Journal of Heat Transfer

Published Monthly by ASME

VOLUME 132 • NUMBER 6 • JUNE 2010

RESEARCH PAPERS

Combustion and Reactive Flows

Conduction

Evaporation, Boiling, and Condensation

Forced Convection

Heat Exchangers

Melting and Solidification

(Contents continued on inside back cover)

This journal is printed on acid-free paper, which exceeds the ANSI Z39.48-1992 specification for permanence of paper and library materials. ♾™
♻ 85% recycled content, including 10% post-consumer fibers.

Editor, **YOGESH JALURIA (2010)**
Assistant to the Editor, **S. PATEL**

Associate Editors
Yutaka Asako, Tokyo Metropolitan University, Japan (2010)
Cho Lik Chan, The University of Arizona (2010)
Louis C. Chow, University of Central Florida (2010)
Frank J. Cunha, Pratt & Whitney (2011)
Ali Ebadian, Florida International Univ. (2011)
Ofodike A. Ezekoye, Univ. of Texas-Austin (2011)
Srinivas Garimella, Georgia Institute Technology (2012)
Kenneth Goodson, Stanford University (2012)
Satish G. Kandlikar, Rochester Inst. of Tech. (2010)
Sung Jin Kim, KAIST, Korea (2010)
Giulio Lorenzini, University of Bologna (2012)
Jayathi Y. Murthy, Perdue University (2010)
Pamela M. Norris, Univ. of Virginia (2011)
Patrick H. Oosthuizen, Queens University, Canada (2012)
Patrick E. Phelan, National Science Foundation (2011)
Roger R. Schmidt, IBM Corporation (2010)
S. A. Sherif, University of Florida (2010)
Heping Tan, Harbin Institute of Technology (2011)
Wen Q. Tao, Xi'an University, China (2012)
Wei Tong, Danaher Corporation (2012)
Robert Tzou, University of Missouri-Columbia (2012)
Peter Vadasz, Northern Arizona University (2010)
Walter W. Yuen, Univ. of California–Santa Barbara (2011)

Past Editors
V. DHIR
J. R. HOWELL
R. VISKANTA
G. M. FAETH
K. T. YANG
E. M. SPARROW

HEAT TRANSFER DIVISION
Chair, **V. CAREY**
Vice Chair, **L. GRITZO**
Past Chair, **CHANG OH**

PUBLICATIONS COMMITTEE
Chair, **BAHRAM RAVANI**

OFFICERS OF THE ASME
President,
AMOS E. HOLT
Executive Director,
THOMAS G. LOUGHLIN
Treasurer,
WILBUR MARNER

PUBLISHING STAFF

Managing Director, Publishing
PHILIP DI VIETRO

Manager, Journals
COLIN McATEER

Production Coordinator
JUDITH SIERANT

Transactions of the ASME, Journal of Heat Transfer (ISSN 0022-1481) is published monthly by The American Society of Mechanical Engineers, Three Park Avenue, New York, NY 10016. Periodicals postage paid at New York, NY and additional mailing offices. POSTMASTER: Send address changes to Transactions of the ASME, Journal of Heat Transfer, c/o THE AMERICAN SOCIETY OF MECHANICAL ENGINEERS, 22 Law Drive, Box 2300, Fairfield, NJ 07007-2300. **CHANGES OF ADDRESS** must be received at Society headquarters seven weeks before they are to be effective. Please send old label and new address.

STATEMENT from By-Laws. The Society shall not be responsible for statements or opinions advanced in papers or ... printed in its publications (B7.1, Para. 3).

COPYRIGHT © 2010 by The American Society of Mechanical Engineers. For authorization to photocopy material for internal or personal use under those circumstances not falling within the fair use provisions of the Copyright Act, contact the Copyright Clearance Center (CCC), 222 Rosewood Drive, Danvers, MA 01923, tel: 978-750-8400, www.copyright.com. Request for special permission or bulk copying should be addressed to Reprints/Permission Department.

Canadian Goods & Services Tax Registration #126148048

Downloaded 05 Feb 2011 to 141.219.44.39. Redistribution subject to ASME license or copyright; see http://www.asme.org/terms/Terms_Use.cfm

(**Contents continued**)

Journal of Heat Transfer **Volume 132, Number 6** **JUNE 2010**

Micro/Nanoscale Heat Transfer

Natural and Mixed Convection

Thermal Systems

TECHNICAL BRIEFS

The ASME Journal of Heat Transfer is abstracted and indexed in the following:

Applied Science and Technology Index, Chemical Abstracts, Chemical Engineering and Biotechnology Abstracts (Electronic equivalent of Process and Chemical Engineering), Civil Engineering Abstracts, Compendex (The electronic equivalent of Engineering Index), Corrosion Abstracts, Current Contents, E & P Health, Safety, and Environment, Ei EncompassLit, Engineered Materials Abstracts, Engineering Index, Enviroline (The electronic equivalent of Environment Abstracts), Environment Abstracts, Environmental Engineering Abstracts, Environmental Science and Pollution Management, Fluidex, Fuel and Energy Abstracts, Index to Scientific Reviews, INSPEC, International Building Services Abstracts, Mechanical & Transportation Engineering Abstracts, Mechanical Engineering Abstracts, METADEX (The electronic equivalent of Metals Abstracts and Alloys Index), Petroleum Abstracts, Process and Chemical Engineering, Referativnyi Zhurnal, Science Citation Index, SciSearch (The electronic equivalent of Science Citation Index), Theoretical Chemical Engineering

Sophia Haussener
Department of Mechanical and Process Engineering,
ETH Zurich,
8092 Zurich, Switzerland

Wojciech Lipiński
Department of Mechanical Engineering,
University of Minnesota,
Minneapolis, MN 55455

Peter Wyss
Department of Electronics/Metrology,
EMPA Material Science and Technology,
Überlandstrasse 129,
8600 Dübendorf, Switzerland

Aldo Steinfeld[1]
Department of Mechanical and Process Engineering,
ETH Zurich,
8092 Zurich, Switzerland
and
Solar Technology Laboratory,
Paul Scherrer Institute,
5232 Villigen, Switzerland
e-mail: aldo.steinfeld@ethz.ch

Tomography-Based Analysis of Radiative Transfer in Reacting Packed Beds Undergoing a Solid-Gas Thermochemical Transformation

A reacting packed-bed undergoing a high-temperature thermochemical solid-gas transformation is considered. The steam- and dry-gasification of carbonaceous materials to syngas is selected as the model reaction. The exact 3D digital geometrical representation of the packed-bed is obtained by computer tomography and used in direct pore-level simulations to characterize its morphological and radiative transport properties as a function of the reaction extent. Two-point correlation functions and mathematical morphology operations are applied to calculate porosities, specific surfaces, particle-size distributions, and representative elementary volumes. The collision-based Monte Carlo method is applied to determine the probability distribution of attenuation path length and direction of incidence at the solid-fluid boundary, which are linked to the extinction coefficient, scattering phase function, and scattering albedo. These effective properties can be then incorporated in continuum models of the reacting packed-bed.
[DOI: 10.1115/1.4000749]

Keywords: packed-bed, radiation, solar energy, gasification, chemical reactors

1 Introduction

Morphological and effective heat/mass transfer properties of complex porous media are needed for the engineering design, optimization, and scale-up of thermochemical reactors and processes in particular for packed beds. Their complex solid-gas structures can be incorporated in direct pore-level simulations for determining their morphological-dependent effective transport properties for continuum domain. This approach has been successfully applied for the geometrical characterization of packed beds and foams [1–5] and for the determination of the effective radiative heat transfer properties of opaque and semitransparent packed beds [3,6–8] and foams [5,9,10], of the effective conductivity of packed beds and foams [11–14], of convective heat transfer properties [13,15], and of the effective fluid flow properties [15,16] through foams. These pore-level computations allow for more in-depth investigations vis-à-vis classical empirical models for radiative [17,18], conductive [19], convective [20], and fluid flow [19,21,22] properties.

In this study, computer tomography (CT) is employed to obtain the exact 3D digital geometrical representation of a packed-bed of carbonaceous materials undergoing high-temperature gasification. Thus, the numerically calculated effective properties are based on the exact morphology of the reacting packed-bed, which varies with time and process parameters (e.g., temperature, gasifying agent, partial pressure, and feedstock size) as the reaction progresses. These effective properties can then be applied for the accurate derivation of the reaction kinetics and for the design and optimization of packed-bed reactors.

2 Gasification Experiments

A packed-bed of tire shreds is selected as the model reactor. The gasification of this waste carbonaceous material into high-quality synthesis gas (syngas, mainly H_2 and CO, used for power generation in efficient combined-cycles and fuel cells or further processed to Fischer–Tropsch liquid fuels) is investigated in a packed-bed reactor using concentrated solar energy as the source of high-temperature process heat [23]. In this study, a laboratory packed-bed reactor, schematically shown in Fig. 1, is used to conduct the gasification reaction at controlled conditions and to produce sample materials at different reaction extents. These samples are then scanned by tomography. Their BET specific surface area is measured by N_2 adsorption (Micromeritics TriStar 3000) and their particle-size distribution is measured by laser scattering (HORIBA LA-950 analyzer). Outlet gas composition is monitored by mass spectrometry (MS, Pfeiffer Vacuum OmniStar GSD 301 O1) and gas chromatography (GC, Varian CP-4900 Micro GC).

Proximity analysis of the tire shreds indicates 63 wt % volatiles, 29 wt % fixed carbon, 7 wt % ash and 1 wt % moisture. Elemental analysis indicates 82 wt % C, 7 wt % H, 3 wt % O, 2 wt % S, and heavy metal impurities. Energy dispersive X-ray spectrometer analysis shows that the main components in the ash are Si, Zn, and Fe based oxides. Samples are first pyrolyzed to release volatiles. Approximately 3 g of pyrolyzed material is loaded in a 2.6 cm inside diameter quartz tube, rapidly heated by a radiative source, and gasified either by steam or CO_2 diluted by Ar. Once the reaction reaches a desired carbon conversion, the quartz tube is removed from the furnace and rapidly cooled. The partially reacted sample is extracted. The carbon conversion (or reaction extent) is defined by

---

[1] Corresponding author.

Contributed by the Heat Transfer Division of ASME for publication in the JOURNAL OF HEAT TRANSFER. Manuscript received May 15, 2009; final manuscript received October 22, 2009; published online March 25, 2010. Assoc. Editor: Walter W. Yuen.

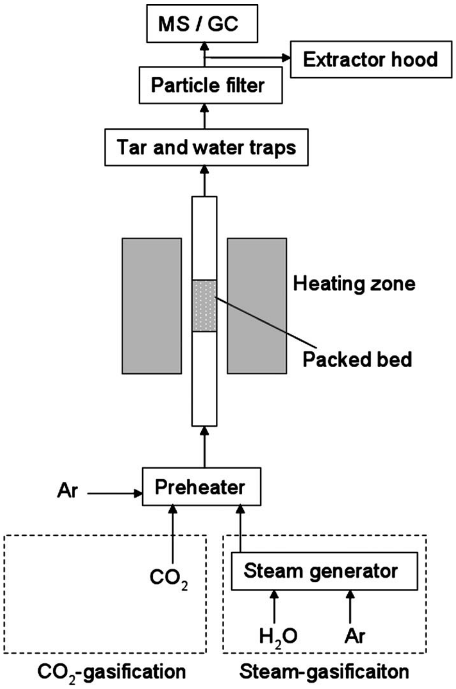

Fig. 1 Schematic of the tubular packed-bed reactor setup used for the gasification of carbonaceous materials

$$X_C = 1 - \frac{n_C}{n_{C,0}} = \frac{\displaystyle\int_0^t \dot{n}_{Ar} x_{Ar}^{-1}(x_{CO_2} + x_{CO} + x_{CH_4})dt}{\displaystyle\int_0^\infty \dot{n}_{Ar} x_{Ar}^{-1}(x_{CO_2} + x_{CO} + x_{CH_4})dt} \qquad (1)$$

The process parameters are listed in Table 1: furnace temperature, type of gasifying agent, partial pressure of gasifying agent, and type of feedstock. Carbon conversions are shown in Fig. 2 as a function of reaction time for the five different experimental runs. Samples at $X_C=0$ (after pyrolysis), 0.3, 0.7, and 1 (ash) obtained in each of the five experiments are selected for the subsequent analysis.

3 Computer Tomography

3.1 CT Scans. Low- and high-resolution computer tomography techniques are employed in this study. Low-resolution tomographic scans of the samples are obtained by exposing them to an unfiltered X-ray beam generated by electrons incident on a wolfram target. The generator is operated at 40–50 keV and a current of 0.2–0.3 mA. A Hamamatsu flat panel C7942 CA-02 protected by a paper filter is used to detect the transmitted X-rays. The samples are scanned at 1800 angles (projections). Each projection consists of an average over six scans at 1.2 s exposure time. The scans are performed for voxel sizes of 10 μm (at $X_C=0, 0.3, 0.7$) and 5 μm (at $X_C=1$). The fields of view investigated are 11.2 $\times$ 11.2 $\times$ 12 mm^3 and 5.6 $\times$ 5.6 $\times$ 6 mm^3, respectively. In addition, high-resolution tomography scans (voxel size of 0.37 μm and field of view 0.76 $\times$ 0.76 $\times$ 0.62 mm^3) are obtained with synchrotron radiation on the TOMCAT beamline at the Swiss Light Source (SLS) [24]. The scans are obtained for 10 keV photon energy, 0.4 mA beam current, 100 μm thick Al filter, 20 times geometrical magnification, 1.5 s exposure time, and 1501 projections. Figure 3 shows tomograms obtained with the low-resolution scans for the reference case sample at $X_C=0$, 0.3, 0.7, and 1 (Fig. 3(*a*)) and with the high-resolution scans for a single particle of the reference case sample at $X_C=0.3$ (Fig. 3(*b*)). The latter scan was performed to examine the amount of pores below 5 μm.

Table 1 Process parameters for the five experimental runs

Case	T (K)	Gasifying agent	p_{ga} (bar)	Feedstock (mm)
Reference	1273	H_2O	0.8	Granular, $d_m=1$
Powder	1273	H_2O	0.8	Powder, $d_m=0.5$
T	1173	H_2O	0.8	Granular, $d_m=1$
Reduced p_{H_2O}	1273	H_2O	0.4	Granular, $d_m=1$
CO_2	1273	CO_2	0.8	Granular, $d_m=1$

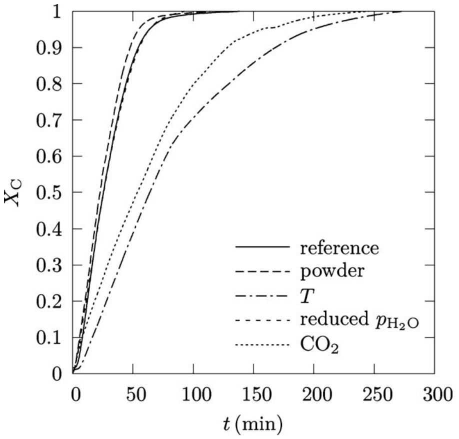

Fig. 2 Carbon extent X_C as a function of reaction time for five different sets of process parameters, as described in Table 1

3.2 Image Processing and Digitalization. The data obtained by tomography consist of 2 byte (0–65535) optical density values, $\alpha(\mathbf{x})$, arranged on a 3D Cartesian grid. The data is digitally improved by brightness and contrast adjustment, and by intensity transformation, obtained via a two-step gamma correction:

$$f_\gamma(\alpha) = \begin{cases} (c^{\gamma_1 - 1}\alpha)^{1/\gamma_1} & \text{for } \alpha < c \\ \left(\dfrac{(2^b-1)^{\gamma_2} - c^{\gamma_2}}{(2^b-1)-c}(\alpha - c) + c^{\gamma_2}\right)^{1/\gamma_2} & \text{for } \alpha \geq c \end{cases} \qquad (2)$$

where b is the number of bits of the image (16), γ_1 and γ_2 are the gamma correction factors, and c denotes the absorption value where the two transformations interchange. For example, for $X_C=0$, $c=0.4(2^b-1)$. When appropriate, median filtering is applied to reduce the noise.

The detailed mathematical methodology to obtain the continuous representation of the optical density values is described in detail elsewhere [9]. A short summary is given here. The discrete values obtained by CT and subsequent image processing are linearly interpolated in three dimensions. The iso-surface describing the phase interface is obtained when the continuous density value equals the threshold value for phase segmentation $\alpha_0(\mathbf{x})$. Due to the highly heterogeneous material containing optically thin carbon-containing compounds and optically thick heavy metal impurities, phase segmentation is complicated. Local multistep threshold segmentation, implemented in MATLAB, is used to allow for more accurate phase detection. A representative rendered 3D geometry is shown in Fig. 4. The pore-space indicator function $\psi(\mathbf{x})$ is defined as

$$\psi(\mathbf{x}) = \begin{cases} 1 & \text{if } \alpha(\mathbf{x}) \geq \alpha_0(\mathbf{x}) \\ 0 & \text{if } \alpha(\mathbf{x}) < \alpha_0(\mathbf{x}) \end{cases} \qquad (3)$$

The distance of a random point in the sample to the phase boundary is found by following a generic ray in small steps (searching for the root). Afterward, the bisection method is used to find the

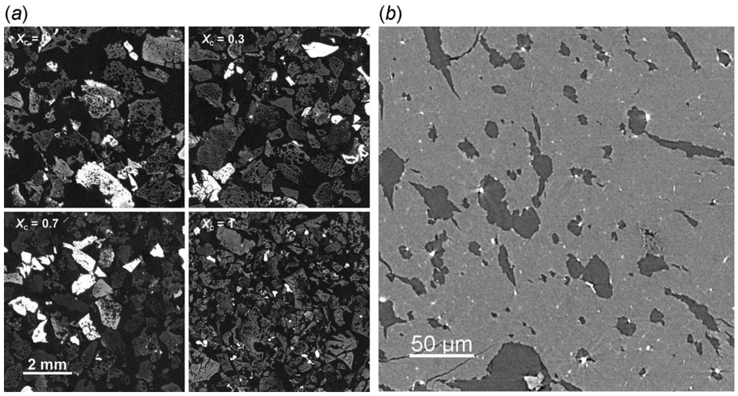

Fig. 3 Tomograms of the reference case sample for: (*a*) scans (voxel size=10 and 5 μm) at $X_C=0$, 0.3, 0.7, and 1, and (*b*) submicron scans (voxel size=0.37 μm) of a particle at $X_C=0.3$

exact value. The normal unit vector at the interface is determined by computing the gradient of the gray values at the specific position.

4 Morphological Characterization

4.1 Experimental. Porosity is determined by weight measurements, assuming the approximate intrinsic density to increase linearly with decreasing carbon content, and is given by $\rho = \rho_{\mathrm{ash}} X_C + \rho_C (1-X_C)$ with $\rho_C = 1700\ \mathrm{kg\ m^{-3}}$ and $\rho_{\mathrm{ash}} = 2500\ \mathrm{kg\ m^{-3}}$. ρ_{tire} of the initial tire shreds (before pyrolysis) is measured by He pycnometry (AccuPyc 1330) to be $1200\ \mathrm{kg\ m^{-3}}$. ε is shown in Fig. 5 as a function of the carbon conversion for the five experimental runs listed in Table 1. The porosity peaks at $X_C=0.55$ as a result of growing pores and break-up of fragile particles [25]. The measured values correspond to a loosely packed-bed of randomly oriented and located non-spherical particles having uniform size and sphericity (fraction of surface area of volume-equivalent sphere to surface area of particle) smaller than 0.25 [26], indicating highly porous particles. The measured porosity is fitted to a second order polynomial function (RMS =0.04).

$$\varepsilon_{\mathrm{ex}}(X_C) = -0.243X_C^2 + 0.269X_C + 0.856 \tag{4}$$

The porosity of the unreacted packed-bed of tire shreds is determined to be $\varepsilon_{\mathrm{ex}} = 0.60 \pm 0.05$, which corresponds to a packed-bed of non-spherical particles of uniform size and with sphericity of 0.55 [26].

The BET specific surface area and the corresponding fraction resulting from nanopores ($d_p < 2$ nm) is shown Fig. 6 as a function of the carbon conversion for the five experimental runs listed in Table 1. Before pyrolysis, BET surface area is $0.6\ \mathrm{m^2\ g^{-1}}$ for the granular and $1.6\ \mathrm{m^2\ g^{-1}}$ for the powder feedstock, and no nanopores are detected. During pyrolysis, it increases to $70\ \mathrm{m^2\ g^{-1}}$ of which a small fraction (~5%) is associated to nanopores. During gasification, the BET specific surface area increases up to $\sim 700\ \mathrm{m^2\ g^{-1}}$ for $X_C=0.7$ and decreases for the residual ash ($X_C=1$), which is consistent with the variation in porosity in Fig. 5. The fraction of nanopores increases and peaks at 60% for $X_C=0.3$. No nanopores are detected in the ash. The different values obtained for H_2O and CO_2 gasifying agents are presumable the result of different mechanisms as CO_2 mainly reacts at the external surface while H_2O diffuses to the particle core [27]. In general, the variation in the reaction temperature, partial pressure, gasifying agent, and particle-size (as described in Table 1) do not significantly affect the morphology of the sample at the same

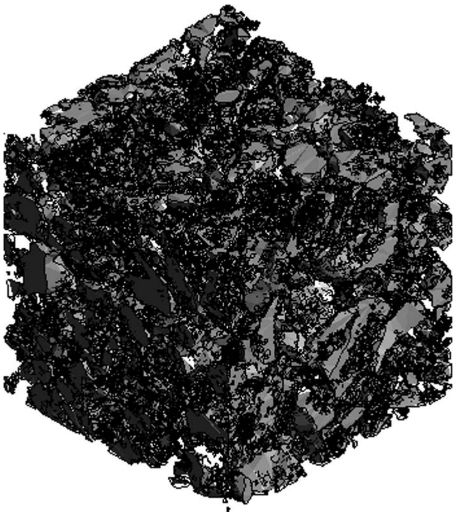

Fig. 4 A 3D rendered geometry of the reference case at $X_C=0$ with cube length of 1.5 cm

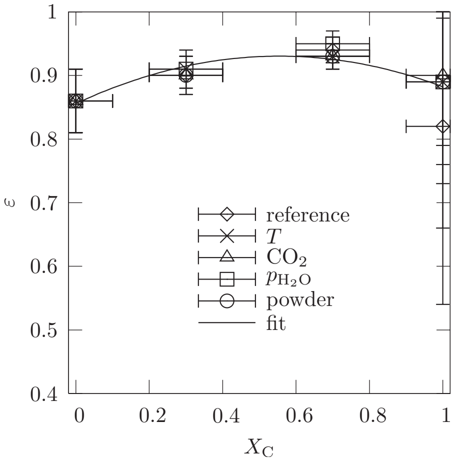

Fig. 5 Experimentally determined porosity for the packed-bed of tire shred as a function of carbon conversion for the five experimental runs listed in Table 1

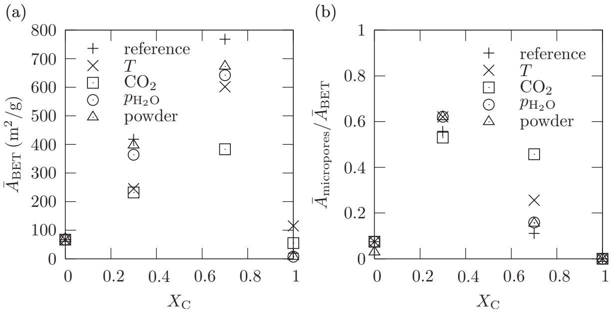

Fig. 6 Experimentally determined specific surface area (*a*) and the corresponding fraction resulting from micropores (*b*) as a function of carbon conversion for the five experimental runs listed in Table 1

carbon conversion.

The experimentally measured particle-size distribution is shown in Fig. 7 for the reference case at $X_\mathrm{C}=0,0.3,0.7,1$. As expected, the main peak shifts to the left as particles shrink, and the small peaks—associated with smaller particles resulting from particle break-up—increase during the reaction. Note that these distributions are qualitative as particles are not spherical.

4.2 Numerical. The two-point correlation function

$$s_2(r)=\frac{\displaystyle\int_V\int_{4\pi}\psi(\mathbf{r})\psi(\mathbf{r}+r\hat{\mathbf{s}})\mathrm{d}\Omega\ \mathrm{d}V}{4\pi V} \tag{5}$$

is applied to calculate the porosity and specific surface area of the sample since $s_2(0)=\varepsilon$ and $\mathrm{d}s/\mathrm{d}r|_{r=0}=-A_0/4$ [1]. The particle-size distribution is calculated by an opening; a morphology operation consisting of an erosion followed by a dilation with the same structuring element [28]. A sphere is used as the structuring element. The determined opening porosity is related to the size distribution by

$$f(d)=\frac{\mathrm{d}}{\mathrm{d}d}\left(1-\frac{\varepsilon_{\mathrm{op}}}{\varepsilon_0}\right) \tag{6}$$

The calculated porosity of the unreacted packed-bed of 0.61 compares well to the experimentally determined one of 0.60 ± 0.05. Figure 8 shows the experimentally measured and numerically calculated porosity as a function of the carbon conversion during gasification for the reference case. The failure in predicting the porosity and its increase with increasing X_C is related to the resolution of the tomographic scans, which is limited by the tomographic setup, the subsequent image processing (especially filtering) and the relative increase in optically thick material, which distorts the tomographic image. The impact of the insufficient scanning resolution and subsequent image processing is roughly calculated to be $(1-\varepsilon)\varepsilon_{\mathrm{sub}}\approx0.1$, where $\varepsilon_{\mathrm{sub}}$ (≈0.2 for $X_\mathrm{C}=0.3$) is the porosity of the particle only detectable by the high-resolution tomography. Nanopores are not detectable but obviously present as indicated by the BET measurements. Calculated specific surface shows an increase up to $X_\mathrm{C}=0.7$ but the experimentally observed decrease for the ash is not elucidated.

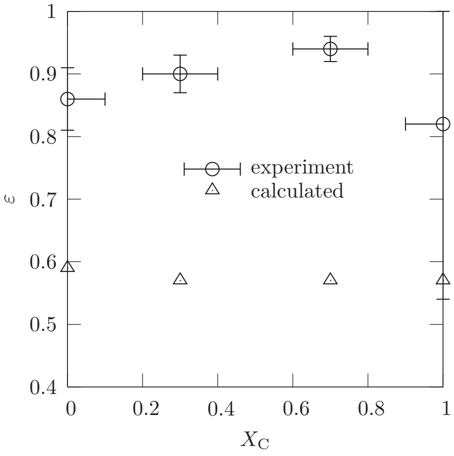

Fig. 8 Experimentally measured and numerically calculated porosity as a function of the carbon conversion for the reference case

The numerically calculated particle-size distributions, shown in Fig. 9 for the reference case at $X_\mathrm{C}=0,0.3,0.7,1$, are based on the largest sphere that fits inside the particle. Therefore, for non-spherical, complex, porous and fractal-like particles, these distributions deviate from those experimentally measured. The calculations are limited by the voxel size of the CT scans ($d_{\mathrm{min}}=4\cdot$voxel size). Since the particle-size distribution is calculated based on the solid phase, the limited resolution of the CT scans leads to an over prediction of the particle-size due to virtual particle agglomeration. The measurements show (see Fig. 7) that the amount of particles in the 10 μm range is small compared with that in the 100 μm range. Therefore the influence of this distortion is assumed negligible on the particle-size distribution in the

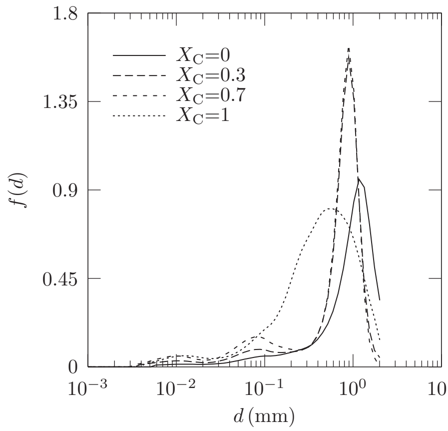

Fig. 7 Experimentally measured size distribution of the particles for the reference case at various carbon conversions $X_\mathrm{C}=0,0.3,0.7,1$

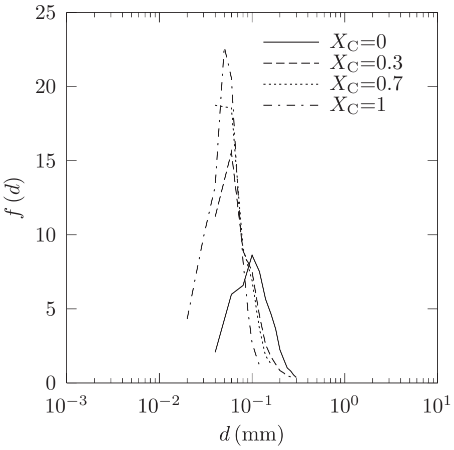

Fig. 9 Numerically calculated particle-size distribution for the reference case at various carbon conversions $X_\mathrm{C}=0,0.3,0.7,1$

range of 60–100 μm. Indeed, an increase in small particles due to shrinkage and breakup of the initial ones during the reaction is observed.

The representative elementary volume (REV)—the smallest volume that can be considered as continuum—is determined by calculating the porosity of a subsequently growing subsample until its variation is within a tolerance band of ±0.05 [3]. The edge length of the REV, l_{REV}, was found to be equal to 5 mm, independent of the process parameters.

5 Radiative Heat Transfer Characterization

The packed-bed of the carbonaceous material is assumed to be opaque for visible and near-infrared radiation, which is the spectral range encountered in the solar-driven reactor [23]. The fluid phase is assumed to be radiatively non-participating. Hence, the variation in the radiative intensity in continuum models is described by a single equation of radiative transfer (RTE) [29,30].

$$\frac{dI_\lambda(s,\hat{\mathbf{s}})}{ds} + \beta_\lambda I_\lambda(s,\hat{\mathbf{s}}) = \kappa_\lambda I_{\lambda,\mathrm{b}}(s,\hat{\mathbf{s}}) + \frac{\sigma_{\mathrm{s},\lambda}}{4\pi}\int_{4\pi} I_\lambda(s,\hat{\mathbf{s}}_{\mathrm{in}})\Phi_\lambda(\hat{\mathbf{s}},\hat{\mathbf{s}}_{\mathrm{in}})d\Omega_{\mathrm{in}} \tag{7}$$

Since the smallest pores or particles detected by CT and consequently employed in the analysis are larger than the voxel sizes of the low-resolution scans, geometric optics can be assumed for radiation wavelengths smaller than 1 μm [17]. Collision-based Monte Carlo (MC) method is applied to compute the cumulative distribution functions of the radiation mean free path $G_{\mathrm{e}}(s)$ and of the cosine of incidence at the solid wall $F_{\mu_{\mathrm{in}}}(\mu_{\mathrm{in}})$ defined as

$$G_{\mathrm{e}}(s) = \int_0^s \frac{1}{N_{\mathrm{r}}}\sum_{j=1}^{N_{\mathrm{r}}} \delta(s' - s_j')ds' \tag{8}$$

$$F_{\mu_{\mathrm{in}}}(\mu_{\mathrm{in}}) = \frac{1}{N_{\mathrm{e}}}\sum_{j=1}^{N_{\mathrm{e}}} \delta(\mu_{\mathrm{in}} - \mu_{\mathrm{in},j}) \tag{9}$$

$G_{\mathrm{e}}(s)$ and $F_{\mu_{\mathrm{in}}}(\mu_{\mathrm{in}})$ are related to β_λ and Φ_λ [2,5,8] by

$$G_{\mathrm{e}}(s) \approx 1 - \exp(-\beta_\lambda s) \tag{10}$$

$$\Phi(\mu_{\mathrm{s}}) = \frac{2\int_{\mu_{\mathrm{in}}=0}^{1}\int_{\varphi_{\mathrm{d}}=0}^{\pi}\int_{\mu_{\mathrm{r}}=0}^{1} \delta\left(\mu_{\mathrm{s}} - \sqrt{(1-\mu_{\mathrm{in}}^2)(1-\mu_{\mathrm{r}}^2)}\cos\varphi_{\mathrm{d}} - \mu_{\mathrm{in}}\mu_{\mathrm{r}}\right)\rho''(\mu_{\mathrm{in}},\mu_{\mathrm{r}},\varphi_{\mathrm{d}})F_{\mu_{\mathrm{in}}}\mu_{\mathrm{r}}d\mu_{\mathrm{r}}d\varphi_{\mathrm{d}}d\mu_{\mathrm{in}}}{\int_{\mu_{\mathrm{in}}=0}^{1}\int_{\varphi_{\mathrm{d}}=0}^{\pi}\int_{\mu_{\mathrm{r}}=0}^{1} \rho''(\mu_{\mathrm{in}},\mu_{\mathrm{r}},\varphi_{\mathrm{d}})F_{\mu_{\mathrm{in}}}\mu_{\mathrm{r}}d\mu_{\mathrm{r}}d\varphi_{\mathrm{d}}d\mu_{\mathrm{in}}} \tag{11}$$

The absorption characteristics of the samples and the contribution of dependent scattering vary with the reaction extent since ash is less absorbing than coal ($\rho_{\mathrm{r,sp,C}}=0.273$, $\rho_{\mathrm{r,d,C}}=0.1$, $\rho_{\mathrm{r,sp,ash}}=0.092$, and $\rho_{\mathrm{r,d,ash}}=0.75$ [31,32]). Gas, packed-sphere, liquid, and modified liquid models are used to estimate the corresponding deviations of the scattering and absorption coefficients from the corresponding values obtained by assuming independent scattering [33]. For a packed-bed with $d_{\mathrm{m}}=0.4$ and 1 mm (d_{m} of particle-size distribution shown in Fig. 7 at $X_{\mathrm{C}}=1$ and 0, respectively), the maximum deviation of the scattering efficiency (appearing at the largest radiation wavelength in our spectral range of interest 1 μm) is 5% and 23% for $\varepsilon_{\mathrm{ex}}=0.88$ and 0.86, respectively, (measured and depicted in Fig. 5 at $X_{\mathrm{C}}=1$ and 0, respectively). Consequently, dependent scattering effects are neglected in the radiative transfer analysis.

The cumulative distribution function of the cosine of incidence at the solid wall and the scattering phase function are computed for two limiting cases: a specular and a diffuse solid-gas interface. For tire shreds, a combination of these two cases is anticipated to be valid. The specular directional-hemispherical reflectivity is calculated using Fresnel's equations for the complex refractive index of the carbon-ash mixture $m=(1-X_{\mathrm{C}})m_{\mathrm{C}}+X_{\mathrm{C}}m_{\mathrm{ash}}$, where m_{C}

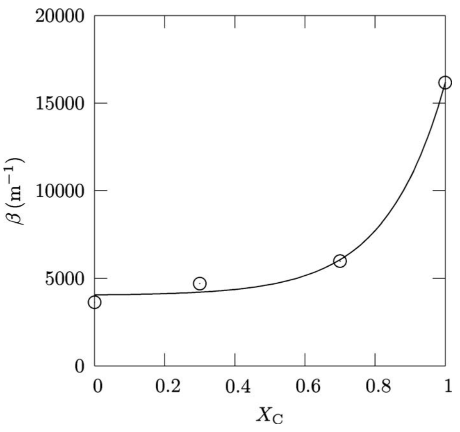

Fig. 10 Extinction coefficient as a function of carbon conversion (markers) and its fit (solid line) given by Eq. (11)

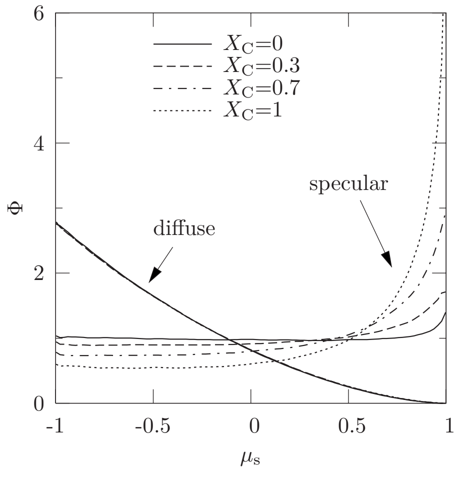

Fig. 11 Scattering phase function for the reference case at various carbon conversions $X_{\mathrm{C}}=0,0.3,0.7,1$ for diffusely and specularly reflecting particles

Table 2 Coefficients of the exponential fit to the scattering phase function for specularly reflecting solid-gas interface as a function of X_C

X_C	A	b	c	RMS
0	0.986	5.031×10^{-7}	13.55	0.017
0.3	0.899	1.415×10^{-2}	4.057	0.001
0.7	0.750	3.622×10^{-2}	4.017	0.009
1	0.614	6.377×10^{-3}	6.697	0.124

$=2.2-1.12i$ is the complex refractive index of carbon and $m_{\mathrm{ash}}=1.5-0.02i$ is the complex refractive index of ash [17,34]. Note that the cumulative distribution function of radiation mean free path, and consequently, the extinction coefficient are independent of the interface reflection type in the geometrical optics range.

The extinction coefficient β and scattering phase function Φ are shown in Figs. 10 and 11, respectively, for the reference case at $X_C=0, 0.3, 0.7, 1$. β increases with X_C as particles shrink and shorten the attenuation path length. An empirical correlation of the extinction coefficient inversely proportional to the characteristic diameter supports this trend [18]. The extinction coefficient is fitted to an exponential function ($\mathrm{RMS}/\beta_{X_C=0}=0.09$):

$$\beta_{\mathrm{MC}}(X_C) = 4024 + 32.14 \exp(5.93X_C) \tag{12}$$

The scattering phase function is independent of the reaction extent for the assumed diffusely reflecting interface. This result is consistent with the small differences obtained between the phase functions for diffuse reflecting identical overlapping transparent spheres and for diffuse reflecting identical overlapping opaque spheres [3,6,9], although largely differing in morphology. Φ is described by a second order polynomial function (RMS=0.01).

$$\Phi_d = 0.565\mu_s^2 - 1.394\mu_s + 0.812 \tag{13}$$

In contrast, the scattering phase function for specularly reflecting particles exhibits a large forward scattering peak. This peak is enhanced with increasing X_C due to the decrease in the real part of the refractive index of the carbon-ash particle. The coefficients of the exponential fit, described by Eq. (14), are listed in Table 2.

$$\Phi_{\mathrm{sp}} = a + b \exp(c\mu_s) \tag{14}$$

The scattering albedo (σ_s/β) can be approximately calculated as

$$\frac{\sigma_s}{\beta} = (1 - X_C)\rho_{r,C} + X_C\rho_{r,\mathrm{ash}} \tag{15}$$

For the specular solid-gas interface, $\sigma_s/\beta=0.273$ and 0.092 at $X_C=0$ and 1, respectively. For the diffuse solid-gas interface $\sigma_s/\beta=0.1$ and 0.75, respectively, [31,32].

6 Conclusions

CT-based computational techniques were used to characterize the morphology (porosity, specific surface, particle-size distribution, and the REV for continuum domain) and the effective radiative heat transfer properties (extinction coefficient, scattering phase function, albedo) of a packed-bed undergoing a thermochemical reaction. The study was performed for the gasification of carbonaceous waste materials (tire shreds) to produce high-quality syngas. The variation in the morphology of the packed-bed was investigated at discrete carbon conversion steps (X_C=0, 0.3, 0.7, and 1) and for different process parameters (feedstock size, furnace temperature, gasifying agent, and partial pressure of gasifying agent). The CT scans were digitally improved to allow for more accurate phase segmentation. Numerical calculated and experimentally measured porosity (by weight), BET surface (by N_2-adsorption), and particle-size distribution (by laser scattering) were compared. Discrepancies were due to limitations in the CT scan resolutions and to image distortions around optically thick heavy metal impurities. The morphological results can be used for the determination of structural parameters [25] needed in kinetic models. The extinction coefficient increased as particles shrank and shortened the attenuation path length. For diffuse reflecting particles, the scattering phase function was found to be independent of the reaction extent. For specularly reflecting particles, the scattering phase function exhibited a strong forward peak and dependency on the refractive index and therefore X_C.

Further studies are directed to the determination of the effective properties for conduction heat transfer (thermal conductivity), convection heat transfer (interfacial heat transfer coefficient), and for fluid flow (permeability and Dupuit–Forchheimer coefficient).

Acknowledgment

This work has been financially supported by the Swiss National Science Foundation under Contract No. 200021-115888 and by the European Commission under Contract No. 212470 (Project HYCYCLES). We thank J. Gaabab for the technical support with the gasification experimental runs and F. Marone for the technical support at SLS.

Nomenclature

A_0 = specific surface, m^{-1}
b = bit number of image
c = constant, indicating gamma correction regime change
d = particle diameter, m
F = probability density function
f = size distribution function, m^{-1}
f_γ = two-step gamma correction function
G_e = cumulative distribution function of extinction length
I = radiative intensity, W m^{-3} sr^{-1}
m = complex refractive index
N_r = number of rays
N_e = number of extincted rays
n = number of moles
$\dot{n}$ = molar flow rate
p = (partial) pressure, bar
r = distance between two points in the sample, m
$\mathbf{r}$ = position vector for spatial coordinates in the sample
s = path length, m
s_2 = two-point correlation function
$\hat{\mathbf{s}}$ = unit vector of path direction
T = temperature, K
t = time, s
V = total sample volume, m^3
X_C = carbon conversion
x = molar fraction
$\mathbf{x}$ = spatial location vector, m

Greek

α = density value of tomographic scans
α_0 = threshold density value for phase segmentation
β = extinction coefficient, m^{-1}
δ = Dirac delta function
ε = porosity
γ_i = gamma constant
κ = absorption coefficient, m^{-1}
λ = radiation wavelength, m
μ = directional cosine
ρ = intrinsic density, kg m^{-3}
ρ_r = hemispherical reflectance
σ_s = scattering coefficient, m^{-1}
φ_d = difference between azimutal angle of incidence and reflection, rad
Φ = scattering phase function

ψ = pore-space indicator function
Ω = solid angle, sr

Subscripts

b = blackbody
C = carbon
d = diffuse
ex = experimental
ga = gasifying agent
in = incidence
m = mean
min = minimal
op = opening
r = reflection
s = scattering
sp = specular
sub = submicron
0 = initial

References

[1] Berryman, J., and Blair, S., 1986, “Use of Digital Image Analysis to Estimate Fluid Permeability of Porous Material: Application of Two-Point Correlation Functions,” J. Appl. Phys., **60**, pp. 1930–1938.

[2] Rintoul, M. D., Torquato, S., Yeong, C., Keane, D. T., Erramilli, S., Jun, Y. N., Dabbs, D. M., and Aksay, I. A., 1996, “Structure and Transport Properties of Porous Magnetic Gel via X-Ray Microtomography,” Phys. Rev. E, **54**, pp. 2663–2669.

[3] Haussener, S., Lipiński, W., Petrasch, J., Wyss, P., and Steinfeld, A., 2009, “Tomographic Characterization of a Semitransparent-Particle Packed Bed and Determination of its Thermal Radiative Properties,” ASME J. Heat Transfer, **131**, p. 072701.

[4] Petrasch, J., Wyss, P., Stämpfli, R., and Steinfeld, A., 2008, “Tomography-Based Multiscale Analyses of the 3D Geometrical Morphology of Reticulated Porous Ceramics,” J. Am. Ceram. Soc., **91**, pp. 2659–2665.

[5] Haussener, S., Coray, P., Lipiński, W., Wyss, P., and Steinfeld, A., 2010, “Tomography-Based Heat and Mass Transfer Characterization of Reticulate Porous Ceramics for High-Temperature Processing,” ASME J. Heat Transfer, **132**, p. 023305.

[6] Tancrez, M., and Taine, J., 2004, “Direct Identification of Absorption and Scattering Coefficients and Phase Function of a Porous Medium by a Monte Carlo Technique,” Int. J. Heat Mass Transfer, **47**, pp. 373–383.

[7] Coquard, R., and Baillis, D., 2004, “Radiative Characteristics of Opaque Spherical Particle Beds: A New Method of Prediction,” J. Thermophys. Heat Transfer, **18**, pp. 178–186.

[8] Coquard, R., and Baillis, D., 2005, “Radiative Characteristics of Beds of Spheres Containing an Absorbing and Scattering Medium,” J. Thermophys. Heat Transfer, **19**, pp. 226–234.

[9] Petrasch, J., Wyss, P., and Steinfeld, A., 2007, “Tomography-Based Monte Carlo Determination of Radiative Properties of Reticulate Porous Ceramics,” J. Quant. Spectrosc. Radiat. Transf., **105**, pp. 180–197.

[10] Zeghondy, B., Iacona, E., and Taine, J., 2006, “Determination of the Anisotropic Radiative Properties of a Porous Material by Radiative Distribution Function Identification (RDFI),” Int. J. Heat Mass Transfer, **49**, pp. 2810–2819.

[11] Logtenberg, S., and Dixon, A. G., 1998, “Computational Fluid Dynamics Studies of Fixed Bed Heat Transfer,” Chem. Eng. Process., **37**, pp. 7–21.

[12] Huai, X., Wang, W., and Li, Z., 2007, “Analysis of the Effective Thermal Conductivity of Fractal Porous Media,” Appl. Therm. Eng., **27**, pp. 2815–2821.

[13] Krishnan, S., Murthy, J. Y., and Garimella, S. V., 2006, “Direct Simulation of Transport in Open-Cell Metal Foam,” ASME J. Heat Transfer, **128**, pp. 793–799.

[14] Petrasch, J., Schrader, B., Wyss, P., and Steinfeld, A., 2008, “Tomography-Based Determination of the Effective Thermal Conductivity of Fluid-Saturated Reticulate Porous Ceramics,” ASME J. Heat Transfer, **130**, p. 032602.

[15] Petrasch, J., Meier, F., Friess, H., and Steinfeld, A., 2008, “Tomography Based Determination of Permeability, Dupuit–Forchheimer Coefficient, and Interfacial Heat Transfer Coefficient in Reticulate Porous Ceramics,” Int. J. Heat Fluid Flow, **29**, pp. 315–326.

[16] Boomsma, K., Poulikakos, D., and Ventikos, Y., 2003, “Simulations of Flow Through Open Cell Metal Foams Using an Idealized Periodic Cell Structure,” Int. J. Heat Fluid Flow, **24**, pp. 825–834.

[17] Modest, M., 2003, *Radiative Heat Transfer*, 2nd ed., Academic, San Diego, CA.

[18] Hendricks, T. J., and Howell, J. R., 1996, “Absorption/Scattering Coefficients and Scattering Phase Functions in Reticulated Porous Ceramics,” ASME J. Heat Transfer, **118**, pp. 79–87.

[19] Kaviany, M., 1995, *Principles of Heat Transfer in Porous Media*, Springer-Verlag, New York.

[20] Incropera, F., and DeWitt, D., 2002, *Fundamentals of Heat and Mass Transfer*, Wiley, New York.

[21] Dullien, F., 1979, *Porous Media Fluid Transport and Pore Structure*, Academic, New York.

[22] Macdonald, I. F., El-Sayed, M. S., Mow, K., and Dullien, F. A. L., 1979, “Flow Through Porous Media—The Ergun Equation Revisited,” Ind. Eng. Chem. Fundam., **18**, pp. 199–208.

[23] Piatkowski, N., Wieckert, C., and Steinfeld, A., 2009, “Experimental Investigation of a Packed-Bed Solar Reactor for the Steam-Gasification of Carbonaceous Feedstocks,” Fuel Process. Technol., **90**, pp. 360–366.

[24] Streun, A., Böge, A., Dehler, M., Gough, C., Joho, W., Korhonen, T., Lüdeke, A., Marchand, P., Muñoz, M., Pedrozzi, M., Rivkin, L., Schilcher, T., Schlott, V., Schulz, L., and Wrulich, A., 2001, “Commissioning of the Swiss Light Source,” *Proceedings of the 2001 Particle Accelerator Conference*, P. Lucas, and S. Webber, eds., IEEE, Piscataway, NJ, pp. 224–226.

[25] Lu, G. Q., and Do, D. D., 1994, “Comparison of Structural Models for High-Ash Char Gasification,” Carbon, **32**, pp. 247–263.

[26] 2003, *Handbook of Fluidization and Fluid-Particle Systems*, W. C. Yang, ed., Marcel Dekker, New York.

[27] Czechowski, F., and Kidawa, H., 1991, “Reactivity and Susceptibility to Porosity Development of Coal Maceral Chars on Steam and Carbon Dioxide Gasification,” Fuel Process. Technol., **29**, pp. 57–73.

[28] Vogel, H., and Roth, H., 2001, “Quantitative Morphology and Network Representation of Soil Pore Structure,” Adv. Water Resour., **24**, pp. 233–242.

[29] Lipiński, W., Petrasch, J., and Haussener, S., 2010, “Application of the Spatial Averaging Theorem to Radiative Heat Transfer in Two-Phase Media,” J. Quant. Spectrosc. Radiat. Transf., **111**, pp. 253–258.

[30] Gusarov, A. V., 2008, “Homogenization of Radiation Transfer in Two-Phase Media With Irregular Phase Boundaries,” Phys. Rev. B, **77**, p. 144201.

[31] Touloukian, Y., Powell, R., Ho, C., and Klemens, P., 1970, *Thermophysical Properties of Matter*, IFI/Plenum, New York.

[32] Jones, M. T., Sparks, R. S., and Valdes, P. J., 2007, “The Climatic Impact of Supervolcanic Ash Blankets,” Clim. Dyn., **29**, pp. 553–564.

[33] Tien, C. L., and Drolen, B. L., 1987, “Thermal Radiation in Particulate Media With Dependent and Independent Scattering,” Annu. Rev. Numer. Fluid Mech. Heat Transfer, **1**, pp. 1–32.

[34] Ruan, L. M., Qi, H., An, W., and Tan, H. P., 2007, “Inverse Radiation Problem for Determination of Optical Constants of Fly-Ash Particles,” Int. J. Thermophys., **28**, pp. 1322–1341.

Simultaneous Measurement of Three-Dimensional Soot Temperature and Volume Fraction Fields in Axisymmetric or Asymmetric Small Unconfined Flames With CCD Cameras

D. Liu
e-mail: liudong@zju.edu.cn

Q. X. Huang

F. Wang

Y. Chi

K. F. Cen

J. H. Yan[1]
e-mail: yanjh@zju.edu.cn

State Key Laboratory of Clean Energy Utilization,
Zhejiang University,
Hangzhou 310027, People's Republic of China

A nonintrusive measurement technique is presented numerically for simultaneous measurement of three-dimensional (3D) soot temperature and volume fraction fields in the axisymmetric or asymmetric flames with charge-coupled device (CCD) cameras. CCD cameras were introduced to capture the flame images for obtaining the line-of-sight radiation intensities. The distributions of local emission source under two wavelengths can be deduced through solving the reconstruction matrix equation by the least-square QR decomposition method from the knowledge of the line-of-sight radiation intensities of the flames. The two-color distributions of the local emission source were used to retrieve the soot temperature and volume fraction distributions. The effects of the discrete ray number of CCD cameras, the number of CCD cameras, and the system signal-to-noise ratio (SNR) on the measurement were investigated. The results show that for accurate measurement of soot volume fraction field, the CCD cameras number should not be less than four and the system SNR can be as low as 54 dB. The proposed technique can be capable for reconstructing the 3D soot temperature and volume fraction fields in both axisymmetric and asymmetric flames well. [DOI: 10.1115/1.4000752]

Keywords: soot temperature, soot volume fraction, axisymmetric flame, asymmetric flame, CCD camera

1 Introduction

Measurements of soot temperature and volume fraction distributions are of practical importance for the studies of the soot formation and radiative heat transfer analyses in the combustion system. In recent years optical soot diagnostic techniques were developed fast and intensively due to their nonintrusive advantages. Hall and Bonczyk [1] investigated emission-absorption tomography for a sooting flame temperature measurement. Greenberg and Ku developed a technique for the measurement of soot volume fractions by laser light-extinction measurements, in which a two-dimensional (2D) array of data was acquired simultaneously [2], and also applied this technique to the soot volume fraction measurement for normal and reduced gravity laminar acetylene jet diffusion flames [3]. De Iuliis et al. [4] used the multiwavelength emission technique for the measurement of soot volume fraction and temperature in an ethylene diffusion flame, and Cignoli et al. [5] developed the 2D two-wavelength emission technique for soot diagnostics. Recently, De Iuliis et al. [6] applied the two-color laser-induced incandescence (2C-LII) technique to the 2D soot volume fraction imaging in an ethylene diffusion flame. Snelling et al. conducted the 2D attenuation measurements for soot volume fraction [7] and developed a multiwavelength flame emission technique for high spatial resolution measurement of soot temperature and soot volume fraction in axisymmetric laminar diffusion flames [8]. Thomson et al. used the spectral soot emission and line-of-sight attenuation measurements for the radially resolved measurements of soot volume fraction and soot temperature at pressures from 0.5 MPa to 4.0 MPa [9] and extended to the technique of diffuse-light 2D line-of-sight attenuation, which can achieve very high levels of sensitivity in transmissivity measurements [10]. Xu and Lee [11] developed and tested a forward-illumination light-extinction soot volume fraction measurement technique.

Many inverse analyses for soot diagnostics were also reported. Liu et al. [12,13] utilized the outgoing monochromatic emission and transmission radiation intensities to reconstruct temperature and absorption coefficient profiles for an axisymmetric free flame by the inverse analyses, used an iteration method to reconstruct the time-averaged temperature distribution in turbulent axisymmetric sooting free flame by the multiwavelength measured data of low time-resolution [14], and also extended an iteration method to analyze the influences of the turbulent fluctuation on the reconstruction of Reynolds time-averaged temperature in turbulent axisymmetric free flames [15]. Ai and Zhou [16] developed a three-color emission method for the simultaneous estimation of temperature and soot volume fraction distributions in these flames. Ayrancı et al. [17] developed an inversion scheme based on tomographic reconstruction of flame emission spectra for nonintrusive characterization of soot temperature and volume fraction fields within an optically thin axisymmetric flame by extracting characteristic information on soot refractive index from spectral gradients of emission spectra, and then conducted the measurement of line-of-sight emission intensity spectra in the near-

---

[1] Corresponding author.

Contributed by the Heat Transfer Division of ASME for publication in the Journal of Heat Transfer. Manuscript received June 10, 2009; final manuscript received October 15, 2009; published online March 31, 2010. Assoc. Editor: He-Ping Tan.

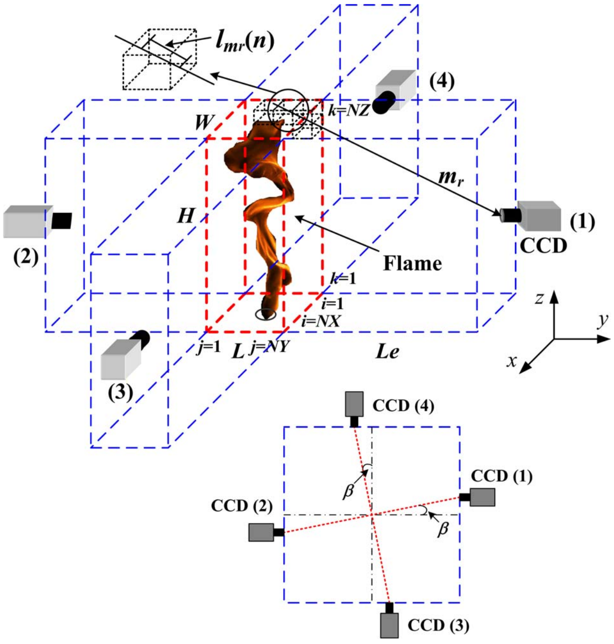

Fig. 1 Reconstruction system

infrared range by Fourier-transform infrared spectrometry to infer soot temperature and volume fraction profiles from an inversion technique [18].

However, all above researches were restricted to the axisymmetric flames and are not applicable for the asymmetric and nonsteady flames. The actual flames are almost asymmetric and nonsteady. Only limited studies have been devoted to the simultaneous measurements of soot temperature and volume fraction distributions in the nonaxisymmetric flames. Liu et al. [19] extended the multiwavelength inversion method to reconstruct the time-averaged temperature distribution in nonaxisymmetric turbulent unconfined sooting flame by the multiwavelength measured data of low time-resolution outgoing emission and transmission radiation intensities. Huang et al. [20] reconstructed soot temperature and volume fraction distributions for the asymmetric diffusive flame using a tomography technique, which was restricted to the reconstructions on the flame cross section from one to another separately, and actual 3D flame imaging of the CCD camera was not considered for the emission measurement technique.

In the present study, the 3D emission measurement technique was developed for the measurements of soot temperature and volume fraction distributions by means of CCD cameras. The 3D pinhole flame imaging of CCD cameras was considered and the 3D soot temperature and volume fraction distributions of the whole flame can be retrieved by solving one reconstruction matrix equation. Both axisymmetric and asymmetric flames were taken into consideration, which allows one to reconstruct the both steady and nonsteady flames.

2 Reconstruction Method

The reconstruction system for both axisymmetric and asymmetric flames was shown in the Fig. 1. Four CCD cameras were used and marked from CCD (1) to CCD (4) were mounted around the flame. The size of the reconstruction area was $W\times L\times H$, and the distance of each CCD camera to the edge of the reconstruction area was L_e. The reconstruction area was divided into the volume elements of $NX\times NY\times NZ$ and the volume elements were numbered from 1 to $N=NX\times NY\times NZ$ by the following sequence (i,j,k): $(1,1,1),(2,1,1),\ldots,(NX,1,1),(1,2,1),\ldots,(NX,NY,1),(1,1,2),\ldots,(NX,NY,NZ)$. The angle between the line connecting the two CCD cameras and the center line of the whole system was β. The discrete ray number M_r in the viewing angle of the CCD camera was assumed.

Following the considerations of the Refs. [17,20], the background radiation, the selfattenuation, and the species scattering were negligible, so the following equation can be obtained for one fixed radiation ray m_r from the flame to the CCD camera

$$\begin{aligned}I_\lambda(m_r)&=\int_0^{s_f}[\kappa_\lambda(s)I_{b,\lambda}(s)]ds=\int_0^{s_f}[H_\lambda(s)]ds\\&=\sum_{n=1}^{N}\kappa_\lambda(n)I_{b,\lambda}(n)l_{m_r}(n)=\sum_{n=1}^{N}H_\lambda(n)l_{m_r}(n),\end{aligned}\tag{1}$$

where $I_\lambda(m_r)$ is the flame monochromatic radiation into CCD camera for the ray m_r, $\kappa_\lambda(s)$ is the local absorption coefficient, $I_{b,\lambda}(s)$ is the local monochromatic blackbody intensity, $H_\lambda(s)$ is the local emission source, $\kappa_\lambda(n)$ is the local absorption coefficient of the volume element n, $I_{b,\lambda}(n)$ is the local monochromatic blackbody intensity of the volume element n, from which temperature $T(n)$ can be obtained by Wien's law, $I_{b,\lambda}(n)=c_1/\{\lambda^5\pi\exp[c_2/(\lambda T_n)]\}$, c_1 and c_2 are the first and second radiation constants, $H_\lambda(n)$ is the local emission source of the volume element n, $H_\lambda(n)=\kappa_\lambda(n)I_{b,\lambda}(n)$, $l_{m_r}(n)$ is the path length of the ray m_r in the volume element n, and N is the total volume element number $N=NX\times NY\times NZ$.

The local absorption coefficient of soot can be represented by Rayleigh approximation as [21]

$$\kappa_\lambda(n)=6\pi f_v(n)E(m)/\lambda=\frac{36\pi nk}{(n^2-k^2+2)^2+4n^2k^2}\frac{f_v}{\lambda}\tag{2}$$

where $f_v(n)$ is the local soot volume fraction of the volume element n, and $E(m)\{\equiv\mathrm{Im}[(m^2-1)/(m^2+2)]\}$ is a function of wavelength dependent soot complex refraction index $m=n-ik$.

n and k were chosen from Ref. [22]

$$n=1.811+0.1263\ln\lambda+0.027\ln^2\lambda+0.0417\ln^3\lambda\tag{3}$$

$$k=0.5821+0.1213\ln\lambda+0.2309\ln^2\lambda-0.01\ln^3\lambda\tag{4}$$

Discrete M_r rays were assumed in 3D directions and M_r equations can be obtained according to Eq. (1)

$$\begin{cases}I_\lambda(1)=\sum_{n=1}^{N}\kappa_\lambda(n)I_{b,\lambda}(n)l_1(n)=\sum_{n=1}^{N}H_\lambda(n)l_1(n)\\ \vdots\qquad\qquad\vdots\qquad\qquad\vdots\\ I_\lambda(m_r)=\sum_{n=1}^{N}\kappa_\lambda(n)I_{b,\lambda}(n)l_{m_r}(n)=\sum_{n=1}^{N}H_\lambda(n)l_{m_r}(n)\\ \vdots\qquad\qquad\vdots\qquad\qquad\vdots\\ I_\lambda(M_r)=\sum_{n=1}^{N}\kappa_\lambda(n)I_{b,\lambda}(n)l_{M_r}(n)=\sum_{n=1}^{N}H_\lambda(n)l_{M_r}(n)\end{cases}\tag{5}$$

Rewrite Eq. (5) to the matrix form

$$\mathbf{I}_\lambda=\mathbf{l}\cdot\mathbf{H}_\lambda\tag{6}$$

where $\mathbf{I}_\lambda$ is the vector of monochromatic intensities received by the CCD camera ($\mathbf{I}_\lambda\in R^{M_r}$), $\mathbf{l}$ is the matrix of the path length in each volume element for each ray ($\mathbf{l}\in R^{Mr\times N}$), and $\mathbf{H}_\lambda$ is the desired local emission source vector ($\mathbf{H}_\lambda\in R^N$).

Equation (6) is a large sparse matrix, and reconstruction problem is an ill-posed problem. The least-square QR (LSQR) decomposition method have been introduced to solve for several inverse problems for temperature field reconstructions by means of CCD cameras and the results were satisfying [20,23–25]. So in the present study, LSQR method was used to solve for Eq. (5).

The linear system of equations is described as

$$\mathbf{A}\boldsymbol{x} = \boldsymbol{b} \quad \mathbf{A} \in R^{m\times n}, \boldsymbol{x} \in R^{n}, \boldsymbol{b} \in R^{m} \tag{7}$$

The LSQR method, which used Lanczos' method [26] for solving least-square (LS) problems

$$\min\|\mathbf{Ax\text{-}b}\|_2 \tag{8}$$

was proposed by Paige and Saunders [27,28] in 1982.

Assuming that k times double diagonalization process have been made and one can obtain $m\times(k+1)$ orthogonal matrix $\mathbf{U_{k+1}}$, $n\times k$ orthogonal matrix $\mathbf{V_k}$, and $(k+1)\times k$ lower double diagonalizations matrix $\mathbf{B_k}$

$$\mathbf{U}_{k+1} = [\boldsymbol{u}_1, \boldsymbol{u}_2, \cdots, \boldsymbol{u}_{k+1}], \mathbf{V}_k = [\boldsymbol{v}_1, \boldsymbol{v}_2, \cdots, \boldsymbol{v}_k]$$

$$\boldsymbol{u}_1, \boldsymbol{u}_2, \cdots, \boldsymbol{u}_{k+1} \in R^{m}, \boldsymbol{v}_1, \boldsymbol{v}_2, \cdots, \boldsymbol{v}_k \in R^{n} \tag{9}$$

$$\mathbf{B}_k = \begin{bmatrix} \alpha_1 & 0 & \cdots & \cdots & 0 \\ \beta_2 & \alpha_2 & \ddots & \cdots & 0 \\ \vdots & \beta_3 & \ddots & \ddots & \vdots \\ \vdots & \vdots & \ddots & \ddots & \vdots \\ \vdots & \vdots & \ddots & \ddots & \alpha_k \\ 0 & \cdots & \cdots & \cdots & \beta_{k+1} \end{bmatrix}_{(k+1)\times k}$$

$$\alpha_1, \alpha_2, \cdots, \alpha_k \in R$$

$$\beta_1, \beta_2, \cdots, \beta_{k+1} \in R \tag{10}$$

The double diagonalization process is described below as

$$\beta_1 = \|\boldsymbol{b}\|_2, \boldsymbol{u}_1 = \boldsymbol{b}/\beta_1, \alpha_1 \boldsymbol{v}_1 = \mathbf{A}^{\mathbf{T}}\boldsymbol{u}_1$$

$$\mathbf{U}_{k+1}(\beta_1 \boldsymbol{e}_1) = \boldsymbol{b}$$

$$\mathbf{AV}_k = \mathbf{U}_{k+1}\mathbf{B}_k$$

$$\mathbf{A}^{\mathbf{T}}\mathbf{U}_{k+1} = \mathbf{V_k}\mathbf{B}_k^{\mathbf{T}} + \alpha_{k+1}\boldsymbol{v}_{k+1}\boldsymbol{e}_{k+1}^{\mathbf{T}} \tag{11}$$

If we define

$$\boldsymbol{x}_k = \mathbf{V}_k \boldsymbol{y}_k \quad \boldsymbol{y}_k \in R^{k}$$

$$\boldsymbol{r}_k = \boldsymbol{b} - \mathbf{A}\boldsymbol{x}_k \tag{12}$$

According to Eqs. (11) and (12), then

$$\begin{aligned} \boldsymbol{r}_k &= \boldsymbol{b} - \mathbf{A}\boldsymbol{x}_k = \mathbf{U}_{k+1}(\beta_1 \boldsymbol{e}_1) - \mathbf{AV}_k\boldsymbol{y}_k = \mathbf{U}_{k+1}(\beta_1 \boldsymbol{e}_1) - \mathbf{U}_{k+1}\mathbf{B}_k\boldsymbol{y}_k \\ &= \mathbf{U}_{k+1}(\beta_1 \boldsymbol{e}_1 - \mathbf{B}_k\boldsymbol{y}_k) \end{aligned} \tag{13}$$

Because $\mathbf{U}_{k+1}$ is an orthogonal matrix and orthogonal transformation does not change the matrix norm, the original Eq. (8) is transformed to

$$\min\|\boldsymbol{r}_k\|_2 = \min\|\beta_1 \boldsymbol{e}_1 - \mathbf{B}_k \boldsymbol{y}_k\|_2 \tag{14}$$

The desired results can be inferred from Eq. (14).

After $\mathbf{H}_\lambda$ under two wavelengths were obtained, the two-color method can be used for the soot temperature and volume fraction computations, that is, for volume element n, the following equation can be obtained:

$$f_1[T(n), f_v(n)] = H_{\lambda 1}(n)$$

$$f_2[T(n), f_v(n)] = H_{\lambda 2}(n) \tag{15}$$

There are two unknown variables and two equations in Eq. (15), so solving this equation can obtain the soot temperature and volume fraction in volume element n.

3 Results and Discussion

The size of the reconstruction system was $W\times L\times H = 7$ mm $\times 7$ mm$\times 36$ mm and $L_e = 0.021$ m. The reconstruction area was divided into the volume elements of $N = NX\times NY\times NZ = 7\times 7 \times 9 = 441$. The viewing angle of each CCD camera was assumed to be about 80 deg. The angle between the line connecting the two CCD cameras and the center line of the whole system was $\beta = 4.67$ deg. The angle β was used to avoid the overlaps of some rays of two CCD cameras face to face. The assumed 3D soot temperature and volume fraction distributions were shown in Fig. 2. The serial numbers $1, 2, \ldots, 441$ of the abscissa is as the following sequence (i, j, k): $(1,1,1), (2,1,1), \ldots, (7,1,1), (1,2,1), (2,2,1), \ldots, (7,7,1), (1,1,2), \ldots, (7,7,9)$, as shown in Fig. 1. The soot temperature and volume fraction distributions on the cross section $k = 5$ of the flame were shown in Fig. 3. Both axisymmetric and asymmetric flames were considered. The two wavelengths used here were 0.7 μm and 0.53 μm.

The measured intensities received by the CCD cameras were simulated by adding random errors of normal distribution with zero average value and mean square deviation σ to the exact intensities, which can be obtained from the direct problem

$$I_{\lambda,\text{measured},j} = (\mu + \sigma\xi)I_{\lambda,j} + I_{\lambda,j} \tag{16}$$

where $I_{\lambda,\text{measured},j}$ is the element of the simulated measured intensity vector, and $I_{\lambda,j}$ is the element of the exact intensity vector, average value μ equals zero, ξ is a random variable of standard normal distribution, and the probability lying in the range of $-2.576 < \xi < 2.576$ is 99%. $j = 1, 2, \ldots, M_r$.

The exact intensities received by the CCD cameras from the direct problem can be computed using assumed soot temperature and volume fraction distributions. For an image sensor-based optical reconstruction system, the three primary broad components of noise are photon, dark, and read noises, all of which are considered in the system signal-to-noise ratio, denoted by *SNR*. *SNR* is defined in terms of the logarithmic decibel scale [20]

$$SNR = 20\log\left(\frac{1}{\left[\frac{1}{M_r}\sum_{j=1}^{M_r}\sigma^2\xi_j^2\right]^{1/2}}\right) \tag{17}$$

The relative errors of the soot temperature and volume fraction in each volume element are defined as

$$E_{T,\text{rel},i} = 100\frac{|T_i^{\text{recon}} - T_i^{\text{exact}}|}{T_i^{\text{exact}}} \tag{18}$$

$$E_{f_v,\text{rel},i} = 100\frac{|f_{vi}^{\text{recon}} - f_{vi}^{\text{exact}}|}{f_{vi}^{\text{exact}}} \tag{19}$$

where T_i^{recon} and f_{vi}^{recon} represent the reconstructed temperature and volume fraction, and T_i^{exact} and f_{vi}^{exact} represent the exact temperature and volume fraction, $i = 1, 2, \ldots, N$.

3.1 Case 1: The Axisymmetric Flame. In this section, the axisymmetric flame was tested and the assumed soot temperature and volume fraction distribution of Figs. 2(*a*) and 2(*b*) were served as the exact ones for validation of the reconstruction method developed in the present study.

3.1.1 The Effects of Different Ray Numbers M_r for Each CCD Camera on the Reconstruction Accuracy. Here, four CCD cameras were used and measurement errors were assumed to be zero. Four different ray numbers M_r (192, 252, 304, and 378) for each CCD camera were used and compared with each other, as shown in Fig. 4.

The condition number of the coefficient matrix **I** in Eq. (6) was first decreased and then increased. Accordingly, the ill-posedness of the inverse reconstruction problem was first alleviated and then became serious. The condition number of the coefficient matrix for ray number 192 was the largest and the ill-posedness of the inverse problem was the most serious, since the ray number was smallest and the radiative information of the flame received by the CCD cameras was the least. When the ray number was increased

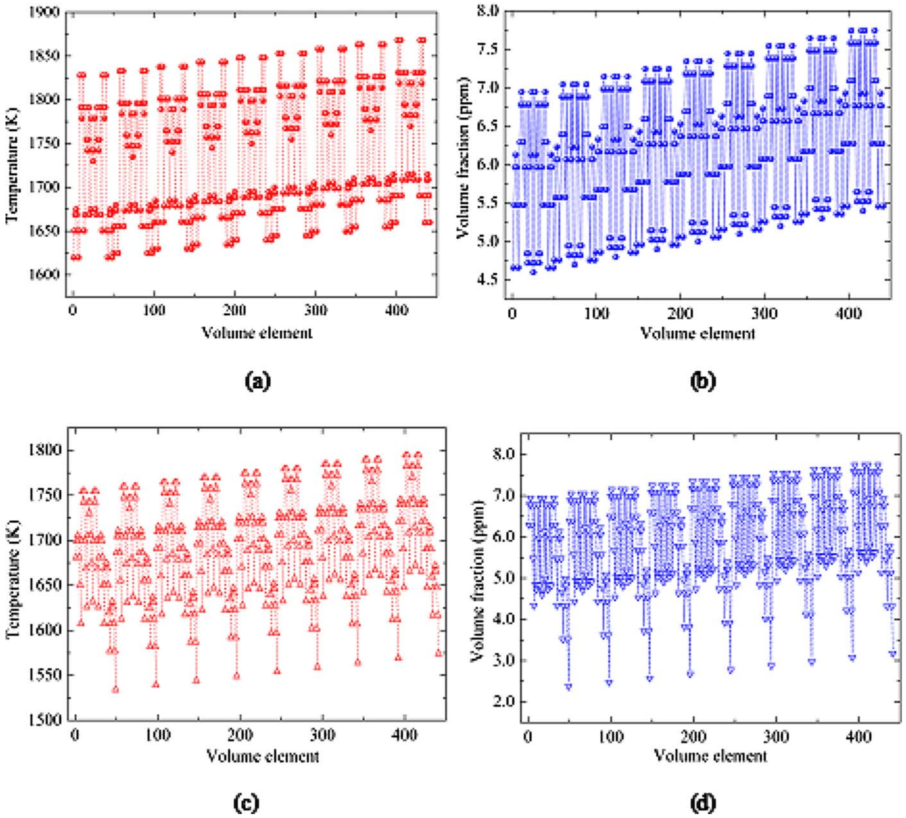

Fig. 2 **Assumed 3D soot temperature and volume fraction distributions: (*a*) axisymmetric temperature distribution; (*b*) axisymmetric volume fraction distribution; (*c*) asymmetric temperature distribution; and (*d*) asymmetric volume fraction distribution**

the condition number was decreased first, because more radiative information of the flame can be obtained by the CCD cameras. But as the ray number was increased to 378, the condition number and ill-posedness were not decreased but increased, since the effect of the increase in the radiative information received by the CCD cameras on the alleviation of the coefficient matrix singularity maybe less compared with the effect of the increase in a large amount of zero elements in the coefficient matrix due to the increase in the rays on the increase in the coefficient matrix singularity.

Among the four kinds of ray numbers, the performance of the ray number 304 was the best. With the ray number of 304, the average relative error of reconstructed temperature distribution was $2.07\times10^{-4}\%$, the average relative error of reconstructed soot volume fraction distribution was 0.0032%, the maximum relative error of reconstructed temperature distribution was $4.56\times10^{-4}\%$, and the maximum relative error of reconstructed soot volume fraction distribution was 0.0067%. It can be found that the simultaneous reconstruction results were very well with ray number 304. The central processing unit (CPU) computing time was about 19 s for ray number 304 on a personal computer with a 2.66 GHz Pentium 4 processor and 1 Gbyte memory. In the later computations, the ray number for each CCD camera was chosen to be 304.

3.1.2 The Effects of Different Combinations of the CCD Cameras on the Reconstruction Accuracy. The measurement errors were assumed to be zero and the ray number was 304 for each CCD camera. Four different combinations of the CCD cameras were tested, that is, CCD (1)(2), CCD (1)(3), CCD (1)(2)(3), and CCD (1)(2)(3)(4), as shown in Fig. 5.

It can be found that when the two CCD cameras were used, the reconstruction results from CCD (1)(3) were better than those from CCD (1)(2), and both of the average relative errors of reconstructed temperature distributions were smaller than 1.7%, but the maximum relative error of reconstructed soot volume fraction was very large, and the reconstructions for soot volume fraction distribution failed. If CCD (1)(2)(3) was used, the average relative error and the maximum relative error of reconstructed temperature distribution were 0.1395% and 2.4291%, respectively. The average relative error of reconstructed soot volume fraction was 1.6480%, but the maximum relative error of that was 16.5673%, which implied that the soot volume fraction distribution also cannot be reconstructed accurately using three CCD cameras. The maximum relative error of the soot volume fraction distribution was only 0.0067% if CCD (1)(2)(3)(4) were used.

Therefore, if only temperature distribution were desired to know, CCD (1)(3) can be used with the maximum relative error of 6.92%, and CCD (1)(2)(3) can also be used for more accurate results with a maximum relative error of 2.42%. If the soot volume fraction distributions were also desired accurately, four CCD cameras should be used, which was the reason why four CCD cameras were used in Sec. 3.1.1.

3.1.3 The Effects of Different Measurement Errors on the Reconstruction Accuracy. Here, four CCD cameras with ray number 304 for each CCD camera were used. Four different measurement errors or *SNR* were assumed, $\sigma=1\times10^{-4}$ (*SNR* is about 80 dB), $\sigma=5\times10^{-4}$ (*SNR* is about 65 dB), $\sigma=1\times10^{-3}$ (*SNR* is about 60 dB), and $\sigma=2\times10^{-3}$ (*SNR* is about 54 dB).

As shown in Fig. 6, due to the random measurement errors used, 20 samples were used to test the stability of the reconstruction method. It was found that for all the four kinds of measurement errors, the temperature reconstruction results were satisfying. When the *SNR* was as low as 54 dB, the maximum relative error and the average relative error of the temperature distribution

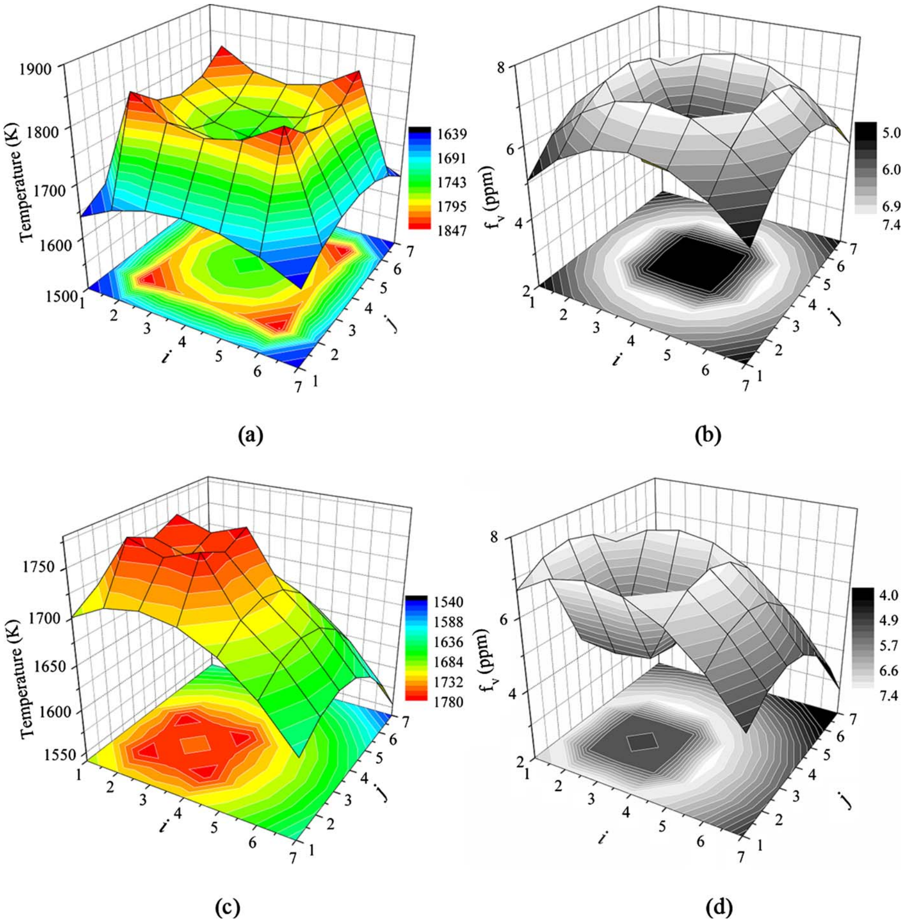

(a)

(b)

(c)

(d)

Fig. 3 Soot temperature and volume fraction distributions on the cross section $k=5$ of the flame: (*a*) axisymmetric temperature distribution; (*b*) axisymmetric volume fraction distribution; (*c*) asymmetric temperature distribution; and (*d*) asymmetric volume fraction distribution

reconstruction were below 1.5% and 0.12% for all 20 samples.

The maximum relative errors of soot volume fraction reconstruction were below 11% for 20 samples when *SNR* was as low as 54 dB. If the *SNR* was decreased further, the soot volume fraction reconstruction can be failed, which implied that if the soot volume fraction distributions were desired to be reconstructed accurately, the system *SNR* should be larger than 54 dB at least. However, in the laboratory, the dynamic range of the camera was about 80 dB at the manufacture settings, and the intensity of a typical flame image pixel was less than 30% of the maximum pixel intensity, so the camera *SNR* was about 69.5 dB. Moreover, if a 4×4 image binning was adopted to render camera noise, the *SNR* can be higher than 93 dB during the experiments [20]. When the *SNR* was about 65 dB, it can be seen that the maximum relative errors of soot volume fraction reconstruction were all below 2.5% for 20 samples and the average relative errors of that

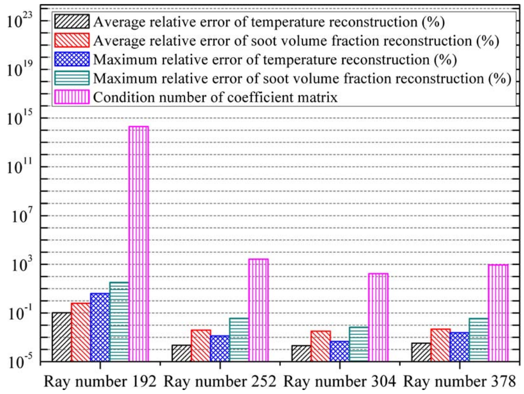

Fig. 4 Effects of different ray numbers on the reconstruction accuracy

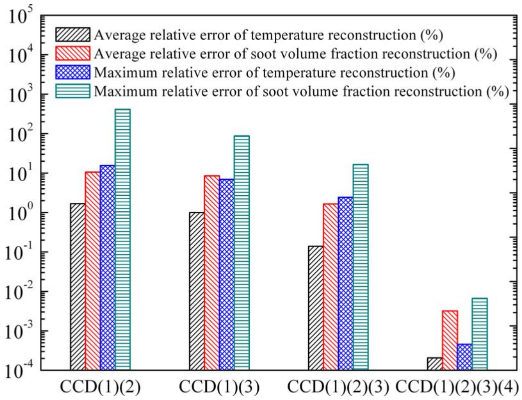

Fig. 5 Effects of different combinations of the CCD cameras on the reconstruction accuracy

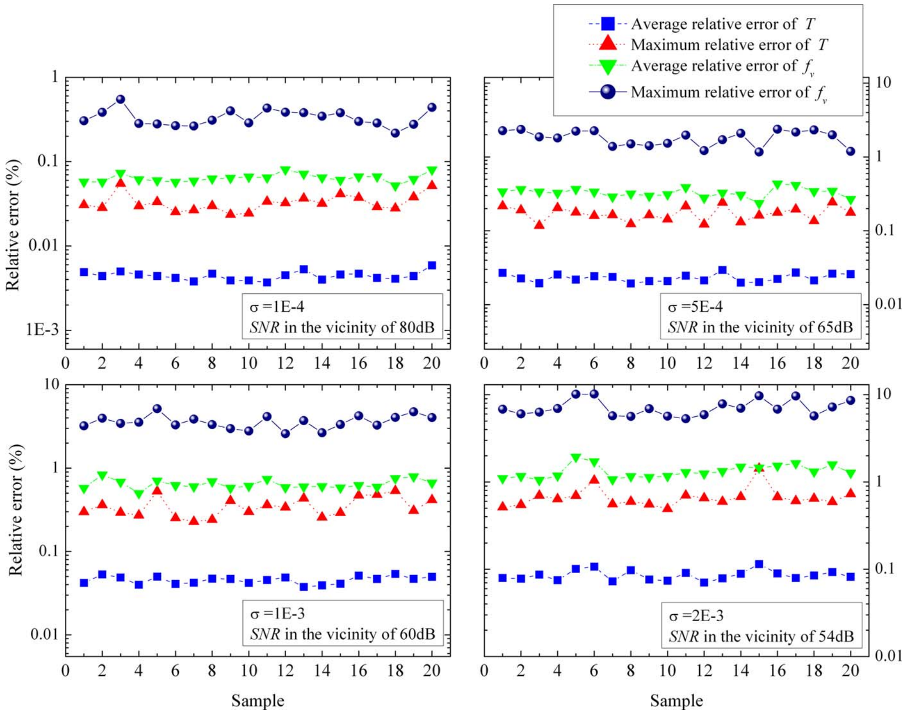

Fig. 6 Effects of measurement errors on the reconstruction accuracy with 20 samples

were only about 0.3%. Therefore, better results than those with *SNR* 65 dB can be expected during the experiments (*SNR* can be higher than 69.5 dB, at least).

Moreover, the effects of the *SNR* on the reconstruction accuracy for the average values of 20 samples were also shown in Fig. 7. It can be found that as the *SNR* increased, all four kinds of average relative errors decreased. When the *SNR* was as low as 54 dB, the average of maximum relative error of the soot volume fraction of 20 samples was about 7.2%.

3.2 Case 2: The Asymmetric Flame. Based on the above discussions of the axisymmetric flame, the reconstruction method was extended to the asymmetric flame, and the assumed soot temperature and volume fraction distribution of Figs. 2(*c*) and 2(*d*) were served as the exact ones for validation of the reconstruction method.

Four different *SNR* values were considered for testing the validity of the reconstruction method for the application of the asymmetric flame. The relative errors of soot temperature and volume fraction in each volume element were shown in Fig. 8. The CPU computing time was about 19 s for each *SNR* on a personal computer with a 2.66 GHz Pentium 4 processor and 1 Gbyte memory.

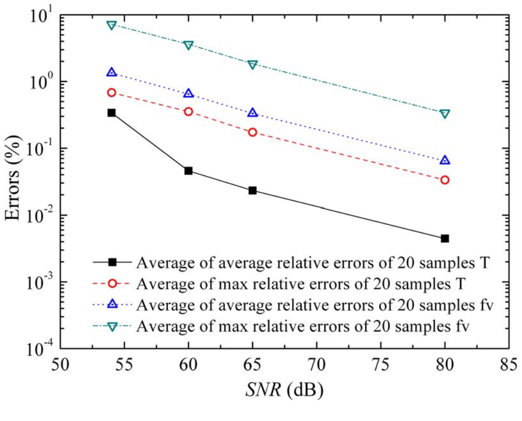

Fig. 7 Effects of ***SNR*** on the reconstruction accuracy

It can be seen that the relative errors of reconstructed temperature in each volume element can be maintained at a low level with four kinds of *SNR*. The maximum of the relative error of temperature reconstruction with $SNR = 53.74$ dB was about 1.07%. Therefore, the temperature reconstructions were satisfying.

The maximum and the average of relative errors of the soot volume fraction was about 7.4% and 1.27% with $SNR = 53.74$ dB, respectively. It implied that the soot volume fraction distribution can be retrieved accurately even when the *SNR* was as low as 53.74 dB, which decreased the requirement of the quality of the CCD cameras for the experiments and also reduced the cost of the devices.

4 Conclusions

All actual flames are almost asymmetric and nonsteady in 3D space. A nonintrusive optical technique was developed for simultaneous measurement of 3D soot temperature and volume fraction distributions in the axisymmetric and asymmetric flames by means of CCD cameras. In the present study, the discrete ray number for each CCD camera in the viewing angle was chosen to be 304 for best reconstruction accuracy. In order to obtain the accurate measurement of soot volume fraction, the CCD cameras number should not be less than four, and the system signal-to-noise ratio can be as low as 54 dB. If only temperature distribution were desired to know, the CCD cameras number can be reduced to be two. Numeral analyses show that the proposed technique can be capable for reconstructing the 3D soot temperature and volume fraction simultaneously in both axisymmetric and asymmetric flames well by means of four CCD cameras.

Acknowledgment

The supports of this study by the National Natural Science Foundation of China (Grant No. 60534030), National Basic Research Program of China (Grant No. 2009CB219802), Zhejiang Provincial Natural Science Foundation of China (Grant No.

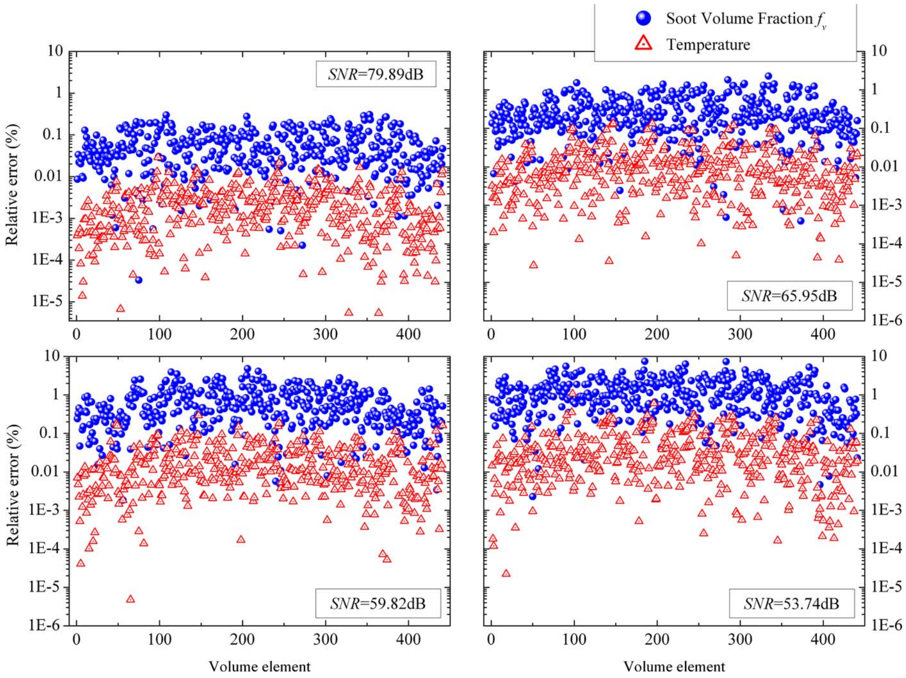

Fig. 8 Relative errors of reconstruction with different measurement errors

Y107387), Program of Introducing Talents of Discipline to University (Grant No. B08026), and the 863 Program (Grant No. 2007AA061302-3) are gratefully acknowledged.

References

[1] Hall, R. J., and Bonczyk, P. A., 1990, "Sooting Flame Thermometry Using Emission/Absorption Tomography," Appl. Opt., **29**, pp. 4590–4598.
[2] Greenberg, P. S., and Ku, J. C., 1997, "Soot Volume Fraction Imaging," Appl. Opt., **36**, pp. 5514–5522.
[3] Greenberg, P. S., and Ku, J. C., 1997, "Soot Volume Fraction Maps for Normal and Reduced Gravity Laminar Acetylene Jet Diffusion Flames," Combust. Flame, **108**, pp. 227–230.
[4] De Iuliis, S., Barbini, M., Benecchi, S., Cignoli, F., and Zizak, G., 1998, "Determination of the Soot Volume Fraction in an Ethylene Diffusion Flame by Multiwavelength Analysis of Soot Radiation," Combust. Flame, **115**, pp. 253–261.
[5] Cignoli, F., De Iuliis, S., Manta, V., and Zizak, G., 2001, "Two-Dimensional Two-Wavelength Emission Technique for Soot Diagnostics," Appl. Opt., **40**, pp. 5370–5378.
[6] De Iuliis, S., Migliorini, F., Cignoli, F., and Zizak, G., 2007, "2D Soot Volume Fraction Imaging in an Ethylene Diffusion Flame by Two-Color Laser-Induced Incandescence (2C-LII) Technique and Comparison With Results From Other Optical Diagnostics," Proc. Combust. Inst., **31**, pp. 869–876.
[7] Snelling, D. R., Thomson, K. A., Smallwood, G. J., and Gülder, Ö. L., 1999, "Two-Dimensional Imaging of Soot Volume Fraction in Laminar Diffusion Flames," Appl. Opt., **38**, pp. 2478–2485.
[8] Snelling, D. R., Thomson, K. A., Smallwood, G. J., Gülder, Ö. L., Weckman, E. J., and Fraser, R. A., 2002, "Spectrally Resolved Measurement of Flame Radiation to Determine Soot Temperature and Concentration," AIAA J., **40**, pp. 1789–1795.
[9] Thomson, K. A., Gülder, Ö. L., Weckman, E. J., Fraser, R. A., Smallwood, G. J., and Snelling, D. R., 2005, "Soot Concentration and Temperature Measurements in Co-annular, Nonpremixed CH4/Air Laminar Flames at Pressures up to 4 MPa," Combust. Flame, **140**, pp. 222–232.
[10] Thomson, K. A., Johnson, M. R., Snelling, D. R., and Smallwood, G. J., 2008, "Diffuse-Light Two-Dimensional Line-of-Sight Attenuation for Soot Concentration Measurements," Appl. Opt., **47**, pp. 694–703.
[11] Xu, Y., and Lee, C. F., 2006, "Forward-Illumination Light-Extinction Technique for Soot Measurement," Appl. Opt., **45**, pp. 2046–2057.
[12] Liu, L. H., Tan, H. P., and Yu, Q. Z., 2000, "Inverse Radiation Problem in Axisymmetric Free Flames," J. Thermophys. Heat Transfer, **14**, pp, 450–452.
[13] Liu, L. H., and Jiang, J., 2001, "Inverse Radiation Problem for Reconstruction of Temperature Profile in Axisymmetric Free Flames," J. Quant. Spectrosc. Radiat. Transf., **70**, pp. 207–215.
[14] Liu, L. H., and Li, B. X., 2002, "Inverse Radiation Problem of Axisymmetric Turbulent Sooting Free Flame," J. Quant. Spectrosc. Radiat. Transf., **75**, pp. 481–491.
[15] Liu, L. H., Tan, H. P., and Li, B. X., 2002, "Influence of Turbulent Fluctuation on Reconstruction of Temperature Profile in Axisymmetric Free Flames," J. Quant. Spectrosc. Radiat. Transf., **73**, pp. 641–648.
[16] Ai, Y. H., and Zhou, H. C., 2005, "Simulation on Simultaneous Estimation of Non-uniform Temperature and Soot Volume Fraction Distributions in Axisymmetric Sooting Flames," J. Quant. Spectrosc. Radiat. Transf., **91**, pp. 11–26.
[17] Ayrancı, I., Vaillon, R., Selçuk, N., André, F., and Escudié, D., 2007, "Determination of Soot Temperature, Volume Fraction and Refractive Index From Flame Emission Spectrometry," J. Quant. Spectrosc. Radiat. Transf., **104**, pp. 266–276.
[18] Ayrancı, I., Vaillon, R., and Selçuk, N., 2008, "Near-Infrared Emission Spectrometry Measurements for Nonintrusive Soot Diagnostics in Flames," J. Quant. Spectrosc. Radiat. Transf., **109**, pp. 349–361.
[19] Liu, L. H., and Man, G. L., 2003, "Reconstruction of Time-Averaged Temperature of Non-Axisymmetric Turbulent Unconfined Sooting Flame by Inverse Radiation Analysis," J. Quant. Spectrosc. Radiat. Transf., **78**, pp. 139–149.
[20] Huang, Q. X., Wang, F., Liu, D., Ma, Z. Y., Yan, J. H., Chi, Y., and Cen, K. F., 2009, "Reconstruction of Soot Temperature and Volume Fraction Profiles of an Asymmetric Flame Using Stereoscopic Tomography," Combust. Flame, **156**, pp. 565–573.
[21] Modest, M. F., 2003, *Radiative Heat Transfer*, 2nd ed., Academic, San Diego, CA.
[22] Chang, H., and Charalampopoulos, T. T., 1990, "Determination of the Wavelength Dependence of Refractive Indices of Flame Soot," Proc. R. Soc. London, Ser. A, **430**, pp. 577–591.
[23] Liu, D., Wang, F., Yan, J. H., Huang, Q. X., Chi, Y., and Cen, K. F., 2008, "Inverse Radiation Problem of Temperature Field in Three-Dimensional Rectangular Enclosure Containing Inhomogeneous, Anisotropically Scattering Media," Int. J. Heat Mass Transfer, **51**, pp. 3434–3441.
[24] Liu, D., Wang, F., Cen, K. F., Yan, J. H., Huang, Q. X., and Chi, Y., 2008, "Noncontact Temperature Measurement by Means of CCD Cameras in a Participating Medium," Opt. Lett., **33**, pp. 422–424.
[25] Wang, F., Liu, D., Cen, K. F., Yan, J. H., Huang, Q. X., and Chi, Y., 2008, "Efficient Inverse Radiation Analysis of Temperature Distribution in Participating Medium Based on Backward Monte Carlo Method," J. Quant. Spectrosc. Radiat. Transf., **109**, pp. 2171–2181.
[26] Lanczons, C., 1950, "An Iteration Method for the Solution of the Eigenvalue Problem of Linear Differential and Integral Operators," J. Res. Natl. Bur. Stand., **45**, pp. 255–281.
[27] Paige, C. C., and Saunders, M. A., 1982, "LSQR: An Algorithm for Sparse Linear Equations and Sparse Least Squares," AMC Trans. Math. Softw., **8**, pp. 43–71.
[28] Paige, C. C., and Saunders, M. A., 1982, "LSQR: Sparse Linear Equations and Least Squares Problems," AMC Trans. Math. Softw., **8**, pp. 195–209.

Hamdy M. Youssef[1]
Department of Mathematics,
Faculty of Education,
Alexandria University,
El-Guish Road, El-Shatby,
Alexandria–21526, Egypt
e-mail: yousefanne@yahoo.com

Theory of Fractional Order Generalized Thermoelasticity

In this work, a new model of thermoelasticity theory has been constructed in the context of a new consideration of heat conduction with fractional order, and its uniqueness theorem has been approved also. One-dimensional application for a half-space of elastic material, which is thermally shocked, has been solved by using Laplace transform and state-space techniques. According to the numerical results and its graphs, conclusion about the new theory of thermoelasticity has been constructed.

[DOI: 10.1115/1.4000705]

1 Introduction

Recently, a considerable research effort has been expended to study anomalous diffusion, which is characterized by the time-fractional diffusion-wave equation by Kimmich [1]

$$\rho c = \kappa I^{\alpha} c_{,ii} \tag{1}$$

where ρ is the mass density, c is the concentration, κ is the diffusion conductivity, i is the coordinate symbol, which takes the values 1, 2, and 3, the subscript "," means the derivative with respect to x_i, and notion I^{α} is the Riemann–Liouville fractional integral is introduced as a natural generalization of the well-known n-fold repeated integral $I^n f(t)$ written in a convolution-type form as in Refs. [2,3]

$$\left.\begin{aligned} I^{\alpha} f(t) &= \frac{1}{\Gamma(\alpha)} \int_0^t (t-\tau)^{\alpha-1} f(\tau) d\tau \\ I^0 f(t) &= f(t) \end{aligned}\right\} \quad 0 < \alpha \leq 2 \tag{2}$$

where $\Gamma(\alpha)$ is the gamma function.

According to Kimmich [1] Eq. (1) describes different cases of diffusion where $0<\alpha<1$ corresponds to weak diffusion (subdiffusion), $\alpha=1$ corresponds to normal diffusion, $1<\alpha<2$ corresponds to strong diffusion (superdiffusion), and $\alpha=2$ corresponds to ballistic diffusion.

It should be noted that the term diffusion is often used in a more generalized sense including various transport phenomena. Equation (1) is a mathematical model of a wide range of important physical phenomena, for example, the subdiffusive transport occurs in widely different systems ranging from dielectrics and semiconductors through polymers to fractals, glasses, porous, and random media. Superdiffusion is comparatively rare and has been observed in porous glasses, polymer chain, biological systems, transport of organic molecules and atomic clusters on surface [4]. One might expect the anomalous heat conduction in media where the anomalous diffusion is observed.

Fujita [5,6] considered the heat wave equation for the case of $1\leq\alpha\leq2$

$$\rho C T = k I^{\alpha} T_{,ii} \tag{3}$$

where C is the specific heat, k is the thermal conductivity, and the subscript "," means the derivative with respect to the coordinates x_i.

Equation (3) can be obtained as a consequence of the non local constitutive equation for the heat flux components q_i is in the form

$$q_i = -kI^{\alpha-1} T_{,i}, \quad 1 < \alpha \leq 2 \tag{4}$$

Povstenko [4] used the Caputo heat wave equation defined in the form

$$q_i = -kI^{\alpha-1} T_{,i}, \quad 0 < \alpha \leq 2 \tag{5}$$

to get the stresses corresponding to the fundamental solution of a Cauchy problem for the fractional heat conduction equation in one-dimensional and two-dimensional cases.

Some applications of fractional calculus to various problems of mechanics of solids are reviewed in the literature [7,8].

2 Theory of Fractional Order Generalized Thermoelasticity

The classical thermoelasticity is based on the principles of the theory of heat conduction, which is called the Fourier law, which relates the heat flux components q_i to the temperature gradient as follows:

$$q_i = -kT_{,i} \tag{6}$$

In combination with the energy conservative law, this leads to the parabolic heat conduction equation, which is considered by Povstenko [4]

$$\rho C \dot{T} = kT_{,ii} \tag{7}$$

where the dotted above T means the derivative with respect to the time t.

Recently, in the nonclassical thermoelasticity theories, Fourier law (6) and heat conduction (7) are replaced by more general equations; these have been formulated. The first well-known generalized of such a type is that of Lord and Shulman [9], and it takes the form

$$q_i + \tau_o \dot{q}_i = -kT_{,i} \tag{8}$$

which leads to the hyperbolic differential equation of heat conduction of Lord and Shulman [9]

$$\rho C(\dot{T} + \tau_o \ddot{T}) = kT_{,ii} \tag{9}$$

where τ_o is a non-negative constant and is called the relaxation time.

According to Eq. (9), Kaliski [10] and Lord and Shulman [9] constructed the theory of generalized thermoelasticity.

Now, a new formula of heat conduction will be considered taking into account considerations (4), (5), and (8) as follows:

$$q_i + \tau_o \dot{q}_i = -kI^{\alpha-1} T_{,i}, \quad 0 < \alpha \leq 2 \tag{10}$$

where I is an integral operator, which is defined in Eq. (2).

In the context of the generalized thermoelasticity, the governing equations for isotropic medium are defined as follows.

For the equation of motion,

---

[1] Present address: Faculty of Engineering, Umm Al-Qura University, P.O. Box 5555, Makkah, Saudi Arabia.

Contributed by the Heat Transfer Division of ASME for publication in the JOURNAL OF HEAT TRANSFER. Manuscript received October 28, 2008; final manuscript received November 24, 2009; published online March 19, 2010. Assoc. Editor: Gautam Biswas.

$$\sigma_{ij,j} + \rho F_i = \rho \ddot{u}_i \tag{11}$$

For the constitution relation,

$$\sigma_{ij} = 2\mu e_{ij} + (\lambda e_{kk} - \gamma\theta)\delta_{ij} \tag{12}$$

where λ and μ are Lamé's constant; u_i is the displacement component; F_i is the body force component; $\theta = |T - T_o|$ is the increment of the dynamical temperature, where T_o is the reference temperature; $\gamma = (3\lambda + 2\mu)\alpha_T$, where α_T is called the thermal expansion coefficient, where δ_{ij} is the Kronecker delta symbol; σ_{ij} is the stress tensor such that $\sigma_{ij} = \sigma_{ji}$; and e_{ij} is the strain tensor that satisfies the relations

$$e_{ij} = \tfrac{1}{2}(u_{i,j} + u_{j,i}) \quad \text{and} \quad e = e_{11} + e_{22} + e_{33} \tag{13}$$

For the heat flux equation,

$$q_{i,i} = -\rho C\dot{\theta} - T_o\gamma\dot{e} \tag{14}$$

The entropy increment equation per unit volume takes the form

$$\rho T_o \eta = \rho C\theta + T_o \gamma e \tag{15}$$

where η is the entropy increment of the material.

For the heat flux-entropy equation,

$$q_{i,i} = -\rho T_o \dot{\eta} \tag{16}$$

For the heat equation without any heat sources

$$q_i + \tau_o \frac{\partial q_i}{\partial t} = -kI^{\alpha-1}\theta_{,i}, \quad 0 < \alpha \leq 2 \tag{17}$$

By using Eqs. (15)–(17), we have the heat equation in the form

$$kI^{\alpha-1}\theta_{,ii} = \left(\frac{\partial}{\partial t} + \tau_o \frac{\partial^2}{\partial t^2}\right)(\rho C\theta + T_o\gamma e) \quad 0 < \alpha \leq 2 \tag{18}$$

Where

$0 < \alpha < 1$ for weak conductivity
$\alpha = 1$ for normal conductivity
$1 < \alpha \leq 2$ for strong conductivity

3 The Uniqueness Theorem

Let V be an open regular region of space with boundary S occupied by the reference configuration of a homogeneous isotropic linear thermoelastic solid. S is assumed closed and bounded. We supplement the equations of two temperature-generalized thermoelasticity (11)–(18) by prescribed boundary conditions as in Ref. [11]

$$u_i = \overline{u_i} \quad \text{on} \quad S_1 \times [0,\infty] \tag{19}$$

$$p_i = \overline{p_i} = \sigma_{ji} n_j \quad \text{on} \quad S - S_1 \times [0,\infty] \tag{20}$$

$$\theta_i = \overline{\theta_i} \quad \text{on} \quad S \tag{21}$$

where $S_1 \subset S$.

In addition, we have prescribed initial conditions

$$u_i = u_{i0}, \quad \dot{u}_i = \dot{u}_{i0}, \quad \theta = \theta_0 \quad \text{in} \quad V \quad \text{at} \quad t = 0 \tag{22}$$

4 Theorem

Given a regular region of space $V+S$ with volume V and boundary S, then there exists at most one set of single valued functions $\sigma_{ij}(x_k,t)$ and $e_{ij}(x_k,t)$ of class $C^{(1)}$, $u_i(x_k,t)$, and $\theta_i(x_k,t)$ of class $C^{(2)}$ in $V+S$, $t \geq 0$, which satisfy Eqs. (11)–(18) and conditions (19)–(22), where k, C, λ, μ, γ, T_o, ρ, and τ_o are all positive.

5 Proof

Let there be two sets of functions $\sigma_{ij}^{(\mathrm{I})}$ and $\sigma_{ij}^{(\mathrm{II})}$, $\mathrm{e}_{ij}^{(\mathrm{I})}$ and $\mathrm{e}_{ij}^{(\mathrm{II})}$, $\theta^{(\mathrm{I})}$ and $\theta^{(\mathrm{II})}\ldots$, etc. and let $\sigma_{ij} = \sigma_{ij}^{(\mathrm{I})} - \sigma_{ij}^{(\mathrm{II})}$, $\mathrm{e}_{ij} = \mathrm{e}_{ij}^{(\mathrm{I})} - \mathrm{e}_{ij}^{(\mathrm{II})}$, $\theta = \theta^{(\mathrm{I})} - \theta^{(\mathrm{II})}\ldots$, etc.

By virtue of the linearity of the problem, it is clear that these differences also satisfy the above-mentioned equations (with $F_i = 0$) and homogeneous counterparts of conditions (19)–(22), namely, they satisfy the following field equations in $V \times (0,\infty)$:

$$\sigma_{ij,j} = \rho \ddot{u}_i \tag{23}$$

$$\sigma_{ij} = \sigma_{ji} \tag{24}$$

$$q_{i,i} = -\rho T_o \dot{\eta} \tag{25}$$

$$\sigma_{ij} = 2\mu e_{ij} + (\lambda e_{kk} - \gamma\theta)\delta_{ij} \tag{26}$$

$$q_i + \tau_o \dot{q}_i = -kI^{\alpha-1}\theta_{,i}, \quad 0 < \alpha \leq 2 \tag{27}$$

$$\rho T_o \eta = \rho C\theta + T_o \gamma_{ij} e_{ij} \tag{28}$$

$$kI^{\alpha-1}\theta_{,ii} = \rho C(\dot{\theta} + \tau_o \ddot{\theta}) + \gamma T_0(\dot{e}_{kk} + \tau_0 \ddot{e}_{kk}) \tag{29}$$

and

$$e_{ij} = \tfrac{1}{2}(u_{i,j} + u_{j,i}) \tag{30}$$

together with the following boundary conditions:

$$u_i = 0 \quad \text{on} \quad S_1 \times [0,\infty) \tag{31}$$

$$p_i = \sigma_{ji} n_j = 0 \quad \text{on} \quad S - S_1 \times [0,\infty) \tag{32}$$

$$\theta_i = 0 \quad \text{on} \quad S \tag{33}$$

where $S_1 \subset S$.

In addition, we have the initial conditions

$$u_i = u_{i0}, \quad \dot{u}_i = \dot{u}_{i0}, \quad \theta = \theta_0 \quad \text{in} \quad V \quad \text{at} \quad t = 0 \tag{34}$$

Now, we will consider the integral

$$\int_v \sigma_{ij}\dot{e}_{ij}dv = \int_v \sigma_{ij}\dot{u}_{i,j}dv = -\int_v \sigma_{ij,j}\dot{u}_i dv \tag{35}$$

Upon inserting Eq. (23) the latter equation is reduced to

$$\int_v (\sigma_{ij}\dot{e}_{ij}dv + \rho\dot{u}_i\ddot{u}_i)dv = 0 \tag{36}$$

Using Eq. (26), we get

$$\int_v [(2\mu e_{ij} + \lambda\delta_{ij}e_{kk} - \gamma\theta\delta_{ij})\dot{e}_{ij} + \rho\dot{u}_i\ddot{u}_i]dv = 0 \tag{37}$$

This can be written as follows:

$$\frac{d}{dt}\int_v \left[\frac{1}{2}\lambda e_{kk}^2 + \mu e_{ij}e_{ij} + \frac{\rho\dot{u}_i\dot{u}_i}{2}\right]dv - \int_v \gamma\theta\dot{e}_{kk}dv = 0 \tag{38}$$

Substituting for $\dot{e}_{kk}$ in Eq. (29), we get

$$T_0\frac{d}{dt}\int_v \left[\frac{1}{2}\lambda e_{kk}^2 + \mu e_{ij}e_{ij} + \frac{\rho\dot{u}_i\dot{u}_i}{2} + \frac{\rho C}{2T_0}\theta^2\right]dv - k\int_v \theta I^{\alpha-1}\theta_{,ii}dv$$
$$+ \tau_o\rho C\int_v \theta\ddot{\theta}dv + \gamma T_0\tau_o\int_v \theta\ddot{e}_{kk}dv = 0 \tag{39}$$

where $\int_v I^{\alpha-1}f(v,t)dv = I^{\alpha-1}\int_v f(v,t)dv$ (v and t are independent variables).

Integrating by parts, we obtain

$$T_0\frac{d}{dt}\int_v\left[\frac{1}{2}\lambda e_{kk}^2+\mu e_{ij}e_{ij}+\frac{\rho\dot{u}_i\dot{u}_i}{2}+\frac{\rho C}{2T_0}\theta^2\right]dv+k\int_v\theta_{,i}I^{\alpha-1}\theta_{,i}dv$$

$$+\tau_o\rho C\int_v\theta\ddot{\theta}dv+\gamma T_0\tau_o\int_v\theta\ddot{e}_{kk}dv=0 \tag{40}$$

From the well-known inequality of the second law of thermodynamics

$$-q_i\theta_{,i}\geq 0 \tag{41}$$

By using Eq. (27), we get

$$k\int_v\theta_{,i}I^{\alpha-1}\theta_{,i}dv+\tau_o\int_v\dot{q}_i\theta_{,i}dv\geq 0$$

Integrating by parts, we obtain

$$k\int_v\theta_{,i}I^{\alpha-1}\theta_{,i}dv-\tau_o\int_v\dot{q}_{i,i}\theta dv\geq 0 \tag{42}$$

Inserting Eqs. (25) and (28) in the last equation, we get

$$k\int_v\theta_{,i}I^{\alpha-1}\theta_{,i}dv+\tau_o\rho C\int_v\theta\ddot{\theta}dv+\gamma T_o\tau_o\int_v\theta\ddot{e}_{kk}dv\geq 0 \tag{43}$$

Hence, we have

$$\frac{d}{dt}\int_v\left[\frac{1}{2}\lambda e_{kk}^2+\mu e_{ij}e_{ij}+\frac{\rho\dot{u}_i\dot{u}_i}{2}+\frac{\rho C}{2T_0}\theta^2\right]dv\leq 0 \tag{44}$$

The integral in the left hand side of Eq. (44) is initially zero since the difference functions satisfy homogeneous initial conditions. By inequality (44), however, this integral either decreases (or therefore becomes negative) or remains equal to zero. Since the integral is the sum of squares, only the latter alternative is possible, that is,

$$\int_v\left[\frac{1}{2}\lambda e_{kk}^2+\mu e_{ij}e_{ij}+\frac{\rho\dot{u}_i\dot{u}_i}{2}+\frac{\rho C}{2T_0}\theta^2\right]dv=0,\quad t\geq 0 \tag{45}$$

It follows that the difference functions are identically zero throughout the body and for all time this completes the proof of the theorem.

6 One-Dimensional Application

We will consider a half-space filled with an elastic material, which has constant elastic parameters. The governing equations will be written in the context of the fractional ordered generalized thermoelasticity theory.

The heat conduction equation takes the form

$$kI^{\alpha-1}\theta_{,ii}=\left(\frac{\partial}{\partial t}+\tau_0\frac{\partial^2}{\partial t^2}\right)(\rho C\theta+\gamma T_0 e),\quad 0<\alpha\leq 2 \tag{46}$$

The constitutive equation takes the form

$$\sigma_{ij}=2\mu e_{ij}+\lambda e_{kk}\delta_{ij}-\gamma\theta\delta_{ij} \tag{47}$$

The equation of motion without body force takes the form

$$\sigma_{ij,j}=\rho\ddot{u}_i \tag{48}$$

Now, we will suppose elastic and homogenous half-space $0\leq x<\infty$, which obey Eqs. (46)–(48) and initially quiescent, where all the state functions are dependent only on the dimension x and the time t.

The displacement components for the one-dimensional medium have the form

$$u_x=u(x,t),\quad u_y=u_z=0 \tag{49}$$

The strain component takes the form

$$e=e_{xx}=\frac{\partial u}{\partial x} \tag{50}$$

The heat conduction equation takes the form

$$kI^{\alpha-1}\frac{\partial^2\theta}{\partial x^2}=\left(\frac{\partial}{\partial t}+\tau_0\frac{\partial^2}{\partial t^2}\right)(\rho C\theta+\gamma T_0 e),\quad 0<\alpha\leq 2 \tag{51}$$

The constitutive equation takes the form

$$\sigma=\sigma_{xx}=(2\mu+\lambda)e-\gamma\theta \tag{52}$$

The equation of motion takes the form

$$\frac{\partial\sigma}{\partial x}=\rho\ddot{u} \tag{53}$$

or

$$\frac{\partial^2\sigma}{\partial x^2}=\rho\ddot{e} \tag{54}$$

For simplicity, we will use the following nondimensional variables:

$$x'=c_0\eta x,\quad \iota'=c_0^2\eta\iota,\quad \tau_0'=c_0^2\eta\tau_0,\quad \theta'=\frac{T-T_0}{T_0},\quad \sigma'=\frac{\sigma}{2\mu+\lambda} \tag{55}$$

where $c_0^2=[(2\mu+\lambda)/\rho]$ and $\eta=\rho C/k$.

Hence, we have (for simplicity, the primes have been dropped)

$$I^{\alpha-1}\frac{\partial^2\theta}{\partial x^2}=\left(\frac{\partial}{\partial t}+\tau_0\frac{\partial^2}{\partial t^2}\right)(\theta+\varepsilon e) \tag{56}$$

$$\sigma=e-\omega\theta \tag{57}$$

$$\frac{\partial^2\sigma}{\partial x^2}=\ddot{e}=\frac{\partial\ddot{u}}{\partial x} \tag{58}$$

where $\varepsilon=\gamma/\rho\mathrm{C}$ and $\omega=\gamma T_0/(\lambda+2\mu)$ are nondimensional constants.

Taking the Laplace transform for the both sides of Eqs. (56)–(58), this is defined as follows:

$$L\{f(t)\}=\overline{f}(s)=\int_0^\infty f(t)e^{-st}dt$$

we obtain

$$\frac{1}{s^{\alpha-1}}\frac{d^2\overline{\theta}}{dx^2}=(s+\tau_0 s^2)\overline{\theta}+(s+\tau_0 s^2)\varepsilon\overline{e} \tag{59}$$

where the rule for the Laplace transform of the Riemann–Liouville fractional integral reads from Ref. [4]

$$L\{I^n f(t)\}=\frac{1}{s^n}L\{f(t)\},\quad n>0 \tag{60}$$

$$\overline{\sigma}=\overline{e}-\omega\overline{\theta} \tag{61}$$

$$\frac{d^2\overline{\sigma}}{dx^2}=s^2\overline{e}=s^2\frac{d\overline{u}}{dx} \tag{62}$$

where all the initial state functions are equal to zero.

Eliminating $\overline{e}$ and $\overline{\theta}$ from Eqs. (59), (61), and (62), we obtain

$$\frac{d^2\overline{\theta}}{dx^2}=L_1\overline{\theta}+L_2\overline{\sigma} \tag{63}$$

where

$$L_1=(s^\alpha+\tau_0 s^{\alpha+1})(1+\varepsilon\omega),\quad L_2=\varepsilon(s^\alpha+\tau_0 s^{\alpha+1})$$

and

$$\frac{d^2\overline{\sigma}}{dx^2} = M_1\overline{\theta} + M_2\overline{\sigma} \tag{64}$$

where

$$M_1 = \omega s^2, \quad M_2 = s^2$$

Choosing as a state variable the temperature of heat conduction $\overline{\varphi}$ and the stress component $\overline{\sigma}$ in the x-direction, then Eqs. (63) and (64) can be written in matrix form, as in Ref. [12], as follows:

$$\frac{d^2\overline{V}(x,s)}{dx^2} = A(s)\overline{V}(x,s) \tag{65}$$

where

$$V(x,s) = \begin{bmatrix} \overline{\theta}(x,s) \\ \overline{\sigma}(x,s) \end{bmatrix} \quad \text{and} \quad A(s) = \begin{bmatrix} L_1 & L_2 \\ M_1 & M_2 \end{bmatrix}$$

The formal solution of system (65) can be written in the form

$$\overline{V}(x,s) = \exp[-\sqrt{A(s)}x]\overline{V}(0,s) \tag{66}$$

where

$$V(0,s) = \begin{bmatrix} \overline{\theta}(0,s) \\ \overline{\sigma}(0,s) \end{bmatrix} = \begin{bmatrix} \overline{\theta}_0 \\ \overline{\sigma}_0 \end{bmatrix}$$

where for bounded solution with large x, we have canceled the part of the exponential that has a positive power.

We will use the well-known Cayley–Hamilton theorem to find the form of the matrix $\exp[-\sqrt{A(s)}x]$. The characteristic equation of the matrix $\sqrt{A(s)}$ can be written as follows:

$$k^2 - k(L_1 + M_2) + (L_1M_2 - L_2M_1) = 0 \tag{67}$$

the roots of this equation, namely, k_1 and k_2, satisfy the following relations:

$$k_1 + k_2 = L_1 + M_2 \tag{68}$$

$$k_1k_2 = L_1M_2 - L_2M_1 \tag{69}$$

Now, we can write the spectral decomposition of $A(s)$, as in Ref. [13]

$$A(s) = k_1E_1 + k_2E_2 \tag{70}$$

where E_1 and E_2 are called the projectors of $A(s)$ and satisfy the following conditions:

$$E_1 + E_2 = I \tag{71a}$$

$$E_1E_2 = \text{zero matrix} \tag{71b}$$

$$E_i^2 = E_i \quad \text{for} \quad i = 1,2 \tag{71c}$$

Then, we have

$$\sqrt{A(s)} = \sqrt{k_1}E_1 + \sqrt{k_2}E_2 \tag{72}$$

where

$$E_1 = \frac{1}{k_1 - k_2}\begin{bmatrix} (L_1 - k_2) & L_2 \\ \dfrac{(k_1 - L_1)(L_1 - k_2)}{L_2} & (k_1 - L_1) \end{bmatrix} \tag{73}$$

and

$$E_2 = \frac{1}{k_1 - k_2}\begin{bmatrix} (k_1 - L_1) & -L_2 \\ \dfrac{(k_1 - L_1)(k_2 - L_1)}{L_2} & (L_1 - k_2) \end{bmatrix} \tag{74}$$

Then, we get

$$B(s) = \sqrt{A(s)} = \frac{1}{\sqrt{k_1} + \sqrt{k_2}}\begin{bmatrix} \sqrt{k_1k_2} + L_1 & L_2 \\ M_1 & \sqrt{k_1k_2} + M_2 \end{bmatrix} \tag{75}$$

The Taylor series expansion for the matrix exponential in Eq. (66) is given by

$$\exp[-B(s)x] = \sum_{n=o}^{\infty} \frac{[-B(s)x]^n}{n!} \tag{76}$$

Using the Cayley–Hamilton theorem, we can express B^2 and higher orders of the matrix B in terms of I, B, where I is the unit matrix of second order.

Thus, the infinite series in Eq. (76) can be reduced to the following form:

$$\exp[-B(s)x] = b_0(x,s)I + b_1(x,s)B(s) \tag{77}$$

where b_0 and b_1 are coefficients depending on s and x.

Consider the characteristic roots p_1 and p_2 satisfy the characteristic equation of the matrix $B(s)$, which takes the form

$$P^2 - P(\sqrt{k_1} + \sqrt{k_2}) + \sqrt{k_1}\sqrt{k_2} = 0 \tag{78}$$

which gives

$$P_1 = \sqrt{k_1} \quad \text{and} \quad P_2 = \sqrt{k_2} \tag{79}$$

By the Cayley–Hamilton theorem, the roots of matrix B must satisfy Eq. (77); thus, we have

$$\exp(-p_1x) = b_0 + b_1p_1 \tag{80}$$

and

$$\exp(-p_2x) = b_0 + b_1p_2 \tag{81}$$

By solving the above linear system of equations, we get

$$b_0 = \frac{1}{p_1 - p_2}[p_1e^{-p_2x} - k_2e^{-p_1x}] \tag{82}$$

and

$$b_1 = \frac{1}{p_1 - p_2}[e^{-p_1x} - e^{-p_2x}] \tag{83}$$

Hence, we have

$$\exp[-B(s)x] = L_{ij}(x,s), \quad i,j = 1,2 \tag{84}$$

where

$$L_{11} = \frac{1}{k_1 - k_2}[e^{-\sqrt{k_2}x}(k_1 - L_1) - e^{-\sqrt{k_1}x}(k_2 - L_1)]$$

$$L_{12} = \frac{L_2}{k_1 - k_2}[e^{-\sqrt{k_1}x} - e^{-\sqrt{k_2}x}]$$

$$L_{22} = \frac{1}{k_2 - k_1}[e^{-\sqrt{k_1}x}(k_2 - M_2) - e^{-\sqrt{k_2}x}(k_1 - M_2)]$$

$$L_{21} = \frac{M_1}{k_1 - k_2}[e^{-\sqrt{k_1}x} - e^{-\sqrt{k_2}x}]$$

We can write the solution of Eq. (65) in the following form:

$$\overline{V}(x,s) = L_{ij}\overline{V}(0,s) \tag{85}$$

Hence, we obtain

$$\overline{\theta} = \frac{1}{k_1 - k_2}[(k_1\theta_0 - L_1\theta_0 - L_2\sigma_0)e^{-\sqrt{k_2}x} - (k_2\theta_0 - L_1\theta_0 - L_2\sigma_0)e^{-\sqrt{k_1}x}] \tag{86}$$

$$\overline{\sigma} = \frac{1}{k_1 - k_2}[(k_1\sigma_0 - M_1\theta_0 - M_2\sigma_0)e^{-\sqrt{k_2}x} - (k_2\sigma_0 - M_1\theta_0 - M_2\sigma_0)e^{-\sqrt{k_1}x}] \quad (87)$$

Now, we will use the boundary conditions on the boundary plane $x=0$, which is given by the following:

(1) Thermal boundary condition

We will suppose that, the boundary plane x=0 is subjected to a thermal shock as follows:

$$\theta(0,t) = \theta_0 = \theta_0^0 H(t) \quad (88)$$

where $H(t)$ is called the Heaviside unite step function and θ_0^0 is constant.

By using Laplace transform as we defined before, we get

$$\overline{\theta}(0,s) = \overline{\theta_0} = \frac{\theta_0^0}{s} \quad (89)$$

(2) Mechanical boundary condition

We will consider that the boundary plane $x=0$ traction free, so we have

$$\sigma(0,t) = \sigma_0 = 0 \quad (90)$$

the above equation gives, after using the Laplace transform, the following equation:

$$\overline{\sigma}(0,t) = \overline{\sigma_0} = 0 \quad (91)$$

Hence, we can use conditions (89) and (91) into the Eqs. (86) and (87) to get the solutions as follows:

$$\overline{\theta} = \frac{\theta_0^0}{s(k_1 - k_2)}[(k_1 - L_1)e^{-\sqrt{k_2}x} - (k_2 - L_1)e^{-\sqrt{k_1}x}] \quad (92)$$

$$\overline{\sigma} = \frac{\theta_0^0 M_1}{s(k_1 - k_2)}[e^{-\sqrt{k_1}x} - e^{-\sqrt{k_2}x}] \quad (93)$$

From Eq. (62), we have

$$\overline{u} = \frac{1}{s^2}\frac{d\overline{\sigma}}{dx} \quad (94)$$

Substituting from Eq. (85) into Eq. (86), we get

$$\overline{u} = \frac{-\theta_0^0 M_1}{s^3(k_1 - k_2)}[\sqrt{k_1}e^{-\sqrt{k_1}x} - \sqrt{k_2}e^{-\sqrt{k_2}x}] \quad (95)$$

Those complete the solution in the Laplace transform domain.

7 Inverse Laplace Transforms

In order to invert the Laplace transforms, we adopt a numerical inversion method based on a Fourier series expansion in Ref. [14].

By this method the inverse $f(t)$ of the Laplace transform $\overline{f}(s)$ is approximated by

$$f(t) = \frac{e^{ct}}{t_1}\left[\frac{1}{2}\overline{f}(c) + R1\sum_{k=1}^{N}\overline{f}\left(c + \frac{ik\pi}{t_1}\right)\exp\left(\frac{ik\pi t}{t_1}\right)\right], \quad 0 < t_1 < 2t \quad (96)$$

where N is a sufficiently large integer representing the number of terms in the truncated Fourier series, chosen such that

$$\exp(ct)R1\left[\overline{f}\left(c + \frac{iN\pi}{t_1}\right)\exp\left(\frac{iN\pi t}{t_1}\right)\right] \leq \varepsilon_1 \quad (97)$$

where ε_1 is a prescribed small positive number that corresponds to the degree of accuracy required. Parameter c is a positive free parameter that must be greater than the real part of all the singularities of $\overline{f}(s)$. The optimal choice of c was obtained according to the criteria described in Ref. [14].

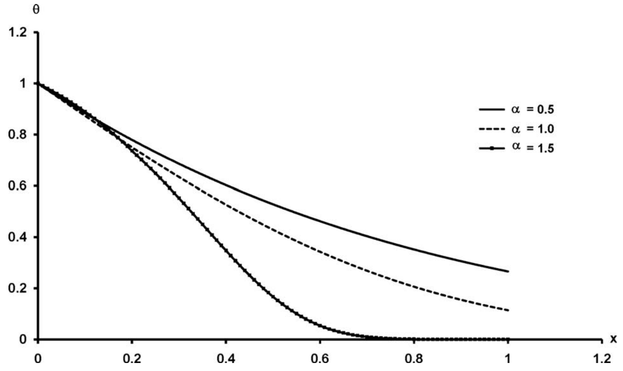

Fig. 1 The temperature distribution at $t=0.2$

8 Numerical Results and Discussion

The copper material was chosen for purposes of numerical evaluations, and the constants of the problem were taken from Refs. [12,15] as follows:

$$k = 386 \text{ N/K s}, \quad \alpha_T = 1.78 \times 10^{-5} \text{ K}^{-1}, \quad C = 383.1 \text{ m}^2\text{/K}$$

$$\eta = 8886.73 \text{ m/s}^2, \quad \mu = 3.86 \times 10^{-10} \text{ N/m}^2$$

$$\lambda = 7.76 \times 10^{-10} \text{ N/m}^2, \quad \rho = 8954 \text{ kg/m}^3, \quad \tau_o = 0.02 \text{ s}$$

$$T_o = 293 \text{ K}, \quad \varepsilon = 1.60861, \quad \omega = 0.0104, \quad \theta_0^0 = 1$$

Figures 1–3 display the temperature distribution q, the stress distribution s, and the displacement distribution u for wide range of x

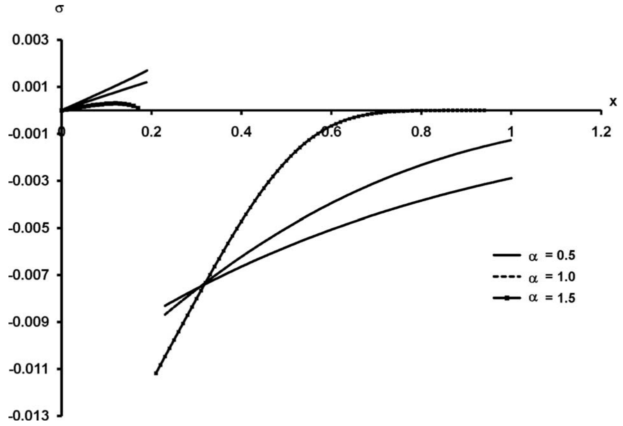

Fig. 2 The stress distribution at $t=0.2$

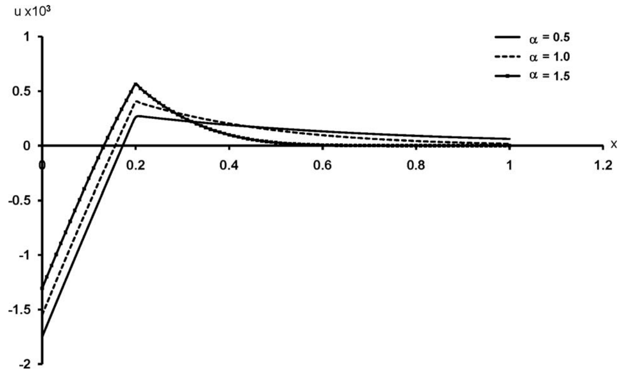

Fig. 3 The displacement distribution at $t=0.2$

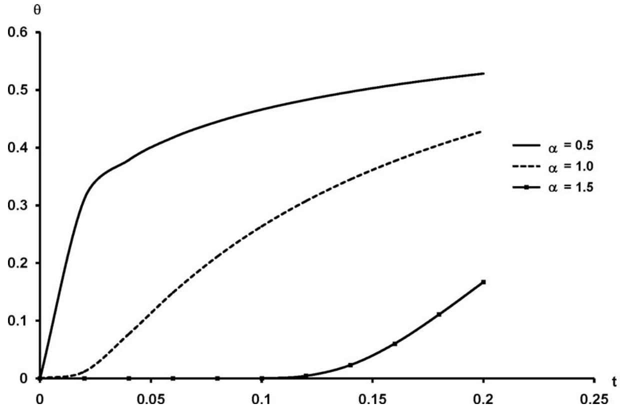

Fig. 4 The temperature distribution at $x=0.5$

$(0<x<1)$ at a small value of time $t=0.2$, and it is noticed that α has a significant effect on all the fields.

In Fig. 1, for a weak conductivity $0<\alpha=0.5<1$, the particle transports the heat to the other particle with difficulty, which makes the particles keep the temperature within itself for a longer time interval, which makes this curve lie above the other two curves. For a normal conductivity $\alpha=1.0$, the results coincide with all the previous results of applications that are taken in the context of the generalized thermoelasticity, as in Refs. [9,12,15]. For strong conductivity (superconductivity) $1<\alpha=1.5\leq 2$, the particles transport the heat to the other particles easily and this makes the decreasing rate of the temperature greater than the other ones.

In Fig. 2, the stress field has the same behavior as the temperature except at discontinuous points. To explain that discontinuous points, the effect of the thermal shock on the boundary generates a wave for small interval $0\leq\alpha\leq 0.19$; after this another wave is generated as a reaction of the first wave in inverse direction.

In Fig. 3, the displacement distribution has been affected by the value of α, where the maximum point of the displacement increases when the value of increases. During the same interval $0\leq\alpha\leq 0.19$, all the displacements increase with a very great rate until the maximum point at $x=0.19$.

Figures 4–6 display the temperature distribution q, the stress distribution s, and the displacement distribution u for wide range of time t $(0\leq t\leq 0.2)$ at $x=0.5$, and it is noticed that α has significant effects on all the fields. It is noticed that all the waves reach the steady state depending on the value of α.

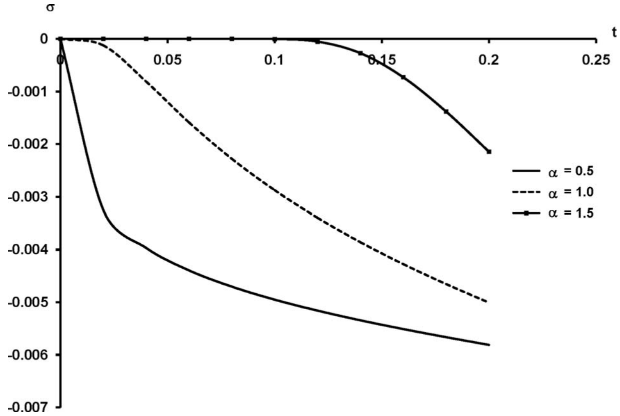

Fig. 5 The stress distribution at $x=0.5$

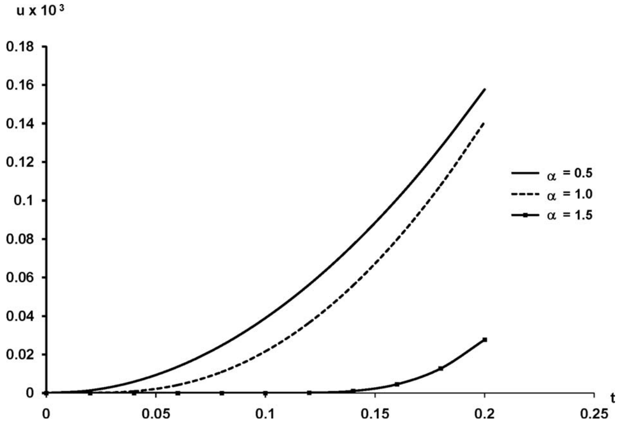

Fig. 6 The displacement distribution at $x=0.5$

9 Conclusion

In general, we have the following system of equations that cover four theorems.

For the equation of motion,

$$\rho\frac{\partial^2 u_i}{\partial t^2} = \rho F_i + (\lambda+\mu)u_{j,ij} + \mu u_{i,jj} - \gamma\left(\theta + \nu\frac{\partial\theta}{\partial t}\right)_{,i} \tag{98}$$

For the generalized heat conduction equation,

$$kI^{\alpha-1}\theta_{,ii} = \rho C\left(\frac{\partial\theta}{\partial t} + \tau_o\frac{\partial^2\theta}{\partial t^2}\right) + \gamma T_o\left(\frac{\partial u_{i,i}}{\partial t} + n_o\tau_o\frac{\partial^2 u_{i,i}}{\partial t^2}\right) \tag{99}$$

where

$$\begin{array}{ll} 0<\alpha<1 & \text{for weak conductivity} \\ \alpha=1 & \text{for normal conductivity} \\ 1<\alpha\leq 2 & \text{for superconductivity} \end{array}$$

and n_o is a constant parameter.

For the constitutive equation,

$$\sigma_{ij} = \lambda e_{kk}\delta_{ij} + 2\mu e_{ij} - \gamma\left(\theta + \nu\frac{\partial\theta}{\partial t}\right) \tag{100}$$

$$e_{ij} = \tfrac{1}{2}(u_{i,j} + u_{j,i}) \tag{101}$$

The previous equations constitute a complete system of fractional order generalized thermoelasticity. This model can be applied to both classical generalizations, the Lord–Shulman theory ($n_0=1$, $\tau_0>0$, $\nu=0$, $\alpha=1$) and the Green–Lindsay theory ($n_0=0$, $\tau_0>0$, $\nu>0$, $\alpha=1$), as well as to the coupled theory ($\tau_0=\nu=0$, $\alpha=1$).

Nomenclature

ρ = the mass density
c = the concentration
κ = the diffusion conductivity
C = the specific heat
k = the thermal conductivity
q_i = the heat flux components
T = the temperature
τ_o = the relaxation time
λ, μ = Lame's constants
u_i = the displacement component
F_i = the body force component
θ = $|T-T_o|$ is the increment of the dynamical temperature
T_o = the reference temperature
α_T = the thermal expansion coefficient

δ_{ij} = the Kronecker delta symbol
σ_{ij} = the stress tensor such that
e_{ij} = the strain tensor
η = the entropy increment
$c_0^2 = (2\mu+\lambda)/\rho$
$\varepsilon = \gamma/\rho C$
$\omega = \gamma T_0/(\lambda+2\mu)$

References

[1] Kimmich, R., 2002, "Strange Kinetics," Porous media, and NMR," J. Chem. Phys., **284**, pp. 243–285.
[2] Podlubny, I., 1999, *Fractional Differential Equations*, Academic, New York.
[3] Mainardi, F., and Gorenflo, R., 2000, "On Mittag-Lettler-Type Function in Fractional Evolution Processes," J. Comput. Appl. Math., **118**, pp. 283–299.
[4] Povstenko, Y. Z., 2004, "Fractional Heat Conductive and Associated Thermal Stress," J. Therm. Stresses, **28**, pp. 83–102.
[5] Fujita, Y., 1990, "Integrodifferential Equation Which Interpolates the Heat Equation and Wave Equation (I)," Osaka J. Math., **27**, pp. 309–321.
[6] Fujita, Y., 1990, "Integrodifferential Equation Which Interpolates the Heat Equation And Wave Equation (II)," Osaka J. Math., **27**, pp. 797–804.
[7] Rabotnov, Y. N., 1966, *Creep of Structure Elements*, Nauka, Moscow, Russia (in Russian).
[8] Rossikhin, Y. A., and Shitikova, M. V., 1997, "Applications of Fractional Calculus to Dynamic Problems of Linear and Non Linear Hereditary Mechanics of Solids," Appl. Mech. Rev., **50**, pp. 15–67.
[9] Lord, H. W., and Shulman, Y., 1967, "A Generalized Dynamical Theory of Thermoelasticity," J. Mech. Phys. Solids, **15**, pp. 299–309.
[10] Kaliski, S., 1965, "Wave Equations of Thermoelasticity," Bull. Acad. Pol. Sci., Ser. Sci. Tech., **13**, pp. 253–260.
[11] Ignaczak, J., 1979, "Uniqueness in Generalized Thermoelasticity," J. Therm. Stresses, **2**, pp. 171–175.
[12] Youssef, H. M., 2005, "State-Space on Generalized Thermoelasticity for an Infinite Material With a Spherical Cavity and Variable Thermal Conductivity Subjected to Ramp-Type Heating," Journal of Canadian Applied Mathematics Quarterly (Applied Mathematics Institute), **13**(4), pp. 369–388.
[13] Cullen, C. G., 1972, *Matrices and Linear Transformations*, 2nd ed., Addison-Wesley, Reading, MA.
[14] Honig, G., and Hirdes, U., 1984, "A Method for the Numerical Inversion of Laplace Transform," J. Comput. Appl. Math., **10**, pp. 113–132.
[15] Youssef, H. M., 2006, "Two-Dimensional Generalized Thermoelasticity Problem for a Half-Space Subjected to Ramp-Type Heating," Eur. J. Mech. A/Solids, **25**, pp. 745–763.

Determination of Time-Delay Parameters in the Dual-Phase Lagging Heat Conduction Model

J. Ordóñez-Miranda
e-mail: eordonez@mda.cinvestav.mx

J. J. Alvarado-Gil
e-mail: jjag@mda.cinvestav.mx

Department of Applied Physics,
Centro de Investigación y de Estudios Avanzados
del I.P.N-Unidad Mérida,
Carretera Antigua a Progreso kilómetro 6,
Apartado Postal 73 Cordemex, Mérida,
Yucatán 97310, México

The study of thermal transport based on the dual-phase lagging model involves not only the well known thermal properties but also two additional time parameters. Those parameters permit to take into account the thermal inertia and the microstructural interactions of the media in such a way that they establish the nonsimultaneity between temperature changes and heat flux. In the dual-phase lagging model, heat transport phenomena are extremely sensitive not only to the size of each time parameter but also to the relative size of them. In order to obtain useful and reliable results, it is important to develop methodologies for the determination of those time parameters. Additionally it is necessary to count with tools that allow evaluating easily the sensitivity of the temperature and heat to the changes in those time parameters. In this work, a system formed by a semi-infinite layer in thermal contact with a finite one, which is excited by a modulated heat flux, is studied. When the thermal effusivities of the layers are quite different, it is shown that a frequency range can be found in which the normalized amplitude and phase of the spatial component of the oscillatory surface temperature show strong oscillations. This behavior is used to obtain explicit formulas for determining simultaneously the time parameters as well as additional thermal properties of the finite layer, under the framework of the dual-phase lagging model of heat conduction. The limits of the corresponding equations for single-phase lagging models of heat conduction are also discussed.

[DOI: 10.1115/1.4000748]

Keywords: dual-phase lagging model, time delays, layered system, heat conduction

1 Introduction

Heat conduction has been studied traditionally using the classical Fourier law, which is supported by extensive and successful results in agreement with experimental data for most of the analyzed experimental conditions [1,2]. However, in situations involving very short times, high heat fluxes, and very low temperatures, the validity of the Fourier approach has been questioned [3–5]. The main objection comes from the fact that the Fourier law predicts an infinite speed of heat propagation, in such a way that a thermal disturbance in any part of a medium results in an instantaneous perturbation anywhere else in the sample [4]. The origin of this fundamental problem is due to the fact that the Fourier law establishes that when a temperature gradient (heat flux) at time t is imposed, the heat flux (temperature gradient) starts instantaneously at the same time t. In this way, the heat flux and the temperature gradient are simultaneous and therefore there is no difference between the cause and the effect of the heat flow. Considering that heat transport is due to microscopic motion and collisions of electrons and phonons, it can be inferred that the condition on the velocity of heat transport in the Fourier law cannot be sustained [3–5].

Different models have been developed to surmount the limitations of the Fourier approach, the simplest one was suggested by Cattaneo [6] and independently by Vernotte [7]. It consists in modifying the Fourier law, considering the finite propagation speed of heat. This hypothesis is incorporated in the heat flux equation by means of the parameter τ, known as the thermal relaxation time for the heat flux. Using the energy conservation equation, a hyperbolic heat conduction equation with a second order time derivative of the temperature is obtained [5]. This equation is known as the Cattaneo–Vernotte (CV) equation and predicts a wave-like behavior for heat transport. Although the CV equation removes the paradox of infinite speed of heat propagation predicted by the Fourier law, it still establishes an instantaneous response between the temperature gradient and the energy transport [8]. Furthermore, it establishes that the temperature gradient is always the cause and the heat flux the effect in the process of heat transport.

To surmount the drawbacks of the CV equation, the dual-phase lagging (DPL) model was proposed by Tzou [8,9]. This model establishes that either the temperature gradient may precede the heat flux or that the heat flux may precede the temperature gradient. This approach has been used to study a wide variety of physical systems, from layered systems [10–13], structures with nonlinear boundary conditions [14], thermoelastic vibration [12], etc.

The DPL model is based on the hypothesis that the heat flux equation can be written in the form

$$q(x,t+\tau_q) = -k\frac{\partial T(x,t+\tau_T)}{\partial x} \tag{1}$$

where x is the spatial coordinate, t is the time, $q(\mathrm{W/m^2})$ is the heat flux, $T(\mathrm{K})$ is the absolute temperature, $k(\mathrm{W/m\,K})$ is the thermal conductivity, τ_q is the phase lag of the heat flux, and τ_T is the phase lag of the temperature gradient. For the case in which $\tau_q > \tau_T$, the heat flux (effect) established across the material is a result of the temperature gradient (cause); while for $\tau_q < \tau_T$, the heat flux (cause) induces the temperature gradient (effect). According to Eq. (1), the temperature gradient established at a point x of the material at time $t+\tau_T$ corresponds to the heat flux at the same point at time $t+\tau_q$, being t the time at which the energy conservation is imposed. The time delay τ_q has been interpreted as the relaxation time due to the fast-transient effects of thermal inertia while the time delay τ_T has been interpreted as the time required for the thermal activation in microscale, caused by the

---

Contributed by the Heat Transfer Division of ASME for publication in the Journal of Heat Transfer. Manuscript received May 3, 2009; final manuscript received October 28, 2009; published online March 25, 2010. Assoc. Editor: Wei Tong.

microstructural interactions such as electron-phonon interaction or phonon scattering [5,8,9]. The DPL model has been shown to be admissible by the second law of extended irreversible thermodynamics [8] and by the Boltzmann transport equation [15].

Assuming that the time delays τ_q and τ_T are much shorter that the typical response time in a transient process ($\tau_q, \tau_T \ll t$), Eq. (1) can be approximated by a first order Taylor series expansion, as follows [12]:

$$q(x,t) + \tau_q \frac{\partial q(x,t)}{\partial t} = -k\left[\frac{\partial T(x,t)}{\partial x} + \tau_T \frac{\partial^2 T(x,t)}{\partial t\, \partial x}\right] \tag{2}$$

After dividing Eq. (2) by τ_q, multiplying it by the factor e^{t/τ_q} and integrating both sides from $-\infty$ to t, the expression for the heat flux is

$$q(x,t) = -\frac{k}{\tau_q} e^{-t/\tau_q} \int_{-\infty}^{t} \left[\frac{\partial T(x,\eta)}{\partial x} + \tau_T \frac{\partial^2 T(x,\eta)}{\partial \eta\, \partial x}\right] e^{\eta/\tau_q} d\eta \tag{3}$$

Equation (3) establishes that the heat flux at a time instant t depends on the history of the temperature gradient established in the whole time interval from $-\infty$ to t. This indicates that the heat flux has thermal memory, consequence of the finite value of the phase lag τ_q. In this way, Eq. (3) predicts a dependence of the time path of the temperature gradient rather than an instantaneous response predicted by the Fourier law.

In order to uncouple the variables q and T, Eq. (1) has to be combined with the energy conservation equation established at time instant t, given by [1]

$$\frac{\partial q(x,t)}{\partial x} + \rho c \frac{\partial T(x,t)}{\partial t} = S(x,t) \tag{4}$$

where $\rho(\mathrm{kg/m^3})$ is the density, $c(\mathrm{J/kg\,K})$ is the specific heat of the medium, and the source term $S(\mathrm{W/m^3})$ represents the rate per unit volume at which the heat flux is generated. Combining Eqs. (2) and (4) and assuming constant thermal properties, the DPL heat conduction equation is obtained [8–11]

$$\frac{\partial^2 T(x,t)}{\partial x^2} + \tau_T \frac{\partial^3 T(x,t)}{\partial t\, \partial x^2} - \frac{1}{\alpha}\frac{\partial T(x,t)}{\partial t} - \frac{\tau_q}{\alpha}\frac{\partial^2 T(x,t)}{\partial t^2} = -\frac{1}{k}\left(S(x,t) + \tau_q \frac{\partial S(x,t)}{\partial t}\right) \tag{5}$$

where $\alpha = k/\rho c$ is the thermal diffusivity of the involved material [1]. Equation (5) constitutes a generalized or unified equation that reduces to the hyperbolic heat conduction equation (based on the CV equation) when $\tau_T = 0$ [4] and to the parabolic heat conduction equation (based on the Fourier law) when $\tau_q = \tau_T = 0$ [5,8,9]. For the case when $\tau_q < \tau_T$, Eq. (5) is of the parabolic type and therefore establishes a non wave-like heat conduction equation which predictions differ from the usual diffusion behavior predicted by the Fourier law. On the other hand, for $\tau_q > \tau_T$, Eq. (5) is of the hyperbolic type and predicts wave-like thermal signals, predominantly [5]. Both of the time phase lags are treated as intrinsic thermal properties of the material and therefore the application of a heat flux (temperature gradient) at the boundary does not guarantee the precedence of the heat flux (temperature gradient) to the temperature gradient (heat flux).

The DPL model depends crucially on the time delays involved; however, experimental or theoretical methodologies permitting to determine such quantities are scarce [8,16]. It is therefore important to explore the DPL effects on the temperature and from them to establish methodologies to measure or constrain the time-delay parameters [17]. For modulated heat sources, it could be expected that the advantages found in photothermal science in the analysis of thermal depth profiles using the Fourier law can also arise when the same kind of heat sources are used with the DPL heat conduction equation [18–21].

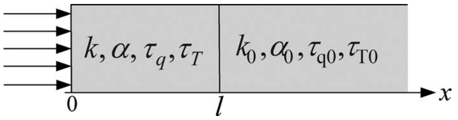

Fig. 1 Schematic diagram of the analyzed system, with $k, \alpha, \tau_q, \tau_T$ and $k_0, \alpha_0, \tau_{q0}, \tau_{T0}$ being the thermal conductivity, thermal diffusivity, phase lag of the heat flux vector, and the phase lag of the temperature gradient of the finite and semi-infinite layers, respectively. The excitation heat source is applied at $x=0$.

In this paper, heat transport governed by DPL model, in a system formed by a finite layer in thermal contact [22,23] with a semi-infinite layer of a different material is analyzed when the first layer is excited with a periodic heat source, in such a way that the heat flux is specified in one of its faces. A normalization procedure of the photothermal signals is performed in order to analyze the behavior of the normalized amplitude and phase of the temperature with the modulation frequency. It is shown that this procedure provides general equations, useful in determining both time delays involved in the DPL model. Approximations on those equations and the simultaneous determination of both phase lags as well as additional thermal properties of the finite layer are discussed.

2 Formulation of the Problem and Solution

Let us consider the configuration shown in Fig. 1, in which the system is excited at the surface $x=0$, with a modulated heat source at frequency f. This situation can be fulfilled when the opaque surface of a material is uniformly illuminated by a laser light beam of periodically modulated intensity. In this case, the heat source is given by [22–27]

$$S(x,t) = I_0 \cos(\omega t)\delta(x) = \mathrm{Re}(I_0 e^{i\omega t})\delta(x) \tag{6}$$

where $\omega = 2\pi f$, $\mathrm{Re}(\xi)$ stands for the real part of ξ, $\delta(x)$ is the Dirac delta function, which guarantees that the electromagnetic energy is converted into heat at the surface $x=0$, and $I_0 = F\eta(1-R')I$, F being a parameter determined by the optical, thermal, and geometric properties of the first layer, η is the efficiency at which the absorbed light is converted into heat, R' is the reflection coefficient of the surface at $x=0$ and $I(\mathrm{W/m^2})$ is the intensity of the light beam. Considering that the sample is uniformly illuminated with a fixed light source, the factor I_0 can be taken as nearly constant and independent of the modulation frequency as it is usually assumed in similar problems [22–27]. For this heat source, the temperature at any point of the sample is given by

$$T(x,t) = T_{\mathrm{amb}} + T_{\mathrm{ac}}(x,t) \tag{7}$$

where T_{amb} corresponds to the ambient temperature and $T_{\mathrm{ac}}(x,t) = \mathrm{Re}[\theta(x)e^{i\omega t}]$ is the periodic component of the temperature, due to the harmonic form of the heat source (Eq. (6)). From now on, the operator Re() will be omitted, taking into account the convention that the real part of the expressions of the temperature must be taken to obtain physical quantities. Our attention will be focused on the spatial component of the oscillatory part of the temperature $[\theta(x)]$, due to the fact that it is the quantity of interest in lock-in and similar detection techniques.

Inserting Eq. (7) into Eq. (5) and considering that there are not any internal heat sources, for $x>0$, the general solution of Eq. (5) for $\theta(x)$ is given by

$$\theta(x) = Be^{px} + Ce^{-px} \tag{8}$$

where B and C are two constants that depend on the boundary conditions of the particular problem and p is given by

$$p = \sqrt{\frac{i\omega}{\alpha}}\sqrt{\frac{1+i\omega\tau_q}{1+i\omega\tau_T}} = \frac{\beta + i\gamma}{\mu} \tag{9a}$$

$$\mu = \sqrt{\frac{2\alpha}{\omega}} = \sqrt{\frac{\alpha}{\pi f}} \tag{9b}$$

$$\beta = \sqrt{\frac{\sqrt{[1+(\omega\tau_q)^2][1+(\omega\tau_T)^2]} - \omega(\tau_q - \tau_T)}{1+(\omega\tau_T)^2}} \tag{9c}$$

$$\gamma = \sqrt{\frac{\sqrt{[1+(\omega\tau_q)^2][1+(\omega\tau_T)^2]} + \omega(\tau_q - \tau_T)}{1+(\omega\tau_T)^2}} \tag{9d}$$

It is important to observe that for low frequencies such that $\omega\tau_q, \omega\tau_T \ll 1$; both parameters β and γ tend to the unity and the parameter p approaches to its classical value $p_c = (1+i)/\mu$ [22–24]. On the other hand, for high frequencies such that $\omega\tau_q, \omega\tau_T \gg 1$; both parameters β and γ tend to $\sqrt{\tau_q/\tau_T}$ and the parameter $p \rightarrow \sqrt{\tau_q/\tau_T}p_c$. These results indicate that the temperature $\theta(x)$ predicted by the Fourier and DPL models would be similar for the high and low frequency regimes. Furthermore, for $\tau_q = \tau_T$, it is found that for any frequency $\beta = \gamma = 1$, and therefore the results predicted by the DPL model must have the same behavior as the ones predicted by the Fourier law.

Considering that there is a thermal resistance $R(\mathrm{m}^2\ \mathrm{K/W})$ at the interface of the layers [23,25], the boundary conditions obtained from the usual requirement of temperature discontinuity and heat flux continuity at the interface $x = l$ are given by

$$\theta(x^-) - \theta(x^+) = Rk(x^+)\frac{1+i\omega\tau_T^+}{1+i\omega\tau_q^+}\frac{d\theta(x^+)}{dx} \tag{10a}$$

$$k(x^-)\frac{1+i\omega\tau_T^-}{1+i\omega\tau_q^-}\frac{d\theta(x^-)}{dx} = k(x^+)\frac{1+i\omega\tau_T^+}{1+i\omega\tau_q^+}\frac{d\theta(x^+)}{dx} \tag{10b}$$

where the superscripts "+" and "−" indicate that the limit $x \rightarrow l$ is taken from the right and left of the point $x = l$, respectively. The form of the Eq. (10*b*) may be derived using Eq. (2) or (3). Furthermore, according to Eq. (6), the boundary condition at $x = 0$ has the following form:

$$- \left. k\frac{1+i\omega\tau_T}{1+i\omega\tau_q}\frac{d\theta(x)}{dx}\right|_{x=0} = I_0 \tag{11}$$

Using Eqs. (8), (10*a*), (10*b*), and (11), it is found that the solution for the spatial part of the thermal wave at $x = 0$ is given by

$$\theta(0) = \frac{I_0}{kp}\frac{1+i\omega\tau_q}{1+i\omega\tau_T}\frac{(1+\lambda+R\lambda_0)e^{pl} + (1-\lambda+R\lambda_0)e^{-pl}}{(1+\lambda+R\lambda_0)e^{pl} - (1-\lambda+R\lambda_0)e^{-pl}} \tag{12}$$

where p is defined by Eqs. (9*a*)–(9*d*) for the thermal properties of the finite layer and

$$\lambda = \frac{\varepsilon_0}{\varepsilon}\sqrt{\frac{1+i\omega\tau_{T0}}{1+i\omega\tau_{q0}}}\sqrt{\frac{1+i\omega\tau_q}{1+i\omega\tau_T}} \tag{13a}$$

$$\lambda_0 = \varepsilon_0\sqrt{i\omega}\sqrt{\frac{1+i\omega\tau_{T0}}{1+i\omega\tau_{q0}}} \tag{13b}$$

with $\varepsilon = k/\sqrt{\alpha}$ being the thermal effusivity of the finite layer and ε_0 the corresponding one of the semi-infinite layer [28,29]. After expressing $\theta(0)$ as a complex function in its polar form, both its amplitude and phase can be obtained. Final expressions are long and complicated, however when the ratio of the thermal effusivities of the layers is quite different from the unity, useful expressions for the determination of the thermal properties can be found.

3 Analysis and Discussions

From Eqs. (12), (13*a*), and (13*b*), it can be observed that $\theta(0)$ depends on the phase lags of the semi-infinite layer through the parameters λ and λ_0. This dependence can be suppressed in the following two limiting cases:

- Semi-infinite layer thermal effusivity much lower than the one of the finite layer: $\varepsilon_0/\varepsilon \ll 1$

  An approximate example of this case is given by a quartz layer ($\varepsilon = 1502.87\ \mathrm{W\ s^{1/2}/m^2\ K}$) in contact with an air layer ($\varepsilon_0 = 5.51\ \mathrm{W\ s^{1/2}/m^2\ K}$) acting as the semi-infinite medium [22]. In this case, from Eq. (13*a*); we have that $|\lambda| \ll 1$ and therefore Eq. (12) reduces to

  $$\theta_1(0) = \frac{I_0}{kp}\frac{1+i\omega\tau_q}{1+i\omega\tau_T}\frac{1+e^{-2pl}}{1-e^{-2pl}} \tag{14}$$

  where it has been assumed that the time delays of each layer are of the same order of magnitude. When $\tau_T = 0$ and $\tau_{T0} = 0$ (CV model) Eq. (14) remains valid if the other time delays (τ_q and τ_{q0}) are also of the same order of magnitude.
- Semi-infinite layer thermal effusivity much higher than the one of the finite layer: $\varepsilon_0/\varepsilon \gg 1$

  A good example of this case is given by a thick diamond layer ($\varepsilon_0 = 64011.33\ \mathrm{W\ s^{1/2}/m^2\ K}$), playing the role of the semi-infinite layer, and a finite layer of quartz ($\varepsilon = 1502.87\ \mathrm{W\ s^{1/2}/m^2\ K}$). In this case, Eq. (13*a*) implies that $|\lambda| \gg 1$ and therefore Eq. (12) reduces to

  $$\theta_2(0) = \frac{I_0}{kp}\frac{1+i\omega\tau_q}{1+i\omega\tau_T}\frac{1-e^{-2pl}}{1+e^{-2pl}} \tag{15}$$

  where the condition $R|\lambda_0| \ll 1$ has been assumed. For time delays of the same order, this condition is fulfilled if $R \ll 1/(\varepsilon_0\sqrt{\omega})$. For materials with thermal effusivity of the order mentioned above, this would be valid for thermal resistances such that $R \ll 10^{-5}/\sqrt{\omega}$. When $\tau_{T0} = 0$ (CV model), the condition $R|\lambda_0| \ll 1$ can also be satisfied when the product $\omega\tau_{q0}$ is of the order of unity.

In order to simplify Eqs. (14) and (15), a normalization procedure has been followed, in such a way that the resulting thermal signal Ω only depends on the thermal properties of the first layer, as follows:

$$\Omega \equiv \frac{\theta_2(x=0)}{\theta_1(x=0)} = \left(\frac{1-e^{-2pl}}{1+e^{-2pl}}\right)^2 \tag{16}$$

The normalized phase ϕ and amplitude A of this signal are given by

$$\phi = 2\ \arctan\left[\frac{\sin(2\gamma l/\mu)}{\sinh(2\beta l/\mu)}\right] \tag{17}$$

$$A = \frac{\sinh^2(\beta l/\mu) + \sin^2(\gamma l/\mu)}{\sinh^2(\beta l/\mu) + \cos^2(\gamma l/\mu)} \tag{18}$$

3.1 Analysis of the Normalized Phase. The normalized phase as a function of the modulation frequency is shown in Fig. 2, for two pairs of time delays $(\tau_q, \tau_T) = (1\times 10^{-7}\ \mathrm{s}, 2\times 10^{-8}\ \mathrm{s})$ and $(5\times 10^{-8}\ \mathrm{s}, 8\times 10^{-9}\ \mathrm{s})$ of the first layer, which are characteristic of semiconductor materials [8,30,31]. The thickness of the finite layer is $l = 10\ \mu\mathrm{m}$ and its thermal diffusivity is taken as $\alpha = 1\times 10^{-4}\ \mathrm{m^2/s}$. The corresponding phase predicted by the Fourier law ($\tau_q = \tau_T = 0$) is shown in the same figure by a dashed line.

In Fig. 2, it can be observed that for low $(\omega\tau_q, \omega\tau_T \ll 1)$ and high $(\omega\tau_q, \omega\tau_T \gg 1)$ frequencies, the normalized phases predicted by the Fourier and DPL models have the same behavior. In contrast, for middle-valued frequencies $(\omega\tau_q, \omega\tau_T \approx 1)$, where dual-

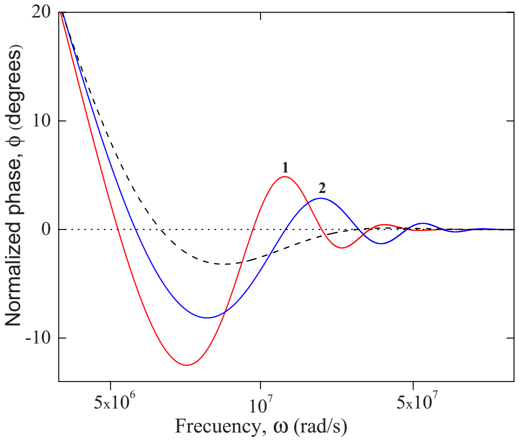

Fig. 2 **Frequency dependence at $x=0$ of the normalized phase of the temperature. The dashed line corresponds to the parabolic model and the solid lines to the DPL one, for two pairs of time delays: $(\tau_q,\tau_T)_1=(1\times10^{-7}\ \mathrm{s}, 2\times10^{-8}\ \mathrm{s})$ and $(\tau_q,\tau_T)_2=(5\times10^{-8}\ \mathrm{s}, 8\times10^{-9}\ \mathrm{s})$.**

phase effects are dominant, the DPL model predicts a remarkable oscillatory behavior, which can be used to determine the times delays τ_q and τ_T as well as additional thermal properties under the framework of the DPL model. The measurement of the frequencies at which the phase vanishes or when its maxima and minima occur would allow establishing methodologies to determine simultaneously the time delays τ_q and τ_T of a layer of thickness l when the thermal diffusivity α is known.

3.1.1 Zeros of the Phase. From Eq. (17), it can be observed that the phase vanishes at frequencies given by $2\gamma l/\mu = n\pi$ with $n=1,2,3,\ldots$. Using Eq. (9*d*), it can be shown that these frequencies satisfy

$$\frac{\sqrt{[1+(\omega\tau_q)^2][1+(\omega\tau_T)^2]}+\omega(\tau_q-\tau_T)}{1+(\omega\tau_T)^2}=\frac{\lambda_n}{\omega} \qquad (19)$$

where $\lambda_n=\omega_c(n\pi/2)^2$, with $\omega_c=2\alpha/l^2$ being the classical cutoff frequency of the finite layer [32,33]. Rewriting Eq. (19), a polynomial of second degree in τ_q and of fourth degree in τ_T is obtained, which can be expressed as follows:

$$P(\omega,\lambda_n,\tau_q,\tau_T)=0 \qquad (20)$$

Assuming that ω_n is the frequency of the nth zero of the normalized phase and ω_m is the frequency of its mth zero, such that $(n\neq m)$, the following system of equations is obtained:

$$P(\omega_n,\lambda_n,\tau_q,\tau_T)=0 \qquad (21a)$$

$$P(\omega_m,\lambda_m,\tau_q,\tau_T)=0 \qquad (21b)$$

which can be solved for τ_q and τ_T, with the constraints that they must be positive real values and satisfy Eq. (19) for any frequency ω_n with $n=1,2,3,\ldots$. These two constraints ensure that the time phase lags τ_q and τ_T are unique for a homogeneous material. The proof of this fact may be performed making the time displacements $\tau_q\to\tau_q+t_q$ and $\tau_T\to\tau_T+t_T$ in Eq. (19) and showing that its right-hand side remains constant if and only if $t_q=t_T=0$.

In this way, for a layer of known thickness and thermal diffusivity (known cutoff frequency), it is possible to determine its phase lags simultaneously by finding experimentally two frequencies at which the normalized phase vanishes. Notice that according to Fig. 2, the determination of the first two frequencies at which the normalized phase vanishes could be easier than the other ones and therefore they could be used preferably. Of course, the use of other frequencies ω_n is also possible, which permits to determine the time delays on different ways, testing our approach and taking an average representative value of the time phase lags. Note also that a convenient form of solving the system of Eqs. (21*a*) and (21*b*) is using a numerical approach with an appropriate software.

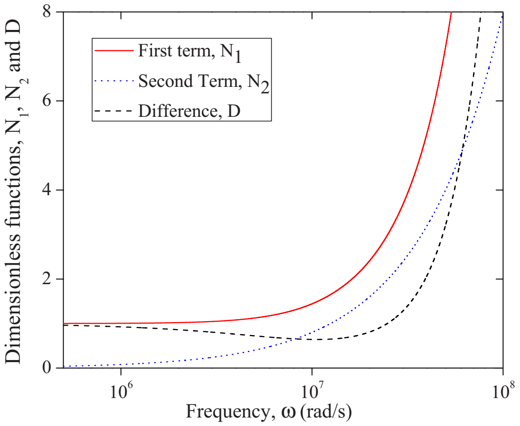

Fig. 3 **Frequency dependence of the dimensionless functions $N_1(\omega)$, $N_2(\omega)$, and $D(\omega)$, for the time delays $\tau_q=1\times10^{-7}$ s and $\tau_T=2\times10^{-8}$ s**

Calculations using modulated heat sources in DPL model have been performed previously by Basirat and Andarwa [26]. Analyzing the thermal impedance, these authors have shown that when the ratio of the time delays $\tau_T/\tau_q=0.1$, it is convenient to perform the measurement of the time delays at frequencies given by $\omega\tau_q\approx1$. As can be observed in Fig. 2, the first frequencies at which the normalized phase vanishes are given by $\omega\approx\tau_q^{-1}$, in agreement with the results of Ref. [26].

It is also possible to obtain approximated analytical results for τ_q and τ_T, observing that for any frequency ω, the first term $N_1(\omega)=\sqrt{[1+(\omega\tau_q)^2][1+(\omega\tau_T)^2]}$ in the numerator of the left-hand side of Eq. (19) is always larger than the second one, $N_2(\omega)=\omega(\tau_q-\tau_T)$ which tends to zero when $\tau_q\to\tau_T$. In this way, Eq. (19) can be approximated by

$$\sqrt{\frac{1+(\omega\tau_q)^2}{1+(\omega\tau_T)^2}}\approx\frac{\lambda_n}{\omega} \qquad (22)$$

In Fig. 3, the behavior of the functions $N_1(\omega)$, $N_2(\omega)$, and their difference $D(\omega)$ is shown, for values of phase lags $\tau_q=1\times10^{-7}$ s and $\tau_T=2\times10^{-8}$ s, which are typical of semiconductor materials [8,30,31]. It can be observed that for the range of middle-valued frequencies (larger than 10^7 rad/s), where the DPL effects are clearly present; the difference $D(\omega)$ increases when the frequency grows. A similar behavior is obtained for other values of the time delays. In this way, it can be concluded that Eq. (22) will provide closer results to the ones obtained with Eq. (19) for larger frequencies.

After writing Eq. (22) in a polynomial form, for a pair of frequencies ω_1 and ω_2, and solving for the square of the phase lags, it is found

$$\tau_q^2=\frac{(\lambda_1\omega_1)^2(\lambda_2^2-\omega_2^2)-(\lambda_2\omega_2)^2(\lambda_1^2-\omega_1^2)}{(\lambda_1\omega_1)^2\omega_2^4-(\lambda_2\omega_2)^2\omega_1^4} \qquad (23a)$$

$$\tau_T^2=\frac{\omega_1^4(\lambda_2^2-\omega_2^2)-\omega_2^4(\lambda_1^2-\omega_1^2)}{(\lambda_1\omega_1)^2\omega_2^4-(\lambda_2\omega_2)^2\omega_1^4} \qquad (23b)$$

Although Eqs. (23*a*) and (23*b*) were written for the first two frequencies at which the normalized phase vanishes, they remain valid for any other pair of frequencies at which the normalized phase has a zero. The results given by these equations will improve when larger frequencies are used.

In order to check up how good are the numerical results obtained with Eqs. (23*a*) and (23*b*) as compared with the exact values obtained with Eqs. (21*a*) and (21*b*), the third and fourth frequencies (at which according to curve 1 of the Fig. 2, the normalized phase vanishes) were determined. These are $\omega_3 = 1.541\times 10^7$ rad/s and $\omega_4 = 2.165\times 10^7$ rad/s. In this case, Eqs. (23*a*) and (23*b*) give the results: $\tau_q = 1.956\times 10^{-7}$ s and $\tau_T = 3.003\times 10^{-8}$ s. Comparing these values with the exact results $(\tau_q,\tau_T) = (1\times 10^{-7}\ \text{s}, 2\times 10^{-8}\ \text{s})$, it can be observed that, in this case, Eqs. (23*a*) and (23*b*) provide acceptable estimates of the order of magnitude of the phase lags τ_q and τ_T. To determine these time delays with more accuracy, Eqs. (21*a*) and (21*b*) have to be used.

3.1.2 Maxima and Minima of the Normalized Phase. From Eq. (17), it can be shown that the normalized phase has maxima and minima at frequencies given by

$$\left(\frac{\beta}{\mu}\right)'\tan\left(\frac{2\gamma l}{\mu}\right) - \left(\frac{\gamma}{\mu}\right)'\tanh\left(\frac{2\beta l}{\mu}\right) = 0 \tag{24}$$

where the prime ($'$) indicates derivative with respect to the frequency ω and it was assumed that $\cos(2\gamma l/\mu)\neq 0$. The transcendental Eq. (24) can be solved approximately, taking into account that according to Eqs. (9*c*) and (9*d*), for any frequency; the parameters β and γ can be approximated by

$$\beta \approx \gamma \approx \sqrt[4]{\frac{1+(\omega\tau_q)^2}{1+(\omega\tau_T)^2}} \tag{25}$$

Notice that according to Fig. 3, this approximation improves for larger frequencies. Under this consideration, Eq. (24) becomes

$$\tan(\xi) - \tanh(\xi) = 0 \tag{26}$$

where $\xi = 2\beta l/\mu$, which can be expressed as

$$\sqrt{\frac{1+(\omega\tau_q)^2}{1+(\omega\tau_T)^2}} \approx \frac{\lambda}{\omega} \tag{27}$$

with $\lambda = \omega_c(\xi/2)^2$. Notice that Eq. (27) has the same form of Eq. (22). Taking into account that the first two solutions of Eq. (26) are $\xi_1 = 3.927$ and $\xi_2 = 7.069$, and considering that the corresponding frequencies for the first two extreme value of the phase are ω_1 and ω_2, respectively; the solutions for the phase lags are given by Eqs. (23*a*) and (23*b*). In this way, it is not only possible to determine the time delays τ_q and τ_T using the zeros of the normalized phase, but also by using the frequencies at which its extreme values occur.

3.2 Analysis of the Normalized Amplitude. The normalized amplitude as a function of the modulation frequency is shown in Fig. 4, for two pairs of time delays $(\tau_q,\tau_T) = (1\times 10^{-7}\ \text{s}, 2\times 10^{-8}\ \text{s})$ and $(5\times 10^{-8}\ \text{s}, 8\times 10^{-9}\ \text{s})$ of the finite layer, which are characteristic of semiconductor materials [8,30,31]. The thickness of the finite layer is $l = 10\ \mu\text{m}$ and its thermal diffusivity is taken as $\alpha = 1\times 10^{-4}\ \text{m}^2/\text{s}$. The corresponding normalized amplitude predicted by the Fourier law $(\tau_q = \tau_T = 0)$ is shown in the same figure by dashed line.

In Fig. 4, it can be observed that for low $(\omega\tau_q,\omega\tau_T \ll 1)$ and high $(\omega\tau_q,\omega\tau_T \gg 1)$ frequencies, the normalized amplitudes predicted by the Fourier and DPL models have a similar behavior. On the other hand, for middle-valued frequencies $(\omega\tau_q,\omega\tau_T \approx 1)$, where the DPL effects are dominant, the DPL model predicts a remarkable oscillatory behavior, which can be used to determine the time delays τ_q and τ_T in a similar form as it was done, using the normalized phase.

3.2.1 Ones of the Normalized Amplitude. From Eq. (18), it can be observed that the normalized amplitude takes the unit value $(A = 1)$ at frequencies given by $\sin^2(\gamma l/\mu) = \cos^2(\gamma l/\mu)$ or $\cos(2\gamma l/\mu) = 0$, from which it is found that

$$\gamma^2 = \frac{\lambda_n}{\omega} \tag{28}$$

where $\lambda_n = \omega_c[(2n-1)\pi/4]^2$, with $n = 1,2,3,\ldots$ and $\omega_c = 2\alpha/l^2$ being the classical cutoff frequency of the finite layer [32,33]. Notice that Eq. (28) has the same form as Eq. (19) and therefore the former one can also be used to determine the phase lags, as it was explained in Sec. 3.1.1.

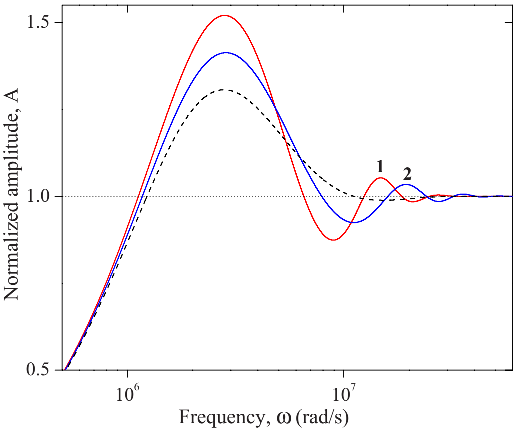

Fig. 4 Frequency dependence at $x=0$ of the normalized amplitude of the temperature. The dashed line corresponds to the parabolic model and the solid lines to the DPL one, for two pairs of time delays: $(\tau_q,\tau_T)_1 = (1\times 10^{-7}\ \text{s}, 2\times 10^{-8}\ \text{s})$ and $(\tau_q,\tau_T)_2 = (5\times 10^{-8}\ \text{s}, 8\times 10^{-9}\ \text{s})$.

3.2.2 Maxima and Minima of the Normalized Amplitude. From Eq. (18), it can be inferred that the normalized amplitude has maxima and minima at frequencies given by solving the equation

$$\left(\frac{\gamma}{\mu}\right)'\tan\left(\frac{2\gamma l}{\mu}\right) + \left(\frac{\beta}{\mu}\right)'\tanh\left(\frac{2\beta l}{\mu}\right) = 0 \tag{29}$$

where the prime ($'$) indicates derivative with respect to the frequency ω and it was assumed that $\cos(2\gamma l/\mu)\neq 0$. Under the condition expressed by Eq. (25), Eq. (29) becomes

$$\tan(\xi) + \tanh(\xi) = 0 \tag{30}$$

where ξ also satisfies Eq. (27), through the parameter $\lambda = \omega_c(\xi/2)^2$. The first two solutions of Eq. (30) are: $\xi_1 = 2.367$ and $\xi_2 = 5.498$, which can also be used to determine the phase lags τ_q and τ_T in a similar form, as it was explained in Sec. 3.1.2.

3.3 Simultaneous Measurement of Thermal Properties. It is important to mention that up to this point, our approach for the determination of the phase lags has been based on the assumption that some of the thermal properties, as the thermal diffusivity or the ratio of thermal effusivities of the materials are known. In homogeneous materials, as the individual layers analyzed in this work, measurements in the range of low modulation frequencies, using the parabolic approach, provide the value of the thermal diffusivity and thermal effusivity of the materials, which could be used in the regime of middle-valued frequencies, where the DPL effects are dominant, for the determination of the phase lags. However, it has been suggested that for a given material, it is important to measure the thermal properties using a single heat conduction model [34,35]. Therefore, it is important to establish the thermal regime in which the experiments are performed and only the simultaneous determination of the thermal properties and time delays, using the same heat transport model is adequate. In our approach, the thermal diffusivity and the time delays using the normalized phase or amplitude spectra can be determined using

Eq. (17) or (18). The thermal effusivity can then be determined using any of the non-normalized amplitudes of the signals given by Eqs. (14) and (15).

Since the parameter λ_n, appearing in the phase or amplitude analysis, depends directly on the classical cutoff frequency $\omega_c = 2\alpha/l^2$; for each value of the number $n=1,2,3,\ldots$, Eq. (20) can be rewritten as follows:

$$P(\omega, \omega_c, \tau_q, \tau_T) = 0 \tag{31}$$

Assuming that ω_1, ω_2, and ω_3 are the frequencies of the first ($n=1$), the second ($n=2$), and the third ($n=3$) zero (one) of the normalized phase (amplitude), respectively; using Eq. (31), the following system of equations is found:

$$P(\omega_1, \omega_c, \tau_q, \tau_T) = 0 \tag{32a}$$

$$P(\omega_2, \omega_c, \tau_q, \tau_T) = 0 \tag{32b}$$

$$P(\omega_3, \omega_c, \tau_q, \tau_T) = 0 \tag{32c}$$

which can be solved for τ_q, τ_T, and ω_c, using an appropriate software and with the constraints that they must be positive real values and satisfy Eq. (19) for any frequency ω_n. The thermal diffusivity can then be determined with the relation $\alpha = \omega_c l^2/2$. In this way, for a layer of known thickness, it is possible to determine its phase lags and thermal diffusivity simultaneously by finding experimentally three frequencies at which the normalized phase (amplitude) vanishes (takes the unit value). It is also possible to obtain approximated analytical formulas for τ_q, τ_T, and α in a similar form, as was done in Sec. 3.1.1 for the time delays τ_q and τ_T only. Notice that Eq. (22), which is valid for the zeros (ones) of the normalized phase (amplitude) can be written in a polynomial form as follows:

$$\rho_n^2\omega_c^2 + (\rho_n\omega)^2(\omega_c\tau_T)^2 - \omega^2\tau_q^2 = 1 \tag{33}$$

where

$$\rho_n = \frac{1}{\omega}\begin{cases}(n\pi/2)^2, & \phi = 0\\ [(2n-1)\pi/4]^2, & A = 1\end{cases} \tag{34}$$

Now, writing Eq. (33) for the frequencies ω_1, ω_2, and ω_3 at which the normalized phase (amplitude) has its first ($n=1$), second ($n=2$), and third ($n=3$) zero (one), respectively, it is found a system of three equations, whose solutions for τ_q, τ_T, and $\alpha = \omega_c l^2/2$ are

$$\tau_q = \sqrt{\frac{(\rho_1\rho_2)^2(\omega_2^2-\omega_1^2) - (\rho_1\rho_3)^2(\omega_3^2-\omega_1^2) + (\rho_2\rho_3)^2(\omega_3^2-\omega_2^2)}{(\omega_1\omega_2)^2\rho_3^2(\rho_2^2-\rho_1^2) - (\omega_1\omega_3)^2\rho_2^2(\rho_3^2-\rho_1^2) + (\omega_2\omega_3)^2\rho_1^2(\rho_3^2-\rho_2^2)}} \tag{35}$$

$$\tau_T = \sqrt{\frac{\omega_3^2(\rho_2^2-\rho_1^2) - \omega_2^2(\rho_3^2-\rho_1^2) + \omega_1^2(\rho_3^2-\rho_2^2)}{(\omega_1\omega_2)^2(\rho_2^2-\rho_1^2) - (\omega_1\omega_3)^2(\rho_3^2-\rho_1^2) + (\omega_2\omega_3)^2(\rho_3^2-\rho_2^2)}} \tag{36}$$

$$\alpha = \frac{l^2}{2}\sqrt{\frac{(\omega_1\omega_2)^2(\rho_2^2-\rho_1^2) - (\omega_1\omega_3)^2(\rho_3^2-\rho_1^2) + (\omega_2\omega_3)^2(\rho_3^2-\rho_2^2)}{(\omega_1\omega_2)^2\rho_3^2(\rho_2^2-\rho_1^2) - (\omega_1\omega_3)^2\rho_2^2(\rho_3^2-\rho_1^2) + (\omega_2\omega_3)^2\rho_1^2(\rho_3^2-\rho_2^2)}}. \tag{37}$$

Equations (35)–(37) remain valid when other frequencies, at which the normalized phase (amplitude) vanishes (takes the unit value) are used, improving their predictions for larger frequencies. In order to test how good numerical results for the phase lags and thermal diffusivity are provided by Eqs. (35)–(37), the second, third, and fourth frequencies at which, according to the curve 1 of the Fig. 2 (Fig. 3), the normalized phase (amplitude) vanishes (takes the unit value) were determined. For the normalized phase it is found that $\omega_2 = 9.470\times10^6$ rad/s, $\omega_3 = 1.541\times10^7$ rad/s, and $\omega_4 = 2.165\times10^7$ rad/s. For these frequencies, using Eqs. (34)–(37), it is found that $\tau_q = 1.480\times10^{-7}$ s, $\tau_T = 2.599\times10^{-8}$ s, and $\alpha = 8.019\times10^{-5}$ m^2/s. On the other hand, for the normalized amplitude, the corresponding frequencies are $\omega_2 = 6.536\times10^6$ rad/s, $\omega_3 = 1.242\times10^7$ rad/s, and $\omega_4 = 1.848\times10^7$ rad/s. For these values, Eqs. (34)–(37), give that $\tau_q = 1.533\times10^{-7}$ s, $\tau_T = 2.724\times10^{-8}$ s, and $\alpha = 8.205\times10^{-5}$ m^2/s. In both cases, it can be observed that these results provides reasonable estimations of the exact values of the corresponding thermal properties ($\tau_q = 1\times10^{-7}$ s, $\tau_T = 2\times10^{-8}$ s, and $\alpha = 1\times10^{-4}$ m^2/s). In addition, if better results are required, higher frequencies must be used or the system of Eqs. (32*a*)–(32*c*) can be solved. It is also important to note that Eqs. (35)–(37) remain valid when using two frequencies at which the normalized phase vanishes and one frequency at which the normalized amplitude takes the unit value or vice versa.

After determining the phase lags τ_q and τ_T, and the thermal diffusivity α, using Eqs. (32*a*)–(32*c*) or Eqs. (33)–(37); additional thermal properties can be determined through the non-normalized signals given by Eq. (14) or (15). For the case of the first one (for example) its amplitude A_1 and phase ϕ_1 are given by

$$A_1 = \frac{I_0}{\varepsilon\sqrt{\omega}}\sqrt[4]{\frac{1+(\omega\tau_q)^2}{1+(\omega\tau_T)^2}}\sqrt{\frac{\sinh^2(\beta l/\mu) + \cos^2(\gamma l/\mu)}{\sinh^2(\beta l/\mu) + \sin^2(\gamma l/\mu)}} \tag{38}$$

$$\phi_1 = -\frac{\pi}{4} + \frac{1}{2}\arctan\left[\frac{\omega(\tau_q - \tau_T)}{1+\omega^2\tau_q\tau_T}\right] - \arctan\left[\frac{\sin(2\gamma l/\mu)}{\sinh(2\beta l/\mu)}\right] \tag{39}$$

After determining the time delays τ_q and τ_T, the thermal diffusivity can also be found ($\mu = \sqrt{2\alpha/\omega}$) using Eq. (39), measuring the phase ϕ_1 for any frequency ω or for a set of them to obtain a better average result. After determining τ_q, τ_T, and the thermal diffusivity α; the thermal effusivity ε can be calculated using Eq. (38), measuring the amplitude A_1 for any frequency ω or for a set of them to get a better average result. Finally, the thermal conductivity can also be determined using the relation $k = \varepsilon\sqrt{\alpha}$.

3.4 Behavior of the Thermal Spectra for Different Time Delays.

In this section, the graphical behavior of the normalized phase and amplitude as a function of the modulated frequency, when $\tau_q > \tau_T$, $\tau_q < \tau_T$, and $\tau_q \to \tau_T$ is analyzed.

3.4.1 Behavior of the Normalized Phase. The normalized phase as a function of the modulation frequency is shown in Fig. 5(*a*) for the case $\tau_q > \tau_T$ and in the Fig. 5(*b*) for the case $\tau_q < \tau_T$. The corresponding normalized phases predicted by the Fourier law ($\tau_q = \tau_T = 0$) are shown in the same figures by dashed lines.

In Fig. 5(*a*) ($\tau_q > \tau_T$), four remarkable characteristic of the normalized phase can be observed. First, for $\tau_T > 0$ (DPL model) the normalized phase has an attenuated oscillatory behavior that re-

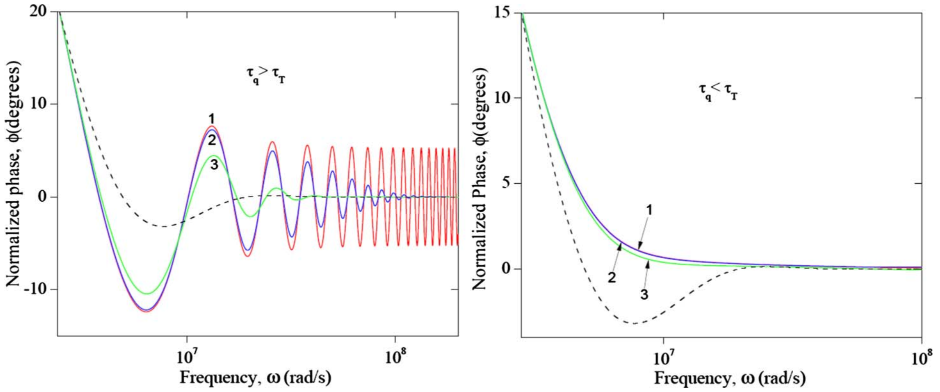

Fig. 5 Frequency dependence at $x=0$ of the normalized phase of the temperature. The dashed line corresponds to the parabolic model and the solid lines to the DPL one, for three pairs of phase lags. (*a*) $(\tau_q,\tau_T)_1=(7\times10^{-8}\ \text{s},0)$, $(\tau_q,\tau_T)_2=(7\times10^{-8}\ \text{s},1\times10^{-9}\ \text{s})$, and $(\tau_q,\tau_T)_3=(7\times10^{-8}\ \text{s},1\times10^{-8}\ \text{s})$; and (*b*) $(\tau_q,\tau_T)_1=(0,7\times10^{-8}\ \text{s})$, $(\tau_q,\tau_T)_2=(1\times10^{-9}\ \text{s},7\times10^{-8}\ \text{s})$, and $(\tau_q,\tau_T)_3=(1\times10^{-8}\ \text{s},7\times10^{-8}\ \text{s})$. In both cases the thickness of the finite layer is $l=10\ \mu\text{m}$ and its thermal diffusivity is taken as $\alpha=1\times10^{-4}\ \text{m}^2/\text{s}$.

duces to the prediction of the Fourier law, for high frequencies $(\omega\tau_q,\omega\tau_T\gg1)$. Second, the size of these oscillations is larger when the difference of the time delays increases. Third, in the extreme case where $\tau_q=\tau_T$, the normalized phase predicted by the DPL model reduces to the one predicted by the parabolic model; as it was expected. Fourth, for $\tau_T=0$ (CV model, line 1) the normalized phase presents a nonattenuated oscillatory behavior, for high frequencies $(\omega\tau_q\gg1)$. This constitutes one of the main differences with the DPL model and can be used to obtain analytical formulas to measure the thermal relaxation time $\tau=\tau_q$ when $\tau_T=0$. Notice that for $\omega\tau\gg1$ and an approximation of first order in $(\omega\tau)^{-1}$, Eq. (17) reduces to

$$\phi = 2\ \arctan\left[\frac{\sin(2\omega\tau a)}{\sinh(a)}\right] \tag{40}$$

where $a=l/\sqrt{\alpha\tau}$. Looking at the oscillatory term in Eq. (40), it can be observed that the maxima and minima of the normalized phase are given by

$$\phi_{\max} = 2\ \arctan\left[\frac{1}{\sinh(a)}\right] \tag{41a}$$

$$\phi_{\max} = -2\ \arctan\left[\frac{1}{\sinh(a)}\right] \tag{41b}$$

which occurs at the following modulation frequencies:

$$f_n = \frac{1}{2l}\sqrt{\frac{\alpha}{\tau}}\begin{cases} n+\dfrac{1}{4}, & \phi=\phi_{\max} \\ n-\dfrac{1}{4}, & \phi=\phi_{\min} \end{cases} \tag{42}$$

where $f_n=\omega_n/2\pi$, $n=1,2,3,\ldots$. Equations (41*a*), (41*b*), and (42) agree with the results presented in Ref. [36]. In this way, the measurement of the maximum and minimum values of the amplitude as well as the frequencies at which they occur, would allow to determine simultaneously the thermal relaxation time τ and the thermal diffusivity $\alpha(a=l/\sqrt{\alpha\tau})$ of a layer of thickness l, by solving the system of Eqs. (41*a*), (41*b*), and (42) for some maximum or minimum. The simultaneous measurement of additional thermal properties under the framework of the CV model, using a similar methodology is also possible [36].

In Fig. 5(*b*) $(\tau_q<\tau_T)$, it can be observed that the normalized phase presents a highly attenuated oscillatory behavior for any of the three curves that belongs to the DPL model. This is due to the fact that for $\tau_q<\tau_T$, the DPL equation of heat conduction (Eq. (5)) is of the parabolic type, whose behavior is similar to the one predicted by the Fourier law.

3.4.2 Behavior of the Normalized Amplitude. The normalized amplitude as a function of the modulation frequency is shown in Fig. 6(*a*) for the case $\tau_q>\tau_T$ and in Fig. 6(*b*) for the case $\tau_q<\tau_T$. The corresponding normalized amplitudes predicted by the Fourier law $(\tau_q=\tau_T=0)$ are shown in the same figures by dashed lines.

In Fig. 6(*a*), it can be observed that the normalized amplitude presents a similar behavior of the normalized phase for different time delays under the constraint $\tau_q>\tau_T$. For $\tau_q<\tau_T$ (see Fig. 6(*b*)), the normalized amplitude has a strongly attenuated oscillatory behavior, which was expected, because in this case Eq. (5) is of parabolic type.

For CV model, in which $\tau=\tau_q$ and $\tau_T=0$, the oscillations of the normalized amplitude can be used to measure the thermal relaxation time, by noting that for $\omega\tau\gg1$ and for a first order approximation in $(\omega\tau)^{-1}$, Eq. (18) becomes

$$A = \frac{\sinh^2(a/2)+\sin^2(\omega\tau a)}{\sinh^2(a/2)+\cos^2(\omega\tau a)} \tag{43}$$

where $a=l/\sqrt{\alpha\tau}$. Notice that the maxima and minima of the normalized amplitude are given by

$$A_{\max} = \frac{\sinh^2(a/2)+1}{\sinh^2(a/2)} = \coth^2(a/2), \tag{44a}$$

$$A_{\min} = \frac{\sinh^2(a/2)}{\sinh^2(a/2)+1} = \tanh^2(a/2), \tag{44b}$$

which occur at the following modulation frequencies:

$$f_n = \frac{1}{2l}\sqrt{\frac{\alpha}{\tau}}\begin{cases} n+\dfrac{1}{2}, & A=A_{\max} \\ n, & A=A_{\min} \end{cases} \tag{45}$$

where $f_n=\omega_n/2\pi$, $n=1,2,3,\ldots$. Equations (44*a*), (44*b*), and (45) agree with the results obtained in Ref. [36]. In this way, the measurement of the maxima and minima values of the amplitude as well as the frequencies at which they occur, would allow to determine the thermal relaxation time τ and the thermal diffusivity α, such as it was explained in Sec. 3.4.1 for the case of the normalized phase.

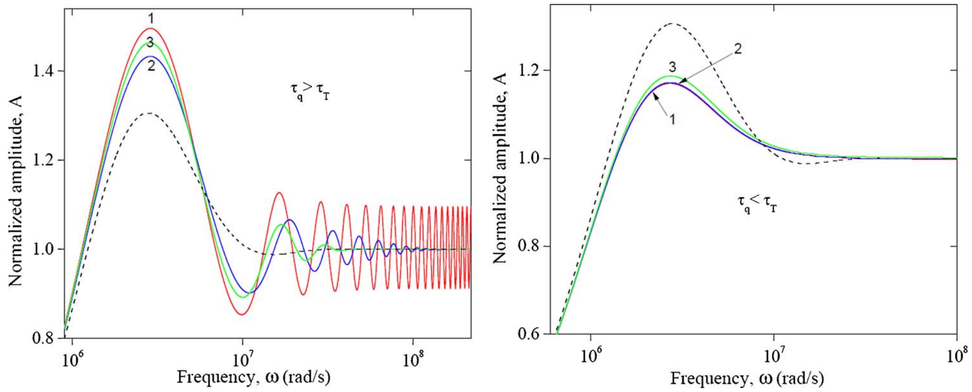

Fig. 6 Frequency dependence at $x=0$ of the normalized amplitude of the temperature. The dashed line corresponds to the parabolic model and the solid lines to the DPL one, for three pairs of phase lags. (*a*) $(\tau_q,\tau_T)_1=(7\times10^{-8}\ \mathrm{s},0)$, $(\tau_q,\tau_T)_2=(7\times10^{-8}\ \mathrm{s},1\times10^{-9}\ \mathrm{s})$, and $(\tau_q,\tau_T)_3=(7\times10^{-8}\ \mathrm{s},1\times10^{-8}\ \mathrm{s})$; and (*b*) $(\tau_q,\tau_T)_1=(0,7\times10^{-8}\ \mathrm{s})$, $(\tau_q,\tau_T)_2=(1\times10^{-9}\ \mathrm{s},7\times10^{-8}\ \mathrm{s})$, and $(\tau_q,\tau_T)_3=(1\times10^{-8}\ \mathrm{s},7\times10^{-8}\ \mathrm{s})$. In both cases the thickness of the finite layer is $l=10\ \mu\mathrm{m}$ and its thermal diffusivity is taken as $\alpha=1\times10^{-4}\ \mathrm{m}^2/\mathrm{s}$.

It is important to mention that the presented methodology is useful when the interface thermal resistance between the layers is sufficiently small to satisfy the condition $R|\lambda_0|\ll1$. Our approach considers that when the thermal effusivities of the layers are quite different, the amplitude and phase of the spatial part of the oscillatory surface temperature must be independent of the thermal properties of the semi-infinite layer. If the interface thermal resistance does not satisfy the condition $R|\lambda_0|\ll1$, the contribution of the time delays τ_{q0} and τ_{T0}, due to the semi-infinite layer cannot be neglected; therefore the presented methodology would not be applicable. In this sense our approach is a first approximation to the real problem and constitutes a limiting case of a more general formulation for the determination of the phase lags (DPL model) or the thermal relaxation time (CV model), as well as additional thermal properties under the framework of these models of heat conduction. Actually our efforts are pointed out to develop a different approach in order to take into account the interface thermal resistance between the layers.

It is important to mention that the values of the time delays that we are using in this work are the ones adequate for semiconductors and metals [30]. In contrast, for granular or porous systems these phase lags are expected to be larger [8,30] and the determination of the time delays using our methodology could be done for lower modulation frequencies and therefore an easier task than in the case of metals.

4 Conclusions

The heat transport governed by DPL model, in a system formed by a finite layer in thermal contact with a semi-infinite layer is studied. The process is induced by a modulated heat flux applied to the finite layer. It has been shown that, in contrast to the predictions of the parabolic model, remarkable oscillations of the normalized amplitude and phase of the spatial component of the surface temperature are obtained for middle-valued frequencies, where DPL effects are dominant. The experimental observation of these oscillations would constitute an unmistakable characteristic of DPL behavior of the materials. Furthermore, it has been shown that these oscillations can be used to determine the time delays for homogeneous layers, by solving polynomial systems of equations. Analytical formulas have been obtained, which provide useful estimations of the thermal properties. Additionally, it has been shown that our approach is useful in cases in which it is necessary to determine simultaneously the time delays as well as additional thermal properties of a material under the framework of the DPL model. This work constitutes a limiting case of a more general formulation considering more complex boundary conditions or higher order dual-phase lagging models and therefore it could be used as the basis for obtaining useful results for the time delays under those approaches.

Nomenclature

a = dimensionless parameter
A = normalized amplitude, K
c = specific heat, J/kg K
D = frequency-dependent function
f = frequency, Hz
F = dimensionless parameter of normalization
I = light beam intensity, $\mathrm{W/m^2}$
I_0 = normalized light beam intensity, $\mathrm{W/m^2}$
k = thermal conductivity, W/m K
l = thickness, m
N_1, N_2 = frequency-dependent functions
p = complex wave number, $\mathrm{m^{-1}}$
P = polynomial
q = heat flux, $\mathrm{W/m^2}$
R = interface thermal resistance
R' = reflection coefficient
Re() = real part
S = heat source, $\mathrm{W/m^2}$
t = time, s
T = temperature, K
x = spatial coordinate, m

Greek Symbols

α = thermal diffusivity, $\mathrm{m^2/s}$
β = dimensionless parameter
γ = dimensionless parameter
ε = thermal effusivity, $\mathrm{W\ s^{1/2}/m^2\ K}$
θ = spatial part of the oscillatory temperature, K
λ = frequency-dependent complex parameter
μ = classical thermal diffusion length, m
ρ = density, $\mathrm{kg/m^3}$
ρ_n = frequency-dependent parameter, s
τ = thermal relaxation time, s
τ_q = phase lag of the heat flux, s
τ_T = phase lag of the temperature gradient, s
ϕ = normalized phase
ω = angular frequency
ω_c = classical cutoff frequency
Ω = normalized thermal signal

Subscripts

ac = relative to the time-dependent temperature
amb = ambient
max = maximum value
min = minimum value
0 = relative to the semi-infinite layer
n = natural number

References

[1] Carslaw, H. S., and Jaeger, J. C., 1959, *Conduction of Heat in Solids*, Oxford University Press, London.

[2] Tikhonov, A. N., and Samarskii, A. A., 1990, *Equations of Mathematical Physics*, Dover, New York.

[3] Frankel, J. I., Vick, B., and Ozisik, M. N., 1987, “General Formulation and Analysis of Hyperbolic Heat Conduction in Composite Media,” Int. J. Heat Mass Transfer, **30**(7), pp. 1293–1305.

[4] Joseph, D. D., and Preziosi, L., 1989, “Heat Waves,” Rev. Mod. Phys., **61**(1), pp. 41–73.

[5] Wang, L., Zhou, X., and Wei, X., 2008, *Heat Conduction: Mathematical Models and Analytical Solutions*, Springer-Verlag, Berlin, Heidelberg.

[6] Cattaneo, C., 1948, “Sulla Coduzione del Calore,” Atti Semin. Mat. Fis. Univ. Modena, **3**, pp. 83–84.

[7] Vernotte, P., 1958, “Les Paradoxes de la Theorie Continue de L’equation de la Chaleur,” Acad. Sci., Paris, C. R., **246**(22), pp. 3154–3155.

[8] Tzou, D. Y., 1997, *Macro-to Microscale Heat Transfer: The Lagging Behavior*, Taylor & Francis, New York.

[9] Tzou, D. Y., 1989, “On the Thermal Shock Wave Induced by a Moving Heat Source,” ASME J. Heat Transfer, **111**(2), pp. 232–238.

[10] Ho, J.-R., Kuo, C.-P., and Jiaung, W.-S., 2003, “Study of Heat Transfer In Multilayered Structure Within the Framework of Dual-Phase-Lag Heat Conduction Model Using Lattice Boltzmann Method,” Int. J. Heat Mass Transfer, **46**(1), pp. 55–69.

[11] Ramadan, K., 2009, “Semi-analytical Solutions for the Dual Phase Lag Heat Conduction in Multilayered Media,” Int. J. Therm. Sci., **48**(1), pp. 14–25.

[12] Al-Huniti, N. S., and Al-Nimr, M. A., 2004, “Thermoelastic Behavior of a Composite Slab Under a Rapid Dual-Phase-Lag Heating,” J. Therm. Stresses, **27**(7), pp. 607–623.

[13] Lee, Y. M., and Tsai, T. W., 2007, “Ultra-fast Pulse Laser Heating on a Two-Layered Semi-infinite Material With Interfacial Contact Conductance,” Int. Commun. Heat Mass Transfer, **34**(1), pp. 45–51.

[14] Liu, K.-C., 2007, “Numerical Analysis of Dual-Phase-Lag Heat Transfer in a Layered Cylinder With Nonlinear Interface Boundary Conditions,” Comput. Phys. Commun., **177**(3), pp. 307–314.

[15] Xu, M., and Wang, L., 2005, “Dual-Phase-Lagging Heat Conduction Based on Boltzmann Transport Equation,” Int. J. Heat Mass Transfer, **48**(25), pp. 5616–5624.

[16] Tzou, D. Y., 1995, “Experimental Support for the Lagging Response in Heat Propagation,” J. Thermophys. Heat Transfer, **9**(4), pp. 686–693.

[17] Quintanilla, R., 2002, “Exponential Stability in the Dual-Phase-Lag Heat Conduction Theory,” J. Non-Equilib. Thermodyn., **27**(3), pp. 217–227.

[18] Tzou, D. Y., 1995, “The Generalized Lagging Response in Small-Scale and High-Rate Heating,” Int. J. Heat Mass Transfer, **38**(17), pp. 3231–3240.

[19] Tzou, D. Y., 1995, “A Unified Field Approach for Heat Conduction From Micro- to Macro-Scales,” ASME J. Heat Transfer, **117**(1), pp. 8–16.

[20] Tzou, D. Y., 1992, *Thermal Shock Phenomena Under High-Rate Response in Solids*, Hemisphere, Washington, DC, Chap. 3.

[21] Khadrawi, A. F., Al-Nimr, M. A., and Hammad, M., 2002, “Thermal Behavior of Perfect and Imperfect Contact Composite Slabs Under the Effect of the Hyperbolic Heat Conduction Model,” Int. J. Thermophys., **23**(2), pp. 581–598.

[22] Almond, D. P., and Patel, P. M., 1996, *Photothermal Science and Techniques*, Chapman and Hall, London.

[23] McDonald, F. A., and Westel, G. C., Jr., 1978, “Generalized Theory of the Photoacoustic Effect,” J. Appl. Phys., **49**(4), pp. 2313–2322.

[24] Salazar, A., Sánchez-Lavega, A., and Terrón, J. M., 1998, “Effective Thermal Diffusivity of Layered Materials Measured by Modulated Photothermal Techniques,” J. Appl. Phys., **84**(6), pp. 3031–3041.

[25] Pichardo, J. L., and Alvarado-Gil, J. J., 2001, “Open Photoacoustic Cell Determination of the Thermal Interface Resistance in Two Layer Systems,” J. Appl. Phys., **89**(7), pp. 4070–4075.

[26] Basirat Tabrizi, H., and Andarwa, S., 2009, “A Method to Measure Time Lag Constants of Heat Conduction Equations,” Int. Commun. Heat Mass Transfer, **36**(2), pp. 186–191.

[27] Myers, G. E., 1971, *Analytical Methods in Conduction Heat Transfer*, McGraw-Hill, New York, pp. 167–172.

[28] Rohsenow, W. M., and Hartnett, J. P., 1973, *Handbook of Heat Transfer*, McGraw-Hill, New York.

[29] Salazar, A., 2003, “On Thermal Diffusivity,” Eur. J. Phys., **24**(4), pp. 351–358.

[30] Vedavarz, A., Kumar, S., and Moallemi, M. K., 1994, “Significance of Non-Fourier Heat Waves in Conduction,” ASME J. Heat Transfer, **116**(1), pp. 221–224.

[31] Sharma, K. R., 2005, *Damped Wave Transport and Relaxation*, Elsevier, The Netherlands.

[32] Vargas, H., and Miranda, L. C. M., 1988, “Photoacoustic and Related Photothermal Techniques,” Phys. Rep., **161**(2), pp. 43–101.

[33] Marín, E., Pichardo, J. L., Cruz-Orea, A., Diaz, P., Torres-Delgado, G., Delgadillo, I., Alvarado-Gil, J. J., Mendoza-Alvarez, J. G., and Vargas, H., 1996, “On the Thermal Characterization of Two-Layer Systems by Means of the Photoacoustic Effect,” J. Phys. D, **29**(4), pp. 981–986.

[34] Roetzel, W., Putra, N., and Das, S. K., 2003, “Experiment and Analysis for Non-Fourier Conduction in Materials With Non-homogeneous Inner Structure,” Int. J. Therm. Sci., **42**(6), pp. 541–552.

[35] Antaki, P. J., 2005, “New Interpretation of Non-Fourier Heat Conduction in Processed Meat,” ASME J. Heat Transfer, **127**(2), pp. 189–193.

[36] Ordóñez-Miranda, J., and Alvarado-Gil, J. J., 2009, “Thermal Wave Oscillations and Thermal Relaxation Time Determination in a Hyperbolic Heat Transport Model,” Int. J. Therm. Sci., **48**(11), pp. 2053–2062.

On the Mechanism of Pool Boiling Critical Heat Flux Enhancement in Nanofluids

Hyungdae Kim[1]
Department of Nuclear Engineering,
Kyung Hee University,
Yongin-city 446-701, Republic of Korea
e-mail: hdkims@khu.ac.kr

Ho Seon Ahn

Moo Hwan Kim
Professor
e-mail: mhkim@postech.ac.kr

Department of Mechanical Engineering,
POSTECH,
Pohang,
Gyungbuk 790-784, Republic of Korea

The pool boiling characteristics of water-based nanofluids with alumina and titania nanoparticles of 0.01 vol % were investigated on a thermally heated disk heater at saturated temperature and atmospheric pressure. The results confirmed the findings of previous studies that nanofluids can significantly enhance the critical heat flux (CHF), resulting in a large increase in the wall superheat. It was found that some nanoparticles deposit on the heater surface during nucleate boiling, and the surface modification due to the deposition results in the same magnitude of CHF enhancement in pure water as for nanofluids. Subsequent to the boiling experiments, the interfacial properties of the heater surfaces were examined using dynamic wetting of an evaporating water droplet. As the surface temperature increased, the evaporating meniscus on the clean surface suddenly receded toward the liquid due to the evaporation recoil force on the liquid-vapor interface, but the nanoparticle-fouled surface exhibited stable wetting of the liquid meniscus even at a remarkably higher wall superheat. The heat flux gain attainable due to the improved wetting of the evaporating meniscus on the fouled surface showed good agreement with the CHF enhancement during nanofluid boiling. It is supposed that the nanoparticle layer increases the stability of the evaporating microlayer underneath a bubble growing on a heated surface and thus the irreversible growth of a hot/dry spot is inhibited even at a high wall superheat, resulting in the CHF enhancement observed when boiling nanofluids. [DOI: 10.1115/1.4000746]

Keywords: critical heat flux, evaporating meniscus, nanofluids, nanoparticle deposition, wetting

1 Introduction

Nucleate boiling is a highly efficient heat-transfer mode for removing large amounts of heat at a low temperature difference. However, a maximum value of the heat flux, known as a critical heat flux (CHF), exists at which nucleate boiling transitions to film boiling, which is a very poor boiling heat-transfer regime. As a result of the CHF phenomenon, the temperature of the heated surface increases tremendously, thus causing serious damage to the thermal systems. Obviously, a higher CHF is desirable. Accordingly, various techniques to enhance the boiling CHF have been proposed and studied. Typical approaches that have been considered include the following: (a) oxidation or selective fouling of a heater surface to increase the wettability of the liquid; (b) vibration of heaters to promote the departure of bubbles from a heater surface; (c) coating or extending the heater surface to increase the heat-transfer area; (d) heater rotation to promote bubble departure from, and liquid deposition onto, the heater surface; (e) fluid vibration to promote bubble departure and liquid supply; and (f) application of electric fields to promote bubble departure from the surface using dielectrophoretic forces to increase liquid renewal [1].

A nanofluid is a colloidal suspension in which many nanosized particles are uniformly and stably dispersed. You et al. [2] introduced a new CHF enhancement approach using nanofluids and demonstrated that adding tiny amounts (less than 0.001% by volume) of alumina nanoparticles to a conventional cooling liquid could significantly increase the CHF up to ∼200%. However, such a large CHF enhancement in nanofluids cannot be interpreted using traditional hydrodynamic instability models. Because of its potential for a remarkable CHF enhancement and scientific interest about its mechanism, boiling heat-transfer studies for nanofluids have attracted considerable attention, especially those concerned with the CHF.

Many experimental studies [3–5] have found that a major deposition of nanoparticles occurs on the heater surface during nanofluid boiling. Particle type, size, concentration, and pH of the nanofluids affected morphology of the porous deposition layer, which seemed to be responsible for the greatest increase in CHF [6,7]. Kim et al. [8,9] carried out pool boiling experiments with pure water on a nanoparticle-fouled heater that was prepared using preboiling in water-based nanofluids and found that the significant CHF increase in nanofluids could be reproduced only due to the nanoparticle-surface deposition. The same results were recently obtained by Golubovic et al. [10]. Therefore, it was suggested that interfacial parameter improvements due to the nanoparticle fouling could be a key factor in the significant increase in the nanofluid CHF. Kim et al. [11] reported that the nanoparticle-fouled surfaces significantly improved wettability as measured by a reduction in the static equilibrium contact angle. They based their suggestion on a review of the prevalent CHF theories stating that the improved wettability caused by the nanoparticle layer could explain the CHF enhancement. Kim and Kim [12] also found that a porous layer of nanoparticles significantly improved the surface wettability, but noted that the effect of wettability alone could not explain the CHF enhancement in nanofluids. Focusing on the role of the heater surface capillarity in the CHF, they demonstrated that the liquid spreads dynamically on nanoparticle-coated surfaces due to capillarity. They concluded that the significant CHF enhancement of nanofluids during pool boiling is a consequence of not only the increased surface wettability but also the improved capillarity due to the surface deposition of nanopar-

---

[1] This author is currently working at Massachusetts Institute of Technology. This work was performed when he was working at POSTECH.

Contributed by the Heat Transfer Division of ASME for publication in the JOURNAL OF HEAT TRANSFER. Manuscript received April 7, 2009; final manuscript received October 2, 2009; published online March 25, 2010. Assoc. Editor: Satish G. Kandlikar.

ticles. Liu and Liao [13] and Coursey and Kim [14] performed pool boiling experiments of water-based and alcohol-based nanofluids on a plain heated surface. Both studies confirmed with the static contact angle measurement that the nanoparticle layer formed on the heater surface improved the wettability significantly. Coursey and Kim [14] also showed that the surface treatment, like oxidation, alone resulted in a similar CHF enhancement to nanofluids. In summary, various previous studies suggest that the likely CHF enhancement mechanism for nanofluids appears to be an improvement in the ability of the fluid to wet the surface due to the thin nanoparticle sorption layer.

On the other hand, Sefiane [15] proposed a different approach to clarify the mechanism through which the presence of nanoparticles affects the heat transfer and CHF during boiling. He showed experimentally that the nanoparticles in the liquid promote the pinning of the contact angle line of the evaporating meniscus and sessile drops. He explained that the observed results were due to the structural disjoining pressure stemming from the ordered layering of nanoparticles in the confined wedge of the evaporating meniscus [16] and suggested that an analysis of the boiling heat transfer of nanofluids might account for the strong effect of nanoparticles on the contact line region through the structural disjoining pressure. Wen [17] further investigated the influence of nanoparticles on the structural disjoining pressure. He calculated the equilibrium meniscus shape in the presence of nanoparticles in liquid and found that the vapor-liquid-solid line could be significantly displaced toward the vapor phase in the presence of nanoparticles in liquid. Thus, he concluded that the structural disjoining pressure due to nanoparticles in liquid could significantly increase the wettability of the fluids and inhibit the development of dry patches, which trigger the CHF.

The preceding literature review has demonstrated that the remarkable CHF enhancement in nanofluid pool boiling is likely due to the improved ability of the fluid to wet the surface, though it is not clear whether the wetting improvement is obtained by surface wettability enhancement or structural disjoining pressure due to the ordered layering of nanoparticles. At this stage, to understand the mechanism of the CHF enhancement in nanofluids, the first question of interest must be whether this enhancement is caused by the nanoparticles suspended in liquid or the nanoparticles deposited on the surface. After this question is answered clearly, we can focus on exploring the exact mechanism by which the improved ability of the fluid to wet the surface increases the CHF. The present work was designed to resolve these two issues.

In this paper, we introduce the results from two experimental studies. The first is pool boiling experiments to judge whether the nanofluid CHF enhancement is due to the nanoparticles dispersed in the liquid (the actual nanofluid) or the nanoparticle layer deposited on the heater surface during boiling. For the same purpose, Kim et al. [8,9] and Golubovic et al. [10] have carried out the similar experiments on thin electrically heated metallic wires. However, applying the electric potential to heat the thin wire can cause nanoparticles in liquid to migrate and accumulate on the heater surface, which is well known as the electrophoretic phenomenon in electrolytes [18]. Thus, the direct electric heating technique of the boiling surface could be suspected of the nanoparticle deposition distorting the boiling characteristics of nanofluids. In addition, the CHF studies on the flat plate are of importance for the practical application, as the geometries of actual heat-transfer components in thermal systems are either a flat surface or a cylinder with a large diameter, and thus boiling tests on the flat surfaces (versus thin wires) are required. Therefore, we decided to reinvestigate pool boiling characteristics of nanofluids using a horizontal flat surface heated by conduction heat transfer. Using the new experimental facility, the boiling curves for nanofluids on clean surfaces and for pure water on a nanofluid-preboiled surface are obtained. As a result, a comparison of the CHF values reveals that the CHF increase in nanofluids resulted from the surface changes caused by the nanoparticle deposition during nanofluid boiling.

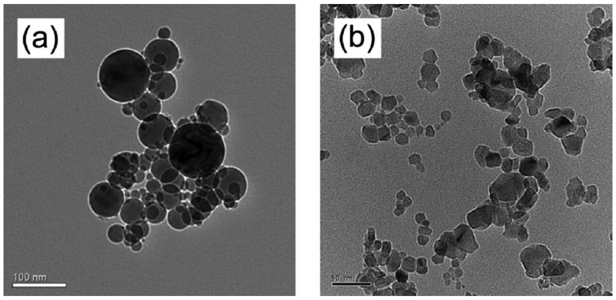

Fig. 1 TEM photographs of nanoparticles dried after dispersion into pure water: (*a*) alumina and (*b*) titania

The second experiment is a photographic investigation of a water droplet impinging on a clean and a nanoparticle-deposited surface at surface temperatures ranging from 100°C to 200°C, which includes the temperatures at which the CHF transition occurred in the pool boiling experiments with both pure water and nanofluids. To examine the effect of the nanoparticle layer on the ability to wet the heated surface, the behavior of the evaporating meniscus is carefully examined by measuring the dynamic contact angles at the edges of the droplet. The results are analyzed based on a force balance of the evaporation vapor recoil and the surface tension force on the steady-state evaporating meniscus. Finally, the most plausible mechanism for the CHF enhancement during nanofluid pool boiling is deduced based on the experimental results and their analyses.

2 Experimental

2.1 Preparation and Characterization of Nanofluids. Two types of nanoparticle materials were used in this study: alumina (Al_2O_3) and titania (TiO_2). The nanosized powders of these materials were purchased from NanoPhase Technologies Corp. (alumina) and Advanced Nano Products (titania). The average sizes of the dry nanoparticles supplied by the vendors were 47 nm and 45 nm for alumina and titania, respectively. Water-based nanofluids were prepared by dispersing the dry powders into de-ionized, distilled water with 3 h of ultrasonic vibration. No additives such as dispersants or surfactants were used to stabilize the nanoparticle suspensions because they alone can influence boiling heat transfer significantly [19]. The nanoparticles were dried after the dispersion and visualized with transmission electron microscopy (TEM) to observe their shape. As shown in Figs. 1(*a*) and 1(*b*), the shapes of the alumina and titania nanoparticles were spherical and polygonal, respectively. The individual particle sizes seems consistent with the vendor-specified particle sizes, but some larger nanoparticle clusters were observed that might have been due to agglomerations of the individual particles in the fluid.

The thermophysical properties relevant to the boiling phenomena were measured or estimated for water-based alumina and titania nanofluids with 0.01 vol % of nanoparticle concentration. The surface tension, thermal conductivity, and viscosity of the nanofluids were measured by means of a SenaDyne QC6000 surface tensiometer (CSC Scientific), a transient hot wire, and a SV10 viscometer (A&D Corporation), respectively. All the nanofluids properties were very close to those of pure water (within ±3%) due to the low nanoparticle concentration in the nanofluids. Accordingly, we do not believe that the boiling phenomena were significantly affected by changes in the thermophysical properties of the nanofluids in this study.

2.2 Pool Boiling Apparatus. Figure 2 shows a schematic diagram of the pool boiling experimental facility. It consisted of a

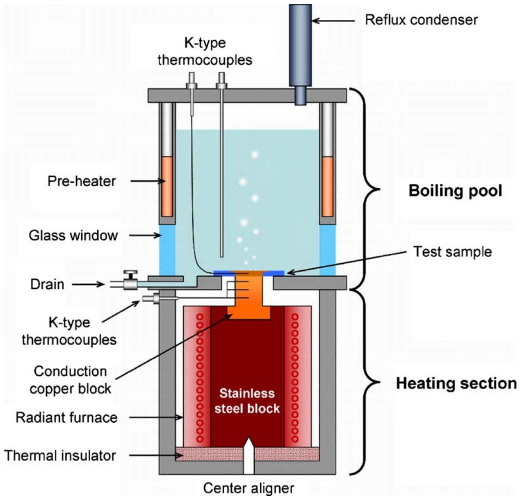

Fig. 2 Schematic diagram of the pool boiling facility

boiling pool, test sample, heating section, and data acquisition system. The boiling pool, which contained either de-ionized distilled water or nanofluids, was a 150-mm-inner-diameter cylindrical stainless steel chamber with a height of 200 mm. Eight cartridge heaters with a peak heating power of 250 W were embedded into the wall of the chamber to preheat the working fluid. A reflux condenser was located at the top of the chamber to condense the phase-changed vapor into liquid. Four K-type thermocouples were immersed into the pool to measure the temperature of the bulk fluid. During the experiment, the bulk temperature was maintained at 100°C using a feedback control of the thermocouples and preheaters. Two glass windows were located in the side wall of the boiling pool to visualize the boiling phenomenon on the heater surface. The test sample for the boiling experiment was placed at the bottom of the boiling pool. During the experiment, the test sample was heated by conduction heat transfer from the heater, which consisted of a cylindrical copper block, a conductive stainless steel block, and a radiant furnace. The radiant furnace with a peak heating power of 4 kW increased the temperature of the stainless steel block, and the thermal energy was transferred through the cylindrical copper block to the test sample via conduction heat transfer.

2.3 Heater Design. Figure 3 shows a detailed schematic diagram of the test sample and cylindrical conduction copper block. The test sample consisted of a high-grade (99.999%) copper disk with a thickness of 7 mm and a diameter of 20 mm, and side insulation made of Peek high-temperature plastic with a very low thermal conductivity (~ 0.5 W/m/K) relative to copper (~ 400 W/m/K). The microsized crevices between the boiling surface and side insulation are the preferred cavities of bubble nucleation, and premature bubble nucleation from these unpredictable cavities severely distorts the boiling heat-transfer characteristics, eventually resulting in poor repeatability of the boiling experiments. In this regard, to prevent the nucleation of premature bubbles and to enhance the accuracy of the experiments, the top surface of the circular copper disk was extended to include a 0.1-mm-thick, 28-mm-diameter disk fin. This heater geometry successfully prevented the unpredictable bubble generation around the edge of the heater surface, as shown in Fig. 4. Such a clear boiling phenomenon resulted in very good experimental repeatability for the pool boiling curves of pure water, which are shown later in Sec. 3. A 0.5-mm-diameter K-type thermocouple was horizontally inserted into the center of the test sample through the Peek insulator to measure the temperature of the boiling surface. The thermocouple was located 2.5 mm below the boiling surface.

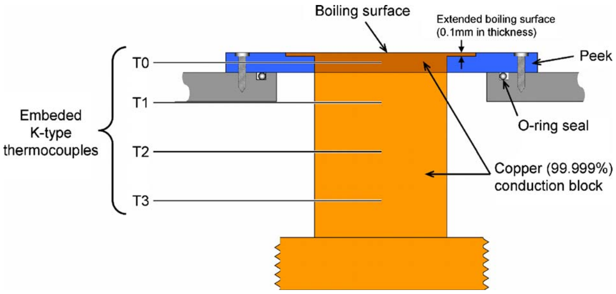

Fig. 3 Detailed design of the test heater

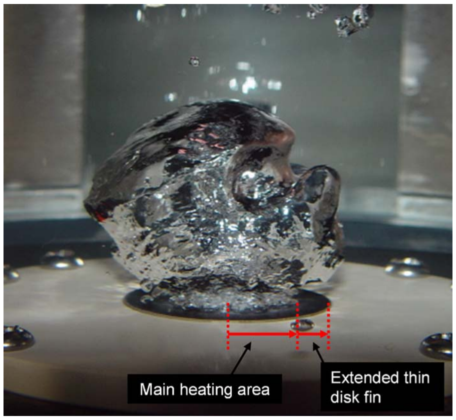

Fig. 4 Visualization of boiling phenomena of pure water at $q'' \sim 1300$ kW/m^2 on the present flat surface heater with the thin disk fin to prevent the undesired bubble nucleation from the heater edge

The cylindrical conduction copper block was made of high-grade copper materials. It transferred the thermal energy from the heating section to the test sample. The side wall of the block was insulated with ultrahigh-temperature insulating material with a thermal conductivity of 0.1 W/m/K. Three 0.25-mm-diameter K-type thermocouples were horizontally embedded at the center axial line of the cylindrical copper block and separated by gaps of 7 mm.

2.4 Measurement and Uncertainty. The heat flux and surface temperature of the test sample during the experiment must be measured to obtain the boiling curve. The heat flux was measured using the temperature data gathered in the cylindrical conduction copper block. We assumed that the heat loss through the insulation was negligible in the conduction block surrounded by the thermal insulator since the thermal conductivity of the copper was three orders of magnitude higher than that of the insulation material. The heat flux can be described by the one-dimensional, steady-state conduction heat-transfer equation

$$q'' = k\frac{T_2 - T_1}{\Delta x} \tag{1}$$

The surface temperature of the test sample was calculated by extrapolating the measured temperature inside the sample using the heat flux obtained by Eq. (1)

$$\Delta T_{\mathrm{wall}} = T_{\mathrm{wall}} - T_{\mathrm{sat}} = \left(T_0 - \frac{q''d}{k}\right) - T_{\mathrm{sat}} \tag{2}$$

The experimental uncertainty can be represented using the method proposed by Holman [20] as follows:

$$\frac{U_{q''}}{q''} = \sqrt{\left(\frac{U_{T_2-T_1}}{T_2 - T_1}\right)^2 + \left(\frac{U_{\Delta x}}{\Delta x}\right)^2} \qquad (3)$$

$$\frac{U_{\Delta T_{\text{wall}}}}{\Delta T_{\text{wall}}} = \sqrt{\left(\frac{U_{T_0-T_{\text{sat}}}}{T_0 - T_{\text{sat}}}\right)^2 + \left(\frac{U_{q''}}{q''}\right)^2 + \left(\frac{U_d}{d}\right)^2} \qquad (4)$$

The accuracy of the K-type thermocouples used in the present experiments was ±0.5°C. The maximum fabrication error of the temperature measuring positions was 0.15 mm. In addition, another important source of uncertainty in the heat flux measurement was the heat conduction from the heating block to the thin disk fin. This heat flow introduced the only positive error in the heat flux measurement. The error due to this heat loss was evaluated through a two-dimensional numerical heat-transfer analysis for our heater geometry using the FLUENT® commercial CFD code. To calculate the maximum conduction heat loss, the same boiling heat-transfer coefficient was applied to both the main boiling surface and thin-fin region, even though the latter must have a lower heat-transfer coefficient due to the steep temperature drop on the disk. As a result, the estimated maximum heat loss through the thin disk fin was 10.4% when the heat flux from the conduction block was 2000 kW/m^2. Thus, the overall maximum uncertainties in the CHF and wall superheat measurements were 12.8% and 13.2%, respectively.

2.5 Experimental Procedure. The surface of a test sample was uniformly polished with No. 220 sandpaper and thoroughly rinsed with distilled water before each initial boiling test. The arithmetic surface roughness was found to be 0.21 μm. The test sample was mounted at the center of the bottom of the boiling pool, and then it was mechanically clamped to the heater. Distilled water or nanofluid was poured into the boiling pool and preheated to 100°C using the cartridge heaters in the wall. The electric power to the furnace of the heating section was increased slightly until the temperature of the test sample reached the temperature of the working fluid. Then, the AGILENT 34970A data acquisition system was turned on to gather data from the temperature sensors. The heat flux was stepwise increased with an average increasing rate of 14 $\text{kW/m}^2\text{/min}$ during the entire boiling experiment. Each data point was gathered under the steady-state conditions of heat flux and wall superheat. The occurrence of the CHF was detected by a sudden increase in the temperature T_0 of the thermocouple embedded in the test sample. Just after the CHF occurred, the experiment was stopped and the boiling pool with the test sample was quickly disassembled from the heating section to preserve the condition of the boiling surface at the CHF point.

3 Pool Boiling Results

3.1 Boiling Curves for Pure Water and Nanofluids. Prior to the nanofluid tests, a set of pool boiling tests was performed in distilled water on the copper surface to verify the procedure and repeatability. As shown in Fig. 5, the experimental data for pure water showed good repeatability for nucleate boiling heat transfer and the CHF, with a scatter within ±10% and ±5%, respectively. This result indicates that the basic parameters, such as the roughness of the heating surface and the temperature of the bulk fluid, were uniformly maintained. The data for the nucleate boiling region were in good agreement with the Rohsenow and Griffith [21] correlation for a water-copper surface. The CHF values were considerably higher than the prediction by the Zuber [22] correlation for an infinite flat surface, but close to the prediction by the Haramura and Katto [23] correlation for a small horizontal disk, which included the effect of an inflow of liquid to the heater surface from the surrounding. The present CHF results, about 13% higher than the Haramura and Katto [23], appear to be reasonable in light of the heat-conduction heat loss through the thin disk fin. In addition, we carried out ad hoc tests of pure water on the 1-cm-diameter circular heater without the extended fin and obtained the CHF value of 1540 kW/m^2, which is remarkably close to the prediction by the Haramura and Katto [23] correlation. This result revealed that the deviation of ~13% in the CHF values was truly due to the conduction heat loss through the increased heat-transfer area, and thus that the CHF results obtained in the present experimental study were reasonable. Accordingly, the repeatability and reproducibility of the pool boiling facility appeared sufficient to systemically investigate the nucleate boiling heat transfer and CHF in nanofluids.

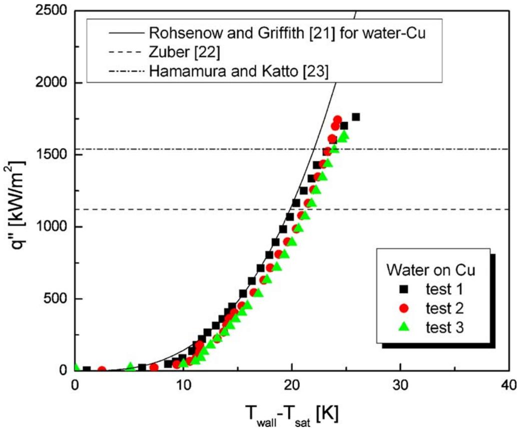

Fig. 5 Boiling curves for distilled water on a copper surface

Figure 6 shows representative pool boiling curves for pure water and 0.01 vol % alumina nanofluid on a copper surface. Both fluids had almost an identical heat-transfer performance under the natural convection regime. As the surface heat flux increased, the onset of nucleate boiling (ONB) occurred at a similar wall superheat of ~12°C, but the nucleate boiling heat-transfer performance of the nanofluid was degraded when compared with pure water, which had a higher wall superheat. However, the alumina nanofluid provided a ~30% enhancement in the CHF above the value of pure water, and the wall superheat at the CHF point also increased significantly by 50°C: $q''_{\text{CHF}} = 1740\ \text{kW/m}^2$ at $\Delta T_{\text{wall}} = 26°\text{C}$ for pure water, and $q''_{\text{CHF}} = 2260\ \text{kW/m}^2$ at $\Delta T_{\text{wall}} = 76°\text{C}$ for the alumina nanofluid. The increased CHF was considerably higher than the Zuber [22] correlation or the Haramura and Katto [23] correlation predictions. It is worthwhile to mention that the CHF values for pure water and alumina nanofluids observed in the present study were remarkably close to the CHF

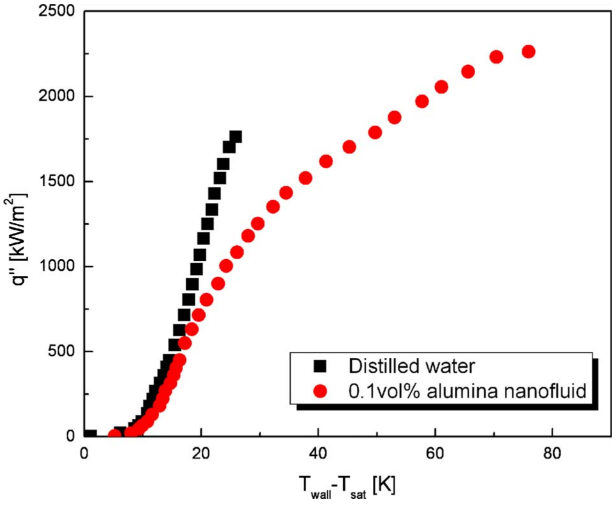

Fig. 6 Boiling curves for pure water and alumina nanofluid on a copper surface

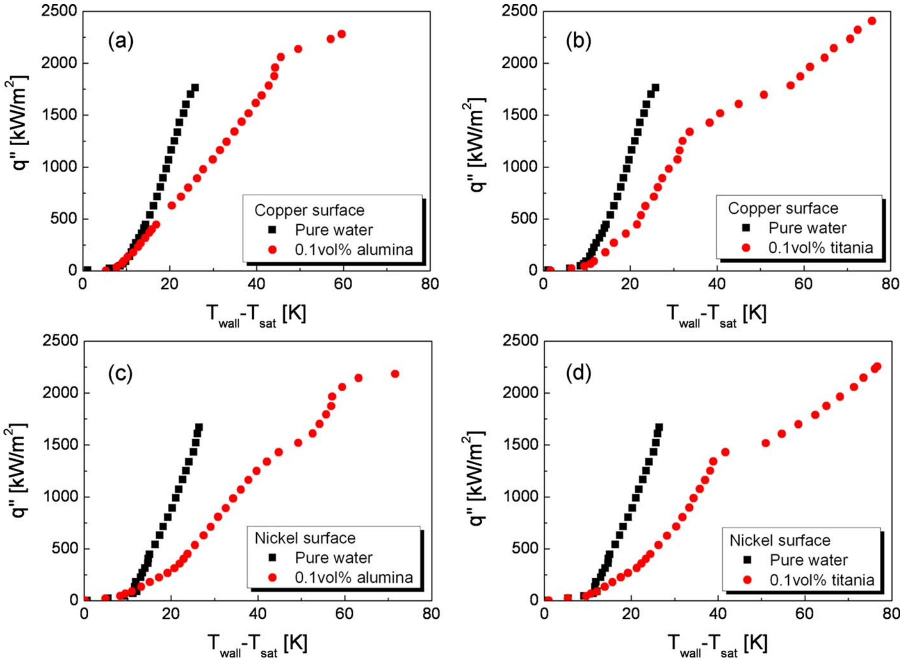

Fig. 7 Boiling curves for nanofluids: (*a*) alumina on copper, (*b*) titania on copper, (*c*) alumina on nickel, and (*d*) titania on nickel

values obtained by Bang and Chang [4] on the rectangular plain surface: for water and alumina nanofluids, $1740\ \text{kW/m}^2$ and $2260\ \text{kW/m}^2$, respectively, at 0.01 vol % in the present study versus $1740\ \text{kW/m}^2$ and $2300\ \text{kW/m}^2$, respectively, at 0.5 vol % in Ref. [4]. The trends of the nucleate boiling heat transfer and CHF for the alumina nanofluid were fairly similar to those for the titania nanofluid, regardless of whether the heater surfaces were made of copper or nickel-plated copper, as shown in Figs. 7(*a*)–7(*d*).

3.2 Nanoparticle Deposition During Nanofluid Boiling. A nanoparticle deposit layer formed on the heater surface during the nanofluid boiling, as shown in Figs. 8(*a*)–8(*d*), which was consistent with other nanofluid boiling studies. Many previous nanofluid boiling experiments were carried out using an electrically heated thin-metal wire or plate. However, the direct electric heating of the boiling surface has been suspected as the reason for the nanoparticle deposition because the electric field generated around the heater surface might have caused the dispersed nanoparticles to migrate and accumulate on the electrodes [18]. Therefore, the boiling surface used in this study was thermally heated by conduction without the influence of an electric field. As a result, the nanoparticle deposition layer shown in Figs. 8(*a*)–8(*d*) must have been due to the nanoparticle-surface interaction during the nanofluid boiling. Kim et al. [11] explained that the evaporation of the microlayer with the subsequent settlement of the nanoparticles initially contained in it was responsible for the formation of the porous layer.

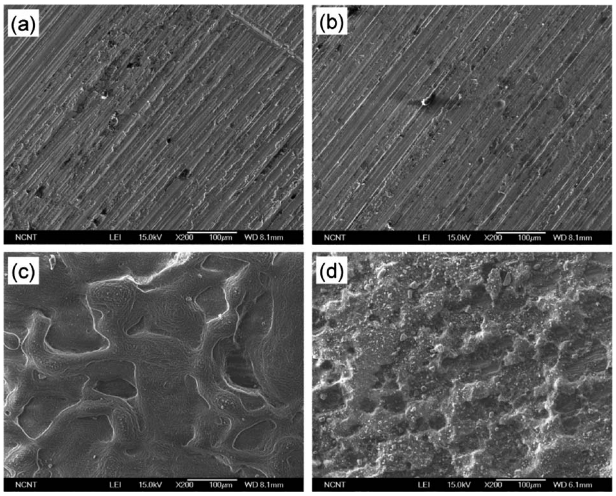

Fig. 8 SEM photographs of various copper heater surfaces: (*a*) fresh, (*b*) water-boiled, (*c*) alumina nanofluid-boiled, and (*d*) titania nanofluid-boiled

3.3 Effect of the Nanoparticle Deposition on the CHF. To experimentally examine the effect of the nanoparticle deposition on the CHF in pool boiling with nanofluids, two successive boiling experiments were performed. First, a nanofluid pool boiling experiment on a clean heater surface was carried out using the same procedure as the normal boiling experiment, but the heat flux was increased up to ~90% of the CHF value for the specific nanofluid. Next, a subsequent pool boiling experiment of pure water on the nanofluid-boiled (or nanoparticle-fouled) surface was conducted by changing only the working fluid from the nanofluid to pure water. Figure 9 shows the results of the successive boiling tests for the alumina nanofluid. The nucleate boiling initiated at the higher wall superheat on the nanoparticle-fouled surface, and the nucleate boiling heat transfer was considerably degraded compared with that on the clean surface. However, an appreciable CHF enhancement for pure water occurred due to the nanoparticle layer $q''_{\text{CHF}} \sim 2200\ \text{kW/m}^2$ on the nanoparticle-fouled surface versus $q''_{\text{CHF}} \sim 1740\ \text{kW/m}^2$ on the clean surface.

Figures 10(*a*)–10(*c*) compare the boiling curves for nanofluids on an initially clean surface and pure water on a nanoparticle-fouled surface. On the fouled surface, the nucleate boiling initiated at a higher wall superheat, and the heat-transfer rate was lower in the low heat flux range below $1500\ \text{kW/m}^2$. However, the slope of the boiling curve for pure water was steeper, and thus in the high heat flux region, the heat-transfer rate became higher than that of the nanofluids. However, the CHF values for two cases appeared to be close.

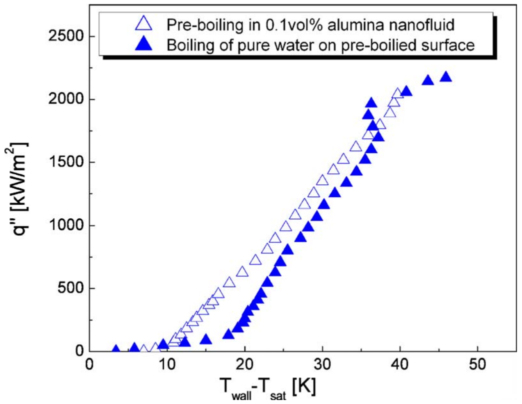

Fig. 9 Boiling curves for preboiling of alumina nanofluids on a fresh copper surface and subsequent boiling of pure water on a nanofluid-boiled surface

For a better understanding of the influence of the nanoparticle deposition, the comparison of the measured heat flux and wall superheat values at the CHF points are summarized in Table 1. Regardless of the substrate and nanoparticle material, the CHF data for pure water on the fouled surface were within ±12.4% of the nanofluid CHF values, which is close to the maximum uncertainty of the present pool boiling experiments. This observation is identical with those of Kim et al. [8,9] and Golubovic et al. [10] on the electrically heated thin wires though each CHF increase in nanofluids is different due to the difference in heater geometry, as shown in Fig. 11. Therefore, those results suggest that the CHF increase in the nanofluids is due to the nanoparticle layer on the heater surface. Furthermore, this conclusion is compatible with the recent work of Kim et al. [24], who studied pool boiling heat transfer by quenching hot spheres into nanofluids. Their results showed that the CHF was enhanced not in the initial quenching of the clean sphere into the nanofluids, but in the subsequent quenching of the same sphere. If the nanoparticles in liquid had played an important role in the nanofluid CHF enhancement, the initial quenching should have resulted in a considerable increase in the CHF because the nanoparticles could hardly have been deposited on the heated surface during film boiling. Based on all of the available experimental results, we can conclude that the main cause of the CHF increase in nanofluids appears to be the nanoparticle deposition on the heater surface that occurs during the nucleate boiling process. That is, when dispersing a small amount of alumina or titania nanoparticles into pure water, the boiling-induced deposition of the nanoparticles modifies the heater surface to have better properties for effectively delaying the CHF.

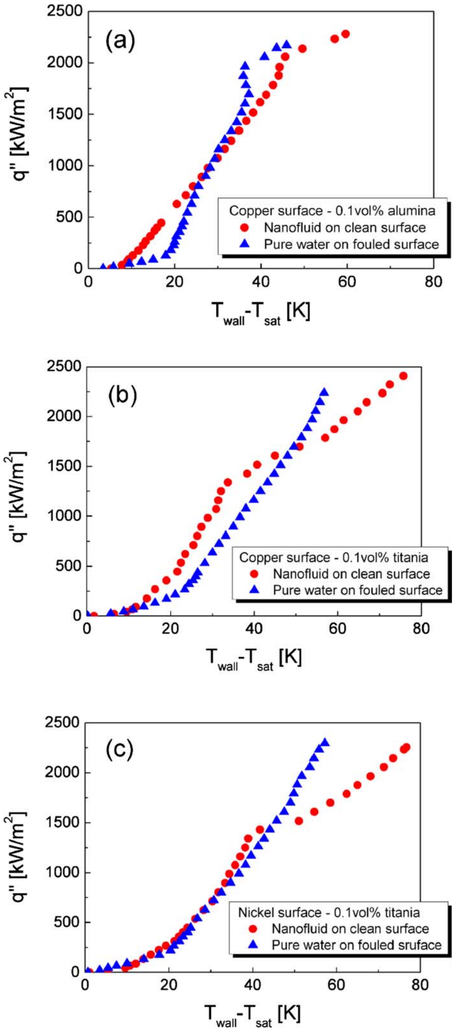

Fig. 10 Comparison of boiling curves for nanofluids on a fresh surface and pure water on a nanoparticle-fouled surface: (*a*) alumina on copper, (*b*) titania on copper, and (*c*) titania on nickel

The wall superheat at the CHF point marked a considerable difference between a nanofluid on a clean surface and pure water on a fouled surface: the latter showed a 20°C lower wall superheat than the former. Note that this trend is exactly the same as the results obtained by Coursey and Kim [14] in nanofluid pool boiling experiments on a clean surface and pure fluid pool boiling experiments on an oxidized surface. They explained that a surface treatment (i.e., surface oxidation) alone resulted in a similar CHF enhancement, but at a ~20°C lower wall superheat than what was observed using nanofluids. In the light of the present work and the one done by Coursey and Kim [14], another effect of nanofluids on the wall superheat increase may exist, but it does not seem to be directly involved with the nanofluid CHF enhancement.

An interesting phenomenon was observed in the boiling curve for pure water on the alumina nanoparticle-fouled surface: in the vicinity of the CHF, the wall superheat decreased as the heat flux approached the CHF. This phenomenon is known as the inverted boiling crisis [25], which is occasionally observed during boiling on a porous coating layer. Recently, Kim [26] and Chen et al. [27] also observed this phenomenon on surfaces with titania nanoparticle deposition and on a Si nanowire array, respectively. According to Chen et al. [27], this phenomenon can be attributed to the activation of submicrometer cavities on the nanoparticle-fouled surfaces, where both microsized and nanosized cavities are expected to coexist; the surface deposition of the nanoparticles forms submicron pores among them, and the agglomeration of the nanoparticles generate micron-sized structures. The submicrometer cavities among those need high superheat to be activated as nucleation sites. As the heat flux approaches the CHF, the wall superheat becomes higher than the required wall superheat. Therefore, a large amount of submicrometer cavities can be activated and more bubbles are produced, resulting in a decrease in the wall superheat near the CHF. Another possible explanation for the inverted boiling crisis is that some deposited nanoparticles are detached by the vigorous vapor generation, and then those detachments not only reduce the thermal resistance of the coating but also increase the number of the microsized cavities, which then decreases wall superheat.

4 Evaporating Meniscus on Hot Surfaces: Effect of Nanoparticle Deposition

The pool boiling experiments presented in Sec. 3 have shown that the CHF enhancement in nanofluids is due to the nanoparticle layer formed during nanofluid nucleate boiling. Therefore, the

Table 1 Heat flux and wall superheat at the CHF points during nanofluid boiling on a clean surface and pure water boiling on a nanoparticle-fouled surface. (The average CHF values of pure water were 1710 $\mathrm{kW/m^2}$ for copper and 1690 $\mathrm{kW/m^2}$ for nickel, respectively. The values in parenthesis indicate the enhancement above the CHF values of pure water on the same substrate material.)

		Nanofluids on a clean surface		Pure water on a fouled surface	
Substrate	Nanoparticle	q''_{CHF} ($\mathrm{kW/m^2}$)	ΔT_{wall} (K)	q''_{CHF} ($\mathrm{kW/m^2}$)	ΔT_{wall} (K)
Copper	Alumina	2400 (1.40)	67	2640 (1.51)	45
		2280 (1.33)	60	2170 (1.27)	46
		2260 (1.32)	76	2240 (1.31)	31
	Titania	2410 (1.41)	76	2240 (1.31)	57
Nickel	Alumina	2185 (1.29)	72	N/A	N/A
	Titania	2260 (1.34)	77	2300 (1.36)	57

mechanism of the nanofluid CHF increase should be sought from the surface effects due to the nanoparticle layer. The deposition of the alumina or titania nanoparticles on a clean surface caused a significant reduction in the static equilibrium contact angle of a water droplet (see Figs. 12(*a*)–12(*c*)), which is consistent with the results of other studies on the wettability of the nanoparticle layer due to nanofluid boiling (e.g., Ref. [28]). The characterization of the surface properties with only the static equilibrium contact angle gives some insights; however, it is not sufficient to identify the exact mechanism of the CHF enhancement phenomenon. In this section, we examine how the nanoparticle deposition layer affects the dynamic wetting behavior of a liquid meniscus evaporating on a heated surface, which plays an important role in boiling heat transfer. In addition, plausible mechanisms to link the hydrophilic nanoparticle layer and CHF enhancement are discussed based on the obtained wetting experimental results.

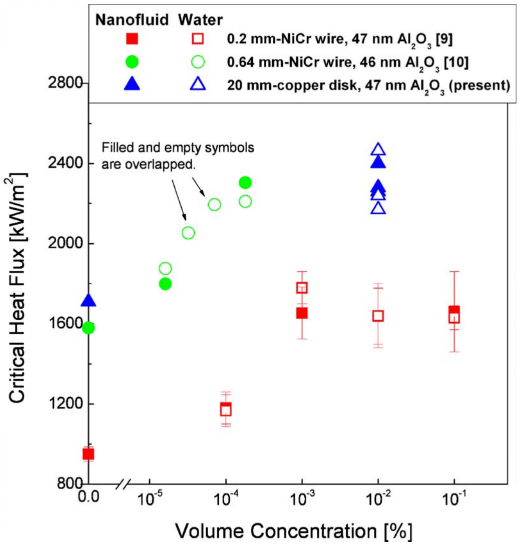

Fig. 11 Influence of the nanoparticle deposition in CHF increases in water-based alumina nanofluids. The average particle sizes were 47 nm in the present study and in Ref. [9], and 46 nm in Ref. [10]. The filled and open symbols indicate the nanofluid tests on the fresh surfaces and the water tests on the alumina nanoparticle-fouled surface, respectively.

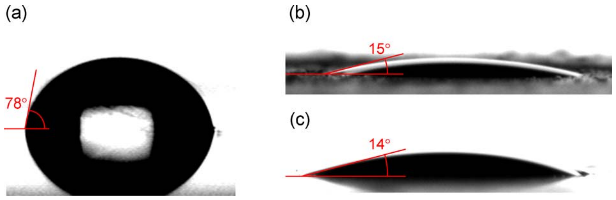

Fig. 12 Static contact angles of a water droplet on (*a*) a water-boiled surface, (*b*) an alumina nanoparticle-fouled surface, and (*c*) a titania nanoparticle-fouled surface

4.1 Wetting Experiments With a Water Droplet on Hot Surfaces.

Subsequent to the boiling experiments, wetting experiments with a water droplet at 22°C were performed on the water- and nanofluid-boiled surfaces at various wall temperatures from 100°C to 200°C. The behavior of the evaporating droplets was visualized with a high-speed camera at a sampling rate of 5000 frames/s. The dynamic contact angles of the evaporating meniscus near the edge of the droplets were measured using the captured high-speed images. The diameter and velocity of the impinged droplets were estimated to be 2.8 mm and 0.4 m/s, respectively, and thus the Weber number was 6.2.

Figure 13 shows droplets evaporating on a clean copper surface at three values of wall temperature T_{wall}. At $T_{\mathrm{wall}}=120°\mathrm{C}$, the surface temperature was 20°C above the boiling point of water. The impinged droplet oscillated on the surface during an initial period soon after the impact, and then stabilized with a constant contact angle. Stable evaporation of the liquid took place on the edges of the stabilized droplet. At $T_{\mathrm{wall}}=140°\mathrm{C}$, many bubbles nucleated within the liquid and evaporation near the contact line became intensive. However, the evaporating meniscus was stable during the evaporation process. When T_{wall} was raised to 160°C, the evaporating meniscus receded toward the liquid, causing a significant increase in the contact angle.

The instantaneous contact angles of the evaporating meniscus with the surface temperature are shown in Figs. 14(*a*) and 14(*b*). Extracting a single representative dynamic advancing or receding contact angle from a fast evaporating droplet appeared to be arbitrary. Instead, we present all contact angle measurement results during the entire evaporation process of a droplet before levitation occurs. As a result, the contact angles at specific surface temperatures had large scatter due to oscillation of the impinged droplet and the consequent wave of the liquid-vapor interface. However, a clean distinction was observed below and above the temperature at which the evaporating meniscus suddenly receded toward the liquid on the heated surface. For $T_{\mathrm{wall}} \leq 150°\mathrm{C}$, the evaporating meniscus showed contact angles in the range from 20 deg to 100 deg. When the surface temperature was 150°C, the contact angle dramatically jumped to the range between 110 deg and 140 deg. Such a large jump in contact angle, known as the vapor cutback phenomenon [29], was caused by the rapid receding motion of the liquid-vapor interface to liquid. This phenomenon is attributed to vapor recoil force due to evaporation at the liquid-vapor interface. The intense evaporation on a heated surface exerts a vapor recoil pressure on the meniscus as a result of the momentum transfer from the escaping molecules. The pressure is correspondingly

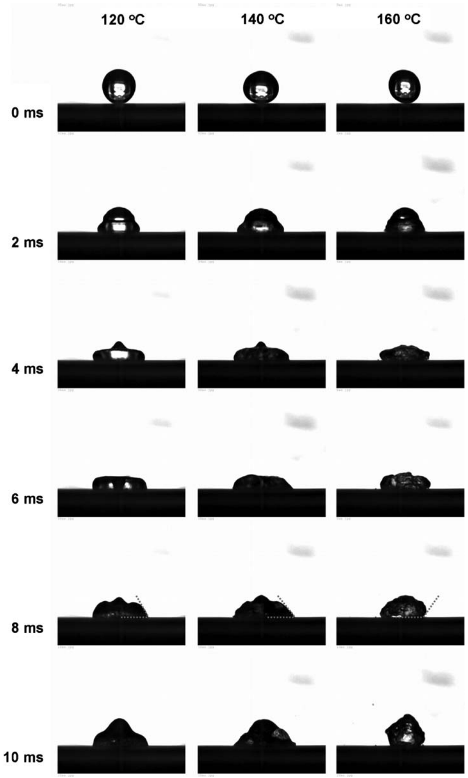

Fig. 13 Wetting of a water droplet on a water-boiled copper surface at 120°C, 140°C, and 160°C

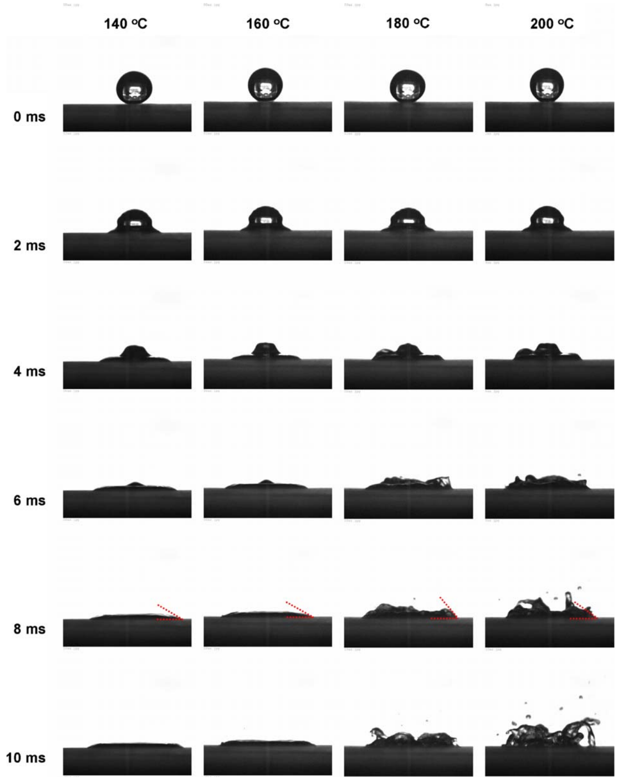

Fig. 15 Wetting of a water droplet on a titania nanoparticle-fouled copper surface at 140°C, 160°C, 180°C, and 200°C

stronger near the contact line since the mass flux of evaporation is stronger in this region [30]. The nonuniform pressure distribution causes the meniscus to stand up and quickly recede toward the liquid along the heated surface [31].

The droplets impinged on a nanoparticle-deposited surface with surface temperatures ranging from 140°C to 200°C are shown in Fig. 15. The wetting phenomenon on the nanoparticle-fouled surface appeared to be quite different from that on the copper surface. The evaporation meniscus had smaller contact angles within a narrower scattering range: $\theta_{\text{ave}} \sim 30$ deg with a scattering range between 10 deg and 50 deg on the nanoparticle-fouled surface versus $\theta_{\text{ave}} \sim 60$ deg between 20 deg and 100 deg on the clean surface (see Figs. 16(*a*) and 16(*b*)). At the initial moment of contact, the advancing contact angle of the spreading meniscus was remarkably small: ~30 deg on the fouled surfaces versus ~100 deg on the clean surface. Its maximum spreading diameter was approximately two times larger. At $T_{\text{wall}} = 160°\text{C}$, the surface temperature was 60°C above the boiling point of water. The evaporating meniscus at the edges of the droplet was quite stable, while the meniscus on the clean surface showed a jump in contact angle. When T_{wall} was raised to 180°C and 200°C, more and more bubbles were nucleated in the liquid, and the shape of the liquid-vapor interface was severely distorted due to the departing bubbles. The evaporating meniscus on the alumina nanoparticle-fouled surface seemed to recede at 190°C, resulting in a contact angle jump; however, a decisive transition was not observed. As a result, the contact angle jump observed on the clean surfaces near 150°C was not found on the nanoparticle-fouled surfaces even at 200°C, which is higher than the CHF point temperatures in pool boiling of nanofluids. The significant subcooling (~78 K) of the impinging water droplet might be a reason to delay the vapor cutback phenomenon to the higher temperature, e.g., the contact angle jump on a clean surface was observed at 150°C, which is obviously higher than the CHF point temperature of pure water 127°C at the pool boiling experiments. Therefore, the contact line jump on the fouled surface is likely to be observed at the higher surface temperature. However, the maximum allowable tempera-

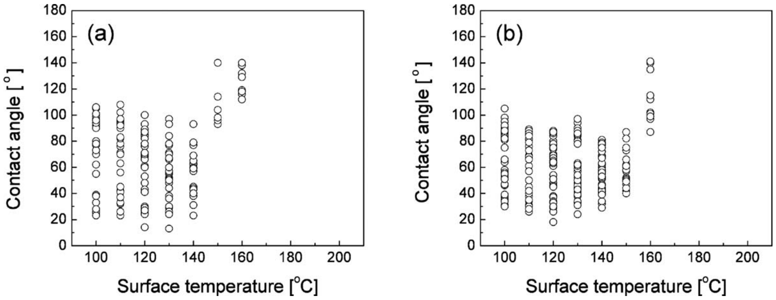

Fig. 14 Contact angle of a liquid meniscus evaporating on water-boiled surfaces: (*a*) copper and (*b*) nickel

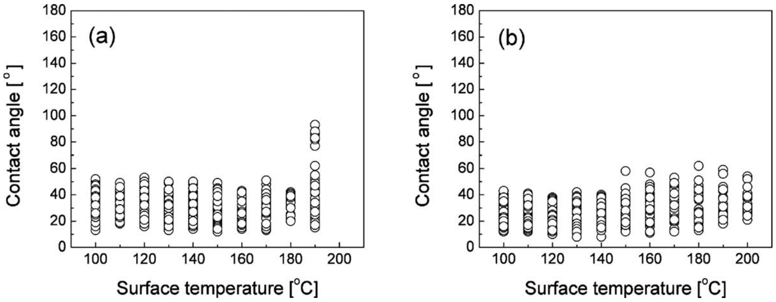

Fig. 16 Contact angle of a liquid meniscus evaporating on nanoparticle-fouled copper surfaces: (*a*) alumina and (*b*) titania

ture of the plastic insulating material used on the heater specimen was about 200°C and thus the temperature range explored in this study was limited.

4.2 Relationship Between the Nanoparticle Deposition and Stability of the Evaporating Meniscus. To interpret the wetting experimental data, we shall consider a steady-state evaporating meniscus on a heated surface. Two dominant forces play a key role in interpreting the behavior of the evaporating meniscus: the evaporation recoil force, which drives the meniscus to recede, and the surface tension force, which drives the liquid to flow into the meniscus. The *evaporation recoil force* on the meniscus can be evaluated as a dynamic pressure [32]

$$F_V \sim \tfrac{1}{2}\rho_v U_v{}^2 \tag{5}$$

where U_v is related to the heat flux q'', vapor density, and latent heat of evaporation as follows:

$$U_V = q''/(\rho_v h_{lv}) \tag{6}$$

Wang et al. [33] obtained an analytical solution for the total heat transfer in a liquid meniscus evaporating on a heating surface

$$q_t = \sqrt{\frac{2Ah_{lv}h_e(T_{\text{wall}} - T_v)}{v}\ln\left(\frac{k_l}{h_e\delta_0} + 1\right)} \tag{7}$$

where A is the dispersion constant, h_e is the evaporative heat-transfer coefficient, and δ_{o} is the nonevaporating region thickness. Using Eqs. (5)–(7), the vapor recoil force exerted on an evaporating meniscus is approximately

$$F_V \sim \frac{Ah_e(T_{\text{wall}} - T_v)}{v\rho_v h_{lv}}\ln\left(\frac{k_l}{h_e\delta_0} + 1\right) \tag{8}$$

The *surface tension force* is the counterforce of the evaporation recoil force and holds the liquid meniscus in place. The force is due to surface tension and interfacial curvature R [32]

$$F_s = \sigma/R \tag{9}$$

According to Kim et al. [11], the average radius of curvature of the meniscus with the contact angle can be estimated as

$$R = \sqrt{\frac{\sigma}{g(\rho_l - \rho_v)}}\Big/\sqrt{1 - \frac{\sin\theta}{2} - \frac{\pi/2 - \theta}{2\cos\theta}} \tag{10}$$

The evaporation recoil force increases linearly proportional to the wall superheat. The surface tension force is determined by the interfacial curvature of the meniscus, which is associated with the contact angle (or surface wettability). When the evaporation recoil force becomes larger than the surface tension force, the liquid meniscus near the contact line suddenly recedes, causing a dramatic jump in contact angle.

In our wetting experiments, the evaporating meniscus was stable at a wall superheat up to ∼50°C for the clean surface and ∼100°C for the nanoparticle-fouled surface. For these results, Eq. (8) suggests that the evaporation recoil force exerted on the meniscus was approximately two times larger on the nanoparticle-fouled surface than on the clean surface $F_{v,\text{fouled}}/F_{v,\text{clean}} \sim 100°\text{C}/50°\text{C}$. Such enhancement in the maximum allowable recoil force is certainly due to the change in the surface tension force of the solid surface. The average contact angles of the evaporating meniscus prior to the vapor cutback were ∼60 deg and ∼30 deg on the clean and nanoparticle-fouled surfaces, respectively[2], and thus Eq. (9) suggests that the surface tension forces on the fouled surface are larger by a factor of $F_{s,\text{clean}}/F_{s,\text{fouled}} \sim 1.83$ or 83%. This enhancement in the surface tension force is in good agreement with the increase in the maximum allowable recoil force due to the nanoparticle layer (see Fig. 17). Also, the improved stability of the meniscus evaporating on the nanoparticle layer causes a 41% enhancement in the maximum heat-transfer rate $q_{t,\text{fouled}}/q_{t,\text{clean}} \sim \sqrt{100°\text{C}/50°\text{C}} = 1.414$, based on Eq. (7). This estimation is fairly close to the CHF enhancement observed in our pool boiling experiments. In summary, the high wettability of the nanoparticle layer improved the stability of the evaporating meniscus on a heated surface so that the meniscus could sustain the stronger evaporation recoil force at the higher wall superheat and heat flux.

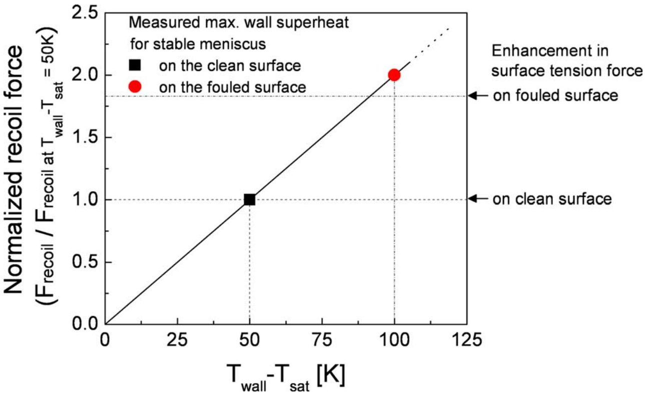

Fig. 17 Comparison between the normalized vapor recoil force at various wall superheats and the surface tension force enhancement on clean and nanoparticle-fouled surfaces

4.3 Relationship Between the Improved Stability of the Evaporating Meniscus and the CHF Enhancement in Nanofluids. Many nanofluid boiling studies in the literature have demonstrated that a link exists between the nanofluid CHF enhancement and the improved surface wettability caused by the nanoparticle deposition. However, the exact mechanism by which

---

[2] The contact angle of the evaporating meniscus had a large scatter between advancing and receding contact angles due to the oscillating interface motion of the impinged droplet, as shown in Figs. 13 and 15. In this study, the averaged values of the measured contact angles were used to estimate the surface tension force on the evaporating meniscus.

the improved wettability due to the nanoparticle layer causes the CHF enhancement has not been clearly explained. Recently, Kim et al. [11] examined the prevalent CHF theories with respect to their ability to explain the CHF gains in nanofluids, and classified them as follows:

- hydrodynamic instability theory
- macrolayer dryout theory
- hot/dry spot theory
- bubble interaction theory

They reported that except for the hydrodynamic instability theory, all the theories properly corroborated the link between increased surface wettability and CHF enhancement in nanofluids. While the macrolayer dryout and bubble interaction theories deal with the amount of trapped liquid or the mutual interaction between bubbles growing and departing on a heated surface, the hot/dry spot theory focuses its attention on the behavior of an individual hot/dry spot and the microhydrodynamics of the thin liquid meniscus at the boundary of the spot to interpret the wettability effect [34]. Our wetting experiments showed that the individual liquid meniscus evaporating on the heated surface became significantly more stable due to the nanoparticle layer with high wettability. Furthermore, the magnitude of the heat flux gain estimated for the individual meniscus was remarkably close to our experimental observation of the CHF enhancements in nanofluids. In addition, to describe the microhydrodynamic behaviors of the vapor-liquid interface of a single bubble at the heater surface, Kandlikar [35] proposed a contact angle based CHF model, which utilizes the evaporation momentum force and receding contact angle as parameters

$$q''_{\mathrm{CHF}} = h_{fg}\rho_g^{1/2}\left(\frac{1+\cos\beta}{16}\right)\left[\frac{2}{\pi}+\frac{\pi}{4}(1+\cos\beta)\cos\phi\right]^{1/2}[\sigma g(\rho_l - \rho_g)]^{1/4} \qquad (11)$$

When applying the average contact angles measured in the present work (60 deg for the water-boiled surface versus 30 deg for the nanoparticle-fouled surface), Eq. (11) predicts a CHF enhancement of 34% for the fouled surface, which is consistent with our experimental observation. This result supports our argument on the interaction of the CHF enhancement in nanofluid boiling and the improved microhydrodynamics of the evaporating liquid meniscus on the nanoparticle-fouled surface. Therefore, with all experimental and analytical results presented, it can be concluded that the hot/dry spot theory incorporated with the microhydrodynamics of the evaporating meniscus is a very plausible mechanism for the CHF enhancement observed during pool boiling of nanofluids.

5 Conclusions

In this study, the mechanism for the CHF enhancement during pool boiling of nanofluids was investigated through pool boiling and droplet-wetting experiments. The pool boiling in nanofluids with 0.01 vol % alumina and titania nanoparticles showed 30–40% CHF enhancements. A visual observation of the nanofluid-boiled surface revealed that some nanoparticles were deposited on the heater surface during the boiling. Through comparisons of the CHF values for nanofluids on a clean surface and the values obtained for pure water on a nanoparticle-fouled surface, we demonstrated that the main cause for the CHF enhancement in nanofluids was the nanoparticle deposition on the surface. Subsequent to the boiling experiments, wetting tests of a water droplet revealed that the high surface wettability on the nanoparticle layer improved the stability of the meniscus evaporating on the heated surface. The critical wall superheat at which the evaporating liquid meniscus suddenly receded due to the evaporation recoil force was about 50°C on the clean surface and at least 100°C on the nanoparticle-fouled surface. This suggests that the evaporating microlayer with its improved stability against the evaporating recoil force can keep dissipating the thermal energy of the heated surface at the higher surface temperature, inhibiting the irreversible growth of a hot/dry spot. Therefore, it is concluded from this study that a very plausible CHF model to explain the physical mechanism of the nanofluid CHF enhancement is the hot/dry spot theory incorporated with the microhydrodynamics of a thin liquid meniscus.

Acknowledgment

This research was supported by the Korea Science and Engineering Foundation (KOSEF) via Nuclear R&D Programs. The authors are grateful to Mr. Seon Tae Kim and Mr. Hangjin Jo for providing valuable help on the construction and operation of the experimental apparatus.

Nomenclature

A = dispersion constant (J)
d = depth of the temperature measurement point T_0 from the boiling surface (m)
F_S = surface tension force (N)
F_V = vapor recoil force due to evaporation (N)
g = acceleration of gravity (m/s^2)
h_e = evaporative heat-transfer coefficient (W/m^2 K)
h_{lv} = latent heat of evaporation (J/Kg)
k = thermal conductivity (W/m K)
q_t = total heat-transfer rate (W/m)
q'' = heat flux (W/m^2)
R = radius of curvature (m)
T_0 = temperature inside the test sample (°C)
T_1 = temperature of the first thermocouple in the conduction block (°C)
T_2 = temperature of the second thermocouple in the conduction block (°C)
T_3 = temperature of the third thermocouple in the conduction block (°C)
vol % = volume percent
ΔT_{sat} = wall superheat (K)
Δx = distance between temperature measurement points in the conduction copper block (m)

Greek Symbols

δ_0 = nonevaporating region thickness (m)
θ = contact angle (deg)
ρ = density (kg/m^3)
σ = surface tension (N/m)
υ = kinematic viscosity (m^2/s)

Subscripts

ave = average
CHF = critical heat flux
l = liquid
sat = saturation
v = vapor
wall = heater surface

References

[1] Chang, S. H., and Baek, W. P., 2003, “Understanding, Predicting, and Enhancing Critical Heat Flux,” *Proceedings of the Tenth International Topical Meeting on Nuclear Reactor Thermal Hydraulics*, Seoul, Republic of Korea, pp. 5–9.
[2] You, S. M., Kim, J. H., and Kim, K. H., 2003, “Effect of Nanoparticles on Critical Heat Flux of Water in Pool Boiling Heat Transfer,” Appl. Phys. Lett., **83**, pp. 3374–3376.
[3] Vassallo, P., Kumar, R., and D’Amico, S., 2004, “Pool Boiling Heat Transfer Experiments in Silica-Water Nano-fluids,” Int. J. Heat Mass Transfer, **47**, pp. 407–411.
[4] Bang, I. C., and Chang, S. H., 2005, “Boiling Heat Transfer Performance and Phenomena of Al_2O_3-Water Nano-fluids From a Plain Surface in a Pool,” Int. J. Heat Mass Transfer, **48**, pp. 2407–2419.
[5] Milanova, D., and Kumar, R., 2005, “Role of Ions in Pool Boiling Heat Trans-

fer of Pure and Silica Nanofluids," Appl. Phys. Lett., **87**, p. 233107.

[6] Milanova, D., and Kumar, R., 2008, "Heat Transfer Behavior of Silica Nanoparticles in Pool Boiling Experiment," ASME J. Heat Transfer, **130**, p. 042401.

[7] Kumar, R., and Milanova, D., 2009, "Dispersion and Surface Characteristics of Nanosilica Suspensions," Ann. N.Y. Acad. Sci., **1161**, pp. 472–483.

[8] Kim, H., Kim, J., and Kim, M. H., 2006, "Experimental Study on CHF Characteristics of Water-TiO_2 Nanofluids," Nuclear Engineering Technology, **38**, pp. 61–68.

[9] Kim, H., Kim, J., and Kim, M. H., 2006, "Effect of Nanoparticles on CHF Enhancement in Pool Boiling of Nano-fluids," Int. J. Heat Mass Transfer, **49**, pp. 5070–5074.

[10] Golubovic, M., Hettiarachchi, M. H. D., and Worek, W. M., 2008, "Nanofluids and Critical Heat Flux," ASME Paper No. MNHT2008-52204.

[11] Kim, S. J., Bang, I. C., Buongiorno, J., and Hu, L. W., 2007, "Surface Wettability Change During Pool Boiling of Nanofluids and Its Effect on Critical Heat Flux," Int. J. Heat Mass Transfer, **50**, pp. 4105–4116.

[12] Kim, H. D., and Kim, M. H., 2007, "Effect of Nanoparticle Deposition on Capillary Wicking That Influences the Critical Heat Flux in Nanofluids," Appl. Phys. Lett., **91**, p. 014104.

[13] Liu, Z., and Liao, L., 2008, "Sorption and Agglutination Phenomenon of Nanofluids on a Plane Heating Surface During Pool Boiling," Int. J. Heat Mass Transfer, **51**, pp. 2593–2602.

[14] Coursey, J. S., and Kim, J., 2008, "Nanofluid Boiling: The Effect of Surface Wettability," Int. J. Heat Fluid Flow, **29**, pp. 1577–1585.

[15] Sefiane, K., 2006, "On the Role of Structural Disjoining Pressure and Contact Line Pinning in Critical Heat Flux Enhancement During Boiling of Nanofluids," Appl. Phys. Lett., **89**, p. 044106.

[16] Wasan, D. T., and Nikolov, A. D., 2003, "Spreading of Nanofluids on Solids," Nature (London), **423**, pp. 156–159.

[17] Wen, D., 2008, "Mechanisms of Thermal Nanofluids on Enhanced Critical Heat Flux (CHF)," Int. J. Heat Mass Transfer, **51**, pp. 4958–4965.

[18] Santillán, M. J., Membrives, F., Quaranta, N., and Boccaccini, A. R., 2008, "Characterization of TiO_2 Nanoparticle Suspensions for Electrophoretic Deposition," J. Nanopart. Res., **10**, pp. 787–793.

[19] Hetsroni, G., Mosyak, A., Pogrebnyak, E., Sher, I., and Segal, Z., 2006, "Bubble Growth in Saturated Pool Boiling in Water and Surfactant Solution," Int. J. Multiphase Flow, **32**, pp. 159–182.

[20] Holman, J. P., 2001, *Experimental Methods for Engineers*, 7th ed., McGraw-Hill, New York.

[21] Rohsenow, W. M., and Griffith, P., 1956, "Correlation of Maximum Heat Flux Data for Boiling of Saturated Liquids," Chem. Eng. Prog., Symp. Ser., **52**, pp. 47–49.

[22] Zuber, N., 1959, "Hydrodynamic Aspects of Boiling Heat Transfer," Ph.D. thesis, University of California, Los Angeles, CA.

[23] Haramura, Y., and Katto, Y., 1983, "A New Hydrodynamic Model of Critical Heat Flux, Applicable Widely to Both Pool and Forced Convection Boiling on Submerged Bodies in Saturated Liquids," Int. J. Heat Mass Transfer, **26**, pp. 389–399.

[24] Kim, H., DeWitt, G., McKrell, T., Buongiorno, J., and Hu, L. W., 2009, "On the Quenching of Steel and Zircaloy Spheres in Water-Based Nanofluids With Alumina, Silica and Diamond Nanoparticles," Int. J. Multiphase Flow, **35**, pp. 427–438.

[25] Cieslinski, J. T., 2002, "Nucleate Pool Boiling on Porous Metallic Coatings," Exp. Therm. Fluid Sci., **25**, pp. 557–564.

[26] Kim, H., 2007, "Experimental Investigations of Pool Boiling CHF Enhancement in Nanofluids," Ph.D. thesis, POSTECH, Pohang, Republic of Korea.

[27] Chen, R., Lu, M. C., Srinivasan, V., Wang, Z., Cho, H. H., and Majumda, A., 2009, "Nanowires for Enhanced Boiling Heat Transfer," Nano Lett., **9**, pp. 548–553.

[28] Jeong, Y. H., Chang, W. J., and Chang, S. H., 2008, "Wettability of Heated Surfaces Under Pool Boiling Using Surfactant Solutions and Nano-fluids," Int. J. Heat Mass Transfer, **51**, pp. 3025–3031.

[29] Kandlikar, S. G., and Steinke, M. E., 2002, "Contact Angles and Interface Behavior During Rapid Evaporation of Liquid on a Heated Surface," Int. J. Heat Mass Transfer, **45**, pp. 3771–3780.

[30] Moosman, S., and Homsy, G. M., 1980, "Evaporating Menisci of Wetting Fluids," J. Colloid Interface Sci., **73**, pp. 212–223.

[31] Sefiane, K., Benielli, D., and Steinchen, A., 1998, "A New Mechanism for Pool Boiling Crisis, Recoil Instability and Contact Angle Influence," Colloids Surf., A, **142**, pp. 361–373.

[32] Theofanous, T. G., and Dinh, T. N., 2006, "High Heat Flux Boiling and Burnout as Microphysical Phenomena: Mounting Evidence and Opportunities," Multiphase Sci. Technol., **18**, pp. 251–276.

[33] Wang, H., Garimella, S. V., and Murthy, J. Y., 2008, "An Analytical Solution for the Total Heat Transfer in the Thin-Film Region of an Evaporating Meniscus," Int. J. Heat Mass Transfer, **51**, pp. 6317–6322.

[34] Theofanous, T. G., and Dinh, T. N., 2002, "The Boiling Crisis Phenomenon. Part II: Dryout Dynamics and Burnout," Exp. Therm. Fluid Sci., **26**, pp. 793–810.

[35] Kandlikar, S. G., 2001, "A Theoretical Model to Predict Pool Boiling CHF Incorporating Effects of Contact Angle and Orientation," ASME J. Heat Transfer, **123**, pp. 1071–1079.

Heat Transport Capability and Fluid Flow Neutron Radiography of Three-Dimensional Oscillating Heat Pipes

B. Borgmeyer

C. Wilson

R. A. Winholtz

H. B. Ma[1]
LaPierre Professor
e-mail: mah@missouri.edu

Department of Mechanical and Aerospace Engineering,
University of Missouri-Columbia,
Columbia, MO 65201

D. Jacobson

D. Hussey

National Institute of Standards and Technologies,
100 Bureau Drive,
Gaithersburg, MD 20899

An experimental investigation into the parameters affecting heat transport in two three-dimensional oscillating heat pipes (OHPs) was implemented. A three-dimensional OHP is one in which the center axis of the circular channels containing the internal working fluid do not lie in the same plane. This novel design allows for more turns in a more compact size. The OHPs in the current investigation is made of copper tubings (3.175 mm outside diameter, 1.65 mm inside diameter) wrapped in a three-dimensional fashion around two copper spreaders that act as the evaporator and condenser. The two OHPs have 10 and 20 turns in both the evaporator and condenser. The 20-turn OHP was filled to 50% of the total volume with a high performance liquid chromatography grade water. Transient and steady state temperature data were recorded at different locations for various parameters. Parameters such as heat input, operating temperature, and filling ratio were varied to determine its effect on the overall heat transport. Neutron radiography was simultaneously implemented to create images of the internal working fluid flow at a rate of 30 frames per second. Results show the average temperature drop from the evaporator to condenser decreases at higher heat inputs due to an increase in temperature throughout the condenser region due to greater oscillations. These large oscillations were visually observed using neutron radiography. As the operating temperature is increased, the thermal resistance is reduced. A decrease in filling ratio tends to create more steady fluid motion; however, the heat transfer performance is reduced. [DOI: 10.1115/1.4000750]

Keywords: oscillating heat pipe, heat transfer, fluid flow, neutron radiography

1 Introduction

Oscillating heat pipes (OHPs) have become widely investigated due to their capability to transfer large amounts of heat. Oscillating heat pipes are a two phase heat transfer device that transfers heat through oscillating fluid flow. In an OHP, a channel is partially filled with an internal working fluid at saturated conditions. If the tube has a small enough diameter, then surface tension forces overcome gravitational forces and the liquid and vapor form distinct plugs and slugs, respectively. In order to create the distinct plugs and slugs, the maximum tube diameter can be calculated by $D_{\max}=1.84\sqrt{\sigma/g(\rho_l-\rho_v)}$, where 1.84 is the critical Bond number. By creating the tube inner diameter small enough based on this equation, the vapor and liquid flow in the tube flow in the same direction, which avoids entrainment limits as seen in conventional heat pipes. Applying heat to one end and removing heat from the other creates temperature gradients, which result in pressure differences that when coupled with vapor expansion and contraction cause oscillating fluid flow between the evaporator and condenser regions.

There are many parameters that affect the heat transport in an OHP. The structural parameters, such as the tube size, length, number of turns, and closed or open looped, significantly influence the oscillating motion and heat transfer performance. While the unlooped OHP, in which the working fluid is unable to circulate, can produce the oscillating motion, the closed looped OHP, in which the channel forms a complete loop, has a better heat transfer performance [1]. The number of serpentine turns also affects the overall performance. As the number of turns in a given range increases, the overall heat transfer performance of the OHP increases [2]. The functional parameters such as working fluid, heat input, orientation, and operating temperature also play important roles in an OHP. Khandekar et al. [3] discussed the properties of working fluids and how they aid or inhibit the performance of the OHP. A high pressure gradient due to the temperature gradient produces the pumping action of the OHP. This is desired because it is this pressure difference that allows the working fluid to flow without the aid of a mechanical pump or the use of wick structures as in conventional heat pipes. Khandekar and Groll [4] stated that low heat inputs are unable to generate sufficient pressure perturbations resulting in a lack of pumping action, which is necessary for optimal performance. Charoensawan et al. [2] conducted an experimental investigation into the effects of device orientation on heat transfer performance. Operating temperature was investigated by Ma et al. [5] and they noted that an increase in operating temperature results in reduced temperature drops. All these investigations have been focused on the two-dimensional OHPs, which cannot transfer heat with a higher heat flux. In addition, for a two-dimensional OHP, it is not easy to produce the bulk circulation due to the turn number limitation in a given heating area.

In the current investigation, two new three-dimensional OHPs have been conducted experimentally and examined the effects of certain parameters such as turn number, operating temperature, charging ratio, and power input in order to develop an OHP that removes heat with a higher heat flux level. In addition to understanding the parameters' effect on heat transfer capabilities, it is also necessary to determine fluid flow characteristics associated with the temperature oscillations. A number of experimental in-

---

[1] Corresponding author. Present address: Department of Mechanical and Aerospace Engineering, University of Missouri-Columbia, Columbia, MO 65211.

Contributed by the Heat Transfer Division of ASME for publication in the JOURNAL OF HEAT TRANSFER. Manuscript received May 20, 2009; final manuscript received November 10, 2009; published online March 31, 2010. Assoc. Editor: Louis C. Chow.

(*a*) (*b*) (*c*)

Fig. 1 20-turn (*a* and *b*) and 10-turn (*c*) OHPs

vestigations have been conducted utilizing glass tubing to visually track fluid motion within OHPs [6,7]. Due to the low thermal conductivity of glass, it is more difficult to simultaneously monitor temperature with slug flow. The investigation presented herein uses neutron radiography, which allows for fluid flow visualizations at a rate of 30 frames per second (fps) while recording temperature data at several locations.

2 Experiment Setup and Procedure

The OHPs shown in Figs. 1(*a*)–1(*c*), 2(*a*), and 2(*b*) were constructed from copper tubings with outer and inner diameters of 3.175 mm and 1.65 mm, respectively. The evaporator and condenser were constructed from copper blocks. Semicircular channels were milled into the copper blocks to create maximum contact between the two regions and the tubing. The condenser regions have holes dilled through the center for water bath controlled condenser temperature. Similarly, holes were drilled in the evaporator to hold cylindrical cartridge heaters that would serve as the controlled heat input. The copper tubing was laid in the semicircular channels of the evaporator and condenser blocks. Thermal paste was also added to the grooves to reduce contact resistance. The copper block attaching with the copper tubing for the 20-turn OHP has an evaporator section and condenser section of $7.62 \times 8.89 \times 2.54\ \text{cm}^3$. The length of the adiabatic section was set at 10.16 cm for the 20-turn OHP. In order to achieve a higher heat flux, the 10-turn OHP was designed to be smaller with dimensions of $3.81 \times 7.62 \times 2.54\ \text{cm}^3$ for the evaporator and $6.35 \times 7.62 \times 2.54\ \text{cm}^3$ for the condenser. The adiabatic section was set to a length of 7.62 cm. The tubing for the 10-turn OHP was staggered to achieve a clearer image of the fluid flow.

Both OHPs were backfilled to a given charging ratio with a high performance liquid chromatography (HPLC) grade water using a vacuum pump. The OHP was then sealed to maintain subatmospheric pressure conditions. 400 W cartridge heaters were covered in thermal paste and inserted into the holes. Cooling bath water was passed through a heat exchanger to control the temperature of the deuterium oxide (^2H_2O) circulating in a separate loop through the OHP. The deuterium oxide (also known as heavy water) does not scatter as many neutrons as water; therefore, images in the condenser region can be recorded more clearly. T thermocouples were placed in different locations in the evaporator, adiabatic, and condenser regions. Prior to experimentation, thermocouples were calibrated to a maximum error of $\pm 0.25°C$. The locations for the thermocouples are shown in Figs. 2(*a*) and 2(*b*). The thermocouples were connected to a National Instruments[2] data acquisition (DAQ) system and a personal computer for temperature recording, as shown in Fig. 3. The DAQ system was relayed to record data at the moment the neutron imaging software was initiated to capture images. This allowed for simultaneous visual and temperature data. The neutron imaging setup, as shown in Fig. 4, was developed at the National Institute of Standards and Technologies' (NIST) research reactor. In this system, the OHP is bombarded with neutrons from the reactor and the hydrogen in the HPLC grade water scatters the neutrons, while a neutron detector downstream from the reactor records the image. The scattering of the neutrons by the water creates a darker image than where there is no water in the OHP. The detector has the capability of record-

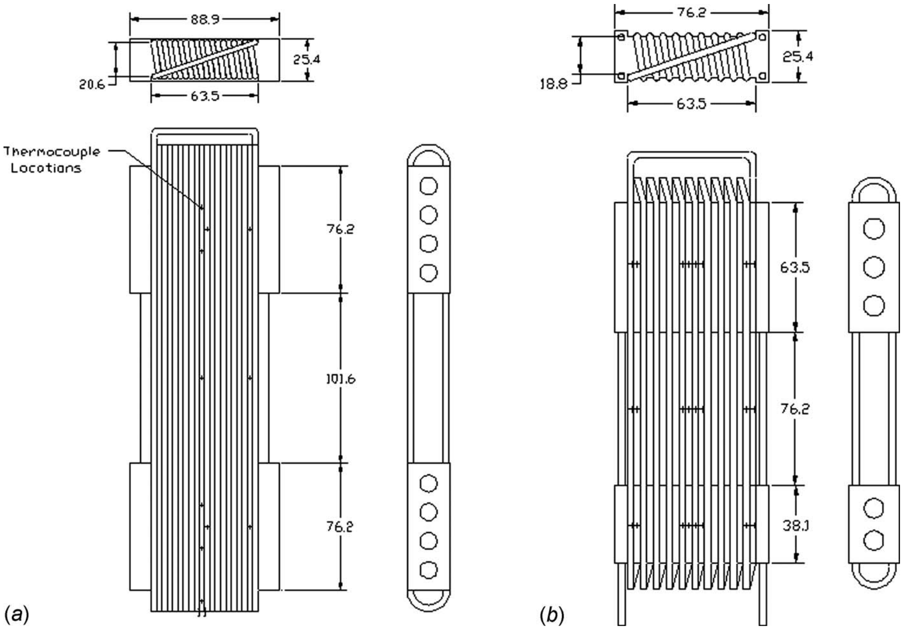

Fig. 2 Dimensions and thermocouple locations for the 20-turn (*a*) and 10-turn (*b*) OHPs (dimensions in mm)

---

[2] Certain trade names and company products are mentioned in the text or identified in an illustration in order to adequately specify the experimental procedure and equipment used. In no case does such identification imply recommendation or endorsement by the National Institute of Standards and Technology, nor does it imply that the products are necessarily the best available for the purpose.

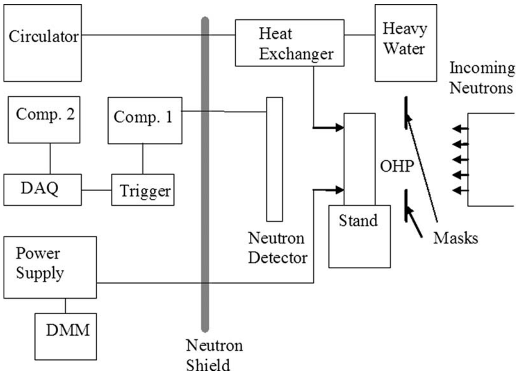

Fig. 3 Experimental setup

ing images at a rate of 30 fps and its resolution is based on neutron flux, OHP material and inner channel diameter, and location from the sensor.

A Staco power supply was wired in parallel with the cartridge heaters and a multimeter to accurately gauge the input power. The entire OHP was surrounded with insulation material to prevent heat transfer with the environment. The insulation was then covered with aluminum foil to prevent airborne radiological contamination. The 20-turn OHP was set up in only the vertical position with bottom heating, whereas the 10-turn was only arranged in the horizontal position. Two condenser settings (20°C and 60°C) were tested at numerous heat inputs for the 20-turn OHP, while only one setting (60°C) was tested for the 10-turn OHP due to time constraints at the NIST. Heat input was increased by increments of 50 W from 0 W to 400 W for the 20-turn OHP. Due to the smaller size and fewer turns for the 10-turn, heat input was incremented by 25 W from 0 W to 100 W and by 50 W from 100 W to 200 W. Temperature data and neutron images were recorded during both the initial increase in heat input (transient) and when the temperatures in all three regions fluctuated about an average value (steady state). Each heat pipe was allowed to cool to room temperature and temperature data and neutron imaging was recorded for a step input from zero to the maximum heat input. Recordings were also taken during shut down from the maximum heat input.

3 Results and Discussion

The experiments were conducted to determine the effect of turn number, heat input, operating temperature, and filling ratio on the heat transfer performance. Using the neutron images, the circulation and oscillating motion occurring in the OHP can be readily observed including flow patterns. The OHPs developed herein performed well overall and the frequency and amplitude of temperature oscillations were very consistent, especially at higher heat fluxes where sustained oscillations and bulk circulation occurred. The consistency of amplitude and frequency of the 20-turn OHP is greater than the 10-turn in general.

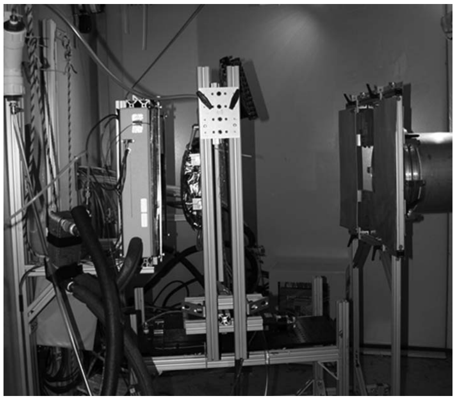

Fig. 4 Neutron imaging setup

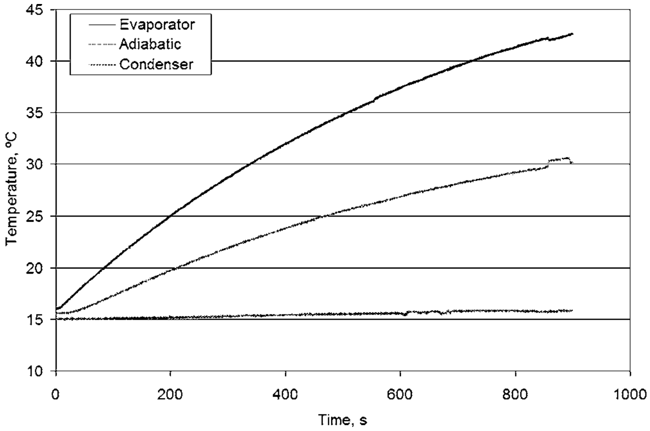

Fig. 5 Temperature data for the startup stage for the 20-turn OHP

3.1 20-Turn OHP. The 20-turn OHP was tested in the vertical position (bottom heating) for heat inputs up to 400 W. Because semicircular channels were milled into the copper block to create maximum contact between the heating block and the tubing, the contact area between the copper block and the tubing can be found as 152.0 cm^2. The calculated area is based on half the circumference of the tubing times evaporator length time the number of semicircular grooves. Given this contact area, the heat flux level reached at a heat input of 400 W is 2.63 W/cm^2. Two condenser settings of 20°C and 60°C were tested to determine operating temperature effect.

3.1.1 Heat Input Effect. From the experiments and neutron images conducted in this investigation, there appears to be three stages of fluid flow associated with this novel three-dimensional OHP. The first stage occurs at startup (0–50 W). This stage is shown thermally by a gradual increase in evaporator and adiabatic temperature with a steady condenser temperature. Figure 5 shows the temperature data associated with the startup period. The temperature data shows a steady curve; however, the neutron images show small movements. Also, at the low heat inputs, the growing vapor plugs in the evaporator slowly push the liquid slugs to the condenser. Further increase in heat input creates sufficient unsteady vapor growth required to develop pressure perturbations necessary for fluid exchange between adjacent turns.

The second stage of fluid flow in the OHP is intermittent flow starting at about 50 W up to 150 W for the 20-turn OHP investigated herein. This is where the fluid exchange between the evaporator and condenser regions is occasionally hindered. The stoppage in fluid exchange corresponds to a short steady increase in temperature following sustained temperature oscillations. The stoppage in fluid flow resumes once the temperature difference has increased enough to provide sufficient driving force to transfer the fluid. Figure 6 shows a large stoppage in fluid motion between the time 60–80 s that corresponds to a large increase in temperature. Results shown in Fig. 6 correspond to the 20-turn OHP in a vertical position (bottom heating) maintaining a heat input of 50 W and a condenser temperature of 60°C. Figure 6 shows that the frequency of temperature oscillation is roughly 0.17 Hz with amplitudes ranging from 2°C to 7°C. The majority of the temperature oscillations have amplitudes around 3°C. Figures 7(*a*)–7(*d*) display the neutron images at four separate points in time. Figures 7(*a*)–7(*c*) are during this period of temperature increase and it can be seen that during this time little movement

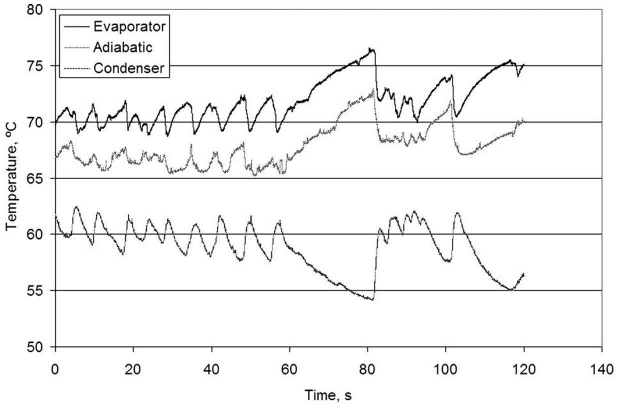

Fig. 6 Temperature data for the intermittent stage for the 20-turn OHP (heat input: 50 W, condenser setting: 60°C)

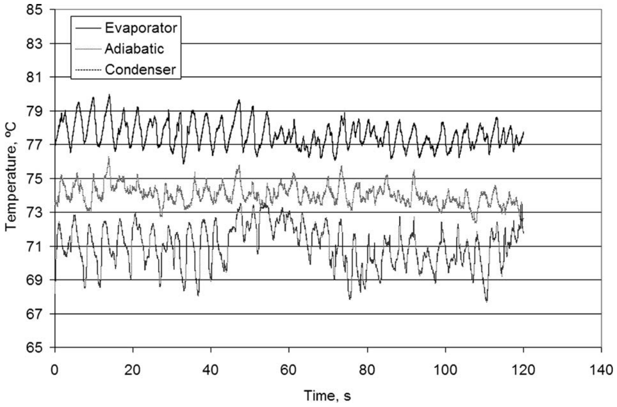

Fig. 8 Temperature data for the bulk circulation stage for the 20-turn OHP (heat input: 300 W, condenser setting: 60°C)

occurs. At 85 s (Fig. 7(*d*)), we start to see a change in the location of the slugs. As heat input is increased, the intermittent flow becomes more periodic.

The third stage of fluid flow occurs at high heat flux (>150 W) in which there are sustained oscillations and bulk circulation. This stage corresponds to steady fluid flow through the OHP with uniform frequency and amplitude. Figure 8 shows the oscillatory temperature readings associated with a 300 W heat input (1.97 W/cm^2) and a condenser setting of 60°C. At this heat input, consistent bulk circulation can be observed from the neutron images. The frequency of temperature oscillation for this heat input is roughly 0.275 Hz. This indicates an increase in frequency with increases in heat input. The amplitudes of oscillations range from about 2°C to 3°C. The amplitudes of oscillations seem to become more consistent at higher heat inputs. Figures 9(*a*)–9(*d*) display the neutron images at times where the evaporator thermocouple peaks and when it reaches its low point. The circulating flow tends to match the frequency of the temperature data. It should also be noted that at higher heat inputs, the velocities of the liquid slugs exceed the capture rate of the detector. The blurring associated with it makes it difficult to track the fluid meniscus. Figure 10 shows the average temperature drop from the

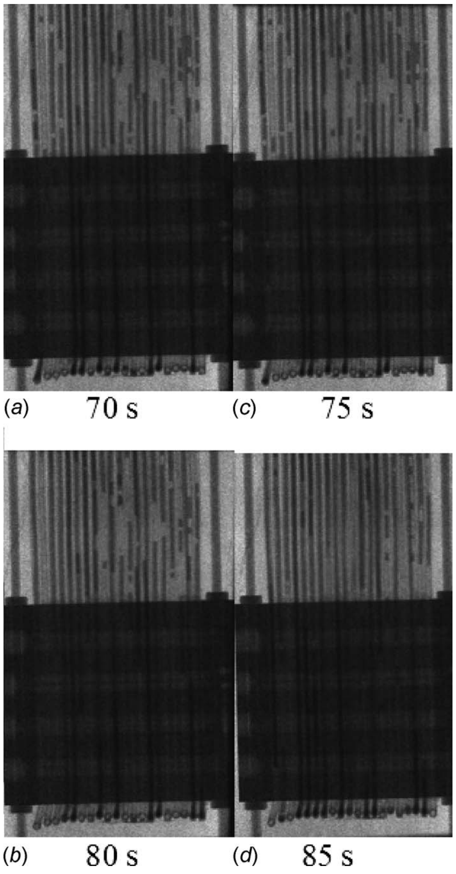

Fig. 7 Neutron images of the intermittent stage for the 20-turn OHP at (*a*) 70 s, (*b*) 75 s, (*c*) 80 s, and (*d*) 85 s

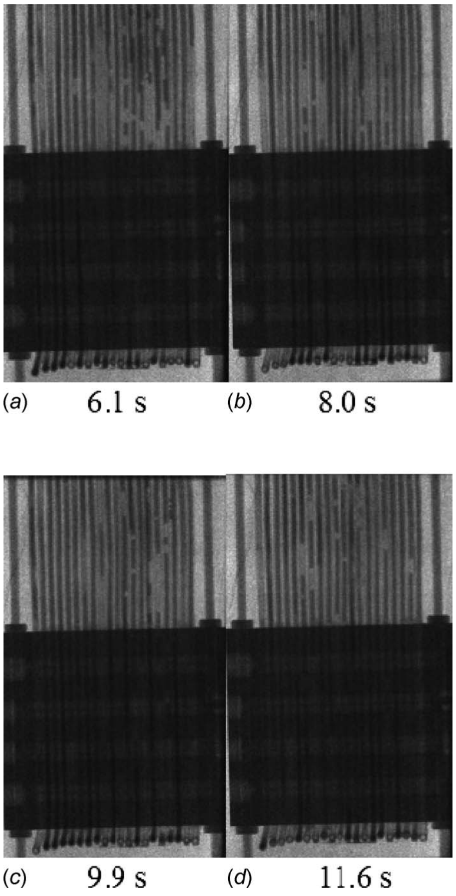

Fig. 9 Neutron images of the circulation stage for the 20-turn OHP at (a) 6.1 s, (*b*) 8.0 s, (*c*) 9.9 s, and (*d*) 11.6 s

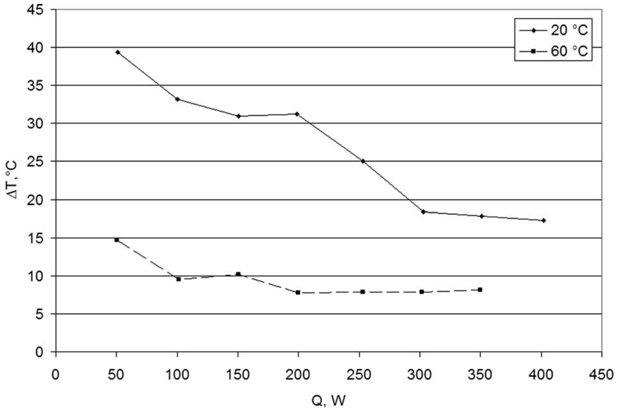

Fig. 10 Temperature drop versus heat flux for the 20-turn OHP

evaporator to the condenser in the 20-turn OHP for condenser setting of 20°C and 60°C. Temperature drop decreases as the heat input increases due to increased fluid flow.

3.1.2 Operating Temperature Effect. The neutron images comparing operating temperatures show unnoticeable differences; however, it is clear that oscillations start up more easily given a higher condenser setting. Figure 10 shows a decrease in temperature drop with an increase in condenser setting. Consequently, this means a reduced thermal resistance, as seen in Fig. 11. As expected from the results for the heat input effect, the thermal resistance decreases with increase in power input. In addition to the decrease in thermal resistance with heat input, the performance is enhanced as the condenser setting was raised. This increase in performance is based on the change in fluid properties associated with temperature change. For example, the viscosity of water decreases with an increase in temperature, which would allow for greater fluid motion. There appears to be no discernable differences between the fluid flow images at different condenser settings.

3.2 10-Turn OHP. The 10-turn OHP was tested in the horizontal position for heat inputs up to 200 W. The contact area for the 10-turn OHP was calculated to be 38.0 cm^2. This corresponds to a maximum heat flux of 5.26 W/cm^2 at a heat input of 200 W. The filling ratio was decreased in situ during the experiments. The first filling ratio was roughly 50% with the two subsequent ratios being less. Exact values are unknown due to the inability to weigh the OHP during the process. However, from the images it was determined that the three filling ratios were roughly 53%, 35%, and 30%, respectively. A startup similar to the 20-turn OHP was noticed. The liquid slugs were slowly forced out of the evaporator section, as shown in Figs. 12(*a*) and 12(*b*). Small oscillation exists until the pressure perturbations are sufficient to force the liquid back into the evaporator (Fig. 12(*c*)).

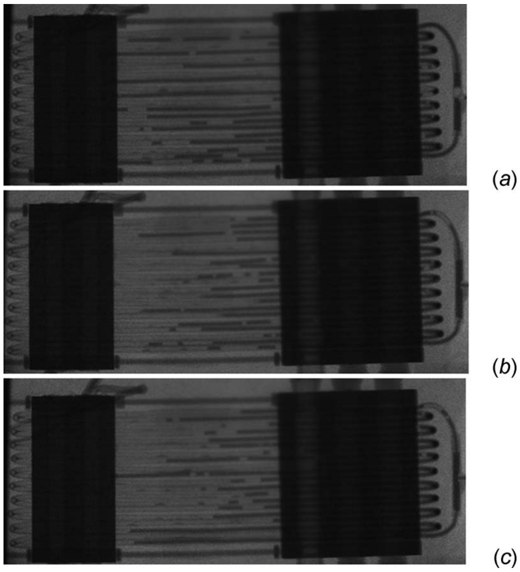

Fig. 12 Startup of the 10-turn OHP at (*a*) 0 s, (*b*) 400 s, and (*c*) 600 s

3.2.1 Filling Ratio Effect. The filling ratio has an inverse effect on both the fluid motion and heat transfer. The filling ratio of 53% showed good heat transfer; however, at the lower heat input of 50 W (Fig. 13), the fluid motion in hindered by the large mass of fluid. The filling ratio of 35% shows a slightly lower average evaporator temperature than the higher filling ratio. This may be due to the increase in amplitude and frequency of oscillation. Figure 14 shows the increased temperature oscillations for the filling ratio of 35%. A further decrease in filling ratio to 30% results in a large increase in evaporator temperature at the same heat input of 50 W (Fig. 15). Temperature and imaging data suggest an increase in fluid motion in the OHP; however, the reduction in liquid slugs to carry heat from the evaporator to condenser causes an increase in temperature. Also, a decreased filling ratio was noticed to cause the fluid run toward gravity. This causes the majority of the liquid to fill only one side of the OHP, as seen in Figs. 16(*a*)–16(*c*). Figures 16(*a*)–16(*c*) show the typical fluid distribution for the three filling ratios at 50 W (1.32 W/cm^2). Because of this tendency, full circulation through the OHP is hin-

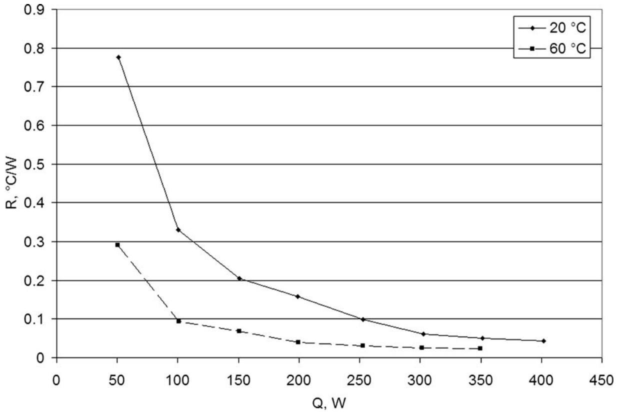

Fig. 11 Thermal resistance versus heat flux for the 20-turn OHP

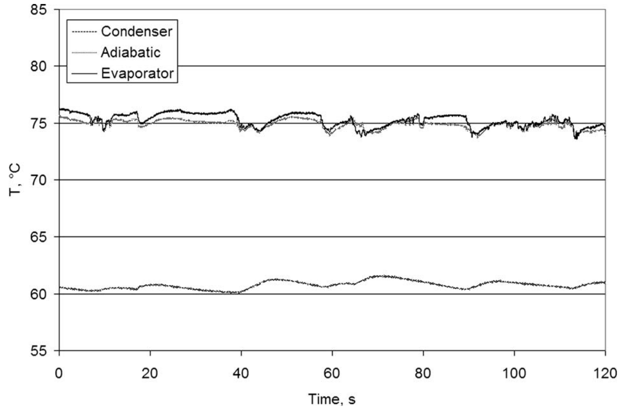

Fig. 13 Temperature fluctuations at a filling ratio of 53% for the 10-turn OHP

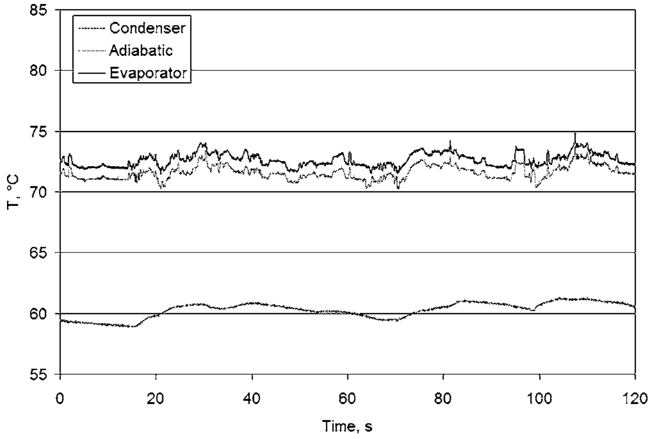

Fig. 14 Temperature fluctuations at filling ratio of 35% for the 10-turn OHP

dered and the liquid slug will only oscillate within the same channel or occasionally with the adjacent one. Figures 17 and 18 show the temperature drop and thermal resistance versus heat input for the three filling ratios. There is an obvious decrease in heat transfer performance with the filling ratios less than 53%.

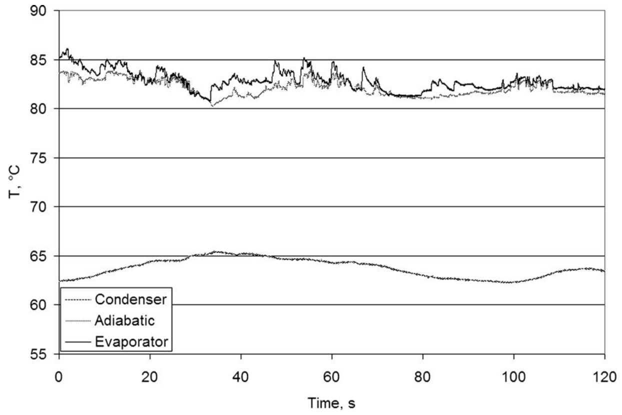

Fig. 15 Temperature fluctuations at a filling ratio of 30% for the 10-turn OHP

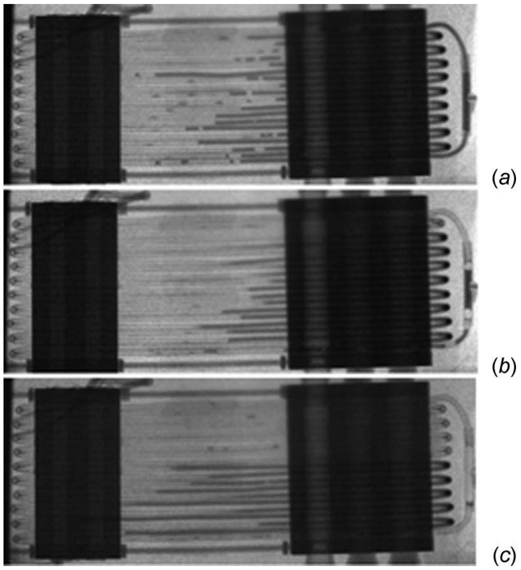

Fig. 16 Typical fluid distribution at low heat input for filling ratio of (*a*) 53%, (*b*) 35%, and (*c*) 30%

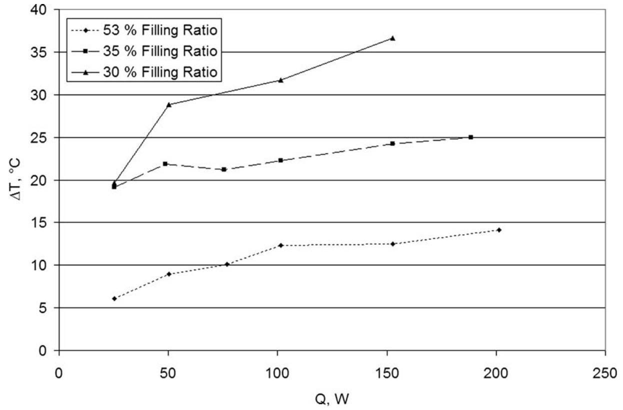

Fig. 17 Temperature drop given different filling ratios for the 10-turn OHP

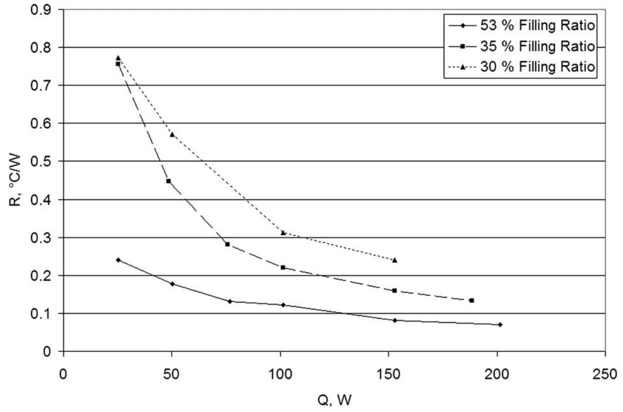

Fig. 18 Thermal resistance given different filling ratios for the 10-turn OHP

4 Conclusions

An experimental investigation was implemented to determine the heat transfer and fluid flow characteristics of two novel three-dimensional OHP. The effects of filling ratio, turn number, power input, and operating temperature were investigated to determine their effect on heat transport performance. Results show that when the turn number is different, the effect of power input on the heat transfer performance is different. The neutron images show that both oscillating motion and circulation exist when the power input is higher than 150 W for the 20-turn OHP investigated herein. As the power input increases for the 20-turn OHP, the temperature difference between the evaporator and condenser or effective thermal resistance decreases, which is very different from the conventional heat pipe or most of heat transfer devices. When the turn number was reduced to 10, the temperature difference between the evaporator and condenser or the effective thermal resistance is almost constant or increases slightly as the power input increases. In addition, it is found that the frequency for both OHPs increases as the input power increases. The operating temperature significantly affects the heat transfer performance for both OHPs. As the operating temperature increases, the temperature difference or effective thermal resistance decreases for both OHPs. A lower filling ratio results in larger and more frequent fluid motions; however, heat transport capability is reduced. The novel design of this three-dimensional OHP creates a high performance device with consistent frequencies and amplitudes not commonly observed in OHPs.

Acknowledgment

The work presented in this article was funded by the Office of Naval Research under Grant No. N00014-06-1-1119, which was directed by Dr. Mark Spector. The authors would also like to acknowledge the National Institute of Standards and Technology, U.S. Department of Commerce, for providing the neutron research facilities used in this work.

Nomenclature

D = diameter, m
g = gravity, $\mathrm{m/s^2}$
ρ = density, $\mathrm{kg/m^3}$
σ = surface tension, N/m

Subscripts

max = maximum
l = liquid
v = vapor

References

[1] Wilson, C., Borgmeyer, B., Winholtz, R. A., Ma, H. B., Jacobson, D., and Hussey, D., 2008, “Thermal and Visual Observation of Water and Acetone Oscillating Heat Pipes,” ASME Summer Heat Transfer Conference, Jacksonville, FL, Jul. 10–14.

[2] Charoensawan, P., Khandekar, S., Groll, M., and Terdtoon, P., 2003, “Closed Loop Pulsating Heat Pipes Part A: Parametric Experimental Investigations,” Appl. Therm. Eng., **23**, pp. 2009–2020.

[3] Khandekar, S., Dollinger, N., and Groll, M., 2003, “Understanding Operational Regimes of Closed Loop Pulsating Heat Pipes: An Experimental Study,” Appl. Therm. Eng., **23**(6), pp. 707–719.

[4] Khandekar, S., and Groll, M., 2003, “On the Definition of Pulsating Heat Pipes: An Overview,” *Proceedings of the Fifth Minsk International Seminar*, Minsk, Belarus.

[5] Ma, H. B., Wilson, C., Borgmeyer, B., Park, K., Yu, Q., Choi, U. S., and Tirumala, M., 2006, “Nanofluid Effect on the Heat Transport Capability in an Oscillating Heat Pipe,” Appl. Phys. Lett., **88**(14), p. 143116.

[6] Xu, J. L., Li, Y. X., and Wong, T. N., 2005, “High Speed Flow Visualization of a Closed Loop Pulsating Heat Pipe,” Int. J. Heat Mass Transfer, **48**, pp. 3338–3351.

[7] Khandekar, S., Schneider, M., Schafer, P., Kulenovic, R., and Groll, M., 2002, “Thermofluid Dynamic Study of Flat-Plate Closed-Loop Pulsating Heat Pipes,” Microscale Thermophys. Eng., **6**, pp. 303–317.

Effect of Return Bend and Entrance on Heat Transfer in Thermally Developing Laminar Flow in Round Pipes of Some Heat Transfer Fluids With High Prandtl Numbers

Predrag S. Hrnjak
Research Professor
Mem. ASME
e-mail: pega@illinois.edu

S. H. Hong

Department of Mechanical Science and Engineering,
University of Illinois at Urbana Champaign,
1206 West Green Street,
Urbana, IL 61801

The paper presents experimental results and analysis of heat transfer in a thermally developing region of round pipes for three fluids typically used as low temperature coolants, in the range of 0– −40°C. The experiments were performed at low Re (200–1000) and high Pr (80–140) numbers that are typically found in secondary refrigeration loop conditions. The effect of horizontal U-bend is also presented. It is shown that the positive effect of thermal development (high Nu number) lasts long because of the technically significant length of the thermally developing region. Secondary flows developed in and after the U-bend are so significant that they have almost an identical effect as the thermal development at the pipe entrance. That is a reason for the extremely good performance of the heat exchangers with secondary refrigerants in laminar flow regimes. Experimental data are presented with developed empirical correlations, which show good relationships to several existing correlations. [DOI: 10.1115/1.4000704]

Keywords: laminar flow, effect of U-bend, high Pr number, secondary coolant

1 Introduction

Heat transfer in hydraulically and thermally developing regions of laminar flows in channels is well explained and characterized by numerous authors. Appendix C gives an overview of some of the most important correlations. It is perhaps less known to some engineers that the thermally developing regime for some secondary refrigerants especially after U-bends could positively affect heat transfer in technically significant lengths, 0.5–1.5 m.

In this paper we will present results of the experimental program to measure the change in local heat transfer coefficients as a function of the length following entrance to circular pipe and after the U-bend. The examination of the local heat transfer in the pipe, averaged over a certain region was followed by the second part of the work to determine the effects of the same phenomena in a typical air cooler operating with the same fluids and in the same regime. This paper presents the results of the first part with reference to the result in the other. The rest of the details could be found in Ref. [1].

Figure 1 presents the explanation of the phenomena in the U-bend that causes the increase in the heat transfer. In the laminar flow of heated fluid in the horizontal tube, the core is colder and thus heavier than annulus closer to heated walls. Due to that fact, fluid in the central zone sinks and generates secondary flow that moves upward in the vicinity of vertical heated walls (see Fig. 1). The effects of the denser central zone are even more significant in fluid turning, like in U-bends or elbows. Greater inertial force impinges the stream to the bend or elbow wall causing stronger secondary flows and significant mixing. That effectively increases heat transfer bringing central cold stream in contact with the walls.

The objective of the experimental program was to quantify the effects of the phenomena described in realistic conditions and with the most promising secondary fluids at this time. Experiments are done with warm liquid heating the secondary coolant (object of the study) in the central pipe in a counterflow mode so it is in between a case with constant heat flux and constant wall temperature.

Three fluids were examined: propylene glycol (PG), potassium acetate (PA), and potassium formate (PF). These fluids were mixed with water in the following concentrations: PG 35%, PA 42.5%, and PF 46%. These fluids are the strongest candidates for secondary refrigeration loops in the range of −10– −40°C. Potassium acetate and potassium formate are less known and to our best knowledge this was the first experimental heat transfer study

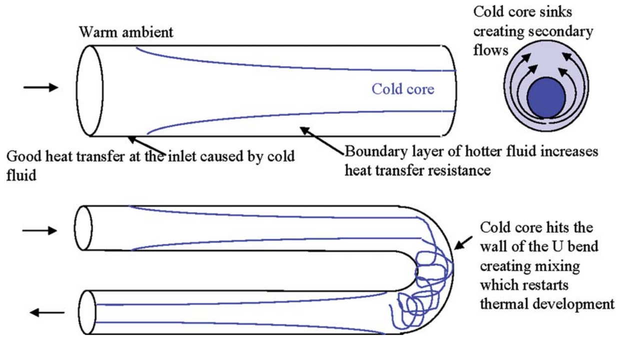

Fig. 1 Elements of heat transfer characteristics in a laminar developing flow

---

Contributed by the Heat Transfer Division of ASME for publication in the JOURNAL OF HEAT TRANSFER. Manuscript received July 2, 2008; final manuscript received October 20, 2009; published online March 19, 2010. Assoc. Editor: Gautam Biswas.

using them. Both are very attractive due to good thermophysical properties and their environmental friendliness. The exact concentrations and thermophysical properties of examined fluids are given in Appendix B.

2 Experimental Setup

More details of the facility shown schematically in Fig. 2 could be found in Ref. [1]. Two identical coriolis type mass flow meters nominal accuracy of 0.1% full scale (FS) are installed in the system: one for the refrigerant and the other for the heating fluid.

The test section consists of a pair of 3 m long annular coaxial heat exchanger tubes placed side-by-side in the horizontal plane with a U-bend functioning as a return line between the two tubes. Refrigerant flows through the inner copper tube and water flows through the outer annular spacing between copper and PVC tubes. Flow through the annulus is articulated with a spiral insert, as shown in Figs. 5(*a*), 5(*b*), and 6. Each heat exchanger tube has three test sections: 0.5 m, 0.5 m, and 2 m long. A schematic of the test coaxial heat exchanger is shown in Fig. 3. The shorter sections at the inlet are used to capture rapidly changing heat transfer rate. The two annular coaxial heat exchangers before and after the U-bend are identical in construction. The only difference is their function. Inlet to the upstream heat exchanger section has a uniform cross section temperature profile. The uniform profile is obtained by a long adiabatic section in the hose leading to the heat exchanger and one static mixer in it. The other identical heat exchanger is positioned downstream of the U-bend to measure the effect of the U-bend on local heat transfer coefficient. The data collection from a side-by-side setup of the heat exchanger sections allows direct comparison of the effect of the horizontal U-bend to a uniformly temperature distributed thermally developing inlet regime.

The inner tubes are mandrel expanded 9.53 mm copper tubes as normally used in round tube plate fin heat exchangers. As mentioned earlier in conjunction to the experiments shown here, the performance of the entire heat exchanger was explored and the intention was to have identical tubes. The inside surface of the copper tube is assumed to be smooth and thus the roughness factor for the smooth wall was used when needed.

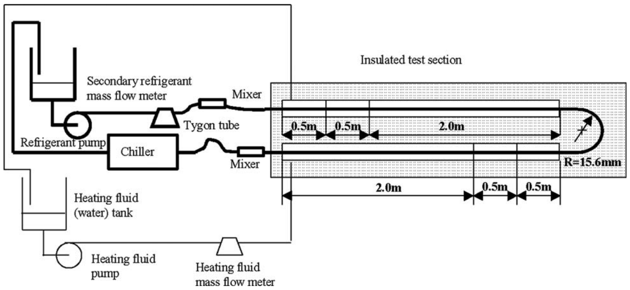

Fig. 2 Experimental facility (thermocouple configuration discussed later)

Table 1 Physical dimensions

	ID (mm)	*OD* (mm)	Total length of each straight section (m)	Radius of curvature (center to center) (mm)
Copper tube	9.14	9.78	3.1 (0.5+0.5+2.1)	
Copper tube bend	9.14	9.78		15.6
Articulator–ten gage stranded copper wire		4.2		

Dimensions of the copper tubes received and installed in the test sections and a spiral flow articulator in the annulus are listed in Table 1. The wire was wound around the copper tube at an angle approximately 45 deg. Figure 4 shows a cross section view of the joint of two sections where the spiral could be seen. Once PVC tube was sled in place, the wire was released, and it became unsprung due to the natural elasticity of the wire. Therefore, the wire is pressing against the PVC tube and not against the copper tube heat exchanger surface creating a small gap between the wire and the copper tube, which is 0.3–0.5 mm. Figure 4 also shows a continuous copper pipe and two sections being connected through a plastic ring. Detail design of this ring is shown in Fig. 5(*a*). There are three holes in the ring. The center hole is for the copper tube and two other holes serve to narrow down the passage of the heating fluid and thus ensure accurate reading of the heating fluid bulk temperature. Two radial holes that lead from the perimeter to two holes, 1.6 mm in diameter are for heating fluid thermocouple probes. Locations of those thermocouples are shown in Fig. 4. Two other small radial holes (1.6 mm) that protrude to the center hole and later the copper tube are for refrigerant thermocouple probes or thermocouple wires, as shown in Fig. 4.

Figure 5(*b*) shows another ring, used at the inlet and outlet of each of the heat exchanger tubes and is inserted into T-fittings. The ring has only one tube, either for the copper tube or heating fluid. The radial hole 1.6 mm in diameter is for the thermocouple probe.

Figure 4 also shows thermal insulation over the PVC pipe, spiral flow articulator, and location of thermocouples.

Thermal insulation has been used to minimize heat transfer exchange with the environment. The entire outside area of the coaxial heat exchanger was insulated with a total of 5 cm thermal

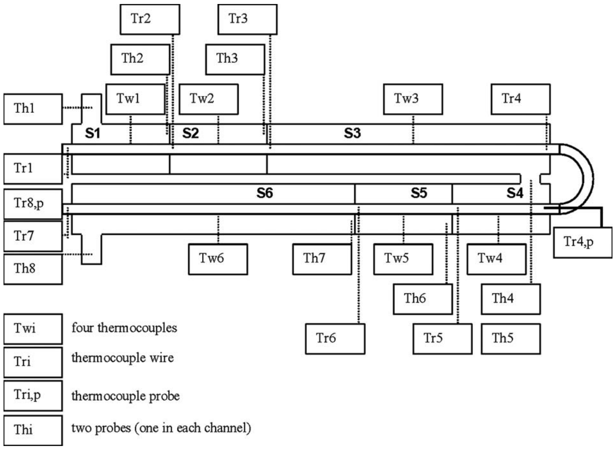

Fig. 3 Schematic of the test section

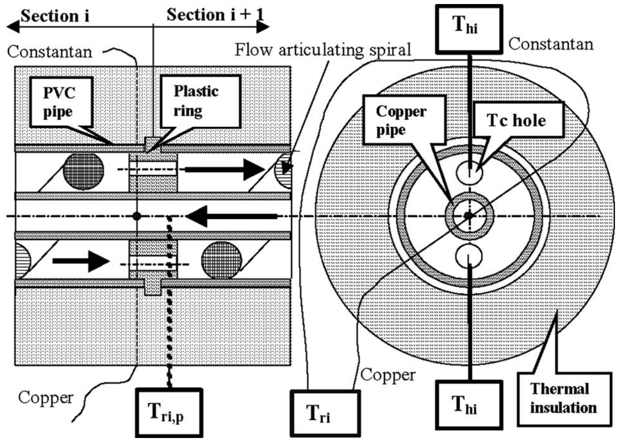

Fig. 4 Joint of two sections

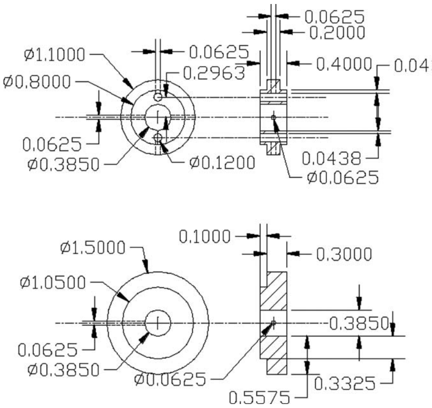

Fig. 5 Hard plastic rings. The top ring (*a*) separates the test sections and the bottom ring (*b*) is the end cap for each end of the coaxial heat exchanger tubes (numbers are in inches).

insulation (Armaflex®). The hoses for the refrigerant are also insulated to keep heat loss to a minimum. The fact that the temperature of the heating fluid in the annulus is kept close to room temperature reduces the heat transfer even further. Calibration was performed to verify heat losses. They were so small that they were hardly measurable.

All thermocouple wires and probes used are of a special limit of error type-T thermocouples, copper-constantan joined at the end. The thermocouple probes are exposed, with a special limit of error type-T probes and are used to measure heating fluid temperature at the beginning and end of each of the outer annular test sections. To reduce the effect of heat conduction in refrigerant temperature measurements through the thermocouple probe sheath, thermocouple wires were used instead of thermocouple probes. To immerse thermocouple wires into the fluid stream, the insulation of the thermocouple wires was removed, and copper and constantan wires were pulled apart to form a straight line with the welded joint in the middle. The welded joint was then carefully inserted into the center of the copper tube for each of the positions. The two opposite holes where the two thermocouple wires entered the copper tube were then epoxied leak-tight. A schematic of these thermocouple probes and wires is shown in Figs. 4, 5(*a*), and 5(*b*).

For wall temperature measurement, the same special limit of error type-T thermocouple wires are used. Four of these wires were cemented onto the groove in the outer side of the copper tube at the top, bottom, right, and left of each of the test sections along the middle. Highly conductive thermal epoxy is used as the cement for wall thermocouples. Figure 6 shows the locations of wall thermocouples. In the calibration phase, signals of these wall thermocouples were collected separately to check the uniformity of the reading. Results were very good, as shown in Appendix H of Ref. [1]. Finally, wall thermocouples are bundled thus averaging the signal.

All thermocouples were carefully checked simultaneously in a vacuum insulated container at two temperatures: 0°C and 22°C.

Details and further information about the test facility could be found in Ref. [1].

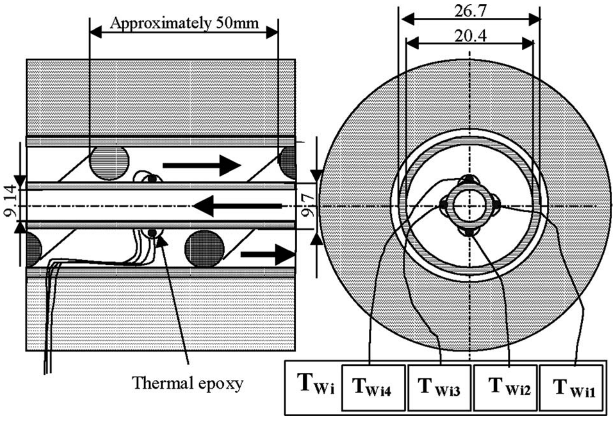

Fig. 6 Positions of the thermocouples for wall temperature measurements

Table 2 Test matrix for a coaxial heat exchanger run

	$T_{r,i}$ (°C)	$T_{h,i}$ (°C)	V_r (m/s)
Propylene glycol	−2.1−−8.5	25–17	0.27–0.95
Potassium acetate	−20−−23	24–20	0.17–0.61
Potassium formate	−20−−23	24–19	0.17–0.61

3 Test Procedure and Data Reduction

The temperature and mass flow rates were monitored continuously. Data were collected over an interval of at least 10 min in the steady state preceded by a 20 min steady state. The test range for fluids examined is shown in Table 2.

Physical parameters and properties needed to compute local heat transfer coefficients are: (1) temperature readings at the inlet and the outlet of each of the test sections, (2) wall temperatures, and (3) mass flow readings of the refrigerant and heating fluids. Figure 7 shows a schematic of a test section and the location of its thermocouples. The heat exchanged between the refrigerant and the heating fluid (water) could be determined for both fluids based on the measurements of temperature and mass flow given its specific heat value.

The heat transfer is then found from the energy balance on the heating fluid side. The refrigerant side energy balance is not used except for calibration because the bulk temperature of the refrigerant cannot be measured accurately with thermocouple wires. The thermocouples that measure refrigerant temperatures are located at the center of the copper tube, as shown in Fig. 4. The center location should give close to the lowest temperature inside the tube. Since the cold fluid in laminar flow is heated from the outside, the coldest streamline sinks below the center line in the horizontal laminar flow due to gravity creating a secondary flow. Additional difficulty in measurement is a very small temperature difference at the inlet and the exit of the refrigerant.

In addition, the heating fluid side is not subjected to a similar temperature measurement error because water flow is kept turbulent assuring reasonably uniform temperatures. Even more, flow is purposefully forced to go through two tiny holes in the rings, where an exposed thermocouple probe is inserted directly into the fluid stream of each hole for temperature measurement. Therefore, the energy balance on the heating side is believed to be more

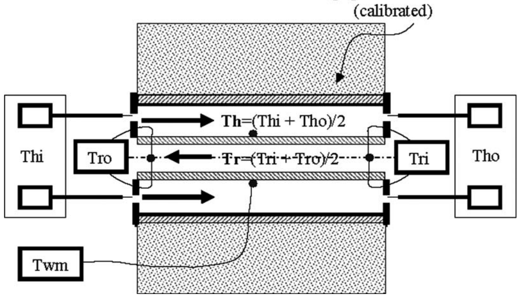

Fig. 7 Schematic of a test section

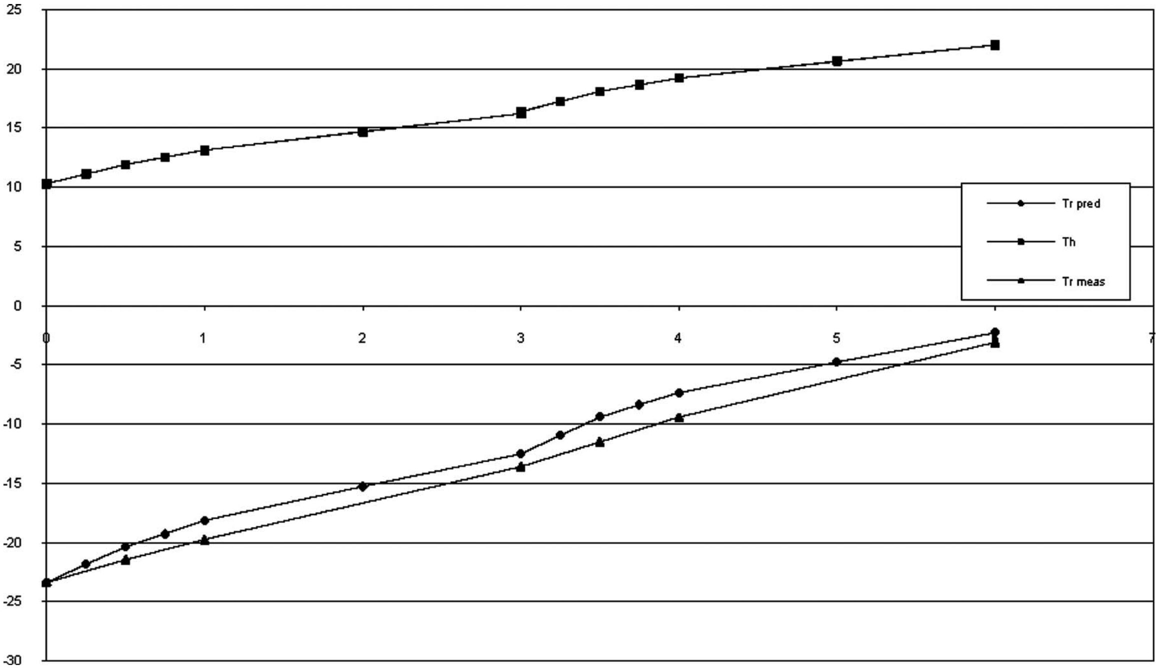

Fig. 8 Comparison of refrigerant temperature predictions to potassium formate data

reliable and is used in subsequent calculations to determine the refrigerant heat transfer coefficient. Very careful analysis was performed for each test run to check for refrigerant and heating fluid balances. It is given in Appendix I of Ref. [1]. This analysis shows that overall heat balance is very good, where the heat balance deviations are 4.50%, 16.4%, and 5.41% for PG, PA, and PF, respectively. The heat balance deviation for PA is higher because of incorrect specific heat data determined later. This is discussed more in detail in Sec. 4.4.1 of Ref. [1]. Good agreement in refrigerant and water side overall heat balances is a consequence of the static mixer at the exit of the pipe and compounded temperature difference.

Having determined the energy balance for each segment using the heating fluid side, the heat transfer coefficient was solved given the heat exchanged, area, and temperatures at the inlet, outlet, and wall as

$$h_r = \frac{Q_h}{A_{r,\mathrm{in}} \cdot (T_w - T_{r,m})}$$

Wall temperature T_w is obtained as an average from the measurement of four thermocouples attached to the surface of the copper tube. It is obvious that these four temperatures are not equal as the consequence of the secondary flows in the tube. This was not the objective of this study and readers could find more details in Ref. [2].

The $T_{r,m}$ term is the average of the refrigerant bulk temperature at the inlet and the outlet of a test section

$$T_{r,m} = \frac{T_{b,i} + T_{b,o}}{2}$$

However, the calculation of the $T_{r,m}$ term in the above equation still requires the determination of the refrigerant bulk temperature, and thermocouples measure temperature at the center. A good measurement of bulk refrigerant temperature cannot be obtained due to secondary flow effects, as discussed previously.

In order to solve for the heat transfer coefficient with reasonable confidence, the effect of measurement error on the heat transfer coefficient was studied. The average bulk refrigerant temperature $T_{r,m}$ is determined by refrigerant inlet and outlet bulk temperatures using heating fluid balance. This temperature prediction procedure is illustrated for one typical run and is shown in Fig. 8. It is a plot of a run with potassium formate.

This graph has three temperature lines: heating fluid T_h, refrigerant temperature measured in the center $T_{r,\mathrm{meas}}$, and bulk refrigerant temperature determined by the heating fluid $T_{r,\mathrm{pred}}$. The effect of the difference $T_{r,\mathrm{pred}} - T_{r,\mathrm{meas}}$ on the determination of the heat transfer coefficient is significantly reduced due to a large temperature difference between wall and refrigerant. Average error induced by this difference is 6.0%. Figure 9 shows the comparison between refrigerant heat transfer coefficients using predicted temperature values to experimental data.

Nevertheless, this difference increases the wall to refrigerant temperature and consequently reduces the Nusselt number or heat transfer coefficient. This error is on the "safe" side because measured values are higher than the existing correlation, as it will be shown later.

The resulting heat transfer coefficient values were than converted to dimensionless Nusselt number

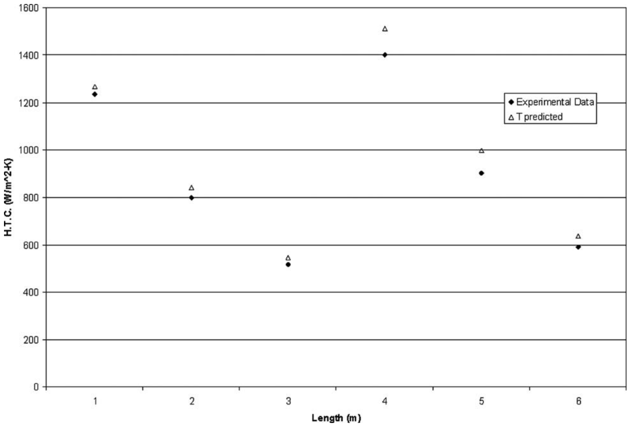

Fig. 9 Comparison of predicted refrigerant heat transfer coefficients to measured values with potassium formate ($V_r = 0.62$ m/s)

$$\mathrm{Nu} = \frac{h_r \cdot ID_{\mathrm{in}}}{k_r}$$

and plotted versus x^*, where

$$x^* = \frac{x}{ID_{\mathrm{in}} \cdot \mathrm{Re} \cdot \mathrm{Pr}}$$

a dimensionless number incorporating length, Reynolds number, and Prandtl number, as accepted in earlier studies like those by Shah and London [3], the inverse of Graetz (Gz) number. For the cases with variable thermophysical properties, corrections should be made to account for the differences in thermophysical properties in radial locations. Sieder and Tate [4], and Popovska [5] are among those that have proposed correction factors. The classic correlation given by Sieder and Tate [4] for flow of viscous oils described their own data for vertical tubes and data of other investigators for horizontal tubes

$$\left(\frac{\mathrm{Nu}}{\mathrm{Nu}_{\mathrm{cp}}}\right) = \left(\frac{\mu_b}{\mu_w}\right)^{0.14}$$

4 Experimental Results and Comparison to Existing Correlations and Other Published Experimental Results

Appendices A and J in Ref. [1] present a complete set of data for each coaxial heat exchanger experimental run and give additional information. For each run there are:

- measured data in tabular form
- graph showing local heat exchanged in each test section
- temperature profiles along the tube
- the heat transfer coefficient that has been calculated and plotted against the length of each test section

All data presented in this paragraph are shown as is, with no adjustments for variable thermophysical properties. However, the correlation used for comparison, in this case the Gnielinski [6] correlation, has been adjusted for variable property using the correlation by Sieder and Tate [4].

Open symbols in Fig. 10 are data obtained in the test tube before the U-bend, and closed symbols are after the U-bend. Solid lines are curve-fit, while dashed lines are from the Gnielinski [6] correlation. For the curve-fit of each fluid, or correlation proposed, the asymptote at a small x^* value is found from a curve-fit of the data points of all three fluids combined, while the asymptote at a large x^* value was determined for each fluid separately. The standard deviations of the curve-fits are 5.91 and 4.42 for before and after the U-bend, respectively. In addition, two lines are shown for the Gnielinski [6] correlation: index T represents the constant wall temperature case while H is the case of constant heat flux on the heat exchanger surface. It is already being discussed that this experiment, as most of the real applications, does not fit into any of these boundary conditions but lies somewhere in between. We have chosen the Gnielinski [6] correlation as a reference on this graph because it is closest to the experimental data obtained in this work. There is also a curve given in the plot that lists the curve-fit of the Nu numbers of all three fluids combined before the U-bend. This curve gives some idea of how the curve-fit of propylene glycol compares to the average curve-fit. In addition, authors recognize that asymptotes in curve-fits (correlations) do not reach expected values for fully developed flows. That is true also for the results internally: asymptotes are not identical for the cases before and after the U-bend.

Results show almost equal Nu numbers for open and closed symbols at small x^* values preceding and following the U-bend. That means that the effect of the U-bend is as strong as the complete restart of the thermally developing region. At higher x^*, which is here mostly further downstream, or for faster flow or less viscous (such as in higher temperature) cases, effects of secondary flow in the U-bend are even stronger. For these conditions, heat transfer downstream of the U-bend is even higher than at the same distance from the entrance with a uniform temperature in the radial direction.

The data points in Fig. 11 show similar experimental results for runs with potassium acetate. The Nu number does not increase as sharply as in experiments with propylene glycol at small x^* values. However, the curve exhibits the overall same behavior—a larger Nu number at a small x^* value and a more or a less constant value at a large x^*. At large x^* values, the asymptotic curve flattens out to a Nu number of around 7. The standard deviations of the curve-fits for potassium acetate are 1.77 and 1.40 for before and after the U-bend, respectively.

The data points in Fig. 12 show experimental results for runs with potassium formate. The Nu number is the highest among all three fluids. The data points are especially higher in the middle region than the other two fluids. However, the curve exhibits the same overall behavior as the other fluids—a larger Nu number at a small x^* value and a more or less constant value at a large x^* value. The standard deviations of the curve-fits for potassium formate are 1.75 and 1.84 for before and after the U-bend, respectively.

Figure 13 gives the curve-fit as well as a 99% confidence interval and R^2 for the data-fit curve for all three fluids together. Its standard deviation is 3.92.

Assuming the same effect as those of variable thermophysical properties, one would expect that results for all three fluids will fall on top of each other. However, Fig. 13 shows some variation among fluids. Potassium formate has the highest Nu number while propylene glycol and potassium acetate are more or less on top of each other.

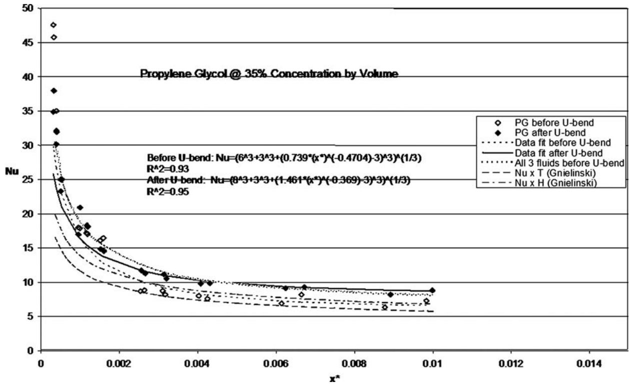

Fig. 10 Heat transfer preceding and following the U-bend for propylene glycol

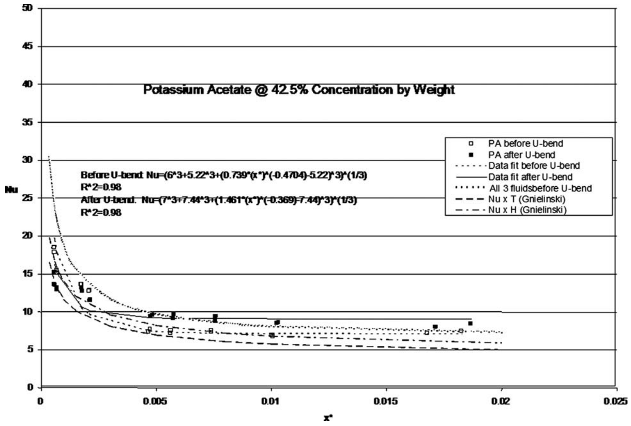

Fig. 11 Heat transfer preceding and following the U-bend for potassium acetate

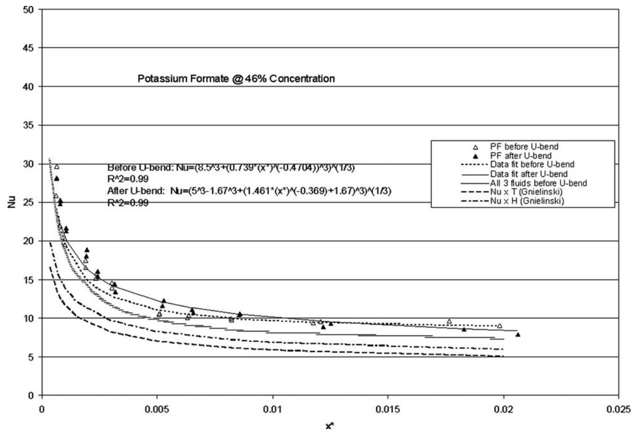

Fig. 12 Heat transfer preceding and following the U-bend for potassium formate

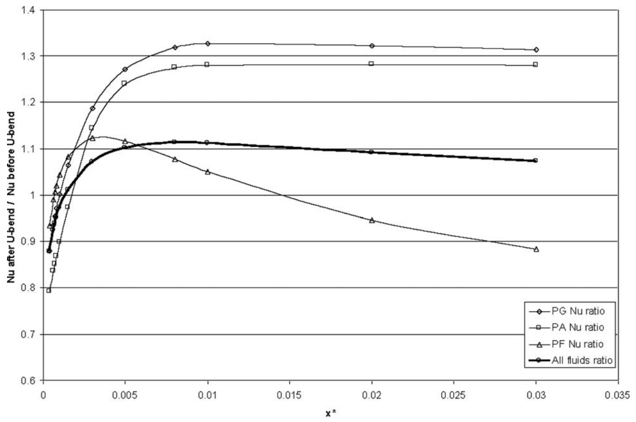

Fig. 15 Ratio of the Nusselt number preceding and following the U-bend for each of the three fluids, individually and together

The same procedure is repeated for the data points after the U-bend. The plot below, Fig. 14, gives a 99% confidence interval and R^2 for the data-fit curve of the data after the U-bend. Its standard deviation is 3.64.

4.1 Effect of the U-Bend. The graphs in Figs. 13 and 14 allow the direct comparison between the effect of the thermal entry region and the effect of the U-bend. The ratio between a curve-fit of data points for a straight section before the U-bend to that of after the U-bend for all three fluids presented in Fig. 15. The ratio for all three fluids shows that the Nusselt number after the U-bend is slightly less than before the U-bend for x^* less than 0.0011 but becomes greater after that point. At a large value of x^*, the ratio reaches an asymptotic value near 1. This result clearly shows that even a smooth U-bend will have an effect of remixing the thermal stratification of a laminar flow sufficiently well that essentially a thermally developing flow occurs after the U-bend.

4.2 Comparison to Other Correlations. Figures 16 and 17 present data obtained in this work for all three fluids along with two correlations by Gnielinski [6]—one is constant heat flux cor-

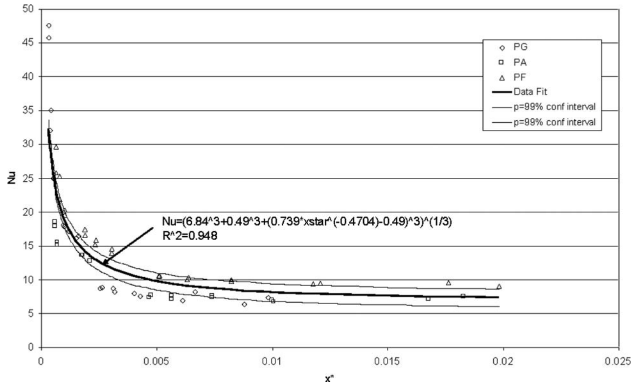

Fig. 13 Local Nusselt number versus *x preceding the U-bend. Figure 13 gives the curve-fit as well as a 99% confidence interval and R^2 for the data-fit curve for all three fluids together. Its standard deviation is 3.92.**

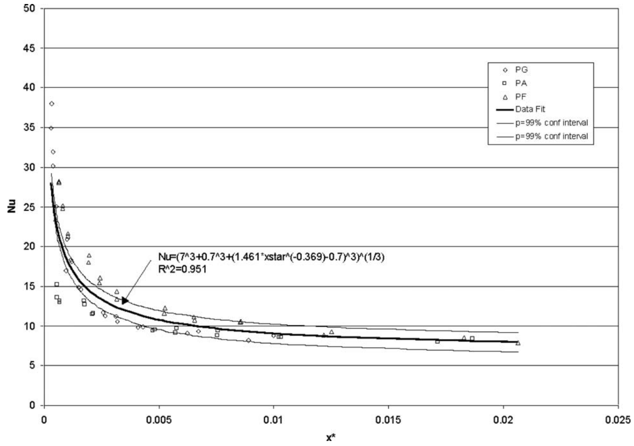

Fig. 14 Nusselt number versus *x in a straight section following the U-bend**

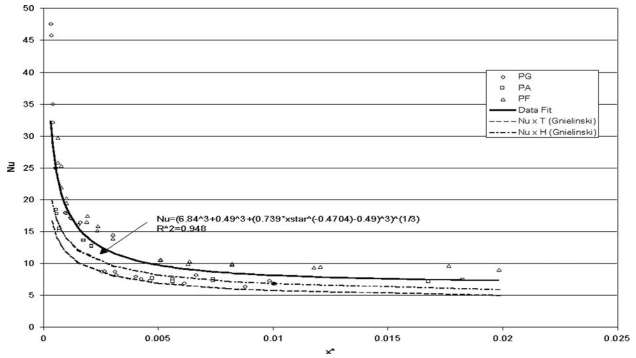

Fig. 16 Nusselt number before the U-bend with published correlations

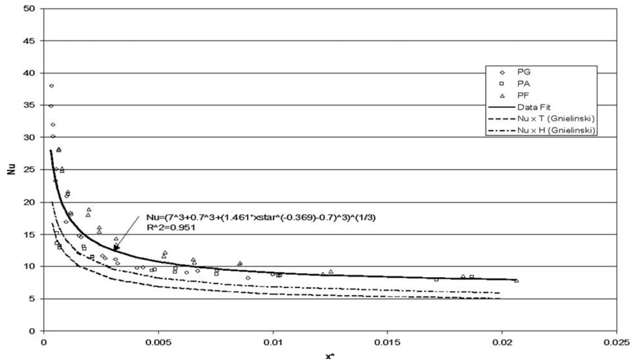

Fig. 17 Nusselt number after the U-bend with published correlations

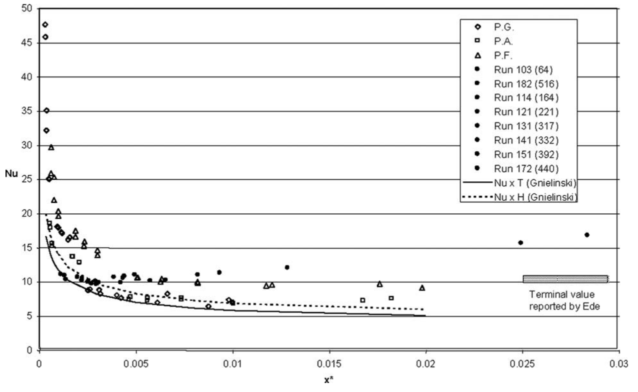

Fig. 18 Heat transfer in the coaxial heat exchanger experimental results preceding the U-bend—comparison of several experimental results: from Ref. [2] (solid circles), from Ref. [7], and from this work (open symbols)

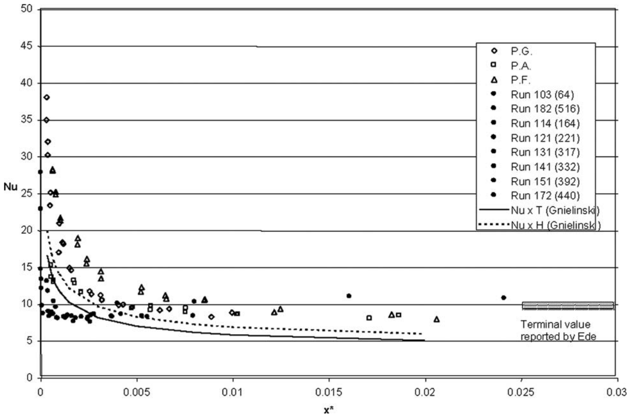

Fig. 19 Heat transfer in the coaxial heat exchanger experimental results following the U-bend—comparison of several experimental results: from Ref. [2] (solid circles), from Ref. [7], and from this work (open symbols)

relation and the other is constant temperature correlation. The Nu number of experimental data is expected to be bounded by the two correlation curves. However, the graphs show the Nusselt number of data in this investigation to be higher than both of the correlations. In addition, the correlations by Gnielinski [6] have been adjusted with the temperature dependent viscosity ratio by Sieder and Tate [4]. In addition, the asymptote of each of the correlations developed here are higher than expected. The authors wanted to report actual experimental data.

For laminar flow through a U-bend, Mehta and Bell [2] reported very extensive experimental data of the effect of return bends. They presented the radial temperature distribution after the U-bend.

The experimental setup was a coaxial heat exchanger type similar to this work, but the heat exchanger was electrically heated. Its electrical heating method gives a different boundary condition than the coaxial heat exchanger tested in this case, so a direct comparison may not be justified. The other significant difference between this work and the one by Mehta and Bell [2] is that their U-bend is on a vertical plane with its outlet on top. Even with the above mentioned and other differences between the experiment by Mehta and Bell [2] and this coaxial heat exchanger setup, comparisons of the results between the two experiments are conducted to aid in the understanding of the thermally developing flow. Since Mehta and Bell [2] did not present the development of the heat transfer coefficient along the tube, authors extracted appropriate dimensionless variables.

Figure 18 shows data points by Mehta and Bell [2] preceding a U-bend. Those results are shown with filled symbols. Open symbols are data obtained in this work for each individual fluid. At the higher x^* values, the Nu number for the developed region as reported by Ede [7] is shown. Solid and dotted lines are the correlations by Gnielinski [6].

The comparison shows a qualitatively better correlation of current results to the correlation by Gnielinski [6]. The difference in offset comes from the effect of different thermophysical properties at the wall and in the center of the flow and phenomena associated with the secondary flow induced by this effect. That issue was discussed in Sec. 3. Nevertheless, the results by Mehta and Bell [2] do not indicate the same change in the heat transfer coefficient with x^* as expected and found here. Values are less or more unaffected by x^*. The data shown by solid circles are calculated from original data based on average values in the circumferential direction to fit into the Nu number versus x^* variables. Experimental values reported by Ede [7] in sketchy form agree with the data obtained in this work. Figure 19 plots the data for locations after the U-bend. A steep asymptotic curve at the region right after the U-bend is clearly evident in the results by Mehta and Bell [2]. However, the effect of the U-bend is evident at a much smaller value of the parameter x^* than those found in this work with the coaxial heat exchanger or what the correlation by Gnielinski [6] would predict.

5 Summary Conclusion

This paper presents results of heat transfer experiments in laminar flow with three fluids: propylene glycol (35%), potassium acetate (42.5%), and potassium formate (46%). To our best knowledge, this is the first experimental heat transfer result for potassium acetate and potassium formate. These fluids are very attractive due to their good properties as secondary coolants in the range of −10–−40°C and their environmentally benign character. Concentration and the range explored reflect these applications as the secondary coolants in indirectly refrigerated systems.

The thermally developing region is found to be extremely long and technically significant (0.5–1.5 m). That fact could be extremely important in heat exchanger design. Experimental results are compared with existing correlations. Experimental results show somewhat higher values than predicted.

The equation

$$\mathrm{Nu} = (6.84^3 + 0.49^3 + (0.739x^{*(-0.4704)} - 0.49)^3)^{1/3} \qquad (1)$$

was found to represent the best heat transfer in the thermally developing region of the laminar flow. Compared with some other correlations, the asymptotic value 6.84 is on the high end (see Fig. 20, Appendix A).

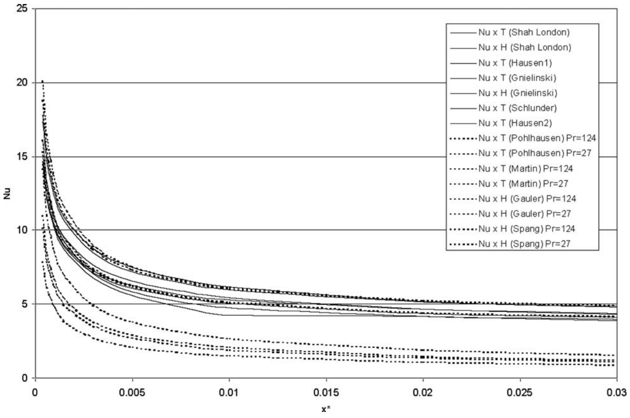

Fig. 20 Published correlations for thermally and simultaneously developing flows

Effects of mixing in the return U-bend in a horizontal orientation show almost a full recovery of heat transfer rates to the value at the inlet to the pipe, so the heat transfer rates can be predicted assuming a full restart of the thermally developing region after the return U-bend. For the two fluids explored, heat transfer after the U-bend was even increased compared with inlet to the tube (Fig. 15).

Nomenclature

A = area
C_p = specific heat
fd = fully developed
Gn = correlation by Gnielinski [6]
Gz = Graetz number
h = heat transfer coefficient
H1 = correlation by Hausen (1943)
H2 = correlation by Hausen (1959)
D = diameter
ID = inside diameter
k = conductivity
L = length
m = mass flow
Ma = correlation by Martin
N = number
Nu = Nusselt number
OD = outside diameter
Re = Reynolds number
Po = correlation by Pohlhausen
Pr = Prandtl number
Q = heat transfer
R = resistance
Sc = correlation by Schlunder
SL = correlation by Shah and London [3]
Sp = correlation by Spang
T = temperature
V = velocity
x = local length
x^* = dimensionless length (the inverse of Gz)

Greek Symbols

μ = viscosity

Subscripts

b = bulk
cp = constant physical property
h = heating fluid
H = constant heat flux
heater = heater
i = inlet
in = inside
m = mean
meas = measured
o = outlet
out = outside
pred = predicted
r = refrigerant
R = tubes
x = local
T = constant temperature
tot = total
w = wall

Appendix A

A.1 Error Analysis. A simulation code was used to calculate the numerical derivatives of the heat transfer and local heat transfer coefficient equations to be applied to Eq. (C1) with the appropriate uncertainty values from Tables 3–6. Uncertainties for tem-

Table 3 Uncertainty values of coaxial heat exchanger measurements

Variable	Uncertainty
T_{r1}–T_{r7}	±0.082°C
T_{h1}–T_{h8}	±0.045°C
T_{w1}–T_{w6}	±0.026°C
m_r	±0.1%
m_h	±0.1%

Table 4 Coaxial heat exchanger error analysis for propylene glycol

		$V_r=0.95$ m/s		$V_r=0.78$ m/s		$V_r=0.60$ m/s		$V_r=0.38$ m/s		$V_r=0.27$ m/s	
	Unit	Run 1 (052499-1)	Run 2 (060499-1)	Run 1 (052499-2)	Run 2 (060499-2)	Run 1 (060399-1)	Run 2 (060599-1)	Run 1 (060399-2)	Run 2 (060599-2)	Run 1 (052499-3)	Run 2 (060599-3)
x_1^*	-	$0.0003168\pm3.188\times10^{-7}$	$0.0003285\pm3.307\times10^{-7}$	$0.0003868\pm3.893\times10^{-7}$	$0.0003947\pm3.973\times10^{-7}$	$0.0005301\pm5.335\times10^{-7}$	$0.0005016\pm5.048\times10^{-7}$	$0.0007643\pm7.704\times10^{-7}$	$0.0008227\pm8.292\times10^{-7}$	0.001092 ± 0.0000011	0.00122 ± 0.000001229
x_2^*	-	$0.0009514\pm9.575\times10^{-7}$	$0.000988\pm9.944\times10^{-7}$	0.001162 ± 0.000001169	0.001187 ± 0.000001195	0.001593 ± 0.000001606	0.001509 ± 0.000001521	0.002298 ± 0.000002316	0.002478 ± 0.000002497	0.003284 ± 0.00000331	0.003675 ± 0.000003692
x_3^*	-	0.00254 ± 0.000002557	0.002641 ± 0.000002658	0.003107 ± 0.000003132	0.003172 ± 0.000003192	0.004253 ± 0.000004286	0.00403 ± 0.000004062	0.006132 ± 0.00000618	0.006639 ± 0.00000667	0.008771 ± 0.000008839	0.00983 ± 0.000009874
x_4^*	-	$0.0003186\pm3.211\times10^{-7}$	$0.0003308\pm3.334\times10^{-7}$	$0.0003902\pm3.932\times10^{-7}$	$0.0003972\pm4.003\times10^{-7}$	$0.0005339\pm5.380\times10^{-7}$	$0.0005049\pm5.088\times10^{-7}$	$0.0007706\pm7.765\times10^{-7}$	$0.0008345\pm8.383\times10^{-7}$	0.001103 ± 0.000001108	0.001238 ± 0.000001243
x_5^*	-	$0.0009586\pm9.660\times10^{-7}$	0.0009949 ± 0.000001003	0.001173 ± 0.000001182	0.001196 ± 0.000001206	0.001609 ± 0.000001617	0.001522 ± 0.000001534	0.002324 ± 0.000002334	0.002509 ± 0.000002521	0.003326 ± 0.000003341	0.003733 ± 0.000003749
x_6^*	-	0.002566 ± 0.000002585	0.002664 ± 0.000002684	0.00314 ± 0.000003155	0.003205 ± 0.00000323	0.00431 ± 0.00000433	0.00408 ± 0.000004098	0.00623 ± 0.000006258	0.006712 ± 0.000006741	0.008913 ± 0.000008953	0.009983 ± 0.00001003
$\mathrm{Nu}_{r,1}$	-	47.57 ± 2.531	45.76 ± 2.455	32.11 ± 2.008	35 ± 1.993	24.97 ± 1.576	25 ± 1.504	19 ± 1.476	15.49 ± 1.409	11.3 ± 1.411	9.748 ± 1.41
$\mathrm{Nu}_{r,2}$	-	18 ± 2.247	17.87 ± 2.275	17.19 ± 1.824	17.06 ± 1.873	16.45 ± 1.456	16.09 ± 1.423	14.18 ± 1.411	14.88 ± 1.415	12.88 ± 1.39	13.88 ± 1.473
$\mathrm{Nu}_{r,3}$	-	8.698 ± 0.5231	8.839 ± 0.5471	8.747 ± 0.4394	8.179 ± 0.4383	7.573 ± 0.331	8.004 ± 0.3297	6.904 ± 0.3238	8.191 ± 0.3632	6.346 ± 0.3318	7.288 ± 0.375
$\mathrm{Nu}_{r,4}$	-	34.89 ± 2.418	37.98 ± 2.446	30.14 ± 2.066	31.95 ± 1.94	25.04 ± 1.506	23.29 ± 1.427	21.45 ± 1.454	22.48 ± 1.726	18.1 ± 1.518	19.49 ± 1.881
$\mathrm{Nu}_{r,5}$	-	16.96 ± 2.455	20.91 ± 2.561	18.32 ± 2.083	18.11 ± 2.059	14.55 ± 1.598	14.85 ± 1.478	11.63 ± 1.609	12.16 ± 1.76	8.726 ± 1.736	11.03 ± 2.265
$\mathrm{Nu}_{r,6}$	-	11.7 ± 0.6171	11.28 ± 0.6207	11.15 ± 0.5127	10.5 ± 0.5121	9.878 ± 0.4211	9.798 ± 0.3966	9.114 ± 0.4622	9.296 ± 0.4716	8.194 ± 0.5289	8.789 ± 0.6309

Table 5 Coaxial heat exchanger error analysis for potassium acetate

		V_r=0.61 m/s		V_r=0.51 m/s		V_r=0.39 m/s		V_r=0.29 m/s		V_r=0.17 m/s	
	Unit	Run 1 (061599-1)	Run 2 (061699-3)	Run 1 (061599-2)	Run 2 (061699-4)	Run 1 (061599-3)	Run 2 (061699-5)	Run 1 (061699-1)	Run 2 (061699-6)	Run 1 (061699-2)	Run 2 (061699-7)
x_1^*	-	0.0005811 ± 5.830×10^{-7}	0.0005917 ± 5.936×10^{-7}	0.0007001 ± 7.024×10^{-7}	0.0007018 ± 7.041×10^{-7}	0.0009174 ± 9.203×10^{-7}	0.0009181 ± 9.211×10^{-7}	0.001249 ± 0.000001253	0.00124 ± 0.000001245	0.002059 ± 0.000002067	0.002234 ± 0.000002243
x_2^*	-	0.001748 ± 0.000001753	0.001779 ± 0.000001785	0.002106 ± 0.000002113	0.00211 ± 0.000002119	0.002761 ± 0.000002772	0.002761 ± 0.000002772	0.003755 ± 0.00000377	0.003731 ± 0.000003745	0.006216 ± 0.00000624	0.006756 ± 0.000006782
x_3^*	-	0.004671 ± 0.00000469	0.004757 ± 0.000004775	0.005632 ± 0.000005655	0.005648 ± 0.00000567	0.007401 ± 0.000007429	0.007407 ± 0.000007436	0.01008 ± 0.00001012	0.01002 ± 0.00001006	0.01679 ± 0.00001685	0.01828 ± 0.00001835
x_4^*	-	0.0005855 ± 5.878×10^{-7}	0.0005965 ± 5.989×10^{-7}	0.0007068 ± 7.095×10^{-7}	0.0007092 ± 7.119×10^{-7}	0.0009293 ± 9.329×10^{-7}	0.0009294 ± 9.330×10^{-7}	0.001273 ± 0.000001277	0.001264 ± 0.000001269	0.002123 ± 0.000002128	0.002312 ± 0.000002318
x_5^*	-	0.00177 ± 0.000001777	0.001803 ± 0.00000181	0.002137 ± 0.000002145	0.002147 ± 0.000002155	0.002807 ± 0.000002818	0.002807 ± 0.000002818	0.003843 ± 0.000003858	0.003818 ± 0.000003832	0.006399 ± 0.000006413	0.00697 ± 0.000006986
x_6^*	-	0.004763 ± 0.000004782	0.004855 ± 0.000004874	0.005753 ± 0.000005775	0.005785 ± 0.000005806	0.007569 ± 0.000007597	0.00759 ± 0.000007608	0.01032 ± 0.00001035	0.01026 ± 0.00001028	0.01715 ± 0.00001718	0.01868 ± 0.00001872
$\mathrm{Nu}_{r,1}$	-	18.45 ± 0.7492	17.8 ± 0.6963	15.49 ± 0.7366	15.1 ± 0.6774	11.77 ± 0.7008	12.37 ± 0.6357	7.934 ± 0.7771	8.753 ± 0.7849	5.338 ± 0.7229	4.686 ± 0.7102
$\mathrm{Nu}_{r,2}$	-	13.58 ± 0.6978	13.59 ± 0.6463	12.7 ± 0.6971	12.75 ± 0.6345	12.15 ± 0.6788	11.92 ± 0.6023	11.24 ± 0.7532	11.29 ± 0.765	11.7 ± 0.7928	12.19 ± 0.8003
$\mathrm{Nu}_{r,3}$	-	7.296 ± 0.1654	7.643 ± 0.1533	7.164 ± 0.169	7.529 ± 0.1549	7.273 ± 0.1735	7.549 ± 0.1553	6.721 ± 0.2034	6.85 ± 0.2073	7.125 ± 0.2501	7.436 ± 0.2625
$\mathrm{Nu}_{r,4}$	-	15.16 ± 0.6851	13.55 ± 0.6255	12.87 ± 0.6949	13.14 ± 0.639	11.38 ± 0.7036	11.22 ± 0.6159	12.97 ± 0.9716	12.95 ± 0.97	13.94 ± 1.388	13.83 ± 1.519
$\mathrm{Nu}_{r,5}$	-	13.12 ± 0.7811	12.67 ± 0.708	11.44 ± 0.8097	11.54 ± 0.7498	9.245 ± 0.8063	8.444 ± 0.6805	8.684 ± 1.152	7.955 ± 1.125	6.453 ± 1.712	6.306 ± 1.911
$\mathrm{Nu}_{r,6}$	-	9.329 ± 0.219	9.486 ± 0.2021	9.099 ± 0.2389	9.666 ± 0.2255	8.762 ± 0.261	9.357 ± 0.2382	8.527 ± 0.3764	8.469 ± 0.3788	7.948 ± 0.6276	8.371 ± 0.7237

Table 6 Coaxial heat exchanger error analysis for potassium formate

		V_r=0.62 m/s		V_r=0.50 m/s		V_r=0.39 m/s		V_r=0.27 m/s		V_r=0.17 m/s	
	Unit	Run 1 (062499-1)	Run 2 (062699-1)	Run 1 (062499-2)	Run 2 (062699-2)	Run 1 (062499-3)	Run 2 (062699-3)	Run 1 (062499-4)	Run 2 (062699-4)	Run 1 (062499-5)	Run 2 (062699-5)
x_1^*	-	0.0006249 ± 6.338×10^{-7}	0.0006285 ± 6.373×10^{-7}	0.0007733 ± 7.843×10^{-7}	0.0007791 ± 7.900×10^{-7}	0.001006 ± 0.000001021	0.001004 ± 0.000001018	0.00147 ± 0.00000149	0.001433 ± 0.000001452	0.002121 ± 0.00000215	0.002377 ± 0.00000241
x_2^*	-	0.001885 ± 0.000001911	0.001897 ± 0.000001923	0.002331 ± 0.000002364	0.002352 ± 0.000002384	0.003033 ± 0.000003075	0.00303 ± 0.000003071	0.004439 ± 0.000004499	0.004331 ± 0.000004389	0.006445 ± 0.00000653	0.00725 ± 0.000007345
x_3^*	-	0.005082 ± 0.000005151	0.00511 ± 0.000005178	0.006291 ± 0.000006375	0.006353 ± 0.000006436	0.00822 ± 0.000008328	0.008209 ± 0.000008314	0.01207 ± 0.00001222	0.01176 ± 0.00001191	0.01764 ± 0.00001785	0.01983 ± 0.00002007
x_4^*	-	0.0006427 ± 6.510×10^{-7}	0.0006466 ± 6.548×10^{-7}	0.000798 ± 8.083×10^{-7}	0.0008051 ± 8.152×10^{-7}	0.001047 ± 0.00000106	0.001045 ± 0.000001057	0.001535 ± 0.000001554	0.001494 ± 0.000001512	0.002246 ± 0.000002271	0.002528 ± 0.000002557
x_5^*	-	0.001939 ± 0.000001964	0.001958 ± 0.000001982	0.00241 ± 0.000002441	0.002431 ± 0.000002461	0.003166 ± 0.000003205	0.003158 ± 0.000003195	0.00463 ± 0.000004684	0.004509 ± 0.000004562	0.006772 ± 0.000006847	0.007649 ± 0.000007733
x_6^*	-	0.005231 ± 0.000005295	0.005277 ± 0.00000534	0.00651 ± 0.000006588	0.00656 ± 0.000006637	0.008566 ± 0.000008665	0.008535 ± 0.000008631	0.0125 ± 0.00001264	0.01218 ± 0.00001231	0.01829 ± 0.00001848	0.02063 ± 0.00002085
$\mathrm{Nu}_{r,1}$	-	25.81 ± 1.016	29.63 ± 1.017	21.89 ± 0.9495	25.24 ± 0.9473	19.53 ± 0.8467	20.28 ± 0.8561	11.58 ± 0.9451	13.49 ± 0.9656	10.13 ± 0.8487	9.556 ± 0.8334
$\mathrm{Nu}_{r,2}$	-	16.56 ± 0.872	17.43 ± 0.8812	15.19 ± 0.8413	15.83 ± 0.8545	13.87 ± 0.7746	14.57 ± 0.7934	14.04 ± 0.9409	14.33 ± 0.9712	14.28 ± 0.9377	14.68 ± 0.9637
$\mathrm{Nu}_{r,3}$	-	10.55 ± 0.2202	10.59 ± 0.2175	9.976 ± 0.2173	10.34 ± 0.2232	9.795 ± 0.2119	9.95 ± 0.216	9.491 ± 0.2812	9.361 ± 0.2851	9.608 ± 0.3155	9.052 ± 0.3147
$\mathrm{Nu}_{r,4}$	-	28.18 ± 1.046	28.07 ± 1.03	24.77 ± 1.033	25.13 ± 1.055	21.3 ± 1.006	21.65 ± 1.03	18.07 ± 1.37	18.69 ± 1.353	18.73 ± 1.613	18 ± 1.639
$\mathrm{Nu}_{r,5}$	-	18.01 ± 1.025	18.91 ± 1.086	15.41 ± 1.044	16.06 ± 1.066	13.39 ± 1.066	14.37 ± 1.077	9.917 ± 1.468	10.53 ± 1.458	7.163 ± 1.754	6.845 ± 1.981
$\mathrm{Nu}_{r,6}$	-	11.61 ± 0.2661	12.21 ± 0.2735	11.11 ± 0.2863	10.68 ± 0.2865	10.57 ± 0.3137	10.43 ± 0.3127	9.259 ± 0.4778	8.818 ± 0.4698	8.523 ± 0.6732	7.874 ± 0.7511

perature measurements are determined in Appendix H of Ref. [1]. The values are deviations from average values for each set of thermocouples (refrigerant, heating fluid, and wall). These values are not uncertainties of temperature readings but temperature differences.

Appendix B: Thermophysical Properties of Fluids Examined

B.1 Propylene Glycol. Propylene glycol is 35% concentration by volume [8]; linear interpolation.

B.2 Potassium Acetate (Pekasol 50). Potassium acetate (pekasol 50) is 42.5% by weight—interpolation from Table 7.

B.3 Potassium Formate. Potassium formate is 46% by weight. Temperature T is in Celsius (°C).

$$\text{Density}\ \ (\mathrm{kg/m^3}) = -\,0.530754^{*}T + 1328.7$$

$$\text{Viscosity}\ \ (\mathrm{cP}) = 0.0899^{*}\ \exp(479.09/T + 126.55)$$

$$\text{Conductivity}\ \ (\mathrm{W/m\ K}) = 0.001674^{*}T + 0.4750$$

Table 7 Physical properties of potassium acetate

Temperature (°C)	Specific heat (kJ/kg K)	Conductivity (W/m K)	Viscosity (mPa s)	Density (g/cm^3)
20	3.311	0.517	2.2	1.221
0	3.258	0.497	3.8	1.229
−10	3.234	0.486	5.7	1.233
−20	3.216	0.476	9.3	1.237
−30	3.193	0.466	17.5	1.241

$$\text{Specific heat (kJ/kg K)} = 0.0023^{*}T + 2.578$$

Appendix C: Thermally Developing Flow Correlations

In the hydrodynamically and thermally fully developed flow, the Nu number ($\mathrm{Nu}=hD/K$) for a uniform wall temperature is found to be the constant 3.66 [9]. This is for the conditions of the absence of flow work, thermal energy sources, and fluid axial conduction. For the case of uniform heat flux with negligible viscous dissipation and no thermal energy source, the Nu number is found to be 4.36 [10]. In a thermally developing flow, a fluid with a fully developed velocity distribution and a uniform temperature flows into the entrance, and the fluid axial conduction, viscous dissipation flow work, and energy resource are negligible in most cases. Graetz and Nusselt solved this problem with the boundary conditions of constant surface temperature and presented the solution in the form of an infinite series of eigenvalues and constants. However, the eigenvalue solution is very slowly convergent at the region close to the entry, and the asymptotic solution by Leveque is utilized at the entry region. The uniform heat flux thermal entry region problem is very similar to the constant surface temperature problem. Shah and London [3] formulated the following equations to correlate the infinite series within 3% accuracy:

$$\begin{aligned}\mathrm{Nu}_{x,T} &= 1.077x^{*-1/3} - 0.7 \quad \text{for } x^{*} \le 0.01\\ &= 3.657 + 6.874(10^{3}x^{*})^{-0.488}e^{-57.2x^{*}} \quad \text{for } x^{*} > 0.01\end{aligned} \tag{C1}$$

$$\begin{aligned}\mathrm{Nu}_{m,T} &= 1.615x^{*-1/3} - 0.7 \quad \text{for } x^{*} \le 0.005\\ &= 1.615x^{*-1/3} - 0.2 \quad \text{for } 0.005 < x^{*} < 0.03\\ &= 3.657 + 0.0499/x^{*} \quad \text{for } x^{*} \ge 0.03\end{aligned} \tag{C2}$$

$$\begin{aligned}\mathrm{Nu}_{x,H} &= 1.302x^{*-1/3} - 1 \quad \text{for } x^{*} \le 0.00005\\ &= 1.302x^{*-1/3} - 0.5 \quad \text{for } 0.00005 < x^{*} < 0.0015\\ &= 4.364 + 8.68(10^{3}x^{*})^{-0.506}e^{-41x^{*}} \quad \text{for } x^{*} \ge 0.0015\end{aligned} \tag{C3}$$

$$\begin{aligned}\mathrm{Nu}_{m,H} &= 1.953x^{*-1/3} \quad \text{for } x^{*} \le 0.03\\ &= 4.364 + 0.0722/x^{*} \quad \text{for } x^{*} > 0.03\end{aligned} \tag{C4}$$

where $x^{*}=x/(D*\mathrm{Re}*\mathrm{Pr})$.

Hausen, as prescribed by Ebadian and Dong [11], presented the following correlation for the mean Nusselt numbers of the solution by Graetz for the entire range of x^{*}:

$$\mathrm{Nu}_{m,T} = 3.66 + \frac{0.0668}{x^{*1/3}(0.04 + x^{*2/3})} \tag{C5}$$

Shah and Bhatti [10] took the above correlation by Hausen and calculated the local Nusselt numbers of the solution by Graetz

$$\mathrm{Nu}_{x,T} = 3.66 + \frac{0.0018}{x^{*1/3}(0.04 + x^{*2/3})^{2}} \tag{C6}$$

Hausen's two predictions given above in Eqs. (C5) and (C6) are higher than the tabulated values obtained from the infinite series by amounts ranging from 14% for $x^{*} < 0.0001$ to 0% as x^{*} goes to infinity [10].

Shah and London [3] presented the numerical solutions of the well-known Nusselt–Graetz problem for heat transfer to an incompressible fluid with constant properties flowing through a circular duct having a uniform wall temperature and a fully developed laminar velocity profile. The asymptotes for the local Nusselt number with a uniform wall temperature are presented below. The two asymptotes for a uniform temperature boundary condition are

$$\mathrm{Nu}_{x,T} = 1.077x^{*-1/3} \quad \text{for } x^{*} < 0.01 \tag{C7}$$

and

$$\mathrm{Nu}_{x,T} = 3.66 \quad \text{for } x^{*} > 0.01 \tag{C8}$$

The two corresponding asymptotes of the mean Nusselt number integrated from 0 to x are as follows:

$$\mathrm{Nu}_{m,T} = 1.61x^{*-1/3} \quad \text{for } x^{*} < 0.001 \tag{C9}$$

and

$$\mathrm{Nu}_{m,T} = 3.66 \quad \text{for } x^{*} > 0.01 \tag{C10}$$

Schlunder, in Ref. [12], derived a correlation of the two mean Nusselt number asymptotes by superpositioning them. This correlation claims to give sufficiently good results for most technical purposes

$$\mathrm{Nu}_{m,T} = (3.66^{3} + 1.61^{3}/x^{*})^{1/3} \tag{C11}$$

Hausen, as in Ref. [13], obtained a different correlation, which deviates only slightly from the equation given by Schlunder

$$\mathrm{Nu}_{m,T} = 3.66 + \frac{0.19x^{*-0.8}}{1 + 0.117x^{*-0.467}} \tag{C12}$$

Both equations by Schlunder and by Hausen are valid for gases and liquids in the range of $0.0001 < x^{*} < 10$.

Shah and London [3] also considered the two asymptotes for the case of a uniform heat flux boundary condition. The two asymptotes are given below

$$\mathrm{Nu}_{x,H} = 1.302x^{*-1/3} \quad \text{for } x^{*} < 0.0001 \tag{C13}$$

and

$$\mathrm{Nu}_{x,H} = 4.36 \quad \text{for } x^{*} > 0.001 \tag{C14}$$

The corresponding asymptotes for the mean Nusselt numbers are as follows:

$$\mathrm{Nu}_{m,H} = 1.953x^{*-1/3} \quad \text{for } x^{*} < 0.01 \tag{C15}$$

and

$$\mathrm{Nu}_{m,H} = 4.36 \quad \text{for } x^{*} > 0.1 \tag{C16}$$

Gnielinski [14] has also compiled a comprehensive list of correlations for heat transfer to an incompressible fluid with constant properties in the thermal entry region of a circular tube, and he presents local as well as mean Nusselt numbers for a uniform temperature and a uniform heat flux boundary conditions. The correlations given in the paper by Gnielinski [14] are mainly superpositions of the asymptotes, and the asymptotes used are given in Eqs. (C7)–(C10) and (C13)–(C16).

For the case of hydrodynamically fully developed and thermally developing region, the following correlations superposition the two corresponding asymptotes in a way similar to the methods by Schlunder and by Hausen. The correlation for the local Nusselt number for a uniform temperature boundary condition covers the entire range of x^* and is accurate to within 6% in the range of $0.01 < x^* < 0.1$, while the correlation for the mean Nusselt number is accurate to within 1% for the same range

$$\mathrm{Nu}_{x,T} = (3.66^3 + 0.7^3 + (1.077x^{*-1/3} - 0.7)^3)^{1/3} \qquad \text{(C17)}$$

and

$$\mathrm{Nu}_{m,T} = (3.66^3 + 0.7^3 + (1.615x^{*-1/3} - 0.7)^3)^{1/3} \qquad \text{(C18)}$$

The correlations presented in the paper by Gnielinski [14] for a uniform heat flux boundary condition are very similar to those for a uniform wall temperature in that they also superposition the two asymptotes in an appropriate manner. The correlation given below for a local Nusselt number in a uniform heat flux covers the entire range of x^* and is accurate to within 4% in the range of $0.001 < x^* < 0.01$, while the correlation for the mean Nusselt number is accurate to within 1% for the same range

$$\mathrm{Nu}_{x,H} = (4.364^3 + 1 + (1.302x^{*-1/3} - 1)^3)^{1/3} \qquad \text{(C19)}$$

and

$$\mathrm{Nu}_{m,H} = (4.364^3 + 0.6^3 + (1.953x^{*-1/3} - 0.6)^3)^{1/3} \qquad \text{(C20)}$$

There is also a correlation proposed by Eubank and Proctor, see Ref. [14]. They critically surveyed the available data for laminar flow [15,16] of petroleum oils in horizontal steam-heated tubes. Equation (C21) gives the correlation with a maximum deviation of 60% for small D and temperature difference. This equation is also referred to as the Farr equation in discussions hereon. The equation seems to be for the mean value of the heat transfer coefficient

$$\mathrm{Nu} = 1.86 \cdot x^{*-1/3} \qquad \text{(C21)}$$

C.1 Correlations for the Simultaneously Developing Flow. The case of both hydrodynamically and thermally developing flow is also known as the simultaneously developing flow. The simultaneously developing flow usually occurs when the fluid exhibits a moderate Prandtl number, which is when Pr equals 1. In such a flow, the velocity and the temperature profiles develop simultaneously along the flow direction. However, laminar flow develops very quickly, and for a Prandtl number greater than about 5, the velocity profile develops so much faster than the temperature profile that even if both temperature and velocity are uniform at the tube entrance, the hydrodynamically fully developed idealization introduces little error. Shah and London [3] presented tables of eigenvalues of the simultaneously developing flow for uniform wall heat flux and uniform wall temperature conditions.

Gnielinski [14] gave compiled correlations of local and mean Nusselt numbers for the simultaneously developing flow in the cases of a uniform wall temperature and a uniform wall heat flux. Pohlhausen has obtained the following correlations for the simultaneously developing flow for a uniform wall temperature, which is valid for $\mathrm{Pr} > 0.1$:

$$\mathrm{Nu}_{x,T} = 0.332\ \mathrm{Pr}^{1/3}\left(\frac{x}{D\ \mathrm{Re}}\right)^{-1/2} \qquad \text{(C22)}$$

and

$$\mathrm{Nu}_{m,T} = 0.664\ \mathrm{Pr}^{1/3}\left(\frac{x}{D\ \mathrm{Re}}\right)^{-1/2} \qquad \text{(C23)}$$

Martin has calculated the correlations for the simultaneously developing flow for a uniform wall temperature by using a superposition method, and they are presented below

$$\mathrm{Nu}_{x,T} = \left(3.66^3 + 0.7^3 + (1.077x^{*-1/3} - 0.7)^3 + \left(0.5\left(\frac{2}{1+22\ \mathrm{Pr}}\right)^{1/6} x^{*-1/2}\right)^3\right)^{1/3} \qquad \text{(C24)}$$

and

$$\mathrm{Nu}_{m,T} = \left(3.66^3 + 0.7^3 + (1.615x^{*-1/3} - 0.7)^3 + \left(\left(\frac{2}{1+22\ \mathrm{Pr}}\right)^{1/6} x^{*-1/2}\right)^3\right)^{1/3} \qquad \text{(C25)}$$

Gauler has studied the simultaneously developing laminar flow for a uniform heat flux case and has presented the following correlations:

$$\mathrm{Nu}_{x,H} = 0.459\ \mathrm{Pr}^{1/3}\left(\frac{x}{D\ \mathrm{Re}}\right)^{-1/2} \quad \text{for } \mathrm{Pr} = 1 \qquad \text{(C26)}$$

and

$$\mathrm{Nu}_{x,H} = 0.464\ \mathrm{Pr}^{1/3}\left(\frac{x}{D\ \mathrm{Re}}\right)^{-1/2} \quad \text{for } \mathrm{Pr} = \infty \qquad \text{(C27)}$$

Spang has used a superposition method to derive correlations for the simultaneously developing laminar flow for a uniform heat flux and the correlations are presented below

$$\mathrm{Nu}_{x,H} = \left(4.364 + 1 + (1.302x^{*-1/3} - 1)^3 + \left(0.462\ \mathrm{Pr}^{1/3}\left(\frac{x}{D\ \mathrm{Re}}\right)^{-1/2}\right)^3\right)^{1/3} \qquad \text{(C28)}$$

and

$$\mathrm{Nu}_{m,H} = \left(4.364 + 0.6^3 + (1.953x^{*-1/3} - 0.6)^3 + \left(0.924\ \mathrm{Pr}^{1/3}\left(\frac{x}{D\ \mathrm{Re}}\right)^{-1/2}\right)^3\right)^{1/3} \qquad \text{(C29)}$$

The correlations by Spang are valid for $0.7 < \mathrm{Pr} < 1000$.

Figure 20 plots the correlations discussed above in Nusselt number versus x^* for comparison. The graph shows thermally developing flow correlations in solid lines and simultaneously developing flow correlations in dashed lines. For the simultaneously developing flow, the Nusselt number is also a function of the Prandtl number, and two different Prandtl numbers, which cover the whole range of the experimental data ($\mathrm{Pr} = 124$ and 27), are calculated and plotted. As can be seen in Fig. 20, thermally developing flow correlations and simultaneously developing flow correlations are close to each other except for simultaneously developing flow correlations by Pohlhausen and Gauler. The reason for their outlying prediction is because their equations, Eqs. (C22), (C23), (C26), and (C27), do not incorporate a terminal asymptote value at a large x^* value. Therefore, their Nusselt number continues to decrease for a large x^* value.

References

[1] Hong, S. H., and Hrnjak, P. S., 1999, "Heat Transfer in Thermally Developing Flow of Fluids With High Prandtl Numbers Preceding and Following U-Bend," ACRC Report No. CR-24.

[2] Mehta, N. D., and Bell, K. J., 1981, "Laminar Flow Heat Transfer in a Tube Preceded by a 180° Bend," Heat Transfer-Sov. Res., **13**(6), pp. 71–80.

[3] Shah, R. K., and London, A. L., 1978, *Laminar Flow Forced Convection in Ducts*, Academic, New York.

[4] Sieder, E. N., and Tate, G. E., 1936, "Heat Transfer and Pressure Drop of Liquids in Tubes," Ind. Eng. Chem., **28**, pp. 1429–1435.

[5] Popovska, F., 1975, Ph.D. thesis, University of Bradford, Bradford, UK.

[6] Gnielinski, V., 1976, "New Equations for Heat and Mass-Transfer in Turbulent Pipe and Channel Flow," Int. Chem. Eng., **16**, pp. 359–368.

[7] Ede, A. J., 1966, "The Effect of a 180° Bend on Heat Transfer to Water in a Tube," *Proceedings of the Third International Heat Transfer Conference*, Vol. 1, pp. 99–103.

[8] ASHRAE, 1997, "ASHRAE Handbook-Fundamentals."

[9] Bhatti, M. S., 1985, "Fully Developed Temperature Distribution in a Circular Tube With Uniform Wall Temperature," Owens-Corning Fiberglass Corporation, Granville, OH, unpublished paper.

[10] Shah, R. K., and Bhatti, M. S., 1987, *Handbook of Single-Phase Convective Heat Transfer*, S. Kakac, R. K. Shah, and W. Aung, eds., Wiley, New York, Chap. 3.

[11] Ebadian, M. A., and Dong, Z. F., 1998, *Handbook of Heat Transfer*, W. M. Rosennow, J. P. Hartnett, and Y. I. Cho, eds., McGraw-Hill, New York, Chap. 5.
[12] Gnielinski, V., 1983, *Heat Exchanger Design Handbook*, Hemisphere, New York, Chap. 2.
[13] Gnielinski, V., 1997, *VDI-Waermeatlas*, Springer-Verlag, Berlin.
[14] McAdams, W. H., 1954, *Heat Transmission*, 3rd ed., McGraw-Hill, New York.
[15] Abdelmesih, A. N., and Bell, K. J., 1999, "Effect of Mixed Convection and U-Bends on the Design of Double-Pipe Heat Exchangers" Heat Transfer Eng., **20**(3), pp. 25–36.
[16] Clarke, R., and Finn, D. P., 2008, "The Influence of Secondary Refrigerant Air Chiller U-Bends on Fluid Temperature Profile and Downstream Heat Transfer for Laminar Flow Conditions," Int. J. Heat Mass Transfer, **51**(3–4), pp. 724–735.

Effect of Pin Density on Heat-Mass Transfer and Fluid Flow at Low Reynolds Numbers in Minichannels

N. K. C. Selvarasu

Danesh K. Tafti[1]
e-mail: dtafti@vt.edu

Department of Mechanical Engineering,
Virginia Polytechnic Institute and State University,
114-I Randolph Hall,
Mail Code 0238,
Blacksburg, VA 24061

Neal E. Blackwell
U.S. Army RDECOM CERDEC,
Fort Belvoir, VA 22060-5816

Previous investigations on the performance of straight pins, pins with tip clearance, and profiled fins showed that closely packed cylindrical pin fins are very competitive with the modified pins. Therefore, the objective of this paper is to investigate the effect of pin density on performance. Steady/time-dependent calculations are performed to investigate the effect of pin density on friction and heat transfer. Pins packed at distances of $S_D = 1.1$*, 1.2, 1.3, 1.4, 1.5, 2.0, 2.5, and 3 pin diameters (D) are investigated for* $10 \leq Re_D \leq 600$*. Two performance measures are used to compare the different pin fin densities. The first measure is to maximize heat transfer capacity for a given pumping power compared with a plane channel. The second measure used is based on entropy generation minimization (EGM), where the objective is to reduce the total irreversibility of the pin fin array to obtain an optimal spacing. Based on the performance measure of maximizing heat capacity, it is shown that for plain channels operating in the laminar range using denser pin packing has distinct advantages with* $S_D = 1.1$ *providing the best augmentation. However, the augmentation in heat capacity becomes relatively independent of the pin density for a channel operating in the turbulent regime. Based on the EGM method, at* $Re_D > 200$*,* $S_D = 1.3$*, 1.4, and 1.5 are the most suitable, with the least entropy generation observed at* $S_D = 1.4$*. At* $Re_D < 200$*,* $S_D = 1.1$*, 1.2, and 1.3 are also suitable for keeping entropy generation low.* [DOI: 10.1115/1.4000949]

Keywords: heat transfer, pin fins, low Reynolds number, thermal performance, entropy generation minimization (EGM), minichannels

1 Introduction

Heat transfer from or to a surface can be augmented by the use of extended surfaces or fins primarily by increasing the heat transfer area and/or increasing heat transfer coefficient. Cylindrical or pin fins are widely used in electronics cooling and turbine blade internal cooling applications, both of which operate at high Reynolds numbers in the turbulent regime. Hence, considerable past research has been devoted to developing heat transfer and friction correlations under turbulent conditions.

Whereas most of the previous studies were performed at high Reynolds numbers and high slenderness ratio pins [1–11], the miniaturization of geometrical scales in the quest for compactness and the broadening of the application base into other areas of heat and mass transfer augmentation require that careful consideration be given to the performance of the pin fin geometries at low Reynolds numbers. Peles et al. [12] studied the heat transfer and pressure drop over a bank of micropin fins, derived an expression for the thermal resistance, and concluded that micropin fin heat transfer to be a very effective mode of heat transfer. Koşar et al. [13] investigated the laminar flow across a bank of low aspect ratio micropin fins and obtained pressure drop and friction data for low Reynolds numbers in the range of 5–128. In an extension of this work, Peles and co-workers [14,15] conducted a heat transfer and pressure drop study for a micropin fin with slenderness ratio of 2.43 and Reynolds number range of 14–112. The results were compared with existing long tube correlations and it was observed that the variations were high for $Re < 50$ and less for $Re > 50$. The variations from the existing long tube correlations were explained as being induced by end wall effects.

Recently, numerical studies on low Reynolds number flows for minichannels with pin fins have been presented by Rozati and co-workers [16–18]. Rozati et al. [16] investigated the effect of pin fin density, spanwise pitch, and streamwise pitch for heat transfer and friction factor characteristics at Reynolds number ranging from 5 to 400. Wake recirculation was found to have a detrimental effect on pin and end wall heat transfer. Increasing the fin density by decreasing the spanwise pitch had a favorable effect on heat transfer and friction by reducing the size of the wake. Conductance augmentation in the range of 1.6–3.5 was obtained for high density pins in comparison to a plain channel flow. Friction augmentation ratio of 8 was reported for high density pins.

The motivation for this investigation resulted from our past results. Sreedharan et al. [18] compared the performance of straight pins [16], pins with tip clearance [17], and profiled pins [18]. The performance measure was based on the percentage increase in heat conductance over a plain channel for the same pumping power. It was found that all different configurations were successful in augmenting the conductance by 50–400% in a Reynolds number range of 5–350. However, it was found that closely packed plain pins remained very competitive with the modified pins. Therefore, the objective for this paper is to investigate the effect of pin density on performance. A range of pin densities from $S_D=1.1$ to $S_D=3$ is investigated over a Reynolds number range of 10–600. Two performance measures are used to find optimal pin densities, one that gives a maximum increase in conductance over a plain channel and another that has minimal operating costs based on the entropy generation minimization (EGM) criterion. The study is the first to comprehensively investigate the

---

[1] Corresponding author.

Contributed by the Heat Transfer Division of ASME for publication in the JOURNAL OF HEAT TRANSFER. Manuscript received December 23, 2008; final manuscript received December 14, 2009; published online April 2, 2010. Assoc. Editor: Roger Schmidt.

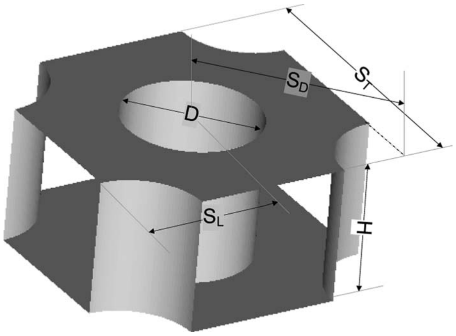

Fig. 1 Schematic of a pin fin array

effect of pin density on heat transfer and friction at low Reynolds numbers suitable for heat and mass transfer augmentation in minichannels and microchannels.

2 Mathematical and Computational Model

The time-dependent, incompressible continuity, momentum, and energy equations with constant properties are solved in a generalized coordinate system. Fully developed hydrodynamic and thermal conditions are assumed. Radiation and free convection effects are neglected, as it has been shown in Ref. [18] that they have a negligible influence on heat transfer in minichannels and at low temperatures. The channel walls and the pin fin walls are subjected to a uniform constant heat flux boundary condition $q^{*\prime\prime}$. The equations are nondimensionalized using D^* as the pin diameter for the length scale, the friction velocity as the velocity scale ($u_\tau^* = \sqrt{\Delta P^*/\rho}$), ρu_τ^{*2} as the pressure scale, D^*/u_τ^* as the time scale, and $q^{*\prime\prime}D^*/k$ as the temperature scale. The computer program used for these computations has been tested extensively for various similar applications [18–24]. Detailed information can be found in Ref. [21].

The computational domain consists of an array of cylindrical pins of circular cross section. Eight pin fin array configurations are studied. The schematic of the pin fin array under consideration including the dimensions of interest are listed in Fig. 1. The summary of the geometrical parameters is listed in Table 1. Calculations were carried out for $5 < \mathrm{Re}_D < 600$. The slenderness ratio is set to 1. For all unsteady cases, time-averaged results are presented and the time averaging is started after the flow becomes stationary, and is performed for 20 time units to produce the time-averaged results.

The nondimensionalized friction factor is based on the tube bundle approach [25] and is given as follows:

$$f = \frac{\Delta P}{N}\frac{1}{0.5u_{\max}^2} \tag{1}$$

The local instantaneous nondimensionalized Nusselt number is defined, as shown below, based on the pin fin diameter

Table 1 Nondimensional geometric parameters of the domains studied

Domain	S_D	S_L	S_T	H
1	1.1	0.778	1.556	1
2	1.2	0.849	1.697	1
3	1.3	0.919	1.838	1
4	1.4	0.990	1.980	1
5	1.5	1.061	2.121	1
6	2.0	1.414	2.828	1
7	2.5	1.768	3.536	1
8	3.0	2.121	4.243	1

Table 2 Grid size used for different interfin spacings S_D

Domain	S_D	No. of cells
1	1.1	196,608
2	1.2	196,608
3	1.3	196,608
4	1.4	131,072
5	1.5	131,072
6	2.0	282,240
7	2.5	653,184
8	3.0	1,048,576

$$\mathrm{Nu}_D = \frac{1}{(\theta_w - \theta_{\mathrm{ref}})} \tag{2}$$

where θ_w is the local modified nondimensional wall temperature and θ_{ref} is the modified reference temperature, which is defined below as [17]

$$\theta_{\mathrm{ref}} = \frac{\int\int\int \theta |u| dydzdx}{\int\int\int |u| dydzdx} \tag{3}$$

The instantaneous surface average Nusselt number is calculated as follows by integrating over the fin surface area:

$$\frac{1}{\overline{\overline{\mathrm{Nu}_D}}} = \frac{1}{A_{\mathrm{Total}}}\int\int dA(\theta_w - \theta_{\mathrm{ref}}) \tag{4}$$

3 Grid Independency and Validation

Over the range of Reynolds number studied, the flow is in the laminar to unsteady laminar or transitional regime, which does not put very high demands on the grid density. Rozati and co-workers [16,17] performed a detailed grid and domain independency study on domain 5 with $S_D = 1.5$ at the Reynolds number $\mathrm{Re}_D \approx 400$, which would guarantee the independency of the results at the lower Reynolds numbers as well as in the present case. The grids used for the different interpin spacings are listed in Table 2. As the pin density decreases, the grid size increases to compensate for the larger open flow volume. On the other hand, as the pin density increases, a different block structure is used which results in a finer grid than the intermediate grid.

An attempt was also made to compare and validate the heat transfer and pressure drop with previous correlations but it was found that most correlations and experimental data available in the literature are for high Reynolds number turbulent flow regimes and for high slenderness ratios. Koşar [14] studied the heat transfer and pressure drop of de-ionized water over a bank of shrouded staggered micropin fins for the Reynolds number range of 14–112. To compare the current study with the experiments done by Koşar et al. [14], a computational domain with the dimensions given in Table 3 was used.

The result of the numerical study for the above domain is shown in Fig. 2. It is seen that the current model predictions are in good agreement with experiments for $\mathrm{Re}_D > 50$ but deviates substantially from the experiments for $\mathrm{Re}_D < 50$. In their comparison of experimental data with correlation, Koşar et al. [14] observed that their measurements of heat transfer coefficient were comparable for $\mathrm{Re}_D > 50$ but had large variations for $\mathrm{Re}_D < 50$. The comparison of the friction factor from this study and Koşar and co-

Table 3 Geometric parameters for validation based on Ref. [14]

Domain	S_D	S_L	S_T	H
9	1.6771	1.5	1.5	2.43

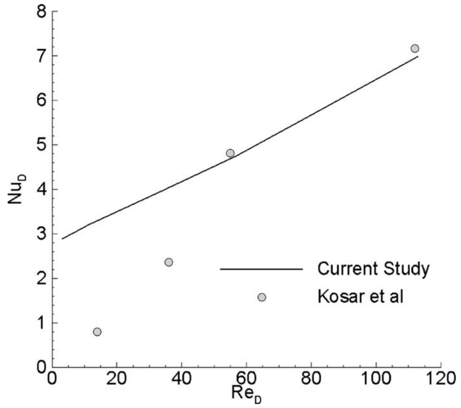

Fig. 2 Validation of the current study—Nu_D versus Re_D

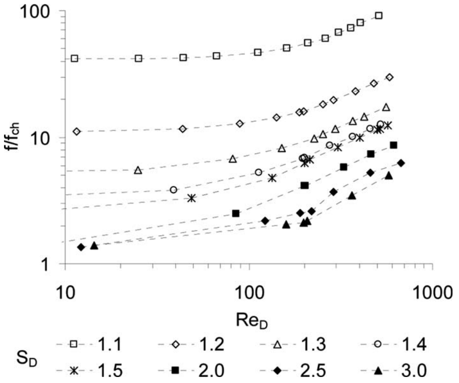

Fig. 4 Variation in friction factor ratio with Re_H for all S_D values

workers [13,14] is shown in Fig. 3. The trend in the change in friction factor with Re_D is in good agreement but discrepancies in friction factor are observed at $Re_D < 25$. Similar trends were reported by Rozati and co-workers [17,18]. The reason for these discrepancies is not clear. With the relatively low Reynolds numbers and the high grid densities used in the calculations, it is unlikely that the model suffers from numerical errors. There could be a possibility that either the physical model assumptions of constant properties breakdown at low Reynolds numbers or the possibility that experimental uncertainties increase at low Reynolds numbers.

4 Friction Factor Ratio and Heat Transfer Augmentation

Flow characterization for pin fins with different densities and configurations have been reported in detail by Rozati and co-workers [16–18]. The increase in heat transfer and the friction factor is compared with that of an equivalent plane channel. The plane channel expressions are as expressed below [26]

$$f = \frac{48}{Re_H} \tag{5}$$

$$Nu_H = 4.115, \quad \text{for laminar flows} \tag{6}$$

The variation in the ratio of the calculated friction factor to the plane channel friction factor with Re_D is shown in Fig. 4. It is observed that the friction factor is higher for configurations with higher pin fin density ($S_D \leq 1.5$). At very low Reynolds numbers, the losses are dominated by friction drag, but as the Reynolds number increases and wake recirculation develops, form drag dominates. As the pin density increases, both friction and form drag increase. The friction drag increases due to the flow acceleration between pins and the larger induced shear stresses on the sides of the pin and the end wall, whereas in spite of the size of the wake decreasing, larger pressure losses are also incurred resulting in an increase in form drag. Thus, from the stand point of friction factor augmentation, low pin densities are desirable.

The heat transfer coefficient augmentation with respect to an equivalent plane channel is compared in Fig. 5. It is observed that the configurations with $S_D > 1.5$ exhibit augmentation ratios less than unity at low Reynolds numbers, which gradually increase above unity with the development of wake instabilities. The low values are mostly caused by the end wall viscous effects and by the large recirculating wakes. As the pin fin density increases, flow acceleration near heat transfer surfaces and smaller wakes has a large favorable impact on the augmentation ratio, which is greater than unity, even at low Reynolds numbers. The augmentation in thermal conductance, which takes into effect the increase in area due to the pins over an equivalent channel is shown in Fig. 6. The trends are similar to the heat transfer coefficient. The high density pins provide a larger augmentation in surface area over an equivalent channel and hence the heat conductance augmentation increases with pin density. The augmentation ranges from 0.9 to 2.5 at low densities to a maximum of 4–10 at the highest pin density of $S_D = 1.1$.

5 Performance Measures

It is apparent from the results that high pin densities increase the ability to transfer more heat but at the same time increase the friction also. In choosing an optimal configuration, we entertain the scenario of an existing heat exchanger using plain channels as the basic heat exchange conduit, which is to be replaced with channels populated with pin fins to increase the overall heat ca-

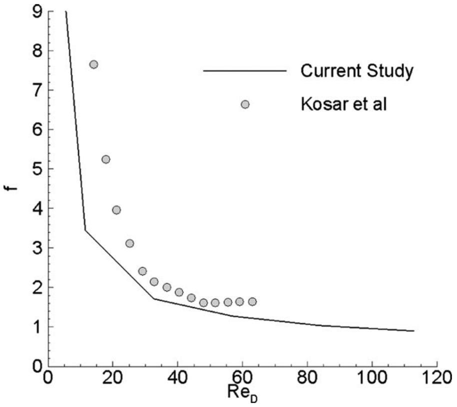

Fig. 3 Validation of the current study—*f* versus Re_D

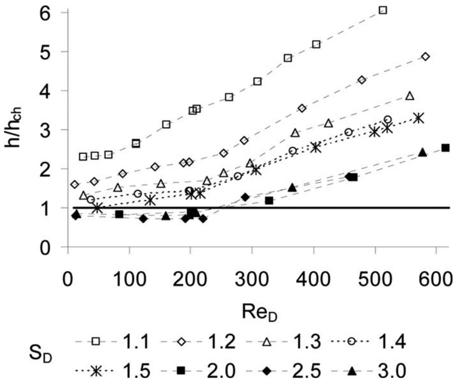

Fig. 5 Variation in heat transfer coefficient with Re_D

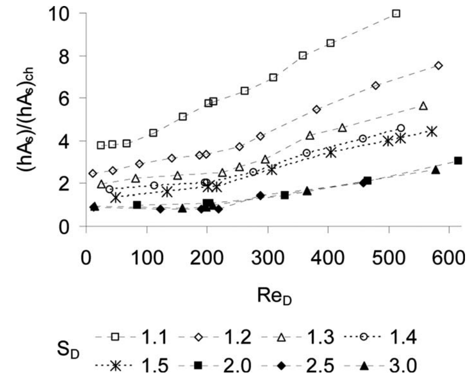

Fig. 6 Variation in thermal conductance with Re_D

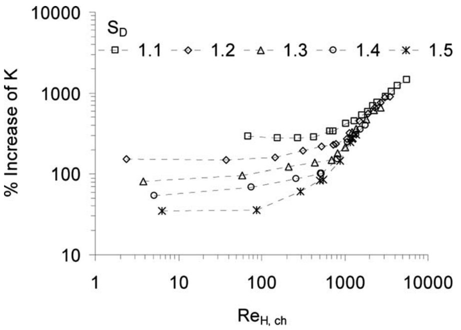

Fig. 7 Increase in thermal conductance compared with plane channel for the same pumping power for higher density configurations

pacity. Two objectives are investigated for the conversion: one in which the configuration with the largest augmentation in conductance is selected but at the same pumping power as expended in a plain channel and another in which an increase in conductance is desirable at the same pumping power but at minimal entropy generation or operating costs. In both cases, the gains in heat conductance can be passed onto decreasing the effective surface area or volume to increase the compactness of the heat exchanger.

5.1 Increase in Heat Transfer Capacity for a Given Pumping Power. The objective of the first performance measure is to find the augmentation in heat capacity afforded by placing pin fins in a plain channel keeping the pumping power the same. The dimensions of the plane channel are the same as that of the pin finned channel with the pins removed. To facilitate the analysis we first obtain an equivalent flow rate in a plain channel by removing pins from an existing channel. In this scenario, to maintain the same pumping power, the flow rate in the plane channel will increase due to the reduced friction. The heat transfer in the plane channel with this increased flow rate is then compared with the pin finned channel. The ratio of pumping power between a pin finned and plane channel is given as

$$\frac{\text{Power}}{\text{Power}_{\text{ch}}} = \frac{ND_h^*}{L}\frac{A_c^*}{A_{\text{ch}}^*}\frac{f}{f_{\text{ch}}}\left(\frac{u_{\max}^*}{u_{\text{ch}}^*}\right)^3 \qquad (7)$$

The plane channel Reynolds number is obtained, as shown below

$$\text{Re}_{D_H} = \text{Re}_D\frac{u_{\text{ch}}^*}{u_{\max}^*}\frac{D_H^*}{D} \qquad (8)$$

In Eq. (7), the friction factor is expressed in terms of the equivalent Reynolds number for a plane channel $\text{Re}_{D_H,\text{ch}}$, as in Eq. (8), and the ratio of channel velocity and pin finned channel maximum velocity ($u_{\text{ch}}^*/u_{\max}^*$) is obtained in terms of $\text{Re}_{D_H,\text{ch}}$ with the power ratio set to unity. This ratio is then used to compute the equivalent plane channel Reynolds number from Eq. (8). No more iteration is needed if the obtained plane channel Reynolds number is laminar. If the plane channel Reynolds number obtained from the above procedure is not in the laminar range ($\text{Re}_{D_H,\text{ch}} > 2300$), Eq. (8) is revisited and the friction factor is expressed using the Petukhov [26] correlation for turbulent flow (Eq. (9)). The turbulent correlation for f is used with Eqs. (7) and (8) to obtain a corrected $\text{Re}_{D_H,\text{ch}}$

$$f_{\text{ch}} = (0.790\ln(\text{Re}_{D_H} - 1.64))^{-2} \qquad (9)$$

The calculated equivalent plane channel Reynolds number ($\text{Re}_{H,\text{ch}} = 0.5\ \text{Re}_{D_H,\text{ch}}$) can be plotted against the Reynolds number of the pinned channel based on pin fin diameter. This figure (not shown) can be used to obtain the required operating Reynolds number Re_D of a pin finned channel, for a given plane channel operating at Reynolds number $\text{Re}_{H,\text{ch}}$, under the condition of same pumping power for both. For example, to replace a plain channel operating at $\text{Re}_{H,\text{ch}} = 150$ with the same power consumption, a pin finned channel with $S_D = 1.1$ would operate at $\text{Re}_D = 25$, whereas for $S_D = 1.2$ at $\text{Re}_D = 44$. Using the relationship between $\text{Re}_{H,\text{ch}}$ and Re_D for the same power consumption Fig. 7 for $S_D \leq 1.5$ and Fig. 8 for $S_D > 1.5$ show the increase in thermal conductance if the plain channel is replaced with a pin finned channel of a given pin density. It is observed that for channels operating at $\text{Re}_H < 200$, pins placed at $S_D <= 1.5$ are necessary to provide any augmentation in conductance—pins at $S_D > 1.5$ decrease the overall heat capacity. Channels operating in the laminar range $\text{Re}_H < 1000$ are very dependent on the pin fin density S_D for augmenting the heat capacity. For example, at $\text{Re}_H = 500$, inserting pin fins with $S_D = 1.1$ would provide an augmentation of about 300%, whereas a configuration with $S_D = 1.5$ would provide an augmentation of 70%. However, the augmentation in heat capacity becomes relatively independent of the pin density for a channel operating in the turbulent regime.

5.2 Entropy Generation Minimization. The objective with this measure is to find a thermodynamic optimum spacing, whereby the system destroys the least amount of exergy [25]. In a convective heat transfer process, the competing losses are the heat transfer and friction losses, which account for the thermodynamic irreversibility. The friction irreversibility increases with Reynolds number, whereas the irreversibility due to heat transfer decreases. This leads to an optimum Reynolds number at which the irreversibility is minimized. The second law analysis for a pin fin array is studied assuming the fin has a small Biot number (Bi < 0.1), constant thermal conductivity of the pin fin material, and insulated pin fin tip. The last assumption is valid due to the symmetry of the flow conditions along the midplane at $0.5H$, thus simplifying the

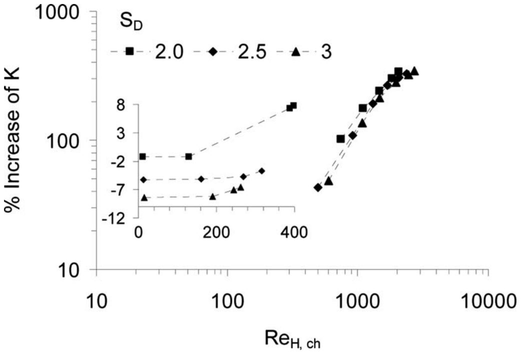

Fig. 8 Increase in thermal conductance compared with plane channel for the same pumping power for lower density configurations

geometry, with an insulated pin fin of height one-half of the pin fins inside the channel.

The array of pin fins is assumed to contain N rows and V columns. The total heat transfer rate in terms of the temperature difference between the freestream and the fin base is obtained by solving the heat equation for a pin fin with an insulated tip [26]. Using the characteristic scales defined earlier, the nondimensional form of the above equation is obtained as

$$\theta_B = \frac{Q_B}{\frac{\pi}{2}NV\left(\mathrm{Nu}_s\frac{k^*}{k_w^*}\right)^{0.5}\tanh\left(H\left(\mathrm{Nu}_s\frac{k^*}{k_w^*}\right)^{0.5}\right)+\mathrm{Nu}_w\left(A-\frac{\pi}{4}NV\right)} \tag{10}$$

The entropy generation rate for a fluid flowing around a submerged body is expressed by Bejan [27] as follows:

$$S_{\mathrm{gen}}^* = \frac{Q_B^*\theta_B^*}{T_\infty^{*2}} + \frac{\dot{m}^*\Delta P^*}{\rho T_\infty^*} \tag{11}$$

The first term in Eq. (11) is the entropy generation term due to heat transfer and the second term corresponds to the entropy generation due to friction losses. The mass flow rate for a section of the pin fin array is given in terms of the maximum average velocity $u_{\max}^*$ as follows:

$$\dot{m}^* = \rho u_{\max}^*\frac{H^*}{2}(V-0.5)(S_T^*-D^*) \tag{12}$$

The characteristic entropy generation rate scale is defined as follows [27]:

$$S^* = \frac{Q_B^{*2}u_{\max}^*}{k_w^*\nu^*T_\infty^{*2}} \tag{13}$$

Following Bejan [27], the nondimensional entropy generation number is given as follows:

$$N_S = N_{S,H} + N_{S,F} = S_{\mathrm{gen}}^*/S^* \tag{14}$$

Simplifying the above terms the entropy generation number due to heat transfer is given as follows:

$$N_{S,H} = \left\{\mathrm{Re}_D\left[\frac{\pi}{2}NV\left(\mathrm{Nu}_s\frac{k^*}{k_s^*}\right)^{0.5}\tanh\left(H\left(\mathrm{Nu}_s\frac{k^*}{k_s^*}\right)^{0.5}\right)+\mathrm{Nu}_w\frac{\lambda^*}{k^*}\left(A - \frac{\pi}{4}NV\right)\right]\right\}^{-1} \tag{15}$$

Similarly, the entropy generation number due to the friction losses is given as follows:

$$N_{S,F} = \frac{1}{4}NH(V-0.5)(S_T-1)f\ \mathrm{Re}_D^2\ B \tag{16}$$

In the above Eqs. (15) and (16), the nondimensional groups are defined as listed below

$$\mathrm{Nu}_s = \frac{h^*D^*}{k^*}, \quad \mathrm{Nu}_w = \frac{h_w^*D^*}{k^*}$$

$$\mathrm{Re}_D = \frac{u_{\max}^*D^*}{\nu^*}, \quad \mathrm{Re}_\Gamma = \frac{u_\Gamma^*D^*}{\nu^*}$$

$$B = \frac{\rho k^*\nu^{*3}T_\infty^*}{Q_B^{*2}}$$

Following Taufiq et al. [28], the nondimensional cost of operation is considered. If the capital cost of the fin material per unit volume is assumed as negligible, the total operating cost of the system is given as follows:

$$\Gamma = N_{S,H} + \left(\frac{\lambda_{S,F}^*}{\lambda_{S,H}^*}\right)N_{S,F} \tag{17}$$

The above Eq. (17) is nondimensionalized using the unit cost of lost work due to heat transfer irreversibility as the characteristic cost. The ratio $(\lambda_{S,F}^*/\lambda_{S,H}^*)$ is typically set to unity [28], reducing the total operating cost given in Eq. (17) to the total entropy generation number. This provides an additional interpretation of the total entropy generation number. Thus, an interpin spacing that provides the least entropy generation number also provides the least total operating cost. In above Eqs. (15) and (16), the Nusselt number and Reynolds number and the friction factors are obtained from the present numerical studies and not based on existing experimental correlations.

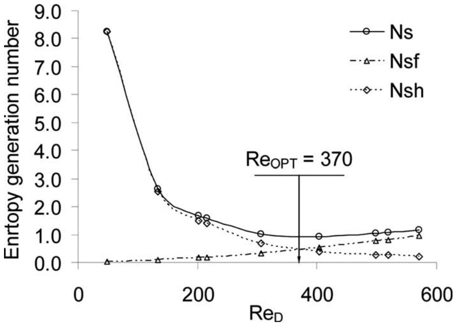

Fig. 9 Entropy generation number for $S_D=1.5$, $B=0.00001$

Differentiating Eq. (14) with respect to S_D and setting it to zero results in an optimum S_D. Similarly, for a given S_D, an optimum Re_D can be obtained by differentiating Eq. (14) with respect to Re_D and setting it to zero. For all the calculations, the parameter B is set to 0.00001, which is for laminar flows [27–29] and the ratio of the fluid to solid coefficient of thermal conduction is set to 0.0001 [27–29]. Figure 9 shows the variation in the total entropy generation number with Reynolds number for $S_D=1.5$. The entropy generation number due to heat transfer tends to decrease with increasing Reynolds number due to increased heat transfer coefficients at higher Reynolds numbers and the entropy generation number due to friction increases with increasing Reynolds numbers, due to the increasing friction losses with Reynolds numbers [25]. It is observed that there is an optimum operating Reynolds number of 370 at which the entropy generation number is a minimum. Similar results are obtained for all geometries, where an optimum Reynolds number is observed. The relative importance of the two irreversibility mechanisms is described by the irreversibility distribution ratio Φ, which is defined as [25]

$$\phi = \frac{\text{Fluid flow irreversibility}}{\text{Heat transfer irriversibility}} = \frac{N_{S,F}}{N_{S,H}} \tag{18}$$

A plot of the above parameter is shown in Fig. 10. For all S_D values, when $\mathrm{Re}_D<250$, the heat transfer irreversibility tends to dominate, with Φ being less than 1. Beyond $\mathrm{Re}_D=250$, the irreversibility distribution ratio is more than 1 for $S_D=1.1$, indicating that the fluid flow friction irreversibility tends to dominate. This is

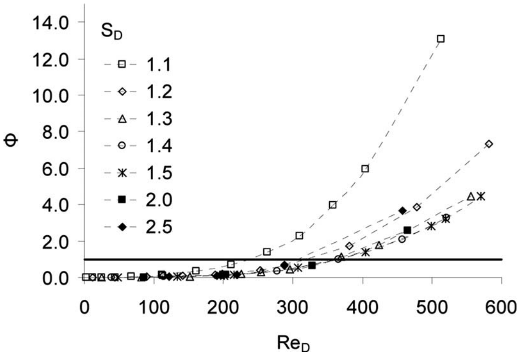

Fig. 10 Variation in irreversibility distribution ratio with Reynolds number for all S_D values

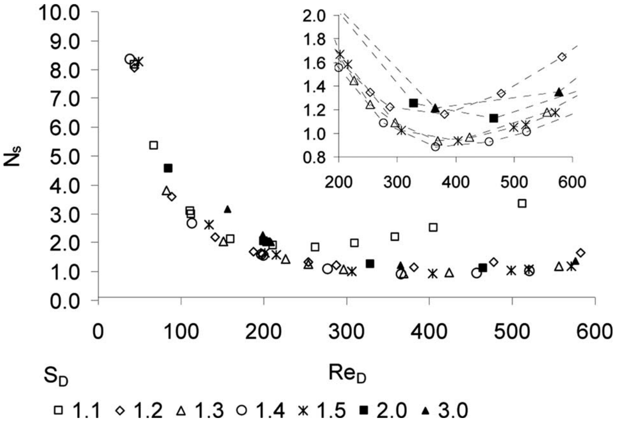

Fig. 11 Total entropy generation rate N_s versus pin finned channel Reynolds number Re_D

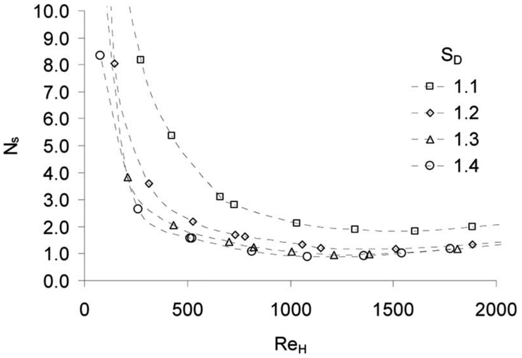

Fig. 12 Total entropy generation rate N_s versus plane channel Reynolds number $Re_{H,ch}$

the case for all domains beyond $Re_D = 300$. The variation in the total entropy generation number with the Reynolds number for all S_D values is shown in Fig. 11. The configuration with the least entropy generation number is preferable. At relatively higher Reynolds numbers ($Re_D > 200$), configurations with $S_D = 1.3$, 1.4, and 1.5 are comparable, with the least entropy generation number observed for $S_D = 1.4$, as seen from the inlaid plot for the relatively higher Reynolds numbers. For this range of Reynolds numbers, the entropy generation number is much higher for $S_D = 1.1$, which increases with Reynolds number due to the irreversibility caused by much higher friction losses, thus causing adverse exergy losses. Conversely, at low $Re_D < 200$, $S_D = 1.1$ is quite competitive with the other configurations because of the relatively high heat transfer coefficient and conductance, which reduces the irreversibility.

5.3 Discussion on Combining Both Performance Measures. Using the equivalent pin fin channel Reynolds number Re_D (with the same pumping power) for a given plane channel Reynolds number $Re_{H,ch}$, the increase in conductance (Fig. 7) and irreversibility (Fig. 11) for $S_D = 1.1$, 1.2, 1.3, and 1.4 are summarized in Table 4. Table 4 compares the two selection criterion (maximum gain in conductance versus minimum irreversibility) for three plane channel Reynolds numbers of 100, 1000, and 1700. The variation in N_s with the equivalent plane channel Reynolds number $Re_{H,ch}$ is given in Fig. 12 for these four pin fin spacings. For all three channel Reynolds numbers, using a pin configuration with $S_D = 1.1$ gives the largest augmentation in heat capacity, whereas using $S_D = 1.4$ gives the smallest irreversibility or operating costs, as seen in Table 4 and also in Fig. 12. At the low Reynolds number ($Re_{H,ch} = 100$), the percentage increase in thermal conductance for interpin fin spacing of 1.1 is more than three times than that for an interfin spacing of 1.4, but at the same time, the operating cost associated with the spacing of 1.1 is almost four times more when compared with an interfin spacing of 1.4. The comparative increase in thermal conductance decreases as the plane channel Reynolds number increases with a corresponding decrease in the operating cost for $S_D = 1.1$ with respect to $S_D = 1.4$. The ratio of increase in thermal conductance and operating cost are almost equal when the plane channel Reynolds number is in the turbulent regime at $Re_{H,ch} = 1700$. If the largest increase in conductance or compactness is the prime objective irrespective of other costs, then the obvious choice is $S_D = 1.1$. If the operating costs are of prime importance, then $S_D = 1.4$ is the most suitable configuration. However, there might be some situations that may be forgiving of some deviations from the prime objective. In such cases, both criteria can be used to come up with a near optimal design. For example, at $Re_{H,ch} = 1000$, use of $S_D = 1.2$ reduces the irreversibility or operating cost by a factor of 1.5 while reducing the heat capacity by only 1.13. Thus, it can be seen that the developed and presented methods in this work can be effectively used to design a pin fin array based on the application constraints.

6 Summary and Conclusion

Cylindrical pin fins of intermediate slenderness ratio in cross flow at low Reynolds numbers ($Re_D < 600$) in a minichannel have been investigated numerically to determine the effect of pin den-

Table 4 Comparison of $S_D = 1.1$, 1.2, 1.3, and 1.4 for $Re_{H,ch} = 100$, 1000, and 1700

S_D	$Re_{H,ch}$	Re_D	Percent increase in K	N_S	$\%K/\%K_{1.4}$	$N_S/N_{S,1.1}$
1.1	100	16.16	283.68	23.37	3.90	3.79
1.2	100	30.11	149.31	15.98	2.05	2.59
1.3	100	41.58	104.85	10.28	1.44	1.67
1.4	100	61.48	72.69	6.16	1.00	1.00
S_D	$Re_{H,ch}$	Re_D	Percent increase in K	N_S	$\%K/\%K_{1.4}$	$N_S/N_{S,1.1}$
1.1	1000	154.74	406.46	2.19	1.91	2.49
1.2	1000	234.82	249.54	1.43	1.18	1.63
1.3	1000	294.15	216.66	1.096	1.02	1.25
1.4	1000	413.53	212.34	0.88	1.00	1.00
S_D	$Re_{H,ch}$	Re_D	Percent increase in K	N_S	$\%K/\%K_{1.4}$	$N_S/N_{S,1.1}$
1.1	1700	278.68	539.31	1.88	1.39	1.74
1.2	1700	430.21	507.5	1.24	1.31	1.15
1.3	1700	522.73	439.1	1.11	1.13	1.03
1.4	1700	705.43	387.02	1.08	1.00	1.00

sity on the heat transfer and fluid flow. In the studied range of Reynolds numbers, the heat transfer is primarily affected by the size and the extent of the pin wake recirculation zone. Any augmentation technique that might affect the pin wake would thus contribute to the increased heat transfer augmentation. In this study, the effect of accelerating the flow around the pins by increasing the pin fin density is investigated.

Denser configurations provide the maximum heat transfer augmentation, with a corresponding increase in the friction factor augmentation. Two performance measures are used to compare the different pin fin densities in a scenario in which a plain channel is replaced with a pinned channel at the same pumping power. The first measure is the increase in heat transfer capacity compared with a plane channel. It is shown that channels operating in the laminar range are very dependent on the pin fin density S_D for augmenting the heat capacity—denser pin packing has distinct advantages. However, the augmentation in heat capacity becomes relatively independent of the pin density for a channel operating in the turbulent regime.

The second measure used is based on EGM. The contribution of friction irreversibility to the total irreversibility tends to dominate when the Reynolds number is higher than 250 for most S_D values. At Reynolds numbers $(\mathrm{Re}_D > 200)$, configurations with $S_D=1.3$, 1.4, and 1.5 are comparable in minimizing entropy generation, with the least entropy generation observed with $S_D=1.4$. For this range of Reynolds numbers, the entropy generation is much higher for $S_D=1.1$ due to the irreversibility caused by much higher friction losses, and which increases with Reynolds number. At low $\mathrm{Re}_D < 200$, $S_D=1.1$, 1.2, and 1.3 are quite competitive with the other configurations because of the relatively high heat transfer coefficient and conductance, which reduces the irreversibility.

It is shown that both measures can be used independently without regard to the other depending on the objective or can be used together to obtain near optimal solutions.

Nomenclature

A = area
B = heat dissipation number, dimensionless group
Bi = Biot number
D = pin diameter
D_H = hydraulic diameter
H = domain height, slenderness ratio
K = thermal conductance
L = domain length
N = number of pin rows
N_S = total entropy generation number
$N_{S,F}$ = entropy generation number due to friction
$N_{S,H}$ = entropy generation number by heat transfer
Nu = Nusselt number
P, p = pressure
Pr = Prandtl number
Q = heat transfer
Re = Reynolds number based on pin diameter
S = entropy generation rate characteristic scale
S_D = interpin spacing
S_{gen} = entropy generation rate
S_L = streamwise pitch
S_T = spanwise pitch
T = temperature
t = time
V = number of pin rows
f = friction factor
h = convective heat transfer coefficient
k = thermal conductivity
k_w = thermal conductivity of end wall
$\dot{m}$ = mass flow rate
q'' = constant heat flux on the pin fin and channel walls
u = streamwise velocity
x = streamwise direction
$\vec{x}$ = direction vector
β = mean pressure gradient
γ = mean temperature gradient
Γ = nondimensional total operating cost
θ = modified temperature
$\lambda_{S,F}$ = unit cost of lost work for fluid flow
$\lambda_{S,H}$ = unit cost of lost work for heat transfer
ν = kinematic viscosity
ρ = fluid density
Φ = irreversibility distribution ratio

Subscripts

B = pin fin base or end wall based values
D = values based on pin diameter
D_H = hydraulic diameter based values
H, h = values based on channel height
c = cross section
ch = smooth channel
max = maximum values
ref = reference values
s = values at the surface
w = values based on the end wall
τ = values based on friction velocity
∞ = freestream values

Superscripts

* = dimensional values

References

[1] Chyu, M. K., Hsing, Y. C., and Natarajan, V., 1998, "Convective Heat Transfer of Cubic Fin Arrays in a Narrow Channel," ASME J. Turbomach., **120**, pp. 362–367.
[2] Jubran, B. A., Hamdan, M. A., and Abdulah, R. M., 1993, "Enhanced Heat Transfer, Missing Pin and Optimization for Cylindrical Pin Fin Arrays," ASME J. Heat Transfer, **115**, pp. 576–583.
[3] Uzol, O., and Camci, C., 2005, "Heat Transfer, Pressure Loss and Flow Field Measurement Downstream a Staggered Two-Row Circular and Pin Fin Arrays," ASME J. Heat Transfer, **127**, pp. 458–471.
[4] Metzger, D. E., Berry, R. A., and Bronson, J. P., 1982, "Developing Heat Transfer in Rectangular Ducts With Staggered Arrays of Short Pin Fins," ASME J. Heat Transfer, **104**, pp. 700–706.
[5] Armstrong, J., and Winstanley, D., 1988, "A Review of Staggered Array Pin Fin Heat Transfer for Turbine Cooling Applications," ASME J. Turbomach., **110**, pp. 94–103.
[6] Short, B. E., Jr., and Raad, P. E., 2002, "Performance of Pin Fin Cast Aluminum Cold Walls, Part 1: Friction Factor Correlations," J. Thermophys. Heat Transfer, **16**(3), pp. 389–396.
[7] Short, B. E., Jr., Raad, P. E., and Price, D. C., 2002, "Performance of Pin Fin Cast Aluminum Cold Walls, Part 2: Colburn j-Factor Correlations," J. Thermophys. Heat Transfer, **16**(3), pp. 397–403.
[8] Ko, J. H., Ewing, M. E., Guezennec, Y. G., and Christensen, R. N., 2002, "Development of a Low Reynolds Number Enhanced Heat Transfer Surface Using Flow Visualization Techniques," Int. J. Heat Fluid Flow, **23**, pp. 444–454.
[9] Sahiti, N., Lemouedda, A., Stojkovic, D., Durst, F., and Franz, E., 2006, "Performance Comparison of Pin Fin in Duct Flow Arrays With Various Pin Cross Sections," Appl. Therm. Eng., **26**, pp. 1176–1192.
[10] Won, S. Y., Mahmood, G. I., and Ligrani, P. M., 2004, "Spatially-Resolved Heat Transfer and Flow Structure in a Rectangular Channel With Pin Fins," Int. J. Heat Mass Transfer, **47**, pp. 1731–1743.
[11] Dong, S., Liu, S., and Su, H., 2001, "An Experimental Investigation of Heat Transfer in Pin Fin Array," Heat Transfer Asian Res., **30**, pp. 533–541.
[12] Peles, Y., Koşar, A., Mishra, C., Kuo, C. J., and Schneider, B., 2005, "Forced Convection Heat Transfer Across a Pin Fin Micro Heat Sink," Int. J. Heat Mass Transfer, **48**, pp. 3615–3627.
[13] Koşar, A., Mishra, C., and Peles, Y., 2005, "Laminar Flow Across a Bank of Low Aspect Ratio Micro Pin Fins," ASME J. Fluids Eng., **127**, pp. 419–430.
[14] Koşar, A., and Peles, Y., 2006, "Thermal-Hydraulic Performance of MEMS-Based Pin Fin Heat Sink," ASME J. Heat Transfer, **128**, pp. 121–131.
[15] Koşar, A., and Peles, Y., 2007, "TCPT-2006-096.R2: Micro Scale Pin Fin Heat Sinks—Parametric Performance Evaluation Study," IEEE Trans. Compon. Packag. Technol., **30**, pp. 855–865.
[16] Rozati, A., Tafti, D. K., and Blackwell, N. E., 2007, "Thermal Performance of Pin Fins at Low Reynolds Numbers in Mini-Micro-Channels," ASME Paper No. HT2007-32158.
[17] Rozati, A., Tafti, D. K., and Blackwell, N. E., 2008, "Effect of Tip Clearance

on Flow and Heat Transfer at Low Reynolds Numbers, ASME J. Heat Transfer, **130**(7), p. 071704.
[18] Sreedharan, S. S., Tafti, D. K., and Rozati, A., 2008, "Heat-Mass Transfer and Friction Characteristics of Profiled Pins at Low Reynolds Numbers," Numer. Heat Transfer, Part A, **54**(2), pp. 130–150.
[19] Zhang, L., Tafti, D. K., Najjar, F., and Balachander, S., 1997, "Computations of Flow and Heat Transfer in Parallel Plate Fin Heat Exchangers on the CM-5: Effect of Flow Unsteadiness and Three-Dimensionality," Int. J. Heat Mass Transfer, **40**(6), pp. 1325–1341.
[20] Patankar, S. V., Liu, C. H., and Sparrow, E. M., 1977, "Fully Developed Flow and Heat Transfer in Ducts Having Streamwise Periodic Variations of Cross-Sectional Area," ASME J. Heat Transfer, **99**, pp. 180–186.
[21] Tafti, D. K., 2001, "GenIDLEST—A Scalable Parallel Computational Tool for Simulating Complex Turbulent Flows," *Proceedings of the ASME Fluids Engineering Division*, **FED-256**, ASME, New York.
[22] Tafti, D. K., 2005, "Evaluating the Role of Subgrid Stress Modeling in a Ribbed Duct for Internal Cooling of Turbine Blades," Int. J. Heat Fluid Flow, **26**(1), pp. 92–104.
[23] Sewall, E. A., Tafti, D. K., Thole, K. A., and Graham, A., 2006, "Experimental Validation of Large Eddy Simulation of Flow and Heat Transfer in Stationary Ribbed Duct," Int. J. Heat Fluid Flow, **27**(2), pp. 243–258.
[24] Elyyan, M. A., and Tafti, D. K., 2008, "Investigation of Dimpled Fins for Heat Transfer Enhancement in Compact Heat Exchangers," Int. J. Heat Mass Transfer, **51**(11-12), pp. 2950–2966.
[25] Bejan, A., 1987, "The Thermodynamic Design of Heat and Mass Transfer Processes and Devices," Int. J. Heat Fluid Flow, **8**(4), pp. 258–276.
[26] Incropera, F. P., and DeWitt, D. P., 2006, *Fundamentals of Heat and Mass Transfer*, 6th ed., Wiley, New York.
[27] Bejan, A., 1996, *Entropy Generation Minimization, The Method of Thermodynamic Optimization of Finite Size Systems and Finite Time Processes*, CRC, Boca Raton, FL.
[28] Taufiq, B. N., Masjuki, H. H., Mahlia, T. M. I., Saidur, R., Faizul, M. S., and Niza Mohamad, E., 2007, "Second Law Analysis for Optimal Thermal Design of Radial Fin Geometry by Convection," Appl. Therm. Eng., **27**, pp. 1363–1370.
[29] Lin, W. W., and Lee, D. J., 1997, "Second Law Analysis on a Pin Fin Array Under Cross Flow," Int. J. Heat Mass Transfer, **40**(8), pp. 1937–1945.

Heat and Mass Transfer on the Unsteady Magnetohydrodynamic Flow Due to a Porous Rotating Disk Subject to a Uniform Outer Radial Flow

Mustafa Turkyilmazoglu
Department of Mathematics,
Hacettepe University,
06532 Beytepe, Ankara, Turkey
e-mail: turkyilm@hacettepe.edu.tr

An unsteady flow and heat transfer of an incompressible electrically conducting fluid over a porous rotating infinite disk impulsively set into motion are studied in the present paper. The disk finds itself subjected to a uniform normal magnetic field. The particular interest lies in searching for the effects of an imposed uniform outer radial flow far above the disk on the behavior of the physical flow. The governing Navier–Stokes and Maxwell equations of the hydromagnetic fluid, together with the energy equation, are converted into self-similar forms using suitable similarity transformations. A compact, unconditionally stable, and highly accurate implicit spectral numerical integration algorithm is then employed in order to resolve the transient behavior of the velocity and temperature fields. The time evolution and steady state case of some parameters of fundamental physical significance such as the surface shear stresses in the radial and tangential directions and the heat transfer rate are also fully examined for the entire family of magnetic interaction, radial flow, and suction/blowing parameters. [DOI: 10.1115/1.4000963]

Keywords: radial flow, unsteady MHD flow, porous rotating disk, heat transfer

1 Introduction

The mathematical modeling of a rotating disk flow is an interesting problem from a mathematical point of view since it is, to some degree, less difficult to deal with the governing equations as compared with the other complicated fluid flow phenomena in fluid mechanics. The magnetohydrodynamic (MHD) fluid flow problem of a rotating disk also finds special places in several science and engineering applications, for instance, in turbomachinery, in cosmical fluid dynamics, in meteorology, in computer disk drives, in geophysical fluid dynamics, in gaseous and nuclear reactors, in MHD power generators, flow meters, pumps, and so on. Moreover, in a close connection with the uniform radial outer flow case, as considered in this paper, the rotating disk flow is relevant to the chemical vapor deposition reactors used for depositing thin films of optical and electrical materials on substrates in the electrochemical industry. The gas flow for the operation of such reactors can be considered as a uniform axial flow incident on a rotating disk and it is desirable that the flow close to the substrate be laminar and free from instability to ensure uniform deposition.

The pioneering work of Kármán [1] has shed light upon many further studies on the rotating disk flow. The effects of unsteadiness on the Kármán flow were investigated by Yoo [2]. The recent work by Takeda et al. [3] explored the permeable wall conditions. The analogous heat transfer problem for steady and unsteady flow cases were examined in Refs. [4,5]. Hossain et al. [6] and Maleque and Sattar [7] investigated the influence of variable properties on the physical quantities of the rotating disk problem by obtaining a self-similar solution of the Navier–Stokes equations along with the energy equation. Kumar et al. [8] and Turkyilmazoglu [9] covered the effects of a uniform external magnetic field on the steady flow over a rotating disk.

The present work is mainly motivated by the lack of investigation in the literature on the rotating disk flow imposed upon a radial outer flow. To fill this gap, we consider the unsteady flow and heat transfer of a viscous electrically conducting fluid over an infinite porous rotating disk. The disk is subject to a uniformly applied magnetic field in the wall-normal direction and also to a uniform radial outer flow far above the disk. The uniform radial flow assumption yields a radial pressure gradient upon the disk owing to the potential flow theory. A set of transformations is used then to reduce the governing equations of motion. The constructed unsteady flow equations as well as the steady flow equations of Navier–Stokes, Maxwell, and energy are solved later using an implicit spectral Chebyshev collocation technique, which is free of the numerical oscillation problem encountered in Refs. [6,10] using a finite difference numerical integration procedure due to the differences between the initial and boundary conditions.

2 The Problem Formulation

Let us consider the unsteady flow motion of a viscous, incompressible, electrically conducting fluid over an infinite porous disk, which is rotating with an angular velocity Ω about its axis of rotation z. Figure 1 shows the axisymmetric flow model and the cylindrical polar coordinate system (r,ϕ,z). A uniform magnetic field of strength B_0 is applied in the z direction. The disk is electrically insulated so that induced electric currents cannot penetrate it. It is assumed that the magnetic Reynolds number $\mathrm{Re}_m = \mu_0\sigma VL$ is negligibly small. Moreover, a uniform radial outer flow above the porous disk affects the flow field given by $u_e = \Omega Cr$. Although not necessary, we suppose C to be a positive constant in the subsequent analysis. The application of the potential flow theory at the edge of the boundary layer signifies that a radial pressure gradient is induced in the form, see Ref. [11]

$$-\frac{\partial p}{\partial r} = (\Omega^2 C^2 \rho + \Omega C \sigma B_0^2) r$$

Contributed by the Heat Transfer Division of ASME for publication in the Journal of Heat Transfer. Manuscript received May 4, 2009; final manuscript received December 14, 2009; published online April 2, 2010. Assoc. Editor: Wei Tong.

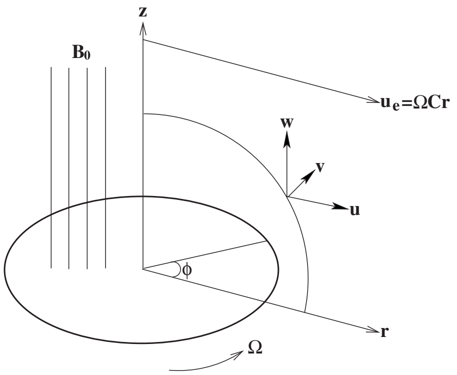

Fig. 1 Configuration of the flow and geometrical coordinates

The dimensionless mean flow velocities, pressures, and temperatures develop alongside a boundary layer coordinate $Z = (\sqrt{\Omega/\nu})z$ in accordance with the self-similarity variables, see Ref. [6]

$$(u,v,w) = (\Omega r F(t,Z), \Omega r G(t,Z), \sqrt{\Omega\nu}H(t,Z))$$
$$(p,T) = (\Omega\mu P(t,Z), T_\infty + (T_w - T_\infty)\theta(t,Z)) \qquad (1)$$

where the similarity functions F, G, H, P, and θ satisfy the following nonlinear partial differential equations:

$$\frac{\partial F}{\partial t} + F^2 - G^2 + F'H - F'' + MF - C^2 - MC = 0$$
$$\frac{\partial G}{\partial t} + 2FG + G'H - G'' + MG = 0$$
$$\frac{\partial H}{\partial t} + P' + H'H - H'' = 0 \qquad (2)$$
$$2F + H' = 0$$
$$\frac{\partial \theta}{\partial t} - \frac{1}{\mathrm{Pr}}\theta'' + H\theta' = 0$$

A symmetry is present in system (2) for C, if the non-MHD flow is taken into consideration. In addition to this, a prime denotes a derivative with respect to Z, $M = \sigma B_0^2/\rho\Omega$ is the magnetic interaction parameter representing the ratio of magnetic to inertial forces and the boundary conditions accompanying the system (2) for all time t are given as

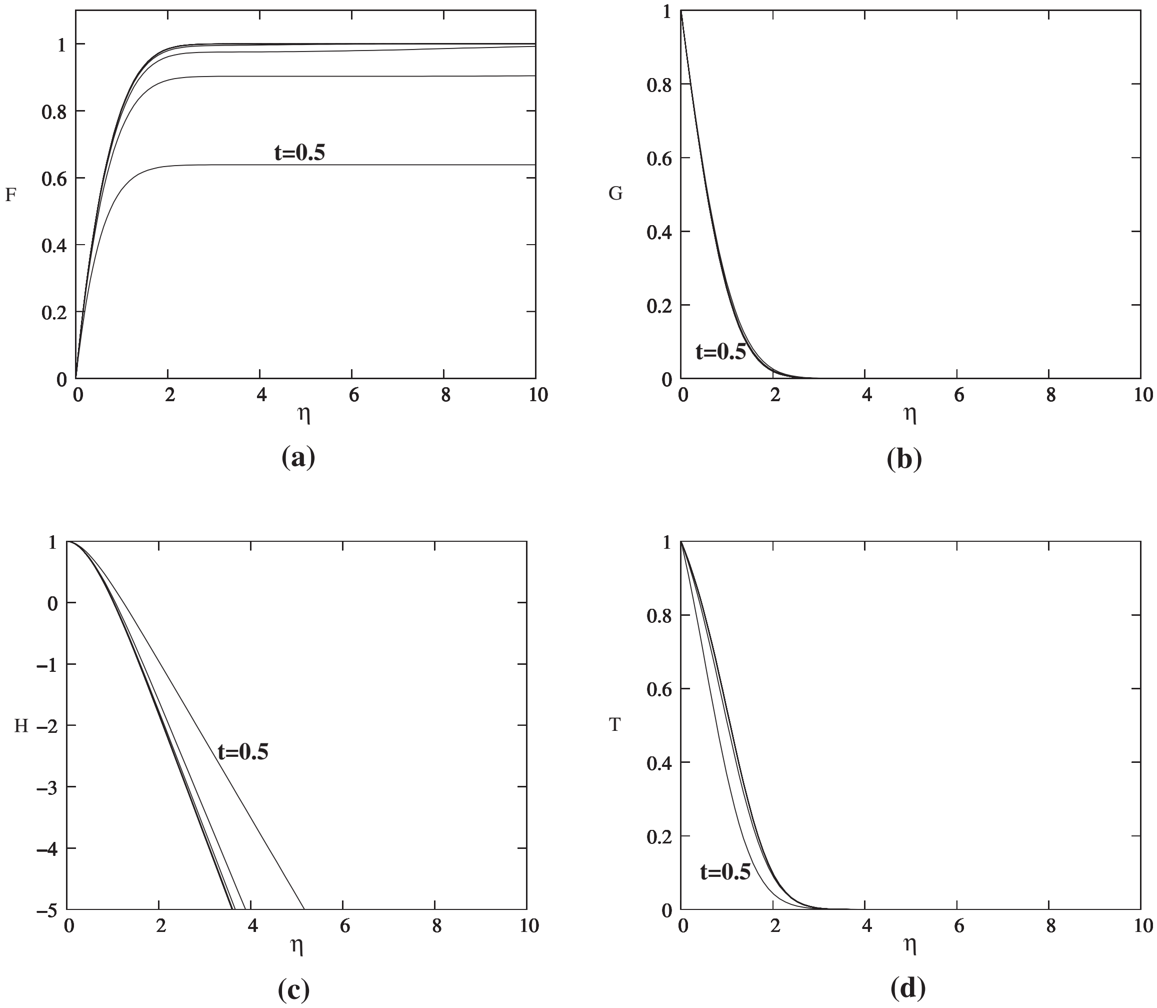

Fig. 2 The time progression of basic flow quantities for the rotating disk flow are shown for an MHD ($M=1$) and permeable wall case ($s=1$), respectively, in (*a*) the radial velocity profiles, (*b*) the circumferential velocity profiles, (*c*) the wall-normal velocity profiles, and (*d*) the temperature profiles. The snapshots are given at 0.5 increments in time. The dot-dashed curves correspond to the large time limit as well as the steady solution.

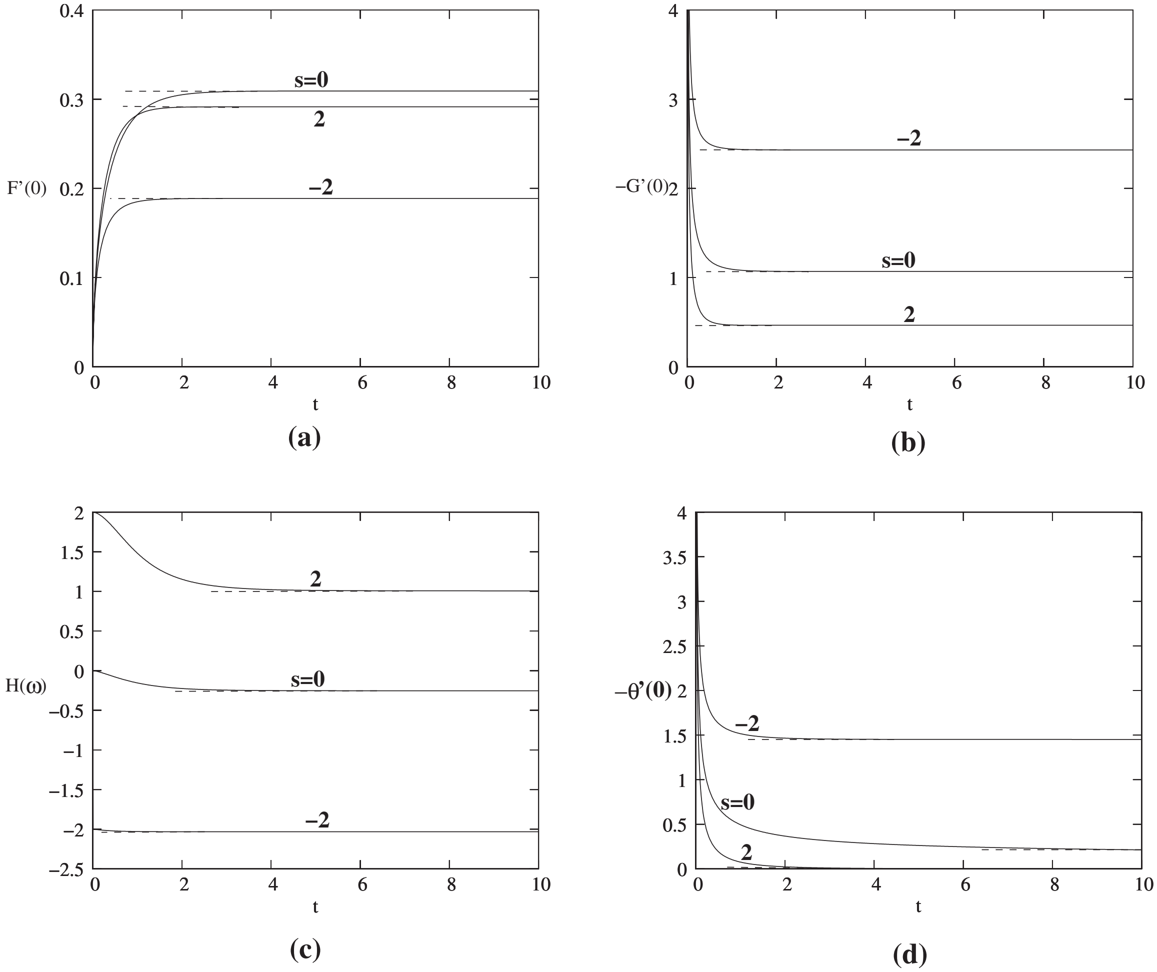

Fig. 3 The time progression of physically significant parameters are shown for the conducting flow case with $M=1$ and $C=0$, respectively, in (*a*) $F'(0)$, (*b*) $-G'(0)$, (*c*) $H(\infty)$, and (*d*) $-\theta'(0)$. A dashed line corresponds to the steady state value.

$$
\begin{gathered}
Z=0, \quad F=0, \quad G=1, \quad H=s, \quad P=0, \quad \theta=1 \\
Z\to\infty, \quad F\to C, \quad G\to 0, \quad \theta\to 0
\end{gathered}
\tag{3}
$$

The system is also supplemented with the subsequent initial values valid for all Z

$$
t=0, \quad F=0, \quad G=0, \quad H=0, \quad P=0, \quad \theta=0 \tag{4}
$$

Equations (2)–(4) represent the unsteady Navier–Stokes equations along with the energy equation, whose corresponding steady state counterparts are identical to those of Kumar et al. [8], if C is also removed from the corresponding equations. It may be remarked that Eqs. (2)–(4) and the corresponding steady state equations also represent the flow over a rotating sphere or cone, see Ref. [12].

The action of the viscosity in the fluid adjacent to the disk sets up a tangential shear stress, which opposes the rotation of the disk. As a consequence, it is necessary to provide a torque at the shaft to maintain a steady rotation. To find the tangential shear stress τ_θ and radial shear stress τ_r, we apply the Newtonian formulae

$$
\begin{gathered}
\tau_\theta = \left.\left[\frac{\partial v}{\partial z}\right]\right|_{z=0} = \Omega r\sqrt{\frac{\Omega}{\nu}}G'(t,0) \\
\tau_r = \left.\left[\frac{\partial u}{\partial z}\right]\right|_{z=0} = \Omega r\sqrt{\frac{\Omega}{\nu}}F'(t,0)
\end{gathered}
\tag{5}
$$

The rate of heat transfer from the disk surface to the fluid is computed by the application of Fourier's law, as given below

$$
q = -\left.\frac{\partial T}{\partial z}\right|_{z=0} = -\sqrt{\frac{\Omega}{\nu}}\theta'(t,0) \tag{6}
$$

from which the normalized Nusselt number can be obtained. The torque generated by the disk is then expressed as

$$
-2\pi\int_0^R \mu v_z|_{z=0} r^2 dr = -2\pi\Omega\mu\frac{R^4}{4}\sqrt{\frac{\Omega}{\nu}}G'(t,0)
$$

Therefore, in what follows, we numerically compute $F'(t,0)$, $G'(t,0)$, and $\theta'(t,0)$ to understand the underlying physics of the problem.

3 Numerical Procedure

It can be immediately noticed that a discontinuity is present between initial values and boundary conditions in Eqs. (3) and (4). There are a number of numerical procedures to discretize system (2)–(4). The most frequently used are the classical explicit or implicit finite difference techniques. But no matter the type of differencing, the resulting numerical algorithm gives rise to numerical oscillations. The numerical oscillations were often reported during the numerical simulation of the unsteady rotating disk flows, see, for instance, Refs. [6,10]. To cope with these deficiencies and obtain the unsteady solution at one go, we propose here

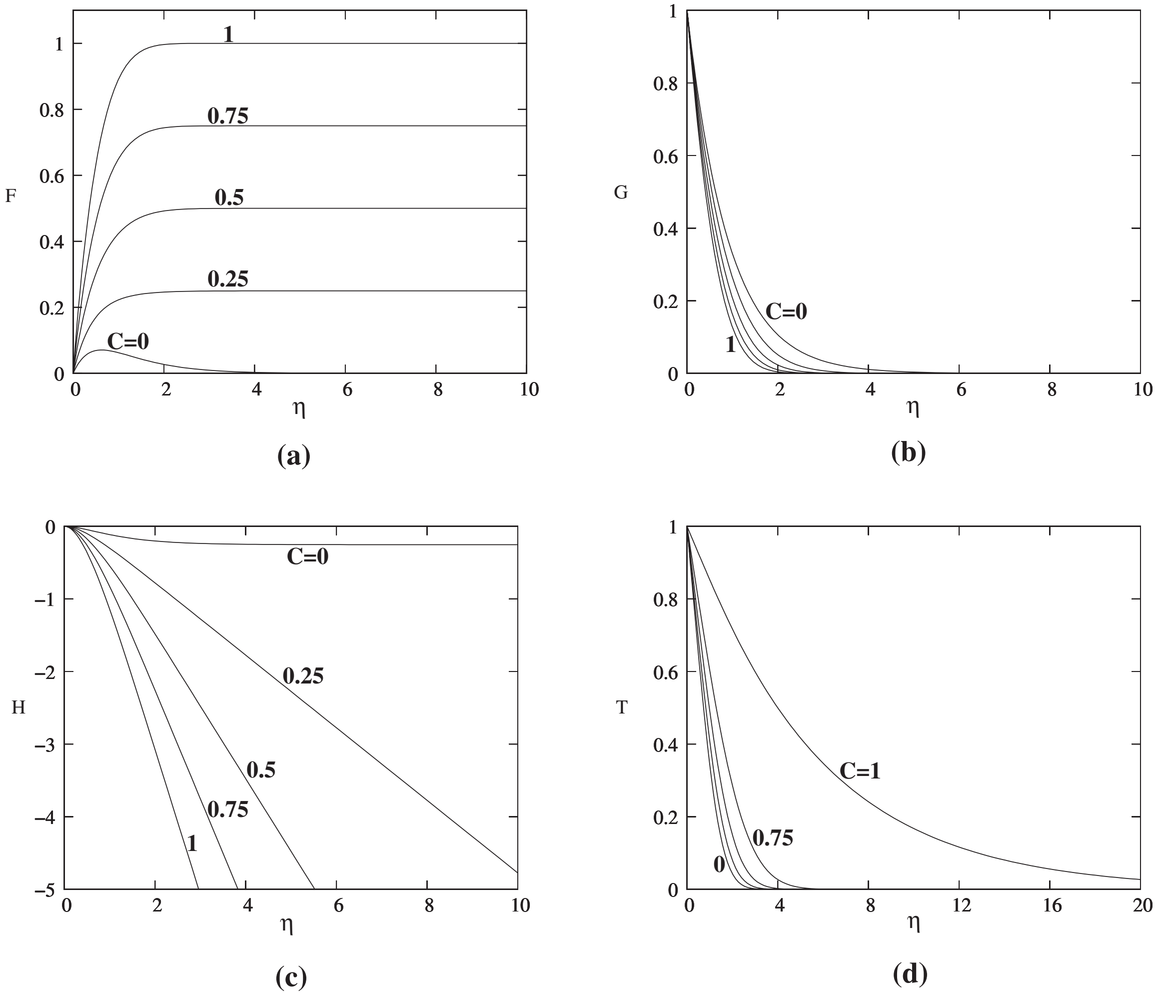

Fig. 4 Effects of the uniform outer radial flow on the basic flow quantities for the rotating disk flow are shown for a non-MHD and impermeable wall case, respectively, in (*a*) the radial velocity profiles, (*b*) the circumferential velocity profiles, (*c*) the wall-normal velocity profiles, and (*d*) the temperature profiles. The increment in *C* is 0.25 units.

to use the spectral Chebyshev method, see Ref. [13]. In compliance with this purpose, the infinity physical domain of computation is mapped first onto the interval $\eta \in [-1,1]$ via the linear transformation $\eta = -1 + 2Z/Z_{\max}$. Next, the nonlinear terms in Eq. (2) are linearized with the usual Newton linearization technique. A forward time differencing for the derivative of F is appropriate at this stage in the form

$$\frac{\partial F}{\partial t} = \frac{F_{j+1} - F_j}{\Delta t}$$

Taking into account the advantage of implicit schemes, the linearized terms are also imposed at the time $t+\Delta t$. A Chebyshev collocation based on the well-known Chebyshev polynomials is later employed in the wall-normal direction η. In view of the above remarks, system (2)–(4) can be cast into a matrix form

$$\mathbf{A}\delta\mathbf{U}_{j+1} = \mathbf{B} \tag{7}$$

which is eventually solved with an *LU* matrix decomposition technique.

As compared with the finite difference methods, the method devised here is robust, unconditionally stable, and easy to program due to its compact matrix form in Eq. (7). More details of the integration scheme without the time derivatives (steady state) can be found in Ref. [14].

4 Results and Discussion

4.1 Unsteady Flow Results. Starting from the zero initial state, the ideal flow over a disk evolves impulsively by a sudden action of rotation of the disk, and as time passes, the flow settles down to a steady state. This action of the fluid flow is shown in Figs. 2(*a*)–2(*d*) for a magnetic ($M=1$) and porous disk ($s=1$) with $C=1$, respectively. Figures are displayed for the time development of the flow quantities by a time step $\Delta t=0.05$, but taken at a snapshot of $t=0.5$. The sufficiently large time solution as well as the steady solution are also shown by the dot-dashed curves. Figures show how the impulsive motion ends up with a steady state, which were calculated by ignoring the time derivative terms in Eqs. (2)–(4). It is further noticeable from the figures that the circumferential velocity attains its steady state quickest as compared with the other physical variables. It is no surprising to witness that the magnetic field helps the velocities to reach their asymptotic limit faster, even though it delays the attendance for the temperature field due to the well-known increasing temperature impact of the magnetic field through the wall-normal velocity H. What is surprising here is that, the presence of a uniform radial outer flow leads the whole flow field to settle down to its steady state counterpart as rapidly as possible, which was found to be the case for all values of the parameters accounted for.

Table 1 Comparison of the numerical solutions of the vertical suction velocity ($H(\infty)$) and the heat transfer coefficient ($-\theta'(0)$) obtained for Pr=1 and $M=0.5$ for a variety of s. Superscripts ^{1} and ^{2}, respectively, refer to the values from the present and Ref. [8].

s	$H(\infty)^1$	$-\theta'(0)^1$	$H(\infty)^2$	$-\theta'(0)^2$
−4	−4.00700706	4.00239513	−4.00700	4.002395
−3	−3.01528894	3.00532198	−3.01530	3.005322
−2	−2.04131653	2.01505125	−2.04130	2.015051
−1	−1.14101328	1.05911937	−1.14100	1.059119
0	−0.45888005	0.28265593	−0.45888	0.282656
1	−0.03213052	0.00343275	−0.03213	0.003433

It is next demonstrated in Figs. 3(*a*)–3(*d*) the time development of $F'(0)$, $-G'(0)$, $H(\infty)$, and $-\theta'(0)$, respectively, for the ($M=1$) case with no outer radial flow, which are closely related to the radial skin friction, azimuthal skin friction (also torque), axial velocity at infinity, and the local rate of heat transfer for Pr $=0.72$ and all computed with a step size of $\delta t=0.01$. The known effects of a uniform suction and injection are well captured in the figures. The steady state values are also shown by the broken lines in each figure. It can again be seen that the method successfully generates the steady state values of the physically important parameters, the fastest for the case of tangential skin frictions consistent with Figs. 2(*a*)–2(*d*).

4.2 Steady Flow Results. In order for assessing the accuracy of the numerical technique, a comparison is made in Table 1 between the steady state results corresponding to system (2)–(4) for $M=0.5$, $C=0$, and Pr=1.0 with those of Kumar et al. [8]. An excellent agreement can be observed from the table.

Effects of the radial flow parameter C on the radial, tangential, and axial velocity profiles F, G, H and on the temperature profile θ for $M=1$ and Pr=0.72 are presented in Figs. 4(*a*)–4(*d*) for an impermeable wall. From the figures, it is evident that the radial velocity F, the axial velocity $-H$, and the temperature θ increase everywhere as C increases but the tangential velocity G is reduced. The physical reason for this behavior is that an increase in C implies an increase in the radial outer flow, which imports extra momentum into the boundary layer near the disk. This increases the axial inflow, radial outflow, and temperature. As a result, the radial, axial velocity, and temperature increase with C. Furthermore, the tangential velocity is reduced, thinning the boundary layer thickness, whereas thickening the thickness of thermal boundary layer.

The variation in the surface shear stresses on the radial and tangential directions $F'(0)$, $-G'(0)$, and the surface heat transfer $-\theta'(0)$ with C for $0\leq M\leq 6$ and Pr=0.72 is shown in Figs.

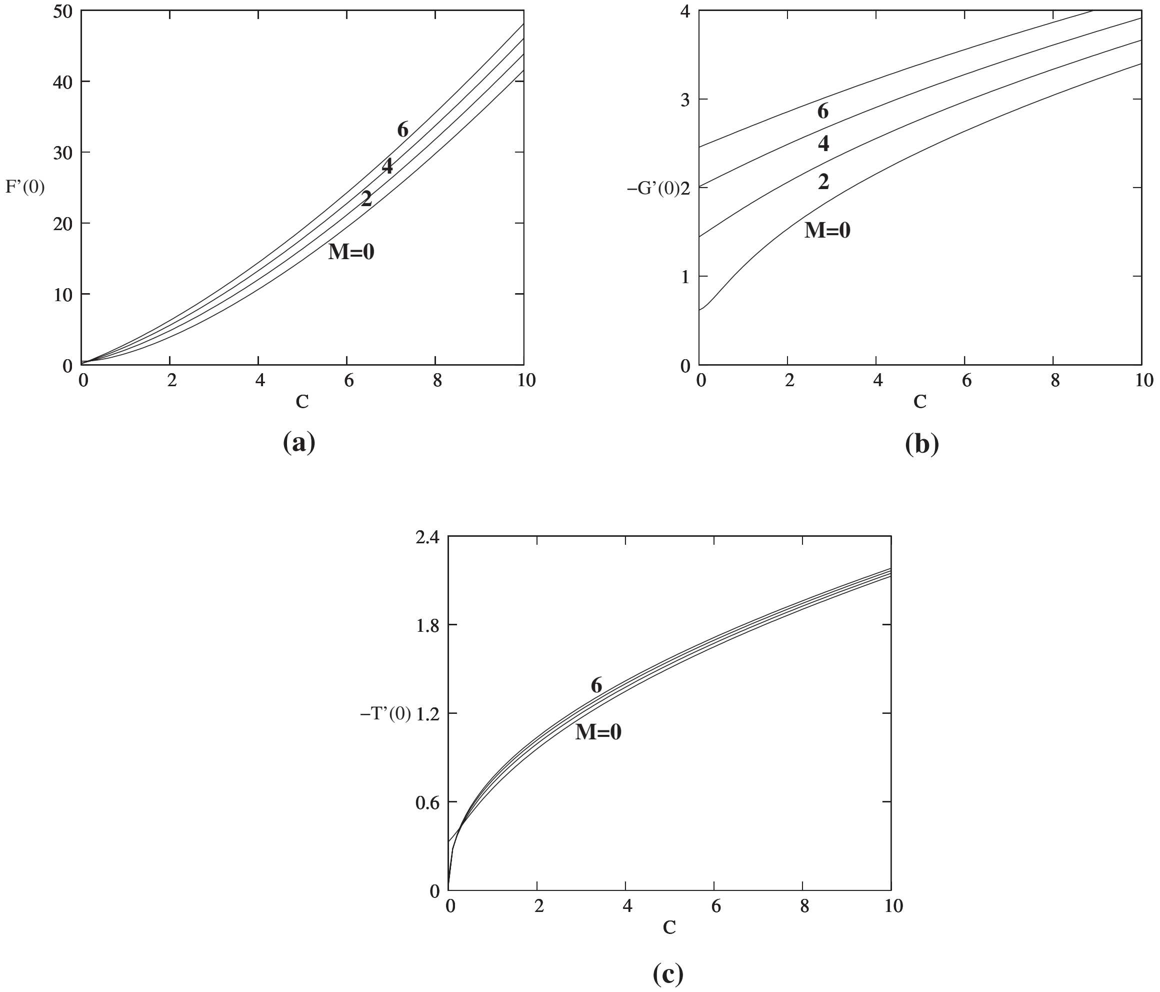

Fig. 5 The variation in physically significant parameters are shown against the radial flow parameter C for the conducting flow with a variety of M, respectively, in (*a*) $F'(0)$, (*b*) $-G'(0)$, and (*c*) $-\theta'(0)$. The increment in M is 2 units.

5(*a*)–5(*c*), respectively, for a nonporous disk. For a fixed M, it is seen that they all increase with increasing C, since an increase in C enhances the radial outer flow, which accelerates the fluid near the surface. On the other hand, for a fixed C, the tangential skin friction increases with M. The contribution appears to be twofold on $F'(0)$ and $-\theta'(0)$. Both decrease initially with small values of C near 0, and then they start increasing with an increase in C for all values of M. Hence, the three physical parameters increase for increasing values of C for all M. It can be deduced that the well-known enhancing heat transfer rate property of a vertically applied uniform magnetic field is delayed under the action of a uniform radial outer flow, particularly for small values of radial flow parameters.

5 Conclusions

A new solution of the Navier–Stokes along with the energy equations governing the unsteady viscous MHD flow over an infinite disk rotating in a fluid upon which a uniform radial outer flow is imposed has been obtained in the present work. The self-similar steady and unsteady equations resulting from some suitable transformations have been numerically solved using an implicit spectral Chebyshev collocation scheme, whose efficiency and accuracy have been verified first solving the model problem in the absence of the radial flow. The subsequent conclusions may be drawn from the outcomes.

(1) The exploration of the transient character of the flow field has shown that the circumferential velocity attains its steady state quickest and the contribution of the uniform radial outer flow is to accelerate the settle down process of the unsteady flow into its steady state.
(2) The steady state solution has shown that the radial and axial velocities, and also temperature, increase as the radial flow parameter increases, unlike the tangential velocity.
(3) For a fixed magnetic interaction parameter, the radial and tangential skin friction coefficients, as well as the rate of heat transfer, increase with an increasing radial flow parameter for a nonporous rotating disk.
(4) For very small values of the radial flow parameter, the heat transfer near the wall is reduced initially, even in the presence of a strong magnetic field.

Nomenclature

Ω = angular velocity
(r,ϕ,z) = variables of cylindrical polar coordinates
(p,T) = pressure and temperature fields
(u,v,w) = velocity field
η = wall-normal coordinate
C = dimensionless radial flow parameter
s = wall suction or injection parameter
(T_w,T_∞) = constant temperature at the wall and infinity
(ρ,ν,σ) = density, kinematic viscosity, and electrical conductivity of the fluid
(c_p,κ) = specific heat at a constant pressure and coefficient of thermal conductivity
μ_0 = magnetic permeability
(F,G,H) = similarity variables for velocities
(P,θ) = similarity variables for pressure and temperature
$(\mathrm{Re}_m,\mathrm{Pr})$ = magnetic Reynolds and Prandtl numbers
M = magnetic interaction parameter
(V,L) = characteristic velocity and length
(τ_r,τ_θ) = shear stresses on the wall
q = heat flux

References

[1] Kármán, T. V., 1921, “Uber laminare und turbulente reibung,” Z. Angew. Math. Mech., **1**, pp. 233–252.
[2] Yoo, J. S., 1997, “Unsteady Heat Transfer From a Rotating Disk With Solidification,” Numer. Heat Transfer, Part A, **31**, pp. 765–781.
[3] Takeda, K., Baev, V. K., and Minaev, S. S., 2007, “An Analytical and Experimental Investigation of Flow Characteristics Generated by Rotating Porous Disk,” Int. J. Heat Mass Transfer, **43**, pp. 623–628.
[4] Shevchuk, I. V., 2009, “Turbulent Heat and Mass Transfer Over a Rotating Disk for the Prandtl or Schmidt Numbers Much Larger Than Unity: An Integral Method,” Int. J. Heat Mass Transfer, **45**, pp. 1313–1321.
[5] Awad, M. M., 2008, “Heat Transfer From a Rotating Disk to Fluids for a Wide Range of Prandtl Numbers Using the Asymptotic Model,” ASME J. Heat Transfer, **130**, p. 014505.
[6] Hossain, M. A., Hossain, A., and Wilson, M., 2001, “Unsteady Flow of Viscous In-Compressible Fluid With Temperature-Dependent Viscosity Due to a Rotating Disc in the Presence of Transverse Magnetic Field and Heat Transfer,” Int. J. Therm. Sci., **40**, pp. 11–20.
[7] Maleque, K. A., and Sattar, M. A., 2005, “Steady Laminar Convective Flow With Variable Properties Due to a Porous Rotating Disk,” ASME J. Heat Transfer, **127**, pp. 1406–1409.
[8] Kumar, S. K., Thacker, W. I., and Watson, L. T., 1988, “Magnetohydrodynamic Flow and Heat Transfer About a Rotating Disk With Suction and Injection at the Disk Surface,” Comput. Fluids, **16**, pp. 183–193.
[9] Turkyilmazoglu, M., 2009, “Exact Solutions Corresponding to the Viscous Incompressible and Conducting Fluid Flow Due to a Porous Rotating Disk,” ASME J. Heat Transfer, **131**, p. 091701.
[10] Attia, H. A., 2003, “Time Varying Rotating Disk Flow and Heat Transfer of a Conducting Fluid With Suction or Injection,” Int. Commun. Heat Mass Transfer, **30**, pp. 1041–1049.
[11] Evans, H., 1968, *Laminar Boundary Layer Theory*, Addison-Wesley, Reading, MA.
[12] Banks, W. H. H., 1976, “The Laminar Boundary Layer on a Rotating Sphere,” Acta Mech., **24**, pp. 273–287.
[13] Canuto, C., Hussaini, M. Y., Quarteroni, A., and Zang, T. A., 1988, *Spectral Methods in Fluid Dynamics*, Springer-Verlag, Berlin.
[14] Turkyilmazoglu, M., 1998, “Linear Absolute and Convective Instabilities of Some Two- and Three Dimensional Flows,” Ph.D. thesis, University of Manchester, Manchester, UK.

H. Huisseune
e-mail: henk.huisseune@ugent.be

C. T'Joen
e-mail: christophe.tjoen@ugent.be

P. Brodeoux

S. Debaets

M. De Paepe

Department of Flow, Heat, and Combustion Mechanics,
Ghent University,
Sint-Pietersnieuwstraat 41,
B9000 Gent, Belgium

Thermal Hydraulic Study of a Single Row Heat Exchanger With Helically Finned Tubes

In this study, the heat transfer and friction correlation of a single row heat exchanger with helically finned tubes are experimentally determined. The transversal tube pitch was parametrically varied. A detailed description of the test rig and the data reduction procedure is given. A thorough uncertainty analysis was performed to validate the results. The proposed heat transfer correlation can describe 95% of the data within ±11% and shows a 4.49% mean deviation. The friction correlation predicts 95% of the data within ±19% with a mean deviation of 6.84%. The new correlations show the same trend as most correlations from open literature, but none of the literature correlations are able to accurately predict the results of this study. [DOI: 10.1115/1.4000706]

Keywords: helical fin, single row, heat exchanger, heat transfer, friction

1 Introduction

Fin-and-tube heat exchangers are widely used to transfer heat between liquid and gas. Examples include condensers and evaporators in HVAC&R applications (heating, ventilation, air conditioning and refrigeration), water and oil cooling in vehicles or process plants, etc. The dominant heat transfer resistance (up to 85% of the total thermal resistance) in these processes is located on the gas side due to the lower thermal conductivity of the gas. In order to improve the heat transfer rate, the exterior surface area is increased by adding fins. The disadvantage of adding fins is that the gas side frictional pressure drop increases.

This study focuses on individually finned tubes for compressed air cooling using water. These tubes are more rugged than the continuous fin designs, but also less compact. Commonly used fin designs are the plain circular fin, the helical fin, and annular enhanced designs such as segmented or slotted wire loop fins [1,2]. There are various ways of manufacturing these finned tubes; the fins can be attached to the tubes by a tight mechanical fit, tension winding, adhesive bonding, soldering, brazing, or welding [3]. These processes result in a contact resistance between the tube and the fin. In most studies this effect is neglected. In a recent combined experimental and numerical study, Kim et al. [4] determined thermal contact conductances in the order of $6000-10,000\ \mathrm{W/m^2\,K}$, which is two orders of magnitude larger than the air side convective heat transfer coefficient, but depending on the liquid velocity, only a few times larger than the convective heat transfer coefficient on the liquid side. So, for the target application the impact of the contact resistance will be small. Kim et al. [4] also showed that the value of the contact resistance is strongly dependent on manufacturing parameters. So care should be taken to ensure good metallic contact. In this study, monofinned tubes are considered. The helical fins are extruded out of the base tube, eliminating the contact resistance. The helically finned tube and the cross section studied in this work are shown in Fig. 1. These tubes were used to manufacture a single row heat exchanger with varying tube pitch.

Heat exchangers consisting of individually finned tubes have been studied extensively in the past. However, most data are focused on multirow heat exchangers [5–13]. Jameson and Schenectady [5] performed an experimental study on the effect of the tube spacing on the pressure drop and heat transfer of helically finned tubes. For various tested tube arrangements, the values of the proportionality constants, which are needed to evaluate the suggested pressure drop equations, are tabulated. Jameson and Schenectady [5] also deduced a relation similar to the fanning equation, relating the pressure drop data for all the tube sizes and arrangements tested. A pressure drop correlation applicable to both bare and finned tube bundles was established by Gunter and Shaw [6]. In the discussion accompanying this article, Jameson validated the correlation with his own test data and suggested a revised expression. Other authors have also questioned the Gunter–Shaw relationship [1,7,8]. Two widely cited correlations for a staggered tube layout are the Briggs–Young [9] (heat transfer) and Robinson–Briggs [8] (pressure drop) correlation. These relations are recommended by Webb [1] based on "the rigorous manner in which the correlations were developed and the wide range of the data which they are based on." Mirkovic [10] performed tests on heat exchangers with helically finned tubes in a staggered eight row configuration to determine the thermal and hydraulic characteristics. He reported correction factors for other numbers of tube rows. The heat transfer and pressure drop correlations suggested by the Engineering Sciences Data Unit (ESDU) [14] are based on data for bundles containing four or more tube rows. For bundles less than four rows deep, the ESDU [14] advised to multiply the Nusselt number with a correction factor as recommended by Huber and Rabas [15]. The pressure loss coefficient of a single row bundle is about 80% of that of a deep bundle [16]. Using experimental data from open literature, Genic et al. [13] established new pressure drop correlations for in-line and staggered helically finned tube bundles. The staggered bundles are divided into two groups: normal and densely-packed tube bundles. They suggested the correction factors of Brauer [17–19], Yudin [20], and Weierman [21] to calculate the pressure drop for a one row heat exchanger. Eckels and Rabas [16] demonstrated that the effect of the row number on heat transfer in finned tube bundles is dependent on the Reynolds number, a point which is not considered in the previously mentioned correction factors. Depending on the Reynolds number, the heat transfer coefficient for a single row bank is 20–30% smaller than the asymptotic value of a deep bank. Eckels and Rabas [16] also discussed the row effect on the pressure drop. Comparing the data of several authors, they concluded that the friction factor can increase or decrease with the row number. Moreover, the influence of the number of rows on the pressure drop is not only dependent

---

Contributed by the Heat Transfer Division of ASME for publication in the Journal of Heat Transfer. Manuscript received November 12, 2008; final manuscript received October 16, 2009; published online March 19, 2010. Assoc. Editor: He-Ping Tan.

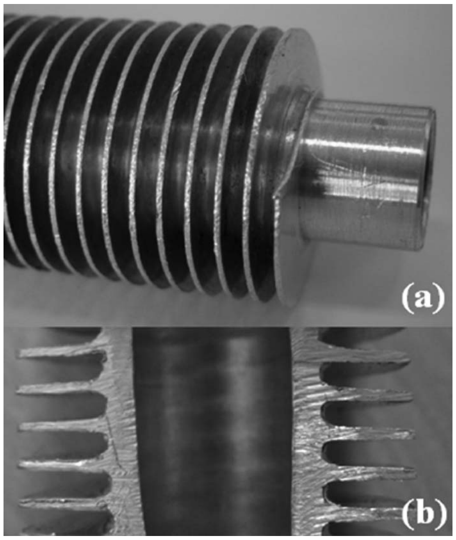

Fig. 1 Tested monofinned tube: (*a*) tube with helical fins and (*b*) cross section

on the Reynolds number but also on the tube diameter, tube pitch, and fin density. Consequently, correcting the correlation of a multiple row tube bank to obtain the heat transfer coefficient or pressure drop of a single row heat exchanger (as studied in this work) does not result in accurate predictions. However, very little research has been done on the thermal hydraulic behavior of heat exchangers with one row of tubes. Jameson and Schenectady [5] reported pressure drop data for a single row bundle. Lapin and Schurig [22] experimentally determined the effect of the number of staggered rows on the air side convective heat transfer coefficient. They studied finned tube banks with one to eight tube rows. Schmidt [23] established a Nusselt correlation for one tube row of a multirow heat exchanger. Sparrow and Samie [24] determined the heat transfer and pressure drop characteristics for one and two row tube bundles. For the one row tube bundle, the transversal tube pitch was parametrically varied. They concluded that the Nusselt numbers increase with decreasing transversal pitch due to the higher velocities in the minimum cross section. The same trend is found in the ESDU correlation [14]. However, Mirkovic [10] observed that the Nusselt numbers increase when the transversal tube pitch is enlarged. This result of Mirkovic [10] is questionable. By correlating the Nusselt numbers with the minimum-area Reynolds number Re_c, Sparrow and Samie [24] established a heat transfer expression independent of the transversal tube pitch. Most authors reported similar results [5,9,16,12,23]. The transversal tube pitch also has an important influence on the pressure drop over the bundle: The pressure drop increases with decreasing pitch, due to the increasing blockage [5,8,9,12,14,24]. Again Mirkovic [10] observed the opposite effect: An increase in pressure drop with transversal pitch.

The above discussion reveals the need for more experimental data of single row annular finned tubes. These heat exchangers are used in applications where a rugged configuration and low pressure drop are desirable, e.g., compressed air cooling. To the authors' knowledge, only two heat transfer correlations [22,24] and one pressure drop correlation [5], deduced from data of single row heat exchangers, are available in open literature for design purposes. The application ranges of these correlations differ and, as will be shown, none of the literature correlations result in satisfactory predictions for the heat transfer coefficients and friction factors of the studied one row heat exchanger.

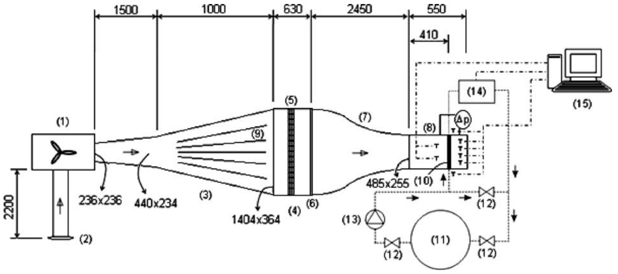

Fig. 2 Experimental setup: open air wind tunnel and a closed water cycle. The dimensions of the wind tunnel are also indicated (in mm) (→: air flow; →: water flow)

2 Experimental Equipment

The test rig consists of an open air wind tunnel and a closed water cycle (see Fig. 2). This test setup and the measurement procedures were previously validated extensively. It is the same setup as used by T'Joen et al. [25,26] to study the heat transfer of a compact fin-and-tube heat exchanger in maldistributed flow. The exit section area was reduced in order to obtain a higher exit velocity. Measurements are performed on both the air and water sides of the heat exchanger.

A radial fan (1) sucks air through a calibrated nozzle (ISO5167) (2). To determine the air mass flow rate, the pressure drop over the nozzle is measured using a differential pressure transducer. The fan is driven by a frequency controller, which allows setting an air mass flow rate between 0.1 kg/s and 1.1 kg/s (corresponding with a velocity range from 0.7 m/s to 7.4 m/s at the inlet of the test section). After the diffuser (3), settling chamber (4) (with honeycomb (cell size 1/2 inch (12.7 mm) – length 4 inch (101.6 mm)) (5) and screen flow straightener (6)) and sinusoidal contraction section (7), a uniform air flow enters the test section (8). To avoid flow separation, the diffuser angle is reduced using baffles (9). The dimensions of the wind tunnel are indicated in Fig. 2. The flow uniformity at the inlet of the test section was illustrated by T'Joen et al. [26] using a heated sphere anemometer and a bladed rotor measuring device. Hotwire measurements performed at the start of this measuring campaign confirmed these local velocity measurements and the uniform inlet flow conditions.

A single row array of helicoidally monofinned tubes (10) is placed in the test section (8), which has a cross-sectional area of $485 \times 255\ \mathrm{mm}^2$. Depending on the transversal tube pitch, eight or ten tubes are positioned. The remaining gap is filled to $X_t/2$ to prevent excessive flow bypass. The geometry of the tubes is listed in Table 1. During the experiments these dimensions are fixed. Only the transversal tube pitch is varied, yielding the dimensionless values X_t/d_{ext}=1.92, 2.27, 2.45, 2.84, and 3.27.

The closed water cycle consists of an electric boiler (11) with a power limit of 6 kW, several valves (12) and a circulation pump (13). The inlet water temperature is controlled with a proportional-integral-derivative (PID) controller. The pump is driven by a frequency controlled motor, thus allowing for a flow rate to be set. The water mass flow rate is measured with a calibrated electromagnetic flow meter (14). To prevent damage to the heat exchanger by overpressure, pressure gauges monitor the overall pressure level in the system. The test section, the tubes, and the distributors bringing the hot water to the heat exchanger

Table 1 Dimensions of the tested monofinned tubes

d_{ext} (mm)	13.0 ± 0.2
d_{in} (mm)	10.3 ± 0.2
t_{fin} (mm)	0.65 ± 0.05
D_{fin} (mm)	24.8 ± 0.05
F_p (mm)	2.4 ± 0.05

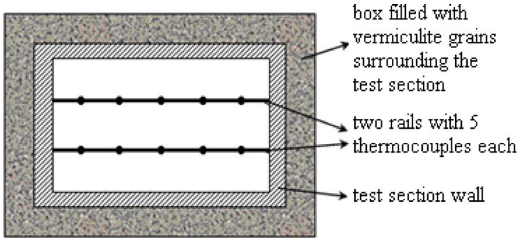

Fig. 3 View of the outlet section of the wind tunnel: position of the thermocouples measuring the outlet air temperature

are surrounded by a box filled with vermiculite grains to avoid heat losses to the environment during the measurements (see Fig. 3). The water flows through the heat exchanger in two passes (4 ×4 or 5×5 depending on the transversal tube pitch).

3 Procedure

All temperatures were measured using calibrated K-type thermocouples (indicated with T symbols in Fig. 2) and read with a Keithley 2700 multimeter/data acquisition system ((15) in Fig. 2). Because of uniform inlet conditions, it was sufficient to insert only two thermocouples in the test section upstream the heat exchanger to measure the incoming air temperature. The averaged value was used in the calculations. Downstream the heat exchanger. the temperature profile of the cross section was no longer uniform. Exit air temperatures were simultaneously measured on ten different locations: two rails of each five thermocouples were positioned in a cross section downstream the heat exchanger (see Fig. 3). The average of these ten values was used as the overall average air exit temperature. A similar technique was used by T'Joen et al. [25,26]. The water inlet and exit temperatures were measured with two thermocouples placed in the center of the inlet and outlet of the respective distributors. The pressure drop over the heat exchanger and across the nozzle was measured with a differential pressure transducer. A summary of the measurement equipments and their uncertainties can be found in Table 2.

The measurements were performed under steady state conditions for different Reynolds numbers. The steady state regime was verified by monitoring the water temperature variation. Once steady state was reached, each thermocouple took a series of 500 samples over a period of 2000 s and the measurements were then averaged. Twice the standard deviation of the 500 temperature measurements was used as uncertainty on these averaged temperatures, as suggested by Moffat [27]. The signal of the water flow meter was also logged every 4 s and averaged. As mentioned in Table 2, the uncertainties on the water and air mass flow rates are ±2% and ±1.5%, respectively. The test conditions can be found in Table 3.

In order to be able to indicate the quality of the measurements, a thorough uncertainty analysis was performed according to Moffat [27]. The uncertainties on the calculated results were determined with the root-sum-square method [27], unless it is mentioned otherwise. The errors estimated on the thermodynamic properties of water and air are tabulated in Table 4 and were determined based on recommendations in open literature [28–30].

Table 2 Measurement equipments and their accuracies

Measurement equipment	Accuracy
Differential pressure transducer (<200 Pa) (Pa)	±0.5
Differential pressure transducer (>200 Pa) (Pa)	±1
Electromagnetic flow meter (water) (%)	±2
Calibrated ISO5167 nozzle (air) (%)	±1.5
K-type thermocouple (°C)	±0.1

Table 3 Test conditions during the measurements

Quantity	Range
Air mass flow rate (kg/s)	0.1020–1.0963
Water mass flow rate (kg/s)	0.0674–0.2187
Air inlet temperature (°C)	14.6–23.1
Water inlet temperature (°C)	66.9–69.1
Water pressure (bar)	2

The air density was calculated from the ideal gas law and its uncertainty resulted from the uncertainties on air temperature and atmospheric pressure. The thermodynamic properties of water were calculated based on the International Association for the Properties of Water and Steam Industrial Formulation 1997 (IAPWS IF-97) [30].

4 Data Reduction

The air and water mass flow rates and temperature measurements are used to determine the overall heat balance on the water and air sides of the single row bundle, according to Eqs. (1) and (2). $T_{\text{air,in}}$ and $T_{\text{air,out}}$ are the averaged air temperatures at the inlet and outlet of the heat exchanger, respectively. The specific heat capacities $\overline{c_p}$ are determined at the averaged temperature between the inlet and outlet and the corresponding pressure.

$$\dot{Q}_{\text{air}} = \dot{m}_{\text{air}} \cdot \overline{c_{p,\text{air}}} \cdot (T_{\text{air,out}} - T_{\text{air,in}}) \tag{1}$$

$$\dot{Q}_{w} = \dot{m}_{w} \cdot \overline{c_{p,w}} \cdot (T_{w,\text{in}} - T_{w,\text{out}}) \tag{2}$$

$$\dot{Q}_{m} = \frac{\dot{Q}_{\text{air}} + \dot{Q}_{w}}{2} \tag{3}$$

The difference between both heat transfer rates is for all measurements smaller than 5%. The mean heat transfer rate $\dot{Q}_m$ (Eq. (3)) is used to determine the overall heat transfer coefficient U using the effectiveness-number of transfer units (NTU) method. The effectiveness ε is determined using Eq. (4), where $C_{\min}$ is the minimum of the water and air heat capacities ($\dot{m} \cdot c_p$). Because there is only one tube row, the water is considered mixed [31]. Also the air is assumed to be mixed, because the fins of neighboring tubes do not touch each other ($X_t > D_{\text{fin}}$), and thus, the fins do not form closed flow channels. Therefore, the NTU for the single row bundle is calculated using Eq. (5) (crossflow configuration—mixed/mixed arrangement) [31], where C^* is the heat capacity ratio. Table 5 gives the ranges of the calculated values of ε, C^*, and NTU. The overall heat transfer resistance $(\text{UA})^{-1}$ can then be determined using Eq. (6)

$$\varepsilon = \frac{\dot{Q}_m}{C_{\min} \cdot (T_{w,\text{in}} - T_{\text{air,in}})} \tag{4}$$

$$\varepsilon = \left(\frac{1}{1 - e^{-\text{NTU}}} + \frac{C^*}{1 - e^{-\text{NTU} \cdot C^*}} - \frac{1}{\text{NTU}} \right)^{-1} \tag{5}$$

Table 4 Uncertainties on the thermodynamic properties of water and air

	Water	Air
Dynamic viscosity μ (%)	1	2
Density ρ (%)	0.001	0.02–0.1
Specific heat capacity c_p (%)	0.1	2
Thermal conductivity k (%)	1.8	2

Table 5 Ranges of the effectiveness, heat capacity ratio, and number of transfer units

Quantity	Range
Effectiveness ε	0.074–0.287
Heat capacity ratio C^*	0.26–0.99
NTU	0.079–0.354

$$\frac{1}{\mathrm{UA}} = \frac{1}{C_{\min}\mathrm{NTU}} \tag{6}$$

As is clear from Eq. (7), the overall heat transfer resistance $(\mathrm{UA})^{-1}$ consists of convection and fouling on the air side, contact resistance between the fins and tube, conduction through the tube wall, and fouling and convection on the water side. The contact resistance of the tested heat exchanger is zero, because the fins are extruded out of the base tube. Clean air and filtered water are used during the experiments, resulting in negligible fouling. For the tested heat exchanger configuration, the thermal resistance on the water side contributes on average 15.08% to the overall heat transfer resistance, while the contributions of the thermal resistances of the tube material and the air side are 0.35% and 84.57%, respectively. Hence, the controlling heat transfer resistance is located on the air side. The Gnielinski correlation [32] was used to calculate the water side heat transfer coefficient h_{in}. In principle this correlation is applicable for transitional and turbulent tube flows ($\mathrm{Re}_w = v_w . d_{\mathrm{in}}/v_w > 2300$). However, Abraham et al. [33] found that the Gnielinski correlation is only supported by experimental data in the range of $\mathrm{Re}_w > 4800$ and should not be used below that value. In the current study the Gnielinski correlation was applicable as Re_w varied between 5750 and 21,200 during the measurements. An uncertainty of ±10% on the calculated water side Nusselt number was taken into account in the uncertainty analysis

$$\frac{1}{\mathrm{UA}} = \frac{1}{\eta_{\mathrm{ext}} h_{\mathrm{ext}} A_{\mathrm{ext}}} + R_{f,\mathrm{ext}} + R_c + \frac{\ln\left(\frac{d_{\mathrm{ext}}}{d_{\mathrm{in}}}\right)}{2\pi\lambda_T L_T} + R_{f,\mathrm{in}} + \frac{1}{h_{\mathrm{in}} A_{\mathrm{in}}} \tag{7}$$

The surface efficiency η_{ext} was calculated from Eq. (8) using the fin efficiency η_{fin}. The fin efficiency η_{fin} of thin circular fins of uniform thickness is given by Eqs. (9) and (10). This equation can also be used to evaluate the fin efficiency of helical fins [31]. Since B involves evaluating six Bessel functions, approximations have been proposed using simpler expressions for hand calculations. The Schmidt approximation [34], which was used in this study, is listed in Eqs. (10)–(12). For $0.5 \leq D_{\mathrm{fin}}/d_{\mathrm{ext}} \leq 8$, the approximation is accurate within 1%. The tested fins do not have a perfectly uniform thickness due to the extruding process, but the fin efficiencies are very close to unity ($\eta_{\mathrm{fin}} \geq 0.97$). In this case, Rabas and Taborek [35] did not recommend any corrections to the Schmidt approximation to account for nonuniform thickness and nonuniformity of the heat transfer coefficients over the height of the fin. An uncertainty of 1% on the fin efficiency was taken into account in the error propagation

$$\eta_{\mathrm{ext}} = 1 - (1 - \eta_{\mathrm{fin}})\left(\frac{A_{\mathrm{fin}}}{A_{\mathrm{ext}}}\right) \tag{8}$$

$$\eta_{\mathrm{fin}} = \frac{4 \cdot d_{\mathrm{ext}} \cdot B}{m \cdot (D_{\mathrm{fin}}^2 - d_{\mathrm{ext}}^2)} \tag{9}$$

$$m = \sqrt{\frac{2 \cdot h_{\mathrm{ext}}}{t_{\mathrm{fin}} \cdot \lambda_{\mathrm{fin}}}} \tag{10}$$

$$\eta_{\mathrm{fin,Schmidt}} = \frac{\tanh(m \cdot l^*)}{m \cdot l^*} \tag{11}$$

Table 6 Variable relative uncertainties: minimum, maximum, and mean values

Symbol	Uncertainty range (%)	Average uncertainty (%)
$\dot{Q}_m$	3.27–8.30	4.48
ΔT_{air}	1.30–10.01	4.89
ΔT_w	4.14–8.92	6.11
ε	3.87–8.59	5.08
NTU	4.37–9.24	5.72
A_{in}	1.95	-
A_{fin}	2.47	-
A_{ext}	2.27	-
A_c	1.10–2.86	1.83
$(\mathrm{UA})^{-1}$	4.81–9.45	6.15
η_u	1.01–1.44	1.20
Re_w	4.88	-
Nu_w	10	-
Re_c	3.13–4.10	3.50
$\mathrm{Nu}_{\mathrm{air}}$	7.38–11.52	8.42
f	4.58–17.26	5.83
j_c	8.14–11.99	9.20

$$l^* = \left(\frac{D_{\mathrm{fin}}}{2} - \frac{d_{\mathrm{ext}}}{2}\right)\left(1 + \frac{t_{\mathrm{fin}}}{D_{\mathrm{fin}} - d_{\mathrm{ext}}}\right)\left(1 + 0.35 \cdot \ln\left(\frac{D_{\mathrm{fin}}}{d_{\mathrm{ext}}}\right)\right) \tag{12}$$

The air side convection coefficient h_{ext} was then determined from Eq. (7). Because the fin efficiency is dependent on the external convection coefficient (Eq. (10)), it resulted from iterative calculations. The dimensionless air side convection coefficient is represented using the Nusselt number (Eq. (13))

$$\mathrm{Nu} = \frac{h_{\mathrm{ext}} \cdot d_{\mathrm{ext}}}{\lambda_{\mathrm{air}}} \tag{13}$$

The friction factor is calculated as proposed by Kays and London [36], using Eq. (14)

$$f = \frac{A_c}{A_{\mathrm{ext}}} \cdot \frac{\rho_{\mathrm{air,in}}}{\rho_{\mathrm{air},m}} \cdot \left[\frac{2\Delta p \cdot \rho_{\mathrm{air,in}}}{G_c^2} - (1 - \sigma^2)\left(\frac{\rho_{\mathrm{air,in}}}{\rho_{\mathrm{air,out}}} - 1\right)\right] \tag{14}$$

Because the pressure measurements were performed under isothermal conditions, Eq. (14) reduces to Eq. (15)

$$f = \frac{A_c}{A_{\mathrm{ext}}}\left[\frac{2\Delta p \cdot \rho_{\mathrm{air,in}}}{G_c^2}\right] \tag{15}$$

5 Results and Discussion

5.1 Uncertainties of Calculations. As stated above, an uncertainty analysis was performed using the procedures found in Ref. [27]. Table 6 presents the minimum, maximum, and average relative uncertainty for most of the calculated variables. The average relative uncertainty is 8.42% on the air side Nusselt number and 5.83% on the air side friction factor.

5.2 Air Side Heat Transfer. A decrease in X_t results in an increase in the Nusselt number because of the higher local velocities in the minimum cross-sectional area [14,24]. This is also seen in our measurement data. To take the effect of X_t into account, Sparrow and Samie [24] suggested correlating the Nusselt number results by using the minimum-area Reynolds number Re_c (Eq. (16)). Figure 4 shows the experimental data as function of Re_c parameterized by the dimensionless transversal tube pitch X_t/d_{ext}

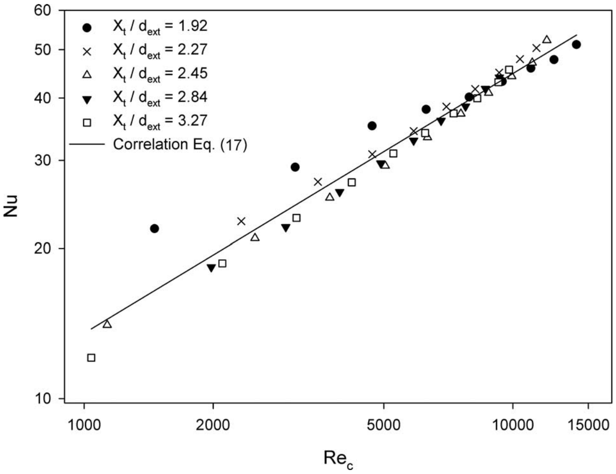

Fig. 4 Experimental data and Nu correlation independent of X_t/d_{ext} (Eq. (17)) plotted versus the minimum-area Reynolds number Re_c

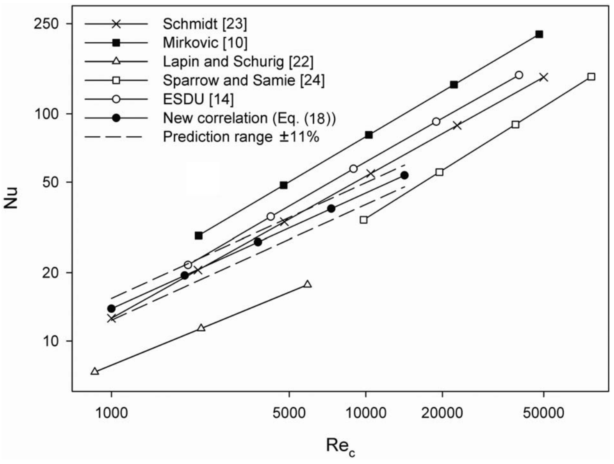

Fig. 6 Comparison of Eq. (18) with heat transfer characteristics from open literature

$$\text{Re}_c = \frac{\rho v_c d_{\text{ext}}}{\mu} \tag{16}$$

A correlation independent of the transversal tube pitch is determined via a least-mean-squares fit

$$\text{Nu} = 0.372\text{Re}_c^{0.520} \tag{17}$$

This correlation, also plotted in Fig. 4, is able to predict 95% of the experimental data within ±15% with a mean deviation of 4.87%.[1] The prediction capability of the correlation is poorer for small values of Re and X_t. To obtain a better match with the experimental data, a dimensionless group dependent on the transversal tube pitch X_t is added to the correlation in addition to using the minimum-area Reynolds number Re_c. The regression analysis resulted in

$$\text{Nu} = 0.495\text{Re}_c^{0.509}\left(\frac{X_t}{d_{\text{ext}}}\right)^{-0.209} \tag{18}$$

Figure 5 compares Eq. (18) with the experimental data. The proposed heat transfer correlation can describe 95% of the data within ±11% and shows a 4.49% mean deviation.

Figure 6 compares the new correlation with correlations for a single row heat exchanger with annular finned tubes found in literature. Table 7 shows the data ranges for which the different correlations are valid. Data from open literature were recalculated to Reynolds numbers based on the external tube diameter and the air velocity at the minimal cross-sectional area (Eq. (16)). The Nusselt numbers are evaluated for the heat exchanger geometry in Table 8. The transversal tube pitch is set to the value of Lapin and Schurig's tests [22]. Mirkovic [10] and the ESDU [14] predicted the highest Nusselt numbers. However, these are multiple tube row correlations, which are corrected with a constant factor to apply them on a single row heat exchanger. The correction factor applied on the Mirkovic correlation is 0.71 [10]. The ESDU recommended a correction factor equal to 1 for forced draught air-cooled heat exchangers [14]. Figure 6 shows that correcting multiple row correlations for single row arrays does not result in reliable predictions. Moreover, Eckels and Rabas [16] showed that the influence of the number of rows on the heat transfer in finned tube bundles depends on the Reynolds number, a point which is

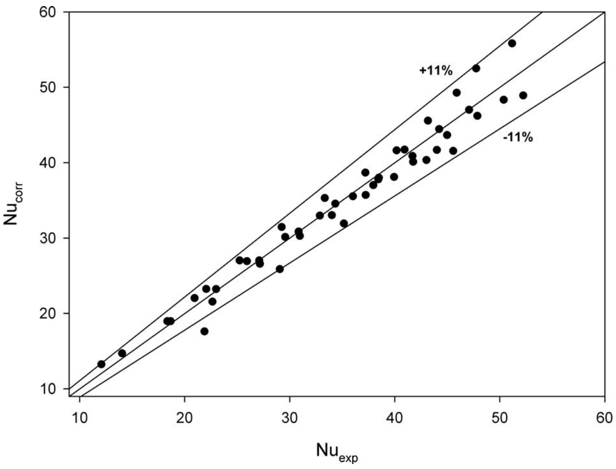

Fig. 5 Comparison of the heat transfer correlation (Eq. (18)) with the experimental data

Table 7 Application ranges of heat transfer correlations from open literature

Authors	Re_c	d_{ext} (mm)	X_t/d_{ext}	$D_{\text{fin}}/d_{\text{ext}}$	s/d_{ext}
Mirkovic [10]	2200–48,000	25.4–50.8	1.969–4.724	1.375–1.75	0.053–0.142
ESDU [14]	2000–40,000	9.5–51	$1.15 < X_t/X_l < 1.72$	1.220–4.474	0.014–0.990
Lapin and Schurig [22]	960–4800	15.875	2.4	2.4	0.1712
Schmidt [23]	1000–50,000	9.7–27.9	1.72–3.83	1.8–2.6	0.07–0.36
Sparrow and Samie [24]	9800–77,000	31.75	1.926–6.408	1.8	0.1
New correlation (Eq. (18))	1000–14,100	13	1.92–3.27	1.91	0.135

---

[1] Mean deviation $= (1/M)(\Sigma_1^M(|\text{Nu}_{\text{corr}} - \text{Nu}_{\text{exp}}|/\text{Nu}_{\text{exp}}))100\%$.

Table 8 Heat exchanger geometry used for comparison with literature correlations

d_{ext} (mm)	13
$D_{\mathrm{fin}}/d_{\mathrm{ext}}$	1.91
$t_{\mathrm{fin}}/d_{\mathrm{ext}}$	0.05
s/d_{ext}	0.135
X_t/d_{ext}	2.4
X_l/d_{ext}	1.91

not considered in the correction diagram of Mirkovic [10] and by the ESDU [14]. It should be noted that the use of data for multiple rows' heat exchangers and a comparison with data for a single row are always speculative. The geometry listed in Table 8 is within the application range of Schmidt [23]. Schmidt presented a Nusselt correlation for one tube row of a multirow tube bundle. The increase in flow turbulence in a tube bank at higher Reynolds numbers leads to an increase in heat transfer of the inner tubes, as compared with the first row [37]. Thus, for high Reynolds numbers, the average Nusselt number of one tube row in a multirow bundle is higher than the Nusselt number of a single row heat exchanger. This corresponds with our findings in Fig. 6: For higher Reynolds numbers, Schmidt's correlation lies above our Eq. (18). The correlations of Lapin and Schurig [22] and Sparrow and Samie [24] are correlations for single row heat exchangers. The slope of Eq. (18) (i.e., the exponent of Re_c) agrees well with the slope of the correlation of Lapin and Schurig [22]. However, their correlation underestimates our result (Eq. (18)). A possible explanation is that their tests are performed on a heat exchanger with larger fin spacing. The correlation of Sparrow and Samie [24] is only applicable for higher Reynolds numbers (which were not reached in our tests because of fan restrictions).

5.3 Air Side Pressure Drop. The friction factors, calculated according to Eq. (15), are presented in Fig. 7. They are plotted as function of Re_c for the different values of the transversal tube pitch. Unlike the heat transfer data, the use of the minimum-area velocity does not bring the pressure drop data together (compare Fig. 7 with Fig. 4). This is due to the vena contracta effect: The geometrically minimum free flow area is not the actual minimum free flow area [24]. For a given X_t, the friction factor decreases with increasing Reynolds number. For a fixed Re_c, the pressure drop across the heat exchanger increases with decreasing transversal tube pitch (i.e., increasing blockage). This is in accordance with the results of most authors [5,8,9,12,14,24]. The finding of Mirkovic [10]—the pressure drop increases with the transversal tube pitch—should be questioned.

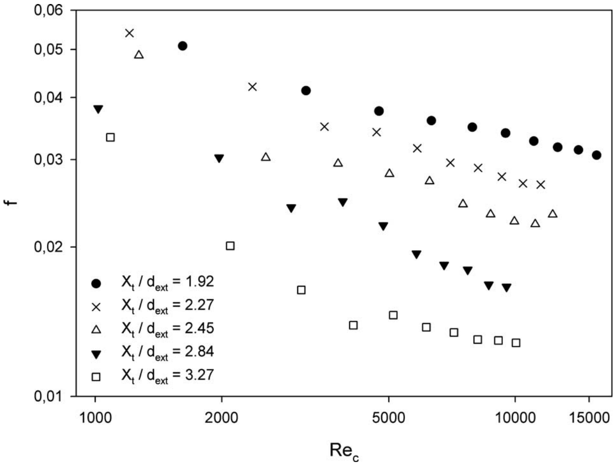

Fig. 7 Experimental friction factors plotted versus the minimum-area Reynolds number Re_c for different transversal tube pitches

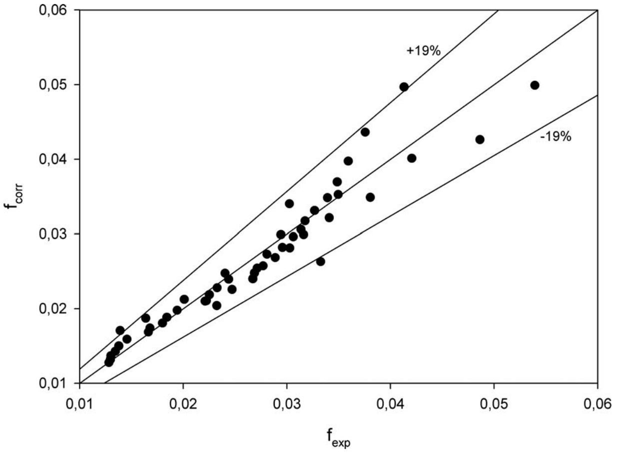

Fig. 8 Comparison of the friction correlation (Eq. (19)) with the experimental data

These experimental data were correlated via a least-mean-squares fit, resulting in

$$f = 2.271\mathrm{Re}_c^{-0.325}\left(\frac{X_t}{d_{\mathrm{ext}}}\right)^{-1.849} \tag{19}$$

Figure 8 compares Eq. (19) with the experimental data. This friction correlation predicts 95% of the data within ±19% and gives a mean deviation of 6.84%.

Figure 9 compares the new friction characteristic with correlations from literature. Their application ranges are listed in Table 9. Data from open literature were recalculated to friction factors, as defined by Eq. (15), and Reynolds numbers based on the external tube diameter and the air velocity at the minimal cross-sectional area (Eq. (16)). The correlations are plotted for the heat exchanger geometry in Table 8. Jameson and Schenectady [5] reported data to calculate the friction factors of a single row heat exchanger. The higher values compared with the results of this paper are probably due to the fact that their correlation is not applicable to the heat exchanger geometry in Table 8. Their general expression, which correlates the data for all the tube sizes and arrangements tested (ranging from one to eight tube rows), shows better agree-

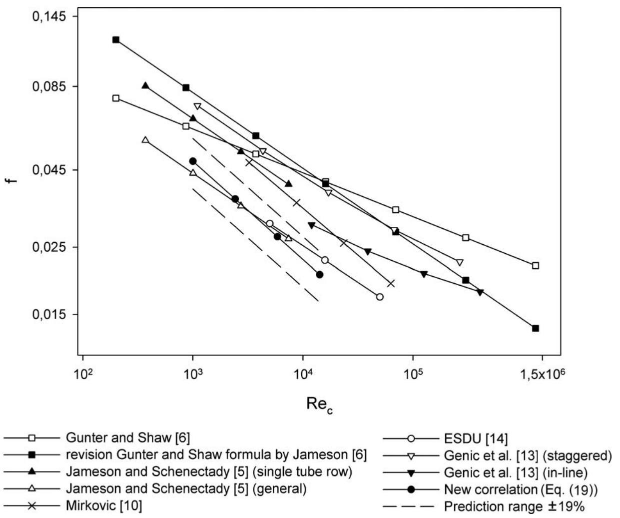

Fig. 9 Comparison of Eq. (19) with friction characteristics from open literature

Table 9 Application ranges of friction correlations from open literature

Authors	Re_c	d_{ext} (mm)	X_t/d_{ext}	$D_{\mathrm{fin}}/d_{\mathrm{ext}}$	s/d_{ext}
Gunter and Shaw [6]	200–1,300,000	25.4	1.313	1.5	0.113
Jameson [6]	200–1,300,000	15.875–25.4	1.959–3.633	1.737–1.951	0.102–0.213
Jameson and Schenectady [5] (single tube row)	370–7400	15.875	1.971	1.794	0.168
Jameson and Schenectady [5] (general correlation)	370–7400	15.875–25.4	1.959–3.633	1.737–1.951	0.102–0.213
Mirkovic [10]	3250–63,000	25.4–50.8	1.969–4.724	1.375–1.75	0.053–0.142
ESDU [14]	5000–50,000	9.5–51	1.85–4.75	1.220–4.474	0.014–0.990
Genic et al. [13] Staggered	1100–265,000	9.65–32	0.952–3.5	0.841–4.572	0.068–0.350
Inline	12,000–406,000	32	2–4	1.563	0.147
New correlation (Eq. (19))	1000–14,100	13	1.92–3.27	1.91	0.135

ment. The Gunter–Shaw relationship [6] predicts friction values which are much too high. This was also observed by other authors [1,6–8]. The slope differs from most other correlations and shows similarity with the in-line configuration of Genic et al. [13]. In the discussion accompanying their article, Jameson suggested a revised version of the Gunter–Shaw equation [6]. The slope shows better agreement with our results, but the friction factors are still overestimated. Mirkovic [10] and the ESDU [14] presented a per row pressure drop correlation for staggered, multirow arrays. Mirkovic's correlation [10] is based on heat exchangers with large tube diameters. This may explain the higher friction values. The ESDU [14] suggested a correction factor of 0.8 for a single row bundle, which results in a better match with the correlation developed in this study. Genic et al. [13] considered staggered and in-line multiple row tube bundles. They advised the correction factors of Brauer [17–19], Yudin [20], and Weierman [21] for a heat exchanger with one tube row. In Fig. 9 the correction factors of Yudin [20] are used to evaluate the correlations of Genic et al. (1.325 for the staggered layout; 2.4 for the in-line layout) [13]. Similar to the heat transfer results, correcting multirow pressure drop expressions for a single row heat exchanger does not lead to accurate predictions.

6 Conclusions

In this study the heat transfer and friction characteristic of a single row heat exchanger with helically finned tubes were determined. The transversal tube pitch was parametrically varied. A thorough error analysis was performed to validate the results. The measurements show that a decrease in transversal tube pitch results in larger heat transfer coefficients (due to higher velocities in the minimum cross-sectional area) and larger pressure drops (due to increasing blockage). The Nusselt numbers and friction factors are correlated using the minimum-area Reynolds numbers. The heat transfer correlation can describe 95% of the data within ±11% and shows a 4.49% mean deviation. The friction correlation predicts 95% of the data within ±19% and gives a mean deviation of 6.84%. Both equations depend on the transversal tube pitch ratio. The correlations were compared with correlations from open literature. Experimental data on single row heat exchangers are rare. It is illustrated that correcting multirow expressions does not lead to reliable predictions. In general, the new correlations show the same trend as most literature correlations, but none of the literature correlations are able to accurately predict the results of this study.

Acknowledgment

The authors would like to express gratitude for the financial support provided by the Flemish Research Foundation (FWO Vlaanderen) and the BOF fund of Ghent University (Contract No. B/05864/01 IV 1).

Nomenclature

A_c = minimum free flow area (m^2)
A_{fin} = fin surface area (m^2)
A_{front} = frontal area of the heat exchanger (m^2)
C = heat capacity rate, ($=\dot{m}\cdot c_p$) (W/K)
C^* = heat capacity ratio, ($=C_{\min}/C_{\max}$)
$\overline{c_p}$ = specific heat capacity at average temperature (J/kg K)
d = tube diameter (m)
D_{fin} = fin diameter (m)
f = friction factor
F_p = fin pitch (m)
G_c = mass flux of air based on minimum flow area (kg/m^2 s)
h = convective heat transfer coefficient (W/m^2 K)
J = Colburn j-factor
$\dot{m}$ = mass flow rate (kg/s)
Nu = Nusselt number
Δp = pressure drop (Pa)
$\dot{Q}$ = heat transfer rate (W)
R_c = Contact resistance (K/W)
R_f = Fouling resistance (K/W)
Re_c = Reynolds number based on the velocity in the minimum cross section
s = fin spacing (m)
T = temperature (K)
t_{fin} = fin thickness (m)
$(\mathrm{UA})^{-1}$ = overall heat transfer resistance (K/W)
v_c = air velocity evaluated at the minimum cross section (m/s)
v_∞ = air velocity evaluated at the inlet of the test section (m/s)
X_l = longitudinal tube pitch (m)
X_t = transversal tube pitch [m]

Greek Symbols

ε = heat exchanger effectiveness, ($=\dot{Q}/\dot{Q}_{\max}$)
η_{ext} = surface efficiency
η_{fin} = fin efficiency
λ = thermal conductivity (W/m K)
μ = dynamic viscosity (Pa s)
ρ = density (kg/m^3)
σ = contraction ratio of the cross-sectional area, ($=A_c/A_{\mathrm{front}}$)

Subscripts

corr = correlation
exp = experimental
ext = exterior (air side)

in = interior (water side)
T = tube
w = water

References

[1] Webb, R. L., 1980, “Air-Side Heat Transfer in Finned Tube Heat Exchangers,” Heat Transfer Eng., **1**(3), pp. 33–49.

[2] Kreith, F., 2000, *The CRC Handbook of Thermal Engineering*, CRC, Boca Raton, FL.

[3] Kuppan, T., 2000, *Heat Exchanger Design Handbook*, Marcel Dekker, Inc., New York.

[4] Kim, C. N., Jeong, J., and Youn, B., 2003, “Evaluation of Thermal Contact Conductance Using a New Experimental-Numerical Method in Fin-Tube Heat Exchangers,” Int. J. Refrig., **26**(8), pp. 900–908.

[5] Jameson, S. L., 1945, “Tube Spacing in Finned-Tube Banks,” Trans. ASME, **67**, pp. 633–642.

[6] Gunter, A. Y., and Shaw, W. A., 1945, “A General Correlation of Friction Factors for Various Types of Surfaces in Crossflow,” Trans. ASME, **67**, pp. 643–660.

[7] Ward, D. J., and Young, E. H., 1963, “Heat Transfer and Pressure Drop of Air in Forced Convection Across Triangular Pitch Banks of Finned Tubes,” Chem. Eng. Prog., Symp. Ser., **59**(41), pp. 37–44.

[8] Robinson, K. K., and Briggs, D. E., 1966, “Pressure Drop of Air Flowing Across Triangular Pitch Banks of Finned Tubes,” Chem. Eng. Prog., Symp. Ser., **62**(64), pp. 177–184.

[9] Briggs, D. E., and Young, E. H., 1963, “Convection Heat Transfer and Pressure Drop of Air Flowing Across Triangular Pitch Banks of Finned Tubes,” Chem. Eng. Prog., Symp. Ser., **59**(41), pp. 1–10.

[10] Mirkovic, Z., 1974, “Heat Transfer and Flow Resistance Correlation for Helically Finned and Staggered Tube Banks in Crossflow,” *Heat Exchangers: Design and Theory Source Book*, N. H. Afgan and E. U. Schlunder, eds., Hemisphere, Washington, DC, pp. 559–584.

[11] Nir, A., 1991, “Heat Transfer and Friction Factor Correlations for Crossflow Over Staggered Finned Tube Banks,” Heat Transfer Eng., **12**(1), pp. 43–58.

[12] Krupiczka, R., Rotkegel, A., Walczyk, H., and Dobner, L., 2003, “An Experimental Study of Convective Heat Transfer From Extruded Type Helical Finned Tubes,” Chem. Eng. Process., **42**, pp. 29–38.

[13] Genic, S. B., Jacimovic, B. M., and Latinovic, B. R., 2006, “Research on Air Pressure Drop in Helically-Finned Tube Heat Exchangers,” Appl. Therm. Eng., **26**, pp. 478–485.

[14] 1986, “High-Fin Staggered Tube Banks: Heat Transfer and Pressure Drop for Turbulent Single Phase Gas Flow,” ESDU Paper No. 86022.

[15] Huber, F. V., and Rabas, T. J., 1985, “The Effect of Geometry on the Heat Transfer Row Correction for Typical Finned Tube Bundles,” AIChE National Heat Transfer Conference, Denver, CO.

[16] Eckels, P. W., and Rabas, T. J., 1985, “Heat Transfer and Pressure Drop of Typical Air Cooler Finned Tubes,” ASME J. Heat Transfer, **107**, pp. 198–204.

[17] Brauer, H., 1961, “Wärme- und Strömungstechnische Untersuchungen an Quer Angeströmten Rippenrohrbündeln, Teil 1: Versuchsanlagen und Meßergebnisse bei Höheren Drücken,” Chem.- Ing.- Tech., **33**, pp.327–335.

[18] Brauer, H., 1961, “Wärme- und Strömungstechnische Untersuchungen an Quer Angeströmten Rippenrohrbündeln, Teil 2: Einfluß der Rippen- und der Rohranordnung,” Chem.- Ing.- Tech., **33**, pp. 431–438.

[19] Brauer, H., 1962, *Wärmeubertragung und Strömungswiderstand bei Fluchtend und Versetztargeordneten Rippenrohren*, Dechema Monograpic, Vol. 40.

[20] Yudin, V. F., 1982, *Teploobmen Poperechno Orebrennykh Trub*, Mashinostroenie, Leningrad.

[21] Weierman, C., 1977, “Pressure Drop Data for Heavy-Duty Finned Tubes,” Chem. Eng. Prog., **73**(2), pp. 69–72.

[22] Lapin, A., and Schurig, F., 1959, “Heat Transfer Coefficients for Finned Exchangers,” Ind. Eng. Chem., **51**(8), pp. 941–944.

[23] Schmidt, E., 1963, “Der Wärmeübergang an Rippenrohren und die Berechnung von Rohrbündel-Wärmeaustauschern,” Kältetechnik, **15**(12), pp. 370–378.

[24] Sparrow, E. M., and Samie, F., 1985, “Heat Transfer and Pressure Drop Results for One- and Two-Row Arrays of Finned Tubes,” Int. J. Heat Mass Transfer, **28**(12), pp. 2247–2259.

[25] T’Joen, C., Steeman, H. J., Willockx, A., and De Paepe, M., 2006, “Determination of Heat Transfer and Friction Characteristics of an Adapted Inclined Louvered Fin,” Exp. Therm. Fluid Sci., **30**, pp. 319–327.

[26] T’Joen, C., Willockx, A., Steeman, H. J., and De Paepe, M., 2007, “Performance Prediction of Compact Fin-and-Tube Heat Exchangers in Maldistributed Airflow,” Heat Transfer Eng., **28**(12), pp. 986–996.

[27] Moffat, R. J., 1988, “Describing the Uncertainties in Experimental Results,” Exp. Therm. Fluid Sci., **1**, pp. 3–17.

[28] Kadoya, K., Matsunaga, N., and Nagashima, A., 1985, “Viscosity and Thermal-Conductivity of Dry Air in the Gaseous-Phase,” J. Phys. Chem. Ref. Data, **14**(4), pp. 947–970.

[29] 1996, “IAPWS Release on the IAPWS Formulation 1995 for the Thermodynamic Properties of Ordinary Water Substance for General and Scientific Use (IAPWS-95),” available at http://www.iapws.org.

[30] 2007, “Revised Release on the IAPWS Industrial Formulation 1997 for the Thermodynamic Properties of Water and Steam (IAPWS-IF97),” available at http://www.iapws.org.

[31] Shah, R. K., and Sekulic, D. P., 2003, *Fundamentals of Heat Exchanger Design*, Wiley, Hoboken, NJ.

[32] Gnielinski, V., 1976, “New Equations for Heat and Mass Transfer in Turbulent Tube and Channel Flow,” Int. Chem. Eng., **29**, pp. 359–368.

[33] Abraham, J. P., Sparrow, E. M., and Tong, J. C. K., 2009, “Heat Transfer in All Pipe Flow Regimes: Laminar, Transitional/Intermittent, and Turbulent,” Int. J. Heat Mass Transfer, **52**, pp. 557–563.

[34] Schmidt, T. E., 1949, “Heat Transfer Calculations for Extended Surfaces,” Refrig. Eng., April, pp. 351–357.

[35] Rabas, T. J., and Taborek, J., 1987, “Survey of Turbulent Forced Convection Heat Transfer and Pressure Drop Characteristics of Low Finned Tube Banks in Crossflow,” Heat Transfer Eng., **8**, pp. 49–62.

[36] Kays, W. M., and London, A. L., 1984, *Compact Heat Exchangers*, 3rd ed., McGraw-Hill, New York.

[37] Zukauskas, A., 1972, “Heat Transfer From Tubes in Crossflow,” Adv. Heat Transfer, **8**, pp. 93–160.

Melting of Phase Change Materials With Volume Change in Metal Foams

Zhen Yang

Suresh V. Garimella[1]
e-mail: sureshg@purdue.edu

Cooling Technologies Research Center,
School of Mechanical Engineering,
Purdue University,
West Lafayette, IN 47907-2088

Melting of phase change materials (PCMs) embedded in metal foams is investigated. The two-temperature model developed accounts for volume change in the PCM upon melting. Volume-averaged mass and momentum equations are solved, with the Brinkman–Forchheimer extension to Darcy's law employed to model the porous-medium resistance. Local thermal equilibrium does not hold due to the large difference in thermal diffusivity between the metal foam and the PCM. Therefore, a two-temperature approach is adopted, with the heat transfer between the metal foam and the PCM being coupled by means of an interstitial Nusselt number. The enthalpy method is applied to account for phase change. The governing equations are solved using a finite-volume approach. Effects of volume shrinkage/expansion are considered for different interstitial heat transfer rates between the foam and PCM. The detailed behavior of the melting region as a function of buoyancy-driven convection and interstitial Nusselt number is analyzed. For strong interstitial heat transfer, the melting region is significantly reduced in extent and the melting process is greatly enhanced as is heat transfer from the wall; the converse applies for weak interstitial heat transfer. The melting process at a low interstitial Nusselt number is significantly influenced by melt convection, while the behavior is dominated by conduction at high interstitial Nusselt numbers. Volume shrinkage/expansion due to phase change induces an added flow, which affects the PCM melting rate.
[DOI: 10.1115/1.4000747]

1 Introduction

Heat transfer associated with solid-liquid phase change is central to a wide range of applications such as thermal energy storage [1,2], transient thermal management of electronics cooling [3,4], freezing/thawing of biological tissues [5], and alloy solidification [6]. Solidification and melting of phase change materials (PCMs) including the effects of melt convection have been extensively investigated [7–11]. Phase change in materials embedded in porous structures is widely encountered in applications such as ice melting/solidification in soils and in biological tissues as well as thermal storage in PCMs enhanced with metal foams. Unlike in the case of phase change in a PCM alone, the existence of a porous matrix enhances heat transfer rates and may change the behavior of the melt front. The interstitial heat transfer between the porous matrix and the PCM is an important determinant of the phase change process in this case, but is not well understood. Assumption of thermal equilibrium between the porous matrix and PCM can greatly simplify the analysis, and under this assumption, a one-temperature model, which treats the matrix and PCM as a homogeneous mixture with averaged properties is sufficient to predict the heat transfer behavior. Beckermann and Viskanta [12] conducted an experimental and numerical investigation of phase change with gallium in a matrix of glass beads. Their numerical predictions of the solid-liquid interface shape and temperature distribution with a one-temperature model agreed reasonably well with the experimental results. However, if the thermal diffusivity of the porous matrix significantly exceeds that of PCM, the assumption of thermal equilibrium does not hold. Chellaiah and Viskanta [13,14] studied the melting of ice in two different situations, one with a bed of glass beads [13] and the other with a bed of aluminum beads [14]. The assumption of local thermal equilibrium in the numerical model yielded reasonable agreement with the experimental results for glass beads (low thermal diffusivity), but showed poor agreement for aluminum beads (high thermal diffusivity) at high Rayleigh numbers. The validity of assuming local thermal equilibrium in porous media saturated with a fluid has been discussed in a number of studies [15,16].

The introduction of a porous matrix can also change the behavior of the melt front. Ellinger and Beckermann [17] experimentally investigated the heat transfer enhancement in a rectangular domain partially filled by a porous layer of aluminum beads. The porous layer was found to cause the solid-liquid interface to move faster initially during the conduction-dominated regime, but the overall melting and heat transfer rates were lower due to the lower porosity and permeability. To improve the convective heat transfer, especially in natural convection with high Rayleigh numbers, it was suggested that high-porosity and high-permeability porous matrices such as metal foams should be used. Tong and Khan [18] numerically demonstrated the enhancement in heat transfer obtained during outward freezing of a low-thermal-conductivity PCM in a vertical annulus by employing a high-porosity metal matrix. Their results included the interface propagation rate, isotherms, streamlines, and heat transfer rates. Alawadhi and Amon [19] conducted numerical and experimental studies on the effectiveness of a thermal control unit composed of an organic PCM and a metal matrix. Their model used modified effective thermophysical properties and showed that the effective thermal conductivity of the unit was two orders higher than that with the PCM alone.

Metal foams used for heat transfer enhancement are characterized by thermal conductivities, which are two orders of magnitude higher than that of the PCM, which renders invalid the thermal equilibrium assumed between the porous matrix and the PCM. To describe transport in this system correctly, a two-temperature model is necessary. The two-temperature model treats the porous matrix and PCM as having different temperatures, and accounts for interstitial heat transfer between these two phases. Krishnan et al. [20] used a two-temperature model to study solid-liquid

---

[1] Corresponding author.

Contributed by the Heat Transfer Division of ASME for publication in the Journal of Heat Transfer. Manuscript received April 9, 2009; final manuscript received October 20, 2009; published online March 24, 2010. Assoc. Editor: W. Q. Tao.

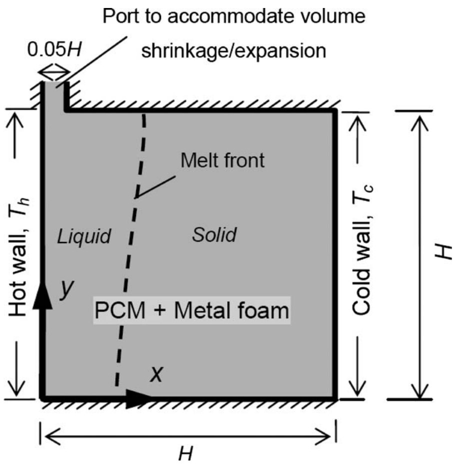

Fig. 1 Schematic illustration of the physical problem

phase change in metal foams. They considered the influence of Rayleigh number, Stefan number, and interstitial Nusselt number on the transport process, and found that while a one-temperature treatment is sufficient at interstitial Nusselt numbers greater than 5.9, the metal foam and PCM are sufficiently out of equilibrium for lower levels of interstitial heat transfer that a two-temperature model is necessary.

Although a number of researchers have investigated the characteristics of melting and solidification of PCM in porous media, many aspects need further attention, such as the effects of volume change in the PCM during phase change and the behavior of the melting region under different interstitial heat transfer rates. The objective of the present work is to investigate the heat transfer processes associated with melting of PCM embedded in a porous metal foam in a rectangular domain by employing a two-temperature model to account for the thermal nonequilibrium between the PCM and metal foam. The effects of volume change in the PCM during phase change as well as those of interstitial heat transfer rate on the heat transfer process (particularly in the melting region) are explored.

2 Mathematical Modeling

A schematic illustration of the physical problem is shown in Fig. 1. The height and width of the enclosure are both H. The hot left wall and the cold right wall of the domain experience constant-temperature thermal boundary conditions, while the other two walls are adiabatic. The temperature on the hot wall T_h is higher than the melting temperature of the PCM T_m, while that of the cold wall T_c is lower than T_m. The domain is filled with a PCM embedded in a metal foam matrix of porosity ε_0. A small port (of width 0.05H) at the top left of the domain, which is open to atmosphere, accommodates volume expansion/shrinkage of the PCM during melting. Initially, the PCM is in a solid state and its temperature, as well as that of the metal foam, is set to T_c. Once the left wall temperature is raised to T_h at time $t=0$, the temperature of the PCM near the hot wall rises and it begins to melt. The melt front propagates from left to right. The thermophysical properties of the PCM are assumed to be constant in the temperature range of interest. In its liquid state, the PCM is assumed to be an incompressible, Newtonian liquid. Due to the low thermal expansion of the liquid phase, the effect of buoyancy can be adequately modeled using the Boussinesq approximation. Thermal dispersion effects are ignored due to the lack of available models for metal foams, although it may be important for very high Rayleigh numbers [21]. The volume-averaged governing continuity and momentum equations for the liquid phase are

$$\rho_l \frac{\partial u_i}{\partial x_i} = (\rho_s - \rho_l)\frac{\partial \varepsilon}{\partial t} \tag{1}$$

$$\begin{aligned}\rho_l \frac{\partial (u_i)}{\partial t} + \rho_l \frac{\partial}{\partial x_j}\left(\frac{u_j u_i}{\varepsilon}\right) = \Bigg[&-\varepsilon \frac{\partial p}{\partial x_i} + \mu \frac{\partial^2 u_i}{\partial x_j\, \partial x_j} + \frac{\mu}{3}\frac{\rho_s - \rho_l}{\rho_l}\frac{\partial}{\partial x_i}\left(\frac{\partial \varepsilon}{\partial t}\right) \\ &+ \varepsilon \rho_l \beta (T - T_{\mathrm{melt}}) g \delta(i,2) - \varepsilon \Bigg(\frac{\mu}{K} u_i \\ &+ \frac{F}{\sqrt{K}} \rho u_{\mathrm{mag}} u_i\Bigg)\Bigg]\end{aligned} \tag{2}$$

where u is the superficial velocity, and ε the local porosity for the liquid phase, which changes from 0 (completely solid) to ε_0 (completely liquid) as the PCM melts. The difference in densities of the liquid and solid phases of the PCM is accounted for in these equations, unlike the assumption of no density difference in the formulation in Ref. [20]. If there were no volume change during the melting of the PCM $\rho_s = \rho_l$, then the right hand side of Eq. (1) and the third term on the right hand side of Eq. (2) reduce to zero.

The governing energy equation for the PCM (including the liquid and solid phases) is

$$\begin{aligned}\frac{\partial}{\partial t}[(\varepsilon \rho_l Cp_l + \varepsilon_s \rho_s Cp_s) T_1] + \frac{\partial}{\partial x_i}(\rho_l u_i Cp_l T_1) = \frac{\partial}{\partial x_i}\left(k_{e,\mathrm{PCM}} \frac{\partial T_1}{\partial x_i}\right) \\ - \frac{\rho_s u_i u_i}{2}\frac{\partial (1/\varepsilon)}{\partial t} - p \frac{\rho_s - \rho_l}{\rho_l}\frac{\partial \varepsilon}{\partial t} + 2\mu \Bigg[S_{ij} S'_{ij} \\ - \frac{1}{3}\left(\frac{\rho_s - \rho_l}{\rho_l}\right)\frac{\partial \varepsilon}{\partial t}\frac{\partial (u_k/\varepsilon)}{\partial x_k}\Bigg] - \rho_s h_L \frac{\partial \varepsilon}{\partial t} + h_i (T_2 - T_1)\end{aligned} \tag{3}$$

where

$$S_{ij} = \frac{1}{2}\left(\frac{\partial u_i}{\partial x_j} + \frac{\partial u_j}{\partial x_i}\right)$$

and

$$S'_{ij} = \frac{1}{2}\left(\frac{\partial (u_i/\varepsilon)}{\partial x_j} + \frac{\partial (u_j/\varepsilon)}{\partial x_i}\right)$$

and the corresponding energy equation for the metal foam is

$$\frac{\partial}{\partial t}[(1 - \varepsilon_0)\rho_m Cp_m T_2] = \frac{\partial}{\partial x_i}\left(k_{e,\mathrm{MF}} \frac{\partial T_2}{\partial x_i}\right) - h_i (T_2 - T_1) \tag{4}$$

where $k_{e,\mathrm{PCM}}$ and $k_{e,\mathrm{MF}}$ are the effective thermal conductivities of the PCM and metal foam, respectively. According to Ref. [22], the effective thermal conductivity k_e of a metal foam filled with a second material such as a PCM can be expressed as

$$k_e = A[\varepsilon_0 \times k_l + (1 - \varepsilon_0) k_m] + \frac{1 - A}{\varepsilon_0/k_l + (1 - \varepsilon_0)/k_m}$$

where k_l is the PCM thermal conductivity assumed to be identical in the liquid and solid phases, k_m is the thermal conductivity of the metal foam, and $A=0.35$, as found from a curve fit to experiments in Ref. [22]. Assuming $k_m=0$ in the above equation, the effective thermal conductivity of the embedded PCM alone is estimated as

$$k_{e,\mathrm{PCM}} = A \times \varepsilon_0 \times k_l$$

And similarly, the effective thermal conductivity for the metal foam alone is obtained by assuming $k_l=0$ as

$$k_{e,\mathrm{MF}} = A \times (1 - \varepsilon_0) \times k_m$$

Introducing the following nondimensional variables

$$X=\frac{x}{H},\quad Y=\frac{y}{H},\quad \tau=\frac{t\nu}{H^2},\quad U_i=\frac{u_iH}{\nu},\quad P=\frac{pH^2}{\rho_l\nu^2},\quad \theta_1=\frac{T_1-T_c}{T_h-T_c},\quad \theta_2=\frac{T_2-T_c}{T_h-T_c},\quad f_\rho=\frac{\rho_s}{\rho_l},\quad f_{Cp}=\frac{Cp_s}{Cp_l},\quad f_{k,\mathrm{PCM}}=\frac{k_{e,\mathrm{PCM}}}{k_l},\quad f_{k,\mathrm{MF}}=\frac{k_{e,\mathrm{MF}}}{k_l},\quad f_k=\frac{k_m}{k_l},\quad \Omega=\frac{\rho_mCp_m}{\rho_lCp_l},\quad \mathrm{Pr}=\frac{\nu}{\alpha_l},\quad \mathrm{Ra}=\frac{\beta gH^3(T_h-T_c)}{\alpha\nu},\quad \mathrm{Da}=\frac{\sqrt{K}}{H},\quad \mathrm{Ste}=\frac{Cp_l(T_h-T_C)}{h_L},\quad \mathrm{Nu}_i=\frac{h_iH^2}{k_l},\quad Rh=\frac{\nu^2}{h_LH^2},\quad \Phi=\frac{d_p}{H}$$

we obtain the nondimensional forms of the governing equations as follows:

(a) continuity equation

$$\frac{\partial U_i}{\partial X_i}=(f_\rho-1)\frac{\partial\varepsilon}{\partial\tau} \tag{5}$$

(b) momentum equation for the liquid PCM

$$\frac{\partial U_i}{\partial\tau}+\frac{\partial}{\partial X_j}\left(\frac{U_jU_i}{\varepsilon}\right)=\left[-\varepsilon\frac{\partial P}{\partial X_i}+\frac{\partial^2U_i}{\partial X_j\,\partial X_j}+\frac{1}{3}(f_\rho-1)\frac{\partial}{\partial X_i}\left(\frac{\partial\varepsilon}{\partial\tau}\right)+\frac{\mathrm{Ra}}{\mathrm{Pr}}\varepsilon(\theta-\theta_{\mathrm{melt}})\delta(i,2)-\varepsilon\left(\frac{1}{\mathrm{Da}^2}U_i+\frac{F}{\mathrm{Da}}U_{\mathrm{mag}}U_i\right)\right] \tag{6}$$

(c) energy equation for the PCM (both liquid and solid)

$$\mathrm{Pr}\frac{\partial}{\partial\tau}[(\varepsilon+(\varepsilon_0-\varepsilon)f_\rho f_{Cp})(\theta_1-\theta_m)]+\mathrm{Pr}\frac{\partial}{\partial X_i}[U_i(\theta_1-\theta_m)]=\frac{\partial}{\partial X_i}\left(f_{k,\mathrm{PCM}}\frac{\partial\theta_1}{\partial X_i}\right)-\frac{\mathrm{Pr}\times f_\rho}{\mathrm{Ste}}\frac{\partial\varepsilon}{\partial\tau}+\frac{\mathrm{Nu}_i}{\Phi^2}(\theta_2-\theta_1)+\frac{\mathrm{Pr}\times Rh}{\mathrm{Ste}}\left[2\hat{S}_{ij}\hat{S}'_{ij}-\frac{2}{3}(f_\rho-1)\frac{\partial\varepsilon}{\partial\tau}\mathrm{tr}(\hat{S}'_{ii})-P(f_\rho-1)\frac{\partial\varepsilon}{\partial\tau}-f_\rho\frac{U_iU_i}{2}\frac{\partial(1/\varepsilon)}{\partial\tau}\right] \tag{7}$$

(d) energy equation for metal foam

$$\mathrm{Pr}\frac{\partial}{\partial\tau}[(1-\varepsilon_0)\Omega(\theta_2-\theta_{\mathrm{melt}})]=\frac{\partial}{\partial X_i}\left(f_{k,\mathrm{MF}}\frac{\partial\theta_2}{\partial X_i}\right)-\frac{\mathrm{Nu}_i}{\Phi^2}(\theta_2-\theta_1) \tag{8}$$

Equations (5)–(8) are applicable to phase change processes in a general porous medium. The Darcy number Da and inertial coefficient F, which reflect the effect of the structural properties of the porous medium on fluid dynamics, can be adjusted to represent specific porous structures.

The porosity ε in Eqs. (5)–(7) is related to the temperature θ_1 as follows:

$$\varepsilon=\begin{cases}\varepsilon_0 & \text{for } \theta_1>\theta_m+\Delta\theta\\ \varepsilon_0\left(\dfrac{\theta_1-\theta_m}{2\Delta\theta}+\dfrac{1}{2}\right) & \text{for } \theta_m-\Delta\theta<\theta_1<\theta_m+\Delta\theta\\ 0 & \text{for } \theta_1<\theta_m-\Delta\theta\end{cases} \tag{9}$$

where $\Delta\theta$ is a small number less than 0.01 to ensure numerical stability. The melting rate $\partial\varepsilon/\partial\tau$ in the second term on the right hand side of Eq. (7) is then determined by

$$\frac{\partial\varepsilon}{\partial\tau}=\frac{\varepsilon^{(n)}-\varepsilon^{(n-1)}}{\Delta\tau} \tag{10}$$

where $\varepsilon^{(n)}$ and $\varepsilon^{(n-1)}$ are the porosity at the current and previous time steps, respectively; and $\Delta\tau$ is the time step.

A zero velocity boundary conditions, i.e., $U_i=0$, is employed on all the walls of the enclosure. The temperatures on the hot left wall and the cold right wall are, respectively, $\theta_1=\theta_2=1$ and $\theta_1=\theta_2=0$. The port is open to atmosphere, with gauge pressure $P=0$ and temperature $\theta_1=\theta_2=1$.

The computational domain is discretized into finite volumes. Values at the centers of the square cells are stored for all the variables. A second-order upwind scheme is used for the convective fluxes, while a central-differencing scheme is used for discretizing the diffusion fluxes. A second-order implicit scheme is used for time discretization of the time-derivative terms in Eqs. (5)–(8); the exception is that a first-order scheme is adopted for ε, as shown in Eq. (10). Pressure-velocity coupling is implemented through the PISO algorithm [23]. Iterations at each time step are terminated when the dimensionless residuals for all equations drop below 10^{-4}. The computations are performed using the commercial software FLUENT 6.1 [24]. User-defined functions (UDFs) are developed to account for Eqs. (7) and (8) as well as for the terms containing ε in Eqs. (5) and (6). Dependence of the results on the grid and time step was assessed. Computations with $\Delta X=\Delta Y=0.01$ and $\Delta\tau=1.25\times10^{-5}$ were compared with those with $\Delta X=\Delta Y=0.005$ and $\Delta\tau=6.16\times10^{-6}$; along the line $Y=0.5$ throughout the whole melting process, the temperature with the former conditions was 1% lower than for the latter conditions, indicating a weak dependence on the grid size and time step. The former grid and time step were hence chosen for the remaining computations in this work.

3 Model Validation

The analysis methodology developed above is first validated against available numerical and experimental studies in the literature. Since experimental results on phase change in metal foams that are suitable for validation are scarce, the melting of gallium in a packed bed of glass spheres [12], for which detailed temperature and interface profiles have been reported, is used instead for validation of the current numerical model. The computational domain is the same, as that shown in Fig. 1. The height of the square enclosure containing the gallium and glass beads is 4.76 cm, with the porosity of the enclosure being 0.385. The temperatures on the hot and cold walls are 45°C and 20°C, respectively, while the other walls are maintained adiabatic. The dimensionless governing parameters used for validation against this case are $\mathrm{Ra}=8.41\times10^5$, $\mathrm{Ste}=0.124$, $\mathrm{Pr}=0.0208$, $\mathrm{Da}=3.7\times10^{-3}$, $\Phi=0.126$, $\lambda=0.046$, $\Omega=0.786$, and $\theta_m=0.3912$. The interstitial Nusselt number Nu_i, according to the correlation proposed by Wakao and Kaguei [25], is given by

$$\mathrm{Nu}_i=6(1-\varepsilon)[2+1.1\mathrm{Re}^{0.6}\ \mathrm{Pr}^{1/3}] \tag{11}$$

This correlation was developed for forced convective flow over spheres with $0<\mathrm{Re}<8500$ and $\varepsilon\approx0.4$. Since correlations specific to natural convective flow in porous media are not available in the literature, Eq. (11) is used to account for the heat transfer between gallium and the glass spheres. The Reynolds number in

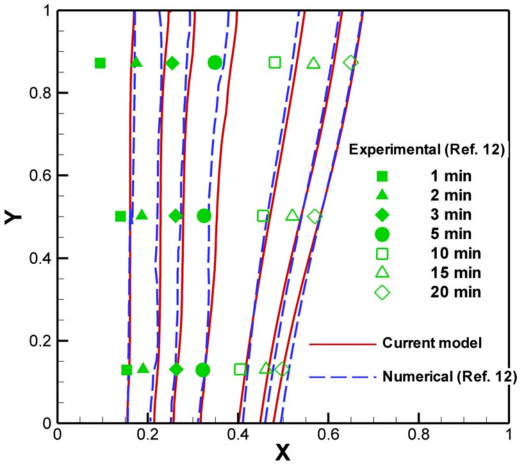

Fig. 2 Comparison of the evolution of the melt front from the present work as well as from experimental and modeling results in the literature [12]

Eq. (11) is defined as $\mathrm{Re}=u_m \times d/\nu$, where d is the diameter of the sphere and u_m is the local mean velocity.

Since the densities for liquid and solid gallium at the melting temperature ($t=29.89\,^\circ\mathrm{C}$) differ by less than 5%, the effects of volume expansion during melting and solidification are expected to be negligible. Previous models [12,20] have treated the density of gallium as a constant, and in order to compare results in the same manner, the solid-liquid PCM density ratio f_ρ in Eqs. (5)–(7) is set at 1 for this comparison; the influence of volume expansion/shrinkage is specifically explored later in this work.

Figures 2, 3(*a*), and 3(*b*), respectively, show comparisons of the interface shapes and temperature profiles between the current model and the previous results in Ref. [12]. Predictions from the current model are shown to agree well with the previous experimental and numerical results. The deviation between predictions and experiment in the early stages of melting in Fig. 2 ($t=1-3$ min) is attributed to uneven packing of the glass beads toward the top of the enclosure, as described by the authors in Ref. [12]. The loose packing causes the local volume fraction of gallium to be larger near the top than in the lower layers, which requires a larger amount of heat for melting and could explain the slower advance of the melt front. Later in the process ($t=20$ min), the melting rate of gallium is greatly reduced due to the lower temperature gradients. As the melting rate (represented in Eq. (7) by the time-differential term of porosity $\partial\varepsilon/\partial\tau$) decreases, heat transfer becomes dominated by conduction and convection in the melt, and the effect of uneven packing of glass beads (volume fraction of gallium) on the temperature profile and melt front is greatly diminished. Under these conditions, good agreement is observed between the measured and predicted melt front locations and temperature profiles, as shown in Fig. 2 ($t=20$ min) and Fig. 3(*b*).

Notwithstanding the effects of uneven packing, the current model is seen to provide predictions in good agreement with experimental results, and may be applied with confidence to the study of melting heat transfer of a PCM embedded in metal foams, wherein the mechanisms of heat transfer are similar to that for gallium melting in a bed of glass beads.

4 Results and Discussion

The parameters Ra, Da, F, Pr, Ste, f_ρ, $f_{k,\mathrm{PCM}}$, $f_{k,\mathrm{MF}}$, f_{Cp}, Ω, and Nu_i, all have an influence on the melting of a PCM in a metal foam, as shown in Eqs. (5)–(8). To limit the parameters explored in this work, a number of these parameters are fixed as follows. The Darcy number Da is set at 0.02, equivalent to a $0.01 \times 0.01\ \mathrm{m}^2$ enclosure with a metal foam of permeability of $4\times10^{-8}\ \mathrm{m}^2$; F is 0.068 for metal foams [26]; Pr is 50 for a typical organic PCM; f_k is 1000 as a typical ratio for thermal conductivities between metals ($\sim 100\ \mathrm{W\,m^{-1}\,K^{-1}}$) and organic PCMs ($\sim 0.1\ \mathrm{W\,m^{-1}\,K^{-1}}$); and f_{Cp} and Ω are fixed at a value of 1, which is common for typical applications. Although the Stephan number Ste is important to the heat transfer process, it is fixed at 1 in this study; a detailed discussion of the effect of Ste was presented in Krishnan et al. [20]. The influence of volume expansion ($f_\rho > 1$) or shrinkage ($f_\rho < 1$) of the PCM embedded in the metal foam during melting under different Ra and Nu_i is the specific focus of the present work. The porosity of metal foam ε_0 is held constant at 0.8, as in Ref. [20], and the ratio between pore diameter and the scale of the enclosure Φ is set at 0.135, corresponding to $d_p=1.35$ mm for a $0.01\times0.01\ \mathrm{m}^2$ enclosure.

4.1 Melt Front Propagation. Figures 4(*a*), 4(*b*), 5(*a*), and 5(*b*) show the development of the melt front, represented by the contour $\varepsilon=0.5\varepsilon_0$, under different conditions. The general behavior of the melt front in all cases is similar. As heat is absorbed at the left wall, the PCM in the region near this wall begins to melt first, and the melt front gradually proceeds toward the right wall. Early in the process, the melt layer is very thin. The heat transfer is governed by conduction driven by the large temperature gradient between the closely spaced hot wall and the melt front (which is maintained at T_m). Convection heat transfer in the melt is severely constrained by the small melt layer thickness. The melt front during this stage is parallel to the hot wall (at $\tau=0.02$ in Fig. 4(*a*) and at $\tau=0.8$ in Fig. 5(*a*)).

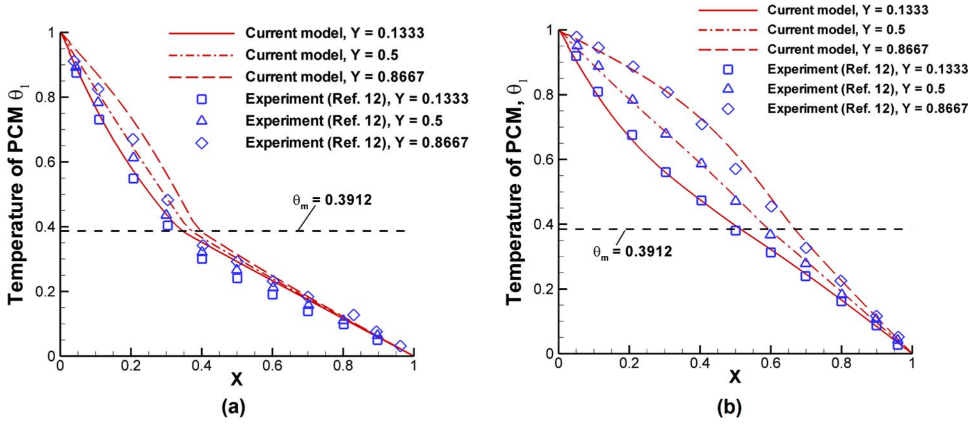

(a)

(b)

Fig. 3 Temperature profiles for the comparison in Fig. 2: (*a*) *t*=5 min and (*b*) *t*=20 min

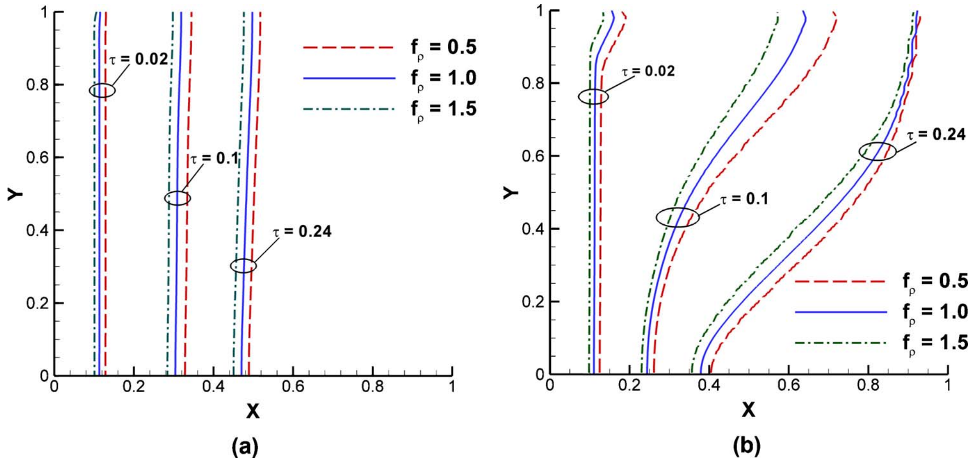

Fig. 4 Melt front at $\varepsilon=0.5\varepsilon_0$ with different solid-liquid density ratios f_ρ at $\mathrm{Nu}_i=1.82$: (*a*) $\mathrm{Ra}=10^6$ and (*b*) $\mathrm{Ra}=10^8$. A larger Rayleigh number is seen to distort the melt front away from the vertical.

As time proceeds, the thickness of the melted PCM increases, which significantly reduces the temperature gradient and the rate of heat conduction into the melt from the hot wall. Since the liquid layer thickness increases, buoyancy induced convection heat transfer in the melt becomes increasingly significant. The hot upward flow of liquid results in a higher melting rate in the upper region of the enclosure. The time at which convective heat transfer sets in scales as $\varepsilon/(\mathrm{Ste}\sqrt{\mathrm{Ra}\times\mathrm{Da}^2})$ in cases without interstitial heat transfer [20], i.e., $\mathrm{Nu}_i=0$. Therefore, an increased Ra value can significantly advance this time. For instance, at $\tau=1.9$, the effect of convection heat transfer on the melting process just begins to appear in Fig. 5(*a*) with $\mathrm{Ra}=10^6$, distorting the melt front from vertical; on the other hand, in the case with a higher Rayleigh number, i.e., $\mathrm{Ra}=10^8$, convection is already well developed by the same time, as indicated by the significantly distorted front shape in Fig. 5(*b*). With interstitial heat transfer occurring between the PCM and foam, the melt front is seen to remain close to parallel with the hot wall; a comparison of the melt fronts with and without interstitial heat transfer at a given Rayleigh number is provided in Figs. 4(*a*), 4(*b*), 5(*a*), and 5(*b*) ($\mathrm{Ra}=10^6$ and 10^8). For instance, for $\mathrm{Ra}=10^8$, the melt front at $\tau=0.1$ with $\mathrm{Nu}_i=1.82$ in Fig. 4(*b*) deviates less from the vertical than does the front at $\tau=1.9$ with $\mathrm{Nu}_i=0$ in Fig. 5(*b*). It is noted that this comparison is made at approximately the same melt fractions in the two cases despite the difference in time scales, due to the different interstitial Nusselt numbers. The interstitial heat transfer from the metal foam to the PCM imprints the linear temperature profile of the foam on to the PCM, and renders the heat transfer in the PCM to behave as if it were conduction-dominated, even when convection in the melt is already fully developed. For larger Nu_i, the liquid temperature approaches that of the foam, and decreases more linearly away from the hot wall, as evident from a comparison of the melt temperature profiles (the portion above the melting temperature $\theta_1=0.3$ on the θ_1 line) in Figs. 6(*b*) and 7(*b*).

The latent heat of the PCM has an important influence on the temperature profiles during melting. The temperature throughout the melting region is maintained at the melting point θ_m, which has a distinct impact on the temperature profiles in the PCM. Without interstitial heat transfer ($\mathrm{Nu}_i=0$), heat energy for melting is delivered solely by conduction and convection through the liquid PCM from the hot wall. The melting process takes place along a sharp front, which results in a change in the slope of the temperature profile at the melting temperature $\theta_1=0.3$, as shown in Figs. 7(*a*) and 7(*b*). Since the metal foam does not lose heat to the PCM, its temperature profile develops much faster than that of the PCM due to its significantly larger thermal diffusivity $\alpha_m=k_m/(\rho_m Cp_m)$, which is two orders of magnitude higher than that of the PCM. At each of the three times considered in Figs. 7(*a*)

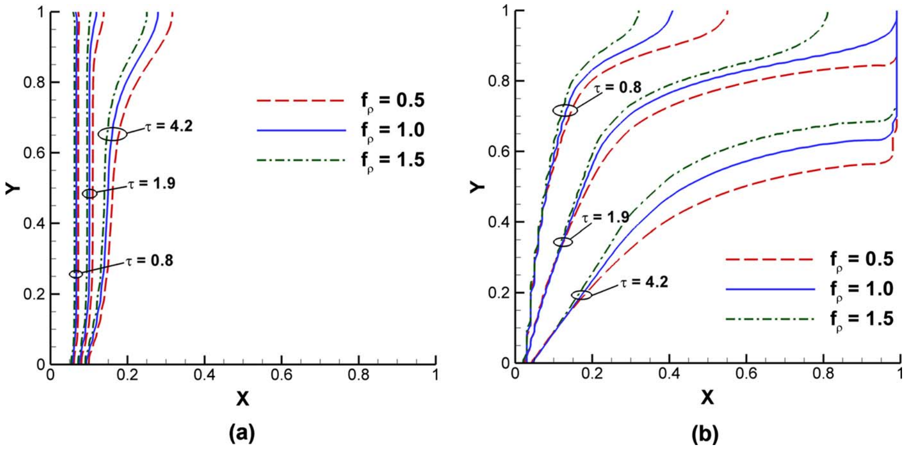

Fig. 5 Melt front at $\varepsilon=0.5\varepsilon_0$ with different solid-liquid density ratios f_ρ at $\mathrm{Nu}_i=0$: (*a*) $\mathrm{Ra}=10^6$ and (*b*) $\mathrm{Ra}=10^8$. Compared with Figs. 4(*a*) and 4(*b*), the melt fronts here deviate much more from the vertical.

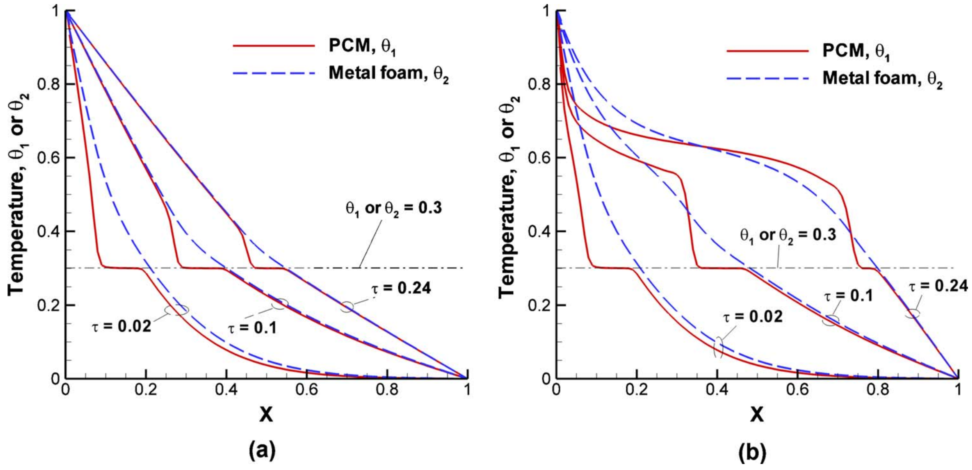

Fig. 6 Temperature profiles at half height ($Y=0.5$) with $\mathrm{Nu}_i=1.82$ and $f_\rho=1$: (*a*) $\mathrm{Ra}=10^6$ and (*b*) $\mathrm{Ra}=10^8$

and 7(*b*), $\tau=0.8$, 1.9 and 4.2, the temperature profile in the metal foam is already well developed into a straight line, with that in the PCM still developing. On the other hand, in the presence of interstitial heat transfer, heat can transfer to the PCM via the metal foam, in addition to conduction and convection in the melt. Even when the PCM close to the hot wall is still in a solid phase, the PCM farther away can be heated by the foam, which could cause a broad melting region rather than a sharp front as in the cases without interstitial heat transfer. The temperature throughout the melting region stays at the melting temperature, as indicated by the plateau in Figs. 6(*a*) and 6(*b*).

The effect of volume change on the movement of the melt front is evident in the results presented in Figs. 4(*a*), 4(*b*), 5(*a*), and 5(*b*). Under the same conditions of Ra and Nu_i, the melt front moves faster when the liquid-phase density of the PCM is larger than for the solid phase, i.e., $f_\rho<1$; conversely, the front moves more slowly when $f_\rho>1$. When $f_\rho<1$, the PCM decreases in volume as it melts, pulling additional liquid toward the melt front and causing an extra component of convection over and above that induced by buoyancy. This extra flow is termed an "added flow" in this paper. This added flow adds hot liquid from near the hot wall to the melting region and increases the melting speed. By a similar but converse argument, the speed of the melt front propagation is reduced when $f_\rho>1$. The nondimensional volume flow rate of the added flow F_a can be estimated as

$$F_a \sim (1-f_\rho)\int_V \frac{\partial \varepsilon}{\partial \tau} dV \tag{12}$$

where V is the 1×1 dimensionless volume of the enclosure. The algebraic sign of F_a is defined in such a way that F_a is positive if the added flow is from the hot wall toward the melt front. The nondimensional convection heat transfer rate induced by the added flow Q_a can then be estimated as

$$Q_a \equiv \frac{q_a}{k(T_h-T_c)} \sim \Pr(\theta_h-\theta_{\mathrm{melt}})(1-f_\rho)\int_V \frac{\partial \varepsilon}{\partial \tau} dV \tag{13}$$

where q_a (W/m) is the heat carried by the added flow in the enclosure over a unit thickness in the direction normal to the 2D coordinate, and the integral in Eq. (13) can be estimated by

$$\int_V \frac{\partial \varepsilon}{\partial \tau} dV \sim -\frac{\mathrm{Ste}(Q_k+Q_c+Q_a)}{\Pr\times f_\rho} \tag{14}$$

Equation (14) signifies that the rate of melting of the PCM volume depends on the total heat transfer rate, i.e., the sum of nondimensional heat transfer rates by conduction Q_k, convection Q_c, and added flow Q_a. Substituting Eq. (14) into Eq. (13), it is readily seen that

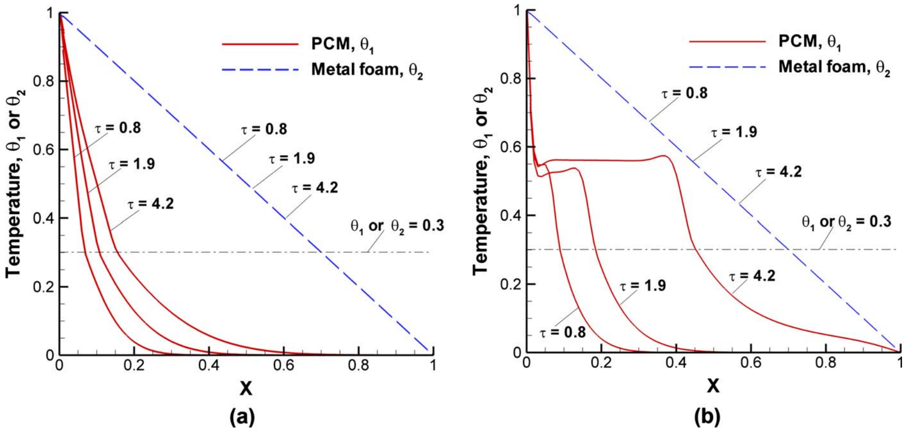

Fig. 7 Temperature profiles at half height ($Y=0.5$) with $\mathrm{Nu}_i=0$ and $f_\rho=1$: (*a*) $\mathrm{Ra}=10^6$ and (*b*) $\mathrm{Ra}=10^8$

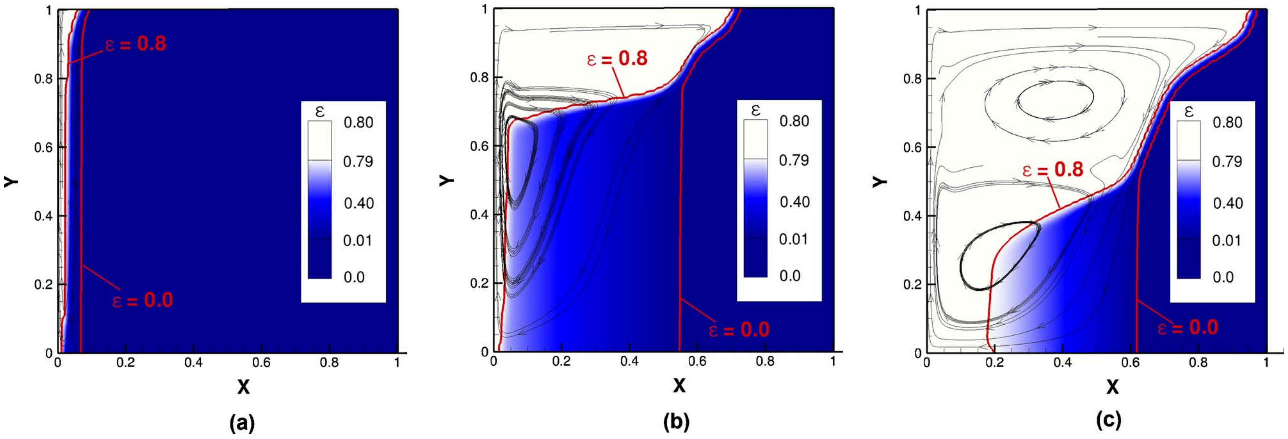

Fig. 8 Melting region colored by ε for $\mathrm{Ra}=10^8$ and $\mathrm{Nu}_i=0.0182$: (*a*) $\tau=0.15$, (*b*) $\tau=0.625$, and (*c*) $\tau=1.125$. To the left of the line $\varepsilon=0.8$ is the liquid area ($\varepsilon=\varepsilon_0$), to the right of the line $\varepsilon=0.0$ is the solid area ($\varepsilon=0$), and between the two lines is the melting region ($0<\varepsilon<\varepsilon_0$). Flow streamlines are also plotted in the melt and mushy zones.

$$r_a \equiv \frac{Q_a}{(Q_k+Q_c+Q_a)} \sim \frac{\mathrm{Ste}(\theta_h-\theta_{\mathrm{melt}})(1-f_\rho)}{f_\rho} \qquad (15)$$

where r_a is the ratio of the heat transfer due to the added flow to the total heat transfer rate. Equation (15) implies that an increase in Ste or the hot wall temperature θ_h can increase the heat transfer due to the added flow. An increase in Ste implies a decrease in latent heat, and a resulting increase in melting speed and stronger expansion/shrinkage of the PCM, leading to an enhanced effect of the added flow on heat transfer. Similarly, increasing the hot wall temperature θ_h enhances the heat transfer rate and thus the melting rate, leading again to an enhanced effect of added flow on heat transfer. It is apparent from Eq. (15) that the contribution of the added flow to the overall heat transfer is positive if the PCM shrinks during melting ($f_\rho<1$), since r_a is positive; the contribution is negative if the PCM expands during melting.

During the initial conduction-controlled period, volume expansion/shrinkage induced by PCM melting has an effect on heat transfer that is uniform over the melt front, as indicated by the front being evenly slower (faster) over its entire extent when $f_\rho>1$ ($f_\rho<1$), relative to the case without volume change ($f_\rho=1$). The melt front remains almost parallel to that for $f_\rho=1$, as shown at $\tau=0.02$ in Fig. 4(*a*) and at $\tau=0.8$ in Fig. 5(*a*). As convection effects set in, the effect of volume expansion/shrinkage of the PCM becomes more nonuniform with the influence being more significant in the upper layers of the enclosure, as revealed in Fig. 4(*b*) at $\tau=0.1$ and Fig. 5(*b*) at $\tau=1.9$. The buoyancy-driven convection of hotter fluid to the top causes larger heat transfer rates in the upper layers. Since the ratio of the heat transfer rate due to the added flow to the overall heat transfer rate is fixed for given Ste, θ_h, θ_m, and f_ρ, as shown in Eq. (15), a larger overall heat transfer rate in the upper layers of the enclosure also implies a larger heat transfer rate due to the added flow; the effect of the added flow on the melting process is thus also larger in the upper layers. This explains the greater deviation of the melting line at $f_\rho=0.5$ or 1.5 from that at $f_\rho=1$ in the upper layers of the enclosure, as shown in Fig. 4(*b*) $\tau=0.1$ and Fig. 5(*b*) $\tau=0.8$ and 1.9. The somewhat different behavior at $\tau=0.24$ in Fig. 4(*b*), wherein the influence of f_ρ in the upper layer seems to be lower than in the middle, may be explained by heat from the hot wall being transmitted directly to the cold wall due to the increased temperature gradient in the remaining solid near the cold wall; the rate of phase change decreases as a result, as does the effect of the added flow.

4.2 Melting Region.

Most of the heat transferred from the hot wall is absorbed as latent heat by the PCM as it melts at a constant temperature. In the current study, the PCM is embedded in the pores of the metal foam, and the volume fraction of the liquid phase is represented by porosity ε, which varies from 0 (completely solid) to ε_0, i.e., the pore is completely occupied by liquid PCM. Values of ε between 0 and ε_0 signify that the PCM is partially melted in the pores of the metal foam; this region of the foam in which liquid and solid PCM co-exist in the pores is referred to as the melting region in this work. Since a metal foam has much greater thermal conductivity than the embedded PCM, the primary heat flow path is from the metal foam to the PCM. In a single pore, PCM adjacent to the metal foam ligaments melts first; as heat diffuses gradually through the melt, PCM in the interior regions of the pore experiences melting. Although the pore is still partially blocked by solid PCM, the melt in the pore may flow subject to buoyancy or a pressure gradient. Therefore, it is necessary to consider the change in permeability of the partially blocked pores in the melting region. A literature review reveals that a model specifically targeting permeability of a metal foam with partially blocked pores is unavailable. In this work, it is assumed that the permeability K in the melt region has a simple linear relationship with porosity, as follows

$$K = K_0 \times \varepsilon/\varepsilon_0 \qquad (16)$$

where K_0 is the permeability for pores completely occupied by liquid PCM, and ε_0 is the porosity of the metal foam. Equation (16) ensures that permeability becomes zero when the pores of the metal foam are completely occupied by solid PCM.

Figures 8(*a*)–8(*c*) and 9(*a*)–9(*c*) show the melting region ($0<\varepsilon<\varepsilon_0$) under different levels of interstitial heat transfer. The porosity takes values between those representing the lines $\varepsilon=0$ and $\varepsilon=0.8\varepsilon_0$, which bound the melting region. The area to the left of the boundary $\varepsilon=0.8$ is completely occupied by liquid with a porosity equaling that of the foam ($\varepsilon_0=0.8$); the area to the right of the right boundary is occupied by a solid PCM with $\varepsilon=0$. For convenience, the left boundary of the melting zone is hereafter referred to as the melt front.

As explained earlier, when the interstitial Nusselt number is zero, melting takes place along a sharp line, and the temperature profile shows a sharp change in slope at the melting temperature. As the interstitial Nusselt number increases, heat is transferred through the metal foam past the melt front causing melting to occur in a region rather than along a single line. Perhaps counterintuitively, the melting region is quite large at a low interstitial Nusselt number ($\mathrm{Nu}_i=0.0182$), as shown in Fig. 8(*b*), but rather narrow at a high Nu_i ($\mathrm{Nu}_i=1.82$), as shown in Fig. 9(*b*). At low Nu_i, the heat transfer rate between PCM and foam is small. The

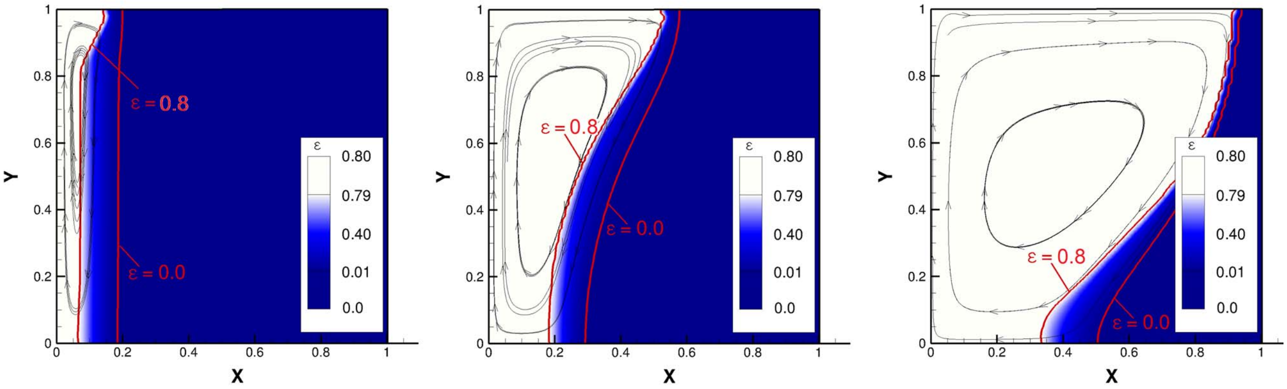

(a) (b) (c)

Fig. 9 Melting region colored by ε for $\mathrm{Ra}=10^8$ and $\mathrm{Nu}_i=1.82$: (*a*) $\tau=0.02$, (*b*) $\tau=0.08$, and (*c*) $\tau=0.25$. To the left of the line $\varepsilon=0.8$ is the liquid area ($\varepsilon=\varepsilon_0$), to the right of the line $\varepsilon=0.0$ is the solid area ($\varepsilon=0$), and between the two lines is the melting region ($0<\varepsilon<\varepsilon_0$). It is noted that the melting times at this higher interstitial Nusselt number are significantly smaller than in Figs. 8(*a*)–8(*c*). Flow streamlines are also plotted in the melt and mushy zones.

temperature in the foam develops much faster than in the PCM, resulting in a wide extent of PCM in which its local temperature is lower than that of the foam. The PCM temperature in this zone gradually rises to the melting point before melting can take place. The melt front at the left side of the melting region propagates slowly since heat transfer from the metal foam is quite limited, while the melting region continues to expand on the right side since the metal foam retains its high temperature, which is available to raise the PCM temperature. This results in a wide melting region at low interstitial Nusselt numbers. At a high interstitial Nusselt number of $\mathrm{Nu}_i=1.82$, the temperature difference between the PCM and foam is small, as evident from a comparison of Figs. 6(*a*) and 6(*b*) and Figs. 7(*a*) and 7(*b*). Due to the strong interstitial heat transfer, the melt front on the left side of the melting region moves rapidly, while advancement on the right side is hampered since the foam has already lost its heat to the PCM earlier along the heat flow path. This results in a narrow melting region with the left boundary tracking the right closely.

As the interstitial Nusselt number goes to infinity (not shown here), the left and right boundaries of the melting region become one, and the melting region shrinks to a sharp melting front. Due to the very strong interstitial heat transfer, the temperature difference between the foam and PCM reduces to almost zero, and a one-temperature model is sufficient to study the melting process in this case.

The morphology and extent of the melting region also develop with time. In the initial stages, the melting region is relatively narrow (Fig. 8(*a*)), since the temperature profile in the foam is still developing. As time proceeds and the metal foam has heated up, the melting region expands (Fig. 8(*b*)). As the melting region shifts toward the cold wall, the rate of heat loss to the cold wall increases (Figs. 6(*a*) and 6(*b*), $\tau=0.24$), significantly reducing the speed of the right boundary of the melting zone. This results in shrinking of the melting region, as shown in Figs. 8(*c*) and 9(*c*).

Convection has an important influence on the melting region morphology, since it enhances heat transfer from the hot wall and speeds up the melt front motion. As discussed earlier, convection heat transfer is most prominent in the upper layers of the enclosure; the melt front (the left boundary of the melting region) is significantly accelerated to follow the right boundary more closely in the upper layers, which results in this part of the melting region being thinner (Figs. 8(*a*)–8(*c*) and 9(*a*)–9(*c*)). At lower Rayleigh numbers, e.g., $\mathrm{Ra}=10^6$, when convection is weak, the melting region has a uniform width from the top to bottom (not shown here), unlike the behavior at the higher Rayleigh number considered in Figs. 8(*a*)–8(*c*) and 9(*a*)–9(*c*).

4.3 Melt Volume Fraction and Melting Rate. Figure 10 shows the variation in melt volume fraction with time for different interstitial Nusselt numbers. The melt volume faction is defined as (V_m/V_0), where V_m and V_0 are the melted volume and the total volume of the PCM, respectively. As expected, an increase in the interstitial Nusselt number expedites the melting rate. For instance, to melt 40% of the total PCM with $f_\rho=1.0$, it takes $\tau=0.1$ at $\mathrm{Nu}_i=1.82$, $\tau=0.75$ at $\mathrm{Nu}_i=0.0182$, and $\tau=2.65$ at $\mathrm{Nu}_i=0$. Toward the end of the melting process, the melt volume fraction reaches a limit when the melt front attains a static position near the cold wall determined by a heat balance. This value of maximum melt volume fraction for $\mathrm{Nu}_i=1.82$ is approximately 0.85, as shown in Fig. 10, while it is even larger for $\mathrm{Nu}_i=0.0182$ (0.95) and $\mathrm{Nu}_i=0$ (>0.98). However, at a lower Rayleigh number of $\mathrm{Ra}=10^6$, the maximum melt volume fraction is approximately $(1-\theta_m)$ [20], i.e., 0.7, for all cases.

When the effect of convection is small as for $\mathrm{Ra}=10^6$, the temperature profiles in the PCM are conduction-dominated, with the temperature contours and melt front being parallel to the hot wall. At the end of the melting process, the temperature in the PCM decreases linearly from the hot wall to the cold wall and the position of the melt front, where the temperature is θ_m, is at a nondimensional distance of approximately $(1-\theta_m)$ away from the hot wall, which results in the maximum melt volume fraction also

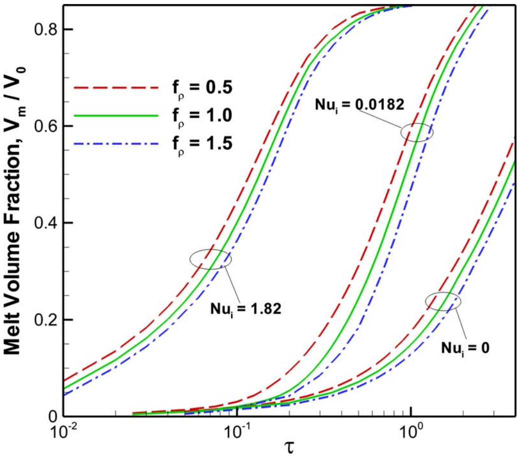

Fig. 10 Melt volume fractions at different times with $\mathrm{Ra}=10^8$

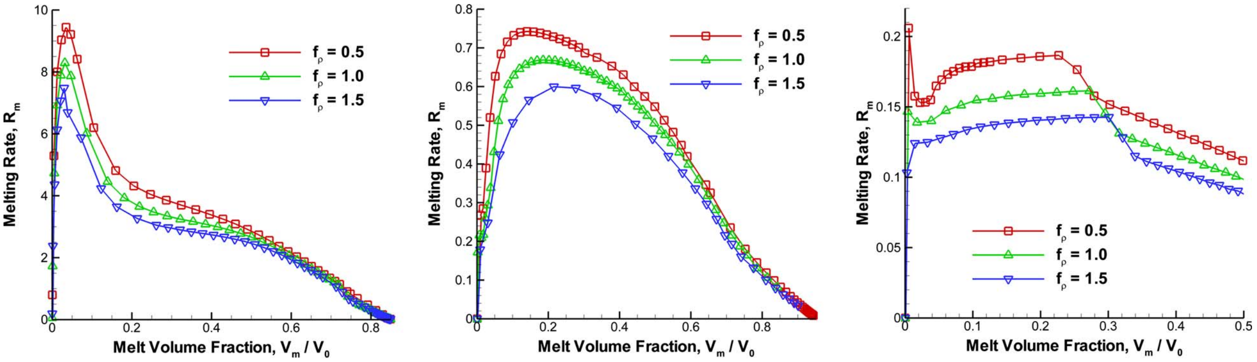

(a) (b) (c)

Fig. 11 Variation in melting rate as a function of melt volume fraction for different interfacial Nusselt numbers: (*a*) $\mathrm{Nu}_i=1.82$, (*b*) $\mathrm{Nu}_i=0.0182$, and (*c*) $\mathrm{Nu}_i=0$. The influence of volume expansion and shrinkage is also brought out.

being $(1-\theta_m)$. On the other hand, for greater levels of convection as with $\mathrm{Ra}=10^8$, the temperature profiles in the PCM deviate significantly from being conduction-dominated (see, for example, Fig. 5(*b*), $\tau=4.2$). PCM beyond a distance of $(1-\theta_m)$ from the hot wall can also melt due to the convective heat transfer, leading to higher melt volume fractions than in the conduction-dominated cases.

It is noted that even at a fixed Rayleigh number, the maximum melt volume fraction can be different under different interstitial heat transfer conditions. Convection becomes relatively important in melting at small interstitial Nusselt numbers. The greater the role of convection in the melting process, the larger is the maximum melt volume fraction, as illustrated in Fig. 10. This is because larger interstitial heat transfer causes the temperature profile of the metal foam to be imprinted on the PCM, making it resemble a conduction-dominated shape, which leads to a lower maximum melt volume fraction, as discussed earlier.

The effect of volume change in the PCM during melting on the evolution of the melt volume fraction is evident from Fig. 10. Volume shrinkage ($f_\rho=0.5$) expedites the melting process, while expansion ($f_\rho=1.5$) suppresses the process, as signified by the $f_\rho=0.5$ (1.5) curves being above (below) that for $f_\rho=1.0$ in Fig. 10.

The variation in the melting rate R_m as a function of melt volume fraction is shown in Figs. 11(*a*)–11(*c*). The melting rate is defined as

$$R_m = \partial(V_m/V_0)/\partial\tau \tag{17}$$

Since both (V_m/V_0) and τ are dimensionless parameters, the melting rate R_m is also nondimensional. At the beginning, the melting rate is zero for all cases. This is because the temperature of the solid PCM is initially set to the cold wall temperature at $\theta_1=0$. The subsequent variation in the melting rate is strongly influenced by the interstitial Nusselt number. At a high interstitial Nusselt number, $\mathrm{Nu}_i=1.82$ (Fig. 11(*a*)), the melting rate R_m rises quickly to a peak value at $(V_m/V_0)\approx 0.05$, and then rapidly drops until $(V_m/V_0)\approx 0.2$ and continues to drop more gradually over $0.2<(V_m/V_0)<0.5$; beyond this melt volume fraction, the melting rate again drops rapidly. The initial quick rise of R_m is due to the rapid growth of the melting region in the PCM. At $\tau\approx 0.02$, when (V_m/V_0) reaches ~ 0.05, the melting region has expanded to its maximum extent, as shown in Fig. 9(*a*), due to the quick spread of the high-temperature region in the metal foam; this corresponds to the maximum melting rate seen in Fig. 11(*a*). During the period $0.02<\tau<0.1$ when (V_m/V_0) is between 0.05 and 0.5, the melting region does not change much in extent as it translates to the right, as is clear from a comparison of Figs. 9(*a*) and 9(*b*). Early in this period, i.e., $0.02<\tau<0.04$ $(0.02<(V_m/V_0)<0.2)$, conduction is more important than convection due to the limited melt thickness, and the melting rate decreases rapidly with increased conduction resistance as the melt volume fraction increases. Later in this period, $(0.04<\tau<0.1,\ 0.2<(V_m/V_0)<0.5)$, convection becomes more important due to the increased liquid space. Since convection does not diminish at the same rate as conduction when the melt volume fraction increases, the decrease in melting rate occurs more slowly in this period. At the final stage, for $\tau>0.1$ $((V_m/V_0)>0.5)$, the melt region has shrunk, especially in the upper part of the enclosure, as shown in Fig. 9(*c*), and heat loss to the cold wall becomes significant, as shown in Fig. 6(*b*) at $\tau=0.24$; this causes the melting rate to decrease rapidly for melt volume fractions greater than 0.5, as shown in Fig. 11(*a*).

For zero interstitial heat transfer ($\mathrm{Nu}_i=0$), on the other hand, the melting of PCM is not enhanced by the metal foam. The melting speed is thus significantly lower than at a high interstitial Nusselt number, as evident from a comparison between Figs. 11(*a*) and 11(*c*). Convection plays a more important role in the melting process under these conditions, which changes the development of the melting rate during the intermediate portions of the melting process. In Fig. 11(*c*), as the melt volume fraction exceeds 0.05, the melting rate increases and remains at a high level until the melt volume fraction reaches ≈ 0.25. The gradual increase in melting rate in this period corresponds to a gradual improvement in convection heat transfer as the extent of the melt region increases. The subsequent decrease in R_m as the melt volume fraction exceeds 0.25 ($\tau>1.9$) in Fig. 11(*c*) is a result of the proximity of the melt to the cold wall on the right in the upper part of the enclosure ($\tau=1.9$ in Fig. 5(*b*)).

At an intermediate interstitial Nusselt number $\mathrm{Nu}_i=0.0182$, the behavior of the melting rate combines features of the behavior at $\mathrm{Nu}_i=1.82$ and 0: convection contributes an expanded high-melting rate region in the range $0.1<(V_m/V_0)<0.5$ as it does under a zero interstitial Nusselt number condition, while the heat transfer from the metal foam leads to a decrease in the melting rate with increasing melt volume fraction in this region, as shown in Fig. 11(*b*).

Compared with the case without volume change during melting ($f_\rho=0$), volume shrinkage ($f_\rho=0.5$) increases the melting rate in all cases, while volume expansion ($f_\rho=1.5$) reduces the melting rate, as shown by the entire set of profiles of R_m in Figs. 11(*a*)–11(*c*).

4.4 Wall Nusselt Number. As discussed in Sec. 4.3, the participation of metal foam in the melting of the PCM can improve the melting rate, and thus enhance the heat transfer process. The heat transfer performance under different conditions of interstitial heat transfer and volume change can be quantified using the following definition of the average Nusselt number on the hot wall

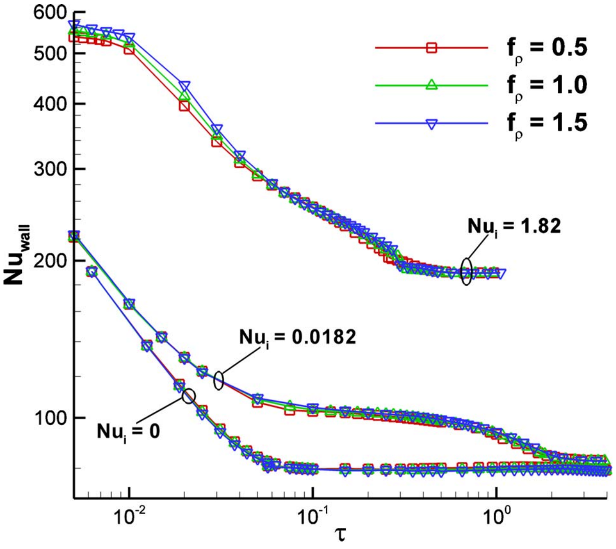

Fig. 12 Variation in wall Nusselt number with time for different interstitial Nusselt numbers, and under volume expansion/ contraction upon melting

$$\mathrm{Nu}_w = \frac{h_w H}{k_{\mathrm{PCM}}} = \int_0^1 \left(A\varepsilon_0 \frac{\partial \theta_1}{\partial X} + A(1-\varepsilon_0) f_k \frac{\partial \theta_2}{\partial X} \right) \times dY \quad (18)$$

Figure 12 shows the change in wall Nusselt number with time. It is clear that interstitial heat transfer greatly enhances wall heat transfer, as shown by a comparison of the profiles at $\mathrm{Nu}_i = 1.82$ with those at $\mathrm{Nu}_i = 0.0182$ and 0. For $\mathrm{Nu}_i = 0$, the wall Nusselt number initially decreases rapidly corresponding to the reduction in heat conduction as the melt front moves away from the hot wall, and then is governed by convection over a relatively long time period of $0.08 < \tau < 2$.

As the interstitial Nusselt number increases, Nu_w decreases monotonically with time, indicating the dominant effect of conduction heat transfer in these cases. Although the effect of convection is still evident for $\mathrm{Nu}_i = 0.0182$, as indicated by the slow decrease in the lines during the time period of $0.05 < \tau < 1$ in Fig. 12, it almost disappears for $\mathrm{Nu}_i = 1.82$ where the conduction heat transfer enhanced by the metal foam is very strong.

Volume change during melting does not appear to have a strong effect on the wall Nusselt number at the hot wall in Fig. 12. Since the heat transfer in the metal foam dominates the overall heat transfer, any differences in heat transfer rate caused by volume change appear to be swamped in terms of the effect on the wall Nusselt number.

5 Conclusions

A two-temperature model is developed for an investigation of the melting of phase change materials embedded in metal foams. The influence of volume change in the PCM during melting and of interstitial Nusselt number on the melting region behavior are treated in detail.

Volume shrinkage/expansion of the PCM during melting causes an added flow that expedites (suppresses) the propagation of the melt front, and consequently increases (decreases) the melting rate by over 10% at the solid-liquid density ratio of 0.5 (1.5) in the earlier stages of melting ($V_m/V_0 < 0.4$).

Interstitial heat transfer between the metal foam and PCM can significantly enhance the melting process and improve the overall heat transfer rates, as well as alter the melt front propagation and the behavior of the melting region. With a high interstitial Nusselt number, the melting and heat transfer processes display conduction-dominant behavior.

At the highest interstitial Nusselt number of 1.82 considered in this paper, the wall Nusselt number exceeds three times that found in the absence of interstitial heat transfer, which shows the importance of the choice of the interstitial Nusselt number value in accurately modeling the melting of PCM in metal foams. A more faithful treatment of the structure-related interstitial heat transfer, as conducted in Refs. [27,28], is important for improved modeling accuracy in such problems.

Nomenclature

Cp = specific heat, J kg^{-1} K^{-1}
Da = Darcy number
d_p = pore diameter in metal foam, m
F = inertial coefficient
f_{Cp} = specific heat ratio of solid to liquid PCM phases ($=Cp_s/Cp_l$)
f_k = thermal conductivity ratio of metal foam to liquid PCM ($=k_m/k_l$)
$f_{k,\mathrm{MF}}$ = effective thermal conductivity ratio of metal foam alone to liquid PCM ($=k_{e,\mathrm{MF}}/k_l$)
$f_{k,\mathrm{PCM}}$ = effective thermal conductivity ratio of PCM embedded in metal foam to its liquid phase ($=k_{e,\mathrm{PCM}}/k_l$)
f_ρ = density ratio of solid to liquid PCM phases ($=\rho_s/\rho_l$)
g = acceleration due to gravity, m/s^2
h_i = interstitial heat transfer coefficient, W m^{-3} K^{-1}
h_L = latent heat, J/kg
H = height of the enclosure, m
K = permeability, m^2
k_e = effective thermal conductivity, W m^{-1} K^{-1}
Nu_i = interstitial Nusselt number
P = nondimensional pressure
p = pressure, Pa
Pr = Prandtl number
Ra = Rayleigh number
Rh = nondimensional parameter$=\nu^2/(h_L H^2)$
Ste = Stephan number
t = time, s
T_1 = temperature of PCM, K
T_2 = temperature of metal foam, K
U = nondimensional velocity
u = velocity, m/s
u_{mag} = magnitude of velocity, m/s
X, Y = nondimensional Cartesian coordinates
x, y = Cartesian coordinates, m

Greek Symbols

α_l = thermal diffusivity of liquid PCM, m^2/s
β = coefficient of thermal expansion
$\delta(i,j)$ = delta function
ε = porosity of PCM melt
ε_0 = porosity of metal foam
Φ = ratio of d_p to H
μ = viscosity of liquid PCM, kg m^{-1} s^{-1}
ν = kinematic viscosity of liquid PCM, m^2/s
θ_1 = nondimensional temperature of PCM
θ_2 = nondimensional temperature of metal foam
ρ = density, kg/m^3
τ = nondimensional time
Ω = ratio defined as $\Omega=(\rho_m Cp_m)/(\rho_l Cp_l)$

Subscripts

c = cooling wall
h = heating wall
i, j = indices for directions, 1 (x-direction) or 2 (y-direction)

l = liquid PCM
s = solid PCM
m = metal foam or melting

References

[1] Fath, H. E. S., 1991, "Heat-Exchanger Performance for Latent-Heat Thermal Energy Storage-System," Energy Convers. Manage., **31**, pp. 149–155.
[2] Cao, Y., and Faghri, A., 1991, "Performance-Characteristics of a Thermal-Energy Storage Module—A Transient PCM Forced-Convection Conjugate Analysis," Int. J. Heat Mass Transfer, **34**, pp. 93–101.
[3] Krishnan, S., and Garimella, S. V., 2004, "Thermal Management of Transient Power Spikes in Electronics—Phase Change Energy Storage or Copper Heat Sinks," ASME J. Electron. Packag., **126**, pp. 308–316.
[4] Krishnan, S., and Garimella, S. V., 2004, "Analysis of a Phase Change Energy Storage System for Pulsed Power Dissipation," IEEE Trans. Compon. Packag. Technol., **27**, pp. 191–199.
[5] Zhang, Y. T., and Liu, J., 2002, "Numerical Study on Three-Region Thawing Problem During Cryosurgical Re-warming," Med. Eng. Phys., **24**, pp. 265–277.
[6] Simpson, J. E., and Garimella, S. V., 1998, "An Investigation of Solutal, Thermal and Flow Fields in Unidirectional Alloy Solidification," Int. J. Heat Mass Transfer, **41**, pp. 2485–2502.
[7] Sparrow, E. M., Patankar, S. V., and Ramadhyani, S., 1977, "Analysis of Melting in the Presence of Natural Convection in the Melt Region," Trans. ASME, Ser. C: J. Heat Transfer, **99**, pp. 520–526.
[8] Gau, C., and Viskanta, R., 1986, "Melting and Solidification of a Pure Metal on a Vertical Wall," Trans. ASME, Ser. C: J. Heat Transfer, **108**, pp. 174–181.
[9] Jany, P., and Bejan, A., 1988, "Scaling Theory of Melting With Natural Convection in an Enclosure," Int. J. Heat Mass Transfer, **31**, pp. 1221–1235.
[10] Sun, D., Garimella, S. V., Singh, S. K., and Naik, N., 2005, "Numerical and Experimental Investigation of the Melt Casting of Explosives," Propellants, Explos., Pyrotech., **30**, pp. 369–380.
[11] Jones, B. J., Sun, D., Krishnan, S., and Garimella, S. V., 2006, "Experimental and Numerical Study of Melting in a Cylinder," Int. J. Heat Mass Transfer, **49**, pp. 2724–2738.
[12] Beckermann, C., and Viskanta, R., 1988, "Natural Convection Solid/Liquid Phase Change in Porous Media," Int. J. Heat Mass Transfer, **31**, pp. 35–46.
[13] Chellaiah, S., and Viskanta, R., 1990, "Natural Convection Melting of a Frozen Porous Medium," Int. J. Heat Mass Transfer, **33**, pp. 887–899.
[14] Chellaiah, S., and Viskanta, R., 1990, "Melting of Ice-Aluminum Balls Systems," Exp. Therm. Fluid Sci., **3**, pp. 222–231.
[15] Minkowycz, W. J., Haji-Sheikh, A., and Vafai, K., 1999, "On Departure From Local Thermal Equilibrium in Porous Media Due to a Rapidly Changing Heat Source: The Sparrow Number," Int. J. Heat Mass Transfer, **42**, pp. 3373–3385.
[16] Vafai, K., and Sozen, M., 1990, "An Investigation of a Latent Heat Storage Porous Bed and Condensing Flow Through It," Trans. ASME, Ser. C: J. Heat Transfer, **112**, pp. 1014–1022.
[17] Ellinger, E. A., and Beckermann, C., 1991, "On the Effect of Porous Layers on Melting Heat Transfer in an Enclosure," Exp. Therm. Fluid Sci., **4**, pp. 619–629.
[18] Tong, X., and Khan, J. A., 1996, "Enhancement of Heat Transfer by Inserting a Metal Matrix Into a Phase Change Material," Numer. Heat Transfer, Part A, **30**, pp. 125–141.
[19] Alawadhi, E. M., and Amon, C. H., 2003, "PCM Thermal Control Unit for Portable Electronic Devices: Experimental and Numerical Studies," IEEE Trans. Compon. Packag. Technol., **26**, pp. 116–125.
[20] Krishnan, S., Murthy, J. Y., and Garimella, S. V., 2005, "A Two-Temperature Model for Solid-Liquid Phase Change in Metal Foams," Trans. ASME, Ser. C: J. Heat Transfer, **127**, pp. 995–1004.
[21] Amiri, A., and Vafai, K., 1994, "Analysis of Dispersion Effects and Non-thermal Equilibrium, Non-Darcian, Variable Porosity Incompressible Flow Through Porous Media," Int. J. Heat Mass Transfer, **37**, pp. 939–954.
[22] Bhattacharya, A., Calmidi, V. V., and Mahajan, R. L., 2002, "Thermophysical Properties of High Porosity Metal Foams," Int. J. Heat Mass Transfer, **45**, pp. 1017–1031.
[23] Issa, R. I., 1986, "Solution of Implicitly Discretized Fluid Flow Equations by Operator Splitting," J. Comput. Phys., **62**, pp. 40–65.
[24] FLUENT 6.1 Documentation, http://www.fluent.com/
[25] Wakao, N., and Kaguei, S., 1982, *Heat and Mass Transfer in Packed Beds*, Gordon and Breach, New York.
[26] Hwang, J. J., Hwang, G. J., Yeh, R. H., and Chao, C. H., 2002, "Measurement of Interstitial Convective Heat Transfer Coefficient and Frictional Drag for Flow Across Metal Foams," Trans. ASME, Ser. C: J. Heat Transfer, **124**, pp. 120–129.
[27] Krishnan, S., Garimella, S. V., and Murthy, J. Y., 2008, "Simulation of Thermal Transport in Open-Cell Metal Foams: Effect of Periodic Unit-Cell Structure," Trans. ASME, Ser. C: J. Heat Transfer, **130**, p. 024503.
[28] Krishnan, S., Murthy, J. Y., and Garimella, S. V., 2006, "Direct Simulation of Transport in Open-Cell Metal Foam," Trans. ASME, Ser. C: J. Heat Transfer, **128**, pp. 793–799.

Effect of Particle Migration on Flow and Convective Heat Transfer of Nanofluids Flowing Through a Circular Pipe

M. M. Heyhat
e-mail: mmheyhat@ut.ac.ir

F. Kowsary
e-mail: fkowsari@ut.ac.ir

School of Mechanical Engineering,
College of Engineering,
University of Tehran,
Tehran 1439957131, Iran

This paper aims to study the effect of particle migration on flow and heat transfer of nanofluids flowing through a circular pipe. To do this, a two-component model proposed by Buongiorno (2006, "Convective Transport in Nanofluids," ASME J. Heat Transfer, ***128****, pp. 240–250) was used and a numerical study on laminar flow of alumina-water nanofluid through a constant wall temperature tube was performed. The effects of non-uniform distribution of particles on heat-transfer coefficient and wall shear stress are shown. Obtained results illustrate that by considering the particle migration, the heat-transfer coefficient increases while the wall shear stress decreases, compared with uniform volume fraction. Thus, it can be concluded that the enhancement of the convective heat transfer could not be solely attributed to the enhancement of the effective thermal conductivity, and beside other reasons, which may be listed as this higher enhancement, particle migration is proposed to be an important reason.* [DOI: 10.1115/1.4000743]

Keywords: nanofluids, heat transfer, thermophoresis, Brownian motion, nonuniform particle distribution

1 Introduction

A possible effective way of improving the heat-transfer performance of common fluids is to suspend various types of small solid particles, such as metallic and nonmetallic particles, in conventional fluids, such as water, mineral oils, and ethylene glycol, to form colloidal. Such a technique is not new; however, suspended micron and millimeter sized particles may cause some severe problems in the flow channels. The major problem with the use of such large particles is the rapid settling of these particles in fluids. Furthermore, these conventional suspensions do not work with the emerging miniaturized devices because they can clog the tiny channels of such devices.

Recent developments in nanotechnology and related manufacturing techniques have made possible the production of nanosized particles. Fluids with nanoparticles suspended in them are called nanofluids, as was coined by Choi [1] to describe this new class of nanotechnology-based heat-transfer fluids, which exhibit thermal properties superior to those of their base fluids or conventional particle fluid suspensions.

Many researchers have reported experimental studies on the thermal conductivity and viscosity of nanofluids [2–8]. Moreover, various mechanisms and models have been proposed for explaining the enhancement of thermal conduction of nanofluids using various assumptions. Koo and Kleinstreuer [9] considered the kinetic energy of the nanoparticles due to the Brownian movement and proposed a model for the effective thermal conductivity of nanofluids. Prasher et al. [10] introduced a Brownian-motion-based convective-conductive model, which predicts the right trend with respect to different parameters such as nanoparticle volume fraction, nanoparticle diameter, and temperature. Jang and Choi [11,12] proposed and modeled the Brownian-motion induced nanoconvection as a key nanoscale mechanism governing the thermal behavior of nanofluids. In their model effects of various parameters such as the ratio of the thermal conductivity of nanoparticles to that of a base fluid, volume fraction, nanoparticle size, and temperature on the effective thermal conductivity of nanofluids was included.

To investigate the heat-transfer enhancement by very fine particles suspended in a fluid, two main approaches have been adopted in the literature. The first one is the two-phase model that takes into account the fluid and solid phase role in the heat-transfer process. The second one is the single-phase model where both the fluid phase and the solid particles are in thermal equilibrium state and flow with the same local velocity. This approach is simpler and requires less computational time. Also, if the main interest is focused on the heat-transfer process, the modified single-phase is more convenient than the two-phase model.

The number of studies available in convective heat-transfer area is limited compared with that in the area of thermal conductivity of nanofluids. Wen and Ding [13] reported heat-transfer enhancement due to the addition of γ-Al_2O_3 nanoparticles to de-ionized water flowing through a copper tube in the laminar flow regime. Their results indicate that the Nusselt number increases up to 47% when 1.6% volume fraction of γ-Al_2O_3 nanoparticles is added to water. They proposed that particle migration may be a reason for this enhancement. Zeinali Heris et al. [14] conducted an experimental investigation to study a laminar flow forced convection heat transfer of Al_2O_3/water nanofluid inside a circular tube with constant wall temperature. Raisee and Moghadami [15] performed a numerical study to investigate the hydrodynamic and thermal characteristics of water/γ-Al_2O_3 mixture flows through circular pipes. Their observations show that temperature dependency (Brownian motion) has a significant effect on the heat-transfer characteristics of nanofluids. Hwang et al. [16] measured the pressure drop and convective heat-transfer coefficient of water-based Al_2O_3 nanofluids flowing through a uniformly heated circular tube in the fully developed laminar flow regime. They discussed the various parameter effects on remarkable enhancement of the convective heat-transfer coefficient and showed for the first time the flattened velocity profile due to particle migration induced by Brownian diffusion and thermophoresis.

Contributed by the Heat Transfer Division of ASME for publication in the JOURNAL OF HEAT TRANSFER. Manuscript received March 10, 2009; final manuscript received November 2, 2009; published online March 24, 2010. Assoc. Editor: Patrick E. Phelan.

It is expected that the main reasons for heat-transfer enhancement of nanofluids may be from the various effects of thermal conductivities under static and dynamic conditions [17], energy transfer by nanoparticles dispersion [8,18,19], particle migration due to viscosity gradient, and nonuniform shear rate [20,21], Brownian diffusion, and thermophoresis [22], beside substantial augmentation of the thermal conductivity. Therefore, the convective heat-transfer coefficient of the nanofluids is a function of properties, dimension, and volume fraction of suspended nanoparticles as well as the flow velocity.

Recently, using the order of magnitude analysis, Buongiorno [22] presented seven slip mechanisms and concluded that Brownian diffusion (movement of nanoparticles from the high concentration site to the low concentration site) and thermophoresis (movement of nanoparticles from the high temperature site to the low temperature site) are important slip mechanisms in nanofluids. Based on this finding, he developed a two-component four-equation nonhomogeneous equilibrium model for mass, momentum, and heat transport in nanofluids.

In this paper, by using Buongiorno's model [22], an investigation is carried out to study the effects of particle migration due to Brownian diffusion as well as thermophoresis for explaining further heat-transfer enhancement observed in convective heat-transfer of nanofluids in a laminar tube flow. To do this, the thermophysical properties of nanofluids will be considered as given functions of the temperature and nanoparticle volumetric fraction. Also, it is assumed that the flow is hydrodynamically developed while thermally developing.

2 Thermophysical Properties of Nanofluids

Thermophysical properties of nanofluids are calculated by using the following formulas.

The density of nanofluids is predicted by the mixing theory as [22]

$$\rho = \varphi\rho_p + (1-\varphi)\rho_{\mathrm{bf}} \tag{1}$$

It should be noted that for calculating the specific heat of nanofluid, some of prior researchers have used the following correlation [3,8]:

$$C_p = \varphi C_{p,p} + (1-\varphi)C_{p,\mathrm{bf}} \tag{2}$$

But, in the present work, the more accurate relationship for the specific heat of nanofluid, which is based on the thermal equilibrium model [23], has been used, that is

$$C_p = \frac{\varphi\rho_p C_{p,p} + (1-\varphi)\rho_{\mathrm{bf}}C_{p,\mathrm{bf}}}{\rho} \tag{3}$$

As no generally accepted correlations currently exist for determining the nanofluid dynamic viscosity and thermal conductivity as a function of temperature and volume fraction, simultaneously, we have opted to use the correlations given by Williams et al. [24] as well as by Rea et al. [25], derived for the alumina-water nanofluid

$$\mu(\varphi,T) = \mu_{\mathrm{bf}}(T)\exp[4.91\varphi/(0.2092-\varphi)] \tag{4}$$

$$k(\varphi,T) = k_{\mathrm{bf}}(T)(1+4.5503\varphi) \tag{5}$$

The applicable temperature range of these equations is $20^\circ\mathrm{C} < T < 80^\circ\mathrm{C}$, with volumetric loadings of up to 6% [24,25]. Also, the density and specific heat of alumina are chosen as $3920\ \mathrm{kg/m^3}$ and 880 J/kg K, respectively. These data correspond to the same nanofluid used in Refs. [24,25].

It is important to mention here that Eqs. (4) and (5) have been derived for the alumina-water nanofluid used in Refs. [24,25]. The reason of such utilization resides in the fact that, although there exists some formulas that can be employed to compute for the dynamic viscosity and thermal conductivity of the nanofluid, but these formulas are not general and each has their limitations. Moreover, up to date, there is no generally accepted correlation to predict the dynamic viscosity and the thermal conductivity of nanofluid as a function of temperature and volume fraction. Therefore, under the scope of the present research, which emphasizes the effect of particle migration on heat transfer and pressure drop, using these equations, which presented the dynamic viscosity and thermal conductivity of the alumina-water nanofluid as a function of temperature as well as volume fraction of nanoparticles, seems to be useful in the simulation.

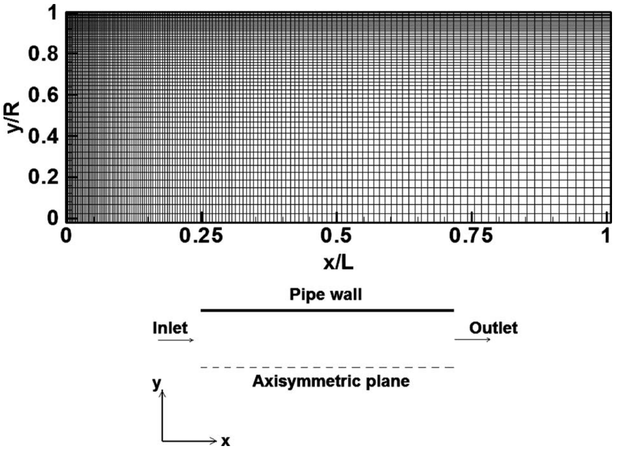

Fig. 1 Grid layout and geometry of problem

3 Mathematical Formulation

The problem under consideration is a two-dimensional (axisymmetric) steady, forced laminar convection flow of a nanofluid flowing inside a straight circular tube. The fluid enters the circular tube with a developed velocity profile and a uniform temperature. The flow and thermal fields are assumed to be axisymetric with respect to the horizontal plane parallel to *x*-axis, as shown in Fig. 1.

The nanofluid is treated as a two-component mixture (base fluid+nanoparticles) with the following assumptions [22]:

(1) incompressible flow
(2) no chemical reactions
(3) negligible external forces
(4) dilute mixture ($\varphi \ll 1$)
(5) negligible viscous dissipation
(6) negligible radiative heat transfer
(7) the nanoparticles and the base fluid are in thermal equilibrium locally

Therefore, under the above assumptions, the continuity equation for the nanofluid, nanoparticle continuity equation, nanofluid momentum equation, and nanofluid energy equation, can be expressed, respectively, as [22]

$$\nabla\cdot V = 0 \tag{6}$$

$$V\cdot\nabla\varphi = \nabla\cdot\left[D_B\nabla\varphi + D_T\frac{\nabla T}{T}\right] \tag{7}$$

$$\rho(V\cdot\nabla V) = -\nabla P + \nabla\cdot\mu\nabla V \tag{8}$$

$$(\rho C_p)V\cdot\nabla T = \nabla\cdot k\nabla T \tag{9}$$

Equation (7) states that nanoparticles not only can move homogeneously with the fluid (first term of the left-hand side), but also they possess a slip velocity relative to the fluid (right-hand side) due to Brownian diffusion and thermophoresis. Brownian motion is proportional to the volumetric fraction of nanoparticles, whereas the thermophoresis is proportional to the temperature gradient. In Eq. (7), D_B represents the Brownian diffusion coefficient, given by the Einstein–Stokes equation, and D_T represents the thermophoretic diffusion coefficient of the nanoparticles

$$D_B = \frac{k_B T}{3\pi\mu d_p} \tag{10}$$

$$D_T = \left(\frac{0.26k}{2k + k_p}\right)\left(\frac{\mu}{\rho}\right)\varphi \tag{11}$$

where K_B is the Boltzmann's constant ($K_B = 1.3807\times 10^{-23}$ J/K).

Note that the expression for D_T (Eq. (11)) was established for particles greater than 1 μm in diameter [26].

Although the phenomenon of thermophoresis in gases is well understood and can be calculated accurately, for liquids, the converse is true [27,28]. Unfortunately there is very little experimental data and considerable confidence is placed on the experimental data of McNab and Meisen [26], which were obtained for particle sizes greater than 1 μm in diameters. However, the thermophoretic velocity appears to be independent of particle size [29]. Thus, we have used Eq. (11) for simulating the thermophoretic effect in the present work (see Refs. [22,30,31]).

The following boundary conditions were used for solving for the coupled nonlinear partial differential equations given above. At the tube inlet section, a parabolic velocity profile, a uniform temperature profile T_{in}, and uniform particle distribution φ_m are specified. The length of the computational domain is chosen large enough so that the flow exits the pipe with fully developed velocity and temperature profiles. Therefore, at the outlet section, the zero normal gradient condition is applied.

On the wall surface of the tube, the no-slip boundary condition and constant wall temperature were imposed. Due to impermeability, the total nanoparticle mass flux at the wall is zero, i.e.

$$\left[D_B \nabla \varphi + D_T \frac{\nabla T}{T}\right]_{\text{wall}} = 0 \tag{12}$$

On the tube center of the pipe, the symmetry boundary condition, which is the zero normal gradient for all variables, was applied.

4 Numerical Method and Validation

The system of governing Eqs. (6)–(9) constitute a complete set of equations from which $\boldsymbol{V}$ (velocity vector field), P (pressure field), φ (particle volume fraction distribution), and T (temperature field) can be calculated, once the boundary conditions and the nanofluid transport coefficients (ρ, C, μ, k, D_B, and D_T) are known as functions of φ and the temperature.

Note that the conservation equations (Eqs. (6)–(9)) are strongly coupled. That is, $\boldsymbol{V}$ depends on φ via viscosity, φ depends on T mostly because of thermophoresis, T depends on φ via thermal conductivity and also via the Brownian and thermophoretic terms in the energy equation, and φ and T obviously depend on $\boldsymbol{V}$ because of the convection terms in the nanoparticle continuity and energy equations, respectively.

In the present study, the system of governing Eqs. (6)–(9) were solved using the finite volume method. In this technique, integrating the governing equations over the finite control-volumes results in a set of algebraic equations that can be solved numerically. Staggered grids have been used, where the velocity components are calculated at the center of the volume interfaces, while the pressure as well as other scalar quantities such as temperature are computed at the center of the control-volume. The algebraic discretization equations have been solved sequentially as well as iteratively throughout the physical domain by combining the line-by-line procedure and the well-known tri-diagonal matrix algorithm (TDMA) technique. Pressure and velocity were coupled using semi-implicit method for pressure linked equations (SIMPLE) [32].

As shown in Fig. 1, the grid used for computations consists of 150×60 grid nodes in the streamwise (x) and radial (y) directions, respectively. The grid spacing of the domain was tested and it was found that further increase in the total number of nodal points did not improve the accuracy appreciably. As can be seen, the grid points are highly packed near the pipe entrance, as well as near the wall in order to resolve the sharp gradients of variables in these regions.

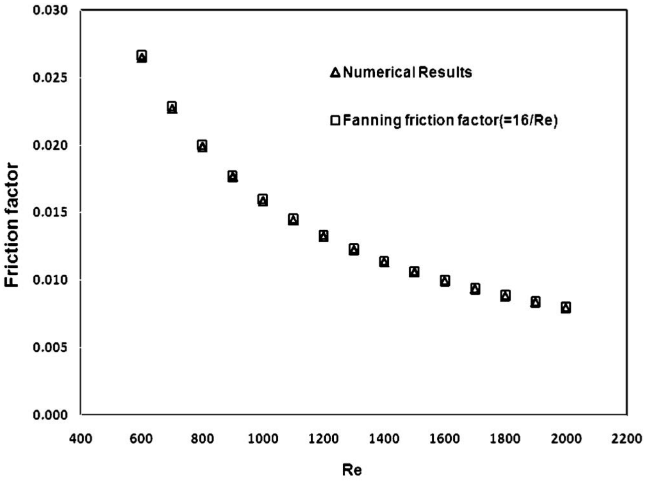

Fig. 2 Comparison of the friction factors in fully developed region

The computer program was successfully validated by comparing the calculated results with the available data in the literature for the classical problem of the laminar flow of pure water in tubes, i.e., $\varphi_m = 0$. To do this, first developing laminar flow and heat transfer of a pure water through a pipe at Re = 1000 is computed. It is assumed that the flow enters the pipe with uniform velocity and temperature. A constant temperature is applied as the wall thermal boundary condition.

Figure 2 shows that the friction factor obtained in the fully developed region of the pipe is in complete agreement with the well-known Fanning friction factor, i.e., $f = 16/\text{Re}$ [33]. Moreover, the local Nusselt number obtained from our computer program is compared with the following Shah equations [33,34] of the local Nusselt number in a circular tube for a constant wall temperature in Fig. 3

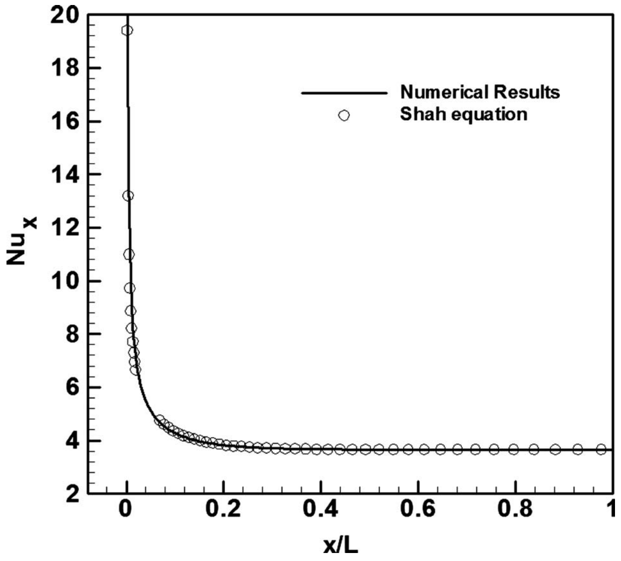

Fig. 3 Comparison of the Shah equation and numerical results for local Nusselt number of pure water

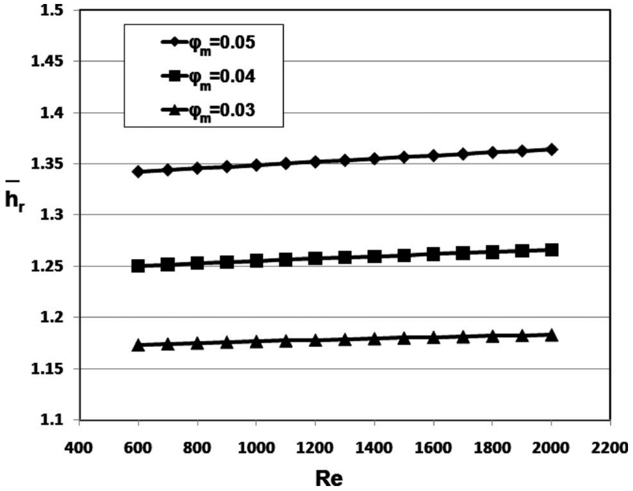

Fig. 4 Effect of nanoparticle volume fraction on the averaged heat-transfer coefficient ratio

$$\mathrm{Nu}_x = \begin{cases} 1.077x_*^{-1/3} - 0.70, & x_* \le 0.01 \\ 3.657 + 6.874(10^3 x_*)^{-0.488} e^{-57.2x_*}, & x_* > 0.01 \end{cases} \tag{13}$$

where

$$\mathrm{Nu}_x = h(x) d_{\mathrm{tube}} / k_{\mathrm{water}}$$

$$x_* = [(x/d_{\mathrm{tube}})/(\mathrm{Re}_{d_{\mathrm{tube}}}\, \mathrm{Pr})].$$

Again, a good agreement is apparently displayed between the results obtained by our computer code and that of the Shah equation [33,34]. Thus, these results confirm the validity of the computational scheme used in the present investigation.

5 Results and Discussion

The working nanofluid used in this simulation is γAl_2O_3-water mixture. The thermophysical properties of water as the base fluid are temperature-dependent and computed by the correlations proposed by Hagen [35].

Numerical simulation has been carried out for the following values and ranges: Re=600–2000, $\varphi_m = 0.03, 0.04, 0.05$, $T_w = 353$ K, and $T_{\mathrm{in}} = 293$ K.

Figure 4 shows the computed average wall heat-transfer coefficient ratio $\overline{h}_r = \overline{h}/\overline{h}_{\mathrm{bf}}$ (ratio of the averaged wall heat-transfer coefficient for nanofluid to the averaged wall heat-transfer coefficient for pure water).

Here the average wall heat-transfer coefficients for the base fluid and nanofluid are calculated as:

$$\overline{h} = \frac{1}{L}\int_0^L \left\{ k \left.\frac{\partial T}{\partial y}\right|_{\mathrm{wall}} / (T_w - T_b) \right\} dx \tag{14}$$

$$\overline{h}_{\mathrm{bf}} = \frac{1}{L}\int_0^L \left\{ k_{\mathrm{bf}} \left.\frac{\partial T}{\partial y}\right|_{\mathrm{wall}} / (T_w - T_b) \right\} dx \tag{15}$$

where T_b is the bulk temperature of the fluid in each section.

As is seen in Fig. 4, addition of alumina nanoparticles to pure water effectively enhances convective heat transfer in the laminar regime. The level of heat transfer increase depends on the volume concentration. For the lowest value of $\varphi_m = 0.03$, the heat-transfer increase is approximately 17%, while at the upper limit of $\varphi_m = 0.05$, the level of heat-transfer augmentation reaches to about 37%. Also, the heat-transfer enhancement increases slightly by increasing the Reynolds number for a fixed value of volume concentration.

In Figs. 5 and 6 the effects of particle volume concentration on the axial wall heat-transfer coefficient ratio distribution of water–γAl_2O_3 nanofluid at Re=600 and Re=2000 are presented, respectively. The influence of the addition of nanoparticles to the base fluid on heat-transfer enhancement is also visible in these figures.

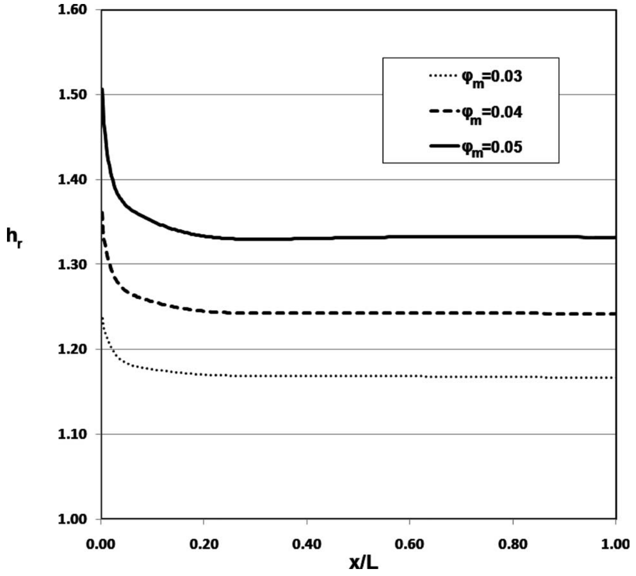

Fig. 5 Wall heat-transfer coefficient ratio distribution at Re =600

This study is based on the model developed by Buongiorno [22]. The difference of this model with single-phase traditional ones is the existence of the nanoparticle continuity equation, i.e., Eq. (7). This equation states that nanoparticles can move homogeneously with the fluid, but they also possess a slip velocity relatively to the fluid, which is due to Brownian diffusion and thermophoresis. This slip phenomenon causes a nonuniform particle distribution, which results in a nonuniform distribution of thermal conductivity and viscosity field and reduces the thermal boundary layer thickness. Prediction of how much can it affect the heat-transfer coefficient and wall shear stress is the main purpose of this article.

The effect of particle migration due to Brownian diffusion and thermophoresis on the averaged heat-transfer coefficient is illustrated in Fig. 7. Here the vertical axis denotes the ratio of the

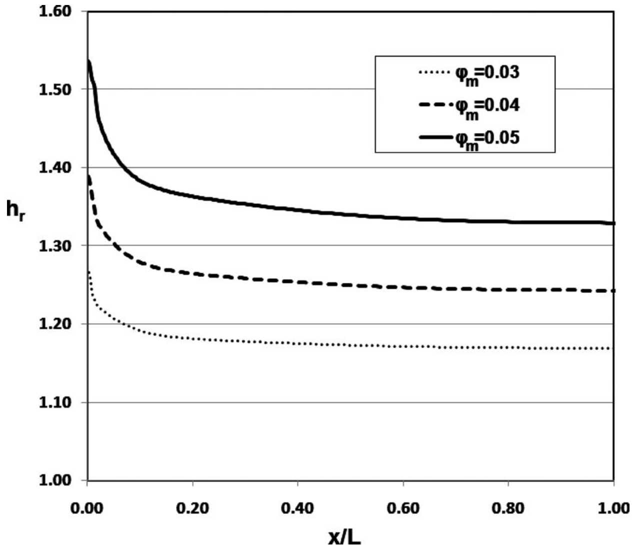

Fig. 6 Wall heat-transfer coefficient ratio distribution at Re =2000

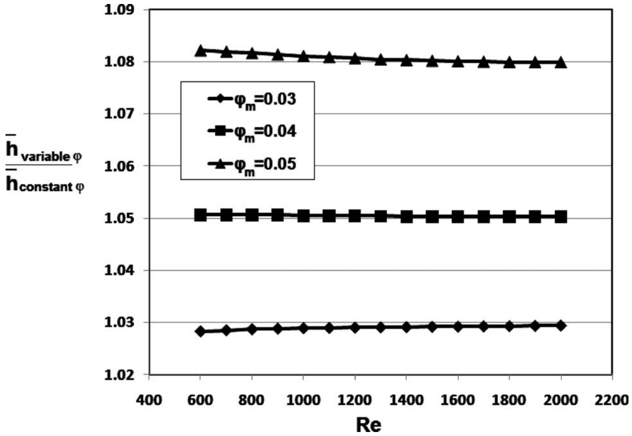

Fig. 7 The effect of particle migration on the averaged heat-transfer coefficient

averaged heat-transfer coefficients with and without consideration of the particle distribution. By eliminating Eq. (7) as a transport equation for nanoparticles and assuming that there is a uniform particle concentration in the flow field, one can solve for Eqs. (6), (8), and (9) as the governing equations and compute for the desired flow and heat-transfer parameters.

With reference to Fig. 7, it is clear that higher heat transfer is achieved by considering a nonuniform distribution of particle concentration caused by thermophoresis and Brownian motion. For the lowest value of $\varphi_m = 0.03$, the heat-transfer enhancement is about 3%, while at the upper limit of $\varphi_m = 0.05$, the level of heat-transfer enhancement reaches to about 8%. Also, computations show that the heat-transfer enhancement due to particle migration is insensitive to the Reynolds number for a fixed value of mean volume concentration of nanoparticles. Moreover, the local heat-transfer coefficients for two lower and upper limits of Reynolds number and the mean volume concentration of nanoparticles are shown in Figs. 8 and 9.

The effect of particle migration on the averaged wall shear stress is demonstrated in Fig. 10. Here the vertical axis denotes the ratio of the averaged wall shear stress with and without consideration of particle distribution.

The local and averaged wall shear stresses of nanofluid are obtained as

$$\tau_w = \mu \left. \frac{\partial u}{\partial y} \right|_{\text{wall}} \tag{16}$$

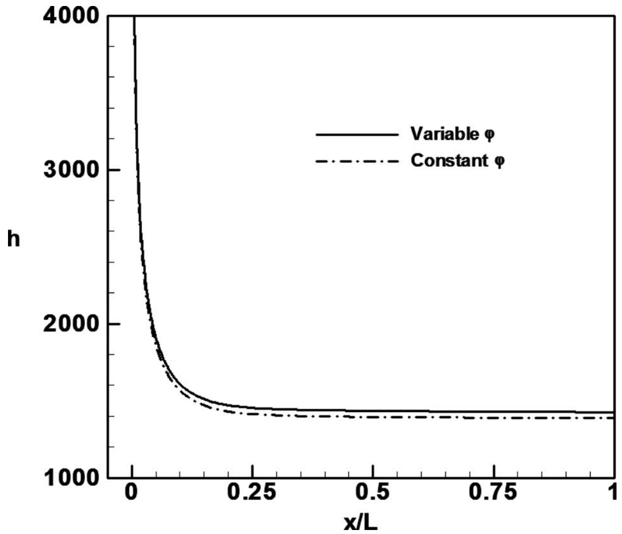

Fig. 8 The effect of particle migration on the local heat-transfer coefficient at Re=600 and $\varphi_m = 0.03$

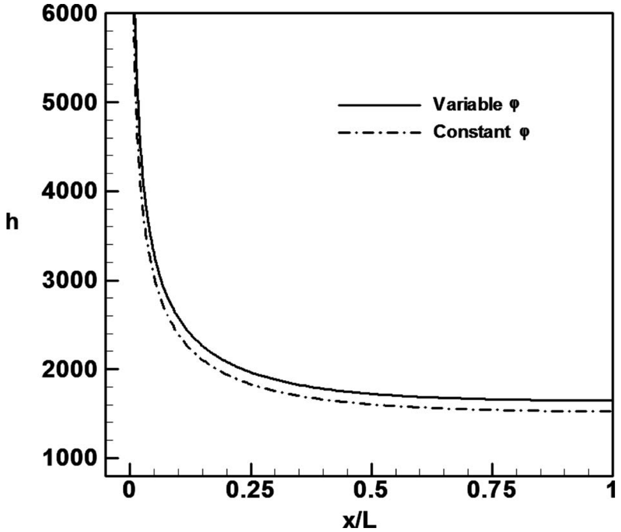

Fig. 9 The effect of particle migration on the local heat-transfer coefficient at Re=2000 and $\varphi_m = 0.05$

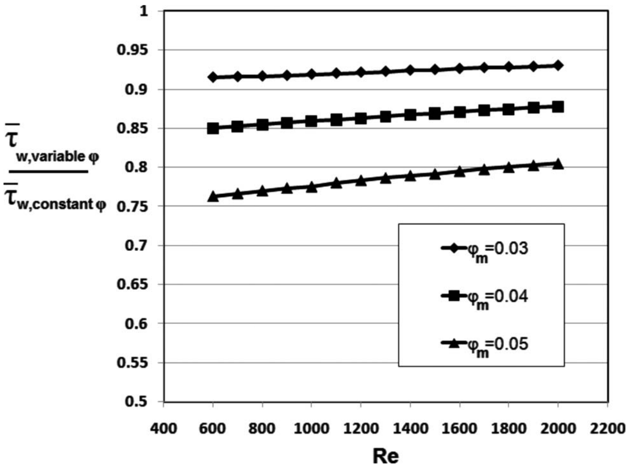

Fig. 10 The effect of particle migration on the averaged wall shear stress

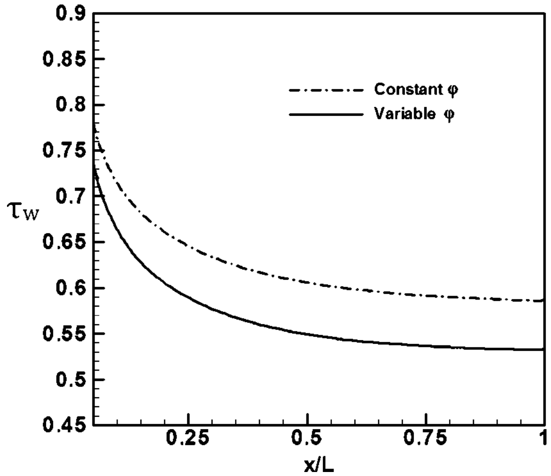

Fig. 11 The effect of particle migration on the local wall shear stress at Re=600 and $\varphi_m = 0.03$

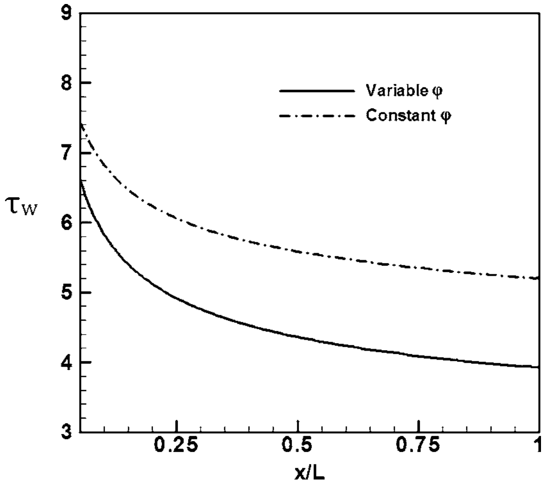

Fig. 12 The effect of particle migration on the local wall shear stress at Re=2000 and φ_m=0.05

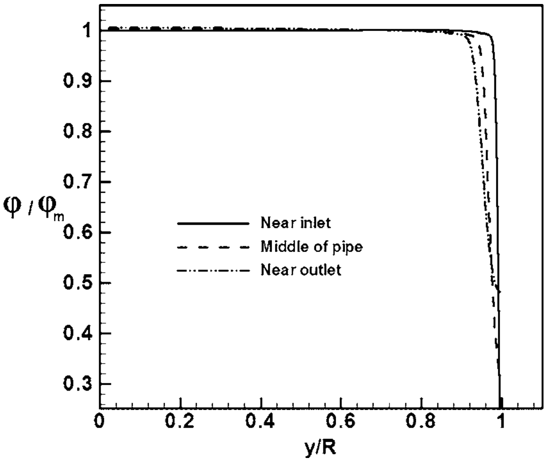

Fig. 13 Radial particle concentration distribution at Re=600 and φ_m=0.03

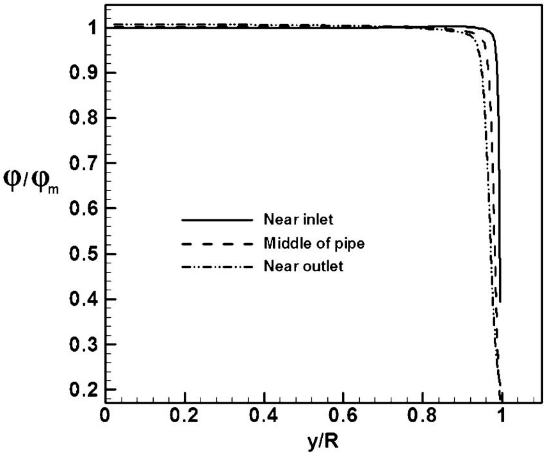

Fig. 14 Radial particle concentration distribution at Re=2000 and φ_m=0.05

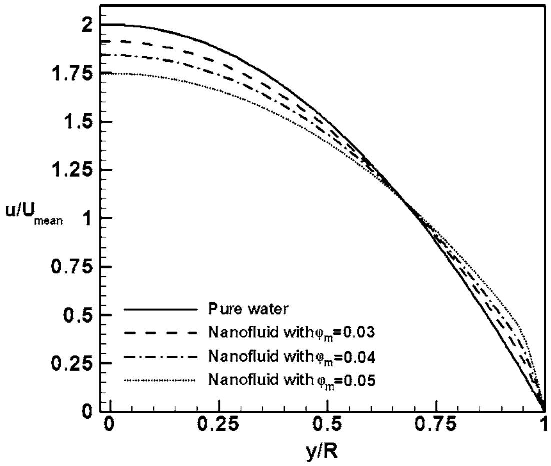

Fig. 15 Dimensionless velocity profile at Re=600

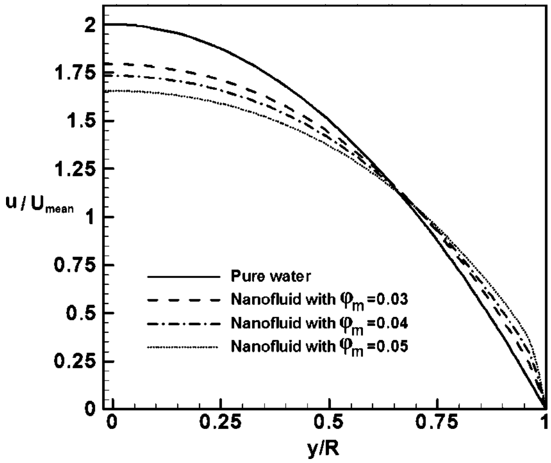

Fig. 16 Dimensionless velocity profile at Re=2000

$$\overline{\tau_w} = \frac{1}{L}\int_0^L \left\{ \mu \left. \frac{\partial u}{\partial y} \right|_{\text{wall}} \right\} dx \tag{17}$$

Obviously, by taking into account the particle migration, the averaged shear stresses are reduced. As shown in Fig. 10, this reduction is roughly between 7% and 24%. Moreover, the local heat-transfer coefficients for two lower and upper limits of Reynolds number and the mean volume concentration of particles are shown in Figs. 11 and 12.

Table 1 Effect of migration mechanisms on heat transfer and wall shear stress

		Re=600 and φ_m=0.03	Re=2000 and φ_m=0.05
Enhancement of averaged heat-transfer coefficient (%)	$(D_B=0,\ D_T=0)$	14.1	26.3
	$(D_B=0,\ D_T\neq 0)$	15.99	31.7
	$(D_B\neq 0,\ D_T\neq 0)$	17.34	36.4
Enhancement of averaged wall shear stress (%)	$(D_B=0,\ D_T=0)$	278.2	693.5
	$(D_B=0,\ D_T\neq 0)$	263.6	604.6
	$(D_B\neq 0,\ D_T\neq 0)$	254.7	558.2

Table 2 Numerical result for computing Eq. (19) (Re=2000, $\varphi_m=0.04$)

Node	y/R	$u_{\mathrm{in}}/U_{\mathrm{mean}}$	$\varphi_{\mathrm{in}}/\varphi_m$	$u_{\mathrm{out}}/U_{\mathrm{mean}}$	$\varphi_{\mathrm{out}}/\varphi_m$	$F_j=0.25\times(A_{j+1}^2-A_j^2)\times B_j\times C_j$ $j=1,2,\ldots,59$	$G_j=0.25\times(A_{j+1}^2-A_j^2)\times D_j\times E_j$ $j=1,2,\ldots,59$
(j)	A_j	B_j	C_j	D_j	E_j	F_j	G_j
1	0.000000	2.000000	1.000000	1.733800	1.005200	0.000252	0.000220
2	0.022471	1.999000	1.000000	1.733800	1.005200	0.001899	0.001656
3	0.065614	1.991400	1.000000	1.729200	1.005200	0.003560	0.003107
4	0.107030	1.977100	1.000000	1.720700	1.005100	0.004988	0.004363
5	0.146790	1.956900	1.000000	1.708600	1.005100	0.006195	0.005437
6	0.184960	1.931600	1.000000	1.693300	1.005000	0.007196	0.006339
7	0.221610	1.901800	1.000000	1.675100	1.004900	0.008002	0.007083
8	0.256790	1.868100	1.000000	1.654300	1.004800	0.008632	0.007681
9	0.290560	1.831200	1.000000	1.631100	1.004700	0.009106	0.008149
10	0.322980	1.791400	1.000000	1.605800	1.004500	0.009437	0.008497
11	0.354100	1.749200	1.000000	1.578600	1.004400	0.009644	0.008742
12	0.383980	1.705100	1.000000	1.549600	1.004300	0.009739	0.008889
13	0.412660	1.659400	1.000000	1.519200	1.004100	0.009744	0.008957
14	0.440200	1.612500	1.000000	1.487400	1.003900	0.009662	0.008947
15	0.466630	1.564500	1.000000	1.454400	1.003800	0.009516	0.008880
16	0.492010	1.515900	1.000000	1.420500	1.003600	0.009309	0.008755
17	0.516370	1.466700	1.000000	1.385700	1.003400	0.009058	0.008587
18	0.539760	1.417300	1.000000	1.350200	1.003200	0.008766	0.008377
19	0.562210	1.367800	1.000000	1.314200	1.003000	0.008449	0.008142
20	0.583770	1.318400	1.000000	1.277800	1.002800	0.008103	0.007876
21	0.604460	1.269300	1.000000	1.241100	1.002500	0.007744	0.007591
22	0.624320	1.220400	1.000000	1.204200	1.002300	0.007376	0.007295
23	0.643390	1.172100	1.000000	1.167200	1.002000	0.007002	0.006987
24	0.661700	1.124300	1.000000	1.130300	1.001800	0.006622	0.006670
25	0.679270	1.077200	1.000000	1.093500	1.001500	0.006249	0.006353
26	0.696140	1.030800	1.000000	1.056900	1.001200	0.005880	0.006036
27	0.712340	0.985140	1.000000	1.020600	1.000900	0.005516	0.005719
28	0.727890	0.940350	1.000000	0.984560	1.000500	0.005162	0.005407
29	0.742820	0.896450	1.000000	0.948980	1.000200	0.004817	0.005100
30	0.757150	0.853460	1.000000	0.913850	0.999820	0.004483	0.004799
31	0.770900	0.811420	1.000000	0.879220	0.999430	0.004167	0.004513
32	0.784110	0.770340	1.000000	0.845140	0.999020	0.003861	0.004231
33	0.796790	0.730260	1.000000	0.811640	0.998580	0.003568	0.003960
34	0.808960	0.691170	1.000000	0.778750	0.998120	0.003289	0.003699
35	0.820640	0.653090	1.000000	0.746490	0.997620	0.003027	0.003452
36	0.831860	0.616020	1.000000	0.714890	0.997090	0.002777	0.003214
37	0.842630	0.579960	1.000000	0.683970	0.996510	0.002542	0.002987
38	0.852970	0.544900	1.000000	0.653730	0.995900	0.002319	0.002770
39	0.862890	0.510840	1.000000	0.624190	0.995220	0.002112	0.002568
40	0.872420	0.477780	1.000000	0.595360	0.994490	0.001915	0.002373
41	0.881560	0.445700	1.000000	0.567230	0.993680	0.001733	0.002192
42	0.890340	0.414580	1.000000	0.539800	0.992770	0.001563	0.002021
43	0.898770	0.384420	1.000000	0.513080	0.991730	0.001404	0.001858
44	0.906860	0.355200	1.000000	0.487050	0.990530	0.001257	0.001707
45	0.914630	0.326900	1.000000	0.461710	0.989100	0.001120	0.001564
46	0.922090	0.299510	1.000000	0.437050	0.987220	0.000993	0.001430
47	0.929250	0.273000	1.000000	0.413020	0.984250	0.000875	0.001302
48	0.936120	0.247360	1.000000	0.389570	0.978140	0.000767	0.001181
49	0.942720	0.222570	1.000000	0.366490	0.963420	0.000666	0.001057
50	0.949050	0.198610	1.000000	0.343360	0.929330	0.000575	0.000924
51	0.955130	0.175450	1.000000	0.319360	0.862250	0.000491	0.000770
52	0.960970	0.153080	1.000000	0.293340	0.756970	0.000413	0.000599
53	0.966570	0.131480	1.000000	0.264140	0.629450	0.000343	0.000433
54	0.971950	0.110620	1.000000	0.231250	0.509220	0.000279	0.000297
55	0.977120	0.090488	1.000000	0.195140	0.414590	0.000219	0.000196
56	0.982070	0.071061	1.000000	0.156870	0.347200	0.000166	0.000128
57	0.986830	0.052319	1.000000	0.117520	0.301870	0.000118	0.000080
58	0.991400	0.034241	1.000000	0.077929	0.272380	0.000075	0.000046
59	0.995790	0.016808	1.000000	0.038682	0.253230	0.000035	0.000021
60	1.000000	0.016808	1.000000	0.038682	0.253230	Sum(F_1,F_{59}) $=0.254776$	Sum(G_1,G_{59}) $=0.252215$

The augmentation of the heat-transfer coefficient and the reduction in the shear stress due to inclusion of particle migration can be explained as follows: From Figs. 13 and 14, one can see that particles migrate to the core region of the pipe. In the vicinity of the wall, the velocity is negligible and the diffusion terms in Eq. (7) become dominant. Thus, the skidding of nanoparticles due to Brownian diffusion and thermophoresis leads to particle depletion in the wall region. On the other hand, the particle volume fraction in the centerline of the pipe increases and leads to the increasing of the viscosity and thermal conductivity of nanofluids near the centerline. Moreover, as a consequence of the viscosity increase near the centerline, velocity profile predicted by Eq. (8) is flattened, as shown in Figs. 15 and 16. Hence, although the slope of velocity near the wall is increased, this effect is countered with the diminishing of nanofluid viscosity at the vicinity of the wall, so the net effect (see Eq. (4)), makes the wall shear stresses smaller. In addition, since the bulk mean temperature and the heat-transfer coefficient are defined as

$$T_b = \frac{1}{U_{\text{mean}} A_c} \int_{A_c} u T dA_c, \quad h = -k \left. \frac{\partial T}{\partial y} \right|_{\text{wall}} / (T_w - T_b) \tag{18}$$

with flattened velocity profile (see Figs. 15 and 16), the bulk mean temperature increases and, as a consequence, the difference between the tube wall temperature (T_w) and bulk mean temperature (T_b) of the nanofluid decreases. Although the numerator decreases slightly compared with constant particle concentration case, the decline of denominator is dominant and the resultant effect of particle migration on heat-transfer is positive, i.e., the heat transfer is increased.

The above results also explain why nanofluids are likely to give higher heat transfer with a relatively lower pressure penalty due to lower viscosity near the wall. Furthermore, as seen from Figs. 13 and 14, for the considered cases, migration of particles to the core region may not encourage the formation of clusters/aggregates and non-Newtonian behavior due to high solid concentrations.

It is worthwhile here to investigate the quantitative contribution of thermophoretic and Brownian diffusion to the overall heat-transfer enhancement. But it should be noted that, as can be seen from Eqs. (7), (10), and (11), these two phenomena are coupled, i.e., the behavior of these two diffusions are such that one affects the another. Therefore, it cannot be concluded that the effects of these two mechanisms are additive. In Table 1 the effects of migration mechanisms on the averaged heat-transfer coefficient and wall shear stress have been shown. These effects have been displayed for two lower and upper bounds of Reynolds numbers and nanoparticle volume fractions, i.e., Re=600 and $\varphi_m=0.03$, and Re=2000 and $\varphi_m=0.05$. The case of $D_B=D_T=0$ certainly shows the enhancement without considering the migration mechanisms. It is clear that the effects of particle migration in these two lower and upper cases are the augmentation of heat transfer from 3.24% to 10.1%, while it reduces the averaged shear stress between 23.5% and 135.3%.

Finally, to verify the integrity of the solution again, here, the condition that the flow bulk concentration of nanoparticles at any cross section should be equal to the initial mean concentration of nanoparticles is checked, i.e.

$$\int_0^R u_{\text{in}} \varphi_m y dy = \int_0^R u \varphi y dy \tag{19}$$

To do this, we consider the typical condition Re=2000 and $\varphi_m=0.04$ and compute for the left and right integrals of the above equation at the inlet and outlet of the pipe, respectively. For computing for these integrals the well known trapezoidal rule has been used in each interval. The numerical results are presented in Table 2. As can be seen from this table, the summation of F_js and G_js, which indicates the left- and right-hand side integrals of Eq. (19), respectively, is very close to each other. The error is less than 1%, which is reasonable. This coincidence of flow bulk concentration indicates the integrity of the solution again.

6 Conclusion

The effect of particle migration duo to Brownian motion and thermophoresis on convective heat-transfer coefficient and wall shear stress has been investigated. Results obtained show that particle migration due to these effects could result in nonuniformity in particle concentration in such a way that, in the vicinity of wall region, the particle concentration is reduced. Also, compared with constant particle concentration, the nonuniform distribution leads to a higher heat-transfer coefficient while the wall shear stress is decreased. Therefore, it seems that particle migration can play an important role and explain the further heat-transfer enhancement observed in convective heat transfer of nanofluids.

Nomenclature

C = nanofluid specific heat (J/kg K)
C_{bf} = base fluid specific heat (J/kg K)
C_p = Nanoparticle specific heat (J/kg K)
d = pipe diameter (m)
D_B = Brownian diffusion coefficient (m^2/s)
D_T = thermal diffusion coefficient (m^2/s)
h = heat-transfer coefficient (W/m^2 K)
k = nanofluid thermal conductivity (W/m K)
k_B = Boltzmann constant (J/K)
k_p = nanoparticle thermal conductivity (W/m K)
L = total length of pipe (m)
P = pressure (Pa)
R = radius of pipe (m)
Re = Reynolds number
T = nanofluid temperature (K)
u = nanofluid axial velocity (m/s)
V = nanofluid velocity (m/s)
x = axial coordinate (m)
y = radial coordinate (m)

Greek Symbols

φ = nanoparticle volumetric fraction
μ = viscosity (Pa s)
ρ = nanofluid density (kg/m^3)
ρ_{bf} = base fluid density (kg/m^3)
ρ_p = nanoparticle density (kg/m^3)
τ_w = shear stress at the wall (Pa)

Subscripts

b = bulk
bf = base fluid
in = inlet
m = mean
out = outlet
p = nanoparticle
w = wall

Superscript

$\bar{\ }$ = averaged property

References

[1] Choi, S., 1995, "Enhancing Thermal Conductivity of Fluids With Nanoparticles," *Developments and Applications of Non-Newtonian Flows*, D. A. Siginer and H. P. Wang, eds., ASME, New York, FED-Vol. 231/MD-Vol. 66, pp. 99–105.
[2] Mintsa, H. A., Roy, G., Nguyen, C. T., and Doucet, D., 2009, "New Temperature Dependent Thermal Conductivity Data for Water-Based Nanofluids," Int. J. Therm. Sci., **48**, pp. 363–371.
[3] Lee, J. H., Hwang, K. S., Jang, S. P., Lee, B. H., Kim, J. H., Choi, S. U. S., and Choi, Ch. J., 2008, "Effective Viscosities and Thermal Conductivities of Aqueous Nanofluids Containing Low Volume Concentrations of Al_2O_3 Nanoparticles," Int. J. Heat Mass Transfer, **51**, pp. 2651–2656.
[4] Murshed, S. M. S., Leong, K. C., and Yang, C., 2008, "Investigations of Thermal Conductivity and Viscosity of Nanofluids," Int. J. Therm. Sci., **47**, pp. 560–568.
[5] Das, S. K., Putra, N., Thiesen, P., and Roetzel, W., 2003, "Temperature Dependence of Thermal Conductivity Enhancement for Nanofluids," ASME J. Heat Transfer, **125**, pp. 567–574.
[6] Hwang, Y., Lee, J. K., Lee, C. H., Jung, Y. M., Cheong, S. I., Lee, C. G., Ku, B. C., and Jang, S. P., 2007, "Stability and Thermal Conductivity Characteristics of Nanofluids," Thermochim. Acta, **455**, pp. 70–74.
[7] Zhu, D., Li, X., Wang, N., Wang, X., Gao, J., and Li, H., 2009, "Dispersion Behavior and Thermal Conductivity Characteristics of $Al_2O_3-H_2O$ Nanofluids," Curr. Appl. Phys., **9**, pp. 131–139.
[8] Pak, B. C., and Cho, Y. I., 1998, "Hydrodynamic and Heat Transfer Study of Dispersed Fluids With Submicron Metallic Oxide Particles," Exp. Heat Trans-

fer, **11**(2), pp. 151–170.
[9] Koo, J., and Kleinstreuer, C., 2004, "A New Thermal Conductivity Model for Nanofluids," J. Nanopart. Res., **6**, pp. 577–588.
[10] Prasher, R., Bhattacharya, P., and Phelan, P. E., 2006, "Brownian-Motion-Based Convective-Conductive Model for the Effective Thermal Conductivity of Nanofluids," ASME J. Heat Transfer, **128**, pp. 588–595.
[11] Jang, S. P., and Choi, S. U. S., 2004, "Role of Brownian Motion in the Enhanced Thermal Conductivity of Nanofluids," Appl. Phys. Lett., **84**, pp. 4316–4318.
[12] Jang, S. P., and Choi, S. U. S., 2007, "Effects of Various Parameters on Nanofluid Thermal Conductivity," ASME J. Heat Transfer, **129**, pp. 617–623.
[13] Wen, D., and Ding, Y., 2004, "Experimental Investigation into Convective Heat Transfer of Nanofluids at the Entrance Region under Laminar Flow Conditions," Int. J. Heat Mass Transfer, **47**, pp. 5181–5188.
[14] Zeinali Heris, S., Nasr Esfahany, M., and Etemad, S. Gh., 2007, "Experimental Investigation of Convective Heat Transfer of Al_2O_3/Water Nanofluid in Circular Tube," Int. J. Heat Fluid Flow, **28**, pp. 203–210.
[15] Raisee, M., and Moghaddami, M., 2008, "Numerical Investigation of LAMINAR Forced Convection of Nanofluids Through Circular Pipes," J. Enhanced Heat Transfer, **15**, pp. 335–350.
[16] Hwang, K. S., Jang, S. P., and Choi, S. U. S., 2009, "Flow and Convective Heat Transfer Characteristics of Water-Based Al_2O_3 Nanofluids in Fully Developed Laminar Flow Regime," Int. J. Heat Mass Transfer, **52**, pp. 193–199.
[17] Sohn, C. W., and Chen, M. M., 1981, "Microconvective Thermal Conductivity in Disperse Two-Phase Mixture as Observed in a Low Velocity Couette Flow Experiment," ASME J. Heat Transfer, **103**, pp. 47–51.
[18] Xuan, Y., and Li, Q., 2003, "Investigation on Convective Heat Transfer and Flow Features of Nanofluids," ASME J. Heat Transfer, **125**, pp. 151–155.
[19] Xuan, Y., and Roetzel, W., 2000, "Conceptions for Heat Transfer Correlation of Nanofluids," Int. J. Heat Mass Transfer, **43**, pp. 3701–3707.
[20] Liu, Sh., 1999, "Particle Dispersion for Suspension Flow," Chem. Eng. Sci., **54**, pp. 873–891.
[21] Wen, D., and Ding, Y., 2005, "Effect of Particle Migration on Heat Transfer in Suspensions of Nanoparticles Flowing Through Minichannels," Microfluid. Nanofluid., **1**, pp. 183–189.
[22] Buongiorno, J., 2006, "Convective Transport in Nanofluids," ASME J. Heat Transfer, **128**, pp. 240–250.
[23] Zhou, S.-Q., and Ni, R., 2008, "Measurement of the Specific Heat Capacity of Water-Based Al_2O_3 Nanofluid," Appl. Phys. Lett., **92**, p. 093123.
[24] Williams, W. C., Buongiorno, J., and Hu, L. W., 2008, "Experimental Investigation of Turbulent Convective Heat Transfer and Pressure Loss of Alumina/Water and Zirconia/Water Nanoparticle Colloids (Nanofluids) in Horizontal Tubes," ASME J. Heat Transfer, **130**, p. 042412.
[25] Rea, U., McKrell, T., Hu, L. W., and Buongiorno, J., 2009, "Laminar Convective Heat Transfer and Viscous Pressure Loss of Alumina-Water and Zirconia-Water Nanofluids," Int. J. Heat Mass Transfer, **52**, pp. 2042–2048.
[26] McNab, G. S., and Meisen, A., 1973, "Thermophoresis in Liquids," J. Colloid Interface Sci., **44**, pp. 339–346.
[27] Brenner, H., and Bielenberg, J. R., 2005, "A Continuum Approach to Phoretic Motions: Thermophoresis," Physica A, **355**, pp. 251–273.
[28] Bielenberg, J. R., and Brenner, H., 2005, "A Hydrodynamic/Brownian Motion Model of Thermal Diffusion in Liquids," Physica A, **356**, pp. 279–293.
[29] Braibanti, M., Vigolo, D., and Piazza, R., 2008, "Does Thermophoretic Mobility Depend on Particle Size?," Phys. Rev. Lett., **100**, pp. 108303.
[30] Tzou, D. Y., 2008, "Instability of Nanofluids in Natural Convection," ASME J. Heat Transfer, **130**, pp. 072401.
[31] Nield, D. A., and Kuznetsov, A. V., 2009, "Thermal Instability in a Porous Medium Layer Saturated by a Nanofluid," Int. J. Heat Mass Transfer, in press.
[32] Patankar, S. V., 1980, *Numerical Heat Transfer and Fluid Flow*, Hemisphere, New York.
[33] Shah, R. K., and London, A. L., 1978, *Laminar Flow Forced Convection in Ducts, Supplement 1 to Advances in Heat Transfer*, Academic, New York.
[34] Shah, R. K., and Bhatti, M. S., 1987, "Laminar Convective Heat Transfer in Ducts," *Handbook of Single-Phase Convective Heat Transfer*, S. Kakac, R. K. Shah, and W. Aung, eds., Wiley, New York, Chap. 3.
[35] Hagen, K. D., 1999, *Heat Transfer With Applications*, Prentice-Hall, Englewood Cliffs, NJ, pp. 637–638.

Heat Transfer Augmentation of Parallel Flows by Means of Electric Conduction Phenomenon in Macro- and Microscales

Miad Yazdani
e-mail: myazdan1@iit.edu

Jamal Seyed-Yagoobi
e-mail: yagoobi@iit.edu

Department of Mechanical, Materials and
Aerospace Engineering,
Two-Phase Flow and Heat Transfer Enhancement
Laboratory,
Illinois Institute of Technology,
Chicago, IL 60616

Electrohydrodynamic conduction phenomenon takes advantage of the electrical Coulomb force exerted on a dielectric liquid generated by externally applied electric field and dissociated charges from electrolytes. The electric conduction phenomenon can be applied to enhance or control mass transport and heat transfer in both terrestrial and microgravity environments with advantages of simplicity and no degradation of fluid properties for isothermal as well as nonisothermal liquids. This paper numerically studies the heat transfer augmentation of externally driven macro- and microscale parallel flows by means of electric conduction phenomenon. The electric conduction is generated via electrode pairs embedded against the channel wall to mainly enhance the heat transfer and not necessarily to pump the liquid. Two cases of Poiseuille and Couette parallel flows are considered where for the former, a constant external pressure gradient is applied along the channel and for the latter, the channel wall moves with a constant velocity. The electric field and electric body force distributions along with the resultant velocity fields are presented. The heat transfer enhancements are illustrated under various operating conditions for both macro- and microscales. [DOI: 10.1115/1.4000977]

Keywords: *EHD conduction, parallel flows, heat transfer enhancement*

1 Introduction

Heat transfer augmentation in forced shear flows has received special attention due to the variety of its applications and numerous industrial advantages. The enhancing effect of a strong electric field on heat transfer rates has been known for over 70 years [1]. Electrohydrodynamic (EHD) induced flow typically allows enhancement of heat transfer without the introduction of large pressure drops and the resulting increase in pump size and power typically associated with conventional methods. Electrically driven flow involves the interaction of electric fields and flow fields in a dielectric fluid medium. For a liquid, one can take the advantage of this interaction to pump the liquid and augment the heat transfer. There are three kinds of EHD pumping mechanisms utilizing the electric body force; i.e., Coulomb force. Ion-drag pumping requires direct injection of free charges into the liquid and is not desirable due to degradation of the liquid properties. Induction pumping is based on charges induced in a liquid due to a gradient or discontinuity of the electric conductivity. Conduction pumping is associated with the heterocharge layers of finite thickness in the vicinity of the electrodes that are based on the process of dissociation of the neutral electrolytic species and recombination of the generated ions [2].

There are numerous studies concentrating on the application of EHD ion-injection and ion-drag pumping to enhance heat transfer in various applications. In particular, the heat transfer enhancement of air flow through ducts and channels was an area of interest for several researchers (see, e.g., Nelson and Ohadi [3] and Molki and Damronglerd [4]). Furthermore, an extensive number of studies have focused on the applications of EHD ion-injection for heat transfer enhancement of dielectric liquids [5,6]. Among the various applications, EHD-enhancement of channel flow has received considerable attention in the past few years. Benetis [7] conducted an experimental study of EHD ion-injection heat transfer enhancement in small scales. In theory and for dielectric liquids, flow destabilization by producing transverse flows is traditionally studied to augment the heat transfer in sheared flows (see, e.g., Ref. [8]) with a major motivation to understand and control the motion of fluids in numerous industrial applications. Paschkewitz and Pratt [9] investigated the role of fluid properties, in particular, viscosity and electrical conductivity, on the enhancement level of a dielectric liquid flow under various operating conditions. Kasayapanand et al. [10] examined EHD-injection heat transfer enhancement in laminar forced convection across a tube bank and found that the heat transfer is significantly enhanced by the EHD mechanism at low Reynolds numbers. However, the heat transfer enhancement was associated with an additional pressure drop due to the presence of the electrodes inside the channel. Later, they conducted similar study on the effect of ion-injection on the heat transfer of wavy channels and drew a similar conclusion [11] and extended their model to investigate enhanced heat transfer in the channel flow with the wire electrodes positioned along the centerline [12].

There are a limited number of published papers concerning heat transfer augmentation with an electric conduction phenomenon. Yazdani and Seyed-Yagoobi [13] proposed an electrically driven impinging liquid jet that provided a considerably high heat transfer performance mainly due to the unique flow distribution at the nozzle exit and over the surface. Furthermore, evaporation and condensation heat transfer enhancement by means of EHD conduction have been studied by the same researchers [14,15].

Despite several studies on heat transfer enhancement of air and liquid flows with ion-injection, the role of EHD conduction mechanism to augment heat transfer of externally driven flows has yet to be investigated. In addition, no studies particularly concern the EHD conduction not as a driving tool, but solely as an augmentation technique. This paper investigates the heat transfer enhancement of channel flow where the external flow forced con-

---

Contributed by the Heat Transfer Division of ASME for publication in the JOURNAL OF HEAT TRANSFER. Manuscript received June 23, 2009; final manuscript received December 9, 2009; published online April 2, 2010. Assoc. Editor: Jayathi Murthy.

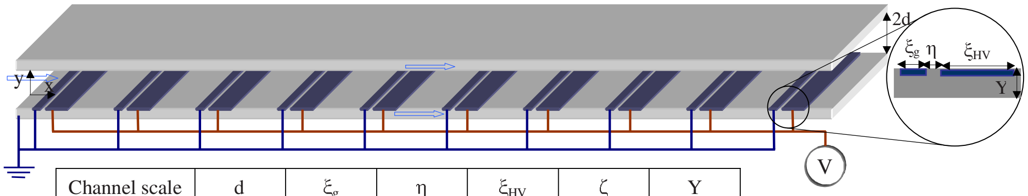

Channel scale	d	ξ_g	η	ξ_{HV}	ζ	Y
Macroscale	4mm	2mm	1mm	6mm	12.4mm	2mm
Microscale	40μm	20μm	10μm	60μm	124μm	20μm

Fig. 1 Schematic of 3D representation of the 2D solution domain (not to scale). Couette flow is studied for two cases. Couette-a: top wall is moving and the lower wall with electrodes is fixed and Couette-b: top wall is stationary and the lower wall with the electrodes is moving.

vection is aimed to be enhanced by EHD conduction phenomenon. While all the EHD ion-injection enhancement techniques are associated with an additional pressure drop penalty due, in part, to the presence of the electrodes within the fluid medium, the EHD conduction mechanism considered here provides a promising advantage of not only avoiding an excess pressure drop, but resulting in a pressure gain throughout the channel. Two cases of Poiseuille and Couette flows in macro- and microscales are considered. The electric field, net charge density, and electric body force contours along with the velocity profiles are presented to illustrate the performance of electric conduction mechanism. The local and average heat transfer enhancements are reported for different operating conditions in a dimensionless form. Finally, this study provides a clear quantitative comparison of EHD conduction performances in macro- and microscale flows.

2 Theoretical Model

Figure 1 illustrates the 3D representation of the 2D numerical domain considered for this study. It also includes the numerical details of the electrode design. A total number of ten electrode pairs are embedded against the channel wall and the channel length is $L=58d$. For the case of Poiseuille flow, only half of the domain is considered due to the symmetry along the centerline, and a constant external pressure gradient is applied along the channel. In the case of Couette flow, only one of the walls is assumed to be equipped with electrodes and two cases are considered: first case where the top wall is moving and the lower wall with the electrodes is stationary (Couette-a) and for the second case, the bottom wall is moving and the top wall remains stationary (Couette-b). A constant dc potential is applied to the wider (HV) electrodes while the narrower electrodes are grounded (see Fig. 1). The net flow is generated due to the electrode asymmetry and is superposed onto the externally driven fluid flow. Per given electrode pair, the net flow direction will be from the narrower electrode toward the wider electrode [16]. The channel wall is assumed to be electrically insulative. For the cases of Poiseuille flow, a constant heat flux is applied along the channel wall, which, due to the symmetry, is equivalent to the heat flux applied on both channel walls. For Couette-a flow, the channel lower wall with electrodes is exposed to a constant heat flux while the upper wall is thermally insulated. Finally, for the case of Couette-b flow, the heat flux is applied on the channel upper (stationary) wall and the lower (moving) wall with electrodes remains thermally insulated.

The following assumptions are incorporated in the theoretical model.

- The solution domain is 2D, steady state, and laminar.
- The channel wall is assumed to be thermally conductive and electrically insulated with no volumetric electric charges.
- Mobility and diffusion coefficients for the positive and negative ions are the same.
- Charge injection is absent.

The theoretical model for EHD conduction phenomenon is adapted from the work by Jeong et al. [17]. The following transport equations govern the fluid dynamics and heat transfer of the flow:

$$\nabla^* \cdot \mathbf{u}^* = 0 \tag{1}$$

$$\mathbf{u}^* \cdot \nabla^* \begin{pmatrix} \mathbf{u}^* \\ T^* \end{pmatrix} = -\begin{pmatrix} \nabla^* P^* \\ 0 \end{pmatrix} + \frac{1}{\mathrm{Re}} \nabla^{*2} \begin{pmatrix} \mathbf{u}^* \\ \frac{1}{\mathrm{Pr}} T^* \end{pmatrix} + \left(\frac{\mathrm{Re}_{\mathrm{EHD}}\ M_o}{\mathrm{Re}}\right)^2 C_0 (p^* - n^*) \begin{pmatrix} \mathbf{E}^* \\ 0 \end{pmatrix} + \begin{pmatrix} 0 \\ J_e^* \end{pmatrix} \tag{2}$$

Note that in all the cases studied in this paper, viscous dissipation is neglected since $\mathrm{Br}=\mu u_0^2/k(T_w-T_m) \ll 1$. The last two terms on the right hand side of Eq. (2) are the direct consequences of the applied electric field and attributed to the electric body force and Joule heating, respectively, and the latter is defined as

$$J_e^* = \sigma |\mathbf{E}|^2 \left(\frac{d}{c_p u_0 T_0}\right) \tag{3}$$

The electric body force and the Joule heating are the results of the applied electric field. These terms require the solution of the following Maxwell's relations:

$$\mathbf{E}^* = -\nabla^* \phi^* \tag{4}$$

$$\nabla^* \cdot \mathbf{E}^* = C_0 (p^* - n^*) \tag{5}$$

and charge conservation equations based on dissociation and recombination of neutral impurities (i.e., electrolytes)

$$\nabla^* \cdot \left[\pm \begin{pmatrix} p^* \\ n^* \end{pmatrix} \mathbf{E}^* + \frac{\mathrm{Re}}{\mathrm{Re}_{\mathrm{EHD}}} \begin{pmatrix} p^* \\ n^* \end{pmatrix} \mathbf{u}^* - \alpha \nabla^* \begin{pmatrix} p^* \\ n^* \end{pmatrix} \right] = 2C_0 (F(\omega) - p^* n^*) \tag{6}$$

with d, u_0, ρu_0^2, V/d, and n_{eq}, respectively, selected as scaling parameters for length, velocity, pressure, electric field, and free charges. The dimensionless temperature is defined as $T^*=(T-T_{\mathrm{in}})/T_{\mathrm{in}}$. $T_{\mathrm{in}}=300$ K has been arbitrarily selected as the reference temperature at the channel inlet and corresponds to refrigerant R-123 saturation temperature at atmospheric pressure where the physical property measurements were made. Therefore, the liquid is assumed to be subcooled with the system pressurized to a beyond-atmospheric pressure value. The resulting dimensionless coefficients in the above equations are defined as follows:

$$\mathrm{Re}_{\mathrm{EHD}} = \frac{bV}{\nu}, \quad \mathrm{Re} = \frac{u_0 D_h}{\nu}$$

$$M_o = \sqrt{\frac{\epsilon}{\rho b^2}}, \quad C_0 = \frac{\sigma d^2}{2b\epsilon V} \tag{7}$$

Table 1 Summary of electrostatic and flow boundary conditions

<table>
<tr><td>Equation</td><td colspan="3">Momentum</td><td colspan="3">Energy</td><td colspan="2">Electrostatics</td></tr>
<tr><td>Flow condition</td><td>Poiseuille</td><td>Couette-a</td><td>Couette-b</td><td>Poiseuille</td><td>Couette-a</td><td>Couette-b</td><td colspan="2">All conditions</td></tr>
<tr><td>Liquid/wall interface, $y=0$</td><td colspan="2" rowspan="3">$\mathbf{u}=0$</td><td rowspan="3">$\mathbf{u}=(u_w,0)$</td><td colspan="3" rowspan="3">$k\nabla_y T=k_s\nabla_y T_s$</td><td colspan="2">$\mathbf{\Phi}=\mathbf{\Phi}_s$, $\nabla_y(p,n)=0$</td></tr>
<tr><td>Ground electrode</td><td>$\mathbf{\Phi}=0$</td><td rowspan="2">$\mathbf{n}\cdot\mathbf{J}_{\pm}=0$</td></tr>
<tr><td>HV electrode</td><td>$\mathbf{\Phi}=V$</td></tr>
<tr><td>$y=d/2$</td><td>Symmetry</td><td>-</td><td>-</td><td>Symmetry</td><td>-</td><td>-</td><td colspan="2" rowspan="4">$\mathbf{n}\cdot\nabla(p,n,\mathbf{\Phi})=0$, $\mathbf{\Phi}=\mathbf{\Phi}_s^{a}$</td></tr>
<tr><td>Liquid/wall interface, $y=d$</td><td>-</td><td>$\mathbf{u}=(u_w,0)$</td><td>$\mathbf{u}=0$</td><td>-</td><td colspan="2">$k\nabla_y T=k_s\nabla_y T_s$</td></tr>
<tr><td>Inlet, $x=0$</td><td>$P=P_0$</td><td colspan="2" rowspan="2">$\mathbf{u}_{\text{in}}=\mathbf{u}_{\text{out}}$, $\nabla_x\mathbf{u}_{\text{in}}=\nabla_x\mathbf{u}_{\text{out}}$</td><td colspan="3">$T=T_{\text{in}}$</td></tr>
<tr><td>Outlet, $x=58d$</td><td>$P=0$</td><td colspan="3">$\nabla_x T=0$</td></tr>
<tr><td>Channel bottom wall, $y=-Y$</td><td colspan="3" rowspan="2">-</td><td colspan="2">$k_s\nabla_y T_s=-q''$</td><td>$\nabla_y T_s=0$</td><td colspan="2" rowspan="2">$\mathbf{\Phi}_s=0$</td></tr>
<tr><td>Channel top wall, $y=2d+Y$</td><td>-</td><td>$\nabla_y T_s=0$</td><td>$k_s\nabla_y T_s=-q''$</td></tr>
</table>

[a] This boundary condition is the continuity of electric potential applied across the solid/liquid interface. The zero flux boundary condition is applied across the inlet and outlet.

$$\alpha_{\text{ch}}=\frac{k_B T}{eV}$$

where u_0 is the selected reference velocity. For the case of Poiseuille flow, $u_0=-(\nabla_x P)_0 d^2/2\mu$ and for the Couette flow, $u_0=u_w$. The charge concentration at equilibrium n_{eq} is defined as $n_{\text{eq}}=\sigma/2b$ and is identical for both positive and negative charges in absolute quantity, which guarantees electrically neutral dielectric liquid at equilibrium. M_o is identified as the mobility ratio [18] and C_0 is expressed as the electric convection-conduction ratio [19]. Note that Langevine's approximation for dielectric fluids [20] is used to relate the recombination constant to the liquid properties; that is, $k_r=2b/\epsilon$.

The liquid is in contact with the channel wall, which is assumed to be thermally conductive and electrically insulative. Assuming no volumetric electric charges within the channel wall, the Laplace equation governs the potential field and temperature distribution

$$\nabla^{*2}\begin{pmatrix}\phi_s^*\\ T_s^*\end{pmatrix}=\begin{pmatrix}0\\ 0\end{pmatrix} \tag{8}$$

The boundary conditions for the dimensional parameters are presented in Table 1. The momentum and thermal boundary conditions at the inlet and outlet for the case of Couette flow are imposed by assuming that the current system resembles the Taylor–Couette flow system where the radii of the rotating/stationary cylinders are assumed to be much larger than the gap between them so as to ignore the Coriolis forces due to the channel curvature. Note that the continuity of potential field is applied across the liquid interface while the wall exterior surface is grounded. No boundary condition is required for velocity and electric charges inside the solid wall since the corresponding equations do not apply within the solid zone. The charge boundary condition at the electrode surfaces is adopted from the theoretical work by González et al. [21]. They argued that the normal components of the ion density currents vanish at the electrodes since they are ideally polarizable as follows:

$$\mathbf{n}\cdot\mathbf{J}_{\pm}=\mp b\begin{pmatrix}p\\ n\end{pmatrix}\frac{\partial\phi}{\partial y}-D\frac{\partial}{\partial y}\begin{pmatrix}p\\ n\end{pmatrix}=0 \tag{9}$$

This is a major departure from the previous works on EHD conduction phenomenon (e.g., Refs. [14,16]) where the charges were simply assumed to have zero flux and zero value on the countersigned electrodes and cosigned electrodes, respectively.

3 Numerical Technique

The code developed by the authors solves the transport equations using finite volume discretization scheme. The discretization equations are solved iteratively by the line-by-line application of the tridiagonal matrix algorithm. Central difference scheme is applied to Gauss' law, and upwind scheme based on the electric field direction is applied to the charge conservation equations. The convergence criterion $|(\psi_{i+1}-\psi_i)/\psi_i|<10^{-5}$ is applied for all involved parameters. The *grid independent* solution is obtained with grid sizes of 600×70 and 600×160 for the Poiseuille and Couette flows, respectively. In addition, an adaptive function is defined to dynamically refine the grid as the solution proceeds. The numerical model has been validated against the available experimental data of Siddiqui and Seyed-Yagoobi [22]. This comparison is provided in Ref. [16].

4 Results and Discussions

The reference values selected to calculate the dimensionless parameters correspond to the properties of refrigerant R-123 as the working fluid [23]. First, the results for Poiseuille flow are presented followed by the heat transfer results for the Couette flow cases. The heat transfer results for pure Poiseuille and Couette flows and pure EHD conduction driven flow will be presented as well, allowing for a clear comparison between enhanced and nonenhanced flows to quantify the heat transfer improvements that EHD conduction can provide. A constant heat flux of $q''=1\ \text{kW/m}^2$ is applied along the channel wall. Throughout this study and in both macro- and microscales, the maximum Re_{EHD} number (i.e., applied potential) corresponds to the maximum electric field intensity of just below the dc breakdown limit of refrigerant R-123 [24] to ensure no ion-injection occurs from the electrodes. The microscale channel flow is characterized by low Reynolds number range of $10<\text{Re}<100$, while the macroscale flow pertains to the moderate laminar range of $100<\text{Re}<2000$.

4.1 EHD Enhanced Poiseuille Flow. For the base case, the macroscale operating conditions $\text{Re}=-2\rho(\nabla_x P)_0 d^3/\mu^2=500$ and $\text{Re}_{\text{EHD}}=\rho bV/\mu=1382$ are selected, which correspond to $(\nabla_x P)_0=-652.5\ \text{Pa/m}$ and applied voltage of 10 kV for refrigerant R-123 as the working fluid. Figures 2–4, respectively, illustrate the distributions of electric field, net charge density, and electric body force over the surface of electrode pair No. 3. The selection of this pair is arbitrary and is solely for illustration purposes. As shown in Fig. 2, a high intensity electric field exists within the

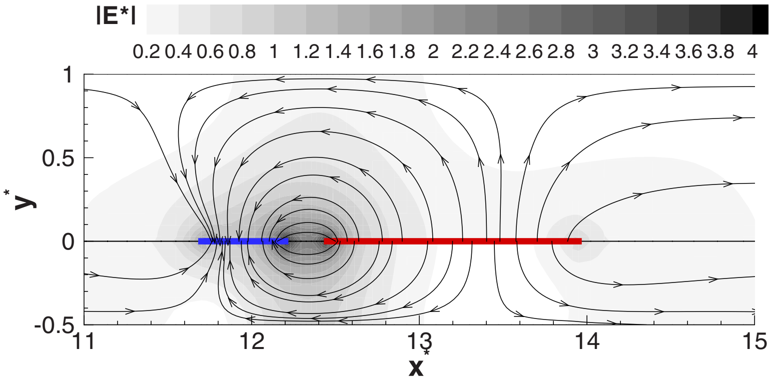

Fig. 2 Dimensionless contours of electric field and electric field streamtraces for electrode pair No. 3 and for the case of Poiseuille flow; scale: macro

interelectrode region. The buildup of the heterocharge layers in the vicinity of the electrodes is the consequence of high electric field intensity in this region, as illustrated in Fig. 3. The electric body force magnitudes embedded by the body force streamtraces are presented in Fig. 4. It is observed that the major part of the electric body force is concentrated around the edges of the electrodes, particularly on those facing toward the interelectrode region, and is directed toward both electrode surfaces. The consequence of electrode asymmetry is the dominance of the body force directed from the narrower electrode toward the wider electrode. In addition, the multidirectional pattern of the electric body force results in considerable secondary velocities in the vicinity of the electrodes as described below.

The velocity and temperature profiles are presented in Fig. 5 for different operating conditions. The cross section of $x^*=12.3$ corresponds to the middle of the interelectrode gap for electrode pair No. 3. Figure 5(*a*) shows that in the flow direction, the external flow has been superposed by an additional liquid flow induced by EHD conduction mechanism. Therefore, the considerable secondary velocity generated by the process of EHD conduction is suppressed as it is imposed onto the external flow. Nevertheless, these EHD-induced secondary velocities play an important role in enhancing the heat transfer performance as discussed later. In addi-

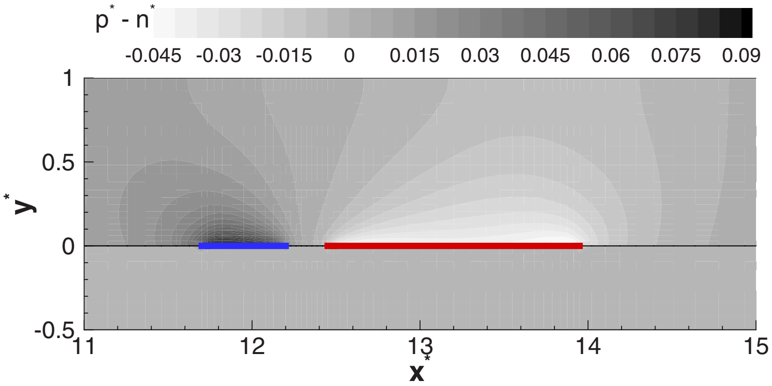

Fig. 3 Dimensionless contours of net charge density for electrode pair No. 3 and for the case of Poiseuille flow; scale: macro

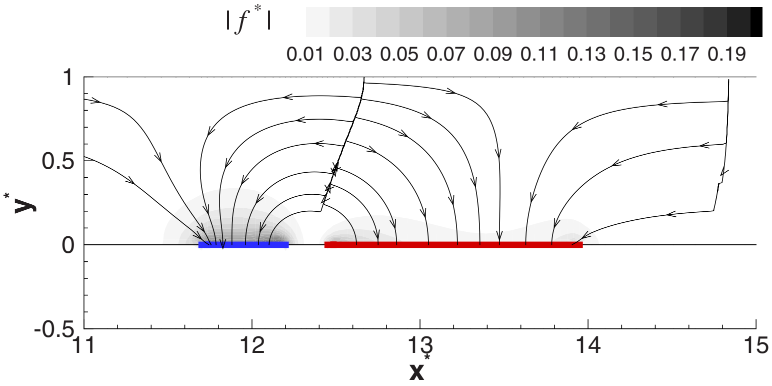

Fig. 4 Dimensionless contours of electric body force and electric body force streamtraces for electrode pair No. 3 and for the case of Poiseuille flow; scale: macro

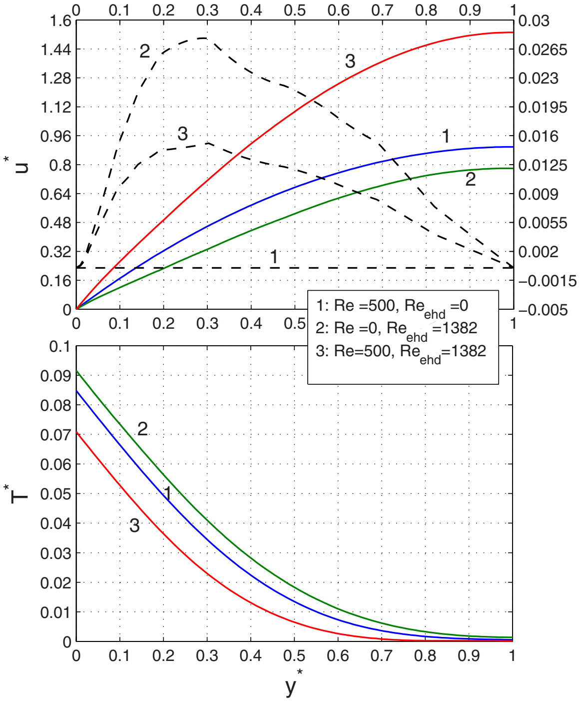

Fig. 5 **The dimensionless (*a*) velocity and (*b*) temperature profiles at $x^*=12.3$ for the case of Poiseuille flow. For the velocity plot, the solid and dashed lines correspond to u^* and v^* profiles, respectively.**

tion, it is observed that the maximum v^*-velocity does not occur along the symmetry line (i.e., $y^*=1$) but rather close to the channel wall where high intensity electric body force exists over the electrode surfaces. The cross-section temperature profile in Fig. 5(*a*) indicates that the maximum impact of the EHD-induced flow is near the channel wall where high intensity electric body force improves the convective heat transfer in this region.

While EHD conduction induced flow not only avoids an additional pressure drop penalty over the system, its contribution through providing a favorable pressure gain of the same order of the external pressure gradient is rather significant. This is unlike the EHD ion-injection enhancement techniques where the system often suffers an excess pressure drop due to the presence of the electrodes within the fluid medium (see, for example, the work by Kasayapanand [12] where wire electrodes were used inside the channel for direct injection of the ions through the fluid medium). Figure 6 quantifies the contribution of electrically driven liquid flow by plotting the ratio of EHD conduction induced pressure gradient and external pressure gradient as a function of the EHD conduction electric power in macro- and microscales. The EHD input power is defined in terms of the electric current, which can be expressed as

$$I = \left| \int_{\text{ground or HV}} \left[\frac{1}{2}\sigma\left(\frac{p+n}{n_{\text{eq}}}\right)\mathbf{E} + (p-n)\mathbf{u} \right] \cdot \mathbf{t}ds \right| \qquad (10)$$

$$W_{\text{in}} = V \times I \qquad (11)$$

where the contribution of the ion diffusion is neglected [25]. The EHD-induced pressure gradient is defined as a tool to measure the significance of the EHD conduction induced flow with respect to the externally generated liquid flow and is expressed as follows:

$$\nabla_x P_e = \frac{1}{A} \oiint_{\mathfrak{R}} (p-n)\nabla_x \phi dxdy \qquad (12)$$

Here, $\mathfrak{R}$ represents the channel domain illustrated in Fig. 1 and A is the channel volume per unit width, encompassing the entire numerical domain. Note that only the x-derivative of the electric potential is considered to isolate the impact of primary velocities in the x-direction. Figure 6 shows that for small and moderate Re numbers, the EHD-induced net flow is of the same order of the external flow. In particular, the EHD-induced favorable pressure gradient grows with a larger slope in microscale where it can approach as much as five times of the externally imposed counterpart. In addition, according to Fig. 6, little input power is required to generate a considerable pumping contribution; in macroscale, the input power barely goes beyond 0.1 W for large applied voltages whereas in microscale, the input power remains below only 10 mW.

Despite the low EHD operating power, the heat transfer enhancement is rather significant. The local heat transfer performance of the channel flow is presented in terms of Nusselt number in Fig. 7 and is defined as follows:

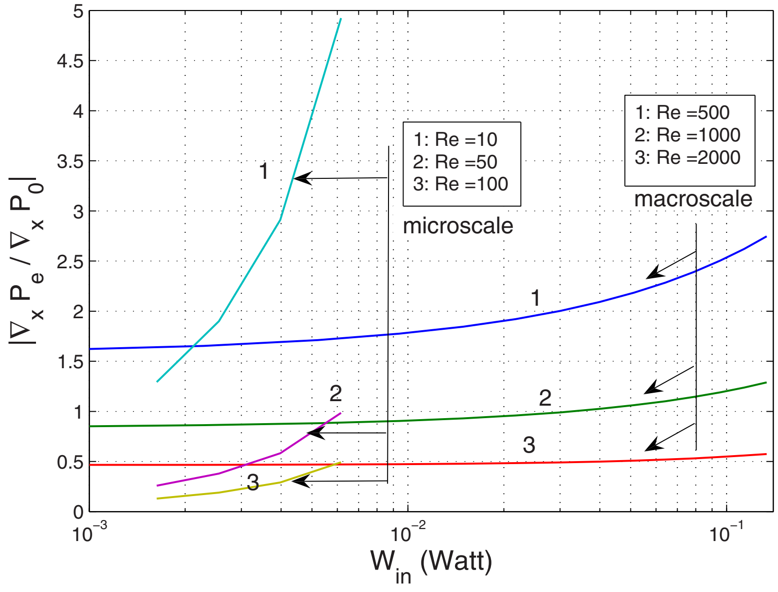

Fig. 6 **EHD-induced pressure gain, Eq. (12), as a function of the input electric power, Eq. (11), for the case of Poiseuille flow**

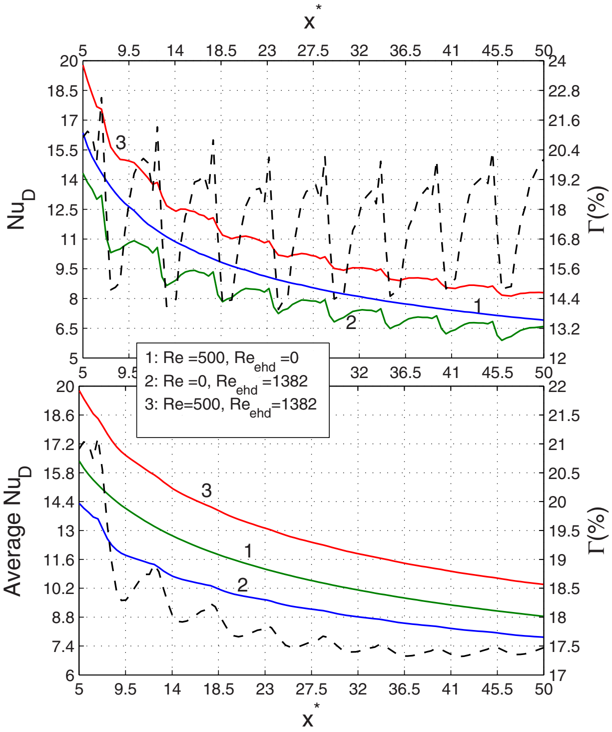

Fig. 7 (***a***) **Local Nusselt number and** (***b***) **axially averaged Nusselt number for the case of Poiseuille flow in the absence and presence of electric conduction mechanism. The solid and dashed lines represent the Nusselt number and heat transfer enhancement, respectively.**

$$\mathrm{Nu}_D = \frac{h(x)D_h}{k}, \quad h(x) = \frac{q''}{T_w(x) - T_m(x)}, \quad D_h = 4d \tag{13}$$

where mean temperature T_m is defined as

$$T_m = \frac{1}{\int_0^d u dy}\int_0^d uT dy \tag{14}$$

The axially averaged Nusselt number is also presented in Fig. 7 and is defined as

$$\text{Average } \mathrm{Nu}_D = \frac{\overline{h(x)}D_h}{k}, \quad \overline{h(x)} = \frac{q''}{\overline{T_w}(x) - \overline{T_m}(x)} \tag{15}$$

with the locally averaged temperature defined as

$$\overline{T}(x) = \frac{1}{x}\int_0^x T(x)dx \tag{16}$$

Additionally, the heat transfer enhancement level with respect to the purely external-driven flow is defined as

$$\Gamma(\%) = \frac{100}{\mathrm{Nu}_0}[\mathrm{Nu}_E - \mathrm{Nu}_0] \tag{17}$$

where Nu_0 and Nu_E represent the nonenhanced and EHD enhanced Nusselt numbers, respectively. Figure 7 also contains the local Nusselt number for pure Poiseuille and pure EHD-driven flows. As expected, the Nusselt number decreases along the channel to eventually approach the Nusselt number dictated by fully developed temperature and velocity profiles. The enhanced local Nusselt number is greater than the Nusselt numbers of any of the sole pumping mechanisms, which is attributed to the higher (superposed) net flow (see Fig. 5(*b*)). In addition, the heat transfer coefficients of the EHD-driven (i.e., Re=0 and $\mathrm{Re}_{\mathrm{EHD}}$=1382) and EHD-assisted (i.e., Re=500 and $\mathrm{Re}_{\mathrm{EHD}}$=1382) flows are discerned by the local raises over the electrode regions due to the significant secondary velocities close to the electrodes. For the latter, however, they are suppressed as the promoted driving flow represses the crosswise flow.

The average Nusselt number and its net enhancement with respect to the pure Poiseuille flow as a function of Reynolds number for several values of EHD Reynolds number are presented in Fig. 8. In macroscale, the considerable EHD-enhancement at a low Re number (and especially at a high $\mathrm{Re}_{\mathrm{EHD}}$ number) decreases as the Re number increases. Beyond Re≈1500, the enhancement is below 5% for all the EHD Reynolds numbers due to the dominance of externally induced heat convection and suppression of EHD conduction induced secondary flows. In microscale, however, the average Nusselt number is considerably more sensitive to the applied electric potential. As $\mathrm{Re}_{\mathrm{EHD}}$ (i.e., applied potential) increases, the EHD conduction induced flow and heat transfer rapidly dominate the external flow and the heat transfer to result in a substantial heat transfer enhancement. In addition, the average

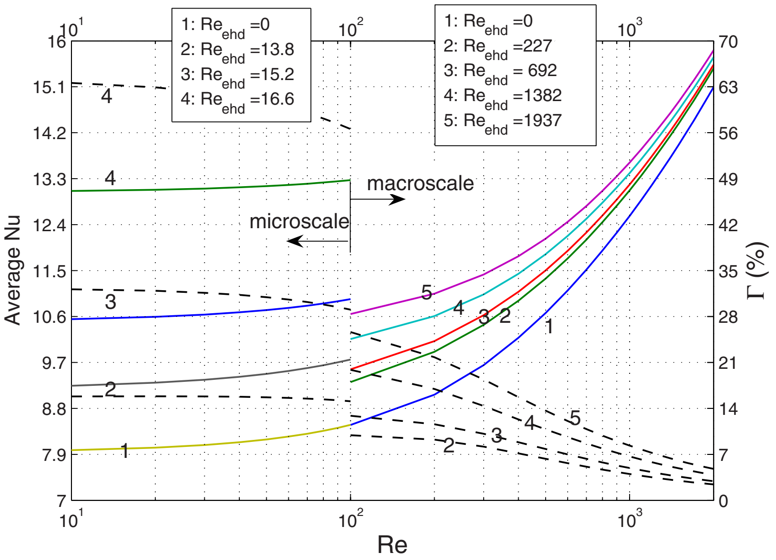

Fig. 8 Average Nusselt number (solid lines) and enhancement level (dashed lines) as a function of Re for different $\mathrm{Re}_{\mathrm{EHD}}$ values and for the case of Poiseuille flow

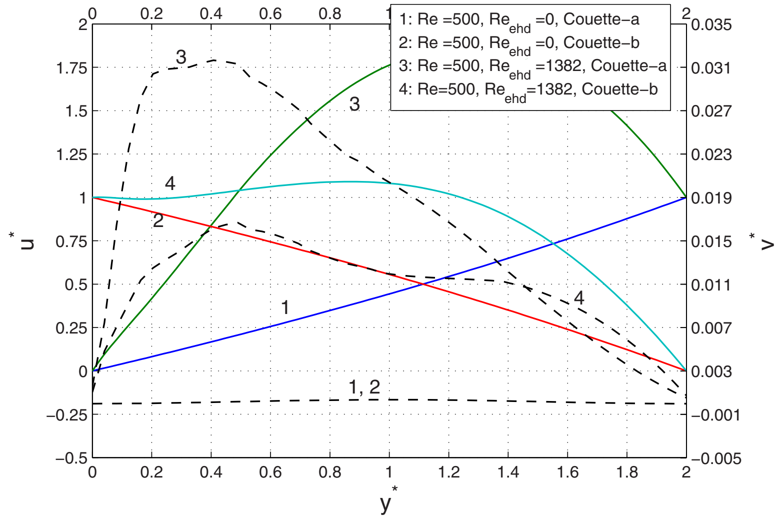

Fig. 9 The dimensionless velocity profiles at $x^*=12.3$ for the cases of Couette-a and Couette-b flows. The solid lines represent the u^* profile and the dashed lines are for the v^* profile.

Nusselt number exhibits slight variation with hydrodynamic Re number in microscale as the EHD conduction generated flow dominates the externally driven counterpart.

4.2 EHD Enhanced Couette Flow. Here, for the base case, $\mathrm{Re}=4u_w d/\nu=500$ that corresponds to $u_w=9$ mm/s. Beyond Re ≈ 1000 and Re ≈ 100, respectively, for macro- and microscales, and particularly for larger $\mathrm{Re}_{\mathrm{EHD}}$, the solution is associated with numerical instabilities regardless of the grid size and convergence criteria. Therefore, the results in this section are limited to the ranges $100<\mathrm{Re}<1000$ and $10<\mathrm{Re}<100$ for macroscale and microscale flows, respectively. Figure 9 illustrates the substantial evolution of the velocity field in the x-direction when EHD conduction is present. The Couette linear profile across the channel height is dominated by the EHD-induced flow with the maximum occurring within the channel. Furthermore, in the case of Couette-b flow, the high intensity electric body force exists over the surface of the moving wall, allowing for a more effective superposition of the two driving mechanisms. Figure 9 also shows that the y-velocity magnitude in Couette-b flow is lower near the channel bottom wall compared with the case of Couette-a flow, which, in part, is attributed to the larger x-velocity near the electrode surfaces for the case of Couette-b flow.

Unlike in the case of Poiseuille flow, the EHD-induced flow remains the dominant driving mechanism at all Re numbers when Couette flow is the primary source of flow generation. Figure 10 illustrates the contribution of EHD-driven flow in terms of the ratio of the electric pressure gradient (i.e., $\nabla_x P_e$; see Eq. (12)) to the Couette flow induced kinetic energy (i.e., $1/2\rho u_w^2$). It is observed that the EHD-driven induced flow provides as much as two orders of magnitude larger pressure gradient than the kinetic energy produced by the sole Couette flow for both macro- and microscales.

The evolution of the velocity profiles presented in Fig. 9 along with a dominant contribution of EHD-induced flow suggests a significant improvement of the heat transfer performance of the Couette flow as the maximum velocity does not occur adjacent to

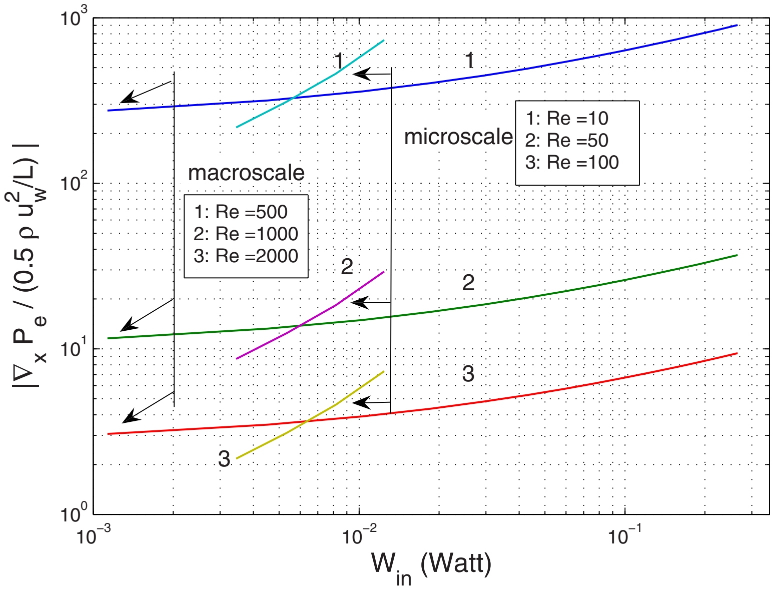

Fig. 10 EHD-induced pressure gain, Eq. (12), as a function of the input electric power, Eq. (11), for the case of Couette-a flow

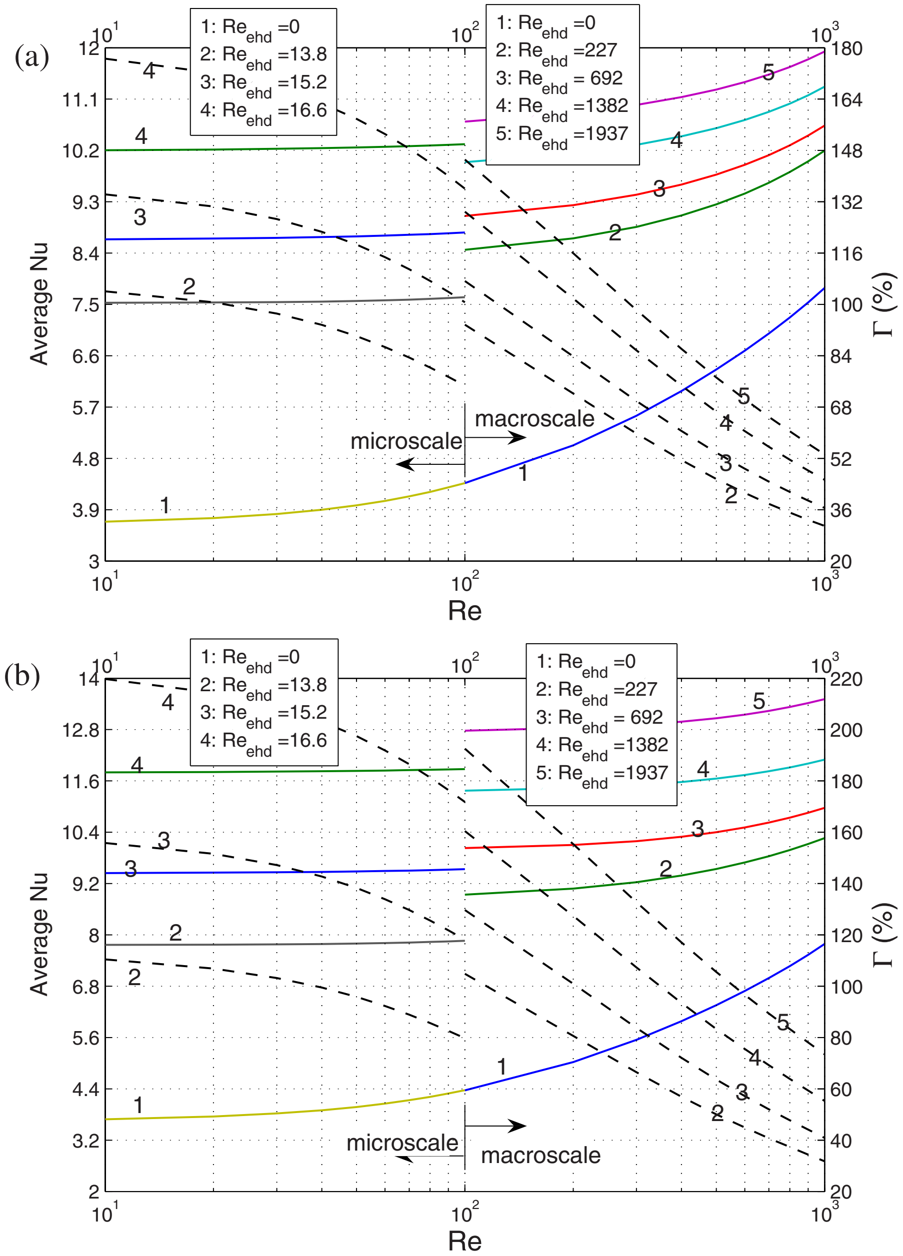

Fig. 11 **Average Nusselt number (solid lines) and enhancement level (dashed lines) as a function of Re for different Re$_{EHD}$ values and for the case of Couette-a flow (*a*) and Couette-b flow (*b*)**

the insulating wall but rather within the channel itself. The plots of average Nusselt number in Figs. 11(*a*) and 11(*b*) show that for macroscale Couette flow, the enhancement is far more significant than that of the Poiseuille flow with similar operating conditions. However, unlike the case of Poiseuille flow, no significant departure is observed when the channel is downscaled to microdimensions; the average Nusselt number and the resulting enhancement level in microscales follow the same trend as the macroscale Nusselt number and enhancement level do. The average Nusselt number, particularly for the Couette-b flow, is substantially less sensitive to the variation of the Re number indicating that the EHD-driven flow becomes the dominant heat transfer mechanism even at high Re numbers. The enhancement level, however, drops with Re number as the result of increasing Nusselt number for the pure Couette flow. The consequence of EHD-dominated velocity profile, particularly in the Couette-b flow, is a substantially better heat transfer performance near the channel walls with the enhancement level approaching to more than 200% for small Re numbers.

5 Conclusions

The application of EHD conduction phenomenon for heat transfer enhancement of channel flow in macro- and microscales was investigated. Two cases of Poiseuille flow and Couette flow were studied. In the case of Poiseuille flow, the enhancement level degraded as the Reynolds number increased due to the diminishing secondary velocities. In microscale, the enhancement was more significant since the external pressure gradient was dominated by the EHD conduction as the primary driving mechanism. For the Couette flow, the enhancement level was considerably higher than the Poiseuille counterpart due, in part, to the dominating EHD conduction driven flow for the enhanced flow. The primary advantage of EHD conduction enhancement technique over ion-injection mechanism was to provide a favorable pressure gain of the same or higher order of the external pressure gradient.

Acknowledgment

This work was financially supported by the NASA Microgravity Fluid Physics Program.

Nomenclature

A = channel volume per unit width
b = charge mobility coefficient
Br = Brinkman number, $\mathrm{Br}=\mu u_0^2/k(T_w-T_m)$
C_0 = EHD dimensionless number, $C_0=\sigma d^2/2b\epsilon V$
c_p = constant pressure specific heat
d = channel half width
D = charge diffusion constant
D_h = hydraulic diameter, $D_h=4d$
e = electron charge
$\mathbf{E}$ = electric field vector
$F(\omega)$ = $I_1(2\omega)/\omega$
h = heat transfer coefficient
I = electric current
k = thermal conductivity
k_B = Boltzmann universal constant
M_o = mobility ratio, $M_o=\sqrt{\epsilon/\rho b^2}$
Nu = Nusselt number
Nu_0 = Nusselt number in the absence of electric field
Nu_E = Nusselt number in the presence of electric field
n = negative charge density
$\mathbf{n}$ = surface normal unit vector
n_{eq} = electric charge concentration at equilibrium
p = positive charge density
P = pressure
Pr = Prandtl number, $\mathrm{Pr}=\nu/\gamma$
q'' = applied heat flux on the channel wall
$\mathrm{Re}_{\mathrm{EHD}}$ = EHD Reynolds number, $\mathrm{Re}_{\mathrm{EHD}}=u_{\mathrm{EHD}}d/\nu_l$
Re = hydrodynamic Reynolds number
T = absolute temperature
T_m = mean temperature
T_w = wall temperature
$\mathbf{u}$ = velocity vector
u_0 = reference velocity
u_{EHD} = EHD reference velocity, $u_{\mathrm{EHD}}=bV/d$
u_w = channel wall velocity
V = applied electric potential
W_{in} = electric input power
$\mathbf{x}$ = Cartesian coordinate unit vector
Y = channel wall thickness
α_{ch} = nondimensionalized charge diffusion constant
Γ = heat transfer enhancement level
γ = thermal diffusivity
ϵ = absolute electric permittivity
ζ = electrode pair distance
η = electrode gap
μ = dynamic viscosity of fluid
ν = kinematic viscosity of fluid
ξ = electrode width
ρ = mass density
σ = electric conductivity of fluid
ϕ = electric potential
ω = dissociation rate coefficient, $\omega=[e^3|E|/4\pi\epsilon k_B^2 T_{\mathrm{sat}}]^{1/2}$

Subscripts

0 = quantity in the absence of electric field
e = quantity in the presence of electric field
g = ground electrode
HV = high voltage electrode
in = channel inlet
out = channel outlet
s = solid zone

References

[1] Allen, P. H. G., and Karayiannis, T. G., 1995, "Electrohydrodynamic Enhancement of Heat Transfer and Fluid Flow," Heat Recovery Syst. CHP, **15**, pp. 389–423.
[2] Seyed-Yagoobi, J., 2005, "Electrohydrodynamic Pumping of Dielectric Liquids," J. Electrost., **63**, pp. 861–869.
[3] Nelson, D. A., and Ohadi, M. M., 1988, "EHD (Electrohydrodynamics) Enhancement of Heat Transfer in Heat Exchangers," Annual Report, Department of Mechanical Engineering and Engineering Mechanics, Michigan Technological University, Houghton, MI.
[4] Molki, M., and Damronglerd, P., 2006, "Electrohydrodynamic Enhancement of Heat Transfer for Developing Air Flow in Square Ducts," Heat Transfer Eng., **27**, pp. 35–45.
[5] Seyed-Yagoobi, J., and Bryan, J. E., 1999, *Enhancement of Heat Transfer and Mass Transport in Single-Phase and Two-Phase Flows With Electrohydrodynamics* (Advances in Heat Transfer Vol. 33), Academic, New York.
[6] Bryan, J. E., and Seyed-Yagoobi, J., 1997, "Heat Transport Enhancement of Monogroove Heat Pipe With Electrohydrodynamic Pumping," J. Thermophys. Heat Trans., **11**(3), pp. 454–460.
[7] Benetis, V., 2005, "Experimental and Computational Investigation of Planar Ion Drag Micropump Geometrical Design Parameters," Ph.D. thesis, University of Maryland, College Park, MD.
[8] Lara, J. L., Castellanos, A., and Pontiga, F., 1998, "Stability Analysis of a Taylor Couette Flow of Insulating Fluid Subjected to Radial Unipolar Injection of Charge," Phys. Fluids, **10**, pp. 3088–3098.
[9] Paschkewitz, J., and Pratt, D., 2000, "The Influence of Fluid Properties on Electrohydrodynamic Heat Transfer Enhancement in Liquids Under Viscous and Electrically Dominated Flow Conditions," Exp. Therm. Fluid Sci., **21**, pp. 187–197.
[10] Kasayapanand, N., Tiansuwan, J., Asvapoositkul, W., Vorayos, N., and Kiatsiriroat, T., 2002, "Effect of the Electrode Arrangements in a Tube Bank on the Characteristic of Electrohydrodynamic Heat Transfer Enhancement: Low Reynolds Number," J. Enhanced Heat Transfer, **9**(5–6), pp. 229–242.
[11] Kasayapanand, N., and Kiatsiriroat, T., 2005, "EHD Enhanced Heat Transfer in Wavy Channel," Int. Commun. Heat Mass Transfer, **32**(6), pp. 809–821.
[12] Kasayapanand, N., 2006, "Numerical Study of Electrode Bank Enhanced Heat Transfer," Appl. Therm. Eng., **26**(14–15), pp. 1471–1480.
[13] Yazdani, M., and Seyed-Yagoobi, J., 2010, "An Electrically Driven Impinging Liquid Jet for Direct Cooling of Heated Surfaces," IEEE Trans. Ind. Appl., to be published.
[14] Yazdani, M., and Seyed-Yagoobi, J., 2008, "Numerical Investigation of Electrohydrodynamic-Conduction Pumping of Liquid Film in the Presence of Evaporation," ASME J. Heat Transfer, **131**, p. 011602.
[15] Yazdani, M., and Seyed-Yagoobi, J., 2007, "Enhancement of External Condensation Heat Transfer by Pumping of Liquid Condensate Circumferentially With Electric Conduction Phenomenon," ASME International Mechanical Engineering Congress and Exposition, Seattle, WA.
[16] Yazdani, M., and Seyed-Yagoobi, J., 2009, "Electrically Induced Dielectric Liquid Film Flow Based on Electric Conduction Phenomenon," IEEE Trans. Dielectr. Electr. Insul., **16**, pp. 768–777.
[17] Jeong, S. I., Seyed-Yagoobi, J., and Atten, P., 2004, "Fluid Circulation in an Enclosure Generated by Electrohydrodynamic Conduction Phenomenon," IEEE Trans. Ind. Appl., **11**, pp. 899–910.
[18] Atten, P., 1996, "Electrohydrodynamic Instability and Motion Induced by Injected Space Charges in Insulating Liquids," IEEE Trans. Dielectr. Electr. Insul., **3**, pp. 1–17.
[19] Crowley, J. M., 1995, *Dimensionless Ratios in Electrohydrodynamics, Handbook of Electrostatic Processes*, Dekker, New York.
[20] Langevin, P., 1903, "Recombmaison et mobilites des ions dans les gag," Ann. Chim. Phys, **28**, p. 433.
[21] González, A., Ramos, A., Green, N. G., Castellanos, A., and Morgan, H., 2000, "Fluid Flow Induced by Nonuniform ac Electric Fields in Electrolytes on Microelectrodes. II. A Linear Double-Layer Analysis," Phys. Rev. E, **61**(4), pp. 4019–4028.
[22] Siddiqui, M., and Seyed-Yagoobi, J., 2009, "Experimental Study of Liquid Film Pumping Based on Conduction Phenomenon," IEEE Trans. Ind. Appl., **45**, pp. 3–9.
[23] Bryan, J. E., 1998, "Fundamental Study of Electrohydrodynamically Enhanced Convective and Nucleate Boiling Heat Transfer," Ph.D. thesis, Texas A&M University, College Station, TX.
[24] Crowley, J. M., and Wright, G. S., 1990, "Selecting a Working Fluid to Increase the Efficiency and Flow Rate of an EHD Pump," IEEE Trans. Ind. Appl., **26**, pp. 42–49.
[25] Feng, Y., and Seyed-Yagoobi, J., 2007, "Electrical Charge Transport and Energy Conversion With Fluid Flow During Electrohydrodynamic Conduction Pumping," Phys. Fluids, **19**(5), p. 057102.

Buoyancy Driven Heat Transfer of Nanofluids in a Tilted Enclosure

Kamil Kahveci[1]
Department of Mechanical Engineering,
Trakya University,
22180 Edirne, Turkey
e-mail: kamilk@trakya.edu.tr

Buoyancy driven heat transfer of water-based nanofluids in a differentially heated, tilted enclosure is investigated in this study. The governing equations (obtained with the Boussinesq approximation) are solved using the polynomial differential quadrature method for an inclination angle ranging from 0 deg to 90 deg, two different ratios of the nanolayer thickness to the original particle radius (0.02 and 0.1), a solid volume fraction ranging from 0% to 20%, and a Rayleigh number varying from 10^4 to 10^6. Five types of nanoparticles, Cu, Ag, CuO, Al_2O_3, and TiO_2 are taken into consideration. The results show that the average heat transfer rate from highest to lowest is for Ag, Cu, CuO, Al_2O_3, and TiO_2. The results also show that for the particle radius generally used in practice ($\beta = 0.1$ or $\beta = 0.02$), the average heat transfer rate increases to 44% for $Ra = 10^4$, to 53% for $Ra = 10^5$, and to 54% for $Ra = 10^6$ if the special case of $\theta = 90$ deg, which also produces the minimum heat transfer rates, is not taken into consideration. As for $\theta = 90$ deg, the heat transfer enhancement reaches 21% for $Ra = 10^4$, 44% for $Ra = 10^5$, and 138% for $Ra = 10^6$. The average heat transfer rate shows an increasing trend with an increasing inclination angle, and a peak value is detected. Beyond the peak point, the foregoing trend reverses and the average heat transfer rate decreases with a further increase in the inclination angle. Maximum heat transfer takes place at $\theta = 45$ deg for $Ra = 10^4$ and at $\theta = 30$ deg for $Ra = 10^5$ and 10^6. [DOI: 10.1115/1.4000744]

Keywords: natural convection, nanofluid, enclosure, PDQ, vorticity, stream function

1 Introduction

As is well known, conventional heat transfer fluids such as water, ethylene glycol, and oil have low thermal conductivities. This is the main drawback in enhancing the performance and the compactness of many engineering devices. Therefore, there is a strong need for advanced heat transfer fluids with substantially higher thermal conductivities. The way to eliminate this need is to use solid particles within a base fluid. Because of technological difficulties, micron-sized particles have been used in the past, but sedimentation and clogging were persistent problems in fluids with micron-sized particles. The introduction of nanofluids has eliminated these drawbacks. The term nanofluid is used to describe a solid and liquid mixture that consists of a base liquid and nanoparticles sized less than 100 nm. Ceramic particles (Al_2O_3, CuO, TiO_2, SiC, and SiO_2), pure metallic particles (Cu, Ag, Au, and Fe), and carbon nanotubes are all used as nanoparticles. The presence of the nanoparticles causes an anomalous increase in the effective thermal conductivity of the fluid. Eastman et al. [1] found that the effective thermal conductivity of ethylene glycol increases up to 40% for a nanofluid consisting of ethylene glycol containing approximately 0.3 vol % Cu nanoparticles of mean diameter less than 10 nm. Choi et al. [2] produced nanotube-in-oil suspensions and measured their effective thermal conductivity. The measured thermal conductivity found to be anomalously greater than theoretical predictions and nonlinear with nanotube loadings. Xuan and Li [3] made a theoretical study of the thermal conductivity of nanofluids. The hot-wire apparatus was used to measure the thermal conductivity of nanofluids with suspended copper nanophase powders. They found that for the water-copper nanoparticle suspension, the ratio of the thermal conductivity of the nanofluid to that of the base liquid varies from 1.24 to 1.78 if the volume fraction of the ultrafine particles increases from 2.5% to 7.5%. Das et al. [4] investigated the increase in thermal conductivity with temperature for nanofluids with water as base fluid and particles of Al_2O_3 or CuO as suspension material. The results indicate an increase in enhancement characteristics with temperature, which makes the nanofluids even more attractive for applications with high energy density than usual room temperature measurements reported earlier. Keblinski et al. [5] investigated four possible mechanisms for this anomalous increase: Brownian motion of the nanoparticles, molecular level layering of the liquid at the liquid-particle interface, the nature of heat transfer in the nanoparticles, and nanoparticle clustering. Keblinski et al. [5] also showed that the Brownian motion is a negligible contributor, and that liquid layering around the nanoparticles could cause rapid conduction.

Thermal conductivity is the most important parameter for the heat transfer enhancement potential of nanofluids. It is known that the thermal conductivity of a nanofluid is a function of the thermal conductivity of both the base fluid and the nanoparticle, the volume fraction, the surface area, the shape of the nanoparticles, and the distribution of the dispersed particles. However, there are no theoretical formulas currently available in the literature for predicting the thermal conductivity of the nanofluids. Some proposed models do exist for solid-liquid mixtures with micrometer-sized particles. In these models, the thermal conductivity of the suspensions depends only on the volume fraction and shape of the suspended solid particles, but not on the size and distribution of the particles. In the absence of a suitable theory for nanofluids, models for the solid-liquid suspensions with relatively large particles may be extended to estimate the thermal conductivity of the nanofluids.

The most popular thermal conductivity model for this type of solid-liquid mixture is the Maxwell model [6]; this is the model on which most later-proposed models for nanofluids are based. In this model, the thermal conductivity is defined as follows:

---

[1] Present address: Muhendislik Mimarlik Fakultesi, Trakya Universitesi, 22030 Edirne, Turkey.

Contributed by the Heat Transfer Division of ASME for publication in the JOURNAL OF HEAT TRANSFER. Manuscript received March 25, 2009; final manuscript received October 9, 2009; published online March 24, 2010. Assoc. Editor: Yutaka Asako.

$$k_{\text{eff}}/k_f = \frac{k_s + 2k_f + 2(k_s - k_f)\phi}{k_s + 2k_f - (k_s - k_f)\phi} \tag{1}$$

where k_s is the thermal conductivity of the particle, k_f is the thermal conductivity of the base fluid, and ϕ is the solid particle volume fraction. In this traditional model, the effective thermal conductivity of the suspensions depends on the thermal conductivity of the spherical particle, the base liquid, and the volume fraction of the solid particles.

The thermal conductivity of nanofluids with nonspherical particles depends not only on the volume fraction of the particles, but also on the shape of the particles. Hamilton and Crosser [7] proposed a model for the effective thermal conductivity of two-component mixtures with nonspherical particles. In this model, given below, thermal conductivity is a function of the conductivity of both the particle and the base fluid, as well as the shape of the particles

$$k_{\text{eff}}/k_f = \frac{k_s + (n-1)k_f + (n-1)(k_s - k_f)\phi}{k_s + (n-1)k_f - (k_s - k_f)\phi} \tag{2}$$

Here, n is the empirical shape factor: $n=3/\Psi$, where Ψ is the sphericity (i.e., the ratio of the surface area of a sphere with a volume equal to that of the particle to the surface area of the particle). The shape factor n can vary from 0.5 to 6.0 (a sphere $=3$, a cylinder$=6$).

An alternative expression for calculating the effective thermal conductivity of solid-liquid mixtures has been proposed by Yu and Choi [8]. They claimed that a structural model of nanofluids might consist of a bulk liquid, solid nanoparticles, and solid-like nanolayers. The solid-like nanolayers act as a thermal bridge between a solid nanoparticle and a bulk liquid. With the assumption of $k_{\text{layer}}=k_p$, the model for spherical nanoparticles is as follows:

$$k_{\text{eff}}/k_f = \frac{k_s + 2k_f + 2(k_s - k_f)(1+\beta)^3\phi}{k_s + 2k_f - (k_s - k_f)(1+\beta)^3\phi} \tag{3}$$

where β is the ratio of the nanolayer thickness to the original particle radius. Yu and Choi [8] compared their model results for $\beta=0.1$ with existing experimental results in literature and obtained a reasonably good agreement. The prediction is effective, most particularly when the nanoparticles have a diameter of less than 10 nm. This model has been used in the present study to define the effective thermal conductivity of the nanofluids.

The viscosity of the nanofluid is generally estimated using existing relations for a two-phased mixture. The following equation given by Brinkman [9] was used as the relation for the effective viscosity in this investigation:

$$\mu_{\text{eff}} = \mu_f/(1-\phi)^{2.5} \tag{4}$$

Xuan et al. [10] experimentally measured the effective viscosity of the transformer oil-water nanofluid and of the water-copper nanofluid in the temperature range of 20–50°C. Their experimental results showed reasonably good agreement with the theory by Brinkman [9].

There is a relatively limited number of studies on convective heat transfer of nanofluids. In one of these studies, Xuan and Li [11] found that nanofluids with oxide particles generally cause a moderate increase in heat transfer while a significant enhancement is obtained for nanofluids with metallic particles. This is because of the fact that a high enhancement rate for metallic nanofluids requires only a small solid volume fraction that does not affect the viscosity significantly. In another study, Eastman et al. [12] found that with less than 1% volume fraction of CuO, the convection heat transfer rate increased by more than 15% in water. Wen and Ding [13] studied laminar heat transfer in the entrance region of a tube flow with an alumina-water nanofluid and found that with a 1.6% solid volume fraction, the local heat transfer coefficient at the entrance region takes on a value that is 41% higher than that at the base fluid with the same flow rate. Wen and Ding [13] also observed that the enhancement is particularly significant in the entrance region and decreases with axial distance. Maiga et al. [14] numerically studied laminar and turbulent flows of nanofluids in a uniformly heated tube for using approximated correlations for experimental data. They found that the heat transfer enhancement due to the nanoparticles becomes more important for the turbulent flow regime with an increase in the Reynolds number. Maiga et al. [15] also studied forced convection flows of nanofluids in a uniformly heated tube and a system of parallel, coaxial, and heated disks. They found that both the Reynolds number and the gap between disks have an insignificant effect on the heat transfer enhancement. Akbarinia and Behzadmehr [16] studied laminar, mixed convection of an Al_2O_3-based nanofluid in a horizontal curved tube. They found that for a given nanoparticle concentration, increasing the buoyancy forces caused a reduction in the skin friction. Mirmasoumi and Behzadmehr [17] studied laminar mixed convection of an Al_2O_3-based nanofluid. The results showed that increasing the nanoparticle volume fraction increases the secondary flow strength. Mirmasoumi and Behzadmehr [17] also observed that the skin friction coefficient in the fully developed region does not notably change with an increasing solid volume fraction, except for at the entrance region. In another study, Izadi et al. [18] made a numerical investigation on developing laminar forced convection of a nanofluid consisting of Al_2O_3 and water in an annulus and observed that the dimensionless axial velocity profile does not significantly change with the nanoparticle volume fraction. However, the temperature profiles are affected by the nanoparticle concentration. Khanafer et al. [19] studied natural convection of copper-based nanofluids in a differentially heated square cavity. Their results show that the presence of nanoparticles enhances heat transfer by about 25% for Gr $=10^4$ and Gr$=10^5$ at a volume fraction of $\varphi=0.2$. In another study similar to that done by Khanafer et al. [19], Santra et al. [20] observed that the heat transfer decreases with an increase in φ for a particular Ra, while it increases with Ra for a particular φ. Buoyancy driven heat transfer of water-based Al_2O_3 nanofluids in a rectangular cavity was studied theoretically by Hwang et al. [21]. They found that water-based Al_2O_3 nanofluids is more stable than base fluid in a rectangular cavity heated from below as the volume fraction of nanoparticles increases, the size of nanoparticles decreases, or the average temperature of nanofluids increases. They also found that the ratio of the heat transfer coefficient of nanofluids to that of the base fluid is decreased as the size of nanoparticles increases, or the average temperature of nanofluids is decreased. The heat transfer enhancement of a copper-based nanofluid in a two-dimensional enclosure was investigated by Jou and Tzeng [22]. It was shown that the average Nusselt number at the hot wall is increased as the aspect ratio decreased. Oztop and Abu-Nada [23] studied buoyancy driven heat transfer and fluid flow in a partially heated enclosure using nanofluids. They observed that the heat transfer enhancement is more pronounced at low aspect ratios than at high aspect ratios of the enclosure. Aminossadati and Ghasemi [24] investigated natural convection cooling of a heat source embedded on the bottom wall of an enclosure filled with nanofluids and found that the type of nanoparticles and the length and location of the heat source affect the heat source maximum temperature significantly. Heat transfer augmentation in a two-sided lid-driven differentially heated square cavity utilizing nanofluids was studied numerically by Tiwari and Das [25]. They observed that when both the vertical walls move upwards in the same direction, the heat transfer is reduced. They also found that when the vertical walls move in opposite directions, the heat transfer is considerably enhanced for forced convection dominated regime regardless of which side moves upwards. Koo and Kleinstreuer [26] investigated the microheat sink and found that a high-Prandtl number base fluid and a high aspect ratio channel give better heat transfer performance.

As also seen from the above literature, there is a relatively limited number of studies on convective heat transfer of nanofluids in an enclosure, while convective heat transfer of conven-

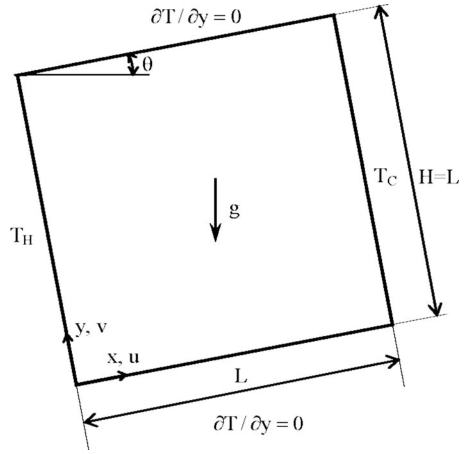

Fig. 1 Geometry and coordinate system

tional heat transfer fluids (see Refs. [27–40]) has been studied extensively. The present study therefore aims to investigate the effects of several pertinent parameters on the flow and heat transfer characteristics of water-based nanofluids in a tilted enclosure using the polynomial differential quadrature (PDQ) method.

2 Analysis

The basic flow configuration used in the analysis is shown in Fig. 1. The tilted square enclosure of height H and width L is bounded by two isothermal walls at temperatures T_H and T_C, and two adiabatic walls. The flow is assumed to be Newtonian, two-dimensional, steady, and incompressible. Despite the fact that a nanofluid is a two phase mixture, since the solid particles are of a very small size, they are easily fluidized and therefore can be considered to behave as a fluid. Therefore, it might be reasonable to treat a nanofluid as a single phase flow. The single phase approach assumes that the fluid phase and particles are in thermal equilibrium and move with the same velocity. This approach, which is simpler and requires less computational effort, is used in this study.

In order to nondimensionalize the governing equations, the following dimensionless variables are used:

$$x=\frac{x^*}{L},\quad y=\frac{y^*}{L},\quad u=\frac{u^*}{\alpha_f/L},\quad v=\frac{v^*}{\alpha_f/L},\quad p=\frac{L^2}{\rho_{fo}\alpha_f^2}p^*$$
$$T=\frac{T^*-T_C}{T_H-T_C} \tag{5}$$

where u^* and v^* are the dimensional velocity components, p^* is the dimensional pressure, T^* is the dimensional temperature, ρ_f is the fluid density, and α is the thermal diffusivity of the fluid. As shown in detail by Gill [41], the scaling in Eqs. (6) and (7) is based on the balance between the convective and conductive terms in the energy equation, and on the balance between the buoyancy and diffusion terms in the momentum equation.

The buoyancy effects are incorporated in the formulation by invoking the Boussinesq approximation. The viscous dissipation terms and the thermal radiation are assumed to be negligible. With the foregoing assumptions, the dimensionless governing equations can be given as follows in the vorticity-stream function formulation:

$$\frac{\partial^2\psi}{\partial x^2}+\frac{\partial^2\psi}{\partial y^2}=-\omega \tag{6}$$

$$u\frac{\partial\omega}{\partial x}+v\frac{\partial\omega}{\partial y}=\frac{\gamma_{\text{eff}}}{\gamma_f}\Pr\left(\frac{\partial^2\omega}{\partial x^2}+\frac{\partial^2\omega}{\partial y^2}\right)+\frac{(\rho\beta_T)_{\text{eff}}}{\rho_{\text{eff}}\beta_{T,f}}\text{Ra}\ \Pr\left[\cos\theta\frac{\partial T}{\partial x}-\sin\theta\frac{\partial T}{\partial y}\right] \tag{7}$$

$$u\frac{\partial T}{\partial x}+v\frac{\partial T}{\partial y}=\frac{\alpha_{\text{eff}}}{\alpha_f}\left[\frac{\partial^2 T}{\partial x^2}+\frac{\partial^2 T}{\partial y^2}\right] \tag{8}$$

Here the Prandtl and Rayleigh numbers are defined as

$$\Pr=\frac{\gamma_f}{\alpha_f},\quad \text{Ra}=\frac{g\beta_{T,f}L^3\Delta T^*}{\gamma_f\alpha_f} \tag{9}$$

where g is the gravitational acceleration, β_T is the coefficient of thermal expansion, and γ is the kinematic viscosity. ΔT^* is the temperature difference between the isothermal walls of the enclosure. The effective properties present in the governing equations can be expressed by the following relations:

$$(\rho C_p)_{\text{eff}}=(1-\phi)(\rho C_p)_f+\phi(\rho C_p)_s \tag{10}$$

$$(\rho\beta_T)_{\text{eff}}=(1-\phi)(\rho\beta_T)_f+\phi(\rho\beta_T)_s \tag{11}$$

where

$$\rho_{\text{eff}}=(1-\phi)\rho_f+\phi\rho_s \tag{12}$$

The dimensionless stream function and vorticity in Eqs. (6) and (7) are defined as follows:

$$u=\frac{\partial\psi}{\partial y},\quad v=-\frac{\partial\psi}{\partial x},\quad \omega=\frac{\partial v}{\partial x}-\frac{\partial u}{\partial y} \tag{13}$$

The appropriate boundary conditions for the governing equations are

$$\psi(x,0)=0,\quad \left.\frac{\partial T}{\partial y}\right|_{x,0}=0,\quad \psi(x,1)=0,\quad \left.\frac{\partial T}{\partial y}\right|_{x,1}=0 \tag{14}$$

$$\psi(0,y)=0,\quad T(0,y)=1,\quad \psi(1,y)=0,\quad T(1,y)=0 \tag{15}$$

There is no physical boundary condition for the value of the vorticity on a solid boundary. However, an expression can be derived from the stream function equation as $\omega_{\text{wall}}=-\partial^2\psi/\partial\eta^2$, where η is the outward direction normal to the surface.

The local variation in the Nusselt number of the nanofluid can be expressed as

$$\text{Nu}=-\frac{k_{\text{eff}}}{k_f}\left.\frac{\partial T}{\partial\eta}\right|_{\eta=0} \tag{16}$$

3 Results and Discussion

The PDQ method [42–45], with the following nonuniform Chebyshev–Gauss–Lobatto grid point distribution, was used to transform the governing equations into a set of algebraic equations

$$x_i=\frac{1}{2}\left[1-\cos\left(\frac{i}{n_x}\pi\right)\right],\quad i=0,1,2,\ldots,n_x$$
$$y_j=\frac{1}{2}\left[1-\cos\left(\frac{j}{n_y}\pi\right)\right],\quad j=0,1,2,\ldots,n_y \tag{17}$$

The points in this grid system are more closely spaced in regions near the walls where the large velocity and temperature gradients are expected to develop. The computational results were obtained by the successive over-relaxation (SOR) iteration method for an inclination angle ranging from 0 deg to 90 deg, a Rayleigh number varying from 10^4 to 10^6, two different ratios of the nanolayer thickness to the original particle radius (0.02 and 0.1), and a solid volume fraction ranging from 0% to 20%. Five types of nanoparticles (Cu, Ag, CuO, Al_2O_3, and TiO_2) were considered. Water

Table 1 Thermophysical properties of base fluid and nanoparticles

Property	Water	Cu	Ag	CuO	Al_2O_3	TiO_2
ρ (kg/m^3)	997.1	8933	10500	6500	3970	4250
C_p (J/kg K)	4179	385	235	536	765	686
k (W/m K)	0.613	400	429	20	40	9
$\alpha \times 10^7$ (m^2/s)	1.47	1163.1	1738.6	57.5	131.7	30.7
$\beta_T \times 10^6$ (1/K)	210	51	54	51	24	24

($\mathrm{Pr}=6.2$) served as the base fluid. The thermophysical properties of the fluid and solid phases are shown in Table 1. The convergence criteria were chosen as $|R|_{\max} \leq 10^{-5}$, where $|R|_{\max}$ is the maximum absolute residual value for the vorticity, stream function, and temperature equations.

A series of grid systems of up to 31×31 points was used to obtain a grid-independent mesh size. The results show that when the mesh size is above 26×26, Nu_a along the hot wall and $|\psi|_{\max}$ remain the same (see Table 2). Therefore, 31×31 was used as the mesh size in this study.

In order to validate the numerical code, a solution for the enclosure filled with air ($\mathrm{Pr}=0.71$) was also obtained and compared with the benchmark results obtained by De Vahl Davis [46] through a standard finite-difference method. The results presented in Table 3 show that there is an excellent agreement between the results of the PDQ method and the benchmark results of Ref. [46]. The numerical code was also validated for several other cases that were different from the aforementioned case (see Refs. [27–30]).

The flow and energy transport in the enclosure for the copper nanofluid case are shown in Figs. 2 and 3 for various values of the inclination angle, ratios of the nanolayer thickness to the original particle radius, solid volume fractions, and the Rayleigh numbers. The heated fluid rises along the left wall as a result of buoyancy forces until it reaches near the top wall, where it turns rightward, toward the sidewalls, while it is cooled. Then it turns downward near those walls. Finally, the restriction imposed by the bottom wall forces the fluid to turn leftward, receiving heat, when it reaches the left wall. The flow path is completed as the colder fluid is entrained to the ascending flow along the heated wall. It can be observed that the flow in the enclosure is unicellular for small values of the Rayleigh number. As the Rayleigh number increases, unicellular flow in the core region breaks up into sev-

Table 2 Grid dependency for a copper-based nanofluid ($\mathrm{Ra}=10^6$)

θ	β	ϕ	Grid size	16×16	21×21	26×26	31×31
0	0.02	0.05	Nu_a	9.80	10.02	9.97	9.96
			$\lvert\psi\rvert_{\max}$	22.37	22.28	22.38	22.39
		0.20	Nu_a	11.97	11.97	11.93	11.92
			$\lvert\psi\rvert_{\max}$	31.40	31.72	31.64	31.65
	0.1	0.05	Nu_a	10.08	10.30	10.25	10.24
			$\lvert\psi\rvert_{\max}$	23.01	22.94	23.01	23.02
		0.20	Nu_a	13.24	13.21	13.17	13.16
			$\lvert\psi\rvert_{\max}$	34.74	34.83	34.86	34.77
45	0.02	0.05	Nu_a	9.61	9.79	9.76	9.76
			$\lvert\psi\rvert_{\max}$	45.37	44.76	44.83	44.86
		0.20	Nu_a	11.73	11.65	11.63	11.63
			$\lvert\psi\rvert_{\max}$	59.20	59.02	59.16	59.18
	0.1	0.05	Nu_a	9.89	10.07	10.03	10.03
			$\lvert\psi\rvert_{\max}$	46.48	45.87	45.89	45.95
		0.20	Nu_a	12.96	12.85	12.83	12.83
			$\lvert\psi\rvert_{\max}$	64.97	64.62	64.51	64.49
90	0.02	0.05	Nu_a	5.45	4.56	4.65	4.63
			$\lvert\psi\rvert_{\max}$	50.48	35.55	35.07	34.98
		0.20	Nu_a	9.42	9.50	9.49	9.49
			$\lvert\psi\rvert_{\max}$	97.12	98.95	98.72	98.78
	0.1	0.05	Nu_a	5.32	4.71	4.80	4.78
			$\lvert\psi\rvert_{\max}$	47.32	36.41	36.08	35.98
		0.20	Nu_a	10.55	10.58	10.58	10.58
			$\lvert\psi\rvert_{\max}$	105.56	107.54	107.44	107.48

Table 3 Validation of the numerical code

	$\mathrm{Ra}=10^4$		$\mathrm{Ra}=10^5$		$\mathrm{Ra}=10^6$	
	De Vahl Davis [46]	Present	De Vahl Davis [46]	Present	De Vahl Davis [46]	Present
$\lvert\psi\rvert_{\max}$	-	5.07	9.61	9.60	16.75	16.72
Nu_a	2.24	2.24	4.52	4.52	8.80	8.82
$\mathrm{Nu}_{\max}$	3.53	3.53	7.72	7.70	17.93	17.56
$\mathrm{Nu}_{\min}$	0.59	0.59	0.73	0.73	0.99	0.98

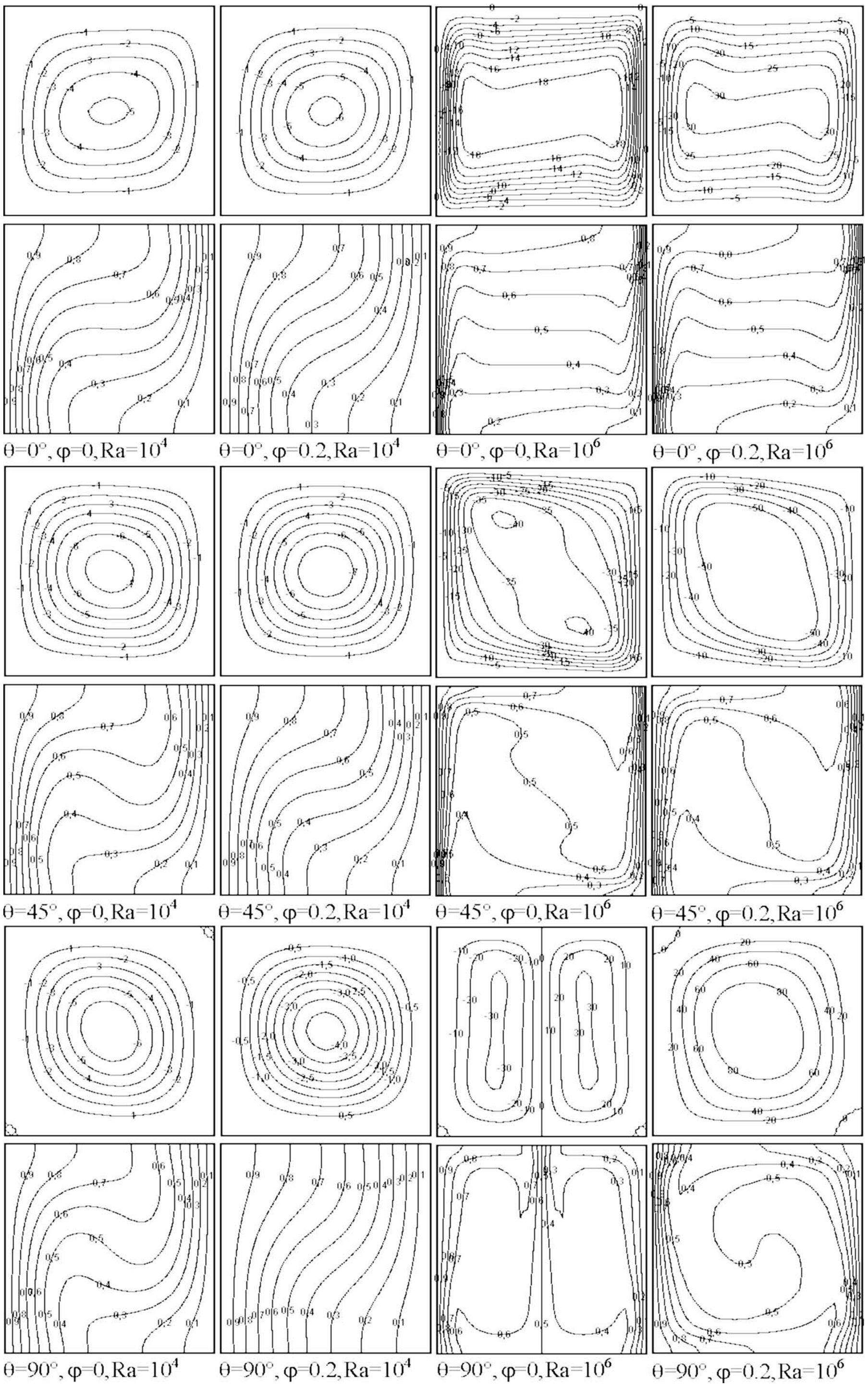

$\theta=0°$, $\varphi=0$, $Ra=10^4$ $\theta=0°$, $\varphi=0.2$, $Ra=10^4$ $\theta=0°$, $\varphi=0$, $Ra=10^6$ $\theta=0°$, $\varphi=0.2$, $Ra=10^6$

$\theta=45°$, $\varphi=0$, $Ra=10^4$ $\theta=45°$, $\varphi=0.2$, $Ra=10^4$ $\theta=45°$, $\varphi=0$, $Ra=10^6$ $\theta=45°$, $\varphi=0.2$, $Ra=10^6$

$\theta=90°$, $\varphi=0$, $Ra=10^4$ $\theta=90°$, $\varphi=0.2$, $Ra=10^4$ $\theta=90°$, $\varphi=0$, $Ra=10^6$ $\theta=90°$, $\varphi=0.2$, $Ra=10^6$

Fig. 2 Streamlines and isotherms of a copper-based nanofluid for $\beta=0.02$

eral cells. As may be observed from the figures, the flow structure evolutes toward the boundary layer regime with increasing Rayleigh numbers. The development of the boundary layer regime with increasing Rayleigh numbers is clearly illustrated by the increasing steepness of the velocity and temperature profiles near the walls, as well as by the formation of a plateau in the core region of the flow. The figures reveal that for a particular Rayleigh number, the strength of circulation increases with an increasing solid volume fraction. This is due to the increase in vertical velocity with increasing thermal energy transport from the hot wall to the fluid particles. This case will also cause a decrease in the critical Rayleigh number. This is consistent with the results of Ref. [47]. He found that the presence of nanoparticles decreases the critical Rayleigh number and therefore enhances heat transfer. As can also be seen from the figure, the multicellular flow in the core region disappears with an increasing solid volume fraction, due to the increase in vertical velocity; as a result, the deformation in the isotherms in the core region decreases. Note that an increase in the viscous forces with increasing solid volume fraction is also a fact, although it does not compensate for the increase in the thermal energy from the hot wall to the nanofluid due to increased thermal conductivity. Hence, convective circulation strengthens

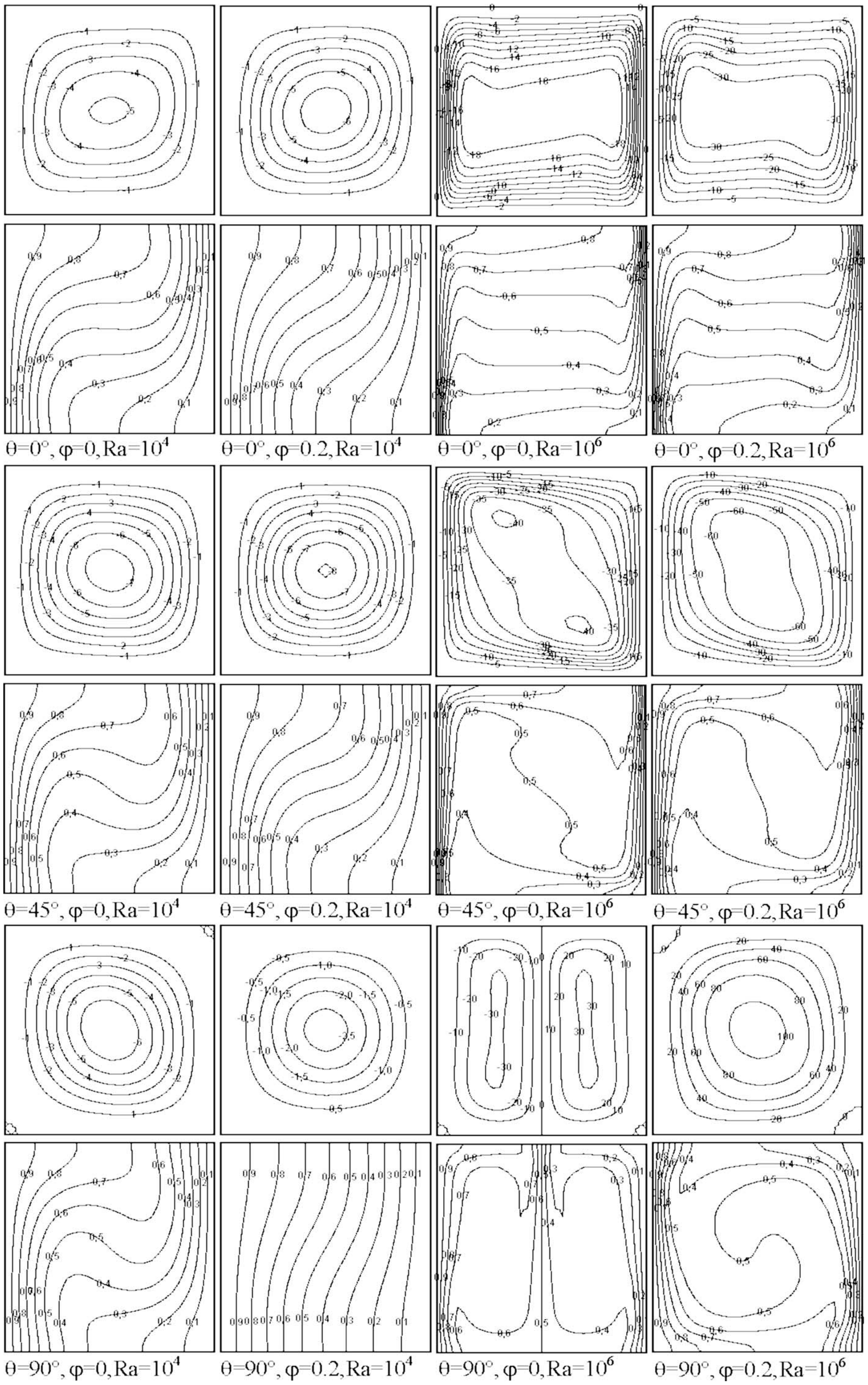
$\theta=0°$, $\varphi=0$, $Ra=10^4$ $\theta=0°$, $\varphi=0.2$, $Ra=10^4$ $\theta=0°$, $\varphi=0$, $Ra=10^6$ $\theta=0°$, $\varphi=0.2$, $Ra=10^6$

$\theta=45°$, $\varphi=0$, $Ra=10^4$ $\theta=45°$, $\varphi=0.2$, $Ra=10^4$ $\theta=45°$, $\varphi=0$, $Ra=10^6$ $\theta=45°$, $\varphi=0.2$, $Ra=10^6$

$\theta=90°$, $\varphi=0$, $Ra=10^4$ $\theta=90°$, $\varphi=0.2$, $Ra=10^4$ $\theta=90°$, $\varphi=0$, $Ra=10^6$ $\theta=90°$, $\varphi=0.2$, $Ra=10^6$

Fig. 3 Streamlines and isotherms of a copper-based nanofluid for $\beta=0.1$

with increasing solid volume fraction. Note also that with an increasing solid volume fraction, the isotherms become gradually parallel to the isothermal walls for low values of the Rayleigh number. As the volume fraction increases, thermal diffusion takes on higher values. Therefore, the isotherms become gradually parallel to the isothermal walls. As may be observed from the figures, thermal stratification in the core region is reduced with an increasing inclination angle, resulting in a stronger flow field. In the case of $\theta=90$ deg (corresponding to the enclosure heated from below), the flow and heat transfer fields show a special character. It has been demonstrated in the past [48] that multiple steady-state solutions can be obtained for this configuration. Possible solutions are given below. The first solution is the single-cellular and counterclockwise rotating flow [40]. The image of this flow through a vertical mirror, which is rotating clockwise, is also a possible solution. Both solutions yield the same average heat transfer. This kind of solution will be referred to as a S1-type solution. The second kind of solution is a bicellular ascending flow [40]. Its determination requires an adequate initial perturbation of the ψ field. The image of this flow through a horizontal mirror is also a possible solution, characterized by a bicellular descending flow. This kind of solution will be stated as a solution of the S2-type.

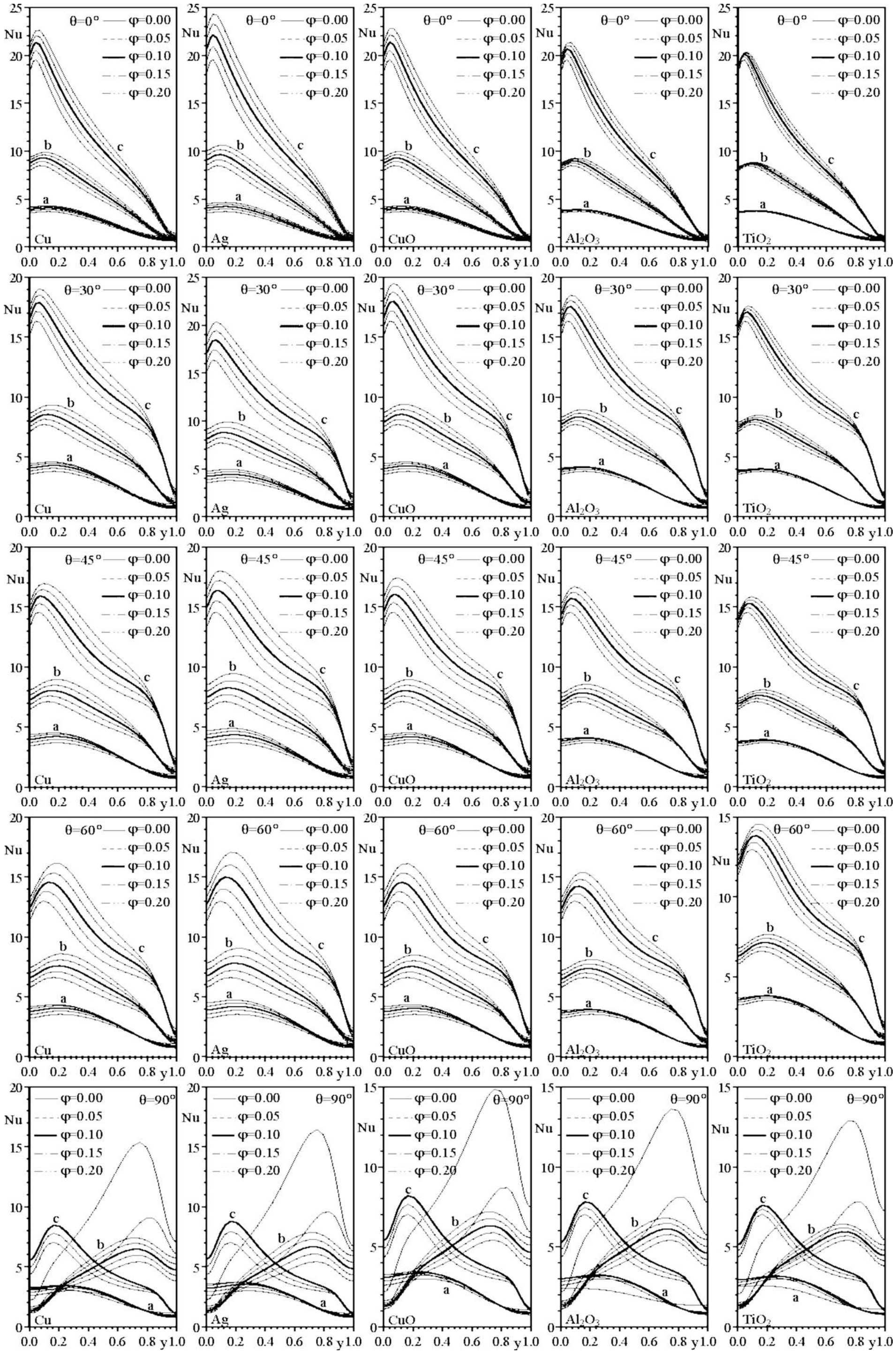

Fig. 4 Local Nusselt number for $\beta=0.02$ and (*a*) $Ra=10^4$, (*b*) $Ra=10^5$, and (*c*) $Ra=10^6$

The third kind of solution is bicellular, characterized by the presence of two horizontal cells: one (the negative cell) of which is above the other (the positive cell) [40]. Each cell is in contact with only one active wall, and the heat transfer occurs from the hot wall to the lower cell, from the lower cell to the upper cell (through the interface between the two cells), and finally from the upper cell to the cold surface. In this case, the image from a vertical mirror is also a solution to the problem, leading to the same average heat transfer. This kind of solution will be called a solution of type S3. Obtaining this solution is a special occurrence. In fact, when Ra exceeds the critical Rayleigh number Ra_c, characterizing the transition from steady-state solution of the S1-type toward an oscillatory one, the flow becomes unsteady and bicellular (S3-type) even if the initial conditions are those of a single-cellular flow [40]. As may be observed from Figs. 2 and 3, the numerical code produces an S1-type solution for $Ra=10^4$, and an S2-type solution for $Ra=10^6$. The S2-type solution changes to an S1-type for $Ra=10^6$ with increasing solid volume fraction. The effect of β on the flow and temperature field can be deduced by comparing Figs. 2 and 3. As the nanoparticle radius does not have an important effect on the solid-like nanolayer [49], higher values

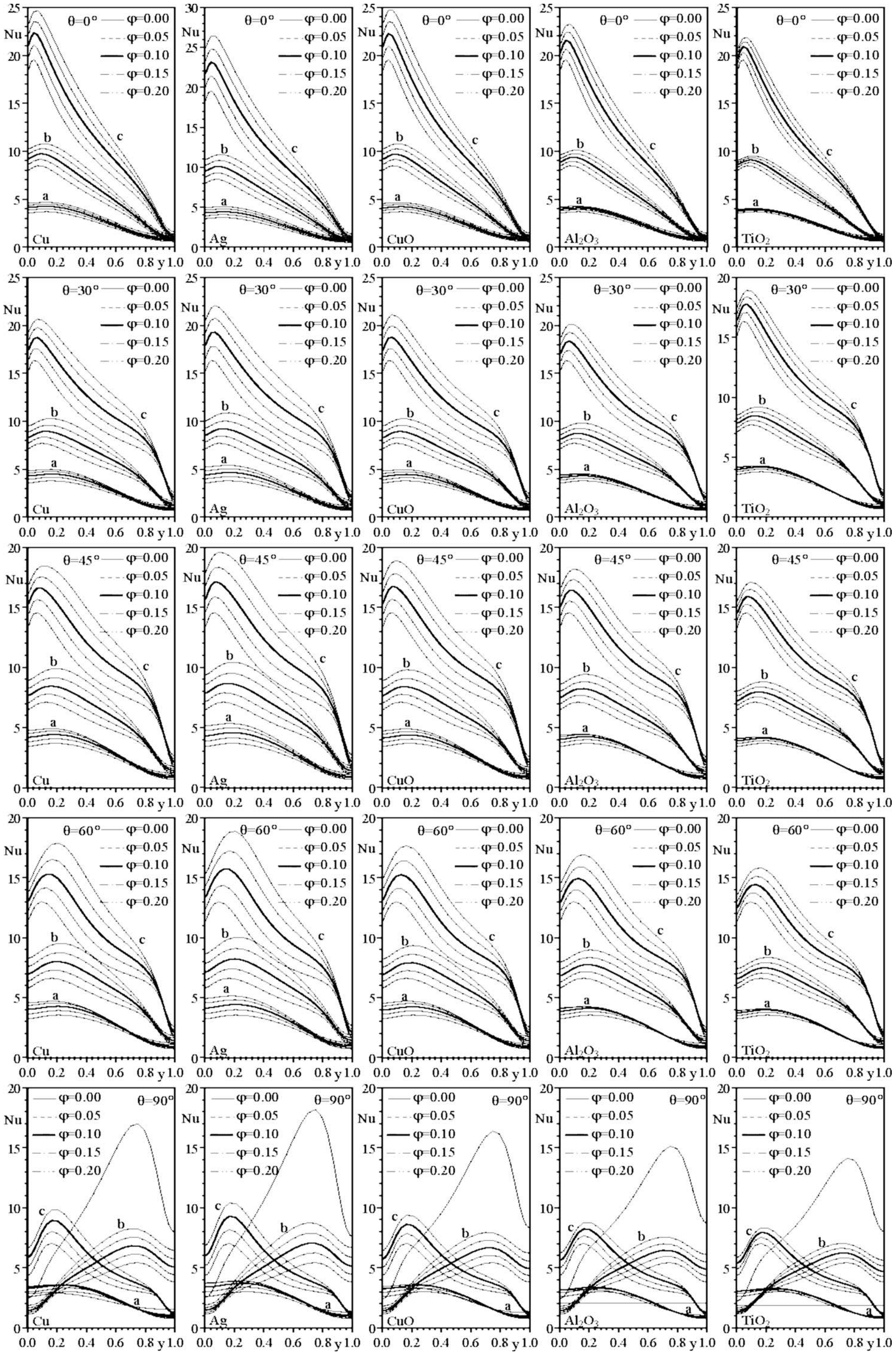

Fig. 5 Local Nusselt number for $\beta=0.1$ and (*a*) $Ra=10^4$, (*b*) $Ra=10^5$, and (*c*) $Ra=10^6$

of β correspond to a lower particle radius. As can be observed from the figures, the circulation intensity takes on higher values as the particle radius decreases.

The variation in the local Nusselt number along the hot wall is presented in Figs. 4(*a*)–4(*c*) for $\beta=0.02$. As the Rayleigh number increases, the circulation strength increases as a result of higher buoyancy forces. This results in an increase in the local Nusselt number. As a result of a stronger circulation resulting from a higher thermal energy transport from the hot wall to the fluid near the surface, therefore the local Nusselt number takes on higher values with an increasing solid volume fraction. In fact, higher values of thermal conductivity are accompanied by higher values of thermal diffusivity. The high value of thermal diffusivity therefore causes a decrease at the temperature gradient and accordingly increases the thermal boundary thickness. This increase in thermal boundary layer thickness has a negative effect on the Nusselt number; however, according to Eq. (16), the Nusselt number is a multiplication of temperature gradient and the ratio of nanofluid conductivity to the base fluid conductivity. Since the effect of the temperature gradient due to the presence of nanoparticles is much smaller than the thermal conductivity ratio, an enhancement in the Nusselt number is seen with an increase in the volume fraction of

Table 4 Average Nusselt number for inclination angle $\theta=0$ deg

Material		Cu			Ag			CuO			Al_2O_3			TiO_2		
β	φ/Ra	10^4	10^5	10^6	10^4	10^5	10^6	10^4	10^5	10^6	10^4	10^5	10^6	10^4	10^5	10^6
0.02	0.00	2.274	4.722	9.230	2.274	4.722	9.230	2.274	4.722	9.230	2.274	4.722	9.230	2.274	4.722	9.230
	0.05	2.421	5.066	9.962	2.463	5.146	10.106	2.410	5.041	9.908	2.370	4.970	9.783	2.338	4.899	9.639
	0.10	2.553	5.384	10.656	2.643	5.554	10.966	2.535	5.344	10.566	2.449	5.191	10.297	2.386	5.050	10.007
	0.15	2.670	5.674	11.310	2.813	5.946	11.808	2.650	5.631	11.204	2.515	5.385	10.771	2.420	5.173	10.332
	0.20	2.776	5.937	11.921	2.974	6.323	12.633	2.756	5.902	11.822	2.574	5.553	11.206	2.445	5.270	10.612
0.1	0.05	2.483	5.202	10.237	2.526	5.284	10.386	2.466	5.165	10.160	2.428	5.098	10.043	2.387	5.008	9.860
	0.10	2.679	5.662	11.227	2.774	5.841	11.554	2.651	5.599	11.089	2.566	5.449	10.830	2.484	5.267	10.454
	0.15	2.866	6.105	12.201	3.020	6.398	12.739	2.829	6.027	12.022	2.692	5.780	11.594	2.567	5.500	11.011
	0.20	3.052	6.537	13.163	3.267	6.962	13.953	3.005	6.452	12.966	2.824	6.095	12.342	2.646	5.711	11.534

nanoparticles. The similar dependency of the Nusselt number to the nanoparticle concentration was also obtained by Heris and co-workers [49,50] who made an experimental investigation on convective heat transfer of oxide nanofluids. As may be observed from the figures, the local Nusselt numbers for all nanofluids taken into consideration in this study have similar forms; only their magnitudes take on different values. The local Nusselt number for nanoparticles with a higher thermal conductivity (such as Ag and Cu) has higher values. This is because of the fact that thermal energy transport from the hot wall is higher for nanoparticles with higher thermal conductivities. This results in an increase in convection intensity and therefore the temperature gradient on the surface and local Nusselt number takes higher values. As shown in the figures, isotherms in the core region for a vertical enclosure are nearly horizontal, while they are oblique for an inclined enclosure. Therefore, for a vertical enclosure, the temperature of the fluid directed from the cold surface to the base of the hot surface is colder, while the temperature of the fluid in the lower part of the hot surface is higher than the corresponding fluid temperature in an inclined enclosure. As a result, the local Nusselt number for a vertical enclosure shows larger changes along the hot wall compared with the corresponding local Nusselt number for an inclined enclosure. For the inclination angle $\theta=90$ deg, the values of local Nusselt numbers are lower than that of other values of inclination angles due to the reduced value of velocity. For high values of the Rayleigh number, the Rayleigh–Bénard type flow is formed inside the enclosure for low values of nanoparticle volume fraction. Therefore, two maximum points for the local Nusselt number are formed. As the nanoparticle volume fraction increases, the Rayleigh–Bénard type flow begins to break down and a relatively stronger clockwise circulation takes place in the flow field; therefore, the local Nusselt number takes relatively higher values. The variation in the local Nusselt number for a smaller value of the nanoparticle radius $\beta=0.01$ is presented in Figs. 5(*a*)–5(*c*). It can be observed that the local heat transfer rate shows a considerable enhancement with a decreasing nanoparticle radius. This enhancement in heat transfer can be attributed primarily to the increased volume fraction of the nanolayer per $\phi_{\text{eff}} = \phi\,(1+\beta^3)$ (see Ref. [8] for details). The similar dependency of the heat transfer rate to the nanoparticle radius was also observed by Mirmasoumi and Behzadmehr [51], who studied the effect of the nanoparticle diameter on mixed convection heat transfer in a

Table 5 Average Nusselt number for inclination angle $\theta=30$ deg

Material		Cu			Ag			CuO			Al_2O_3			TiO_2		
β	φ/Ra	10^4	10^5	10^6	10^4	10^5	10^6	10^4	10^5	10^6	10^4	10^5	10^6	10^4	10^5	10^6
0.02	0.00	2.529	5.057	9.609	2.529	5.057	9.609	2.529	5.057	9.609	2.529	5.057	9.609	2.529	5.057	9.609
	0.05	2.695	5.421	10.338	2.742	5.500	10.474	2.683	5.402	10.305	2.639	5.337	10.201	2.603	5.260	10.049
	0.10	2.837	5.763	11.021	2.940	5.930	11.317	2.819	5.737	10.984	2.720	5.597	10.756	2.651	5.441	10.450
	0.15	2.950	6.088	11.656	3.119	6.354	12.138	2.935	6.063	11.646	2.767	5.837	11.275	2.669	5.602	10.811
	0.20	3.029	6.401	12.241	3.274	6.778	12.941	3.025	6.383	12.291	2.784	6.059	11.760	2.658	5.741	11.131
0.1	0.05	2.764	5.567	10.620	2.812	5.647	10.761	2.746	5.536	10.566	2.703	5.476	10.471	2.658	5.377	10.278
	0.10	2.975	6.063	11.600	3.084	6.238	11.911	2.946	6.013	11.522	2.845	5.879	11.308	2.757	5.678	10.913
	0.15	3.155	6.557	12.545	3.339	6.842	13.066	3.124	6.495	12.481	2.950	6.274	12.126	2.821	5.963	11.516
	0.20	3.303	7.061	13.467	3.575	7.475	14.241	3.277	6.989	13.452	3.025	6.663	12.931	2.854	6.232	12.086

Table 6 Average Nusselt number for inclination angle $\theta=45$ deg

Material		Cu			Ag			CuO			Al_2O_3			TiO_2		
β	φ/Ra	10^4	10^5	10^6	10^4	10^5	10^6	10^4	10^5	10^6	10^4	10^5	10^6	10^4	10^5	10^6
0.02	0.00	2.545	4.915	9.070	2.545	4.915	9.070	2.545	4.915	9.070	2.545	4.915	9.070	2.545	4.915	9.070
	0.05	2.717	5.285	9.758	2.763	5.356	9.882	2.705	5.268	9.733	2.662	5.214	9.645	2.626	5.136	9.500
	0.10	2.864	5.642	10.413	2.967	5.793	10.684	2.846	5.616	10.384	2.746	5.496	10.190	2.677	5.340	9.898
	0.15	2.976	5.988	11.035	3.148	6.232	11.480	2.962	5.960	11.025	2.789	5.762	10.709	2.692	5.525	10.264
	0.20	3.044	6.328	11.632	3.299	6.677	12.275	3.046	6.302	11.660	2.788	6.012	11.203	2.666	5.690	10.599
0.1	0.05	2.787	5.430	10.026	2.835	5.502	10.153	2.769	5.401	9.980	2.728	5.352	9.901	2.682	5.253	9.718
	0.10	3.003	5.942	10.964	3.113	6.101	11.250	2.974	5.893	10.895	2.872	5.779	10.716	2.784	5.577	10.339
	0.15	3.179	6.461	11.893	3.369	6.723	12.373	3.151	6.395	11.822	2.968	6.202	11.523	2.842	5.888	10.936
	0.20	3.308	6.996	12.832	3.595	7.383	13.542	3.292	6.913	12.775	3.017	6.624	12.334	2.855	6.186	11.516

Table 7 Average Nusselt number for inclination angle $\theta = 60$ deg

Material		Cu			Ag			CuO			Al_2O_3			TiO_2		
β	φ/Ra	10^4	10^5	10^6	10^4	10^5	10^6	10^4	10^5	10^6	10^4	10^5	10^6	10^4	10^5	10^6
0.02	0.00	2.496	4.687	8.396	2.496	4.687	8.396	2.496	4.687	8.396	2.496	4.687	8.396	2.496	4.687	8.396
	0.05	2.670	5.062	9.086	2.714	5.127	9.201	2.658	5.042	9.046	2.616	4.994	8.962	2.580	4.918	8.826
	0.10	2.815	5.428	9.762	2.916	5.568	10.014	2.798	5.395	9.694	2.699	5.286	9.509	2.631	5.133	9.231
	0.15	2.919	5.785	10.421	3.092	6.014	10.829	2.908	5.745	10.341	2.730	5.565	10.041	2.638	5.332	9.614
	0.20	2.966	6.137	11.076	3.231	6.466	11.654	2.977	6.094	10.991	2.703	5.830	10.564	2.592	5.513	9.979
0.1	0.05	2.739	5.204	9.343	2.785	5.270	9.461	2.721	5.173	9.282	2.681	5.128	9.206	2.636	5.033	9.033
	0.10	2.951	5.723	10.298	3.060	5.871	10.564	2.923	5.666	10.186	2.822	5.564	10.014	2.735	5.366	9.654
	0.15	3.113	6.252	11.269	3.306	6.499	11.708	3.090	6.172	11.117	2.898	5.999	10.831	2.780	5.689	10.265
	0.20	3.209	6.799	12.289	3.509	7.164	12.921	3.207	6.697	12.092	2.910	6.434	11.677	2.764	6.002	10.878

horizontal tube, and by Anoop et al. [52], who performed an experimental investigation on the convective heat transfer in the developing region of tube flow.

The variation in the average Nusselt number with the Rayleigh number is shown in Tables 4–8 for various values of the governing parameters. The average heat transfer rate takes on different values, ordered from the highest to lowest, in Ag, Cu, CuO, Al_2O_3, and TiO_2. As can be inferred from the results in Tables 4–8, the average Nusselt number does not change significantly with the increasing solid volume fraction for low values of the Rayleigh number, as a result of weak convection. On the other hand, for high values of the Rayleigh number, there is a remarkable increase in heat transfer with increasing solid volume fractions. It can also be concluded from the results that the average Nusselt number shows nearly a linear variation with the volume fraction. The effect of the inclination angle on the average Nusselt number can be revealed by comparing the results in Tables 4–8. The average heat transfer rate shows an increasing trend with an increasing inclination angle and a peak value is detected. Beyond the peak point, the foregoing trend reverses such that the heat transfer rate decreases with further increases in the inclination angle. The minimum heat transfer rates take place for $\theta = 90$ deg due to the low velocity encountered at this angle. The maximum heat transfer takes place at $\theta = 45$ deg for $Ra = 10^4$ and at $\theta = 30$ deg for $Ra = 10^5$ and 10^6.

The percentage increase in the average heat transfer rate is shown in Table 9, which occurs when the solid volume fraction is increased from $\phi = 0$ to $\phi = 0.2$. The thickness of the liquid layering is about 1–2 nm at most [53,54]. Therefore, the nanoparticle radius used in practice corresponds to $\beta = 0.02$ or $\beta = 0.1$. As can be seen from the table, in this case, an increase in the average heat transfer rate, up to 44% for $Ra = 10^4$, 53% for $Ra = 10^5$, and 54% for $Ra = 10^6$, occurs if the special case of $\theta = 90$ deg, which also produces the minimum heat transfer rates, is not taken into consideration. As for $\theta = 90$ deg, the heat transfer enhancement reaches 21% for $Ra = 10^4$, up to 44% for $Ra = 10^5$, and up to 138% for $Ra = 10^6$. At $Ra = 10^4$, for Al_2O_3-based and TiO_2-based nanofluids, which have a relatively small thermal conductivity, an unexpected decrease is observed in the heat transfer rate with in-

Table 8 Average Nusselt number for inclination angle $\theta = 90$ deg

Material		Cu			Ag			CuO			Al_2O_3			TiO_2		
β	φ/Ra	10^4	10^5	10^6	10^4	10^5	10^6	10^4	10^5	10^6	10^4	10^5	10^6	10^4	10^5	10^6
0.02	0.00	2.188	3.877	4.181	2.187	3.877	4.181	2.187	3.877	4.181	2.187	3.877	4.181	2.187	3.877	4.181
	0.05	2.335	4.253	4.632	2.377	4.307	4.693	2.326	4.219	4.582	2.286	4.175	4.530	2.255	4.110	4.458
	0.10	2.431	4.618	5.072	2.534	4.737	5.205	2.424	4.557	4.977	2.313	4.463	4.864	2.264	4.329	4.716
	0.15	2.433	4.974	5.490	2.636	5.165	5.709	2.456	4.892	5.363	2.214	4.742	5.179	2.170	4.5360	4.952
	0.20	2.266	5.320	9.494	2.638	5.596	9.950	2.374	5.227	9.276	1.891	5.013	8.819	1.905	4.729	8.308
0.1	0.05	2.394	4.379	4.775	2.437	4.435	4.838	2.379	4.334	4.712	2.339	4.295	4.664	2.302	4.211	4.571
	0.10	2.533	4.884	5.374	2.647	5.010	5.516	2.521	4.799	5.250	2.399	4.711	5.141	2.339	4.536	4.948
	0.15	2.535	5.397	5.966	2.777	5.605	6.207	2.566	5.276	5.794	2.277	5.131	5.609	2.236	4.856	5.307
	0.20	2.267	5.922	10.574	2.743	6.230	11.086	2.432	5.771	10.277	2.023	5.558	9.827	1.837	5.170	9.125

Table 9 Percentage increase in the average Nusselt number

Material		Cu			Ag			CuO			Al_2O_3			TiO_2		
θ (deg)	β	10^4	10^5	10^6	10^4	10^5	10^6	10^4	10^5	10^6	10^4	10^5	10^6	10^4	10^5	10^6
0	0.02	22	25	29	31	34	37	21	25	28	13	18	21	8	12	15
	0.1	34	38	42	44	47	51	32	37	41	24	29	34	16	21	25
30	0.02	20	27	27	30	34	35	20	26	28	10	20	22	5	14	16
	0.1	31	40	40	41	48	48	30	38	40	20	32	35	13	23	26
45	0.02	20	29	28	30	36	35	20	28	29	10	22	24	5	16	17
	0.1	30	42	42	41	50	49	29	41	41	19	35	36	12	26	27
60	0.02	19	31	32	30	38	39	19	30	31	8	24	26	4	18	19
	0.1	29	45	46	41	53	54	29	43	44	17	37	39	11	28	30
90	0.02	4	37	127	21	44	138	9	35	122	−14	29	111	−13	22	99
	0.1	4	53	153	25	61	165	11	49	146	−7	43	135	−16	33	118

Table 10 A comparison for the average Nusselt number

	ϕ	0	0.04	0.08	0.12	0.16	0.20
Present	$Gr=10^3$	1.94	2.07	2.21	2.34	2.48	2.63
Khanafer et al. [19]	$Gr=10^3$	1.96	2.11	2.25	2.36	2.57	2.75
Present	$Gr=10^4$	4.08	4.41	4.72	5.03	5.33	5.62
Khanafer et al. [19]	$Gr=10^4$	4.07	4.36	4.68	5.00	5.32	5.68

creasing solid volume fraction for an inclination angle of $\theta = 90$ deg. With increasing solid volume fractions, the isotherms gradually become parallel to the isothermal walls (see Figs. 2 and 3), which is the conduction solution ($Ra=10^4$), as a result of a weakening clockwise circulation; therefore, the heat transfer rate decreases.

The problem considered in this paper was also studied by Khanafer et al. [19] for the vertical enclosure case. A comparison of the values of the average Nusselt number obtained in the work done by Khanafer et al. [19] and in this work show that there is a reasonably good agreement (see Table 10). Differences between the results can be attributed to the fact that Khanafer et al. [19] used a different model, which was based on the thermal dispersion of nanoparticles, for his thermal conductivity predictions.

4 Conclusion

Heat transfer enhancement of water-based nanofluids in a differentially heated, tilted enclosure is studied numerically for a range of inclination angles, nanoparticle radii, solid volume fractions, and Rayleigh numbers. It may be concluded from the results that suspended nanoparticles substantially increase the heat transfer rate. It may also be concluded that the variation in the average Nusselt number is nearly linear with the solid volume fraction. The results also show that the average heat transfer rate increases with an increasing inclination angle, and a peak value is detected. Beyond the peak point, the foregoing trend reverses and the average heat transfer rate decreases with a further increase in the inclination angle. Minimum heat transfer takes place at $\theta=90$ deg. Maximum heat transfer takes place at $\theta=45$ deg for $Ra=10^4$ and at $\theta=30$ deg for $Ra=10^5$ and 10^6.

Nomenclature

c_p = specific heat at constant pressure
g = gravitational acceleration
Gr = Grashof number
H = height of the enclosure
k = thermal conductivity
L = width of the enclosure
Nu = Nusselt number
n = shape factor
p = pressure
Pr = Prandtl number
R = residue
Ra = Rayleigh number
T = temperature
u = velocity component in the x direction
v = velocity component in the y direction
x = Cartesian coordinate
y = Cartesian coordinate

Greek Symbols

α = thermal diffusivity
β = ratio of the nanolayer thickness to the original particle radius
β_T = thermal expansion coefficient
γ = kinematic viscosity
η = outward variable normal to the surface
φ = solid volume fraction
μ = dynamic viscosity
θ = inclination angle
ρ = density
Ψ = sphericity
ψ = stream function
ω = vorticity

Subscripts

a = average
C = cold
eff = effective
f = fluid
H = hot
o = reference value
s = solid

Superscript

* = dimensional variable

References

[1] Eastman, J. A., Choi, S. U. S., Yu, W., and Thompson, L. J., 2001, "Anomalously Increased Effective Thermal Conductivity of Ethylene Glycol-Based Nanofluids Containing Copper Nanoparticles," Appl. Phys. Lett., **78**, pp. 718–720.
[2] Choi, S. U. S., Zhang, Z. G., Yu, W., Lockwood, F. E., and Grulke, E. A., 2001, "Anomalous Thermal Conductivity Enhancement in Nanotube Suspension," Appl. Phys. Lett., **79**, pp. 2252–2254.
[3] Xuan, Y., and Li, Q., 2000, "Heat Transfer Enhancement of Nanofluids," Int. J. Heat Fluid Flow, **21**, (1), pp. 58–64.
[4] Das, S. K., Putra, N., Thiesen, P., and Roetzel, W., 2003, "Temperature Dependence of Thermal Conductivity Enhancement for Nanofluids," ASME J. Heat Transfer, **125**, pp. 567–574.
[5] Keblinski, P., Phillpot, S. R., Choi, S. U. S., and Eastman, J. A., 2002, "Mechanisms of Heat Flow in Suspensions of Nano-sized Particles (Nanofluids)," Int. J. Heat Mass Transfer, **45**, pp. 855–863.
[6] Maxwell, J. C., 1881, *A Treatise on Electricity and Magnetism*, Clarendon, Oxford, UK.
[7] Hamilton, R. L., and Crosser, O. K., 1962, "Thermal Conductivity of Heterogeneous Two-Component Systems," Ind. Eng. Chem. Fundam., **1**, pp. 187–191.
[8] Yu, W., and Choi, S. U. S., 2003, "The Role of Interfacial Layers in the Enhanced Thermal Conductivity of Nanofluids: A Renovated Maxwell Model," J. Nanopart. Res., **5**, pp. 167–171.
[9] Brinkman, H. C., 1952, "The Viscosity of Concentrated Suspensions and Solutions," J. Chem. Phys., **20**, pp. 571–581.
[10] Xuan, Y., Li, Q., Xuan, Y., and Li, Q., 1999, "Experimental Research on the Viscosity of Nanofluids," Report of Nanjing University of Science and Technology.
[11] Xuan, Y., and Li, Q., 2003, "Investigation on Convective Heat Transfer and Flow Features of Nanofluids," ASME J. Heat Transfer, **125**, pp. 151–155.
[12] Eastman, J. A., Choi, S. U. S., Li, S., Soyez, G., Thompson, L. J., and DiMelfi, R. J., 1999, "Novel Thermal Properties of Nanostructured Materials," J. Metastable Nanocryst. Mater., **2–6**, pp. 629–634.
[13] Wen, D., and Ding, Y., 2004, "Experimental Investigation Into Convective Heat Transfer of Nanofluids at the Entrance Region Under Laminar Flow Conditions," Int. J. Heat Mass Transfer, **47**, pp. 5181–5188.
[14] Maiga, S. E. B., Nguyen, C. T., Galanis, N., and Roy, G., 2004, "Heat Transfer Behaviours of Nanofluids in a Uniformly Heated Tube," Superlattices Microstruct., **35**, pp. 543–557.
[15] Maiga, S. E. B., Palm, S. J., Nguyen, C. T., Roy, G., and Galanis, N., 2005, "Heat Transfer Enhancement by Using Nanofluids in Forced Convection Flows," Int. J. Heat Fluid Flow, **26**, pp. 530–546.
[16] Akbarinia, A., and Behzadmehr, A., 2007, "Numerical Study of Laminar Mixed Convection of a Nanofluid in Horizontal Curved Tubes," Appl. Therm. Eng., **27**(8–9), pp. 1327–1337.
[17] Mirmasoumi, S., and Behzadmehr, A., 2008, "Numerical Study of Laminar Mixed Convection of a Nanofluid in a Horizontal Tube Using Two-Phase Mixture Model," Appl. Therm. Eng., **28**(7), pp. 717–727.
[18] Izadi, M., Behzadmehr, A., and Jalali-Vahida, D., 2009, "Numerical Study of

Developing Laminar Forced Convection of a Nanofluid in an Annulus," Int. J. Therm. Sci., **48**(11), pp. 2119–2129.
[19] Khanafer, K., Vafai, K., and Lightstone, M., 2003, "Buoyancy Driven Heat Transfer Enhancement in a Two-Dimensional Enclosure Utilizing Nanofluids," Int. J. Heat Mass Transfer, **46**, pp. 3639–3653.
[20] Santra, A. K., Sen, S., and Chakraborty, N., 2008, "Study of Heat Transfer Augmentation in a Differentially Heated Square Cavity Using Copper–Water Nanofluid," Int. J. Therm. Sci., **47**, pp. 1113–1122.
[21] Hwang, K. S., Lee, J. H., and Jang, S. P., 2007, "Buoyancy-Driven Heat Transfer of Water-Based Al_2O_3 Nanofluids in a Rectangular Cavity," Int. J. Heat Mass Transfer, **50**, pp. 4003–4010.
[22] Jou, R.-Y., and Tzeng, S.-C., 2006, "Numerical Research of Nature Convective Hat Transfer Enhancement Filled With Nanofluids in Rectangular Enclosures," Int. Commun. Heat Mass Transf., **33**, pp. 727–736.
[23] Oztop, H. F., and Abu-Nada, E., 2008, "Numerical Study of Natural Convection in Partially Heated Rectangular Enclosures Filled With Nanofluids," Int. J. Heat Fluid Flow, **29**(5), pp. 1326–1336.
[24] Aminossadati, S. M., and Ghasemi, B., 2009, "Natural Convection Cooling of a Localised Heat Source at the Bottom of a Nanofluid-Filled Enclosure," Eur. J. Mech. B/Fluids, **28**(5), pp. 630–640.
[25] Tiwari, R. K., and Das, M. K., 2007, "Heat Transfer Augmentation in a Two-Sided Lid-Driven Differentially Heated Square Cavity Utilizing Nanofluids," Int. J. Heat Mass Transfer, **50**, pp. 2002–2018.
[26] Koo, J., and Kleinstreuer, C., 2005, "Laminar Nanofluid Flow in Microheat-Sinks," Int. J. Heat Mass Transfer, **48**, pp. 2652–2661.
[27] Kahveci, K., 2007, "Numerical Simulation of Natural Convection in a Partitioned Enclosure Using PDQ Method," Int. J. Numer. Methods Heat Fluid Flow, **17**(4), pp. 439–456.
[28] Kahveci, K., 2007, "Natural Convection in a Partitioned Vertical Enclosure Heated With a Uniform Heat Flux," ASME J. Heat Transfer, **129**, pp. 717–726.
[29] Kahveci, K., 2007, "A Differential Quadrature Solution of Natural Convection in an Enclosure With a Finite Thickness Partition," Numer. Heat Transfer, Part A, **51**(10), pp. 979–1002.
[30] Kahveci, K., and Öztuna, S., 2008, "A Differential Quadrature Solution of MHD Natural Convection in an Inclined Enclosure With a Partition," ASME J. Fluids Eng., **130**, p. 021102.
[31] Öztuna, S., 2007, "A Differential Quadrature Solution of Natural Convection in an Enclosure With a Partial Partition," Numer. Heat Transfer, Part A, **52**(11), pp. 1009–1026.
[32] Oztop, H. F., and Dagtekin, I., 2004, "Mixed Convection in Two-Sided Lid-Driven Differentially Heated Square Cavity," Int. J. Heat Mass Transfer, **47**, pp. 1761–1769.
[33] Bilgen, E., and Oztop, H., 2005, "Natural Convection Heat Transfer in Partially Open Inclined Square Cavities," Int. J. Heat Mass Transfer, **48**(8), pp. 1470–1479.
[34] Oztop, H., and Bilgen, E., 2006, "Natural Convection in Differentially Heated and Partially Divided Square Cavities With Internal Heat Generation," Int. J. Heat Fluid Flow, **27**, pp. 466–475.
[35] Oztop, H. F., 2007, "Natural Convection in Tilted Porous Enclosures With Discrete Heat Sources," Journal of Energy, Heat Mass Transfer, **29**, pp. 83–94.
[36] Oztop, H. F., 2007, "Natural Convection in Partially Cooled and Inclined Porous Rectangular Enclosures," Int. J. Therm. Sci., **46**, pp. 149–156.
[37] Lamsaadi, M., Naimi, M., Hasnaoui, M., and Mamou, M., 2006, "Natural Convection in a Vertical Rectangular Cavity With a Non-Newtonian Power Law Fluid and Subjected to a Horizontal Temperature Gradient," Numer. Heat Transfer, Part A, **49**, pp. 969–990.
[38] Bazylak, A., Djilali, N., and Sinton, D., 2006, "Natural Convection in an Enclosure With Distributed Heat Sources," Numer. Heat Transfer, Part A, **49**, pp. 655–667.
[39] Nakhi, A. B., and Chamkha, A. J., 2006, "Effect of Length and Inclination of a Thin Fin on Natural Convection in a Square Enclosure," Numer. Heat Transfer, Part A, **50**(3), pp. 389–407.
[40] Ridouane, E. H., Hasnaoui, M., Amahmid, A., and Raji, A., 2004, "Interaction Between Natural Convection and Radiation in a Square Cavity Heated From Below," Numer. Heat Transfer, Part A, **45**(3), pp. 289–311.
[41] Gill, A. E., 1966, "The Boundary Layer Regime for Convection in a Rectangular Cavity," J. Fluid Mech., **26**, pp. 515–536.
[42] Shu, C., 2000, *Differential Quadrature and Its Application in Engineering*, Springer-Verlag, Berlin.
[43] Bellman, R. E., Kashef, B. G., and Casti, J., 1972, "Differential Quadrature: A Technique for the Rapid Solution of Nonlinear Partial Differential Equations," J. Comput. Phys., **10**, pp. 40–52.
[44] Shu, C., 1992, "Generalized Differential-Integral Quadrature and Application to the Simulation of Incompressible Viscous Flows Including Parallel Computation," Ph.D. thesis, University of Glasgow, Glasgow, UK.
[45] Shu, C., and Richards, B. E., 1992, "Application of Generalized Differential Quadrature to Solve Two-Dimensional Incompressible Navier–Stokes Equations," Int. J. Numer. Methods Fluids, **15**, pp. 791–798.
[46] De Vahl Davis, G. V., 1983, "Natural Convection of Air in a Square Cavity: A Benchmark Numerical Solution," Int. J. Numer. Methods Fluids, **3**, pp. 249–264.
[47] Tzou, D. Y., 2008, "Instability of Nanofluids in Natural Convection," ASME J. Heat Transfer, **130**, p. 072401.
[48] Hasnaoui, M., Bilgen, E., and Vasseur, P., 1992, "Natural Convection Heat Transfer in Rectangular Cavities Partially Heated From Below," J. Thermophys. Heat Transfer, **6**(2), pp. 255–264.
[49] Zeinali Heris, S., Etemad, S. G., and Esfahany, M. N., 2006, "Experimental Investigation of Oxide Nanofluids Laminar Flow Convective Heat Transfer," Int. Commun. Heat Mass Transfer, **33**, pp. 529–535.
[50] Zeinali Heris, S., Esfahany, M. N., and Etemad, S. G., 2007, "Experimental Investigation of Convective Heat Transfer of Al_2O_3/Water Nanofluid in Circular Tube," Int. J. Heat Fluid Flow, **28**, pp. 203–210.
[51] Mirmasoumi, S., and Behzadmehr, A., 2008, "Effect of Nanoparticles Mean Diameter on Mixed Convection Heat Transfer of a Nanofluid in a Horizontal Tube," Int. J. Heat Fluid Flow, **29**, pp. 557–566.
[52] Anoop, K. B., Sundararajan, T., and Das, S. K., 2009, "Effect of Particle Size on the Convective Heat Transfer in Nanofluid in the Developing Region," Int. J. Heat Mass Transfer, **52**, pp. 2189–2195.
[53] Wang, B.-X., Zhou, L.-P., and Peng, X.-F., 2003, "A Fractal Model for Predicting the Effective Thermal Conductivity of Liquid With Suspension of Nanoparticles," Int. J. Heat Mass Transfer, **46**, pp. 2665–2672.
[54] Tillman, P., and Hill, J. M., 2007, "Determination of Nanolayer Thickness for a Nanofluid," Int. Commun. Heat Mass Transf., **34**, pp. 399–407.

Effects of Insulated and Isothermal Baffles on Pseudosteady-State Natural Convection Inside Spherical Containers

Yuping Duan[1]

S. F. Hosseinizadeh[2]
Visiting Research Scholar

J. M. Khodadadi
Professor
Mem. ASME
e-mail: khodajm@auburn.edu

Department of Mechanical Engineering,
Auburn University,
270 Ross Hall,
Auburn, AL 36849-5341

The effects of insulated and isothermal thin baffles on pseudosteady-state natural convection within spherical containers were studied computationally. The computations are based on an iterative, finite-volume numerical procedure using primitive dependent variables. Natural convection effect is modeled via the Boussinesq approximation. Parametric studies were performed for a Prandtl number of 0.7. For Rayleigh numbers of 10^4, 10^5, 10^6, and 10^7, baffles with three lengths positioned at five different locations were investigated (120 cases). The fluid that is heated adjacent to the sphere rises replacing the colder fluid, which sinks downward through the stratified stable thermal layer. For high Ra number cases, the hot fluid at the bottom of the sphere is also observed to rise along the symmetry axis and encounter the sinking colder fluid, thus causing oscillations in the temperature and flow fields. Due to flow obstruction (blockage or confinement) effect of baffles and also because of the extra heating afforded by the isothermal baffle, multi-cell recirculating vortices are observed. This additional heat is directly linked to creation of another recirculating vortex next to the baffle. In effect, hot fluid is directed into the center of the sphere disrupting thermal stratified layers. For the majority of the baffles investigated, the Nusselt numbers were generally lower than the reference cases with no baffle. The extent of heat transfer modification depends on Ra, length, and location of the extended surface. With an insulated baffle, the lowest amount of absorbed heat corresponds to a baffle positioned horizontally. Placing a baffle near the top of the sphere for high Ra number cases can lead to heat transfer enhancement that is linked to disturbance of the thermal boundary layer. With isothermal baffles, heat transfer enhancement is achieved for a baffle placed near the bottom of the sphere due to interaction of the counterclockwise rotating vortex and the stratified layer. For some high Ra cases, strong fluctuations of the flow and thermal fields indicating departure from the pseudosteady-state were observed. [DOI: 10.1115/1.4000753]

1 Introduction

Containment of fluids within spherical vessels is very common in industrial applications in relation to storage and transport of cryogenic liquids and propellants. For example, a great number of supertankers carrying liquid natural gas utilize spherical containers. Schmidt [1] can be credited as the first researcher to have reported on unsteady heat transfer inside spherical containers subject to a step change in wall temperature. Measurements were carried out for five different diameters ranging from 100 mm to 500 mm. By utilizing water and three alcohols (methyl, ethyl, and butyl) with different properties, a range of the Rayleigh numbers ($2\times10^9 - 5\times10^{11}$) was covered. The measurements of surface temperature and fluid velocity within a spherical cavity that was cut into a two-piece Plexiglas block was reported by Shaidurov [2] for Rayleigh number range of $10^4 - 10^6$. It was possible to heat and cool the two parts of the block independently. Moreover, the experimental set-up was designed so as to vary the angle between the imposed temperature gradient and the gravitational acceleration. A correlation relating the governing parameters was presented. Subsequent work on natural convection inside spherical containers [3–5] was reviewed in an earlier paper of one of the authors [6]. Most notably, Chow and Akins [5] presented their experimental investigation of the pseudosteady-state (PSS) natural convection inside spheres. The main feature of the PSS treatment is that the driving force for convection is continuously maintained, i.e., the temperature outside the sphere was increased so that the temperature difference between the outside and the center of the sphere remained constant. During the flow visualization phase of the study, the motion of hollow glass spheres was monitored and the location of the eye of the recirculation pattern was quantified. Comparison of findings of Ref. [5] with the analytical results of Pustovoit [3] and the computational data of Whitley and Vachon [4] were attempted. However, previous mathematical analyses treated a transient phenomenon, whereas Chow and Akins [5] strived to maintain the PSS condition. In view of this, direct comparisons should be considered unwarranted. Finally, Ref. [5] also provided an empirical correlation for the mean Nusselt number in the laminar regime (Rayleigh number below 10^7). Val'tsiferov and Polezhaev [7] referred to a number of articles directed at theoretical and experimental studies of natural convection in spherical vessels filled with a liquid. Among them, only Refs. [3,4] are

---

[1] Currently with China Guodian Corp., Zhongneng Power-Tech Development Co., Ltd., Beijing, China.

[2] At that time, a Ph.D. candidate in the Department of Aerospace Engineering, Sharif University of Technology, I.R. Iran; currently an Assistant Professor, Mechanical Engineering Department, Babol Noshirvani University of Technology, Babol, Iran.

Contributed by the Heat Transfer Division of ASME for publication in the JOURNAL OF HEAT TRANSFER. Manuscript received June 14, 2009; final manuscript received November 11, 2009; published online April 1, 2010. Editor: Yogesh Jaluria.

widely available. They refer to the experimental data for given surface heat flux values with relatively high Rayleigh (10^9–10^{11}) and Prandtl numbers (3–1500) for which the characteristics of convection were found to be contradictory. They continued to present a computational study of natural convection in a sphere with a thin-walled shell for a range of the Rayleigh and Fourier numbers that covered the principal conditions of time-dependent laminar convection due to given heat flux on the surface of the sphere. Detailed computational results for the PSS two-dimensional, natural convection inside spheres were reported by Hutchins and Marschall [8]. Similar to Ref. [4], they utilized a finite-difference-based vorticity-stream function numerical procedure to simulate the flow and temperature fields in the laminar regime ($10^5 < \mathrm{Ra} < 10^8$) and two different Prandtl numbers of 0.7 and 8. In order to compare to the experimental results of Ref. [5], a case of $\mathrm{Pr}=4$ and $\mathrm{Ra}=5.2\times10^7$ was also simulated. The general trends of their computed eye of the recirculation zone and mean Nusselt number variation were similar to the findings of Ref. [5]. The heat transfer data were found to be independent of the Prandtl number. Both streamline and temperature contours were presented, showing their dependence on the Rayleigh number. Finally, they proposed a mean Nusselt number correlation applicable for the Rayleigh number range of 10^5–10^8. The computational results of Ref. [9] were generally in concert with the predictions of Ref. [8] and the experimental observations of Ref. [5]. A study by Khodadadi et al. [10] focused on the analysis of PSS natural convection within rotating spheres. Their results for the limiting case of no rotation were obtained for Ra numbers different than a previous study by Shen et al. [9]. The utilization of baffles for affecting internal natural convection in similar systems has been widespread, as discussed by [11].

In extending the breadth of previous work, the present study was initiated to explore the utilization of baffles within spherical containers in order to control the flow field and consequently heat transfer, through its enhancement and/or degradation. In analyzing the two extreme cases for the thermal condition of the baffle, the pseudosteady-state natural convection within spherical containers due to presence of insulated and isothermal baffles is discussed in this paper. By performing an elaborate computational study, clear conclusions in relation to utilization of insulated or isothermal baffles in spherical containers were obtained.

2 Mathematical Formulation

Consider a spherical container with diameter of $D=2R$ that is completely filled with a motionless fluid held at T_0. The wall temperature (T_w) of the sphere is allowed to vary with time so that it was always above the temperature of the center of the sphere (T_c) by a constant value. In view of the spherical shape, the orthogonal spherical coordinate system is adopted. A thin baffle (extended surface) with length l that makes a right angle with the inner surface of the sphere is positioned at polar angle θ_b (Fig. 1). A three-dimensional cutaway view of the system is also shown in the same figure. The baffle is part of a cone with its apex coinciding with the center of the sphere. The baffle can be either insulated or isothermal (T_w). It is assumed that the following prevails:

1. The dependent variables (velocity, pressure, and temperature) are symmetric with respect to the azimuthal direction (ϕ). Therefore, they are functions of only two spatial coordinates, i.e., radial coordinate (r) and θ. Thus, the flow field is two-dimensional. The gravitational acceleration points downward along the symmetry axis.
2. The fluid is viscous and Newtonian with constant properties except for the variation in density that is modeled using the Boussinesq approximation.
3. Viscous heating effects are ignored.

By utilizing the length and velocity scales to be R and α/R, the dimensionless variables are

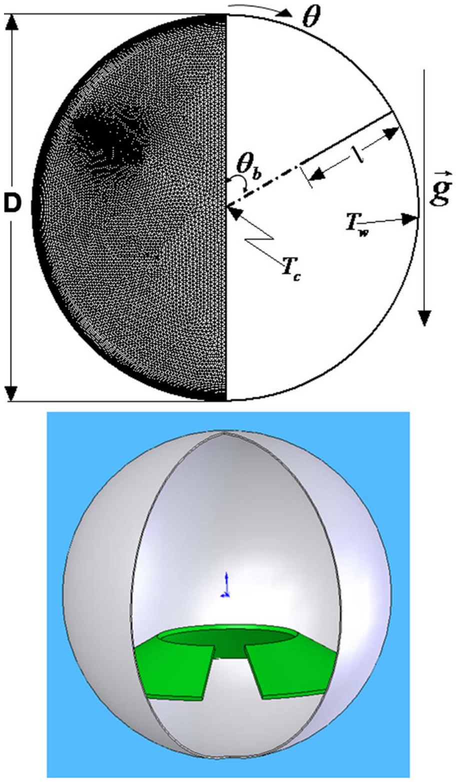

Fig. 1 **Schematic diagram of a spherical container with an insulated or isothermal thin baffle and its three-dimensional cutaway view**

$$r^*=\frac{r}{R},\quad \tau=\frac{\alpha t}{R^2},\quad V_r^*=\frac{V_rR}{\alpha},\quad V_\theta^*=\frac{V_\theta R}{\alpha},\quad p^*=\frac{(p-p_0)R^2}{\rho\alpha^2}$$
$$T^*=\frac{T-T_0}{T_w-T_c},\quad g_r^*=\frac{g_r}{g},\quad g_\theta^*=\frac{g_\theta}{g} \tag{1}$$

Upon introducing these relations, the dimensionless governing equations can be obtained. The continuity equation is

$$\frac{1}{r^{*2}}\frac{\partial}{\partial r^*}(r^{*2}V_r^*)+\frac{1}{r^*\sin\theta}\frac{\partial}{\partial\theta}(V_\theta^*\sin\theta)=0 \tag{2}$$

The momentum equation in the radial (r) and polar (θ) directions are

$$\begin{aligned}\frac{\partial V_r^*}{\partial\tau}+V_r^*\frac{\partial V_r^*}{\partial r^*}+\frac{V_\theta^*}{r^*}\frac{\partial V_r^*}{\partial\theta}-\frac{V_\theta^{*2}}{r^*}\\ =-\frac{\partial p^*}{\partial r^*}-\frac{1}{8}Ra\,\mathrm{Pr}\,g_r^*T^*\\ +\mathrm{Pr}\left[\nabla^{*2}V_r^*-\frac{2}{r^{*2}}V_r^*-\frac{2}{r^{*2}}\frac{\partial V_\theta^*}{\partial\theta}-\frac{2\cot\theta}{r^{*2}}V_\theta^*\right]\end{aligned} \tag{3}$$

and

$$\begin{aligned}\frac{\partial V_\theta^*}{\partial\tau}+V_r^*\frac{\partial V_\theta^*}{\partial r^*}+\frac{V_\theta^*}{r^*}\frac{\partial V_\theta^*}{\partial\theta}+\frac{V_r^*V_\theta^*}{r^*}\\ =-\frac{1}{r^*}\frac{\partial p^*}{\partial\theta}-\frac{1}{8}\mathrm{Ra}\,\mathrm{Pr}\,g_\theta^*T^*+\mathrm{Pr}\left[\nabla^{*2}V_\theta^*+\frac{2}{r^{*2}}\frac{\partial V_r^*}{\partial\theta}-\frac{V_\theta^*}{r^{*2}\sin^2\theta}\right]\end{aligned} \tag{4}$$

with $Ra=g\beta D^3(T_w-T_c)/\alpha\nu$, $\mathrm{Pr}=\nu/\alpha$, and

$$\nabla^{*2} = \frac{1}{r^{*2}}\frac{\partial}{\partial r^*}\left(r^{*2}\frac{\partial}{\partial r^*}\right) + \frac{1}{r^{*2}\sin\theta}\frac{\partial}{\partial\theta}\left(\sin\theta\frac{\partial}{\partial\theta}\right) \tag{5}$$

Finally, the energy equation is

$$\frac{\partial T^*}{\partial\tau} + V_r^*\frac{\partial T^*}{\partial r^*} + \frac{V_\theta^*}{r^*}\frac{\partial T^*}{\partial\theta} = \nabla^{*2}T^* \tag{6}$$

2.1 Boundary and Initial Conditions. The fluid flow boundary conditions on the solid surface of the sphere ($r^*=1$) and baffle are

$$V_\theta^* = V_r^* = 0 \tag{7}$$

The thermal condition of the wall of the sphere becomes

$$T_w^*(\tau) = T_c^*(\tau) + 1 \tag{8}$$

that ensures that the pseudosteady-state condition is maintained. The boundary conditions on the symmetry axis of the sphere ($\theta=0$ and π) are

$$V_\theta^* = \frac{\partial V_r^*}{\partial\theta} = \frac{\partial T^*}{\partial\theta} = 0 \tag{9}$$

For an insulated baffle, the following relation:

$$\frac{\partial T^*}{\partial\theta} = 0 \tag{10}$$

will hold on both sides of the baffle ($(1-2L)\leq r^* < 1$ and $\theta=\theta_b$) with $L=l/D$, whereas for an isothermal baffle, relation (8) will be satisfied.

At the beginning of the computations, the fluid velocity and temperature were set to zero. The pseudosteady-state behavior of this system is characterized by the Rayleigh number, Prandtl number, length of the baffle, and its polar angle position. Previous findings [8–10] have established the weak dependence of the results on the Prandtl number. Therefore, a single Prandtl number equal to 0.7 was used. The Ra number, dimensionless length of the baffle (L) and polar angle position (θ_b) were varied with Ra $=10^4$, 10^5, 10^6, and 10^7 (mainly in the laminar regime), $L=0.05$, 0.1, and 0.25, and $\theta_b=30$ deg, 60 deg, 90 deg, 120 deg, and 150 deg. In effect, a parametric study comprised of 120 cases was performed for both insulated and isothermal baffles.

2.2 Computational Methodology. The SIMPLE method [12] within version 6.2.16 of the commercial code FLUENT [13] was utilized for solving the governing equations. For a thin layer next to the solid wall, a structured grid system with shrinking grid spacing toward the wall was employed. The thickness of this layer was estimated from well-established correlations for natural convection and was fixed to 4% of the diameter. Unstructured grids were laid over the remainder of the sphere. Grid-independence tests were performed for 14 grid densities (e.g., 2084, 8972, 13,868, 23,584, and 35,744 cells) for both baffles with Ra$=10^7$, $L=0.25$, and $\theta_b=90$ deg [14]. The numerical results revealed that the relative errors for the average Nusselt numbers and its root mean square (RMS, to be discussed in the next section) were insignificant for grid density of 5200 and higher. Therefore, a grid density with 13,868 cells was employed for the production runs. Similar time-step independence tests were carried out with 11 time-step increments ranging from 0.1 s to 30 s [14]. For the final runs, a time-step for integrating the temporal derivatives was set to 2 s ($\Delta\tau=1.57\times10^{-4}$). The quadratic upstream interpolation for convective kinematics (QUICK) differencing scheme was used for solving the momentum and energy equations, whereas the pressure staggering option (PRESTO) scheme was adopted for the pressure correction equation. Second-order accurate implicit discretization was utilized for the unsteady terms. The under-relaxation factors for the velocity components, pressure correction, and thermal energy were 0.7, 0.3, and 1, respectively. In satisfying the convergence criteria (10^{-6}), the number of iterations for every time-step was less than 200. The computations were performed on the Cray XD1 supercomputer of the Alabama Supercomputer Authority (Huntsville, AL).

2.3 Evaluation of the Nusselt Numbers and the Criterion for Establishment of the Pseudosteady-State. The instantaneous area-averaged Nusselt number over the surface of the sphere for an insulated baffle is

$$\mathrm{Nu}_m(\tau) = \frac{1}{(T_w^* - T_m^*)}\int_0^\pi \left.\frac{\partial T^*}{\partial r^*}\right|_{r^*=1}\sin\theta d\theta \tag{11}$$

whereas for an isothermal baffle

$$\mathrm{Nu}_m(\tau) = \frac{1}{(T_w^* - T_m^*)}\frac{1}{[1+2(L-L^2)\sin\theta_b]}\left(\int_0^\pi \left.\frac{\partial T^*}{\partial r^*}\right|_{r^*=1}\sin\theta d\theta + \sin\theta_b\int_{1-2L}^{1}\left.\frac{\partial T^*}{\partial\theta}\right|_e dr^*\right) \tag{12}$$

Note that a subscript "m" is used to signify that T_m (mean or bulk temperature) is used in the $\Delta T=T_w-T_m$ expression and the second integral of Eq. (12) covers the surface of the baffle. However, for this specific pseudosteady-state natural convection problem, the temperature difference between the wall and center is held as a constant value. This condition can introduce another Nusselt number that is based on a constant driving force $\Delta T=T_w-T_c$. Then, another Nusselt number can be obtained for insulated and isothermal baffles

$$\mathrm{Nu}_c(\tau) = (T_w^* - T_m^*)\mathrm{Nu}_m(\tau) \tag{13}$$

Another approach to get these Nusselt numbers is to perform a lumped energy balance for the fluid. The Nusselt numbers for insulated baffles are

$$\mathrm{Nu}_m(\tau) = \frac{2}{3}\frac{1}{(T_w^* - T_m^*)}\frac{dT_m^*}{d\tau} = \frac{\mathrm{Nu}_c(\tau)}{(T_w^* - T_m^*)} \tag{14}$$

For an isothermal baffle, these relations are

$$\mathrm{Nu}_m(\tau) = \frac{2}{3}\frac{1}{[1+2(L-L^2)\sin\theta_b]}\frac{1}{(T_w^* - T_m^*)}\frac{dT_m^*}{d\tau} = \frac{\mathrm{Nu}_c(\tau)}{(T_w^* - T_m^*)} \tag{15}$$

In view of the possible unsteady behavior of the flow and thermal fields for certain operating conditions, developing a consistent criterion to determine whether the pseudosteady-state is reached is a critical factor. In view of the current focus on the pseudosteady-state behavior of this system, a criterion based on time-averaging of the Nusselt numbers was favored over other more lengthy analyses [14]. A straight line curve-fitting equation of the fluctuating Nusselt numbers was employed, of the form $\mathrm{Nu}_\xi(\tau)=a+b\tau$, where a and b are constants. For all the cases studied, when b is less than 10^{-6}, it is considered that the statistical stationary PSS natural convection inside spherical containers with and without a thin baffle is reached [14]. Taking the statistical distribution into account, the RMS may be employed to characterize the strength of fluctuations of the Nusselt numbers, i.e.,

$$\mathrm{RMS}|_{\mathrm{Nu}_\xi} = \sqrt{\frac{\sum_{i=1}^{N}(\mathrm{Nu}_\xi(\tau_i) - \mathrm{Nu}_\xi)^2}{N}} \tag{16}$$

with $\xi=c$ or m depending on the choice of the ΔT. In order to make comparison among all the cases, the relative RMS for the Nusselt numbers can be defined as

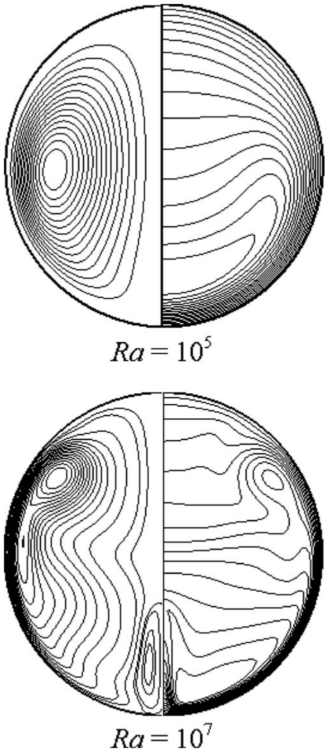

Fig. 2 Pseudosteady-state streamline patterns (left half) and corresponding temperature contours (right half) for cases with no baffles (Ra=10^5 and 10^7)

$$\mathrm{RMS}|_{r\mathrm{Nu}_\zeta} = \frac{1}{\mathrm{Nu}_\xi}\sqrt{\frac{\sum_{i=1}^{N}(\mathrm{Nu}_\xi(\tau_i)-\mathrm{Nu}_\xi)^2}{N}} \tag{17}$$

A similar analysis was performed for the maximum value of the stream function field. This quantity is generally viewed as an appropriate measure of the strength of flow field and its influence on the thermal field.

3 Results and Discussion

Before discussing the present findings, an overview of the pseudosteady-state natural convection within a sphere with no baffles will be presented. This limiting analysis served as a check against the previous findings of Refs. [8,9]. This also served as a check of the computer code in order to make sure that the previous findings were realizable with the commercial package that was adopted.

3.1 Fluid Flow and Thermal Fields With no Baffles. Composite diagrams of the streamline patterns and temperature contours under the pseudosteady-state condition for the Rayleigh numbers of 10^5 and 10^7 with no baffles are presented in Fig. 2. Streamlines are shown on the left half of the sphere, whereas the temperature contours are shown on the right half. For the limiting case of Ra=0 (pure conduction), perfectly concentric circles for the temperature contours would have been observed. As buoyancy-induced convection effects become more dominant, deviations of the temperature contours from concentric ring patterns become more pronounced and the temperature gradients on the bottom of the sphere become stronger. For Ra=10^5, the region around the center of the sphere is composed of constant-temperature stratified layers. The spatial extent of this region is observed to increase as the Ra is raised and natural convection is strengthened next to the wall. As for the flow field, the fluid that is heated adjacent to the wall becomes less dense and rises, replacing the colder fluid that sinks slowly downward along the symmetry axis. The radial and polar angle positions of the eye of the clockwise (CW) recirculating vortex are summarized in Table 1, suggesting that it travels toward the wall of the sphere as the Ra number is raised. At the same time, its polar angle position is lifted from the bottom half to the top half. Similar data of Shen et al. [9] who presented streamline and temperature contours for Ra numbers that were higher by factors of 1.3–1.9 are also summarized in Table 1 showing similar trends for the radial coordinate of the eye of the vortex. However, according to Ref. [9], the polar angle position of the vortex shows almost no sensitivity to the Ra. Whereas the polar angle changes 50 deg in the present study, Ref. [9] only observed 11 deg with the eye always remaining in the lower half. The observations of Ref. [9] were generally supportive of findings of Ref. [8] that reported the data on the eye of the vortex for similar Rayleigh numbers reported here (Table 1). Interestingly, Ref. [10] reported streamline and temperature contours for Ra=10^8, with the vortex eye located at r_e^*/R=0.824 and θ_e =54 deg. This observation is in concert with the data for the present study for a Ra number of 10^7, whereas the data of Ref. [8] for Ra=10^8 exhibit no sensitivity to the Ra number for the polar angle position of the vortex. In view of the commonality of the computational procedure used by previous investigations, the contradictions can be attributed to the differences in spatial grid resolutions among the three studies (about 14,000 cells for the present study compared to ~900 cells for the earlier studies).

Table 1 Radial and angular positions of the eye of the recirculating vortex (cases with no baffles)

	Ra No.				
	10^4	10^5	10^6	10^7	10^8
r_e^*					
Present study	0.605	0.651	0.768	0.814	—
Shen et al. [9][a]	0.617	0.733	0.8	0.9	—
Hutchins and Marschall [8]	—	0.727	0.910	0.850	0.912
θ_e (deg)					
Present study	104.3	91.5	68.5	54.8	—
Shen et al. [9][a]	100	92	89	94	—
Hutchins and Marschall [8]	—	93	94	92	95

[a] The reported Rayleigh numbers were higher than the values shown at the top of the columns by a factor of 1.3–1.9.

An interesting feature of natural convection in a spherical container is the simultaneous existence of thermally *stable* and *unstable* fluid layers in the vicinity of the symmetry axis. This is illustrated schematically in Fig. 3. For the greater portion of the symmetry axis, horizontal stratified fluid layers are observed with

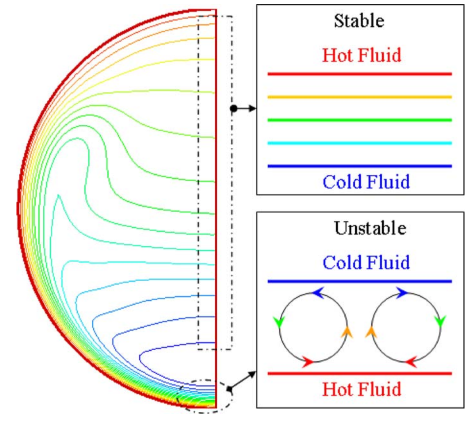

Fig. 3 Thermally stable and unstable flow structures

Table 2 Comparison of the pseudosteady-state Nusselt numbers and the predicted values of the maximum stream function values for cases with no baffles

	Equations (11) and (13)		Equation (14)		Hutchins and Marschall [8]		Maximum stream function	
Ra	Nu_m	Nu_c	Nu_m	Nu_c	Nu_m	Nu_c	Current	Ref. [8]
10^4	11.224	5.7556	11.2246	5.7559	—	—	1.554	—
10^5	16.129	12.8698	16.1298	12.8705	15.8	11.5	7.641	6.01
10^6	25.3452	25.4938	25.3465	25.495	23.8	23.5	19.613	14.51
10^7	40.1974	37.1717	40.1993	37.1735	40.8	36.7	41.428	33.47

the hot lighter fluid sitting on top of cooler dense layers, where fluid motion is negligible and heat conduction dominates. The remaining portion of the symmetry axis is composed of cold fluid layers on top of hotter dense layers. Such a system is thermally unstable and will feature recirculating cells. In the present study, the onset of instabilities through creation of a small counterclockwise (CCW) rotating vortex near the bottom of the sphere was observed for the Rayleigh number of 10^7 (Fig. 2). The strength of this vortex is dictated by the dynamic interaction of the rising hot fluid with the sinking cooler fluid. In connection with this finding, Ref. [4] reports on the existence of a CCW rotating vortex at the bottom of the sphere. Owen and Jalil [15] also reported temperature measurements at the bottom of the sphere exhibiting an oscillating behavior.

3.1.1 Variations in the Nusselt Numbers. Instantaneous Nusselt numbers for the sphere with no baffles are not presented here and can be found elsewhere [14]. Marked variations in $\mathrm{Nu}_c(\tau)$ were observed during the early period ($\tau \leq 0.12$) as the flow is perturbed starting from a motionless state. The frequency of these oscillations increased as Ra number is raised. Beyond the transient period, the RMS and relative RMS values of the Nu_c were of the order of 3×10^{-3} and 3×10^{-4}, respectively, or less. This suggested that the oscillations are weak and the pseudosteady-state was established. The values of the four Nusselt numbers (Eqs. (11), (13), and (14)) under the PSS condition in comparison to those of Ref. [8] are given in Table 2. The reader is reminded that [8] declared establishment of PSS once the relative change in the value of the mean Nusselt number (Nu_m) over a time-step was less than 10^{-6}. Regardless of the Rayleigh number, the relative difference in the predicted values Nu_m and Nu_c using two different approaches in the present study are of the order of magnitude of 10^{-5}. The current results are a little higher than the predictions of Ref. [8] with the relative differences being of the order of 8% for all the Rayleigh numbers. Comparison of the maximum dimensionless stream function (ψ^*_{max}) values ($\mathrm{Pr}=0.7$) with those of Ref. [8] for $\mathrm{Pr}=8$ are also given in Table 2. Recalling the difference in grid densities between the present study and Ref. [8] (about 14,000 versus 900), the comparison among the various quantities in Table 2 are satisfactory. Further details in relation to correlating the Nusselt number data in comparison to previous work was discussed by Duan [14].

Pseudosteady-state flow field streamlines, temperature contours, and the dependence of the time-averaged Nusselt numbers for insulated baffles are presented first, followed by a discussion of the isothermal baffles.

3.2 Fluid Flow and Thermal Fields With Insulated Baffles.

With an insulated baffle, the relative RMS values of the Nusselt numbers and maximum stream function of the primary vortex were small [14], suggesting that the pseudosteady-state was established except for $\mathrm{Ra}=10^7$, indicating that unsteady effects are promoted as the Ra number is raised. Therefore, the case of the highest Ra number will be discussed separately.

3.2.1 Pseudosteady-State Fluid Flow and Thermal Fields for $\mathrm{Ra}=10^5$ *and* 10^6 . The composite diagrams of the streamlines and temperature contours under the pseudosteady-state condition for two insulated baffles with lengths ($L=0.1$ and 0.25) placed at $\theta_b=30$ deg, 60 deg, 90 deg, 120 deg, and 150 deg for $\mathrm{Ra}=10^5$ are presented in Fig. 4. The diagrams in each row correspond to baffles of two lengths positioned at a fixed location, whereas for each column the effects of a baffle with a fixed length at various positions are given. Focusing on the left column of Fig. 4, the presence of a $L=0.1$ baffle does not alter the flow and thermal fields significantly. The distortions are restricted to alteration of the streamlines next to the short baffles, whereas the temperature

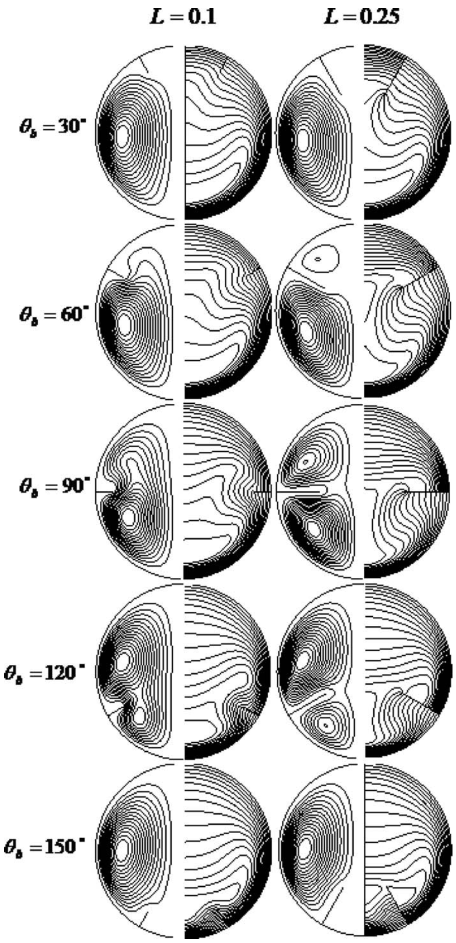

Fig. 4 Pseudosteady-state streamline patterns and temperature contours for two insulated baffles ($L=0.1$ and 0.25) placed at various locations for $\mathrm{Ra}=10^5$

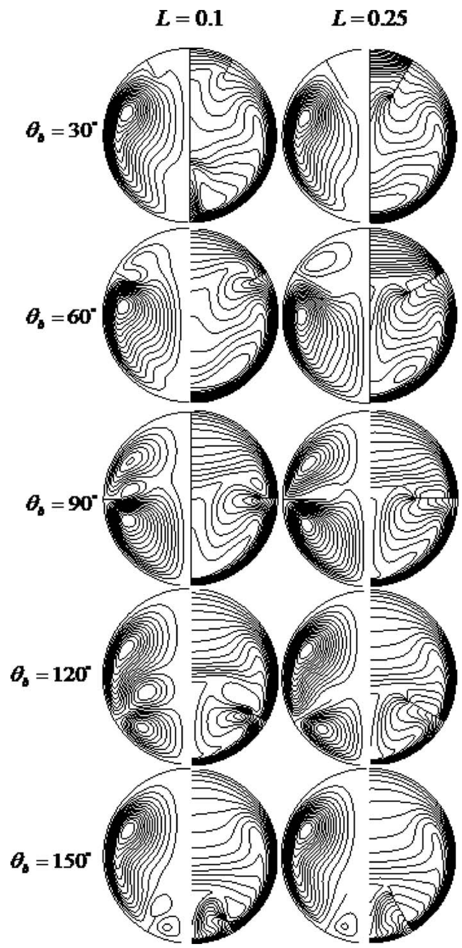

Fig. 5 Pseudosteady-state streamline patterns and temperature contours for two insulated baffles ($L=0.1$ and 0.25) placed at various locations for $\mathrm{Ra}=10^6$

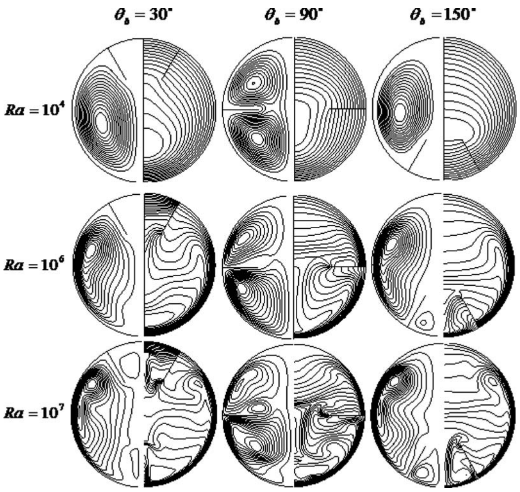

Fig. 6 Pseudosteady-state streamline patterns and temperature contours with an insulated baffle ($L=0.25$) placed at $\theta_b=30$ deg, 90 deg, and 150 deg for $\mathrm{Ra}=10^4$, 10^6, and 10^7

contours are generally unchanged with radial shifting of the contours next to the adiabatic baffle. In contrast, marked changes to the flow field are observed in the right column of Fig. 4 that correspond to the longest baffle ($L=0.25$), especially for the cases when the baffle is located at $\theta_b=60$ deg, 90 deg, and 120 deg. For these cases, two distinct recirculating vortices are observed on both sides of the baffle. These CW rotating vortices lift heated fluid next to the wall and bring down colder fluid. The temperature fields have also been affected by the longer length of the baffle, however the general pseudoconcentric ring temperature contour patterns are preserved. It can clearly be stated that due to the adiabatic nature of the baffle, this structure does not directly participate in perturbation of the thermal field. The presence of the baffle is generally directed at modifying the flow paths for $\mathrm{Ra}=10^5$ cases.

The streamlines and temperature contours for two baffles with lengths ($L=0.1$ and 0.25) placed at various locations for a $\mathrm{Ra}=10^6$ are presented in Fig. 5. Comparing the streamline patterns and temperature fields of Fig. 5 with the case of no baffle (Fig. 2), the presence of the $L=0.1$ baffle modifies the flow and thermal fields for various positions of the baffle. For some positions of the short baffle, two eyes within the CW rotating vortex are observed. As for the effect of this baffle on the temperature contours, the changes were more pronounced in comparison to similar cases of Fig. 4, however, they are still localized in the vicinity of the baffle. The flow modifications are more noticeable when the baffle is located at $\theta_b=60$ deg, 90 deg, and 120 deg. For these cases, the double CW rotating vortex structure is further complicated by appearance of a smaller CCW rotating vortex that is located very near the open end of the baffle. This vortex does not draw energy from the adiabatic thin baffle. Therefore, it is the lifting of the hot fluid below the baffle into the zone above the baffle that is creating this vortex. One can also note that the multivortex structure can clearly rearrange the thermal field when compared to the case of the shortest baffle ($L=0.05$) that exhibited stratified layers in the vicinity of the symmetry axis. In assessing the effect of the long baffle on the flow fields in the right column of Fig. 5, modifications that are very similar to the cases of $\mathrm{Ra}=10^5$ in Fig. 4 are observed. In general, two CW rotating vortices are observed when the baffle is located at $\theta_b=60$ deg, 90 deg, 120 deg, and 150 deg. As for the thermal field, when the baffle is positioned such that $\theta_b \leq 90$ deg, the space above the baffle is clearly composed of stable stratified layers. This suggests that the flow within the top portion is not strong and conduction dominates, whereas the thermal field in the lower half is dominated by natural convection. As a general statement, note that when the long baffle is positioned in the bottom half including the midplane, the thermal field is clearly divided into two zones. Both zones have areas of intense wall heat transfer that are located at the bottom of the sphere and angular positions $\theta < \approx \theta_b$, respectively. A portion of the top zone is a region of stable layers suggesting weak natural convection and dominance of heat diffusion, whereas the bottom zone is where natural convection is very prominent.

3.2.2 Effect of the Rayleigh Number. The effects of the Rayleigh number (10^4, 10^6, and 10^7) and baffle's position ($\theta_b=30$ deg, 90 deg, and 150 deg) on streamlines and temperature contours for the case of the longest baffle ($L=0.25$) are presented in Fig. 6. With the baffle positioned near the top at $\theta_b=30$ deg, the increase in the Rayleigh number brings about stronger convection and fluid flow within the CW rotating vortex. This is accompanied by lifting of the eye of the vortex and its migration outward. For the highest Ra number studied, a weak vortex is observed near the top within the cone part of which is the baffle. Simultaneously, a CCW rotating vortex at the bottom of the sphere that is driven by the thermally unstable stratified layer is still active. The temperature contours exhibit greater deviation from the concentric ring patterns as natural convection strengthens and diffusion is observed to be limited to the small space between the baffle and the symmetry axis. With the baffle located at $\theta_b=90$ deg, two CW rotating vortices occupy the two hemispherical regions with the lower half of the sphere being the site of stronger convection. As the Ra number is raised, the stronger vortex is

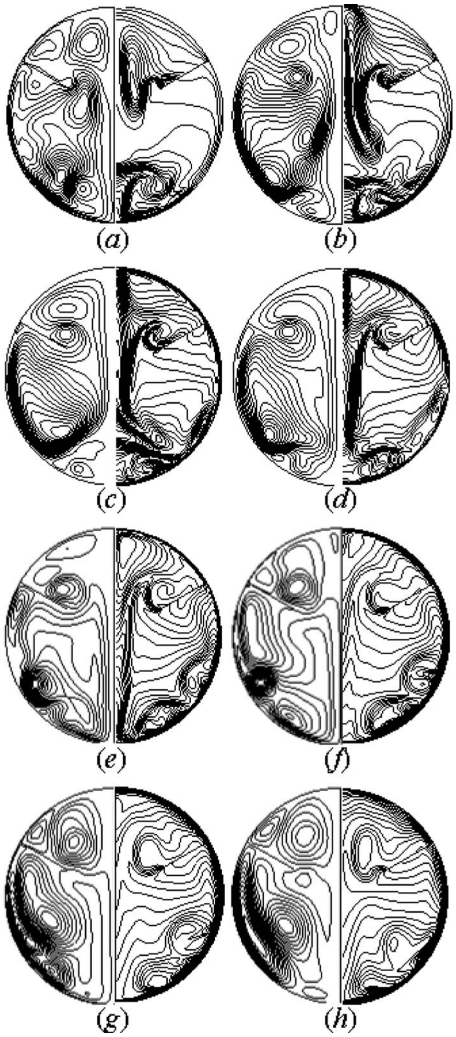

Fig. 7 Streamline patterns and temperature contours in one cycle (a–h with the time instants shown in Fig. 8) with an insulated baffle ($L=0.25$, $\theta_b=60$ deg, and Ra$=10^7$)

observed to penetrate into the top hemisphere and even a third CCW rotating vortex is created next to the free end of the baffle for Ra$=10^6$ and 10^7. The top hemisphere is clearly stratified with stable layers occupying it, whereas the thermal field within the bottom hemisphere is heavily affected by the stronger rotating vortex. The flow fields for the cases with the longest baffle positioned at $\theta_b=150$ deg exhibit many of the features with the baffle located at $\theta_b=30$ deg but in reverse. A CW rotating recirculating vortex that occupies the small space between the baffle and the symmetry line is clearly observed. As for the temperature contours, the alterations appear to be generally confined to the region between the baffle and the symmetry axis. The remainder of the sphere appears to be generally unaffected by the presence of the longest baffle. The reader should know that the last row of Fig. 6 with Ra$=10^7$ is a snapshot of the instantaneous fields. A detailed discussion of a typical case with Ra$=10^7$ is given next.

3.2.3 Time-Dependent Fluid Flow and Thermal Fields for Ra$=10^7$. To illustrate the unsteady nature of the flow, a representative case of Ra$=10^7$, $L=0.25$, and $\theta_b=60$ deg was selected. The instantaneous diagrams of the streamlines and temperature contour fields for this case during a "cycle" are shown in Fig. 7(*a*)–7(*h*). In order to aid the reader, a companion diagram showing the variation in the instantaneous area-averaged Nusselt number is shown in Fig. 8. The cyclic nature of the instantaneous Nusselt number is clearly shown and the instants at which the contours of Fig. 7 were presented are marked by letters a–h. A dynamic flow field is observed within the cycle with distinct growth and decay of a multitude of vortices. The temperature gradients next to the wall of the sphere and the baffle vary markedly during the cycle and are clearly linked to the variation in the Nusselt number shown in Fig. 8. The interested reader may contact the corresponding author to access the animations for the case of Fig. 7.

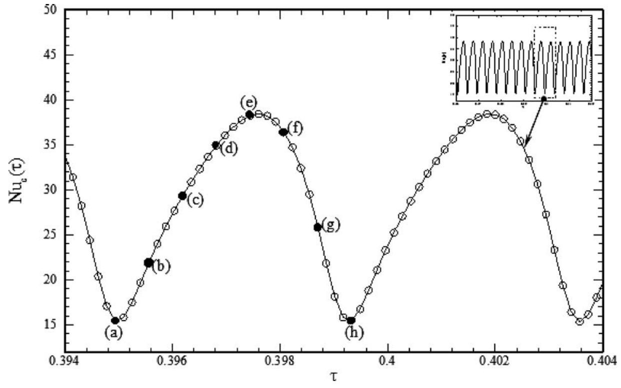

Fig. 8 Cyclic variation in the instantaneous area-averaged Nusselt number for case with an insulated baffle ($L=0.25$, $\theta_b=60$ deg, and Ra$=10^7$)

3.2.4 Variations in the Time-Averaged Nusselt Numbers. The variations in the time-averaged Nusselt number (Nu_c) with Ra for a thin insulated baffle are presented in Fig. 9 for $L=0.05$, as a representative case. The Nusselt number strongly depends on the Rayleigh number and clearly exhibits strengthening trend with the increase in Ra, irrespective of the baffle lengths and locations. For Ra$=10^4$ with conduction being dominant, the flow and temperature fields do not change greatly due to presence of the short insulated baffle. With increase in Ra, the effects of the thin insulated baffle become more noticeable due to the greater importance of convective effects. For a given Ra, the extent of flow and thermal field modifications is directly related to the length of the thin insulated baffle. It was generally observed (56 out of 60 cases) that by adding a thin insulated baffle, Nu_c was lower than the reference case with no baffle. This Nusselt number is directly proportional to the heat that is transferred into the container and the time rate of rise of the bulk temperature (Eq. (14)). Since there is no heat transfer through the surface of the baffle, the presence of the baffle has modified the heat input on the wall of the sphere. This control utility is related to the modified flow and thermal

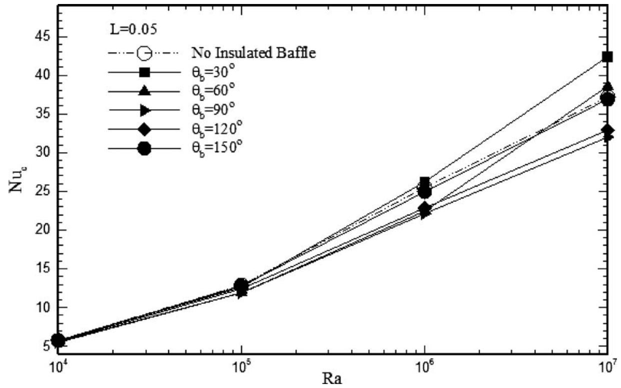

Fig. 9 Dependence of the time-averaged Nusselt number (Nu_c) on Ra among cases with an insulated baffle ($L=0.05$) at various locations and the case without baffle

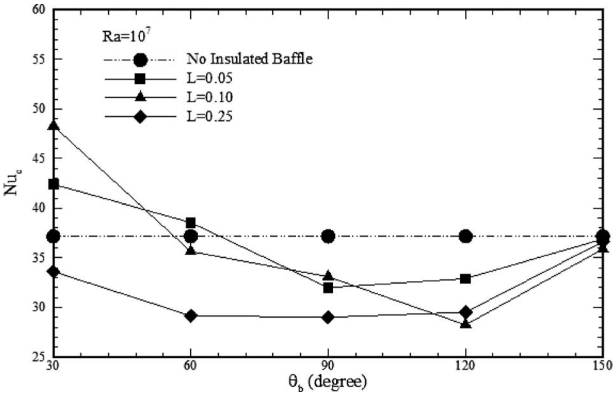

Fig. 10 Dependence of the Nusselt number (Nu_c) on θ_b among a case without baffle and the cases with a thin insulated baffle of different lengths for $\mathrm{Ra}=10^7$

fields presented earlier, where it was observed that presence of a baffle can lead to "confinement" or "compartmentalization." In other words, one can generally state that within the stable stratified layers that are formed in the zone above the baffle conduction dominates, whereas the lower region is dominated by convection. However, it can be observed that the Nusselt numbers for a baffle located at 30 deg and 60 deg are unexpectedly higher than the reference case for $\mathrm{Ra}=10^6$ and 10^7 (also true for $L=0.10$). This is explained as follows. For all the cases with no baffle, the thermal boundary layer becomes thicker as the fluid from the bottom of the sphere rises along the wall of the sphere. For cases with high Ra, the presence of short baffles near the top is beneficial to disturbing the boundary layer, thus allowing extra heat to be drawn into the sphere. This effect can not be sustained if the length of the baffle is increased to $L=0.25$ since the confinement effect of the baffle outweighs the disturbance of the boundary layer.

The dependence of the time-averaged Nusselt number (Nu_c) on the position of the baffles (θ_b) are presented in Fig. 10 for $\mathrm{Ra}=10^7$, as a representative case. As the location of baffle is lowered starting from the top of the sphere and moving toward the bottom, the Nusselt number exhibits trends suggesting that the confinement effect is minimal, when the baffle is placed near the two extremes. The location corresponding to the most marked confinement varies depending on the Ra and length of the baffle. For a fixed location of the baffle and Ra numbers lower that 10^7, one can generally state that as the length of the baffle is raised, the confinement effect becomes more enhanced. This behavior is not observed for the highest Ra studied (Fig. 10). It must be noted that similar trends were observed for the maximum stream function values.

3.3 Fluid Flow and Thermal Fields With Isothermal Baffles. Upon comparing the streamlines for the cases with isothermal baffles for $\mathrm{Ra}=10^4$ and 10^5 with their counterpart cases with insulated baffles (e.g., Fig. 4), the flow fields were found to be very similar. This suggests that for such cases with prevailing weak natural convection, the influence of an isothermal baffle is that of flow blockage, very similar to the effect of an insulated baffle. However, for the same Ra numbers, the pseudoconcentric ring temperature contour patterns were greatly modified in the vicinity of the isothermal baffle. In addition to modifying the flow paths, the isothermal baffle is responsible for bringing in heat into the sphere due to availability of a larger surface area.

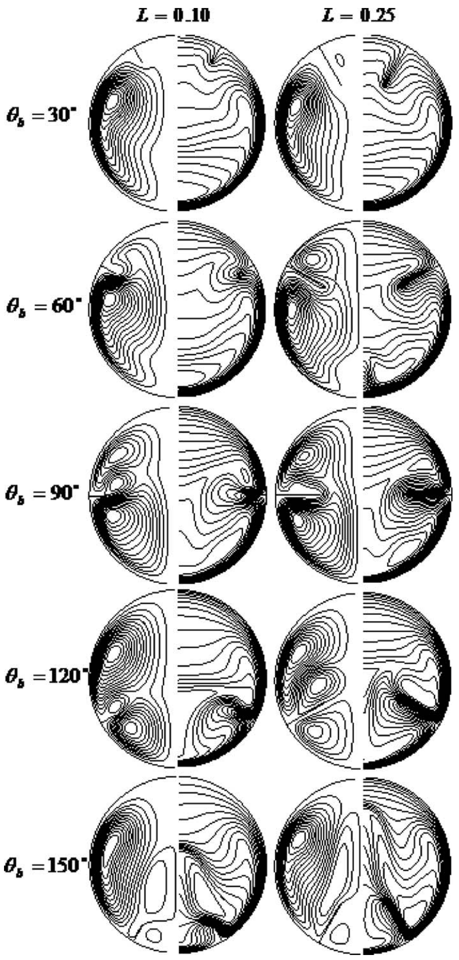

Fig. 11 Pseudosteady-state streamline patterns and temperature contours for two isothermal baffles ($L=0.1$ and 0.25) placed at various locations for $\mathrm{Ra}=10^6$

The streamlines and temperature contours for two isothermal baffles with lengths ($L=0.1$ and 0.25) placed at $\theta_b=30$ deg, 60 deg, 90 deg, 120 deg, and 150 deg for $\mathrm{Ra}=10^6$ are presented in Fig. 11. The flow fields for the baffles located on the midplane or higher are found to be very similar to those shown in Fig. 5. The main contrast between the cases with an isothermal baffle in comparison to the one with an insulated baffle has to do with the CCW rotating vortex that is located partly on top of the baffle. In contrast to a similar vortex that was observed for the same conditions but with an insulated baffle (Fig. 5), this vortex extracts heat from the isothermal baffle and has a bigger spatial coverage. One can also note that the multivortex structure can clearly rearrange the thermal field when compared to the case of the shortest baffle that exhibited stratified layers in the vicinity of the symmetry axis. In assessing the effect of the long baffle on the flow fields in the right column of Fig. 11, two CW rotating vortices are clearly observed for all the cases. In addition, a fresh third CCW rotating vortex with its eye at $\theta <\approx \theta_b$ is created for cases with $\theta_b \geq 90$ deg. This vortex gains more spatial coverage as the baffle is placed deeper into the lower hemisphere and is sandwiched between the two CW rotating vortices when the baffle is located at $\theta_b=120$ deg and 150 deg. The entire top surface of the baffle is in contact with this CCW rotating vortex. By observing the marked temperature gradient next to the top surface of the baffle, this fresh vortex is clearly energized by the extra heat that is brought into the sphere from the top surface of the baffle. As for the effect of the longest baffle on the thermal field, if the baffle is located such that $\theta_b \leq 90$ deg, parts of the interior of the sphere are composed of stable stratified layers. This suggests that the flow within these regions is not strong and conduction mode of transport is dominant. For other positions of the baffle in the lower hemisphere, the remainder of the sphere is greatly affected by the extra heat that is brought into the sphere through the extended surface of the baffle that is shown schematically in Fig. 12. The extra heat coming

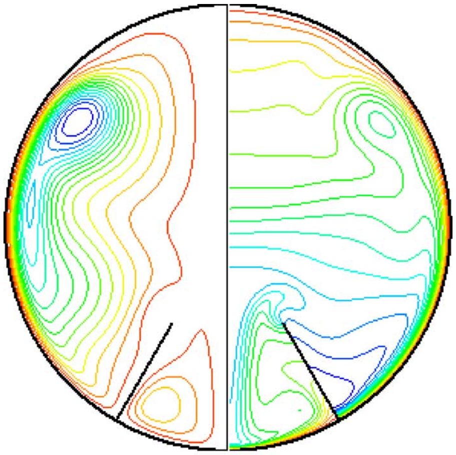

Adiabatic

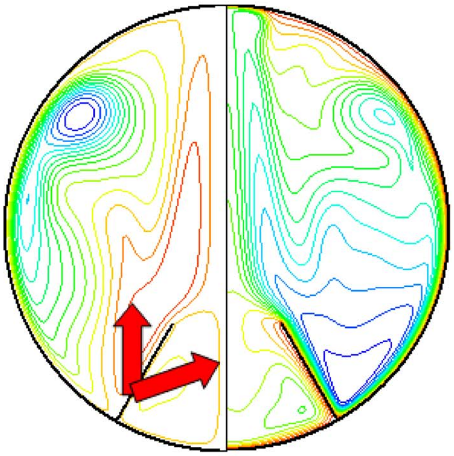

Isothermal

Fig. 12 Comparison of the pseudosteady-state streamline patterns and temperature contours due to insulated and isothermal baffles (Ra=10^7, L=0.25, and θ_b=150 deg)

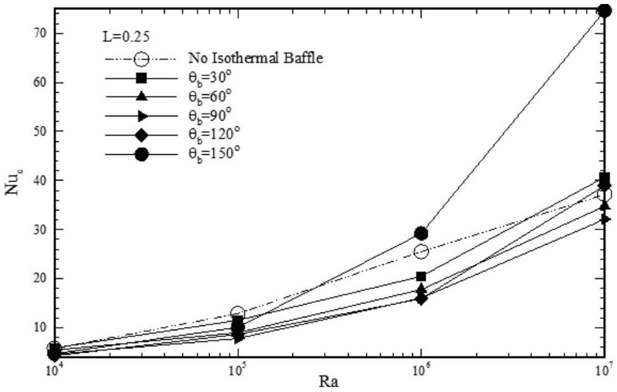

Fig. 13 Dependence of the time-averaged Nusselt number (Nu_c) on Ra among cases with an isothermal baffle (L=0.25) at various locations and the case without baffle

through the baffle energizes a CCW rotating vortex that directs hot fluid toward the center of the sphere, thus reducing thermal stratification. As a general observation, note that the baffle divides the thermal field into two zones. Both zones have areas of intense wall heat transfer that are located at the bottom of the sphere and angular positions $\theta < \approx \theta_b$. The top zone is generally a region of stable layers suggesting weak natural convection and its spatial coverage diminishes as the location of the baffle moves lower. The bottom zone is generally observed to be the site of strong natural convection that is brought about by the extra heating afforded by the baffle.

3.3.1 Variations in Time-Averaged Nusselt Numbers. The variations in the time-averaged Nusselt numbers (Nu_c) with Ra for a thin isothermal baffle (L=0.25) are presented in Fig. 13, as a representative case. Similar to insulated baffles, the Nusselt numbers strongly exhibit a strengthening trend with the increase in Ra, irrespective of the baffle lengths and locations. It was evident (51 out of 60 cases) that by adding a thin isothermal baffle, the Nusselt number was lower than the reference case with no baffle. This means that even though heat is being transferred through the surface of the baffle, the presence of the baffle has adversely caused lowering of the heat input through the wall of the sphere. In other words, the extra heating of the fluid by the baffle is not sufficient to overcome the degraded heat transfer through the surface of the sphere due to compartmentalization. Among the cases that were investigated, it was observed that the Nusselt numbers for some cases for which the baffle is located at 30 deg, 60 deg, 120 deg, and 150 deg are higher than the reference case for Ra=10^6 and 10^7 (four cases shown in Fig. 13). This is explained as follows. For all the cases with no baffle, the thermal boundary layer becomes thicker as the fluid from the bottom of the sphere rises along the wall. For cases with Ra=10^7, the presence of baffles near the top is beneficial to disturbing the thickened boundary layer, thus allowing extra heat to be drawn into the sphere. This effect is even maintained for longer baffles suggesting that the degrading effect of a long baffle through compartmentalization is overcome by extra heating. The enhancement of heat transfer that is observed due to presence of an isothermal baffle near the bottom of a sphere was seen to be limited to the high Ra number cases of 10^6 and 10^7 and the longest baffle (L=0.25). This observation is clearly linked to the creation of a CCW rotating vortex on the upper surface of the baffle. Partly due to the orientation of the baffle and also its longer length, the CCW rotating vortex that is created on the surface of the baffle due to heating directs the hot fluid toward the center of the sphere and penetrates higher into the sphere rising toward the top. This activity, in turn, counteracts the compartmentalization of the baffle by introducing hot fluid into the stable stratified fluid layers above the baffle.

Dependence of the time-averaged Nusselt numbers (Nu_c) on the position of the baffles (θ_b) are presented in Fig. 14 for Ra=10^7, as a representative case. In general, dependence of the degraded heat transfer (due to confinement) on the location of baffle was ob-

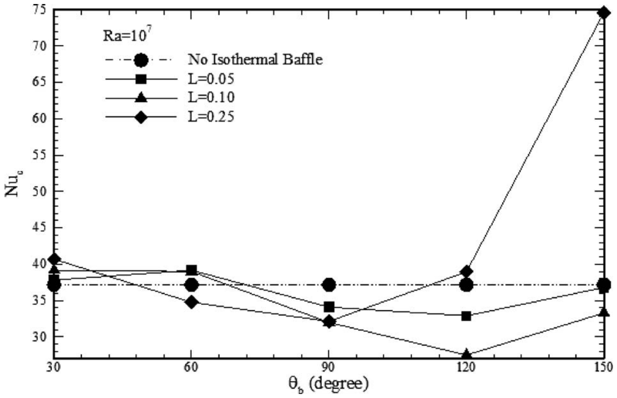

Fig. 14 Dependence of the time-averaged Nusselt number (Nu_c) on θ_b among a case without baffle and the cases with a thin isothermal baffle of different lengths (L=0.05, 0.10, and 0.25) for Ra=10^7

served to be very similar to the case of insulated baffles. For a fixed location of the baffle and $\mathrm{Ra} < 10^7$, one can generally state that as the length of the baffle is raised, the confinement effect becomes more enhanced and marked degradation was observed. This behavior is not observed for the highest Rayleigh number studied (Fig. 14) and opportunities for heat transfer enhancement are observed with the baffle positioned near the top or bottom of the sphere, as discussed when presenting Fig. 13.

4 Conclusions

For the cases with no baffle, PSS natural convection was established and the recirculating streamline patterns and ring-like temperature contours were generally similar to those discussed in previous studies. The major contradiction has to do with the location of eye of the recirculating vortex that is observed to be closer to the wall and its angular position changing drastically as the Rayleigh number is increased. The region in the vicinity of the symmetry axis of the sphere is generally composed of constant-temperature layers. Onset of instabilities due to interaction of the hot rising fluid with the cold sinking fluid along the symmetry axis near the bottom of the sphere was observed for the highest Rayleigh number reported.

The common conclusions pertaining to pseudosteady-state natural convection with adiabatic or insulated baffles are given next and particular deviations are noted.

1. Regardless of the Ra number, the short baffle $(L=0.05)$ alters the flow field and temperature contours to some minor extent in comparison to the corresponding Ra number cases with no baffle. The modifications are limited to the vicinity of the baffle and a possible interaction with the eye of the vortex. With a short insulated baffle, the thermal field is generally unaltered, whereas for an isothermal short baffle, the modified thermal field is linked to the extra heat that is brought into the sphere. The changes in the flow field and thermal fields are observed to be more dramatic for the $L=0.1$ baffle and multiple vortex structures rotating in opposite directions were observed. For the longest baffle $(L=0.25)$, two CW rotating vortices are clearly observed when the baffle is positioned in the intermediate vicinity of the midplane. The ensuing confinement or compartmentalization leads to stable layers above the baffle that are slow-moving and dominated by heat conduction. For the highest Ra number and with the baffle positioned in the lower hemisphere, a CCW rotating vortex is created next to the longest baffle. This vortex is far more pronounced for the case of an isothermal baffle due to extra heating afforded by it and is responsible for directing hot fluid into the sphere and disrupting the stratification.
2. The Nusselt numbers exhibited a strong dependence on the position and length of the baffle and were generally lower than the reference cases with no baffle. For an insulated baffle, the lowest amount of absorbed heat corresponds to a baffle positioned horizontally.
3. Placing a baffle near the top of the sphere for high Ra number cases can lead to heat transfer enhancement that is linked to disturbance of the thermal boundary layer. With isothermal baffles, heat transfer enhancement is achieved for a baffle placed near the bottom of the sphere due to interaction of the CCW vortex and the stratified layer.
4. For various length and position combinations of the baffle, pseudosteady-state can not be achieved and strong flow and thermal field oscillations were observed for the high Ra number cases. This behavior was clearly linked to the establishment of the unstable fluid layers at the bottom of the sphere.

Acknowledgment

The first author acknowledges the Department of Mechanical Engineering at Auburn University for supporting his graduate assistantship. The second author acknowledges the support of the Ministry of Science, Research and Technology of the I.R. Iran through a short-term scholarship. The authors acknowledge Alabama Supercomputer Authority of Huntsville, AL, for providing computing resources on the ASA's Cray XD1 supercomputer.

Nomenclature

D = diameter of the sphere, m
Nu_ξ = area-averaged Nusselt numbers, defined by Eqs. (11)–(15)
p = pressure, Pa
p_0 = static pressure, Pa
r^* = dimensionless radial position, defined as r/R
Ra = Rayleigh number, $g\beta D^3(T_w - T_c)/\alpha\nu$
T_b = temperature of the baffle, K
T_c = temperature at the center of sphere, K
T_m = mean or bulk temperature of the fluid, K
T_w = temperature of the sphere's surface, K
T_0 = initial temperature of the fluid, K
T^* = dimensionless temperature, defined as $(T\text{-}T_0)/(T_w\text{-}T_c)$

Subscripts

b = related to the baffle
e = related to the eye of a vortex
r = related to the radial direction
θ = related to the polar direction

References

[1] Schmidt, E., 1956, "Versuche zum Wärmeübergang bei natürlicher Konvektion," Chem.–Ing.–Tech., **28**(3), pp. 175–180.
[2] Shaidurov, G. F., 1958, "On Convective Heat Transfer Across a Spherical Cavity," Sov. Phys. Tech. Phys., **3**(4), pp. 799–804.
[3] Pustovoit, S. P., 1958, "Transient Thermal Convection in a Spherical Cavity," J. Appl. Math. Mech., **22**(4), pp. 800–806.
[4] Whitley, H. G., III, and Vachon, R. I., 1972, "Transient Laminar Free Convection in Closed Spherical Containers," ASME J. Heat Transfer, **94**, pp. 360–366.
[5] Chow, M. Y., and Akins, R. G., 1975, "Pseudosteady-State Natural Convection Inside Spheres," ASME J. Heat Transfer, **97**, pp. 54–59.
[6] Zhang, Y., Khodadadi, J. M., and Shen, F., 1999, "Pseudosteady-State Natural Convection Inside Spherical Containers Partially Filled With a Porous Medium," Int. J. Heat Mass Transfer, **42**(13), pp. 2327–2336.
[7] Val'tsiferov, Y. V., and Polezhaev, V. I., 1975, "Convective Heat Transfer and Temperature Stratification in a Sphere Completely Filled With a Liquid, With a Given Heat Flux," Fluid Dyn., **10**(5), pp. 828–832.
[8] Hutchins, J., and Marschall, E., 1989, "Pseudosteady-State Natural Convection Heat Transfer Inside Spheres," Int. J. Heat Mass Transfer, **32**(11), pp. 2047–2053.
[9] Shen, F., Khodadadi, J. M., and Zhang, Y., 1995, "Pseudosteady-State Natural Convection Inside Spherical Containers," *Proceedings of the Fourth ASME/JSME Thermal Engineering Joint Conference*, Lahaina, Maui, HI, Vol. 1, pp. 209–216.
[10] Khodadadi, J. M., Li, W., and Shi, X., 1999, "Pseudosteady-State Mixed Convection Inside Rotating Spherical Containers," *Proceedings of the Fifth ASME/JSME Thermal Engineering Joint Conference (CD ROM)*, Paper No. AJTE99-6264, San Diego, CA.
[11] Shi, X., and Khodadadi, J. M., 2003, "Laminar Natural Convection Heat Transfer in a Differentially Heated Square Cavity due to a Thin Fin on the Hot Wall," ASME J. Heat Transfer, **125**(4), pp. 624–634.
[12] Patankar, S. V., 1980, *Numerical Heat Transfer and Fluid Flow*, Hemisphere, Washington, DC.
[13] Fluent, Inc., 2003, FLUENT 6.1 User's Guide, NH, Lebanon.
[14] Duan, Y., 2007, "Effect of a Baffle on Pseudosteady-State Natural Convection Inside Spherical Containers," MS thesis, Department of Mechanical Engineering, Auburn University; available at http://etd.auburn.edu/etd.
[15] Owen, I., and Jalil, J. M., 1986, "Transient Heat Transfer in a Liquid Sphere," *Heat Transfer 1986: Proceedings of the Eight International Heat Transfer Conference*, Taylor & Francis, London, Vol. 4, pp. 1889–1893.

CFD-Based Design of Microtubular Solid Oxide Fuel Cells

Stefano Cordiner

Alessandro Mariani

Vincenzo Mulone[1]
e-mail: mulone@ing.uniroma2.it

Dipartimento di Ingegneria Meccanica,
Università di Roma "Tor Vergata",
via del Politecnico 1,
00133 Roma, Italy

Microtubular solid oxide fuel cells (MT-SOFCs) are interesting for portable and auxiliary power units energy production systems, due to their extremely fast startup time. However, a single cell provides power in the range of 1 W, thus the number of microtubes to reach a kW scale is relevant and packaging design issues arise also. In this paper a specifically developed design procedure is presented to face with system issues and bringing into account fluid-dynamic and thermal influence on system performance. The procedure also simplifies the stack manifold design by means of a modular scale-up procedure starting from a basic optimized configuration. To this aim, a computational fluid dynamics (CFD) model has been integrated with specific models for fuel cell simulation and then validated with tailored experimental data by varying operating conditions in terms of fuel utilization and electric load. A comprehensive three–dimensional (3D) thermal-fluid-dynamic model has then been applied to the analysis of both micro-assembly (i.e., 15 tube assembly) and midi-assembly (up to 45 tubes), showing an important role of local phenomena as current homogeneity and reactant local concentration that have a strong influence on power density and temperature distribution. Microreactor power density in the range of 0.3 kW/l have been demonstrated and a specific manifold design has been realized paving the way toward a modular realization of a 1 kW MT-SOFC. [DOI: 10.1115/1.4000709]

Keywords: heat transfer in fuel cells, solid oxide fuel cells, computational fluid-dynamics, hydrogen

1 Introduction

Solid oxide fuel cells (SOFCs) are characterized by high conversion efficiency and exhaust temperature making them ideal for combined heat and power (CHP) applications, particularly when fuel flexibility is required. On the other hand, material issues [1,2] are challenging as the operating temperature is in the range of 1000–1300 K. For similar reasons, startup and shutdown timings must be controlled to avoid thermal cracking [3]. This mainly limited their application to stationary power plants. In the past years, many research activities have been focused both toward intermediate temperature SOFCs [4] and to downsize tubular SOFCs, down to a tube diameter in the range of 1 mm, for portable and auxiliary power unit (APU) applications, respectively, in the power range of 20–500 W and 1–5 kW [5], paving the way to the microtubular concept (microtubular SOFC (MT-SOFC)). MT-SOFC systems were realized for the first time in the late 1990s [6] including up to 1000 cell reactors: they demonstrated a high potential above all in terms of startup temperature increase (in the order of 200 K/min), due to the limited effects of material dilatation on such small tubes, and to the high active-area/volume ratio. Later on, a temperature increase in the order of 4000 K/min has been demonstrated, leading to reach the operating temperature in about 10s, with no major deterioration problems. Recently, in Ref. [7], zero degradation has been shown after 1000 h of operation under thermal-cycling operating conditions. A general survey on the latest achievements in the field of MT-SOFC is also available in Ref. [8], where allowed temperature increase in the order of 8000 K/min and maximum power density of 1 kW/l are reported [9].

Although the high potential, the experience carried out on MT-SOFCs is based mainly on the choice of proper material and single cell design to get an optimal behavior in terms of durability under cyclic conditions [9]. Thus, simple designs, usually tube array configurations [10], have been tested, still leaving open questions regarding the configuration of multiple tube assemblies, and the analysis of air management issues. Moreover, as a modular scaling-up strategy may be a major solution to realize stacks of the desired power size [11], design issues regarding multiple assemblies to optimize the utilization of the different tubes and the average volumetric power density represent an interesting development of the MT-SOFC concept [12]. Such design issues may be directly addressed experimentally, with high characteristic costs and timings. CFD-based tools have been used otherwise from the middle of 1990s [13] to better understand the coupling among the different occurring phenomena [14] by varying geometrical and operating conditions. In the field of traditional (planar and tubular) designs, several efforts have been carried out in the last years: the recent reviews by Kakac et al. [15], and Bove and Ubertini [16] include some details of micro- and macromodels. The most recent and advanced models have been oriented toward different aspects: models of entire stacks have been developed to compute performance deviation due to manifolding [17,18], and more recently, Kapadia and Anderson [19] developed a comprehensive 3D model to analyze species transport and thermal fields in a tubular stack. Chemical equilibrium, with internal reforming and water gas shift reaction, was discussed by Li and Chyu [20]. Looking at smaller scale phenomena, Janardhanan and Deutschmann [21] developed a detailed model to take into account transport phenomena and chemical multistep chemistry, including also internal reforming processes [22]. Thermal stresses have been studied by Nakajo et al. [23] for a single cell by varying operating conditions. However, none of the cited papers gives details about the effect of geometrical design on cell performance.

Moreover, the efforts performed in the specific field of MT-SOFCs are reported in Refs. [24,25] mainly analyzing the flow

---

[1] Corresponding author.

Contributed by the Heat Transfer Division of ASME for publication in the Journal of Heat Transfer. Manuscript received February 13, 2009; final manuscript received November 12, 2009; published online March 19, 2010. Assoc. Editor: Srinivas Garimella.

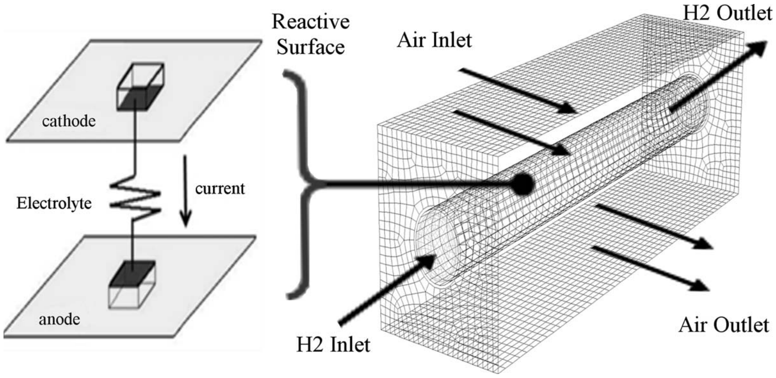

Fig. 1 Basic layout of a single-channel (3D) microtubular SOFC with a schematic description of the modeling approach on the reactive surface (1D)

inside the tubes, while Cui and Cheng [26,27] looked at a single tube by means of a 2D model putting into evidence the link among temperature, species concentration, and current fields. A similar 2D approach has been used by Serincan et al. [28], and validated with experimental data, to compute thermal stresses in a tube.

So, despite the high potential of CFD techniques to support design at such small scales, no definitive results are available in literature in terms of information on the effect of several configurations on performance, especially in the case of MT-SOFCs.

To this aim, the present paper, which is the result of an international joint project [29], is focused on the analysis of the effect of MT-SOFC configurations on performance. Moving from an experimental validation of a single tube, the influence of tube configuration in microreactors (constituted by 15 tubes) and midireactors (constituted by 45 tubes) has been analyzed, studying the effects of air flow management on current and temperature fields and then controlling also the thermal gradient to not exceed stresses on the tubes.

2 Modular Microtubular SOFCs: Design Concept

The MT-SOFC design concept developed in this paper to realize a modular scale-up procedure, moves from the study of a single channel, up towards the analysis of modular assemblies composed by multiple channels and complex reactant flow to simplify air manifolding.

Three different levels of analysis, characterized by increasing complexity, have been identified to realize a kW scale MT-SOFC:

- single-channel level
- microreactor level
- midireactor level

The geometry of the "single-channel level" is represented in the schematic of Fig. 1. It has a simple cross-flow configuration, where fuel flows inside a tube, whose diameter is in the order of 1 mm, and air cross-flows the tube. The study of this basic geometry is crucial to test the electrochemical performance of materials in terms of current/power versus reactant flow rate and load. In the proposed design concept, results achieved for single-channel geometries in terms of power density and maximum allowed thermal gradient, represent a basic point of reference to evaluate the behavior of multiple channel scaled-up assemblies (microreactor and midireactor levels). At this level, the proposed integrated 3D CFD tool has been validated versus specific experimental data to assess the model capabilities. By this way, the analysis of higher level assemblies has been performed only by means of the validated integrated CFD tool, to test a number of different configurations with limited costs/timings otherwise not easily realizable on an experimental basis.

The geometry of the "microreactor level" is shown in Figs. 2(*a*) and 2(*b*) in its baseline version. It is composed by 15 tubes, whose geometries are the same, tested experimentally in the context of the single-channel design level. The main target of the analysis at this level is simplifying air manifolding, realizing a compact and high power density device. However, the homogeneous exploitation of the whole electrochemically active area is not guaranteed, as each tube may have a different temperature and reactant distribution on the surface. Thus, system performance of a microreactor depends mainly on the coupling among fluid-dynamics, heat transfer, and electrochemistry. In this context, the effect of the design, in terms of geometrical parameters (defined in Figs. 2(*a*)

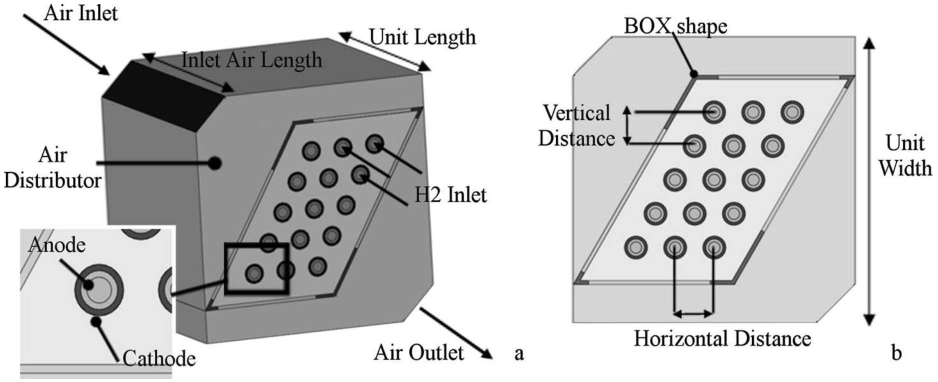

Fig. 2 Basic layout (*a* and *b*) of a microreactor including the definition of the main components and geometrical parameters

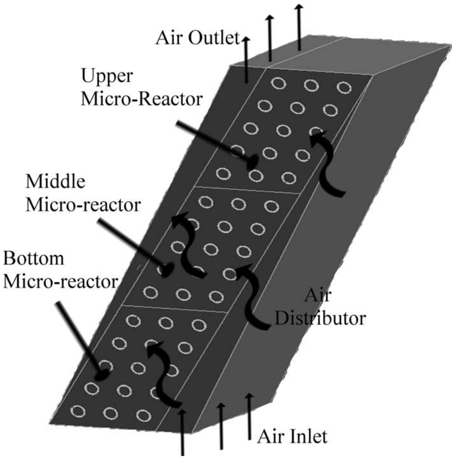

Fig. 3 Basic layout of a midireactor

and 2(*b*)) and reactant flow, is primarily important. Unit width and length, horizontal and vertical distances, the geometry of the surrounding box (box shape), and air distributors define the geometrical parameters varied to study the effect of design on performances. The thermal gradient in each tube has also been analyzed for each case, to look at a significant indicator of thermal-cycling driven damage [30,31].

The geometry of the "midireactor level" is reported in Fig. 3. Like the microreactor geometry, it has a single inlet and a single outlet to manage air flow, and it is realized, in this example, by coupling three microreactors, with a total number of 45 tubes. In this case, the basic idea consists of feeding the three microreactors in parallel by means of an air distributor (indicated in Fig. 3), able to guarantee similar homogeneity and power density performance as for the microreactor level.

The design concept is summarized in Fig. 4. The availability of specific experimental data, related to the single cell geometry and acquired at a different inlet fuel flow and load, first allows to validate the CFD-based model at this level. Moreover, relevant information on the variation in current and temperature distribution, fuel utilization, and temperature gradients are also investigated by varying inlet fuel flow and load operating conditions. The second step (microreactor level) gets as input single cell level results, information on fuel flow rate and on tolerable thermal gradient. It considers assemblies of several tubes with common air flow. In this context the design parameters are defined via the main geometrical parameters discussed above and reactant flow rates. The target of the microreactor level analysis is the achievement of maximum as possible power density (and related current homogeneity), keeping, at the same time, the thermal gradient under control. The last step (midireactor level) gets the analyzed microreactor geometries and results as input, and considers assemblies of microreactors with common air flow. Again, the target is the achievement of maximum power density and current homogeneity, keeping the thermal gradient under control. In this case, air manifold geometry is the main independent parameter.

3 Integrated 3D CFD-Based Model

The integrated 3D CFD model is based on the coupling of FLUENT CFD solver [32] with a separate and specifically developed electrochemical module [33]. The integrated model is valid for any fuel mixture (including H_2, HC, and CO), as it has been already applied to the analysis of biomass fuelled SOFCs by the authors [33].

In the context of the proposed whole model, FLUENT has been used only to solve the multispecies fluid-dynamic equations: in fact, in this field, its reliability has been assessed during the last years. Moreover, the use of FLUENT to model SOFCs has been also proposed in different papers [34,35], mostly for planar [17,30,35–38] and integrated planar technologies [39].

The main assumptions of the model are listed below:

- Fluids are considered as perfect gases (O_2, N_2, H_2, H_2O).
- Fluid-dynamic regime may be assumed as laminar. This conclusion is based on the value of the Reynolds number (Re) that gives a measure of the ratio of inertial forces

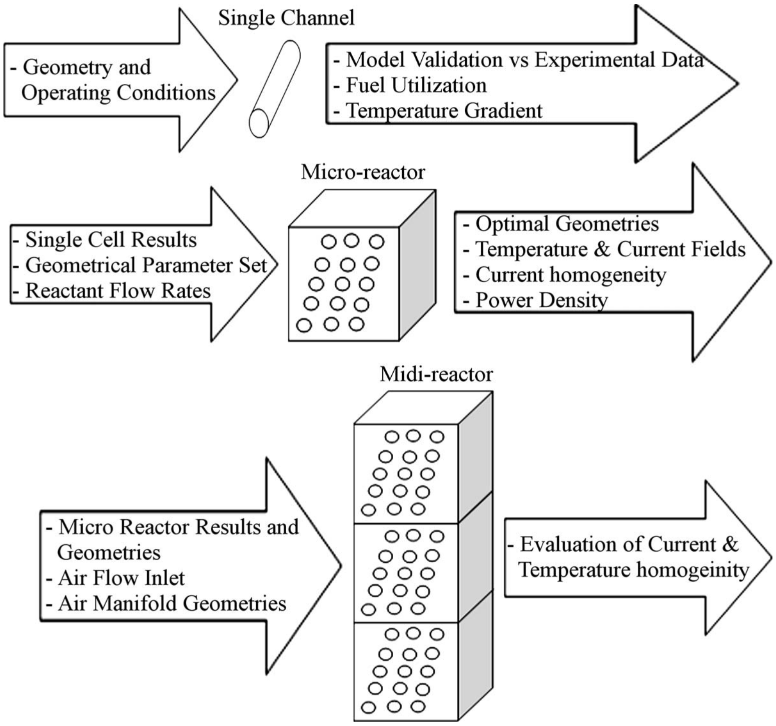

Fig. 4 MT-SOFC design concept

(velocity × density) to viscous forces (dynamic viscosity/characteristic length). The value of Re number, based on tube diameter, is in fact always lower than 1800.
- Equations are solved at steady state.
- Ohmic, activation, and concentration losses are taken into account.
- Fluid-dynamic effects in porous media are taken into account by isotropic Darcy laws.
- Electric conductivity of current collectors is considered infinite. Its contribution has been neglected at a design stage, as it can also be found in literature in some similar examples [40].
- Anode-cathode voltage drop is considered homogeneous.
- Heat transfer to the surrounding environment is neglected.
- Conductive and convective heat transfer mechanisms are taken into account. Radiative heat transfer mechanism is, instead, neglected.

Although radiation is an important heat transfer mechanism [41], at such a high temperature, its contribution strongly depends on solid geometry and boundary conditions [42]. This assumption, also considered in Refs. [24,43–46], has been confirmed by a sensitivity analysis aimed at showing that radiation mechanism gives only a more homogeneous temperature field inside the structure, and therefore allows to get a flatter current distribution. This choice depends also on the other assumption of neglecting heat transfer to the surrounding environment (as the system is considered adiabatic), and leads to a negligible difference (about 0.02 $\mathrm{A/cm^2}$ verified for the presented model) in the calculation of current density [43].

The integrated method is composed of the following modules:

- a 3D CFD module to solve continuity, species, momentum, and energy equations, giving the 3D fields of the fluid-dynamic variables (p, ρ, T, Y_i) in the fuel and oxidant channels and porous electrodes. The input/output parameters of this module are the following:
- input
- material/electrochemical parameters
- geometry
- boundary conditions (cathode and anode inlet parameters: mass flow rate, composition, and temperature)
  - output
- complete thermal-fluid dynamic fields for cathode and anode flows
  - a specifically developed electrochemical module implemented with ANSI-C user defined functions (UDFs), which, getting a local input from the 3D thermo-fluid-dynamic fields on the reactive surfaces, solves at each iteration the mass/current/energy problem across the electrolyte, as reported in the schematic of Fig. 1, based on the following input/output parameters:
- input
- cell voltage
- reactant distribution and composition on cathode and anode sides
- temperature fields
  - output
- current fields on the active area
- cathode and anode outlet parameters: composition, temperature, and fuel utilization

Thus, this module is able to evaluate the local value of current as well as the local reaction rates $(\mathrm{kg/m^2\ s})$ of each of the chemical species. These rates are sent back to the CFD module to update species mass fraction and temperature fields, and are defined by the electrochemical overall reaction

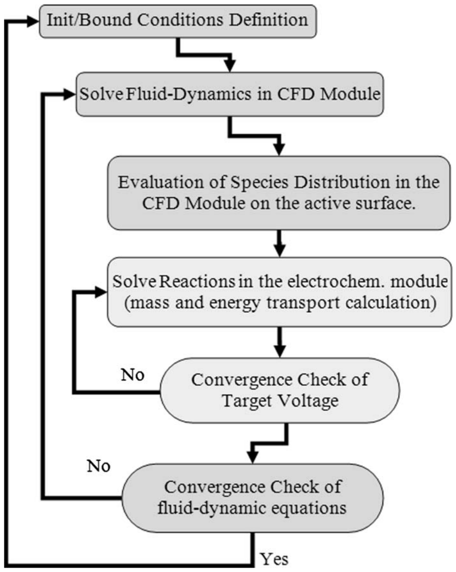

Fig. 5 Algorithm of the integrated CFD model

$$H_2 + \tfrac{1}{2}O_2 \rightarrow H_2O \quad \Delta H = -285.83\ \mathrm{kJ/mol}$$

Equations may be written in terms of two half-reactions occurring at the opposite sides of the electrolyte

$$\tfrac{1}{2}O_2 + 2e^- \rightarrow O^{2-} \text{ at the cathode-electrolyte interface}$$

$$H_2 + O^{2-} \rightarrow H_2O + 2e^- \text{ at the anode-electrolyte interface}$$

The algorithm is given in Fig. 5. It gets started from the assignment of initial/boundary conditions over the full domain. Two main loops constitute the core of the algorithm.

- The inner one refers to the developed electrochemical module (in light-gray) to compute mass/energy/charge fluxes according to Refs. [13,47–51].
- The outer one refers to the convergence of the thermal-fluid-dynamic variables with respect to the CFD module.

Details of the two individual modules are provided below.

3.1 CFD Module Governing Equations. The governing equations of the fluid-dynamic phenomena occurring in a solid oxide fuel cell are summarized below. The electrolyte is considered as an infinitely thin volume (i.e., a surface). Thus, electrochemical and physical processes evolving within this volume are only taken into account by the electrochemical module, and provide boundary conditions toward fuel and air domain in terms of mass and energy fluxes. Conservation of mass is governed by the following:

$$\nabla \cdot \rho \boldsymbol{u} = 0 \tag{1}$$

where ρ is the mixture density and $\boldsymbol{u}$ is the fluid velocity. Species conservation is governed by

$$\nabla \cdot \rho Y_i \boldsymbol{u} - \nabla \cdot (\rho D_i \nabla Y_i) = S_i \tag{2}$$

where Y_i is the mass fraction of the examined species i, D_i is its diffusion coefficient, and S_i is its source term, which is related to the electrochemical reaction mechanism (consumption or production of species i) and local current in each cell immediately adjacent to the electrolyte region in both cathode and anode sides. Momentum conservation (valid for porous and fluid volumes, porosity ε is equal to zero in the latter case) is shown in the following:

$$\nabla \cdot (\rho \boldsymbol{u}\boldsymbol{u} - \mu \nabla \boldsymbol{u}) = -\nabla\left(p + \frac{2}{3}\mu \nabla \cdot \boldsymbol{u}\right) - \frac{\mu}{\mathbf{K}}(\varepsilon \boldsymbol{u}) \tag{3}$$

where K is the isotropic permeability tensor, which allows to take into account the flow in the porous electrodes.

Energy conservation is governed by

$$\nabla \cdot (\rho \boldsymbol{u} h - \lambda \nabla T) = S_h \tag{4}$$

where λ is the local thermal conductivity, which depends on composition and individual species thermal conductivities. In this paper they are calculated locally by means of the ideal gas kinetic theory. In the electrodes, λ expression takes into proper account the solid thermal conductivity ($\lambda_s = 2.25$ W/mK [52]) using a mass-weighted average gas-solid value via the definition of porosity ε. S_h represents the energy source term, which is related to species rate of change by $S_h = \Sigma_i^N h_i S_i$.

3.2 Electrochemical Module Governing Equations. The electrochemical module is called at each iteration by the 3D main solver (external loop, Fig. 5), and provides local 3D current on the basis of reactant and temperature distribution (internal loop, Fig. 5). Species and energy source terms S_i and S_h, represent the link between the electrochemical and the CFD modules, and are provided by the following equations as functions of local current density (j):

- electrolyte on the anode side

$$\text{H}_2 \text{ mass source} \quad S_{\text{H}_2} = -\frac{j}{2F} \cdot M_{\text{H}_2} \tag{5a}$$

$$\text{H}_2\text{O mass source} \quad S_{\text{H}_2\text{O}} = \frac{j}{2F} \cdot M_{\text{H}_2\text{O}} \tag{5b}$$

$$\text{mass balance} \quad \Phi_{\text{mass\_}a} = -\Phi_{\text{mass\_}c} = S_{\text{H}_2} + S_{\text{H}_2\text{O}} \tag{5c}$$

- electrolyte on the cathode side

$$\text{O}_2 \text{ mass source} \quad S_{\text{O}_2} = -\frac{j}{4F} \cdot M_{\text{O}_2} \tag{6a}$$

$$\text{cathode mass balance} \quad \Phi_{\text{mass\_}c} = S_{\text{O}_2} \tag{6b}$$

$$\text{energy source} \quad S_h = \Phi_{\text{energy\_}c} - (1.25V) \cdot j \tag{7}$$

The operating cell potential (V) is imposed across the electrolyte

$$\text{operating cell potential} \quad V = V_0 - \eta_{\text{act}} - \eta_{\text{ohm}} - \eta_{\text{con}} \tag{8}$$

Reversible voltage V_0 (at equilibrium) is calculated by Nernst's equation [53]

$$V_0 = \frac{\Delta G(T)}{2F} + \frac{R \cdot T}{2F} \ln\left[\frac{p_{\text{H}_2} \cdot p_{\text{O}_2}^{0.5}}{p_{\text{H}_2\text{O}}}\right] \tag{9}$$

Activation losses (η_{act}) are directly linked to local current. Electrode polarization is the main cause of these losses [54]; they are evaluated for anode and cathode side by Butler–Volmer equations, where p_0 is the reference pressure, $i_{\text{ex},C}$ and $i_{\text{ex},A}$ are the reference exchange current densities for cathode and anode, respectively. In the presented model these parameters were assigned according to [37]

$$\eta_{\text{act},A} = \frac{2R \cdot T}{F} \sinh^{-1}\left(\frac{i}{2i_{0,A}}\right) \tag{10a}$$

$$\eta_{\text{act},C} = \frac{2R \cdot T}{F} \sinh^{-1}\left(\frac{i}{2i_{0,C}}\right) \tag{10b}$$

$$i_{0,A} = i_{\text{ex},A} \cdot \left(\frac{p_{\text{H}_2}}{p_0}\right) \cdot \left(\frac{p_0}{p_{\text{H}_2\text{O}}}\right)^{0.5} \cdot \exp\left(-\frac{Ea}{RT}\right) \tag{11a}$$

$$i_{0,C} = i_{\text{ex},C} \cdot \left(\frac{p_{\text{O}_2}}{p_0}\right)^{0.25} \cdot \exp\left(-\frac{Ec}{RT}\right) \tag{11b}$$

Ohmic losses (η_{ohm}) are due to resistance of ion flow across the electrolyte and to electrical resistance occurring across the electrodes [48]. Electrolyte constitutes the major part of the overall loss [49]. Voltage drop can be modeled as proportional to current

$$\eta_{\text{ohm}} = i \cdot R_e = \frac{l_e}{\sigma_e} \tag{12}$$

where l_e and σ_e are, respectively, the electrolyte thickness and conductivity; the latter can be expressed as

$$\sigma_e = \beta_1 \exp\left(\frac{-\beta_2}{T}\right) \tag{13}$$

β_1 and β_2 parameters (Table 2) have been set on the basis of similar models available in literature [13,47,49,51].

Concentration losses (η_{conc}) take place when reactant diffusion through electrodes is less efficient than species flow rate requested by electrochemical reactions. These losses are taken into account considering species local partial pressures close to the electrolyte, and then they are directly solved by the CFD module. Thus, Eqs. (8) and (9) can be rewritten as follows, including all the cited losses:

$$V_0 = \frac{\Delta G(T)}{2F} + \frac{R \cdot T}{2F} \cdot \ln\left[\frac{(p_{\text{H}_2}/p_0) \cdot (p_{\text{O}_2}/p_0)^{0.5}}{(p_{\text{H}_2\text{O}}/p_0)}\right] \tag{14}$$

$$V = V_0 - \eta_{\text{act}} - \eta_{\text{ohm}} \tag{15}$$

Once assigned voltage and partial pressures of each species in the electrodes, local current is solved all over the active region by means of a Newton–Raphson algorithm.

4 Analysis of Results

The integrated CFD model has been applied to the analysis of each of the three levels introduced in Sec. 2 (single-channel, microreactor, and midireactor).

The experimental analysis of a single tube has been performed first to directly validate the integrated CFD model in terms of integral parameters, and look at the 3D coupling between thermal-fluid-dynamic and current fields. All material properties refer to a H_2 fuelled MT-SOFC single, anode supported, cell prototype realized in the context of a joint project, at the Upper Austria University of Applied Sciences of Wels [55]. H_2 has been selected as fuel, as basic design issues have been pursued in this context; the same strategy has been followed in several papers available in literature [38,56]. The inner anode is made of $\text{Ni}-\text{ZrO}_2$ cermet, the electrolyte of yttria stabilized zirconia (YSZ), and the outer cathode of a lanthanum strontium manganite coating (Sr-doped LaMnO_3). Cathode current collector is realized by silver wire wrapped around the cells, while an internal wire contact is used for the anode. Currently, several methods to connect the cells electrically are under test [9]. Material properties used in all the calculations are reported in Table 1: their range have been cross-checked with literature available data [57–61].

Electrochemical parameters are common to all the cases and given in Table 2. They are taken from literature available data [37]. Conductivity coefficients β_1 and β_2, and exchange current densities are used to model, respectively, ohmic, and activation losses with regard to electrochemical module equations (Sec. 3.2). Boundary/operating parameters, common to all the simulations, are finally given in Table 3: similar ranges can be found in literature available applications [39,56–61].

Table 1 Material properties

Ni 90%–ZrO_2 (Ni-YSZ) density	5970 $kg\ m^{-3}$
Ni 90%–ZrO_2 thermal conductivity	3 $W\ m^{-1}\ K^{-1}$
Ni 90%–ZrO_2 thermal expansion coefficient (900°C)	$1.164\times10^{-5}\ K^{-1}$
Ni 90%–ZrO_2 specific heat	300 $J\ kg^{-1}\ K^{-1}$
Sr–$LaMnO_3$ (LSM) density	6570 $kg\ m^{-3}$
Sr–$LaMnO_3$ thermal conductivity	3 $W\ m^{-1}\ K^{-1}$
Sr–$LaMnO_3$ thermal expansion	$1.23\times10^{-5}\ K^{-1}$
Sr–$LaMnO_3$ specific heat	573 $J\ kg^{-1}\ K^{-1}$
Solid element density	5000 $kg\ m^{-3}$
Solid element thermal conductivity	5 $W\ m^{-1}\ K^{-1}$
Solid element heat capacity	871 $J\ kg^{-1}\ K^{-1}$
Anode and cathode electrode porosity	35%
Anode and cathode viscous resistance	$10^{13}\ m^{-2}$

Table 5 Comparison between experimental and numerical data (current evaluation)

H_2 flow rate (N ml/min)	Voltage (V)	Current (A)		Power (W)
		Experimental	Numerical	
100	0.612	1.962	1.978	1.201
75	0.607	1.950	2.012	1.184
50	0.601	1.930	2.027	1.160
25	0.583	1.867	1.869	1.088
20	0.566	1.820	1.804	1.030
19	0.566	1.814	1.761	1.027
18	0.557	1.797	1.757	1.001
17	0.560	1.776	1.692	0.995
16	0.550	1.746	1.676	0.960
15	0.550	1.757	1.613	0.966
12	0.499	1.526	1.505	0.762
11	0.449	1.479	1.468	0.664
10	0.443	1.377	1.382	0.610

4.1 Single-Channel Level. Single-channel analysis is of particular importance both as it is the basis of the design concept and as it has been used for the direct validation of the integrated CFD-based model with respect to specific experimental data, whose setup is described below.

4.1.1 Experimental Setup. Geometrical parameters [55] are given in Table 4 while the schematic is provided in Fig. 1. The tube diameter is in the range of 1 mm, while its length is in the order of 1–10 cm. The sum of electrodes and electrolyte thickness is consistently smaller than 1 mm.

Single cell MT-SOFC prototype has been tested in a dedicated rig, containing a humidification section (Bronkhorst HI-Tech), an oven with a controlled temperature cell and an electronic load. Gas flows were controlled, and exhaust gas was analyzed with the use of a Varian CP-3800 gas chromatograph.

Experimental tests were performed in a controlled environment. At the beginning, N_2 flow has been used to clean the anode channel. Then, a wet H_2 mixture (3 mol % steam) [39,55,56] has been delivered to the anode, according to Table 3. Air is provided by a cross impinging flow along a transversal direction onto the tube. Inlet temperature for anode and cathode has been set equal to 1173 K according to the experimental tests; H_2 flow has been varied in the range of 5–100 N ml/min, and a polarization curve has been measured at 50 N ml/min by varying voltage in the range 0.6–1 V. Air flow rate has been set constant for all the tests and equal to 6.3×10^{-5} kg/s.

4.1.2 Integrated CFD Model Validation. The prototype geometry has been represented in the 3D domain to validate the integrated CFD tool. Mass flow rates have been set as in the experiments by means of cathode and anode inlet boundary conditions.

The computational domain has been divided into about 30,000 cells; grid spacing was set, after a sensitivity analysis, to an average size of 0.5 mm. According to this setup, the computational time required for each iteration is about 1 s, and less than 100 iterations are required to get a converged solution.

Quantitative results are given in Tables 5 and 6, where measured and computed H_2 utilizations are reported versus inlet H_2 flow rate. Experimental and numerical polarization curves at 50 N ml/min are also reported in Fig. 6. In both the cases, the integrated CFD-based tool is able to capture the trend of voltage decrease and power increase by varying assigned current and H_2 flow rate.

Error in the evaluation of hydrogen utilization is always lower than 6%, the worst conditions being 50 N ml/min (5.9%). The polarization curve in this (worst) condition is affected by a measurement error equal to 2% (instrument range is 0–30 A), and numerical data (Fig. 6) fit the curve with a similar error (2%). Further considering that electrochemical constants have been selected depending on material properties, that constants have not been tuned at this stage, the integrated CFD-based model was

Table 2 Electrochemical modeling parameters [37]

Electrolyte conductivity coefficient (β_1)	3.34×10^{4} $1/\Omega$ m
Electrolyte conductivity coefficient (β_2)	1.03×10^{4} K
Anode reference exchange current density ($i_{ex,A}$)	5.5×10^{4} A/cm^2
Cathode reference exchange current density ($i_{ex,C}$)	7×10^{4} A/cm^2
Anode activation energy (Ea)	1×10^{5} J/mol
Cathode activation energy (Ec)	1.2×10^{5} J/mol

Table 3 Boundary/operating conditions

Cathode and anode inlet temperature (K)	1173
H_2 anode inlet molar fraction (%)	97
H_2O anode inlet molar fraction (%)	3
Cathode and anode exit pressure (bar)	1

Table 4 Single cell geometrical parameters

Unit width (mm)	5.4
Unit length (mm)	44
Hydrogen channel diameter (mm)	3.91
Reactive cell diameter (mm)	4.3
Reactive cell length (mm)	44

Table 6 Comparison between experimental and numerical data (H_2 utilization)

H_2 flow rate (N ml/min)	H_2 utilization (%)		Percent error (%)
	Experimental	Numerical	
100	13.7	13.6	−0.7
75	18.1	18.8	3.9
50	26.9	28.5	5.9
25	52.0	52.5	1.0
20	63.4	63.3	−0.2
18	69.5	68.5	−1.4
16	76.0	73.5	−3.3
12	88.6	88.2	−0.5
11	93.6	93.8	0.2
10	95.9	94.9	−1.0

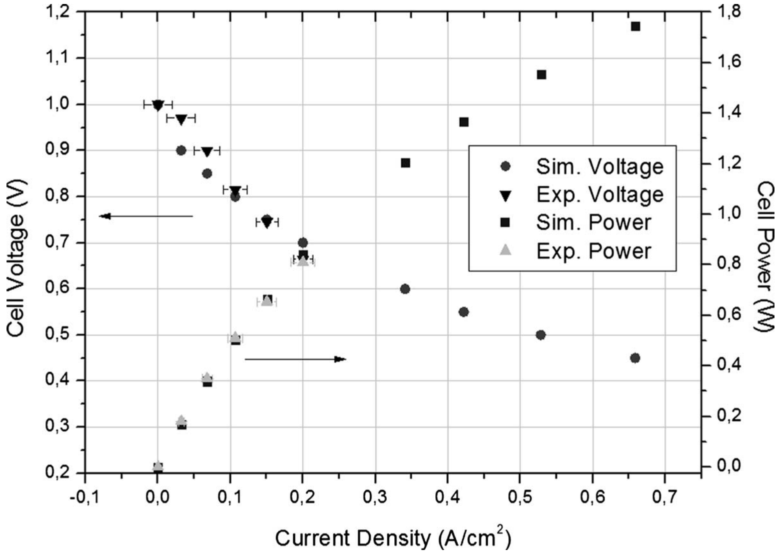

Fig. 6 Polarization curve comparison between experimental (▲) and numerical (■) data

considered validated to predict global performance in the context of the design procedure.

Then, the model has been used to analyze 3D thermal-fluid-dynamic fields over the active surface (Figs. 7(*a*)–7(*d*)) and define the most significant operating conditions in terms of H_2 flow rate. To this aim, a comparison between 20 and 100 N ml/min H_2 flow rate is proposed, according to Table 5 data; quantitative global results are reported in Table 7.

H_2 and H_2O molar fraction fields are plotted on reactive surface in Figs. 7(*a*)–7(*d*) (see row 1). H_2 has a decreasing molar fraction (and then partial pressure) over tube length, while H_2O has an increasing one due to chemical reactions occurring on the active surface. In the case of 100 N ml/min, due to the low H_2 utilization (13.7%) if compared with 20 N ml/min (63.4%), H_2 molar fraction on reactive surface is almost homogeneous (in the range of 0.8–0.96), while this does not occur for 20 N ml/min (in the range of 0.445–0.96). O_2 molar fraction, in both the cases, de-

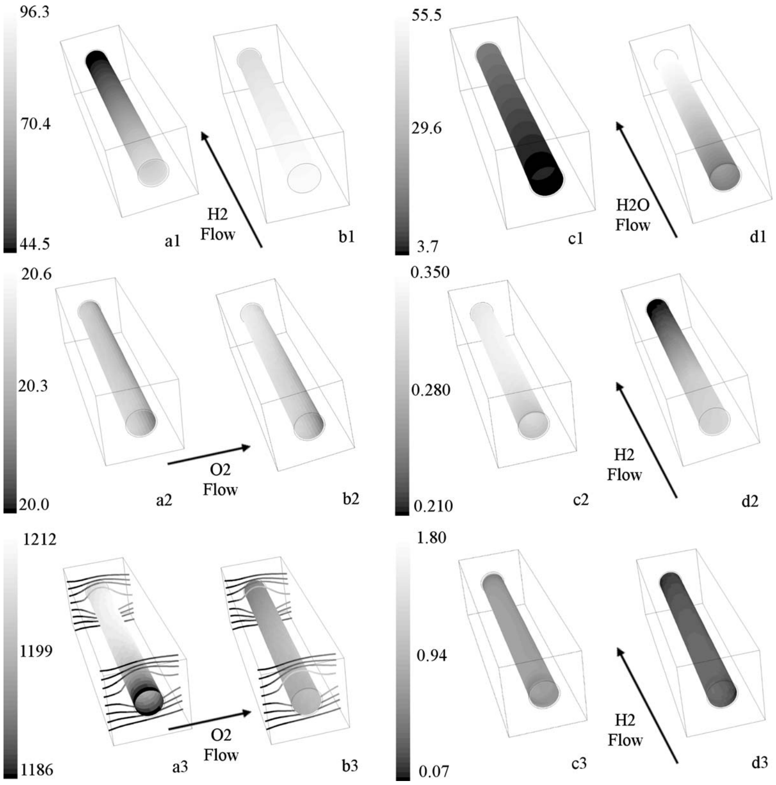

Fig. 7 H_2 (*a*1 and *b*1), H_2O (*c*1 and *d*1), and O_2 (*a*2 and *b*2) molar fractions (%), current density (*c*2 and *b*2, A/cm^2), temperature (*a*3 and *b*3 in K), and temperature gradient magnitude (*c*3 and *d*3 in K/mm) fields on the cell active surface for 100 (*a* and *c*) and 20 (*b* and *d*) N ml/min H_2 flow inlet

Table 7 Single cell performance comparison by varying the H_2 mass flow rate

	Inlet H_2 flow (N ml/min)	
	100	20
Fuel utilization (%)	13.6	63.3
Average current density (A/cm^2)	0.324	0.258
Active surface power density (W/cm^2)	0.198	0.158
Volume specific power density (W/cm^3)	0.186	0.148
Total power (W)	1.17	0.93
Maximum temperature gradient magnitude (K/mm)	1.8	1.4
Average/maximum temperature (K)	1185.9/1219.5	1182.9/1204.9

creases toward air flow direction (Figs. 7(*a*) and 7(*b*), see a2 and b2), but due to the excess air content, it shows a value close to the inlet one all over the active surface.

At 20 N ml/min, power output is lower (1.030 W) with respect to 100 N ml/min (1.201 W). In fact, at 20 N ml/min, current density output (Fig. 7(*d*), see d2) is relevant (i.e., higher than 0.3 A/cm^2) only in the region of the active surface close to H_2 inlet. Temperature field (Fig. 7(*b*), see b3) is rather homogeneous (approximately in the range 1195–1205 K), with a slightly decreasing profile related to a relatively light impact of heat release due to electrochemical losses (according to Eq. (15)) and the cooling effect of impinging air, as reported in Fig. 7(*a*) (see a3), where the air pathlines colored by temperature are plotted. As current output is a function of reactant partial pressure and temperature (according to Eqs. (10*a*), (10*b*), (11*a*), (11*b*), and (12)–(14)), at low mass flow rate the effect of H_2 partial pressure is stronger than temperature field. On the other hand, at 100 N ml/min, it may be observed by the analysis of Figs. 7(*c*) and 7(*a*) (see c2 and a3), that current is higher where temperature gets the maximum value. It is also worth noting that maximum temperature (and current) occur toward the end of the tube, and that maximum temperature is consistently higher than at high fuel utilization operating conditions, giving a range in the order 1190–1210 K.

A further analysis of temperature gradient magnitude, as an indicator of material stress [30,31], reveals that 20 N ml/min (gradient magnitude in the order of 0.5 K/mm) is much less demanding than 100 N ml/min (gradient magnitude in the order of 1 K/mm).

As a final remark on the choice of operating conditions, it may be concluded at this stage that:

- High power density can be achieved by using low H_2 utilization operating conditions. These operating conditions give relatively high stress on materials in terms of maximum temperature and temperature gradient.
- High H_2 utilization operating conditions give lower power density, but the corresponding maximum temperature and temperature gradient are safe for material resistance.

The two fuel flow rates then lead to substantially different strategies to face with design at the microreactor level. Low H_2 utilization operating conditions appear more challenging in terms of power density potential for microreactor design, and then they have been retained primarily important. According to that assumption, the anodes of different cells may also be serially connected to fully exploit H_2 energy content as confirmed in literature [39]. A voltage in the range 0.6 V has been also chosen as a compromise to get at the same time high power density and efficiency.

Accordingly, the previous operating conditions have been considered as primarily important. High H_2 utilization cases have been calculated for the sake of completeness to quantify the difference in terms of power density and thermal field distribution.

As a preliminary conclusion of this analysis, it may be observed that the application of the numerical model at the single-channel level allows, as reported in the schematic of Fig. 4, to perform a detailed evaluation of the effects of fuel utilization on cell behavior, and a more accurate understanding of the 3D coupling between fuel utilization and power output. This information, otherwise unavailable by the sole experimental data, constitutes the point of departure to develop the microreactor design level described below.

4.2 Microreactor Level. A simulation of tubular cells stacked into a microreactor, according to the basic layout of Figs. 2(*a*) and 2(*b*), was performed to estimate the effects of tube assemblies into a whole reactor characterized by a single air inlet and a single air outlet and power in the range 15–20 W. The main advantages of such configuration rely on cost and size reduction.

The design process at the microreactor level aims at analyzing the effects of packaging issues (15 tubes in the specific case of a microreactor) on the average power density and on the distribution of current density and temperature over active areas.

As a result of a number of intermediate simulations, three representative geometries have been selected (A, B, and C). For all the geometries, air inlet is located on the upper left side, and air outlet below on the right side. This is a basic requirement to guarantee easy air manifolding (see midireactor geometry) for further scaling up. Layouts are sketched in Figs. 8(*a*)–8(*c*), while the main geometrical parameters, according also to definitions provided in Figs. 2(*a*) and 2(*b*), are given in Table 8.

The main design characteristics of the three layouts are the following:

- Geometry A is characterized by high compactness, as the distance among the tubes gets the minimum value of the three layouts. Empty air volumes (indicated in the Figs. 2(*a*) and 2(*b*)) are designed to improve air distribution among the different rows.
- Geometry B is larger than A, as it presents an increase in vertical distance among the different rows, to understand the effect of distance on tube performance and thermal fields inside the reactor. Air flow design is similar to geometry A, with a smaller box shape (red baffles).
- Geometry C is finally characterized by average distance among the tubes, and a compact air manifold to have a limited impact of empty air volumes on the total volume.

The three geometries have been divided into about 300,000 computational cells, with an average grid size similar to the single-channel level (0.5 mm). The required average computational timing for each iteration is about 3 min on a state-of-the-art workstation, and 700–800 iterations are required to get a converged solution.

As a preliminary assumption for reactant inlet flow, H_2 and air have been linearly evaluated equal to 15 times higher than the flows rate of single-channel operating conditions, to realize similar air excess ratios of experiments.

Integral results are given in Table 9. It is worth noting that all

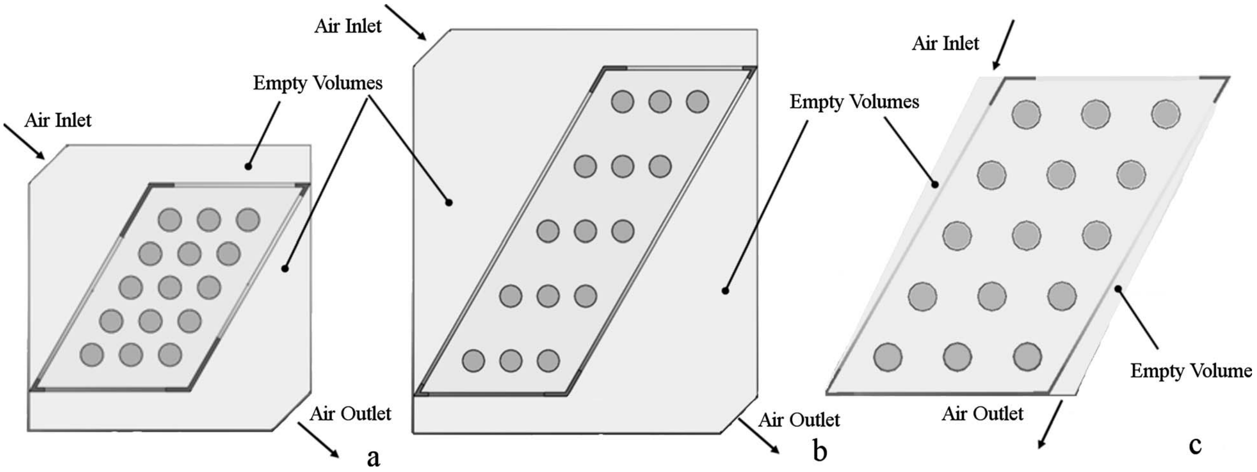

Fig. 8 Microreactor layouts (*a*, *b*, and *c*)

the geometries present an average power density around the value measured in the single-channel experiments, as expected. It is also interesting that geometry C has the highest current density output (Fig. 9(*c*), see c3). The reason for such performance can be found by the analysis of 3D plots.

Temperature field (Figs. 9(*a*)–9(*c*), see row 1), where also air path-lines are plotted colored by temperature), as it is strongly coupled with electrochemistry, is in fact radically different in the three configurations. In geometry A air flow management succeeds in providing homogeneous air flow rate over the different tubes. A small temperature increase may then be observed on active areas. geometry B has, instead, lower air availability in the outer rows; for the effect of the baffles (different box shapes, Figs. 8(*a*)–8(*c*)) air flow is directed mainly toward the center of the stack. In geometry C, this effect is more evident, as temperature gets values up to 1280 K for the row above: this behavior is due to the existence of a large recirculation zone (see path-lines in Fig. 9(*c*) (see c1)).

As commented above, the coupling between temperature and current field is expected to be strong at low H_2 utilization operating conditions, and then, air management, via temperature field, is the main cause of the high current output of geometry C that exhibits a maximum current of 0.502 A/cm^2, and thus the highest power density, although it is characterized by a consistent temperature deviation among the tubes, as average and maximum temperature differ by about 80 K. In geometries B and C, higher air consumption (Figs. 9(*a*)–9(*c*), see row 2) in the "hot tubes" can be observed, due also to the existence of recirculation regions.

As far as material issues are concerned, geometries A and B show different behavior (Table 9) in terms of temperature gradient (and thus stresses); geometry B exhibits higher thermal gradient that at a first sight appears in contrast with the larger distance among the tubes. Looking at the 3D plots of thermal gradient magnitude on active surface (Figs. 9(*a*)–9(*c*), see row 4), it is in fact evident that thermal gradient magnitude is limited only in the core region of air flow, while it increases up to a value in the order of 1.5 K/mm in the tubes closer to the top and the bottom of the microreactor, where also temperature is increased by the coupling of fluid-dynamic (flow recirculation) and heat release effects. Geometry C, due to a higher maximum temperature, presents large regions characterized by gradient in the order of 1.5 K/mm; they are located mostly close to the top of the microreactor where the recirculation zone is highly developed.

Operating conditions have been changed in terms of air flow rate, to compare the different geometries with similar maximum temperature (equal to about 1260 K), too. To this aim, air inlet has been adjusted and set to the values reported in Table 10.

Integral results (Table 10) show an opposite trend, as geometry A provides maximum current density (0.368 A/cm^2) and volumetric power density (0.279 W/cm^3). Temperature 3D plots (Fig. 10(*a*), see a1), reveal that a reduction in air flow rate in geometry A favors a temperature increase above all for tubes closer to air outlet, which take then advantage of heat release of upstream tubes. Accordingly, current output increases for downstream tubes

Table 8 Microreactor (15 cells) geometrical parameters

Configuration	Geometry A	Geometry B	Geometry C
Unit width (mm)	30	54	50
Unit length (mm)	40	44	44
Air inlet length (mm)	30	30	44
Horizontal cells distance (mm)	5.1	5.1	11
Vertical cells distance (mm)	4.4	8.8	10
Air distributor	Large	Large	Small
Box shape	Max	Min	Min
Reactive (AEC) cell length (mm)	36	40	44
Volume (cm^3)	59	112	86

Table 9 Microreactor (15 cells) performance comparison at a constant air flow rate (10^{-3} kg/s)

Configuration	Geometry A	Geometry B	Geometry C
Average current density (A/cm^2)	0.311	0.343	0.360
Active surface power density (W/cm^2)	0.190	0.210	0.218
Volume specific power density (W/cm^3)	0.235	0.152	0.223
Total power (W)	13.88	17.04	19.25
H_2 utilization (%)	10	14	14
O_2 utilization (%)	0.82	0.97	1
Maximum temperature gradient magnitude (K/mm)	0.9	1.5	1.5
Average/maximum temperature (K)	1178/1211	1187/1265	1203/1280

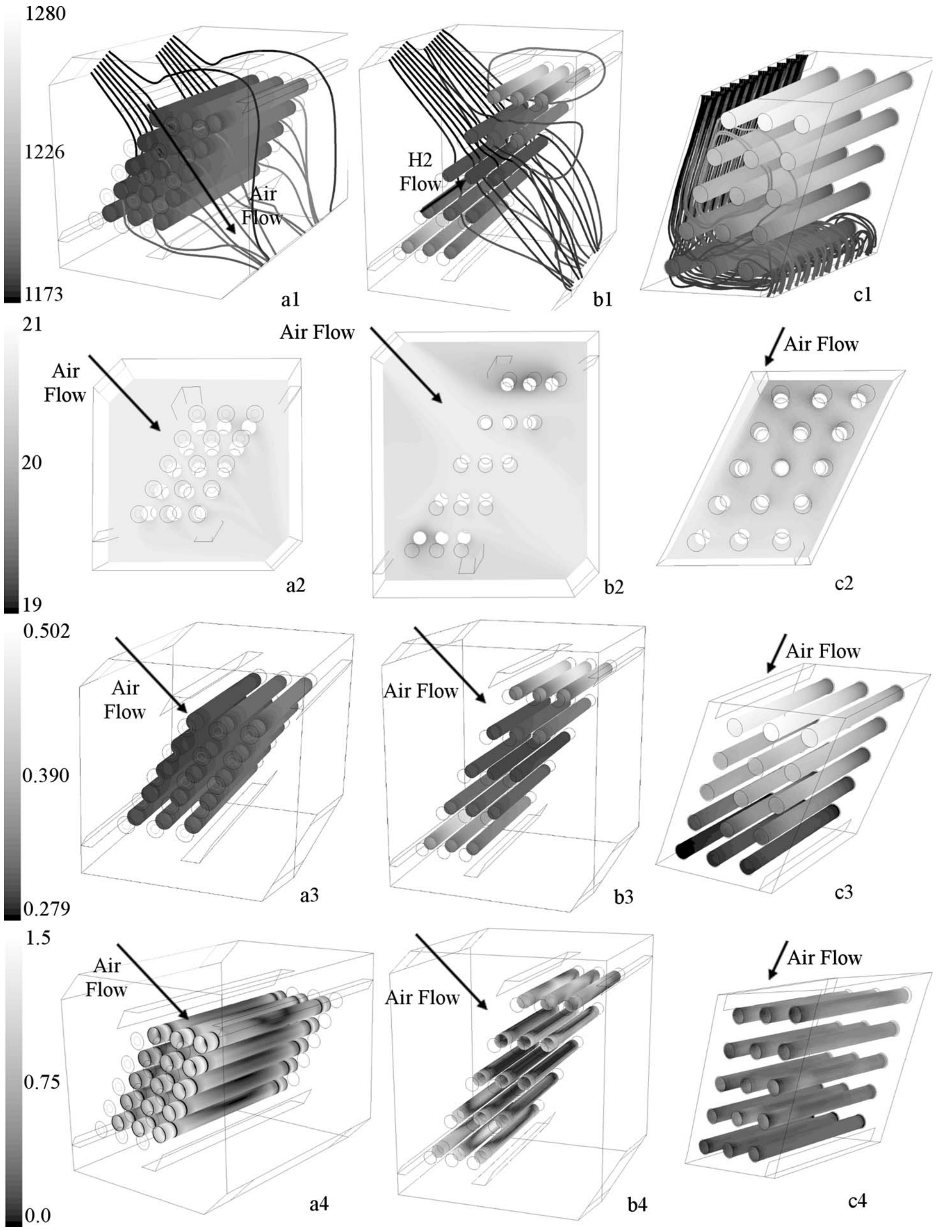

Fig. 9 Temperature fields (K) on the active surface (row 1), O_2 mole fraction (%) on a transversal section (row 2), current density fields (A/cm^2) on the active surface (row 3), and temperature gradient magnitude (K/mm) fields on the active surface (row 4) for the different microreactor geometries at a constant air flow rate (10^{-3} kg/s). (*a*) Geometry A, (*b*) geometry B, and (*c*) geometry C.

Table 10 Microreactor (15 cells) performance comparison at a constant maximum temperature (1260 K)

Configuration	Geometry A	Geometry B	Geometry C
Air inlet (kg/s)	3.5×10^{-4}	1.1×10^{-3}	1.4×10^{-3}
Average current density (A/cm^2)	0.368	0.343	0.337
Active surface power density (W/cm^2)	0.225	0.205	0.206
Volume specific power density (W/cm^3)	0.279	0.149	0.212
Total power (W)	16.43	16.67	18.22
H_2 utilization (%)	12.5	12.7	13.8
O_2 utilization (%)	2.71	0.87	0.79
Maximum temperature gradient magnitude (K/mm)	1.3	1.3	1.4
Average/maximum temperature (K)	1190/1260	1186/1252	1198/1255

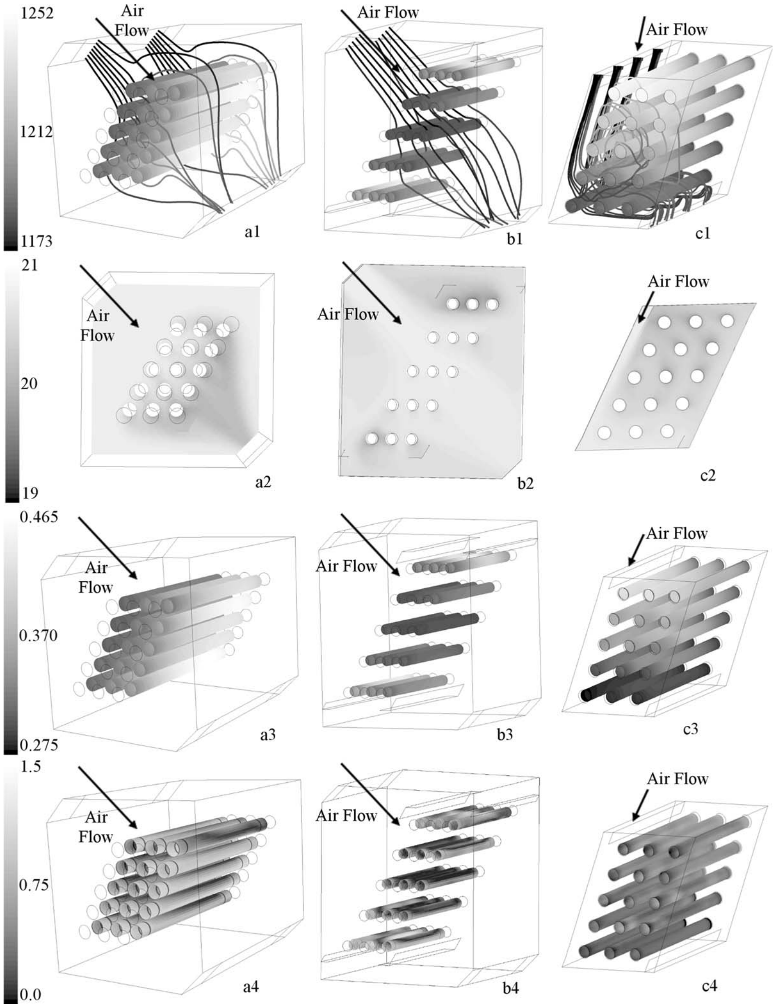

Fig. 10 **Temperature fields (K) on the active surface (row 1), O_2 mole fraction (%) on a transversal section (row 2), current density fields (A/cm^2) on the active surface (row 3) and temperature gradient magnitude (K/mm) fields on the active surface (row 4) for the different microreactor geometries at a constant maximum temperature (1260 K). (*a*) Geometry A, (*b*) geometry B, and (*c*) geometry C.**

(Fig. 10(*a*), see a3). No further differences, although a variation in air flow rate, may be observed for geometries B and C (Figs. 10(*a*)–10(*c*), rows 1 and 3) in terms of temperature and current unless for peak values.

The impact of heat transfer characteristics on microreactor performance may be quantified by the compared analysis of Nusselt number and current density. In fact, as current distribution depends, especially at high fuel utilization (i.e., max temperature operating conditions), on local temperature, heat transfer characteristics determine together with electrochemical reaction rate, current distribution over the different tubes.

Nusselt number and current of each tube are plotted for all the geometries in Figs. 11(*a*)–11(*d*) at constant max temperature conditions. As expected, an anticorrelation occurs between current and Nusselt number for all the geometries. In fact, poor local heat transfer determines a better retaining capability of heat release, thus giving an increase in temperature that is crucial to get high current output.

In geometry A, the row close to the outlet (tubes 3, 6, 9, 12, and 15) is characterized by relatively poor heat transfer, as the tubes are located downstream with respect to the other two rows. In geometry B, instead, upper (1, 2, and 3) and lower (13, 14, and 15) rows are characterized by poor heat transfer characteristics (and thus high current output) for the existence of recirculation zones as underlined above. Geometry C is generally characterized by poor heat transfer in almost all the tubes (but for the lower row 13, 14, and 15): this circumstance allows to get the best current output. It is therefore worth underlying that heat transfer is primarily important to get optimal electrochemical performance, and that the microreactor assembly takes advantage of recirculation zones involving the larger number of tubes as possible.

The analysis of temperature gradient (Figs. 10(*a*)–10(*c*), see row 4) in this case indicates a similar peak for all the geometries that is imposed by air flow rate control. Geometries B and C present similar distribution to the above analyzed. On the other hand, the better performance of geometry A is accompanied by larger temperature gradients occurring mostly in the tubes characterized by higher current performances, and then to those closer to air outlet section. It is also worth noting that a nonhomogeneous current output may be also observed in geometry A as far as higher power density operating conditions are achieved.

At the microreactor level it may then be concluded that geometry B is not optimal in any of the tested conditions, giving low power density and high thermal gradient; hence it was rejected. Then, high fuel utilization operating conditions have been tested by decreasing H_2 mass flow rate by 85% (main performance parameters are reported in Table 11).

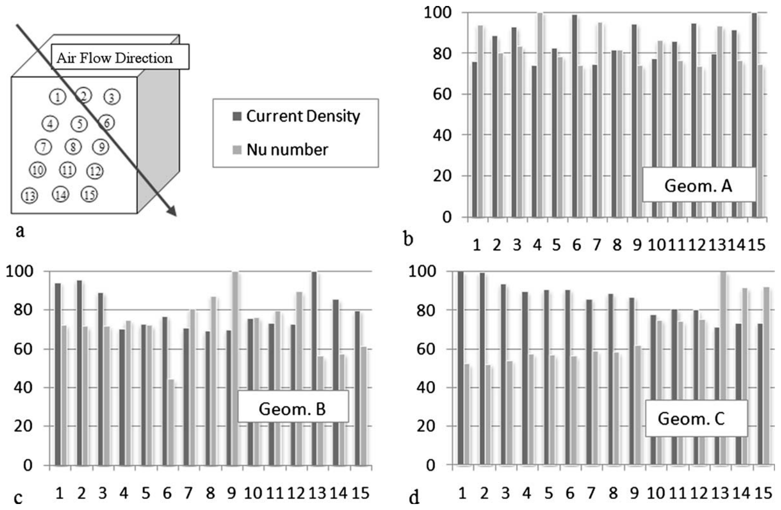

Fig. 11 (*a*) **Cell position in the stack layer, related to air inlet/outlet direction. Evaluation of the relative current density (%) and relative Nusselt number (%) for each channel of (*b*) model A, (*c*) model B, and (*d*) model C at constant maximum temperature (1260 K) operating conditions.**

The comparison of current performance indicate a better performance of geometry A, accompanied by a higher utilization (69.6% for geometry A versus 61% for geometry C). Geometry A performs even better in terms of power density, taking advantage of the smaller volume, although temperature on the active surface has similar range in the two cases (Figs. 12(*b*) and 12(*d*), see b2 and d2). The reasons for the difference in performance may be found again by analyzing the 3D plots. H_2 molar fraction fields (Figs. 12(*a*)–12(*d*), see row 1) show a high utilization for all the 15 tubes in both the geometries. However, the analysis of temperature fields (Figs. 12(*a*)–12(*d*), see row 2), that once again depend on the coupling between electrochemistry, fluid-dynamics, and heat transfer, reveals that high temperature regions are much larger in geometry A than in geometry C, and that in geometry A the five tubes close to air outlet have more or less the same temperature in the order of 1230 K. As underlined above, high utilization conditions give high current only where H_2 mole fraction is high. Thus (Figs. 12(*a*)–12(*d*), see row 3) current field is very low close to H_2 outlets in both the geometries, i.e., where fuel availability is poor, allowing to exploit only a limited percentage of the available active area. In geometry A, however, the already commented high temperature of some tubes allows current to get a peak greater than $0.4\ \text{A}/\text{cm}^2$ over a significant percentage of tube length. Temperature gradient magnitude (Figs. 13(*a*) and 13(*b*)), as expected, has a consistent decrease only for geometry C, as current performance drops down by increasing fuel utilization. In this case, then, the lowest temperature gradient may be observed of all the cases.

Finally, at the microreactor level the following conclusions may be drawn:

- Geometry and air flow management have a noteworthy impact on the performance of the microreactor, i.e., stacked tubes behave in a different way than single tubes. The analysis of the coupling between heat transfer and electrochemistry is primarily important to optimize the microreactor operation. In fact, Nusselt number and current output present an anticorrelation due to the heat transfer capabilities of each "active region" of retaining local heat release due to electrochemical reactions.
- In all the cases, geometry B has the worst performance in both terms of current and temperature gradient, and then it was rejected.
- Geometries A and C have different behaviors. The occurrence of a large recirculation zone allows some of the tubes of geometry C to have better performance, while the same thing may be observed for the downstream row in geometry A. With the same air excess geometry C behaves better, while the opposite can be concluded by controlling air flow rate to limit temperature to a maximum value (i.e., 1260 K).
- 3D plots indicate that each tube behaves differently from the others both in terms of power output and maximum thermal gradient. It was however proved that in none of the proposed geometries temperature gradient exceeded safe values confirmed in literature [30,31], and that, as it was considered in the single-channel, high fuel utilization operating conditions allow to exploit better H_2 and to have limited thermal gradient on the active surface with a reduction in power output. Geometry A demonstrated a lower effect of fuel utilization on performance, if compared with geometry C, as power output decreased by 12%.

Table 11 Microreactor (15 cells) performance comparison at high H_2 utilization

Configuration	Geometry A High FU	Geometry C High FU
Air inlet (kg/s)	3.5×10^{-4}	10^{-3}
Average current density (A/cm^2)	0.324	0.245
Active surface power density (W/cm^2)	0.198	0.149
Volume specific power density (W/cm^3)	0.245	0.153
Total power (W)	14.46	13.2
H_2 utilization (%)	69.6	61
O_2 utilization (%)	2.43	1
Maximum temperature gradient magnitude (K/mm)	1.1	0.9
Average/maximum temperature (K)	1187/1239	1196/1237

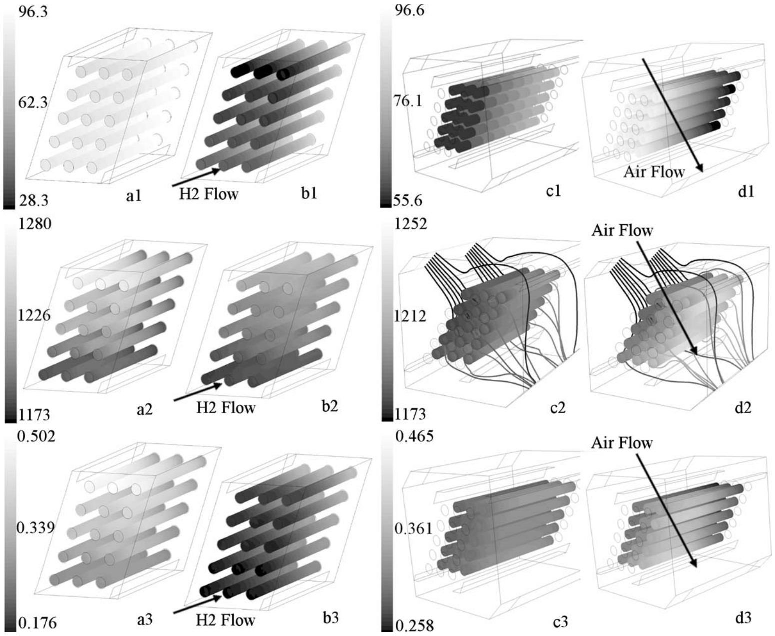

Fig. 12 H_2 mole fraction (%, row 1), temperature fields (K, row 2), and current distribution (A/cm^2, row 3) on the active surface for geometries C (*a* and *b*) and A (*c* and *d*) at low (*a* and *c*) and high (*b* and *d*) fuel utilizations

4.3 Midireactor Level. The analysis of different microreactor geometries allows understanding the effect of geometry and air flow rate on the performance of tube stacks. It is also worth noting that power output of 15 tube microreactors, as reported in Tables 9–11, ranges approximately from 12 W to 19 W. Hence, a single microreactor is not able to provide power enough, for example, for APU applications, where the needed power is in the range 1–5 kW [5]. Thus, the proposed design procedure is based on a modular scale-up methodology to increase the number of tubes, and then power output, by keeping at the same time similar flow configurations to the ones discussed in the section dedicated to the microreactor design level. This simplifying assumption allows to get started from the results computed for simpler configurations, and then limits the complications and the number of degree of freedom of very large tube assemblies and complex flow configurations. Moreover, calculation timings of very large configurations would become prohibitive, especially to compute large parameter range sets.

The midireactor is an example of the application of such a "modular design procedure." According to Fig. 3, an assembly of three microreactors is proposed. The proposed solution aims at preserving as much as possible the geometrical characteristics of geometry C, by designing air distributors able to provide almost homogeneous air flow rates among the different microreactors. Moreover, the proposed distributor layout allows to reduce the volume dedicated to air management, and to confine air distribution only on the sides of the assembly of the microreactors.

Once given the geometry of the midireactor, the integrated CFD tool has been applied to the analysis of current and thermal-fluid-dynamic fields over the active surface, to verify the different output and thermal gradients over the three microreactors. It is worth noting that in this case, to preserve similar accuracy of single-channel and microreactor tests, the computational domain has been divided into about 1*M* cells, and that related computational timing for a single operating condition is about 160 h on a state-of-the-art workstation. This is the main reason why CFD-based design at this stage aims at verifying power output distribution and thermal gradient distribution similar to the microreactor.

Results, classified by the microreactor position, are summarized in Table 12. Operating conditions are similar to constant air flow rate microreactors. The geometry of the single air manifold, used in the midireactor, allows to supply oxygen and to cool every channel without creating zones with lower O_2 concentration (the molar fraction range showed in Fig. 14(*a*) is comparable to microreactor simulations, Figs. 9(*a*)–9(*c*) and 10(*a*)–10(*c*), see row 2), observing only a slight increase in temperature (Fig. 14(*c*)). Current fields are also similar to microreactor results (Fig. 14(*b*)), as recirculation regions let temperature increase in the tubes placed at the bottom of each microreactor (Fig. 14(*c*)). The analysis of the performance of each microreactor (Table 12) indicates that the middle one performs slightly better than the other ones, and that fuel utilization has an almost homogeneous value. Moreover, temperature gradient fields assure that midireactor design does not introduce any misoperation in terms of material failure with respect to microreactor level, as maximum temperature gradient and distribution (Fig. 14(*d*) are similar to the corresponding microreactor fields. Results could be even improved by better de-

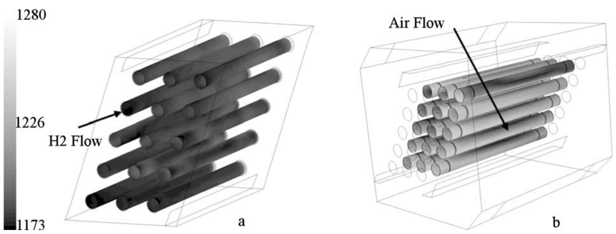

Fig. 13 Temperature gradient magnitude on the active surface for high fuel utilization, geometries C (*a*) and A (*b*)

Table 12 Midireactor results

	Upper microreactor	Mid microreactor	Lower microreactor
Current density (A/cm^2)	0.318	0.354	0.351
Total power (W)	17.19	19.14	18.97
H_2 utilization (%)	13.2	14.6	14.5
O_2 utilization (%)	0.9	1.0	1.0

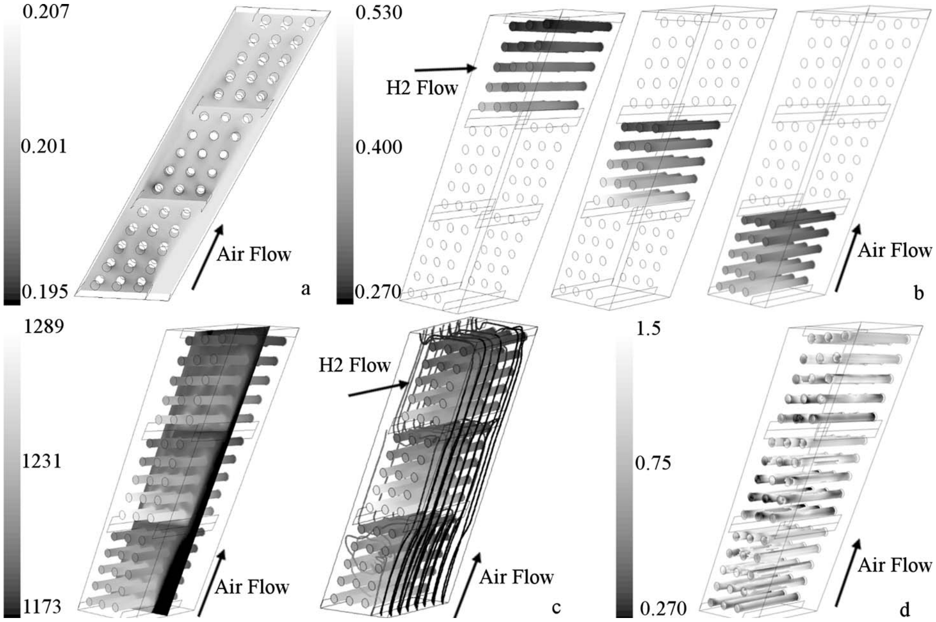

Fig. 14 (*a*) O_2 molar fraction (%) field on a transversal section, (*b*) current density (A/cm^2) on the active surface, (*c*) temperature (K) fields and pathlines colored by temperature on active surface and on a transversal section, and (*d*) temperature gradient magnitude (K/mm) field (d) on the active surface for the midireactor

signing air distributors, but the main target of this section is the demonstration of the potential of the proposed CFD approach to drive the design of a kW-size microtubular SOFC.

5 Conclusions

A specific design procedure for modular MT-SOFCs was presented. It is based on an integrated CFD model able to address all the design issues arising from the complex interaction among fluid-dynamic, heat transfer, and electrochemical phenomena.

The integrated CFD model was first validated versus experimental data with respect to a basic geometry (single-channel level), and then used to evaluate more complex modular scaled-up designs, called micro- and midireactors. Three different microreactor geometries and several operating conditions (i.e., different reactant mass flow rates) have been investigated, leading to the following main conclusions.

- The experimental validation proved that the model is able to represent the coupling among the main phenomena occurring into a microtubular SOFC. The deviation from the experimental data was always lower than 6%. Since no tuning on model constant set was performed, this result has been considered satisfactory for the MT-SOFC design.
- Small size and high temperature of a MT-SOFC make hard a direct analysis, so the 3D computational fluid-dynamic simulation is mandatory to analyze the heat transfer mechanisms inside stacks.
- H_2 utilization was identified as the crucial parameter for cell operation. Low H_2 utilization in fact gives higher power density, although several tubes in series should be adopted to exploit the full H_2 energy content. It was also showed, by means of 3D plots, that at low utilization maximum current output occurs over higher temperature regions of the active area, while at high utilization the zones characterized by low H_2 partial pressure give low current. Moreover, high utilization operating conditions have lower temperature gradient magnitude, and thus materials are less stressed.
- The three proposed microreactor geometries, constituted by 15 channels with common air inlet and outlet sections and characterized by different compactness and tube arrangements, showed a deviation of performance in terms of power output and temperature gradient magnitude. It was showed that by keeping a constant air flow rate, each geometry leads to a different thermal field and then to different power output. Also, by means of 3D plots, it was showed that each tube provides different current output. Current homogeneity and temperature fields are also a strong function of air flow rate and fuel utilization as local heat transfer characteristics have a strong impact on local current performance. Hence, the choice of the optimal solution depends on operating condition management and on heat transfer design issues.
- Temperature gradient magnitude had acceptable values in all the microreactor geometries. However, geometry B, characterized by relevant distance among the tubes, showed a bad trade-off between power output and temperature gradient and then it was not considered suitable for real application.
- Midireactor design was presented as a modular scale-up of a microreactor with common air inlet and outlet. An example of an assembly constituted by three microreactors was analyzed with a specifically designed air manifolding. The final target of this level in the design concept consists of verifying the achievement of most homogeneous as possible power output of each module of the midireactor. The proposed design showed reasonable results with regard to this.

The proposed design procedure and related results aimed at demonstrating the potential of CFD-based tools applied to MT-SOFCs. As far as the design concept is concerned, the next steps foresee the study of even larger assemblies to test geometries characterized by output closer to the 1 kW target, and the realization of midireactor prototypes to finally assess results on an experimental basis.

References

[1] Singhal, S. C., 2000, "Advances in Solid Oxide Fuel Cell Technology," Solid State Ionics, **135**, pp. 305–313.
[2] Wincewicz, K. C., and Cooper, J. S., 2005, "Taxonomies of SOFC Material and Manufacturing Alternatives," J. Power Sources, **140**, pp. 280–296.
[3] Van herle, J., Ihringer, R., Sammes, N. M., Tompsett, G., Kendall, K., Yamada, K., Wen, C., Kawada, T., Ihara, M., and Mizusaki, J., 2000, "Concept and Technology of SOFC for Electric Vehicles," Solid State Ionics, **132**, pp. 333–

342.
[4] Yuan, J., and Sundén, B., 2005, "Analysis of Intermediate Temperature Solid Oxide Fuel Cells Transport Processes and Performance," ASME J. Heat Transfer, **127**(12), pp. 1380–1390.
[5] Minh, N. Q., 2004, "Solid Oxide Fuel Cell Technology—Features and Applications," Solid State Ionics, **174**, pp. 271–277.
[6] Alston, T., Kendall, K., Palin, M., Prica, M., and Windibank, P., 1998, "A 1000-Cell SOFC Reactor for Domestic Cogeneration," J. Power Sources, **71**, pp. 271–274.
[7] Du, Y., Finnerty, C., and Jiang, J., 2008, "Thermal Stability of Portable Microtubular SOFCs and Stacks," J. Electrochem. Soc., **155**, pp. B972–B977.
[8] Kendall K., 2009, "Progress in Microtubular Solid Oxide Fuel Cells," Int. J. Appl. Ceram. Technol., in press.10.1111/j.1744-7402.2008.02350.x
[9] Lawlor, V., Griesser, S., Buchinger, G., Olabi, A. G., Cordiner, S., and Meissner, D., 2009, "Review of the Micro-Tubular Solid Oxide Fuel Cell: Part I. Stack Design Issues and Research Activities," J. Power Sources, **193**, pp. 387–399.
[10] Funahashi, Y., Shinamori, T., Suzuki, T., Fujishiro, Y., and Awano, M., 2007, "Fabrication and Characterization of Components for Cube Shaped Micro Tubular SOFC Bundle," J. Power Sources, **163**, pp. 731–736.
[11] Sammes, N. M., Du, Y., and Bove, R., 2005, "Design and Fabrication of a 100 W Anode Supported Micro-Tubular SOFC Stack," J. Power Sources, **145**, pp. 428–434.
[12] Autissier, N., Larrain, D., Van Herle, J., and Favrat, D., 2004, "CFD Simulation Tool for Solid Oxide Fuel Cells," J. Power Sources, **131**, pp. 313–319.
[13] Ferguson, J. R., Fiard, J. M., and Herbin, R., 1996, "Three-Dimensional Numerical Simulation for Various Geometries of Solid Oxide Fuel Cells," J. Power Sources, **58**, pp. 109–122.
[14] Li, P. W., and Schaefer, L., and Chyu, M. K.,2004, "A Numerical Model Coupling the Heat and Gas Species' Transport Processes in a Tubular SOFC," ASME J. Heat Transfer, **126**(2), pp. 219–229.
[15] Kakac, S., Pramuanjaroenkij, A., and Zhou, X. Y., 2007, "A Review of Numerical Modelling of Solid Oxide Fuel Cells," Int. J. Hydrogen Energy, **32**(7), pp. 761–786.
[16] R. Bove and S. Ubertini, eds., 2008, *Modeling Solid Oxide Fuel Cells, Methods, Procedures and Techniques*, Springer, New York.
[17] Van herle, J., Larrain, D., Autissier, N., Wuillemin, Z., Molinelli, M., and Favrat, D., 2005, "Modeling and Experimental Validation of SOFC Materials and Stacks," J. Eur. Ceram. Soc., **25**, pp. 2627–2632.
[18] Recknagle, K. P., Williford, R. E., Chick, L. A., Rector, D. R., and Khaleel, M. A., 2003, "Three Dimensional Thermo-Fluid Electrochemical Modeling of Planar SOFC Stacks," J. Power Sources, **113**, pp. 109–114.
[19] Kapadia, S., and Anderson, W. K., 2009, "Sensitivity Analysis for Solid Oxide Fuel Cells Using a Three-Dimensional Numerical Model," J. Power Sources, **189**(2), pp. 1074–1082.
[20] Li, P. W., and Chyu, M. K., 2005, "Electrochemical and Transport Phenomena in Solid Oxide Fuel Cells," ASME J. Heat Transfer, **127**(12), pp. 1344–1362.
[21] Janardhanan, V. M., and Deutschmann, O., 2007, "Numerical Study of Mass and Heat Transport in Solid-Oxide Fuel Cells Running on Humidified Methane," Chem. Eng. Sci., **62**, pp. 5473–5486.
[22] Ozgur Colpan, C., Dincer, I., and Hamdullahpur, F., 2008, "Transient Modeling of Direct Internal Reforming Planar Solid Oxide Fuel Cells," ASME Paper No. GT2008-56425.
[23] Nakajo, A., Wullemin, Z., Van Herle, J., and Favrat, D., 2009, "Simulation of Thermal Stresses in Anode-Supported Solid Oxide Fuel Cell Stacks. Part II: Loss of Gas-Tightness, Electrical Contact and Thermal Buckling," J. Power Sources, **193**, pp. 216–226.
[24] Lockett, M., Simmons, M. J. H., and Kendall, K., 2004, "CFD to Predict Temperature Profile for Scale Up of Micro-Tubular SOFC Stacks," J. Power Sources, **131**, pp. 243–246.
[25] Lee, S.-B., Lim, T. H., Song, R. H., Shin, D.-R., and Dong, S.-K., 2008, "Development of a 700 W Anode-Supported Micro-Tubular SOFC Stack for APU Applications," Int. J. Hydrogen Energy, **33**, pp. 2330–2336.
[26] Cui, D., and Cheng, M., 2009 "Numerical Analysis of Thermal and Electrochemical Phenomena for Anode Supported Microtubular SOFC," AIChE J., **55**(3), pp. 771–782.
[27] Cui, D., and Cheng, M., 2009, "Thermal Stress Modeling of Anode Supported Micro-Tubular Solid Oxide Fuel Cell," J. Power Sources, **192**, pp. 400–407.
[28] Serincan, M. F., Pasaogullari, U., and Sammes, N. M., 2008, "Computational Thermal Fluid Analysis of Micro-Tubular Solid Oxide Fuel Cells," J. Electrochem. Soc., **155**, pp. B1117–B1127.
[29] Claassen, P., Grimschitz, G., Kuehn, S., Mariani, A., De Simone, G., Wancura, H., Buchinger, G., Meissner, D., and Raab, T., 2006, Integrated SOFC Systems Based on Microtubular Cells—Reaching the kW-Stage, Fuel Cell Seminar, Honolulu.
[30] Selimovic, A., Kemm, M., Torisson, T., and Assadi, M., 2005, "Steady State and Transient Thermal Stress Analysis in Planar Solid Oxide Fuel Cells," J. Power Sources, **145**, pp. 463–469.
[31] Dikwal, C. M., Bujalski, W., and Kendall, K., 2009, "The Effect of Temperature Gradients on Thermal Cycling and Isothermal Ageing of Micro-Tubular Solid Oxide Fuel Cells," J. Power Sources, **193**, pp. 241–248.
[32] Fluent Inc., 2003, *Fluent User's Guide, Version 6.1*, Fluent Inc., Lebanon, NH.
[33] Cordiner, S., Feola, M., Mulone, V., and Romanelli, F., 2007, "Analysis of a SOFC Energy Generation System Fuelled With Biomass Reformate," Appl. Therm. Eng., **27**(4), pp. 738–747.
[34] Zhang, X., Li, G., Li, J., and Feng, Z., 2007, "Numerical Study on Electric Characteristics of SOFC," Energy Convers. Manage., **48**, pp. 977–989.
[35] Sleiti, A. K., 2008, "Effect of Reduced Temperature and Cathode Porosity on the Performance of Tubular Solid Oxide Fuel Cell," ASME Paper No. GT2008-56447.
[36] Hawkes, G., and Jones, R., 2007, "CFD Model of a Planar Solid Oxide Electrolysis Cell: Base Case and Variations," ASME Paper No. GT2007-32310.
[37] Pasaogullari, U., and Wang, C. Y., 2003, "Computational Fluid Dynamics Modelling of Solid Oxide Fuel Cells," *Proceedings of the SOFC-VIII.*, Vol. 7, Paris, France, pp. 1403–1412.
[38] Mandin, P., Bernay, C., Tran-Dac, S., Broto, A., Abes, D., and Cassir, M., 2006, "SOFC Modelling and Numerical Simulation of Performances," Fuel Cells, **6**(1), pp. 71–78.
[39] Hawkes, G. L., O'Brien, J. E., Martinez Baca, C., Travis, R. P., Haberman, B. A., Marquis, A. J., Costamagna, P., and Tripepi, D., 2008, "Numerical Prediction of the Performance of Integrated Planar Solid-Oxide Fuel Cells With Comparisons of Results From Several Codes," *Proceedings of the Sixth International Conference on Fuel Cell Science, Engineering and Technology*, Denver, Jun. 16–18.
[40] Zhu, H., and Kee, R. J., 2007, "The Influence of Current Collection on the Performance of Tubular Anode-Supported SOFC Cells," J. Power Sources, **169**, pp. 315–326.
[41] Manca, O., and Nardini, S., 2009, "Experimental Investigation of Radiation Effects on Natural Convection in Horizontal Channels Heated From Above," ASME J. Heat Transfer, **131**(6), p. 062503.
[42] Beale, S. B., 2005, *Transport Phenomena in Fuel Cells*, B. Sunden and M. Faghri, eds., MIT, Cambridge, MA, pp. 43–82.
[43] Van der Steen, J. D. J., and Pharoah, J. G., 2004, "The Effect of Radiation Heat Transfer in Solid Oxide Fuel Cell Modelling," Combustion Institute/Canadian Section, Spring Technical Meeting, Queen's University, May 9–12.
[44] Daun, K. J., Beale, S. B., Liu, F., and Smallwood, G. J., 2006, "Radiation Heat Transfer in Planar SOFC Electrolytes," J. Power Sources, **157**, pp. 302–310.
[45] Tanaka, T., Inui, Y., Urata, A., and Kanno, T., 2007, "Three Dimensional Analysis of Planar Solid Oxide Fuel Cell Stack Considering Radiation," Energy Convers. Manage., **48**, pp. 1491–1498.
[46] Burt, A. C., Celik, I. B., Gemmen, R. S., and Smirnov, A. V., 2004, "A Numerical Study of Cell-to-Cell Variations in a SOFC," J. Power Sources, **126**, pp. 76–87.
[47] Singhal, S. C., and Kendall, K., 2004, *High-Temperature Solid Oxide Fuel Cells: Fundamentals, Design and Applications*, Elsevier, New York.
[48] Grew, K. N., Joshi, A. S., and Peracchio, A. A., 2007, "Characterization and Quantification of Charge and Heat Transfer in a Solid Oxide Fuel Cell Anode," ASME Paper No. GT2007-32452.
[49] Chan, S. H., Chen, X. J., and Khor, K. A., 2002, "An Electrolyte Model for Ceramic Oxygen Generator and Solid Oxide Fuel Cell," J. Power Sources, **111**, pp. 320–328.
[50] Larminie, J., and Dicks, A., 2003, *Fuel Cell Systems Explained*, 2nd ed., Wiley, New York.
[51] Wang, C. Y., 2004, "Fundamental Models for Fuel Cell Engineering," Chem. Rev. (Washington, D.C.), **104**, pp. 4727–4766.
[52] Yakabe, H., Ogiwara, T., Hishimuma, M., and Yasuda, I., 2001, "3D Model Calculation for Planar SOFC," J. Power Sources, **102**, pp. 144–154.
[53] Hernandez-Pacheco, E., Mann, M. D., Hutton, P. N., Singh, D., and Martin, K. E., 2005, "A Cell-Level Model for a Solid Oxide Fuel Cell Operated With Syngas From a Gasification Process," Int. J. Hydrogen Energy, **30**, pp. 1221–1233.
[54] Costamagna, P., and Honegger, K., 1998, "Modelling of a SOFC Energy Generation System Integrated Stacks and Simulation at High Fuel Utilization," J. Electrochem. Soc., **145**(11), pp. 3995–4007.
[55] Buchinger, G., Kraut, J., Raab, T., Griesser, S., Lawlor, V., Haiber, J., Hiesgen, R., Sitte, W., and Meissner, D., 2007, "Operating Micro-Tubular SOFCs Containing Nickel Based Anodes With Blends of Methane and Hydrogen," Clean Electrical Power ICCEPP '07.
[56] Cui, D., Liu, L., Dong, Y., and Cheng, M., 2007, "Comparison of Different Current Collecting Modes of Anode Supported Micro-Tubular SOFC Through Mathematical Modeling," J. Power Sources, **174**, pp. 246–254.
[57] Pakalapati, S. R., 2003, "A Numerical Study of Current Distribution Inside the Cathode and Electrolyte of a Solid Oxide Fuel Cell," MS thesis, West Virginia University, Morgantown, WV.
[58] Iwata, M., Hikosaka, T., Morita, M., Iwanari, T., Ito, K., Ondaa, K., Esakib, Y., Sakakib, Y., and Nagata, S., 2000, "Performance Analysis of Planar-Type Unit SOFC Considering Current and Temperature Distributions," Solid State Ionics, **132**, pp. 297–308.
[59] Ullmann, H., Trofimenko, N., Tietz, F., Stover, D., and Ahmad-Khanlou, A., 2000, "Correlation Between Thermal Expansion and Oxide ion Transport in Mixed Conducting Perovskite-Type Oxides for SOFC Cathodes," Solid State Ionics, **138**, pp. 79–90.
[60] Aruna, S. T., Muthuraman, M., and Patil, K., 1998, "Synthesis and Properties of Ni-YSZ Cermet: Anode Material for SOFC," Solid State Ionics, **111**, pp. 45–51.
[61] Li, P.-W., and Suzuki, K., 2004, "Numerical Modeling and Performance Study of a Tubular SOFC," J. Electrochem. Soc., **151**(4), pp. A548– A557.

Semi-Analytical Solution for Heat Transfer in a Water Film Flowing Over a Heated Plane

Adrien Aubert
e-mail: adrien.aubert@emn.fr

Fabien Candelier

Camille Solliec[1]
e-mail: camille.solliec@emn.fr

Department of Energy Systems and Environment,
GEPEA,
Ecole des Mines de Nantes,
4 rue Alfred Kastler,
Cedex 3,
Nantes BP 20722, France

Film flow coupled with heat and mass transfer is a widely open domain due to the range of its applications. However, the coupling between the different phenomena makes the analytical resolution difficult, and thus, coerces most authors into performing numerical studies. Although efficient, the numerical approach does not reveal the real link between the different parameters when studying heat transfer. This lack of meaningful formulation motivates the present paper, which proposes a semi-analytical solution for the establishment of the thermal boundary layer of a film flowing down an inclinated heated plane. The formula is obtained by a truncated sum of Whittaker's functions, and is validated by comparison with a full numerical solution of the problem (assuming the same hypotheses). The semi-analytical nature of the equation provides better understanding of the physical phenomena and could help in reducing numerical computational time.
[DOI: 10.1115/1.4000751]

Keywords: water film, thermal boundary layer, semi-analytical solution, Whittaker's functions

1 Introduction

The study of a liquid film flowing down an inclinated plane is, from the fluid mechanical point of view, quite simple. However, when associated with heat transfer from the wall to the film and with mass transfer between the film and the surrounding atmosphere, it becomes a more difficult problem. Indeed, the high coupling between equations increases considerably the difficulty to find analytical solutions in such cases.

However, due to its widespread applications, this problem has focused the attention of many researchers since the pioneering work of Nusselt [1]. For instance, liquid films have been proved to be efficient to protect glass from radiation [2]. They are also regularly employed as basic principles in desalination plant studies [3,4] or in absorption cooling systems [5].

Considering the complexity of the phenomena taking place in film flows, the numerical approach has been extensively used at the expense of the analytical one (see, for example, Ref. [6]). Despite its powerfulness and its ease of use, numerical approach is limited by the fact that it does not exhibit the explicit relations between governing parameters, such as flow rate or imposed temperature on the wall. Therefore, it does not provide much comprehension of the phenomena, and sometimes, one needs to realize numerous numerical simulations (parametric study) in order to characterize the contributions of a particular parameter. This is the reason why it may be very interesting to seek analytical solutions even if such solutions can only be obtained in simplified cases. In this connection, some interesting studies can be found, concerning film flows coupled with heat and mass transfer, notably those of Nakoryakov and Grigor'eva [7] and Grossman [8], who provided solutions by expansion series or by using the similarity techniques. A very interesting analytical solution of mass transfer obtained for a falling film absorber was also carried out by Conlisk [9], who provided a full analytical solution of the mass transfer equation, with the assumption of a linear temperature profile, which allows avoiding computational work in order to size a vertical tube absorber. More recently, Ren [10] proposed an accurate analytical solution to the heat and mass transfer in counterflow cooling towers.

Nevertheless, those solutions either required strong assumptions or numerical resolution, or lost its physical meaning by projection. Therefore the aim of this paper is to propose an analytical investigation concerning the thermal boundary layer development, where the dependence between the different parameters involved in this study appears explicitly. It is assumed here that the flow is laminar, fully established at the beginning of the heated plane (see Fig. 1), and that the thermal boundary layer does not reach the surface of the film (evaporation is not considered) in the concerned area. The classical hydrodynamic boundary layer hypotheses are also considered.

2 Semi-Analytical Resolution

2.1 Analytical Investigation. Considering the hypotheses presented above, the velocity profile is well known and is given by the Nusselt theory

$$u(y) = \frac{g}{\nu}\sin(\beta)\left(y\delta - \frac{1}{2}y^2\right) \tag{1}$$

where g is the gravitational acceleration, ν is the kinematic viscosity, β is the inclination angle of the plate, y is the normal coordinate, and δ is the film thickness. Concerning the film thickness, one can readily check its link to the flow per unit of length Q by the following relation:

$$\delta = \left(\frac{3Q\nu}{g\,\sin(\beta)}\right)^{1/3} \tag{2}$$

In order to find an analytical solution corresponding to the temperature $T(x,y)$ in the falling film, two main hypotheses were considered. First, it was assumed that the thermal boundary layer thickness δ_T never reaches that of the film. As a consequence the temperature of the free surface is considered as constant and noted T_{water}.

The second hypothesis reads $(\partial^2T/\partial x^2) \ll (\partial^2T/\partial y^2)$, which is very classical in boundary layer problems.

Accordingly, the heat equation takes the following form:

$$u(y)\frac{\partial T}{\partial x} = \alpha\frac{\partial^2 T}{\partial y^2} \tag{3}$$

where α is the thermal diffusivity, and T satisfies the following boundary conditions:

$$\begin{aligned} T(x,y=0) &= T_{\text{wall}} \quad \text{for } x \in [0,L] \\ T(x=0,y) &= T_{\text{water}} \quad \text{for } y \in\ ]0,\delta\,] \\ T(x,y=\delta) &= T_{\text{water}} \quad \text{for } x \in [0,L[\end{aligned} \tag{4}$$

---

[1] Corresponding author.

Contributed by the Heat Transfer Division of ASME for publication in the JOURNAL OF HEAT TRANSFER. Manuscript received June 2, 2009; final manuscript received November 9, 2009; published online March 31, 2010. Assoc. Editor: W. Q. Tao.

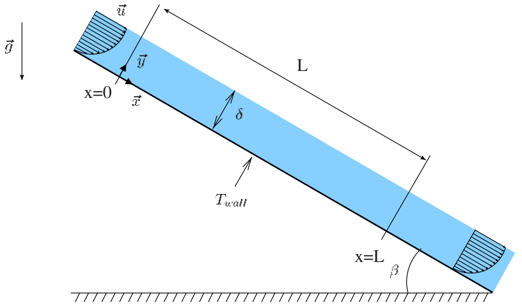

Fig. 1 Schematic representation of the physical system

For later convenience, these equations are now written in a dimensionless form by introducing the following changes: $\theta=(T_{\text{wall}}-T(x,y))/(T_{\text{wall}}-T_{\text{water}})$, $u_*=2\nu u/(g\sin(\beta)\delta^2)=(2y_*-y_*^2)$, and $y_*=y/\delta$ and $x_*=x/(\delta\text{Pe})$. Note that Pe is the Peclet number $\text{Pe}=u(y=\delta)\delta/\alpha$, and also, it should be emphasized that y and x are not normalized with the same length.

In addition, in order to simplify the boundary conditions of the problem, we write

$$\eta=1-y_*$$
$$\theta'=\theta-(1-\eta) \tag{5}$$

In this condition, the governing equation of the normalized temperature reads

$$(1-\eta^2)\frac{\partial\theta'}{\partial x_*}-\frac{\partial^2\theta'}{\partial\eta^2}=0 \tag{6}$$

with the following boundary conditions

$$\theta'(x_*=0,\eta)=\eta \quad \text{for} \quad \eta\in[0,1[$$
$$\theta'(x_*,\eta=1)=0 \tag{7}$$

Following a very common approach in such problems, the solution of Eq. (6) can be sought by using variable separation $f(x_*)h(\eta)$.

This leads to the following relation:

$$\frac{\dfrac{\partial f}{\partial x_*}}{f}=\frac{\dfrac{\partial^2 h}{\partial\eta^2}}{(1-\eta^2)h} \tag{8}$$

Because each part of Eq. (8) is function of a different independent variable, then it is equal to a constant. This constant is taken as $-A^2$ for later convenience, and the left hand side of Eq. (8) led to

$$f(x_*)=C_1e^{-A^2x_*} \tag{9}$$

Concerning the right hand side of the equation, changing $h\sqrt{\eta}$ to h' and $A\eta^2$ to η' lead to an equation that can be identified with Whittaker's equation [11]. The solution h' of this equation is thus given by $M_{A/4,1/4}(\eta')$ and $W_{A/4,1/4}(\eta')$ confluent hypergeometric functions, known as Whittaker special functions (see, for instance, Ref. [11] or the Appendix). Written in terms of h and η

$$h(\eta)=\frac{C_2M_{A/4,1/4}(A\eta^2)+C_3W_{A/4,1/4}(A\eta^2)}{\sqrt{\eta}} \tag{10}$$

where C_1, C_2, and C_3 are integration constants.

Taking now into account the boundary conditions, the solution can be expressed in a more simple way. Indeed, by using the fact that when $\eta\to0:\theta'(x_*,0)=0$, it comes that C_3 is necessarily null, as in these conditions $M_{A/4,1/4}(A\eta^2)\to0$ and $W_{A/4,1/4}(A\eta^2)\neq0$ (assuming that A is not null).

Moreover, when $\eta=1$, the boundary condition imposes that $\forall x_*$, $\theta'(x_*,1)=0$; thus, $h(1)=C_2M_{A/4,1/4}(A)$ must be null. As a consequence, every element A that nullify $h(1)$ can be a solution of the problem; they are the root of the $M_{A/4,1/4}(A)$ Whittaker function and nth is noted as X_n. Because the M function admits an infinity of roots, the general solution of the problem can be written as

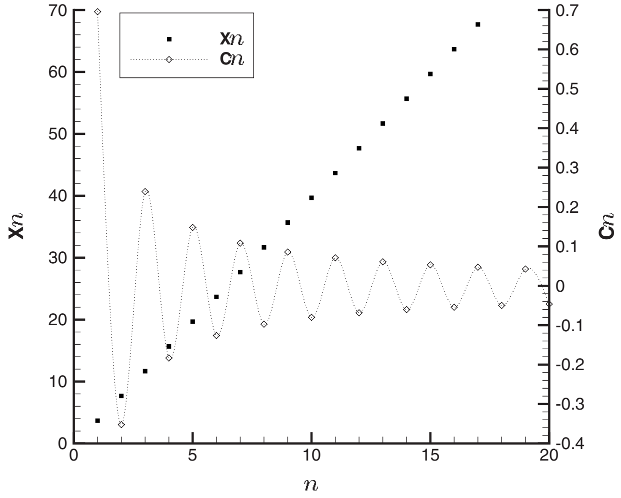

Fig. 2 X_n and C_n coefficients calculated for a 20 element truncature

$$\theta'=\frac{1}{\sqrt{\eta}}\sum_{n=1}^{\infty}C_nM_{X_n/4,1/4}(X_n\eta^2)e^{-X_n^2x_*} \tag{11}$$

where C_n is a constant gathering C_1 and C_2.

2.2 Constant Determination. Here, in contrast with classical problems (e.g., Bessel functions, found in most cylindrical problem) the Whittaker function does not admit, to the author's knowledge, orthogonal properties, which is a necessary condition to determine the constant C_n. This is the reason why it is so difficult to find complete analytical solution to such a problem. It is precisely the aim of the present work to propose an original semi-analytical approach, consisting in determining both X_n and C_n numerically. (Note that even if these coefficients are not obtained analytically, their values remain unchanged whatever the problem parameters are, owing to the dimensionless form of the equation.)

As a first step, the values of the roots of $M_{x_*/4,1/4}(x_*)$, i.e., X_n are calculated accurately with a very classical Newton-like algorithm (the first 20 roots are presented in Fig. 2).

Then we focus our attention on the determination of the C_n coefficients. Let us mention that the boundary condition $\theta'(x_*=0,\eta)=\eta$ imposes that

$$\sum_{n=1}^{\infty}C_nM_{X_n/4,1/4}(X_n\eta^2)=\eta^{3/2} \tag{12}$$

If we consider only a finite number of terms in Eq. (12) and if we define the scalar product $\langle f(\eta)|g(\eta)\rangle=\int_0^1f(\eta)g(\eta)d\eta$, then this equation may be written under the form

$$\mathbf{G}\cdot\mathbf{c}=\mathbf{y} \tag{13}$$

where **G** is a matrix, and **c** and **y** are vectors. The components of these elements are given by

$$G_{ij}=\langle M_{X_i/4,1/4}(X_i\eta^2)|M_{X_j/4,1/4}(X_j\eta^2)\rangle \tag{14}$$

$c(i)=C_i$ (i.e., the constant to be determined), and $y(i)=\langle\eta^{3/2}|M_{X_i/4,1/4}(X_i\eta^2)\rangle$.

It appears that the C_n constant can be found by solving a simple

Table 1 Values of the first 20 coefficients

n	X_n	C_n
1	3.6723	0.6957
2	7.6688	−0.3522
3	11.6679	0.2392
4	15.6675	−0.1832
5	19.6673	0.1481
6	23.6671	−0.1261
7	27.6671	0.1083
8	31.6670	−0.0973
9	35.6669	0.0857
10	39.6669	−0.0800
11	43.6669	0.0711
12	47.6669	−0.0685
13	51.6668	0.0609
14	55.6668	−0.0603
15	59.6668	0.0532
16	63.6668	−0.0543
17	67.6668	0.0473
18	71.6668	−0.0498
19	75.6668	0.0426
20	79.6668	−0.0463

linear system. Note that, in contrast to what happens when dealing with classical orthogonal functions, the value of the C_n coefficient is affected by the number of terms considered in Eq. (12), since $\mathbf{G}$ is not purely diagonal. So it has to be ensured that the values of C_n are not strongly modified by taking more elements in the sum. In this case, by truncating the sum to 50 or 100 elements, it is observed that the first coefficients (at least the first 20) remain almost identical. It will be shown later in this article, by comparing with the numerical results, that this number is sufficient to accurately represent the physics of the problem.

Furthermore, as presented in Fig. 2, it can be noticed that C_n is an alternated and decreasing to a null value sequence. If we refer to the classical Leibniz rule concerning such a series, the error committed by truncating the sequence, in our case, can be estimated by

$$|R_n| = \left| \sum_{k=n+1}^{\infty} C_k \right| \leq |C_{n+1}| \tag{15}$$

Note that the values of the coefficients are also given in Table 1 and in the Appendix for a restriction of 20 elements, in order to avoid any interested reader to reproduce such numerical computation.

In terms of variables θ, x_*, and y_*, Eq. (11) reads

$$\theta = y_* + \sum_{n=1}^{\infty} C_n \frac{M_{X_n/4,1/4}(X_n(1-y_*)^2)}{\sqrt{1-y_*}} e^{-X_n^2 x_*} \tag{16}$$

Under this form other results such as the local heat exchange with the heated plane can be readily extracted

$$\boldsymbol{\varphi} \cdot \boldsymbol{y} = \lambda \frac{T_{\text{wall}} - T_{\text{water}}}{\delta} \left(1 - \frac{1}{2} \sum_{n=1}^{\infty} C_n (3 + X_n) M_{X_n/4+1,1/4}(X_n) e^{-X_n^2 x_*} \right) \tag{17}$$

Figure 3 represents the dimensionless heat flux density $\varphi^* = \varphi\delta/(\lambda(T_{\text{wall}} - T_{\text{water}}))$ along the plate.

2.3 Comparison With a Full Numerical Solution. The solution given by Eq. (16) restricted to 20 elements is now compared with a full numerical solution of the same problem, that is, the heat equation in a falling film (using centered finite differences with second order discretization schemes). A linear temperature profile is assumed as the final boundary condition and a grid of 100 × 100 nodes is chosen.

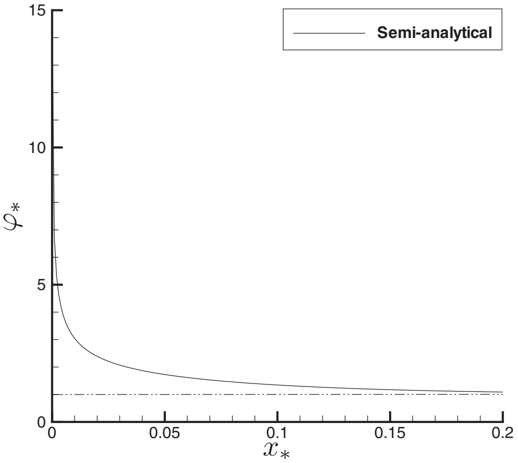

Fig. 3 Local dimensionless heat flux density φ_* versus x_*

Figure 4 depicts θ versus y_* for different fixed x_* ($x_*=0.02$, $x_*=0.05$, $x_*=0.10$, and $x_*=0.25$).

The adequation between the analytical and numerical models is nearly perfect. Indeed, the analytical results fit the numerical results and tend to a linear profile. These results prove that a restriction of the sum presented in Eq. (16) to 20 elements is enough to capture the essential physics of the thermal boundary layer almost everywhere, excepted when x_* tends to 0. This is a classical problem when one needs to approximate an analytical function by a truncated sum. Indeed, the more the function is used close to zero, the more coefficients are required to describe correctly the physics. In the case, for $x_*=0.02$, very small discrepancies can be observed between the semi-analytical and the numerical results.

3 Conclusion

This paper proposes an analytical solution of the heat equation for a water film flowing down a wall heated at a constant temperature, assuming that the flow is laminar and established. This solution had to be restricted to a finite number of elements to enable the calculation of the solution function. It proved though to give similar results as the numerical solution of the same problem. Since the coefficients only have to be computed once and for all, it provides a very fast way of finding a solution to such a problem. Moreover, this solution allows a better understanding of the weight of each parameter involved in the heat transfer, such as the

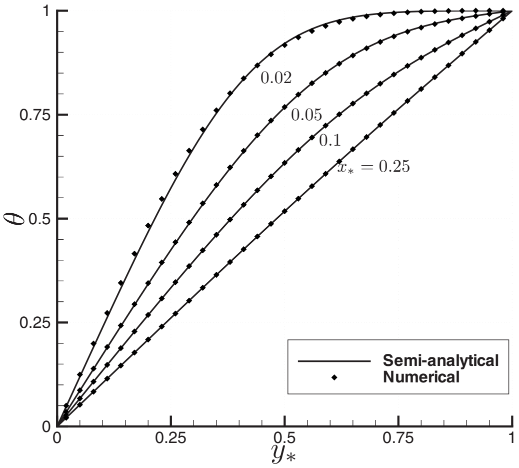

Fig. 4 θ versus y_* at $x_*=0.02$, $x_*=0.05$, $x_*=0.1$, and $x_*=0.25$

flow rate, the temperature, or the inclination of the wall. It can also be used in order to estimate the global or even local heat exchange between the heated plane and water.

Appendix

M is defined by

$$M_{\lambda,\mu}(z) = z^{\mu+1/2}e^{-z/2}\phi\left(\lambda - \mu + \frac{1}{2}, 2\mu + 1, z\right) \tag{18}$$

and W is defined by

$$W_{\lambda,\mu}(z) = \frac{\Gamma(-2\mu)}{\Gamma\left(\frac{1}{2} - \mu - \lambda\right)}M_{\lambda,\mu}(z) + \frac{\Gamma(2\mu)}{\Gamma\left(\frac{1}{2} + \mu - \lambda\right)}M_{\lambda,-\mu}(z) \tag{19}$$

where Γ is the gamma function and the confluent hypergeometric function ϕ is defined as

$$\phi(\alpha,\gamma,z) = 1 + \frac{\alpha}{\gamma}\frac{z}{1!} + \frac{\alpha(\alpha+1)}{\gamma(\gamma+1)}\frac{z^2}{2!} + \frac{\alpha(\alpha+1)(\alpha+2)}{\gamma(\gamma+1)(\gamma+2)}\frac{z^3}{3!} + \dots \tag{20}$$

References

[1] Nusselt, W., 1926, “Die Oberflächenkondensation des Wasserdampfes,” VDI Zeitschrift, **60**, pp. 541–546.

[2] Wu, C. W., and Lin, T., 2007, “Full-Scale Evaluations on Heat Resistance of Glass Panes Incorporated With Water Film or Sprinkler in a Room Fire,” Build. Environ., **42**(9), pp. 3277–3284.

[3] Ben Jabrallah, S., Belghith, A., and Corriou, J. P., 2002, “Study of Heat and Mass Transfer in a Rectangular Cavity: Application to a Distillation Cell,” Int. J. Heat Mass Transfer, **45**(4), pp. 891–904.

[4] Raach, H., and Mitrovic, J., 2005, “Seawater Falling Film Evaporation on Vertical Plates With Turbulence Wires,” Desalination, **183**(1–3), pp. 307–316.

[5] Cui, X.-Y., Shi, J.-Z., Tan, C., and Xu, Z.-P., 2009, “Investigation of Plate Falling Film Absorber With Film-Inverting Configuration,” ASME J. Heat Transfer, **131**(7), p. 072001.

[6] Killion, J. D., and Garimella, S., 2001, “A Critical Review of Models of Coupled Heat and Mass Transfer in Falling-Film Absorption,” Int. J. Refrig., **24**(8), pp. 755–797.

[7] Nakoryakov, V. E., and Grigor’eva, N. I., 1977, “Combined Heat and Mass Transfer During Absorption in Drops and Films,” J. Eng. Phys. Thermophys., **32**(3), pp. 243–247.

[8] Grossman, G., 1987, “Analysis of Interdiffusion in Film Absorption,” Int. J. Heat Mass Transfer, **30**(1), pp. 205–208.

[9] Conlisk, A. T., 1995, “Analytical Solutions for the Heat and Mass Transfer in a Falling Film Absorber,” Chem. Eng. Sci., **50**(4), pp. 651–660.

[10] Ren, C., 2006, “An Analytical Approach to the Heat and Mass Transfer Processes in Counterflow Cooling Towers,” ASME J. Heat Transfer, **128**(11), pp. 1142–1148.

[11] Gradshteyn, I. S., and Ryzhik, I. M., 2000, *Table of Integrals, Series, and Products*, 6th ed., Academic, New York.

Boundary-Condition-Independent Reduced-Order Modeling of Heat Transfer in Complex Objects by POD-Galerkin Methodology: 1D Case Study

Arun P. Raghupathy

Urmila Ghia

Karman Ghia

Computational Fluid Dynamics Research Laboratory,
University of Cincinnati,
Cincinnati, OH 45221-0072

William Maltz
Electronic Cooling Solutions, Inc.,
Mountain View, CA 94043

This technical note presents an introduction to boundary-condition-independent reduced-order modeling of complex electronic components using the proper orthogonal decomposition (POD)-Galerkin approach. The current work focuses on how the POD methodology can be used along with the finite volume method to generate reduced-order models that are independent of their boundary conditions. The proposed methodology is demonstrated for the transient 1D heat equation, and preliminary results are presented. [DOI: 10.1115/1.4000945]

1 Introduction

Practical applications of computational fluid dynamics (CFD) for heat transfer analysis often present situations where a complex 3D object may be used in several locations within a system. In each of those locations, the object may encounter different fluid flow situations and, consequently, have different boundary conditions. Such applications are seen frequently in the field of electronics cooling. If it is possible to deploy a model that offers reduction in the computational resources (reduced-order model) and can provide results in many different flow situations (boundary-condition-independent model), then such a model will accelerate the design and analysis of the end products that make use of these components. Various approaches [1–5] have been proposed to develop models for complex geometries with multiple heat sources. Application of proper orthogonal decomposition has been suggested by various authors [6–11] for the purpose of model reduction for complex electronic systems.

The "Method of Snapshots" introduced by Sirovich [9] is used to construct the original data set from which reduction is done. The POD basis in finite-dimensional Hilbert space can be obtained from the data by the following method. Let the snapshot matrix be defined as the solution matrix that contains temperatures at different spatial and temporal positions resulting from solving the 1D transient heat equation.

$$T_{\text{snap}} = \begin{bmatrix} T(1,\text{time\_initial}) & \dots & T(1,\text{No\_time\_steps}) \\ . & \dots & . \\ . & \dots & . \\ . & \dots & . \\ T(\text{No\_grid\_points},\text{time\_initial}) & \dots & T(\text{No\_grid\_points},\text{No\_time\_steps}) \end{bmatrix} \tag{1}$$

The covariance matrix C is now defined as

$$C = \frac{1}{N} T_{\text{snap}} T_{\text{snap}}^T \tag{2}$$

Here, N is the number of time steps.

Eigenvalue decomposition is done on the covariance matrix C.

$$\text{Eigenvalue decomposition:} C\phi_i = \lambda_i \phi_i \tag{3}$$

Eigenvalues and eigenvectors are obtained from eigenvalue decomposition mentioned in Eq. (3). In the current work, MATLAB is used for identifying all the eigenvectors and eigenvalues of the covariance matrix. The POD basis, Φ, is formed by arranging all the eigenvectors (ϕ_i) in a matrix. These eigenvectors correspond to the largest eigenvalues (λ_i) of the covariance matrix.

The reduced-order model is generated by Galerkin projection of the discrete form of the governing equations onto the POD eigenvector by representing the solution as

$$T(x,t) = \sum_{i=1}^{N} a_i(t)\phi_i(x) \tag{4}$$

where $a_i(t)$ are the POD coefficients defined by the inner product $(T(x,t),\phi_i)$ and ϕ_is are the orthonormal POD basis vectors. The reduced-order model determines the evolution of the POD coefficient and the evolution of the POD coefficients that govern the solution of the reduced-order model. The POD coefficients in the vector form are calculated by Eq. (5) obtained by using the orthonormal nature of the basis vectors from Eq. (4).

$$a(t) = \Phi^T T(x,t) \tag{5}$$

2 Boundary-Condition-Independent Reduced-Order Model

The important contribution of the current work is to show that a boundary-condition-independent reduced-order model can be obtained for an object using the POD-Galerkin methodology. It is possible to obtain a reduced-order model that is boundary condition independent by applying the principle of superposition of the solutions for each type of boundary condition for the heat equation. Since the transient equation captures a majority of the char-

---

Contributed by the Heat Transfer Division of ASME for publication in the JOURNAL OF HEAT TRANSFER. Manuscript received October 16, 2008; final manuscript received December 7, 2009; published online April 1, 2010. Assoc. Editor: Jayathi Murthy.

Table 1 Reduced-order model generating and validation cases

Case	Snapshot	Left	Right
1	1	Insulated	0
	2	Insulated	80
2	3	Insulated	Insulated
3	4	0	Insulated
	5	80	Insulated
4	Validation case	0	0
5	Validation case	−20	200

acteristics of the detailed geometry, transient solutions of different types of boundary conditions are added together to construct the snapshot matrix.

3 Finite-Volume Method for 1D Heat Equation and Order Reduction

The following problem, illustrated by Astrid [6], is used to demonstrate that a boundary-condition-independent reduced-order model can be generated by the POD-Galerkin approach. The governing heat equation is

$$\rho c_p \frac{\partial T}{\partial t} = k\frac{\partial^2 T}{\partial x^2} \tag{6}$$

The length of the 1D rod is 0.1 m. The rod is divided into 400 grid cells. Material properties include a thermal conductivity of $k=100\ \mathrm{W\ m^{-1}\ K^{-1}}$, and $\rho c_p = 10\times 10^6\ \mathrm{J/m^3\ K}$. The power dissipation of the point source is 1×10^{10} W. Heat conduction is simulated for a time period of 240 s by discretizing the time domain into 120 time steps ($\Delta t = 2$ s).

By re-arranging the coefficients of the temperature variable in the discretized form [8] of Eq. (6), and representing the resultant arrangement in a matrix-vector form, the following is obtained:

$$AT(t+\Delta t) = A^0T(t) + Bu(t) \tag{7}$$

where A, A^0, and B are the coefficient matrices.

In order to project this model into the POD subspace, we replace $T(t)=\Phi a(t)$. The Galerkin projection of the discrete form of the equations onto the POD basis Φ then yields

$$\Phi^T A \Phi a(t+\Delta t) = \Phi^T A^0 \Phi a(t) + \Phi^T Bu(t) \tag{8}$$

Equation (8) is the reduced-order model of the 1D heat equation discretized by the finite volume method. This methodology can be readily extended to 2D and 3D geometries as the only change will be in the formation of the coefficient matrices A and A^0. A tridiagonal coefficient A matrix is formed for the 1D case, pentadiagonal for the 2D case, and heptadiagonal for the 3D case. The A^0 matrix is adjusted for the inclusion of boundary conditions for each case. The methodology can be implemented in commercial CFD codes through macros or user-defined functions.

4 1D Heat Equation With Different Boundary Conditions

A heat source is attached to a single cell at the center of the rod. The goal is to identify a single set of POD basis needed to create a boundary-condition-independent reduced-order model for the 1D rod with heat generation. The initial condition is a constant temperature of 100°C. The POD basis is constructed by subjecting the rod to three types of boundary conditions as shown in Table 1. The fourth boundary condition is used for validating the boundary-condition-independent nature of the resulting reduced-order model. The methodology can also be extended to isoflux boundary conditions (by setting heat transfer coefficients on the surface of the package). The difference between isothermal and isoflux boundary conditions arise in the construction of the snapshot matrix. The time required to achieve steady state will be different for different isoflux boundary conditions.

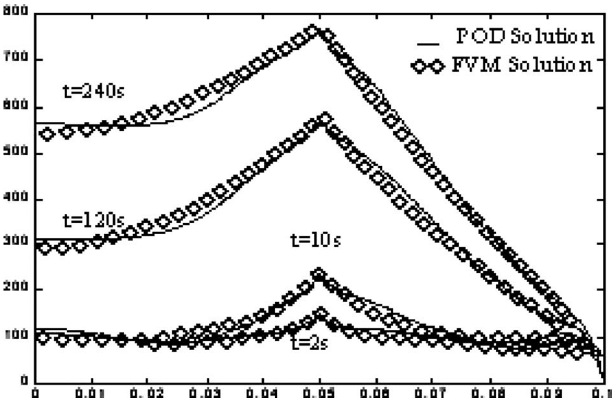

Fig. 1 POD and CFD solutions for a right side temperature of 60°C using six POD basis vectors from only 0°C solution

4.1 Case 1. Initially, the reduced-order model was constructed from six POD basis vectors corresponding to the solution with a boundary value of 0°C alone (snapshot 1 of case 1). This reduced-order model was used to simulate the heat transfer with the right side temperature at 60°C. Figure 1 shows the comparison of the CFD and the reduced-order solutions at $t=2$, 10, 120, and 240 s. The difference in the two solutions can be easily seen in this figure where the results from the reduced-order model do not capture the cooling curve accurately.

In order to overcome this limitation, six POD basis vectors were generated from the single snapshot matrix constructed from the solutions of two fixed temperature values (0°C and 80°C) on the right side, while the left side was insulated. The six POD basis vectors correspond to the first six eigenvalues. The energy contained in rest of the eigenvalues is of the order of 1×10^{-8}% when compared with the total energy. The resulting reduced-order model was employed to simulate the earlier case with a right side temperature of 60°C. Figure 2 shows good agreement with the CFD results at all time steps; the difference in temperature is less than 1°C for all time steps.

4.2 Case 2. From Table 1, case 2 is defined by having insulated boundary conditions on both sides. The reduced-order model is generated by six POD basis vectors obtained from the solution

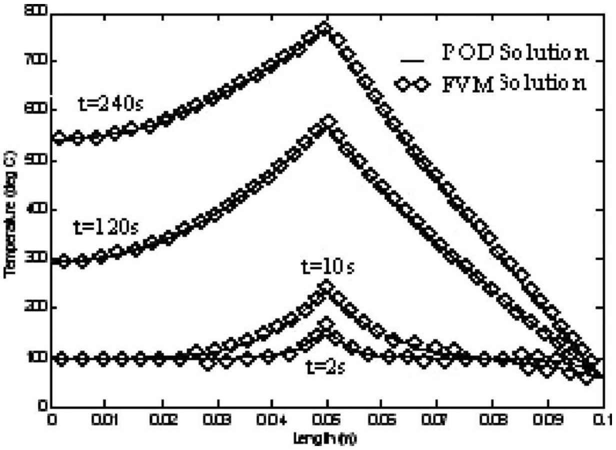

Fig. 2 POD and CFD solution for a right side temperature of 60°C using six POD basis vectors from both 0°C and 80°C solutions

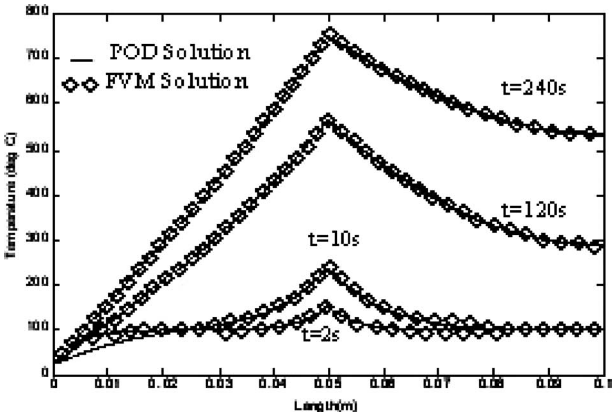

Fig. 3 CFD solution compared with six POD basis vectors for a left side temperature of 25°C

of case 2. A good agreement between the reduced-order model and the CFD solution was observed at all time steps. Using lesser number of POD basis vectors gave significant error.

4.3 Case 3. The first case, case 1, is repeated with the left side at a fixed temperature. Similar to case 1, two extreme boundary conditions (0°C and 80°C) are used for obtaining the CFD solution. The POD basis is constructed from the solution with both these boundary conditions. By using six POD basis vectors, the reduced-order model is used to obtain solution for a boundary condition (25°C) that lies within the two extremes. Figure 3 again shows good agreement between the CFD and reduced-order model solutions with the curves virtually coinciding with each other.

4.4 Case 4: Validation Within Generating Temperature Range. This case serves as the validation case, while cases 1–3 serve as the reduced-order model generation cases. For case 4, a set of POD basis vectors is generated from the snapshot matrix corresponding to the solutions of cases 1–3. The reduced-order model obtained with this POD basis is used for simulating the problem with both ends at a fixed temperature of 0°C. The number of POD basis vectors is increased until an accurate solution is achieved. A POD basis consisting of 12 vectors was found to provide an accurate solution, as seen in Fig. 4. The eigenvalue spectrum for case 4 is shown in Fig. 5. Similar to case 2, the energy contained in the leftout eigenvalues is of the order of $1 \times 10^{-8}\%$ of the total energy. Figure 5 shows deviation to be less than 0.5°C for each time step. Thus this resulting set of 12 POD basis vectors will serve to generate the boundary-condition-independent reduced-order model.

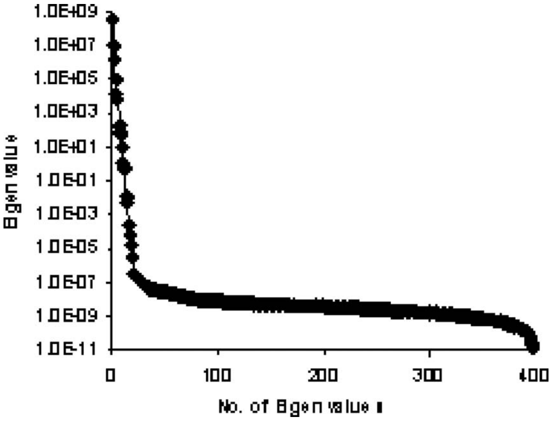

Fig. 4 Eigenvalue spectrum of case 4

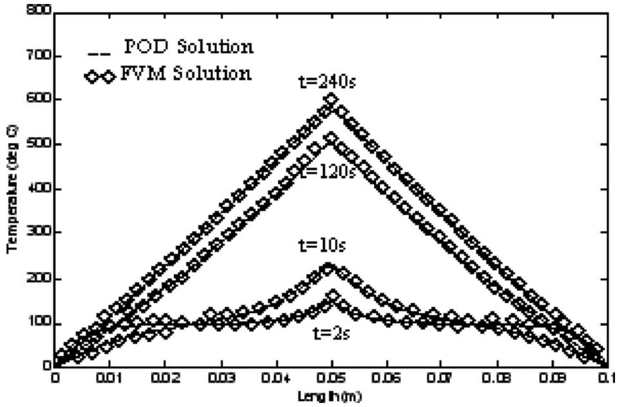

Fig. 5 CFD solution compared with 12 POD basis vectors for both ends at fixed

4.5 Case 5: Validation Outside of Generating Temperature Range. The usage of POD basis vectors in the reduced-order model maximizes capture of the system characteristics with the fewest number of terms. Such a model should be able to reproduce results for any type of boundary condition. This is verified with case 5, where the left end is maintained at −20°C and right end at 200°C. Both these temperatures are outside the range of the generating boundary conditions. The reduced-order model used in case 4, i.e., POD basis consisting of 12 vectors, is used to simulate case 5. Figure 6 shows the comparison of the CFD-generated solution with the solution generated by the reduced-order model. The reduced-order model provides accurate results, with less than 0.5°C deviation. This shows that a truly boundary-condition-independent reduced-order model can be obtained using the POD-Galerkin methodology.

5 Conclusion

A truly boundary-condition-independent reduced-order model is constructed for a rod with a single constant heat source at its center and asymmetric boundary conditions on its ends. The time-averaged error in all cases is less than 1°C. Also, a computation of 400 variables has been reduced to calculation of 12 variables. With the final set of five snapshots and 12 POD basis vectors,

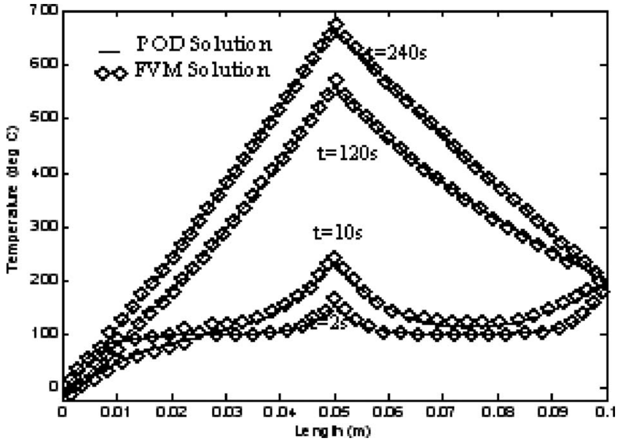

Fig. 6 CFD solution compared with 12 POD basis for left end at −20°C and right end at 200°C temperature of 0°C

conduction heat transfer in a rod with a single heat source can be simulated for any type of boundary condition on its extremities.

Acknowledgment

The authors acknowledge the support of Electronic Cooling Solutions, Inc., Mountain View, CA, for funding this research. Also, communication with Dr. Attila Aranyosi is gratefully acknowledged.

References

[1] Lasance, C., Vinke, H., Rosten, H., and Weiner, K. L., 1995, "A Novel Approach for the Thermal Characterization of Electronic Parts," *Proceedings of the SEMITHERM XI*, San Jose, CA, pp. 1–9.

[2] Sabry, M. N., 2007, "Flexible Profile Compact Thermal Models for Practical Geometries," ASME J. Electron. Packag., **129**, pp. 256–259.

[3] Codecasa, L., D'Amore, D., Maffezzoni, P., and Batty, W., 2002, "Multi-Point Moment Matching Reduction of Distributed Thermal Networks," Eighth International Workshop on Thermal Investigation of ICs and Systems, THERMINIC, Madrid, Spain, pp. 231–234.

[4] Augustin, A., Hauck, T., Maj, B., Czernohorsky, J., Rudnyi, E.-B., and Korvink, J.-G., 2006, "Model Reduction for Power Electronics Systems With Multiple Heat Sources," *Proceedings of 12th International Workshop on Thermal investigations of ICs, THERMINIC*, p. 113–117.

[5] Shapiro, B., 2003, "Creating Compact Models of Complex Electronic Systems: An Overview and Suggested Use of Existing Model Reduction and Experimental System Identification Tools," IEEE Trans. Compon. Packag. Technol., **26**(1), pp. 165–172.

[6] Astrid, P., Huisman, L., Weiland, S., and Backx, A. C. P. M., 2002, "Reduction and Predictive Control Design for a Computational Fluid Dynamics Model," *Proceedings of the 41st IEEE Conference on Decision and Control*, Vol. 3, pp. 3378–3383.

[7] Ghia, U., Shirooni, S., Ghia, K., and Osswald, G., 1991, "Examination of a Vortex-Ring Interaction Phenomenon in an Axisymmetric Flow," AIAA Paper No. AIAA-1991–548.

[8] Versteeg, H. K., and Malalasekera, W. K., 1995, *An Introduction to Computational Fluid Dynamics, The Finite Volume Method*, Pearson Prentice-Hall, Essex.

[9] Sirovich, L., 1987, "Turbulence and Dynamics of Coherent Structures, Part I: Coherent Structures," Q. Appl. Math., **XLV**, pp. 561–571.

[10] Kunisch, K., and Volkwein, S., 2002, "Galerkin Proper Orthogonal Decomposition Methods for a General Equation in Fluid Dynamics," SIAM (Soc. Ind. Appl. Math.) J. Numer. Anal., **40**, pp. 492–515.

[11] Christensen, E. A., Brons, M., and Sorensen, J. N., 1999, "Evaluation of Proper Orthogonal Decomposition-Based Techniques Applied to Parameter Dependent Nonturbulent Flows," SIAM J. Sci. Comput. (USA), **21**(4), pp. 1419–1434.

Combined Effects of Joule Heating and Viscous Dissipation on Magnetohydrodynamic Flow Past a Permeable, Stretching Surface With Free Convection and Radiative Heat Transfer

Chien-Hsin Chen
Professor
Department of Mechanical Design Engineering,
National Formosa University,
Huwei, Yunlin 632, Taiwan
e-mail: chchen@nfu.edu.tw

The combined effects of Joule heating and viscous dissipation on the momentum and thermal transport are studied for the Magnetohydrodynamic (MHD) flow over a stretching sheet. Effects of free convection, thermal radiation, and surface suction/blowing on the flow and heat transfer characteristics are also examined. Results demonstrate that the reduction in heat transfer due to Joule and viscous heating is more pronounced at a higher Prandtl number. The Eckert number changes appreciably the velocity profile as the buoyancy effect becomes significant, while the Eckert number has an unimpressive effect on the velocity when the free convection is week. Increasing the radiation parameter will increase the temperature profile noticeably, and thus reduce the heat transfer rate accordingly. The heat transfer is enhanced markedly by imposing surface fluid suction, while the opposite trend is observed for blowing. [DOI: 10.1115/1.4000946]

Keywords: MHD flow, Joule and viscous heating, stretching surface, free convection, thermal radiation, suction/blowing

1 Introduction

The study of fluid flow and heat transfer over a continuously moving surface has received, through the years, an increasing attention due to its wide-ranging applications in many engineering processes, such as polymer industry, crystal growing, stretching of plastic films, and manufacturing of foods and paper. Since the pioneering work of Sakiadis [1], who investigated the boundary layer flow over a continuous surface moving with constant speed, various flow and thermal aspects of the problem were recently extended in different ways for forced convection (e.g., Refs. [2–4]). In the presence of gravitational force, the density gradient is induced in the fluid medium by the temperature difference; therefore, the free convection effect might alter the heat transfer behavior. As indicated by Karwe and Jaluria [5], the thermal buoyancy effects are more pronounced when the surface moves vertically. Chen [6,7] studied the thermal transport of mixed convection flow over vertical and inclined stretching surfaces. It is well known that the properties of the final product greatly depend on the rate of cooling during manufacturing processes. The cooling rate can be controlled by drawing such strips in an electrically conducting fluid subject to a magnetic field, so as to obtain the final products of the desired characteristics [8]. A number of investigations on the MHD heat transfer for different fluids past stretching surfaces were performed by many authors; for example, Ishak et al. [9] and Pantokratoras [10] for Newtonian fluids, Chen [11] for power-law fluids, Misra et al. [12] for viscoelastic fluids, and Rahman and Sattar [13] for micropolar fluids. In general, the magnetic field is found to increase the temperature profile, but decrease the velocity profile, and thus, it induces a rise in the skin friction coefficient, but a reduction in the rate of heat transfer from the surface. Thermal radiation is another dimension to the problem of boundary layer flow over a stretching sheet. In the absence of the magnetic field, Seddeek and Abdelmeguid [14] explored the effect of thermal radiation on the heat transfer from a stretching sheet with variable heat flux. Abel et al. [15] examined the effect of thermal radiation on viscoelastic MHD flows over a stretching surface embedded in a porous medium. However, the combined effects of Joule heating and viscous dissipation are ignored in the abovementioned studies. As indicated by Chen [16], Joule heating and viscous dissipation may play an important role in the thermal transport of a fluid past a heated surface when a magnetic field is present. Therefore, the object of this paper is to investigate the combined effects of Joule heating and viscous dissipation on the heat transfer characteristics of MHD mixed convection flows over a stretching surface.

2 Mathematical Formulation

Consider a mixed convection flow of an electrically conducting fluid above a stretching sheet that is inclined from the vertical with an acute angle γ (measured in the clockwise direction) and situated in an otherwise quiescent ambient fluid at temperature T_∞. The positive x coordinate is measured along the direction of the moving sheet with the slot as the origin, and the positive y coordinate is measured normal to the sheet in the outward direction toward the fluid. A transverse magnetic field of constant strength B_0 is applied normally to the sheet, which produces a magnetic effect in the x direction. With the usual boundary layer and Boussinesq approximations, the governing equations in the usual notation are

$$\frac{\partial u}{\partial x}+\frac{\partial v}{\partial y}=0 \tag{1}$$

$$u\frac{\partial u}{\partial x}+v\frac{\partial u}{\partial y}=g\beta(T-T_\infty)\cos\gamma+\nu\frac{\partial^2 u}{\partial y^2}-\frac{\sigma B_0^2 u}{\rho} \tag{2}$$

$$u\frac{\partial T}{\partial x}+v\frac{\partial T}{\partial y}=\frac{k}{\rho c_p}\frac{\partial^2 T}{\partial y^2}+\frac{\sigma B_0^2}{\rho c_p}u^2+\frac{\nu}{c_p}\left(\frac{\partial u}{\partial y}\right)^2+\frac{16\sigma_1 T_\infty^3}{3\rho c_p \alpha_R}\frac{\partial^2 T}{\partial y^2} \tag{3}$$

where σ_1 is the Stefan–Boltzmann constant and α_R is the Rosseland mean absorption coefficient. The last term in Eq. (2) characterizes the Lorentz force. The last three terms in Eq. (3) indicate the effects of Joule heating, viscous dissipation, and thermal radiation, respectively. The boundary conditions are

$$\begin{gathered} u_w(x)=Cx, \quad v=v_w, \quad T_w(x)-T_\infty=A\left(\frac{x}{L}\right)^l \quad \text{at } y=0 \\ u\to 0, \quad T\to T_\infty \quad \text{as} \quad y\to\infty \end{gathered} \tag{4}$$

To proceed with the analysis, we introduce the following dimensionless variables

$$\begin{gathered} \xi=\frac{\mathrm{Gr}_x\cos\gamma}{\mathrm{Re}_x^2}, \quad \eta=\frac{x}{y}\mathrm{Re}_x^{1/2}, \quad f(\xi,\eta)=\frac{\psi(x,y)}{\nu\ \mathrm{Re}_x^{1/2}}, \\ \theta(\xi,\eta)=\frac{T(x,y)-T_\infty}{T_w(x)-T_\infty} \end{gathered} \tag{5}$$

where $\psi(x,y)$ is the stream function, $\mathrm{Gr}_x=g\beta(T_w-T_\infty)x^3/\nu^2$ is the local Grashof number, and $\mathrm{Re}_x=u_w x/\nu$ is the local Reynolds number. Using the new variables in Eq. (5), the dimensionless governing equations and boundary conditions become

---

Contributed by the Heat Transfer Division of ASME for publication in the JOURNAL OF HEAT TRANSFER. Manuscript received November 10, 2008; final manuscript received December 6, 2009; published online April 1, 2010. Assoc. Editor: Ben Q. Li.

Table 1 Results of $-\theta'(0)$ for various values of Pr, M, and Ec$(l=2,\ \xi=0,\ R=0,\ f_w=0)$

			$-\theta'(0)$		
Pr	M	Ec	No Joule and viscous heating (Ec=0)	No Joule heating with viscous dissipation	With Joule heating with viscous dissipation
1	1	0	1.215774		
		0.05		1.188896	1.175457
		0.1		1.162018	1.135141
	2	0	1.126901		
		0.05		1.091843	1.068471
		0.1		1.056785	1.010041
10	1	0	4.690210		
		0.05		4.535061	4.457487
		0.1		4.379912	4.224764
	2	0	4.606911		
		0.05		4.392634	4.249783
		0.1		4.178357	3.892654
100	1	0	15.609144		
		0.05		14.943482	14.610650
		0.1		14.277819	13.612157
	2	0	15.529686		
		0.05		14.567006	13.925219
		0.1		13.604325	12.320751

$$f''' + ff'' - (f')^2 - Mf' + \xi\theta = (l-1)\xi\left(f'\frac{\partial f'}{\partial \xi} - f''\frac{\partial f}{\partial \xi}\right) \qquad (6)$$

$$\frac{1}{\Pr}(1+R)\theta'' + f\theta' - lf'\theta + \mathrm{Ec}[(f'')^2 + M(f')^2] = (l-1)\xi\left(f'\frac{\partial \theta}{\partial \xi} - \theta'\frac{\partial f}{\partial \xi}\right) \qquad (7)$$

$$f'(\xi,0) = 1, \quad f(\xi,0) = f_w - (l-1)\xi\frac{\partial f}{\partial \xi}(\xi,0), \quad \theta(\xi,0) = 1$$

$$f'(\xi,\infty) = 0, \quad \theta(\xi,\infty) = 0 \qquad (8)$$

where the primes stand for partial differentiation with respect to η. The dimensionless variables M, Pr, Ec, R, and f_w, appearing in the above equations, represent, respectively, the magnetic field parameter, Prandtl number, Eckert number, thermal radiation parameter, and the suction/blowing parameter. They are given by

$$M = \frac{\sigma B_0^2}{\rho C}, \quad \Pr = \frac{\mu c_p}{k}, \quad R = \frac{16\sigma_1 T_\infty^3}{3\alpha_R k}, \quad \mathrm{Ec} = \frac{u_w^2}{c_p(T_w - T_\infty)}, \qquad (9)$$

$$f_w = -\frac{v_w}{\sqrt{\nu C}}$$

It is noted that a positive f_w is for suction, but a negative f_w is for blowing. If the Joule heating and viscous dissipation are included in the analysis, it requires that $l=2$, so as to hold the Eckert number independent of x, i.e., the surface temperature is given by $T_w - T_\infty = Ax^2$ and the Eckert number becomes $\mathrm{Ec} = C^2L^2/c_pA$. It is interesting to note that a closed form solution exists for the flow field of pure forced convection $(\xi=0)$. In this case, the hydrodynamic problem is uncoupled from the thermal problem, and f satisfies

$$f''' + ff'' - (f')^2 - Mf' = 0 \qquad (10)$$

$$f(0) = f_w, \quad f'(0) = 1, \quad f'(\infty) = 0 \qquad (11)$$

An analytical solution is found to be

$$f(\eta) = f_w + \frac{1}{z}(1 - e^{-z\eta}) \qquad (12)$$

where $z = [f_w + \sqrt{f_w^2 + 4(1+M)}]/2$. Hence, the flow parameter $f''(0)$ is obtained as

$$f''(0) = -\frac{f_w + \sqrt{f_w^2 + 4(1+M)}}{2} \qquad (13)$$

The local skin friction coefficient and the local Nusselt number are defined, respectively, as

$$C_f = \frac{\tau_w}{\rho u_w^2/2}, \quad \mathrm{Nu}_x = \frac{hx}{k} = \frac{xq_w}{k(T_w - T_\infty)} \qquad (14)$$

where $\tau_w = \mu(\partial u/\partial y)_{y=0}$ is the wall shear stress and $q_w = -k(\partial T/\partial y)_{y=0}$ is the surface heat flux. In terms of the new variables (Eq. (5)), we have

$$C_f\ \mathrm{Re}_x^{1/2} = 2f''(\xi,0) \qquad (15)$$

$$\mathrm{Nu}_x\ \mathrm{Re}_x^{-1/2} = -\theta'(\xi,0) \qquad (16)$$

3 Results and Discussion

The present problem is solved numerically by the Keller–Box method [17]. To validate the accuracy of the present results, the results for $-\theta'(0)$ without Joule and viscous heating were compared with those of Grubka and Bobba [2] and Ishak et al. [9] for different values of l and Pr. Excellent agreements were found among these three sets. The effects of viscous dissipation and Joule heating are characterized, respectively, by the Eckert number Ec and the product Ec M. As mentioned previously, when the effects of Joule heating and viscous dissipation are considered, Ec is independent of x, only if $l=2$. We inspect these effects on the heat transfer rate by comparing the corresponding values of $-\theta'(0)$ for $l=2$ and $\xi=0$, as shown in Table 1. As compared with the case of Ec=0 (no Joule and viscous heating), the value of $-\theta'(0)$ decreases when the viscous dissipation is considered. The reduction in $-\theta'(0)$ due to viscous dissipation is amplified as Ec increases. When both the Joule heating and viscous dissipation are included, a further decrease in $-\theta'(0)$ is observed.

Variations of the local Nusselt number, in terms of $-\theta'(\xi,0)$, with the buoyancy parameter ξ, are displayed in Fig. 1(*a*) for

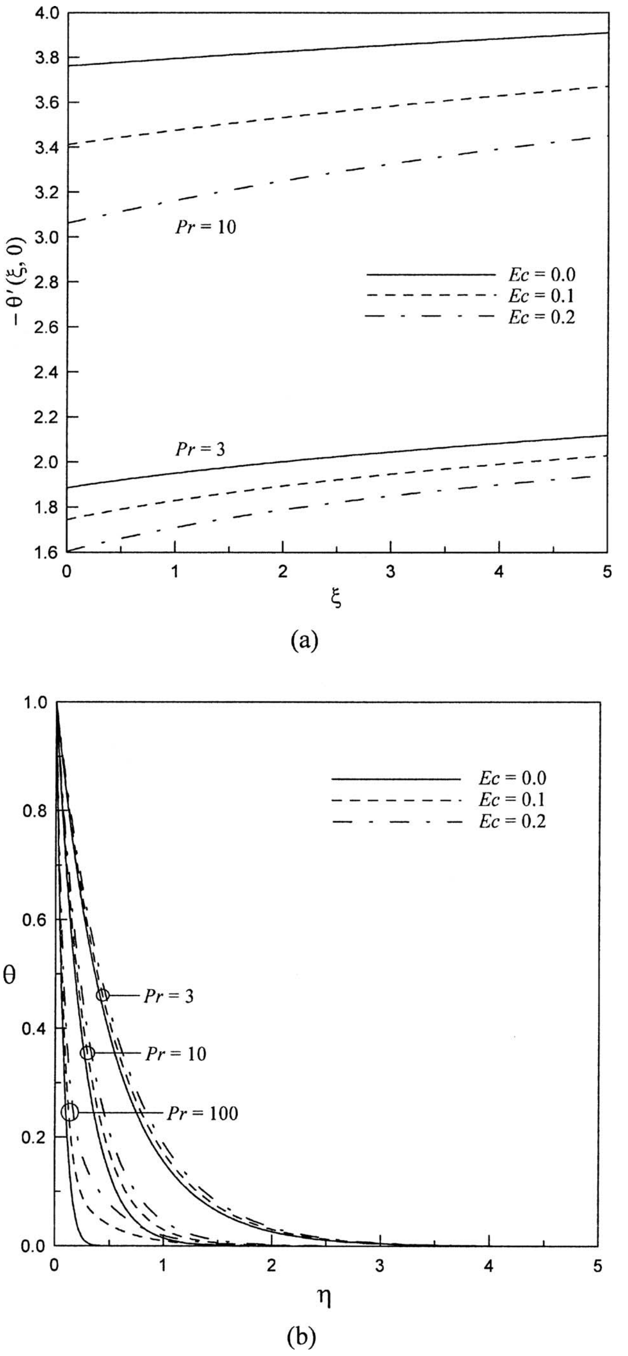

Fig. 1 Combined effects of Joule and viscous heating on (*a*) variations of $-\theta'(\xi,0)$ with ξ and (*b*) the temperature profiles at $\xi=1$ for various values of Ec and Pr($I=2$, $M=1$, $R=0.5$, $f_w=0$)

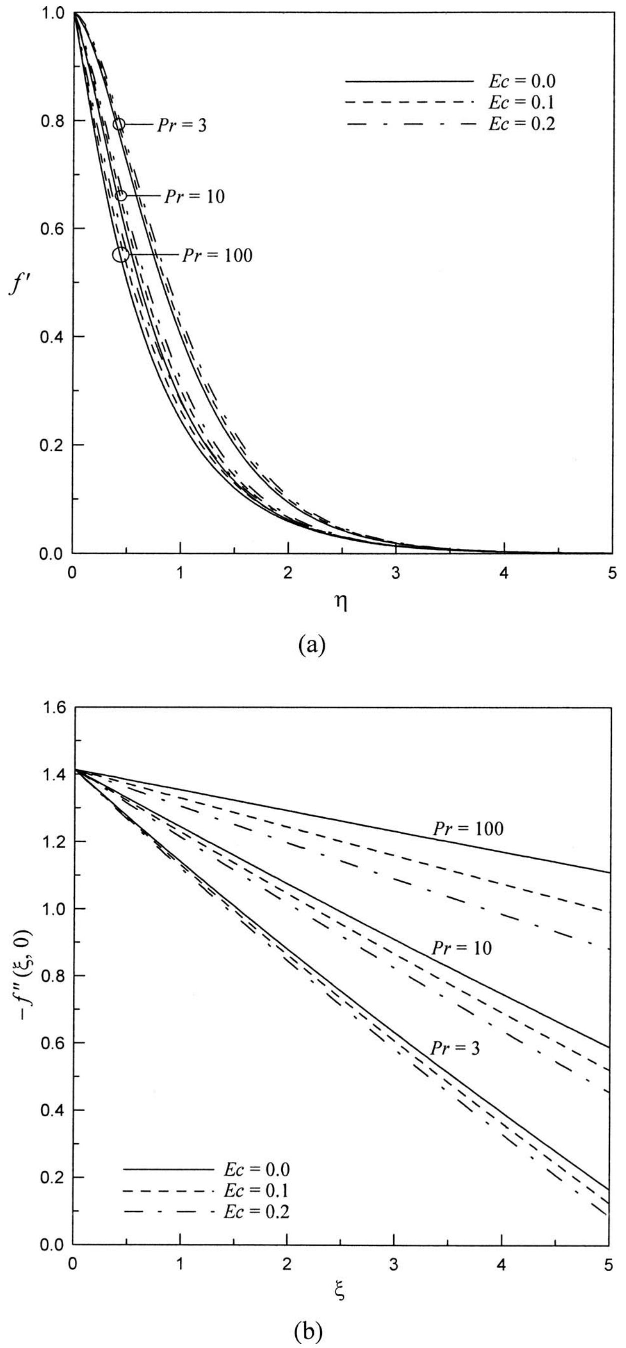

Fig. 2 Combined effects of Joule and viscous heating on (*a*) velocity profiles at $\xi=5$ and (*b*) variations of $-f''(\xi,0)$ with ξ for various values of Ec and Pr($I=2$, $M=1$, $R=0.5$, $f_w=0$)

various values of Ec and Pr. The decrease in the local Nusselt number due to the combined effects of Joule heating and viscous dissipation is seen to be more pronounced at a higher value of Pr. Also, the Nusselt number increases with increasing Pr and ξ, as expected. The temperature profiles shown in Fig. 1(*b*) reveal that increasing Ec will increase the temperature, associated with an increase in the thermal boundary layer thickness, and thus decrease the wall temperature gradient. The effect of Joule and viscous heating on the temperature profile is found to be more prominent as Pr becomes larger. The present calculation shows that the change in the fluid velocity, due to Ec, is not impressive for small ξ (say, $\xi<1$), while appreciable effects of Ec on the velocity are observed for higher values of ξ. The effect of Ec on the velocity profile is shown in Fig. 2(*a*) for $\xi=5$ and for different values of Pr. The inclusion of Joule heating and viscous dissipation is found to increase the fluid velocity. Figure 2(*b*) reveals obviously the reduction in the flow parameter $-f''(\xi,0)$ due to the combined effects of Joule and viscous heating. This outcome is consistent with the velocity behavior close to the wall, as shown in Fig. 2(*a*), where the wall velocity gradient decreases with increasing Ec. In addition, the effect of Ec on $-f''(\xi,0)$ is more noticeable at larger values of Pr and ξ. For the case of pure forced convection flow ($\xi=0$) over an impermeable surface ($f_w=0$), it is interesting to

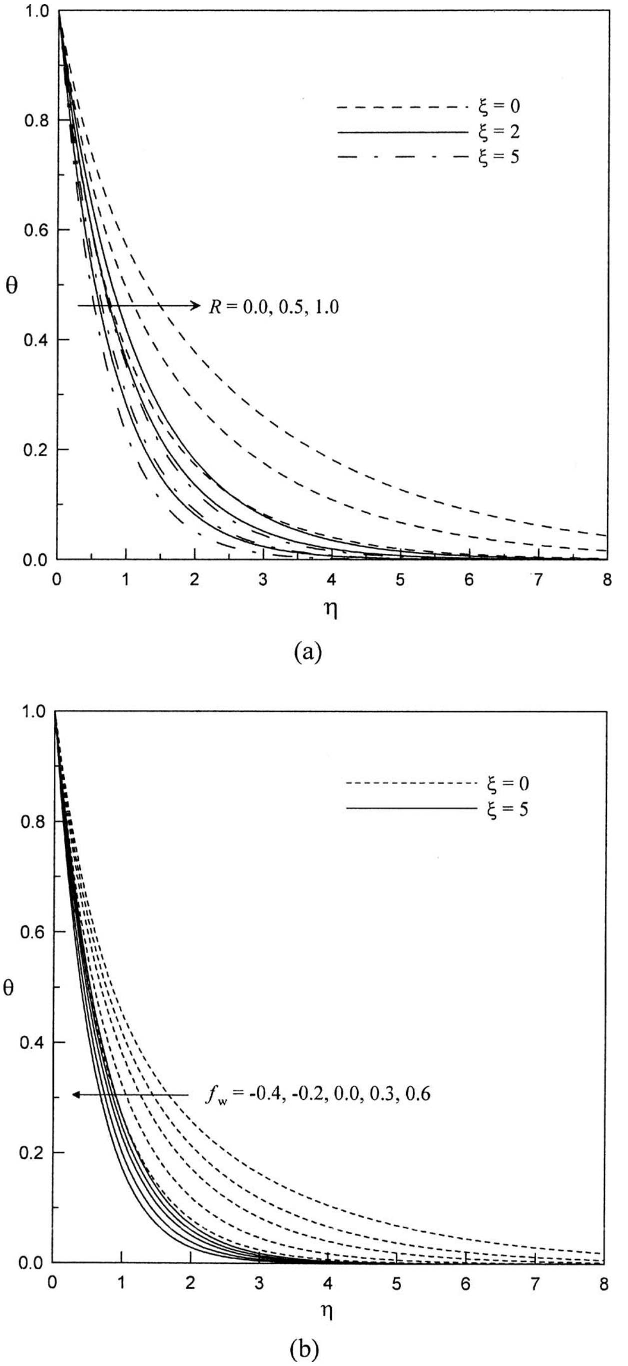

Fig. 3 Influence of (*a*) thermal radiation parameter and (*b*) suction/injection parameter, on the temperature profiles for Pr =1, *l*=2, *M*=1, and Ec=0.1

Table 2 Values of $-f''(\xi,0)$ and $-\theta'(\xi,0)$ for various values of Pr, ξ, R, and f_w ($l=2$, $M=1$, Ec=0.1)

Pr	ξ	R	f_w	$-f''(\xi,0)$	$-\theta'(\xi,0)$
1	0	0	−0.2	1.317745	1.049327
			0.0	1.414214	1.135141
			0.4	1.628286	1.335565
		1	−0.2	1.317745	0.663606
			0.0	1.414214	0.701768
			0.4	1.628286	0.791864
	2	0	−0.2	0.650970	1.230746
			0.0	0.741833	1.315949
			0.4	0.953562	1.506205
		1	−0.2	0.553412	0.873902
			0.0	0.627343	0.914113
			0.4	0.800746	1.000909
10	0	0	−0.2	1.317745	3.333003
			0.0	1.414214	4.224764
			0.4	1.628286	6.600921
		1	−0.2	1.317745	2.464813
			0.0	1.414214	2.923121
			0.4	1.628286	4.068494
	2	0	−0.2	0.952601	3.464466
			0.0	1.093021	4.342441
			0.4	1.383162	6.681909
		1	−0.2	0.876266	2.598970
			0.0	1.005042	3.047392
			0.4	1.283888	4.163782

note that the dimensionless skin friction coefficient can be determined from Eq. (13) to be $-f''(0)=1.41421$, regardless of the values of Pr and Ec.

Typical temperature profiles at selected values of R and f_w are shown in Figs. 3(*a*) and 3(*b*), respectively. It is evident that increasing R will produce an appreciable increase in the temperature distribution. Also, imposing the wall suction ($f_w>0$) will cause the reduction in the thermal boundary layer thickness, which in turn decreases the temperature distributions. However, the behavior is reversed when blowing is imposed on the surface. Some values of $-f''(\xi,0)$ and $-\theta'(\xi,0)$ are listed Table 2 for different values of Pr, ξ, R, and f_w. It can be concluded from this table that the Nusselt number increases with increasing Pr, ξ, and f_w; while it decreases with increasing R. The changes in Pr and R do not alter the skin friction coefficient for forced convection, since the thermal flow is uncoupled in this case. For mixed convection, the skin friction coefficient can be increased, either by increasing Pr or by decreasing R. The effect of increasing f_w is to increase the skin friction coefficient for both forced and mixed convections.

4 Conclusions

In this paper we study the combined effects of Joule heating and viscous dissipation on the momentum and thermal transport characteristics for MHD mixed convection flow over a stretching surface. It is found that Joule heating and viscous dissipation have the effect to increase the fluid velocity, and accordingly decrease the skin friction coefficient. Also, increasing the Eckert number tends to increase the fluid temperature, and consequently to decrease the heat transfer rate from the surface, particularly for a fluid having a higher Prandtl number. Free convection has the effect to reduce the temperature distribution, and thus enhance the heat transfer, whereas thermal radiation shows the opposite effect. Moreover, the local Nusselt number increases by the imposition of fluid suction at the wall, while the opposite trend is true for surface fluid blowing.

Acknowledgment

This work was partially supported by the National Science Council of Taiwan through Grant Nos. NSC 97-2221-E-150-078 and NSC 98-2221-E-150-053.

Nomenclature

B_0 = magnetic field strength
C_f = local skin friction coefficient
Ec = Eckert number
f = dimensionless stream function
f_w = suction/blowing parameter
l = surface temperature exponent
M = magnetic field parameter
Nu_x = local Nusselt number
Pr = Prandtl number

R = thermal radiation parameter
Re_x = local Reynolds number
T = temperature
u,v = fluid velocity components in x and y directions
x,y = streamwise and cross-stream coordinates

Greek Symbols

β = coefficient of thermal expansion
γ = angle on inclination from vertical
η = pseudo-similarity variable
θ = dimensionless temperature
ξ = buoyancy force parameter
σ = electrical conductivity
ψ = stream function

Subscripts

w = wall
∞ = ambient condition

References

[1] Sakiadis, B. C., 1961, “Boundary-Layer Behavior on Continuous Solid Surfaces,” AIChE J., **7**, pp. 26–28.
[2] Grubka, L. J., and Bobba, K. M., 1985, “Heat Transfer Characteristics of a Continuous Stretching Surface With Variable Temperature,” ASME J. Heat Transfer, **107**, pp. 248–250.
[3] Kiwan, S., and Al-Nimr, M. A., 2009, “Flow and Heat Transfer Over a Stretched Microsurface,” ASME J. Heat Transfer, **131**, p. 061703.
[4] Tzirtzilakis, E. E., and Kafoussias, N. G., 2010, “Three-Dimensional Magnetic Fluid Boundary Layer Flow Over a Linearly Stretching Sheet,” ASME J. Heat Transfer, **132**, p. 011702.
[5] Karwe, M. V., and Jaluria, Y., 1988, “Fluid Flow and Mixed Convection Transport From a Moving Plate in Rolling and Extrusion Processes,” ASME J. Heat Transfer, **110**, pp. 655–661.
[6] Chen, C.-H., 1998, “Laminar Mixed Convection Adjacent to Vertical, Continuously Stretching Sheets,” Heat Mass Transfer, **33**, pp. 471–476.
[7] Chen, C.-H., 2000, “Mixed Convection Cooling of a Heated, Continuously Stretching Surface,” Heat Mass Transfer, **36**, pp. 79–86.
[8] Vajravelu, K., and Hadjinicolaou, A., 1997, “Convective Heat Transfer in an Electrically Conducting Fluid at a Stretching Surface With Uniform Free Stream,” Int. J. Eng. Sci., **35**, pp. 1237–1244.
[9] Ishak, A., Nazar, R., and Pop, I., 2008, “Hydromagnetic Flow and Heat Transfer Adjacent to a Stretching Vertical Sheet,” Heat Mass Transfer, **44**, pp. 921–927.
[10] Pantokratoras, A., 2008, “Study of MHD Boundary Layer Flow Over a Heated Stretching Sheet With Variable Viscosity: A Numerical Reinvestigation,” Int. J. Heat Mass Transfer, **51**, pp. 104–110.
[11] Chen, C.-H., 2008, “Effects of Magnetic Field and Suction/Injection on Convection Heat Transfer of Non-Newtonian Power-Law Fluids Past a Power-Law Stretched Sheet With Surface Heat Flux,” Int. J. Therm. Sci., **47**, pp. 954–961.
[12] Misra, J. C., Shit, G. C., and Rath, H. J., 2008, “Flow and Heat Transfer of a MHD Viscoelastic Fluid in a Channel With Stretching Walls: Some Applications to Haemodynamics,” Comput. Fluids, **37**, pp. 1–11.
[13] Rahman, M. M., and Sattar, M. A., 2006, “Magnetohydrodynamic Convective Flow of a Micropolar Fluid Past a Continuously Moving Vertical Porous Plate in the Presence of Heat Generation/Absorption,” ASME J. Heat Transfer, **128**, pp. 142–152.
[14] Seddeek, M. A., and Abdelmeguid, M. S., 2006, “Effects of Radiation and Thermal Diffusivity on the Heat Transfer Over a Stretching Surface With Variable Heat Flux,” Phys. Lett. A, **348**, pp. 172–179.
[15] Abel, S., Prasad, K. V., and Mahaboob, A., 2005, “Buoyancy Force and Thermal Radiation Effects in MHD Boundary Layer Visco-Elastic Fluid Flow Over Continuously Moving Stretching Surface,” Int. J. Therm. Sci., **44**, pp. 465–476.
[16] Chen, C.-H., 2004, “Combined Heat and Mass Transfer in MHD Free Convection From a Vertical Surface With Ohmic Heating and Viscous Dissipation,” Int. J. Eng. Sci., **42**, pp. 699–713.
[17] Cebeci, T., and Bradshaw, P., 1984, *Physical and Computational Aspects of Convective Heat Transfer*, Springer, New York.